IMMOBILISATION OF BIOMOLECULES ON PLASMA-TREATED ULTRA-HIGH-MOLECULAR-WEIGHT POLYETHYLENE

by

MARC BRUGGEMAN



A thesis submitted to the

UNIVERSITY OF BIRMINGHAM

for the degree of

DOCTOR OF PHILOSOPHY

School of Metallurgy and Materials

College of Engineering and Physical Sciences

University of Birmingham

February 2023

UNIVERSITY OF
BIRMINGHAM

University of Birmingham Research Archive

e-theses repository

This unpublished thesis/dissertation is copyright of the author and/or third parties. The intellectual property rights of the author or third parties in respect of this work are as defined by The Copyright Designs and Patents Act 1988 or as modified by any successor legislation.

Any use made of information contained in this thesis/dissertation must be in accordance with that legislation and must be properly acknowledged. Further distribution or reproduction in any format is prohibited without the permission of the copyright holder.

Abstract

Total joint replacements play a vital role in enhancing the quality of life for individuals affected by joint diseases and injuries, a total of 190,223 total joint procedures were performed in the United Kingdom in 2021 alone. In the context of total joint replacements, ultra-high-molecular-weight polyethylene is the primary polymer of choice as the bearing material (i.e., the cup/liners that act as the interface between the implanted artificial joints and corresponding joint sockets) due to its low frictional coefficient, high strength, and bio-inert nature, it was used in at least 93.3% of all hip replacements in 2021. However, surface oxidation and subsequent accelerated debris generation at the polymeric cup insert is a frequent cause of implant rejection as it results in chronic inflammation and joint loosening. To address this, antioxidants like α-tocopherol are embedded into the polymer matrix, as was done in this work.

Next to implant failure due to wear and/or debris, bacterial adhesion and colonization resulting in biofilm formation are responsible for about 20% of biomaterial-associated infections and malfunctions. Fortunately, many of the currently used biomaterials are amenable to modification, allowing the incorporation of antimicrobial agents in/on the surface to combat inflammation and reduce the risk of infection. As polyethylene is chemically-inert, surface modification was required to allow further modification. Due to its non-toxic nature, plasma-nitriding has received increased industrial attention for metals since its initial introduction. To treat non-conductive materials such as polyethylene, the use of an active screen was required to serve as the cathode and allow the formation of plasma near the material surface.

Prior to this work, no research had been conducted on the active screen plasma-nitriding of α-tocopherol-doped ultra-high-molecular-weight polyethylene. The effect of α-tocopherol doping in combination with active screen plasma-nitriding on the ultra-high-molecular-weight polyethylene was investigated using a wide variety of characterisation techniques (e.g., FTIR, Raman, XPS, WXRD, SEM, etc.), to reveal the changes in both chemical and physical material

properties. Amongst others, it was discovered that active screen plasma-nitriding introduced a mixture of polyene, amorphous carbon, and aromatics on the polyethylene-based material surfaces, which drastically increased the surface microhardness. The incorporation of α-tocopherol also resulted in an increased nitrogen presence after active screen plasma-nitriding, reduced surface oxidation, and prevented surface contamination and delamination.

In general, implant-associated infections have been treated by developing materials containing antibiotics and/or biocides. However, the use of antibiotics may result in developing antibiotic-resistant bacteria and the use of biocides comes with the risk of cytotoxicity. A recent alternative are antimicrobial peptides, as used in this work. Antimicrobial peptides are native to the human body and utilise modes-of-action that make it difficult for microbes to become resistant. However, due to the rapid metabolization of natural antimicrobial peptides by proteases, high antimicrobial peptide concentrations may be required to fully prevent infection which can induce cytotoxicity. By immobilizing antimicrobial peptides to the plasma-treated polyethylene-based surface, the cytotoxicity and degradative mechanisms can be reduced. Here, the undoped polyethylene-based surfaces allowed for the immobilisation of antimicrobial peptides and/or amino acids using various coupling chemistries.

The biological response of the polyethylene-based surfaces was evaluated following bacterial attachment and CellTiter-Glo luminescent cell viability assays. The biological evaluation of the polyethylene-based samples with immobilised AMPs were unable to be completed. Nonetheless, the polyethylene-based samples displayed increased bacterial growth of *Staphylococcus aureus* and *Staphylococcus epidermidis* on the plasma-treated samples when compared to their untreated counterparts. On the other hand, the human osteoblast-like *Saos-2* cell proliferation demonstrated increased cell growth on untreated samples when compared to plasma-treated samples. Overall, this research has unveiled the potential of the developed ultra-high-molecular-weight polyethylene-based materials for use in total joint replacements.

Acknowledgments

First of all, I would like to recognize the valuable assistance of my supervisors, Prof Artemis Stamboulis and Dr Mike Jenkins, throughout this study. Without their advice and guidance, this project would not have been possible. Next to that, I am grateful to the School of Metallurgy and Materials for providing a studentship.

I would like to thank everyone involved in the Biomaterials group, especially Hanieh Ijakipour and Christos Softas for their friendship and support, which has made the entirety of my time at this university all the better.

I also wish to express my appreciation to the staff at the School of Metallurgy and Materials, School of Dentistry, and the Institute of Inflammation and Ageing, especially Prof Hanshan Dong, Dr Behnam Dashtbozorg, Dr Sarah Kuehne, Dr Melissa Grant, Prof Zubair Ahmed, and Dr Maryam Esmaeili, for supporting me with the experiments.

I would also like to acknowledge Dr Mark Duffield (T-ERA group, UoB), Aneesa Nabi (Nano-formulation engineering group, UoB), Dr Mark Iscaacs (HarwellXPS facility), and Dr Oliver Fenwick (Queen Mary University of London), for supporting me with analysis.

Last but not least, I am incredibly grateful to my family and partner for their continuous support and patience throughout this study, allowing me to pursue my passion.

"I know you're tired but come, this is the way…"

Rumi

Publications

This thesis incorporates sections as published in the following papers:

Bruggeman, M., Zelzer, M., Dong, H., & Stamboulis, A. (2022). Processing and interpretation of core-electron XPS spectra of complex plasma-treated polyethylene-based surfaces using a theoretical peak model. *Surface and Interface Analysis*. https://doi.org/10.1002/SIA.7125

Author contributions: M.B. devised the main conceptual ideas, carried out the sample preparation and orbital calculations and assembled the developed peak models. M.B. and M.Z. were in charge of spectral interpretation, processed the data and performed the data analysis. M.B. and M.Z. took the lead in writing the manuscript in consultation with A.S. A.S. and H.D. supervised different parts of the project.

Bruggeman, M., Ijakipour, H., & Stamboulis, A. (2019). Defensin-Like Peptides and Their Antimicrobial Activity in Free-Form and Immobilized on Material Surfaces. *Peptide Synthesis*. https://doi.org/10.5772/INTECHOPEN.85508

Author contributions: M.B. and H.I. conceptualized and drafted the manuscript. M.B. took the lead in writing on the surface immobilised peptides and H.I. on the peptides in free-form. M.B. and H.I. revised the final manuscript in consultation with A.S.

Additionally, the following paper was also published:

Trzcińska, Z., **Bruggeman, M.**, Ijakipour, H., Hodges, N. J., Bowen, J., & Stamboulis, A. (2020). Polydopamine Linking Substrate for AMPs: Characterisation and Stability on Ti6Al4V. *Materials*, *13*(17). https://doi.org/10.3390/MA13173714

Table of Contents

Abstract i

Acknowledgments iii

Publications iv

List of Figures viii

List of Tables xvii

Abbreviations xx

Section 1: Introduction 1

1.1. Aims and objectives 6

Section 2: Literature Review 8

2.1. Properties and applications of UHMWPE-based biomaterials 9

2.1.1. History of UHMWPE-based biomaterials 9

2.1.2. Material properties of UHMWPE-based biomaterials 15

2.1.3. Doping of UHMWPE with α-tocopherol 20

2.1.4. Biocompatibility of UHMWPE-based biomaterials 26

2.2. Plasma-nitriding of UHMWPE-based surfaces 34

2.2.1. Direct current plasma-nitriding (DCPN) 37

2.2.2. Active screen plasma-nitriding (ASPN) 38

2.3. Antimicrobial peptides (AMPs) in free-form 40

2.3.1. Classification of AMPs 41

2.3.2. Antimicrobial mechanisms of AMPs 43

2.3.3. LL-37 derivative KR-12 and its analogues 45

2.4. Immobilisation of AMPs on biomaterials 51

2.4.1. History of AMP immobilisation on biomaterials 54

2.4.2. Proposed approach of AMP immobilisation 63

2.5. Theoretical calculations 64

Section 3: Materials and Methods 66

3.1. Sample preparation of UHMWPE-based samples 67
3.1.1. Surface polishing of UHMWPE 67
3.1.2. α-Tocopherol doping of UHMWPE 67
3.1.3. Active screen plasma-nitriding of UHMWPE 68
3.1.4. AMP immobilisation on plasma-treated UHMWPE 69
3.1.5. Sample IDs of UHMWPE-based samples 71
3.2. Characterisation of the UHMWPE-based surfaces 71
3.2.1. Scanning electron microscopy (SEM) 71
3.2.2. Attenuated total reflectance spectroscopy (ATR-FTIR) 71
3.2.3. Raman microspectroscopy 78
3.2.4. Wide-Angle X-Ray Diffraction (WXRD) 82
3.2.5. X-Ray Photoelectron Spectroscopy (XPS) 86
3.2.6. Vickers Microhardness (MH_V) 91
3.2.7. UV Spectrophotometry 92
3.2.8. Wettability 94
3.3. Biological evaluation of the UHMWPE-based surfaces 95
3.3.1. Bacterial adhesion evaluation 95
3.3.2. Biocompatibility evaluation 97
Section 4: Results and Discussion 103
4.1. Effect of αTH on the ASPN of UHMWPE 104
4.1.1. ATR-FTIR spectroscopy 104
4.1.2. Raman microspectroscopy 130
4.1.3. X-ray photoelectron spectroscopy (XPS) survey 151
4.1.4. UV spectrophotometry 158
4.1.5. Wide-angle X-ray diffraction (WXRD) 161
4.1.6. Scanning electron microscopy (SEM) 170
4.1.7. Vickers microhardness (MH_V) test 176

4.1.8. Wettability 179
4.2. Raman mapping of UHMWPE-based samples 186
4.2.1. Crystallinity maps 187
4.2.2. Molecular orientation 191
4.2.3. Presence and localisation of αTH and a-C in the UHMWPE matrix 195
4.3. Interpretation of complex UHMWPE-based surfaces using XPS 207
4.3.1. Functionality evaluation 207
4.3.2. Peak model assembly 208
4.3.3. Effect of functional group positioning 209
4.3.4. Long-range effects of functional groups 211
4.3.5. Comparison and validation of peak models 215
4.3.6. XPS analysis 219
4.4. Biological evaluation of UHMWPE-based surfaces 242
4.4.1. Bacterial adhesion assay 242
4.4.2. Cell viability assay 250
Section 5: Conclusions and Future Perspectives 260
5.1. Conclusions 261
5.2. Future perspectives 263
5.2.1. Limitations and recommendations 264
5.2.2. Proposed future work 265
References 268
Appendices I

List of Figures

Figure 1.	Timeline on the history of commercially available UHMWPE biomaterials used in TJRs.	12
Figure 2.	Simplified schematic of tie molecules connecting neighbouring crystalline lamellae, cilia suspended from the lamellae, and loose loops ending in the same lamellae.	17
Figure 3.	Schematic of (left) total hip replacement components and (right) their placement inside the body.	19
Figure 4.	Simplified reaction scheme of (A) lipid (per)oxidation and (B) the antioxidative action of αTH.	21
Figure 5.	Simplified reaction scheme of the oxidation process of UHMWPE induced by irradiation.	24
Figure 6.	Simplified reaction scheme of the quenching process of αTH in UHMWPE.	25
Figure 7.	Simplified schematics of various DC plasma setups.	36
Figure 8.	Simplified schematic of an electron avalanche following the Townsend theory.	37
Figure 9.	Schematic of conventional active screen plasma-nitriding setup.	39
Figure 10.	Simplified schematic of membrane-mediated mechanisms of AMPs.	44
Figure 11.	Simplified reaction schemes of various coupling chemistries used to immobilise AMPs onto (bio)material surfaces with differing organic functional groups.	56-57
Figure 12.	Simplified schematic of spacer-incorporated immobilized AMPs.	60
Figure 13.	Flowchart of the iterative HF MO method using the LCAO scheme.	64

Figure 14.	Model structures used for the spectral simulations, showing the C20 alkane and αTH.	72
Figure 15.	Settings for '*EDF2*' frequency calculations in '*Spartan'14*'.	73
Figure 16.	The penetration depth and effective penetration estimated for UHMWPE.	75
Figure 17.	Example lineshapes of a pure Lorentzian and Gaussian lineshape, and various asymmetric Lorentzian lineshapes.	77
Figure 18.	Example of lineshape development in a FTIR spectrum.	78
Figure 19.	The raw pixel spectra and the corresponding abstract factors.	81
Figure 20.	The PCA-based noise reduced spectra of UD/UT using the first 12 AFs as a filter mask.	82
Figure 21.	Top-view of the orthorhombic unit cell and the monoclinic unit cell.	84
Figure 22.	Three-dimensional view of the orthorhombic and monoclinic unit cell.	84
Figure 23.	Raw XRD spectrum of UD/UT fitted with a 4-knotted polynomial, separated XRD spectra showing the peak-fitted crystalline components and the peak-fitted amorphous halo, and the raw XRD spectrum peak-fitted with both components.	86
Figure 24.	Simplified schematic of a pyramid-shaped diamond indenter indenting a sample from a side-view and the top-view of an indent in the sample surface.	91
Figure 25.	Correlation of the concentration of the calibration solution versus the UV absorbance at 290 nm.	93
Figure 26.	Schematic representation of the bacterial adhesion assay.	97

Figure 27.	Schematic representation of the cell viability assay experimental setup.	101
Figure 28.	Summed spectral peak fits of the undoped and doped UHMWPE-based sample series between 700 and 750 cm^{-1}, and the corresponding graph displaying the 730:719 cm^{-1} peak area ratios.	107
Figure 29.	Simplified bond structures of the mono-alkyl vinyl, di-alkyl geminal-vinylidene, and di-alkyl trans-vinylene bonds.	108
Figure 30.	Model structures used to predict the absorption band positions for mono-alkyl vinyl, di-alkyl geminal-vinylidene, and di-alkyl trans-vinylene bonds.	109
Figure 31.	Summed spectral peak fits of the undoped and doped UHMWPE-based sample series between 800 and 1050 cm^{-1}, and the corresponding graphs displaying the vinyl endcap, geminal-vinylidene, and trans-vinylene band indices.	110
Figure 32.	Summed spectral peak fits of the undoped and doped UHMWPE-based sample series between 1000 and 1200 cm^{-1}; and the corresponding graphs displaying the 1040 cm^{-1}, 1080 cm^{-1}, 1120 cm^{-1}, and 1165 cm^{-1} band indices.	113
Figure 33.	Summed spectral peak fits of the undoped and doped UHMWPE-based sample series between 1200 and 1400 cm^{-1}, and the corresponding graph displaying the $[CH_2]_{wagging:twisting}$ peak area ratios.	115
Figure 34.	Graph displaying the αTH index as observed in the individual peak fits of the doped sample series.	116
Figure 35.	Summed spectral peak fits of the undoped and doped UHMWPE-based sample series between 1400 and 1500 cm^{-1}, and the corresponding graph displaying the [1472 cm^{-1}]:[1462 cm^{-1}] peak area ratios.	118
Figure 36.	Model structures used to predict the absorption band positions for aldehyde, (top-right) ketone, carboxylic acid, and ester bonds.	120
Figure 37.	ATR-FTIR spectra of D/PT60, αTH, and a-C between 1400 and 1800 cm^{-1}.	120

Figure 38.	Summed spectral peak fits of the undoped and doped UHMWPE-based sample series between 1500 and 1800 cm^{-1}; and the corresponding graphs displaying the $[C=C]_1$, $[C=C]_2$, [C=O], and [O=C−O] band indices.	121
Figure 39.	Summed spectral peak fits of the undoped and doped UHMWPE-based sample series between 2000 and 3000 cm^{-1}, and the corresponding graph displaying the $[CH_2]_{asymmetrical:symmetrical}$ peak area ratios.	123
Figure 40.	Model structures used to predict the absorption band positions for amine, imine, amidine, and amide bonds.	125
Figure 41.	ATR-FTIR spectra of αTH between 3000 and 3800 cm^{-1}.	125
Figure 42.	Summed spectral peak fits of the undoped and doped UHMWPE-based sample series between 1500 and 1800 cm^{-1}; and the corresponding graphs displaying the 3055 cm^{-1}, 3156 cm^{-1}, 3322 cm^{-1}, and 3537 cm^{-1} band indices.	126
Figure 43.	Linear correlations graphs of the $[A_{1300}:A_{1370}]$ ratio versus the $[A_{730}:A_{719}]$, $[A_{1472}:A_{1462}]$, $[C=C]_2$, [C=O], and $[A_{2917}:A_{2849}]$; and the αTH index versus the $[A_{730}:A_{719}]$, vinyl, trans-vinylidene, and $[C=C]_1$.	129
Figure 44.	Overlayed spectra of D/PT60, a-C, and αTH, between 1000 and 1700 cm^{-1}.	132
Figure 45.	Summed spectral peak fit of αTH.	133
Figure 46.	Summed spectral peak fit of a-C.	135
Figure 47.	Linear correlation of the component area at 1485 cm^{-1} and 1080+1200 cm^{-1}, as observed in the individual peak fits of a-C.	136
Figure 48.	Summed spectral peak fits of the undoped and doped UHMWPE-based sample series between 1000 and 1800 cm^{-1}, displaying UHMWPE, αTH, and a-C.	137
Figure 49.	Graph displaying the phase content of the crystalline, amorphous, and interfacial phase in the undoped and doped UHMWPE-based sample series.	139

Figure 50.	Ratios I-IV as determined by the individual peak fits of the undoped and doped UHMWPE-based samples.	141
Figure 51.	Relative elasto-plastic strain (ε) determined by ΔFWHM of the 1130 cm^{-1} band relative to UD/UT.	143
Figure 52.	a-C index as observed in the individual peak fits of the undoped and doped sample series, and the αTH index of the doped sample series.	144
Figure 53.	Summed spectra of the undoped and doped UHMWPE-based sample series, showing the increase in background signal.	145
Figure 54.	Overlayed spectra of D/PT60 and a-C, zoomed-in to display the overlap in bands.	145
Figure 55.	Summed spectral peak fits of the undoped and doped UHMWPE-based sample series between 2750 and 3100 cm^{-1}; and the corresponding graphs displaying the 2848 cm^{-1}, 2857 cm^{-1}, 2883 cm^{-1}, 2894 cm^{-1}, 2931 cm-1 and 2969 cm^{-1} band indices.	148
Figure 56.	XPS survey spectra of the undoped UHMWPE-based sample series before and after ion etching.	152
Figure 57.	XPS survey spectra of the doped UHMWPE-based sample series before and after ion etching.	153
Figure 58.	Elemental surface composition of the undoped and doped UHMWPE-based sample series, showing the At% of the C 1s, N 1s, O 1s, and summed contaminants.	154
Figure 59.	Picture of ASPN working table after a 60-minute treatment of the undoped and doped UHMWPE-based samples, showing the formation of metal oxide rings around the doped samples.	157
Figure 60.	Calculated XRD spectra of the orthorhombic and monoclinic PE unit cells, and the corresponding top-view of the unit cells including the diffraction planes.	161
Figure 61.	Peak fitted WXRD spectra of the undoped and doped UHMWPE-based sample series.	162

Figure 62.	Phase composition of the peak-fitted WXRD spectra of the undoped and doped samples, showing the percentage of the orthorhombic, monoclinic, and amorphous phase.	165
Figure 63.	Unit cell parameters as obtained from the refinement in 'UnitCell', showing the length of the unit cell parameters and the unit cell volume of the undoped and doped sample series.	166
Figure 64.	Schematic representation of the plot used for the modified Scherrer equation.	167
Figure 65.	Crystallite size and lattice strain estimated for the undoped and doped sample series with the Scherrer equation and the most-intense diffraction peak or all diffraction peaks, and the modified Scherrer equation.	168
Figure 66.	Linear correlation between the crystallite size and crystallinity of the UHMWPE-based samples.	169
Figure 67.	Example of histogram threshold and resulting binary image of the black pixels overlayed on the original SEM micrograph of D/PT15 in ImageJ.	172
Figure 68.	Graph displaying the average size of the black pixels and corresponding percentual area coverage observed in the SEM micrographs of undoped and doped samples.	172
Figure 69.	SEM micrographs of UD/UT, UD/PT15, UD/PT30 and UD/PT60, at a 2000x magnification.	173
Figure 70.	SEM micrographs of D/UT, D/PT15, D/PT30 and D/PT60, at a 2000x magnification.	174
Figure 71.	Zoomed-in SEM micrograph of D/PT30 with randomly highlighted sections of the UHMWPE flake-like surface and the bubble-like clusters.	175
Figure 72.	Vickers microhardness for the undoped and doped UHMWPE-based sample series, including the corresponding elastic modulus as determined by the logarithmic correlation from the literature.	176
Figure 73.	Linear correlation between Vickers microhardness and the $[C=C]_{str.}$ band index from FTIR.	178

Figure 74.	Linear correlation between Vickers microhardness and the a-C index from Raman.	178
Figure 75.	Equilibrium contact angles of DI water and diiodomethane for the undoped samples.	180
Figure 76.	Equilibrium contact angles of DI water and diiodomethane for the doped samples.	180
Figure 77.	Surface free energy for the undoped and doped sample series, showing the separated dispersive and polar surface energy components.	183
Figure 78.	Wettability envelopes for the undoped and doped samples, with isolines depicting various contact angles.	185
Figure 79.	Example of UD/UT spectral peak fit and component-based Raman images.	186
Figure 80.	Graph displaying the phase content of the crystalline, amorphous, and interfacial phase in the undoped and doped UHMWPE-based sample series.	187
Figure 81.	Raman images of the crystalline, amorphous, and interfacial fractional phase content for the undoped sample series.	188
Figure 82.	Raman images of the crystalline, amorphous, and interfacial fractional phase content for the doped sample series.	189
Figure 83.	Ratios I-IV as determined by the individual peak fits of the undoped and doped UHMWPE-based samples.	192
Figure 84.	Raman images of the ratios related to the molecular orientation for the undoped sample series.	193
Figure 85.	Raman images of the ratios related to the molecular orientation for the doped sample series.	194
Figure 86.	The (left) peak fitted summed pixel spectrum of the undoped sample series, showing the UHMWPE, αTH, and a-C components; and the synthetic envelope of the a-C components within the D/PT60 summed pixel spectrum overlayed with the spectrum of a-C.	195

Figure 87.	The a-C, oxidation, and αTH indices for the undoped and doped sample series.	196
Figure 88.	Raman images of the a-C index and oxidation index for the undoped sample series.	198
Figure 89.	Raman images of the a-C index, oxidation index, and αTH index for the doped sample series.	199
Figure 90.	The I_D/I_G and $I_{(A+X)}/I_{(D+G)}$ ratios for the undoped and doped sample series.	200
Figure 91.	Derivative Raman images of the respective UHMWPE-related phase contents overlayed with the a-C index for the undoped sample series.	202
Figure 92.	Derivative Raman images of the respective UHMWPE-related phase contents overlayed with the a-C index for the doped sample series.	203
Figure 93.	Derivative Raman images of the respective UHMWPE-related phase contents overlayed with the αTH index for the doped sample series.	204
Figure 94.	Fractional derivative overlap of the a-C index with the crystalline, amorphous, and interfacial phase content, for the undoped sample series.	205
Figure 95.	Fractional derivative overlap of the a-C index with the crystalline, amorphous, and interfacial phase content, for the doped sample series.	205
Figure 96.	Fractional derivative overlap of the αTH index with the crystalline, amorphous, and interfacial phase content, for the doped sample series.	205
Figure 97.	Examples of 3D model structures showing carbon, oxygen, nitrogen, and hydrogen atoms.	210
Figure 98.	Assignment of higher-order carbon shifts in the centred and end-chain model structures, with the [COH] model structure serving as an example.	214
Figure 99.	Linear correlation fits of the HF and wB97X-D calculated ΔCEBEs versus the experimental ΔCEBEs.	217

Figure 100.	High-resolution C 1s spectra peak fits of UHMWPE D/PT60 using a ‘Shirley’ background and the wB97X-D-based peak model, including the respective symmetric higher-order carbon shifts.	229
Figure 101.	Composition of UHMWPE D/PT60 determined by the high-resolution spectra peak fits using a ‘Shirley’ background and the wB97X-D-based peak model including the symmetric higher-order carbon shifts.	230
Figure 102.	High-resolution C 1s, N 1s and O 1s spectra peak fit of UHMWPE D/PT60 using a ‘Shirley’ background and the wB97X-D peak model with the 3° symmetric higher-order carbon shifts.	232
Figure 103.	Composition of UHMWPE UD/UT, UD/PT60, D/UT, and D/PT60, determined by the high-resolution spectra peak fits using a ‘Shirley’ background and the wB97X-D-based peak model including the 3° symmetric higher-order carbon shifts.	233
Figure 104.	High-resolution C 1s spectra peak fits of UHMWPE D/PT60 using a ‘Shirley’ background following conventional reference-based peak fitting, advanced reference-based peak fitting and the wB97X-D-based peak fitting using the 3° symmetric higher-order carbon shifts.	236
Figure 105.	One-way ANOVA with Tukey-Kramer post-hoc analysis on the bacterial concentrations (CFU/mL) for *S. aureus* and *S. epidermidis* on the undoped and doped sample series.	243
Figure 106.	One-way ANOVA with Tukey-Kramer post-hoc analysis on cell count for *Saos-2* on the undoped and doped sample series.	251
Figure 107.	Saos-2 cell viability from various polymers relative to the PS-TC control, polymers are separated by their atomic composition, containing [C], [CO], [CN], or [CNO] atoms.	255

List of Tables

Table 1.	Standard specification for fabricated UHMWPE-based surgical implants, according to ASTM F 648-04.	18
Table 2.	Typical physical/mechanical properties of UHMWPE observed in literature.	18
Table 3.	Effect of annealing on the mechanical properties of γ-irradiated UHMWPE.	20
Table 4.	Results of the alanine and lysine scans on KR-12.	48
Table 5.	Target functionalities and formed bond type of coupling chemistries used for the immobilisation of AMPs to the plasma-treated UHMWPE-based surfaces.	63
Table 6.	Equivalence of the activator and base, temperature, and duration of the coupling chemistries.	70
Table 7.	Sample IDs of UHMWPE-based samples.	71
Table 8.	Structure parameters of the drawn PE unit cells and the bonding of the atoms.	83
Table 9.	Liquid surface free energy and polar/dispersive components of water and diiodomethane.	94
Table 10.	FTIR region ranges of interest and the corresponding present chemical bond information.	105
Table 11.	Expected FTIR absorption band positions for the various vinyl-based bonds according to the literature and as calculated using the vinyl-based model structures between 900 and 1000 cm^{-1}.	109
Table 12.	Expected FTIR absorption band positions according to the literature and as calculated using the C20 alkane / αTH model structure between 1000 and 1200 cm^{-1}.	112

Table 13.	Expected FTIR absorption band positions according to the literature and as calculated using the C20 alkane model structure between 1200 and 1400 cm^{-1}.	114
Table 14.	Expected FTIR absorption band positions according to the literature and as calculated using the αTH model structure between 1200 and 1400 cm^{-1}.	116
Table 15.	Expected FTIR absorption band positions according to the literature and as calculated using the C20 alkane model structure between 1400 and 1500 cm^{-1}.	117
Table 16.	Expected FTIR absorption band positions according to the literature and as calculated using the corresponding vinyl-based and oxygen-based model structures between 1500 and 1800 cm^{-1}.	119
Table 17.	Expected FTIR absorption band positions according to the literature and as calculated using the C20 alkane model structure between 2000 and 3000 cm^{-1}.	122
Table 18.	Expected FTIR absorption band positions according to the literature and as calculated using the vinyl-based, oxygen-based, and nitrogen-based model structures between 3000 and 3800 cm^{-1}.	124
Table 19.	Pearson correlations where $-0.75 > r_p > 0.75$ as observed between the indices and ratios from the individual FTIR spectral peak fits.	128
Table 20.	Expected Raman band positions according to the literature and as calculated using the C20 alkane model structure between 1000 and 1800 cm^{-1}.	131
Table 21.	Raman band positions for αTH as observed in the spectral peak fit and assignments according to the literature and as calculated using the αTH model structure between 1000 and 1800 cm^{-1}.	133
Table 22.	Expected Raman band positions for a-C according to the literature between 1000 and 1800 cm^{-1}.	135
Table 23.	Expected Raman band positions according to the literature and as calculated using the C20 alkane model structure between 2800 and 3000 cm^{-1}.	146
Table 24.	Pearson correlations where $-0.75 > r_p > 0.75$ as observed between the indices and ratios from the individual Raman	149

	spectral peak fits of the undoped and doped UHMWPE-based samples.	
Table 25.	Elemental surface composition of the undoped and doped UHMWPE-based samples before and after ion etching.	155
Table 26.	UV measurements at 290 nm for UD/PT60 and D/PT60, showing the absorbance and degree of substitution.	159
Table 27.	Observed diffraction peak positions of the undoped sample series.	163
Table 28.	Observed diffraction peak positions of the doped sample series.	163
Table 29.	Comparison between the calculated and mean experimental primary carbon CEBE deviations observed for esters/acids and primary/secondary amides in the literature.	211
Table 30.	Statistical analysis of the linear fits between the experimental and calculated ΔCEBE datasets.	216
Table 31.	Atomic composition of UD/UT, UD/PT60, D/UT, and D/PT60, determined by the survey spectra.	221
Table 32.	Composition of the high-resolution spectra peak fits of D/PT60 using a ‘Shirley’ background following conventional peak fitting, reference-based advanced peak fitting, and the wB97X-D-based peak fitting using the 3° higher-order carbon shifts.	237
Table 33.	Pearson and linear regression coefficients between bacterial concentration of *S. Aureus* and *S. Epidermidis* to results obtained by FTIR, Raman, XPS and CA measurements.	247
Table 34.	Relative cell growth rate of *Saos-2* estimated by the linear regression fits on the cell count of the control and samples over the incubation period.	252
Table 35.	Pearson and linear regression coefficients between the cell count at day 1, 4, and 7, and the cell growth rate of *Saos-2* to indices obtained by FTIR, Raman, XPS and CA measurements.	253

Abbreviations

5(6)-FAM	5(6)-Carboxyfluorescein
αTH	α-Tocopherol
(A)S	(Anti-)symmetric
AAc	Amino acid
a-C	Amorphous carbon
a-C:H	Hydrogenated amorphous carbon
AF	Abstract factor
AFM	Atomic force microscope
AMP	Antimicrobial peptide
Amu	Atomic mass unit
APD	Antimicrobial peptide database
ASPN	Active screen plasma-nitriding
ASTM	American Society for Testing and Materials
ATR	Attenuated total reflectance
BE	Binding energy
C20	Alkane model structure of 20 [CH_x] units
Casa	Computer-assisted spectral analysis
CCD	Charge-coupled device
CDI	*1,1'*-Carbonyldiimidazole
CEBE	Core-electron binding energy
CFR	Carbon fibre-reinforcement
CFU	Colony forming units
D/PT#	Doped and plasma-treated UHMWPE

D/UT	αTH-doped and untreated UHMWPE
DCC	*N,N′*-Dicyclohexylcarbodiimide
DCPN	Direct current plasma-nitriding
DFT	Density functional theory
DI	Deionised
DIC	*N,N′*-diisopropylcarbodiimide
DLC	Diamond-like carbon
DMAP	*4*-(Dimethyl-amino)pyridine
DMF	Dimethylformamide
ECA	Equilibrium contact angle
ESEM	Environmental scanning electron microscopy
EtO	Ethylene oxide
Fmoc	Fluorenylmethyloxycarbonyl
FO	Frozen orbital
FR	Fermi resonance
FTIR	Fourier-transform infrared
FWHM	Full-width-half-maximum
GAMESS	General atomic and molecular electronic structure system
GVI	Di-alkyl geminal-vinylidene index
HF	Hartree-Fock
HPC	High-pressure crystallisation
HR	High-resolution
ISO	International Organization for Standardization
KE	Kinetic energy

KS	Kohn-Sham
KT	Koopmans' theorem
LA	pseudo-Voigt lineshape
LCAO	Linear combination of atomic orbitals
LPS	Lipopolysaccharide
MAE	Mean average error
MAX	Maximum absolute error
MH_V	Vickers microhardness
MMFF94	Merck molecular force field
MO	Molecular orbital
NA	Numerical aperture
NBO	Natural bond orbital
NIST	National Institute of Standards and Technology
NMR	Nuclear magnetic resonance
OI	Oxidation index
OT	Overtone
Oxyma Pure	Ethyl-cyano(hydroxyimino)acetate
PBS	Phosphate-buffered saline
PCA	Principal component analysis
PDMS	Polydimethylsiloxane
PIII	Plasma immersion ion implantation
R^2	Regression coefficient
ROS	Reactive oxygen species
r_p	Pearson correlation coefficient

RSF	Relative sensitivity factor
S/N	Signal-to-noise
SA	Steam autoclave
SALC	Symmetry-adapted linear combination
SCF	Self-consistent field
SFE	Surface free energy
SiC	Silicon carbide
STD	Standard deviation
ta-C	Tetrahedral amorphous carbon
TJRs	Total joint replacements
TNF-α	Tumour necrosis factor-α
TSA	Tryptone soya agar
TSB	Tryptone soya broth
TVI	Di-alkyl trans-vinylene index
UD/PT#	Undoped and plasma-treated UHMWPE
UD/UT	Undoped and untreated UHMWPE
uGTS	Unrestricted generalised transition-state
UHF	Unrestricted Hartree-Fock
UHMWPE	Ultra-high-molecular-weight polyethylene
UV	Ultraviolet
VI	Mono-alkyl vinyl index
WXRD	Wide-angle X-ray diffraction
XPS	X-ray photoelectron spectroscopy

Section 1: Introduction

Total joint replacements play a vital role in enhancing the quality of life for individuals affected by joint diseases and injuries, these procedures aim to restore mobility and alleviate pain in daily life routines (Bleß & Kip, 2017). In the context of total joint replacements, ultra-high-molecular-weight polyethylene (UHMWPE) is frequently the polymer of choice as the bearing material (i.e., the cup/liners that act as the interface between the implanted artificial joints and corresponding joint sockets), mostly because of its low frictional coefficient, high strength, and bio-inert nature (Barron & Birkinshaw, 2008; Edidin et al., 1999; Kurtz, 2016; S. Li, 2001; Lustiger & Markham, 1983; Mikić & Lesić, 2013; Sobieraj & Rimnac, 2009). According to the latest available data from the National Joint Registry, a total of 190,223 total joint procedures were performed in the United Kingdom in 2021 (Ben-Shlomo et al., 2022). Most of these procedures, accounting for 89.28% or 169,827 procedures, were primary procedures (i.e., the initial surgeries conducted to replace a joint with an artificial prosthesis) – the other 10.72% or 20,391 procedures were revisions. The distribution of these total joint procedures based on the joint type revealed that 50.26% were related to hip replacements, while 45.32% were knee replacements. Shoulder-related procedures accounted for 3.42% of the total, followed by 0.54% for elbow replacements and 0.46% for ankle replacements.

Focussing on total hip replacements, being the biggest category within total joint replacements, these procedures can be categorized into different types based on the technique and materials used (Ben-Shlomo et al., 2022). The types of replacement techniques are categorised by being cemented (i.e., using bone cement to secure both the femoral stem and acetabular cup), uncemented/cementless (i.e., relying on press-fit or porous coatings to encourage bone ingrowth), hybrid (i.e., combining cemented and cementless components, traditionally, the femoral stem is cemented and acetabular cup uncemented), reverse hybrid (i.e., reversed approach as seen in traditional hybrid replacements), and resurfacing (i.e., capping the existing bone with a metal prosthesis, rather than completely replacing the joint).

From these types of replacement techniques, the traditional hybrid approach was performed the most at 38.1% of all total hip replacements, followed by uncemented and cemented replacement at 35.4 and 21.8%, respectively. Altogether, these three replacement techniques accounted for >95% of all total hip replacements performed in 2021.

The types of materials used are categorised by being combinations of metal-on-polyethylene (MoP), MoM, ceramic-on-polyethylene (CoP), CoM, CoC, MoPoM, CoPoM, and others (Ben-Shlomo et al., 2022). From these types of material combinations, CoP and MoP were found to be most popular at 46.3% and 44.8%, respectively, accounting for >90% of all total hip replacements in 2021. CoP-based implants have become increasingly popular, 15 years ago CoP was only used in ~10% of hip replacements but has become the dominant choice over MoP since 2020. The transition from MoP to CoP implants can be attributed to the advancements in ceramic manufacturing techniques, allowing for improved mechanical properties and wear resistance (Khalifa & Bakr, 2021). Finally, being the polymer of choice for these types of implants, UHMWPE was found to be used in at least 93.3% of all hip replacements in 2021 (Ben-Shlomo et al., 2022).

While the cost for each procedure varies depending on factors such as the implant type, hospital setting, surgery complexity, and postoperative care, total joint replacements are recognized as a significant expense for the healthcare system. For example, according to the national schedule of NHS costs, the costs for a hip procedure varied from £4,401 to £11,034 and for a knee procedure from £3,457 to £9,741 in 2021/22 (NHS, 2022). From these numbers, it is evident that the total cost of total joint replacement procedures ranges from several hundreds of millions to potentially reaching into the billions of pounds each year, which highlights the investment made by the healthcare system to provide joint replacements. A study funded by the National Institute for Health Research (NIHR) revealed that, based on data from national registries and case studies, approximately 85% of total hip replacements lasted for at

least 15 years and 58% for 25 years (Evans et al., 2019). The average patient age undergoing a total joint procedure was approximately 67 years old, whereas the life expectancy in the UK was 81 years old between 2018-2020 (Ben-Shlomo et al., 2022; Office for National Statistics, 2021). Based on the average patient age and their life expectancy in the UK, over 85% of the implants will (statistically speaking) not require revisions.

Nonetheless, the 20,391 implant revisions that did occur in the UK in 2021, have a negative impact on the patient compliance (i.e., the extent to which patients adhere to the recommended medical and post-operative instructions) and the care system due to the additional labour and costs associated with revisions – which underscores the need of optimizing patient outcomes and minimizing healthcare costs through effective prevention of implant rejection/failures (Ben-Shlomo et al., 2022). Major causes of implant rejection and/or failure are the generation of implant debris, surface oxidation, and microbial infection (Renò et al., 2003; Vasconcellos et al., 2007). Over the implants' lifetime, deformation of the cup insert and long-term wear debris generation may result in unsatisfactory implant performance and remains a frequent cause of implant rejection, where the immune system's response to the foreign debris results in the body's rejection and failure to integrate or tolerate the implant (Man et al., 2017). Next to that, the surface oxidation of the UHMWPE implant has an additional negative impact on its performance. Surface oxidation alters the chemical structure and mechanical properties of the UHMWPE surface, initiating or further accelerating the wear debris generation. Altogether, the wear and adverse tissue reactions to debris particles directly accounted for 18% of the revisions in 2021 within the UK, whereas aseptic joint loosening (i.e., the separation of the implant components from the surrounding bone as a result of wear, inflammation, or other factors at the implant-bone interface, occurring without infection) accounted for 39% of the revisions (Ben-Shlomo et al., 2022). Finally, next to influences of a chemical and/or physical nature, microbial infection also remains one of the most devastating

reasons for implant failure (Tanoira, 2019). Although it only affects 1-2% of implantations, microbial infection accounts for up to 20% of the implant revisions and is a significant burden on the care system (Ben-Shlomo et al., 2022; Grindy et al., 2019; Thorn et al., 2022). Patients who endured microbial infection of the implant were also linked with pronounced health problems (e.g., pain, inflammation, impaired mobility, tissue damage, etc.) and recurring infection (i.e., the infection persisted or returned, e.g., due to residual bacteria, inadequate treatment, poor wound healing) after revision (Bauer & Zhang, 2016).

To prevent wear debris generation and surface oxidation, various attempts were made to improve the properties of the UHMWPE implants, including – but not limited to – the crosslinking and/or incorporation of antioxidants. Crosslinking of UHMWPE is also performed to reduce wear debris generation, this process is commonly induced by radiation with γ-rays/*e*-beams, the use of free radical initiators (e.g., organic peroxides), and plasma-based treatments (Machado Rodrigues et al., 2020). However, crosslinking treatments frequently leave residual free radicals, which initiate further crosslinking and surface oxidation. An advantage observed with plasma-treatments is the potential to introduce chemical functionalities which allow conjugation to other molecules, the type of functionalities formed depends on the plasma working gas (López-Santos et al., 2011). The most frequently incorporated antioxidants are α-tocopherol (αTH; i.e., vitamin E) and polyphenols (e.g., gallic acid or dodecyl gallate), which provide partial protection against oxidation after irradiation, *in-vivo* reactive oxygen species (ROS), and reduces the wear debris generation (Y. Ren et al., 2019; Shen et al., 2014, 2015).

To reduce the chance of microbial infection, attempts were also made to incorporate antimicrobial agents (e.g., rifampin and vancomycin) in/on the UHMWPE implant, typically through blending, diffusion, or by covalent immobilisation. However, a drawback with the use of antibiotics is that these most often cannot be used for long-term, due to the increased change of creating antibiotic-resistant microbial strains (B. Li & Webster, 2018). More recently,

antimicrobial peptides (AMPs) have evolved as a promising alternative to the more commonly used antimicrobial agents (J. Wang et al., 2019). AMPs can show antimicrobial activity against bacteria, fungi, parasites, and viruses. AMPs like '*KR-12*' utilise a mode-of-action that lyses the cell membrane, making it more difficult for microbes to become resistant when compared to most antibiotics (G. Wang, 2008). Furthermore, '*KR-12*' is derived from the human host defense cathelicidin '*LL-37*' and allows for selective toxicity towards microbes (i.e., minimum inhibitory concentration of 40 μM against *Escherichia coli*) but not human cells (i.e., no cytotoxicity was observed until at least 63.5 μM) (G. Wang et al., 2008).

When comparing the above-mentioned treatments and minimizing the associated drawbacks, the incorporation of αTH into the polymer matrix, surface functionalisation by plasma-nitriding and subsequent immobilisation of AMPs to the introduced functionalities, presents a promising concept to enhance the performance of UHMWPE-based biomaterials.

1.1. Aims and objectives

The aim of this work is to enhance UHMWPE-based biomaterials used in total joint replacements by addressing implant failure/rejection and improving patient outcomes, through the incorporation of αTH for protection against oxidation, implementing active screen plasma-nitriding (ASPN) for surface crosslinking and the introduction of chemical functionalities, and utilizing immobilized AMPs to combat infection and reduce the risk of implant failure. To achieve this aim and construct well-informed conclusions/recommendations, the project was separated into the following objectives:

1. Investigate the effect of αTH doping in combination with ASPN on UHMWPE using various characterisation techniques. The main goal was to reveal the change in chemical and physical properties (e.g., chemical composition, degree of crystallinity, micro-

hardness, etc.) of the plasma-treated UHMWPE due to the addition of αTH when compared to its undoped counterpart.

2. Study the localisation of the conformational states and other present compounds in the untreated and plasma-treated UHMWPE-based samples with Raman mapping. Raman mapping was used to improve the understanding of the changes visually observed across the sample surface. The observed conformational states were extracted by peak fitting the recorded pixel spectra, which (utilizing various equations) provided insight into, e.g., the surface crystallinity, oxidation, etc.
3. Examine the chemical surface composition of the untreated and plasma-treated UHMWPE-based samples, using X-ray photoelectron spectroscopy (XPS) due to its high surface-sensitivity. There are almost no existing XPS references for ASPN-treated UHMWPE and references for αTH doped UHMWPE treated with ASPN do not exist. To gain a deeper understanding of the modified UHMWPE-based surfaces (e.g., to aid in determining suitable coupling chemistries for surface decoration or assess surface-related properties like biocompatibility), a theoretical peak model was developed. Next to providing a more detailed interpretation of the high-resolution XPS spectra, this theoretical peak model also aims to minimize the need for manual input and potential bias when analysing the spectrum.
4. Evaluate the biological response to all UHMWPE-based surfaces. A bacterial adhesion assay was used to evaluate the anti-bacterial activity on the material surface, the assay was performed using two clinically relevant bacteria associated with implantations: *Staphylococcus aureus* and *Staphylococcus epidermidis*. A cell viability assay was used to evaluate the biocompatibility of the material surface, the assay was performed with the *Sarcoma osteogenic* cell line, which is commonly used for bone-related implants.

Section 2: Literature Review

2.1. Properties and applications of UHMWPE-based biomaterials

2.1.1. History of UHMWPE-based biomaterials

Ultra-high-molecular-weight polyethylene (UHMWPE) has a clinical history for over five decades as a biomaterial for use in total joint replacements (TJRs), including total hip, total knee, and total shoulder protheses. Since its clinical introduction by Sir John Charnley in 1962, it has become the primary bearing/articulating material in TJRs (Mikić & Lesić, 2013). However, during the early stages of clinical implementation, unmodified UHMWPE liners showed signs of degradation over the implants' lifetime inside the body, resulting in reduced material performance. Generation of UHMWPE wear debris at the surface of the liners was a frequent cause of implant rejection, where the immune system's response to the foreign debris resulted in the body's rejection and failure to integrate or tolerate the implant (Man et al., 2017). Therefore, most developments on UHMWPE-based biomaterials focussed on minimising wear debris generation to prevent negative biological reactions like inflammation.

For example, after its clinical introduction, several attempts were performed to improve the performance of UHMWPE-based biomaterials using carbon fibre-reinforcement (CFR), re-crystallisation/crosslinking, and modifying sterilization methods (S. Li, 2001). During the 1970s, CFR-UHMWPE was investigated for use as orthopaedic implants and was commercially introduced (i.e., Poly II, Zimmer, Inc.). However, clinical studies showed short-term failures due to, amongst others, poor crack resistance and fibre rupture at the implant surface, leading to the abandonment of CFR-UHMWPE and leaving a perception that fibre-reinforced UHMWPE materials may not be appropriate for TJRs (Kurtz, 2009). Despite this, fibre-reinforced UHMWPE materials progressed in nonmedical applications (e.g., automotive or protective equipment), and innovations in these fields may pose interesting for future UHMWPE-based biomaterials (Chhetri & Bougherara, 2021).

The use of re-crystallisation and crosslinking to increase the crystallinity levels has also been proposed; this is among others possible using high-pressure crystallisation (HPC) or radiation (e.g., using γ-rays or *e*-beams), respectively (Bassett et al., 1974). In 1968, highly-crosslinked UHMWPE was developed using γ-ray irradiation that served as sterilisation and was released as a commercial product in 1969. However, the γ-ray irradiation leaves residual free radicals on the UHMWPE surface (short-term presence) and, due to the large size of its crystallites, trapped in the lamellae (long-term presence; e.g., the half-life time of the alkyl-radical decay was 26 days when vacuum packaged), which can result in both further crosslinking and surface oxidation (Bhateja et al., 1995; Y. Wang et al., 2013; Y. Zhao et al., 2010). The crosslinking improved the strength and wear resistance of UHMWPE but demonstrated delamination (i.e., flaking-like deterioration) during wear testing (Tomita et al., 1999). Additionally, the free radicals accelerated surface oxidation and corresponding wear debris generation when implanted. Due to this, no significant improvements had been achieved with irradiation-based crosslinking until the development of highly-crosslinked and annealed UHMWPE in 1998, annealing (i.e., heating the material to a specific temperature to promote structural relaxation and reduce radiation-induced defects or stresses) removed most free radicals to ensure oxidative stability (Dumbleton et al., 2009; Oral et al., 2011). However, the material partially melts during annealing, reducing the crystallinity and crack fatigue strength (Oral & Muratoglu, 2011). This raised the need for a process to eliminate free radicals without annealing, Tomita *et al.* reported the first solution to this by incorporating α-tocopherol (αTH; i.e., vitamin E) as a radical scavenger in 1999 (Tomita et al., 1999). These authors showed that, the crack formation at the grain boundaries and subsequent delamination of the surface was negligible when incorporating αTH into UHMWPE before irradiation. Although the surface hardness increased slightly compared to untreated UHMWPE, a much smaller increase was noted compared to the highly-crosslinked UHMWPE without αTH. Nonetheless, the use of

αTH showed to be promising and resulted in increased interest from the scientific community over the subsequent years, improving the understanding of αTH doping in UHMWPE-based biomaterials, showcasing its biocompatibility, anti-oxidative, and anti-inflammatory properties (Oral et al., 2004, 2005; Parth et al., 2002; Shibata & Tomita, 2005; Wolf et al., 2002). Ultimately, this led to the commercial release of irradiation-crosslinked, αTH-doped UHMWPE for total hip and knee implants in 2007 – 2008 (Kurtz, 2016).

In 1974, Bassett *et al.* reported that using HPC at a temperature of 160 °C and a pressure of 300 MPa, UHMWPE was able to reach a crystallinity of about 70%. This unusually high crystallinity for UHMWPE was achieved due to a phase transition of the PE's orthorhombic phase to the hexagonal phase occurring at the before-mentioned processing conditions, which allowed for the crystals to grow larger before transitioning back to the orthorhombic phase at atmospheric conditions (Bassett et al., 1974). A commercial release of UHMWPE processed with HPC was realised in the 1980s by DePuy Orthopaedics, under the name of Hylamer. Unfortunately, this product showed mixed results in clinical trials and its implant performance remains contested (Huddleston et al., 2010; Kurtz et al., 1999). Although HPC could increase the strength of the material, the decrease in ductility due to the high crystallinity was hypothesised to have a negative impact on the long-term wear resistance. To circumvent the increased wear induced by the high-strength, Oral *et al.* proposed to incorporate antioxidative agents to the wear resistance of HPC-UHMWPE in 2006 (Oral et al., 2006). By incorporating αTH into UHMWPE powder prior to HPC, the HPC-treated samples showed improved wear resistance and mechanical properties, displaying a synergistic effect like that observed with irradiation-crosslinked αTH-doped UHMWPE (i.e., both improved wear/mechanical properties and reduced brittleness compared to undoped UHMWPE). A timeline of the commercially available UHMWPE-based biomaterials used in TJRs is visualised in Figure 1.

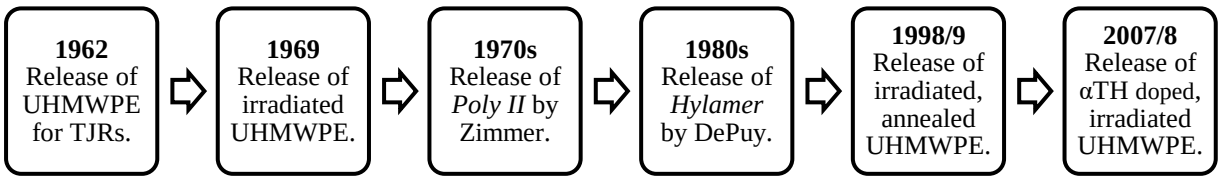


Figure 1. Timeline on the history of commercially available UHMWPE biomaterials used in TJRs.

Prior to the implantation, sterilisation is important to minimize the chance of any microbes being present on the implant before packaging. Besides the sterilisation inherently achieved with, e.g., irradiation-based crosslinking, several alternative sterilisation methods have been reported, such as using ethylene oxide (EtO) diffusion, a steam autoclave (SA), and plasma (Rodrigues et al., 2020). The extent of sterilisation is different for each method and depends on treatment parameters and material compatibility, but all listed methods remain used to meet the sterilisation requirements for medical devices set out in DIN EN 556-1 (i.e., a sterility assurance level of 10^{-6}) (DIN, 2023; IMCD, 2022). Diffusing a mixture of EtO and carbon dioxide near the implant's surface allows for the neutralisation of microbes, to ensure the removal of residual gas, the implants are aerated for 12–24 hours. Costa et al. reported that, when compared to γ-ray irradiation, the use of ethylene oxide resulted in significantly less oxidation (Costa et al., 1998a). However, ethylene oxide was found to be carcinogenic and mutagenic, its use therefore required high safety standards to exclude risk to patients' health. The use of a steam autoclave was proposed as a simple, non-toxic method to ensure sterilisation. Unfortunately, due to the thermo-sensitivity of UHMWPE, using a SA resulted in a change in the implants' dimensions and hydrolysis – limiting its application for UHMWPE-based biomaterials (Clegg & Collyer, 1991). To maintain the thermal stability and reduce the wear generation without the risk of potential toxicity, the use of plasma became increasingly popular and is considered the preferred sterilisation method (Alves et al., 2013; Bistolfi et al., 2021; Goldman & Pruitt, 1998; Nortje, 2021; Patil et al., 2020). Plasma sterilisation can be performed in vacuum chambers or at atmospheric pressure, using a variety of working gases

such as oxygen with hydrogen peroxide, nitrogen, argon, etc. (Shintani et al., 2010). However, the sterilization of the material/implant using plasma is highly parametric-specific, but in general considered faster than most other methods, allowing a log reduction of most microorganisms in approximately one minute. However, plasma sterilisation inherently results in modification of the surface. Etching effects during the plasma treatment also degraded the material surface. It was observed that etching was more frequently present in the amorphous phase, increasing the relative surface crystallinity (Pandiyaraj et al., 2008). To prevent etching, an active screen can be used so the plasma is formed on the active screen instead of on the material surface directly (C. X. Li, 2010; C. X. Li & Bell, 2005). Depending on the working gas, plasma can be used to introduce new functionalities to the material surface. For example, using plasma-nitriding, nitrogen-based functionalities were introduced and can be used for further conjugation – the use of plasma-nitriding of UHMWPE is further discussed in Section 2.2 (Kaklamani et al., 2010; López-Santos et al., 2011).

Unfortunately, sterilisation of the implant cannot fully exclude the presence of microbes in the air during implantation and/or at the implant site (e.g., hip, knee, or shoulder) (Tanoira, 2019). Although it only affects 1-2% of implantations, microbial infection accounts for up to 20% of the implant revisions and is a significant burden on the care system (Ben-Shlomo et al., 2022; Grindy et al., 2019). The main bacteria involved in implant-related infections are coagulase-negative *staphylococci* (30–43%), *Staphylococcus aureus* (12–23%), *streptococci* (9–10%), *enterococci* (3–7%), Gram-negative organisms (3–6%), or anaerobes (2–4%) (Pandey et al., 2000). Patients who endured microbial infection of the implant are linked with pronounced morbidity and recurring infection after revision (Bauer & Zhang, 2016). To reduce the chance of microbial infection, research has been focused towards developing an antimicrobial implant, for example, through ion implantation or by eluting antibiotics (Side et al., 2013; Suhardi et al., 2017). In 2013, Velardi et al. compared the antibacterial properties of

various ions (e.g., Ag, Cu, and Ti) implanted in the UHMWPE surface; it was observed that all ion-implanted surfaces showed an increased bacterial reduction compared to untreated UHMWPE – an increased reduction up to 90% was observed using Ti implanted ions (Side et al., 2013). Next to that, a development by Suhardi *et al.* in 2017 involved two antibiotics, rifampin and vancomycin, which were blended with UHMWPE powder to create an antibiotic-eluting UHMWPE-based biomaterial (Suhardi et al., 2017). In that work, lapine knees infected with *Staphylococcus aureus* were treated with the antibiotic-eluting UHMWPE-based biomaterial and showed a full reduction in bacteria with no detectable side-effects. However, when using antibiotics, the potential concern of developing antibiotic resistance bacterial strains remains an issue for the care system (B. Li & Webster, 2018). More recently, antimicrobial peptides (AMPs) have evolved as a promising alternative to the more commonly used antimicrobial agents (J. Wang et al., 2019). AMPs utilise modes-of-action that lyse the microbial cell membrane, making it difficult for microbes to become resistant. Additionally, various AMPs are native to the human body and show selective toxicity towards bacteria but not human cells. A specifically interesting AMP candidate is KR-12, derived from its parent peptide LL-37 (i.e., a human cathelicidin), as it provides a relatively low-cost, highly antibacterial, and non-cytotoxic AMP for therapeutic use – the use of AMPs is further discussed in free-form in Section 2.3 and immobilised on surfaces in Section 2.4 (Trzcińska et al., 2020; G. Wang, 2008).

Altogether, when comparing the treatments attempted throughout the clinical history of UHMWPE-based biomaterials, the use of αTH doping, plasma-nitriding, and subsequent immobilisation of AMPs to the plasma-treated surface presents a promising concept to enhance the implant performance – whilst minimising the drawbacks (e.g., increased oxidation, reduced mechanical properties, etc.) observed with the other treatments.

2.1.2. Material properties of UHMWPE-based biomaterials

UHMWPE is a subset of the thermoplastic α-olefin ethylene, i.e., an alkene with the general formula [C_nH_{2n}]. The material properties of UHMWPE are rarely found in high-performance polymers, this is due to its simple linear structure and extremely long chains. UHMWPE has attracted significant attention, in both the industrial and medical sectors, as an engineering material for specialty applications. The chemical and physical properties of unmodified UHMWPE have been thoroughly investigated. The properties of UHMWPE vary depending on the manufacturer, due to the use of different processing conditions (e.g., the pressure, temperature, etc.) and additives, complicatedly influencing its properties. Therefore, excessive comparison of the various available grades is typically not considered sensible (Shibata et al., 2006). However, UHMWPE biomaterials used in total joint replacements are only available in two surgical grades (i.e., GUR® 1020 and GUR® 1050). The surgical grades of UHMWPE are produced from premium resins (i.e., without stabilizers and processing aids) according to ASTM F648 and ISO 5834-1 for surgical implants (ASTM, 2021; ISO, 2019).

Chemical properties

UHMWPE does not contain any polar groups and is therefore not able to absorb water and displays poor wetting properties, making bonding to other substrates difficult. In addition, as UHMWPE is aliphatic it inherently cannot take part in π-stacking and is therefore also not susceptible to aromatic solvents. The absence of any functional groups makes UHMWPE highly resistant/unreactive to most chemicals and/or solvents (Chikkali et al., 2017). However, like all polyolefins, UHMWPE is a combustible material. The relatively weak secondary bonding (i.e., van der Waals bonds) among the long PE chains allows for local thermal excitations, which were found to disrupt the crystalline lamellae (Tam & Bhatnagar, 2016). As a result of this, UHMWPE displays a lower heat resistance than most other high-performance polymers. Attempts to improve the thermal stability of UHMWPE involved the use of halogen-

containing compounds (e.g., bromine) or nanoparticles (e.g., carbon nanotubes, nano-clay, etc.) (Handa et al., 1982; W. Zhang et al., 2013). However, such additions frequently resulted in the loss of strength due to lack of interfacial adhesion with the chemically inert UHMWPE. Lastly, most important to its use as a biomaterial in TJRs, unmodified UHMWPE is regarded as non-toxic and its (bio)inert nature results in acceptable biocompatibility – the biocompatibility of UHMWPE will be discussed more in-depth in Section 2.1.4 (Kurtz, 2015).

Physical/Mechanical properties

UHMWPE is a linear semi-crystalline homo-polymer, consisting out of a crystalline phase enclosed within an amorphous phase. UHMWPE used in orthopaedic applications usually has a molecular mass between 3.5 and 7.5 million amu (i.e, atomic mass unit), with a degree of crystallinity between 39–75% as measured by either differential scanning calorimetry or X-ray diffraction (Bracco et al., 2017; Kurtz, 2015). Within the crystalline phase, macromolecules are folded into crystalline lamellae. Additionally, tie molecules connect neighbouring crystalline phases (Edidin et al., 1999). The tie molecules will predominantly determine the ductility of UHMWPE, being the 'cement' that keeps the crystalline 'bricks' together (Lustiger & Markham, 1983). A simplified schematic of this is shown in Figure 2, showing the tie molecules (i.e., chains ending in neighbouring crystalline lamellae), cilia (i.e., loose chains suspended from lamellae), and loose loops (i.e., chains ending in the same lamellae) (Bartczak & Galeski, 2010). Typically, the crystalline lamellae found in UHMWPE are 10-50 nm in thickness and 10-50 μm in length (Oral et al., 2011). Finally, an all-trans non-crystalline interfacial phase is embedded within the amorphous phase - located on/near the crystalline lamellae (Barron & Birkinshaw, 2008).

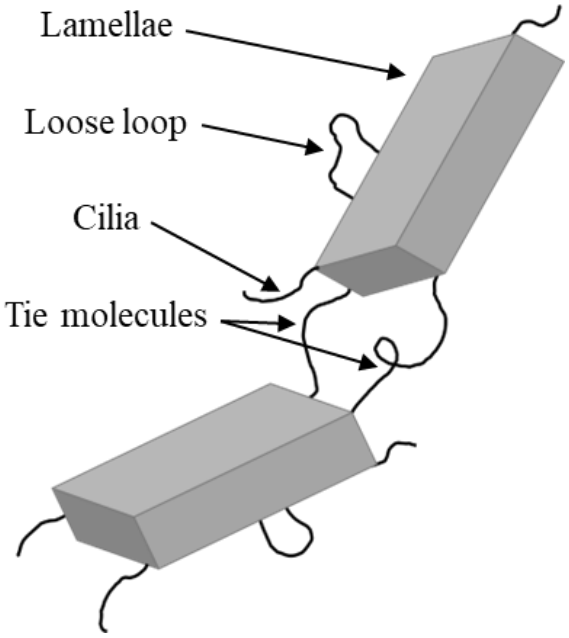


Figure 2. Simplified schematic of tie molecules connecting neighbouring crystalline lamellae, cilia suspended from the lamellae, and loose loops ending in the same lamellae (Bartczak & Galeski, 2010).

When developing implants, it is crucial to maintain the desired mechanical properties over the expected lifetime. Therefore, implants manufactured from UHMWPE must meet mechanical properties set by ASTM F 648-04 as displayed in Table 1 (ASTM, 2021). The elastic properties (i.e., modulus of elasticity and yield stress) and plastic properties (i.e., the elongation at break and ultimate tensile strength) are largely influenced by the morphology of the crystalline phase and the amorphous phase of UHMWPE, respectively (Shibata et al., 2006). Regarding arthroplasty, most deformation in UHMWPE is present during the 'bedding-in' period (i.e., the first 1-2 years after the placement of the implant), where the observed creep deformation is a consequence of the tensile load of the UHMWPE acetabular socket onto the metal or ceramic femoral head as illustrated in Figure 3 (Brach del Prever et al., 2009). At room temperature, the deformation begins with the amorphous phase, but is rapidly exhausted and will start to deform the crystalline lamellae (Lin & Argon, 1994). The ductility of UHMWPE is seen as a drawback for its usage as an implant material because it is relatively easily deformed – especially at high temperatures or stress (Liu et al., 2013). Stress will alter the

microstructure of UHMWPE, influencing the implants' mechanical behaviour continually during its lifetime inside the body. The typical physical/mechanical properties of UHMWPE-based biomaterials observed in the literature are presented in Table 2 (Edidin & Kurtz, 2000).

Table 1. Standard specification for fabricated UHMWPE-based surgical implants, according to ASTM F 648-04 (ASTM, 2021).

Property (Unit)	Method	Requirement
Density (g/cm^3)	ASTM D-792	0.927 – 0.944
Ash (mg/kg)	-	< 300
Tensile yield strength (MPa)	ASTM D-638	> 19
Tensile ultimate strength (MPa)		> 27
Elongation (%)	ASTM D-638	> 250
Izod Impact Strength (kJ/m^2)	ASTM-648 Annex A1	> 25
Charpy Impact Strength (kJ/m^2)	ISO 11542-2	> 30

Table 2. Typical physical/mechanical properties of UHMWPE observed in literature (Edidin and Kurtz, 2000).

Property (Unit)	Value
Crystallinity (%)	39 – 75
Izod Impact Strength (kJ/m^2)	No break
Melting temperature (°C)	125 – 138
Molecular weight (10^6 g/mol)	2 – 6
Tensile modulus of elasticity (GPa)	0.8 – 1.6
Tensile ultimate elongation (%)	350 – 525
Tensile yield strength (MPa)	21 – 28
Tensile ultimate strength (MPa)	39 – 48

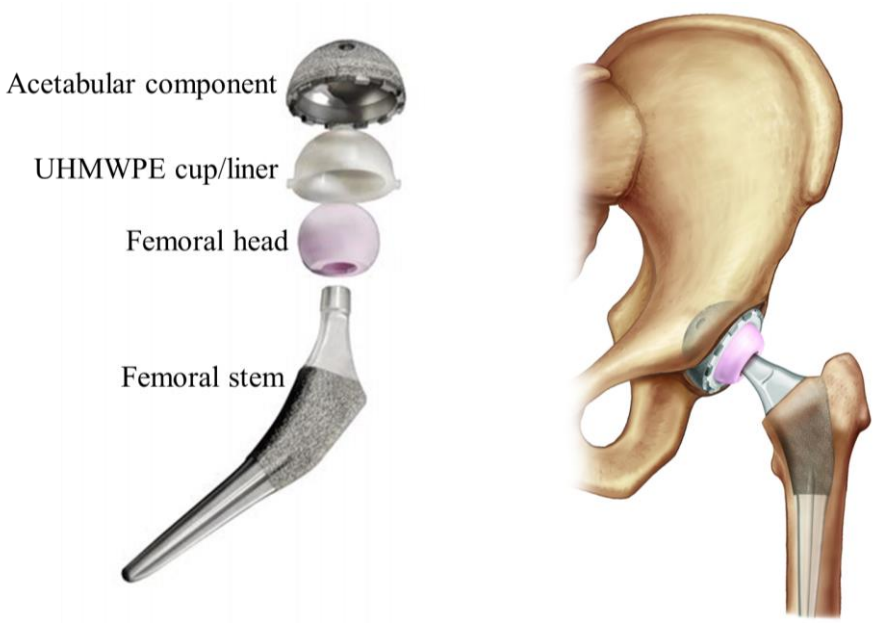


Figure 3. Schematic of (left) total hip replacement components and (right) their placement inside the body – figure was adapted from (OrthopaedicSpecialists, 2022).

As discussed in Section 2.1.1., the highly-crosslinked and annealed UHMWPE developed in 1998 was the first major improvement compared to unmodified UHMWPE (Dumbleton et al., 2009; Oral et al., 2011). As demonstrated by Grobbelaar *et al.* following a sand-slurry abrasion test , the abrasion resistance of the crosslinked UHMWPE increased up to 30% when compared to its unmodified counterpart (Grobbelaar et al., 1978). However, with increased radiation dose and corresponding crosslinking, adverse effects were noted on the ductility, elongation at break, and impact strength of UHMWPE (J. Fu et al., 2011; Kurtz, Pruitt, et al., 1999; Oral, Malhi, et al., 2006). These properties were likely reduced as cross-linking limits the maximum chain stretch and corresponding deformation ability of UHMWPE. Gencur *et al.* have also reported that the uniaxial failure strain of UHMWPE decreases linearly with increasing radiation dose (Gencur et al., 2003). Next to that, Kurtz *et al.* examined γ-ray irradiated UHMWPE annealed at various temperatures and concluded that annealing can adversely affect the mechanical properties (i.e., the elongation at break and ultimate tensile strength) (Kurtz et al., 2003). As shown in Table 3, the authors reported that the decrease in yield and the ultimate strength of 150°C annealed UHMWPE was higher than that observed

with the samples annealed at 110°C and 130°C. However, the ultimate elongation of 150°C annealed UHMWPE was the highest from all samples, due to the partial melting observed at this temperature – which allows for reduction of defects and internal stress relief. Although annealing provided a solution for the removal of free radicals, the decrease in material performance was a drawback and this raised the need for a process without annealing.

Table 3. Effect of annealing on the mechanical properties of γ-irradiated UHMWPE (Kurtz et al., 2003).

Annealing (°C)	Tensile yield strength (MPa)	Tensile ultimate strength (MPa)	Tensile ultimate elongation (%)
RT	23.2 ± 0.2	47.6 ± 2.0	238 ± 13
110	23.0 ± 0.3	47.3 ± 1.5	230 ± 12
130	22.6 ± 0.2	48.5 ± 1.5	231 ± 13
150	19.5 ± 0.3	43.9 ± 3.9	246 ± 12

2.1.3. Doping of UHMWPE with α-tocopherol

Prior to further investigating the use of αTH in UHMWPE-based biomaterials, it is important to understand the functioning of αTH in free-form. αTH is an extremely potent, naturally occurring antioxidant, fundamental for human metabolism (Combs & McClung, 2017). As illustrated in Figure 4A, once a lipid radical (L·) is formed due to a reaction with a free radical (R·; e.g., from reactive oxygen species (ROS)), the lipid radical typically oxidizes into a lipid peroxyl radical (LOO·) and ultimately a lipid hydroperoxide (LOOH) (Niki, 2014; Novo & Parola, 2008; Yamauchi, 1997a). The lipid hydroperoxide may break down into a mixture of lipid peroxyl radicals, lipid alkoxyl radicals (LO·) or regular lipid radicals, propagating the cascade of oxidation and the formation of free radicals. The various free radicals (i.e., L·, LO·, and LOO·) that are present may also form non-radical intermediates (e.g., L–L, L–OO–L, etc.). Within the human body, αTH reduces the accumulation of ROS and free/lipid radicals (Oral & Muratoglu, 2016). This is possible as the hydroxyl group (OH) on

the phenol ring of αTH donates its hydrogen to quench a surrounding ROS and free/lipid radicals, which forms an α-tocopheroxyl radical (αT·) as visualised in Figure 4B (Niki, 2014; Yamauchi, 1997a). The subsequent reactions of an α-tocopheroxyl radical with other radicals are also presented in Figure 4C, introducing several forms of lipid-αTH adducts (depending on type of radical, i.e., L·, LO·, or LOO·) and αTH dimers (i.e., αT–αT). The α-tocopheroxyl radical can also revert to αTH via a redox reaction with another H-donor, e.g., with Vitamin C/ascorbic acid as occurs inside the body (Oral & Muratoglu, 2016). Thus, in theory, αTH can inhibit two free radicals from propagating further and prevent the cascade of oxidation.

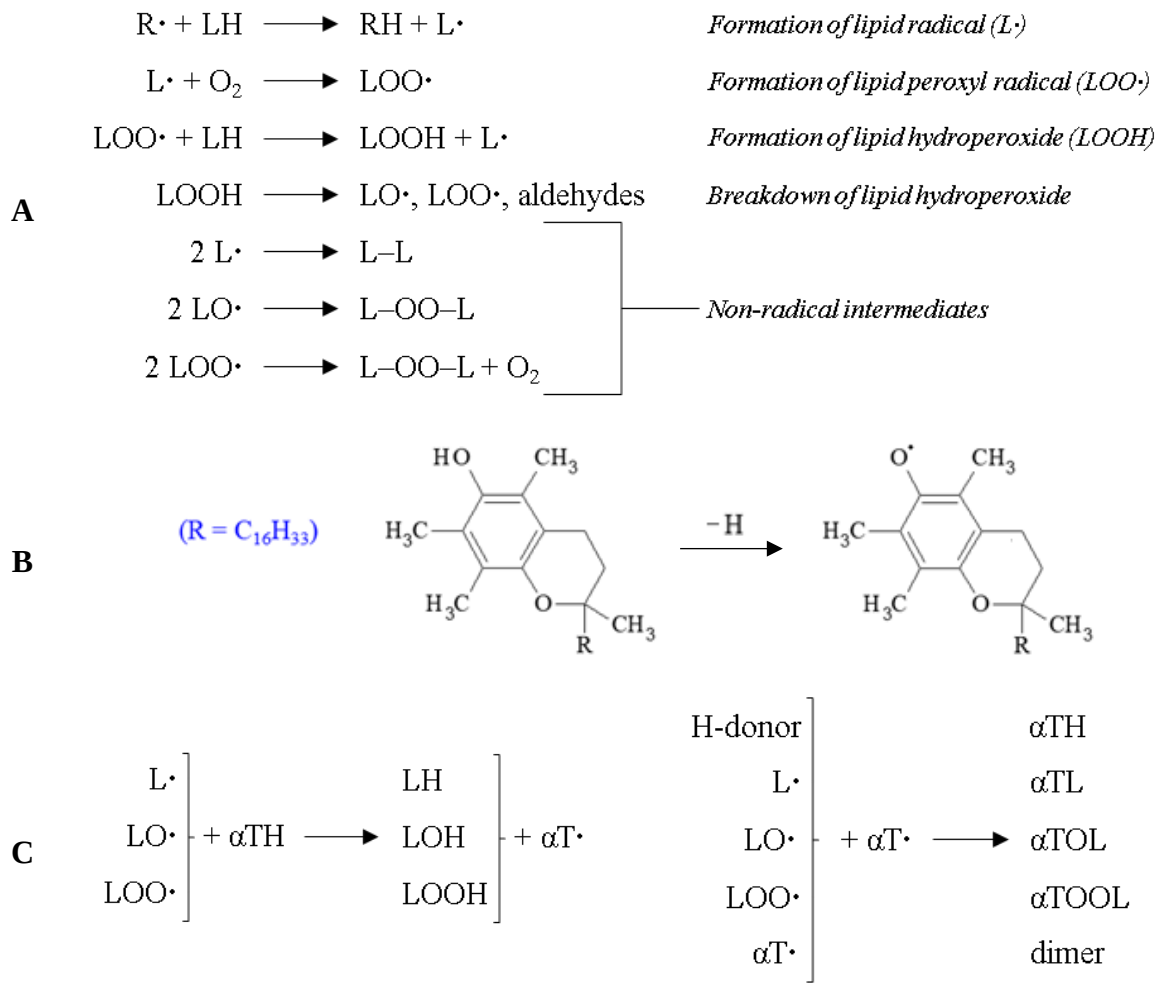


Figure 4. Simplified reaction scheme of (A) lipid (per)oxidation, (B) the H-donation from the hydroxyl group in the phenol ring of αTH, and (C) the reaction scheme of αTH (Combs & McClung, 2017).

The formation of free radicals and subsequent oxidation in UHMWPE is different than of that observed in cell membranes, especially during treatments with sufficient energy to initiate electron-induced fragmentation (e.g., by radiation-based sterilisation/crosslinking or ion bombardment during plasma treatments). The radiation-induced crosslinking/oxidation process and the quenching process of αTH were examined for UHMWPE and visualised in Figure 5 and 6, respectively (Bracco & Oral, 2011; Shibata et al., 2006). Rupture of the UHMWPE chains (i.e., chain scission) forms two primary alkyl radicals, denoted as R(1°) in Figure 5. The carbon-centred alkyl radicals specifically allow for the formation of H/Y-crosslinks and mono-alkyl vinyl endcaps, but can also produce alkyl radicals (Bracco & Oral, 2011). As shown by Zhao *et al.* using electron spin resonance (ESR), the major free radical product in UHMWPE following irradiation is the secondary alkyl radical, denoted as R(2°) in Figure 5 (Y. Zhao et al., 2010). These authors also demonstrated that the secondary alkyl radical initially converted into allyl radicals through radical migration and subsequently into polyenyl radicals. The alkyl to allyl radical conversion plateaued after ~50 days of storage, following the plateau the allyl to polyenyl radical conversion rate increased and was ultimately the only type of free radical left after >100 days of storage in vacuum (Y. Zhao et al., 2010). Next to that, the alkyl radical also specifically allows for the formation of di-alkyl trans-vinylene (Bracco & Oral, 2011). Naturally, both carbon-centred and alkyl radicals are sensitive to oxidation into a peroxy radical and hydroperoxides, ultimately resulting in the formation of various oxidation products (e.g., alcohols, ketones, acids, and esters. In vacuum the relative radical concentration in UHMWPE decreased to ~20% after 140 days (the max. duration of this study), whereas about ~4% was left after an open-air atmosphere (Y. Zhao et al., 2010).

As both (phospho)lipids and UHMWPE are both (almost) entirely composed out of hydrocarbon chains, a practically identical quenching/antioxidative functioning of αTH can be expected when incorporated in UHMWPE-based biomaterials (Bracco & Oral, 2011). For

example, as observed for the (phospho)lipids, it is believed that αTH is capable of quenching alkyl macroradicals and peroxide radicals (Bracco et al., 2007; Costa et al., 2009). As displayed in Figure 6, the formed α-tocopheroxyl radical may interact with another alkyl macroradical to form an adduct, hindering the oxidation cascade in irradiated UHMWPE even at small amounts of αTH (e.g., 0.05 wt%) (Bracco et al., 2007; Kurtz et al., 2009; Lerf et al., 2010). As briefly discussed in Section 2.1.1., doping UHMWPE with αTH was proposed by Aoyama *et al.* in 1999 as an alternative to post-irradiation annealing, for the removal of free radicals introduced during irradiation to prevent the fatigue loss, ensure the oxidative stability of the material, and avoid crack formation at grain boundaries resulting in delamination of the surface (Tomita et al., 1999). The promising results on the use of αTH incorporated in UHMWPE-based biomaterials resulted in growing interest from the scientific community, with further research showcasing its antioxidative, biocompatibility, and anti-inflammatory properties (Oral et al., 2004, 2005; Parth et al., 2002; Ren, Wang, Chen, et al., 2020; Shibata & Tomita, 2005; Wolf et al., 2002; Wolf et al., 2007; Zingg & Azzi, 2012). For example, Oral *et al.* reported that the free radical content in αTH-doped UHMWPE stabilised after one month of shelf ageing, whereas this decay continued for seven months in undoped UHMWPE – limiting the extent to which the material will be oxidised and the corresponding decrease in performance (Oral et al., 2006). Additionally, Sakoda *et al.* demonstrated that the incorporation of αTH contributed to an improved resistance towards delamination of the UHMWPE surface, even after accelerated ageing (Sakoda et al., 2019). The improved wear resistance and reduced free radical content also impacts the long-term biocompatibility, the effects of which are further discussed in Section 2.1.4.

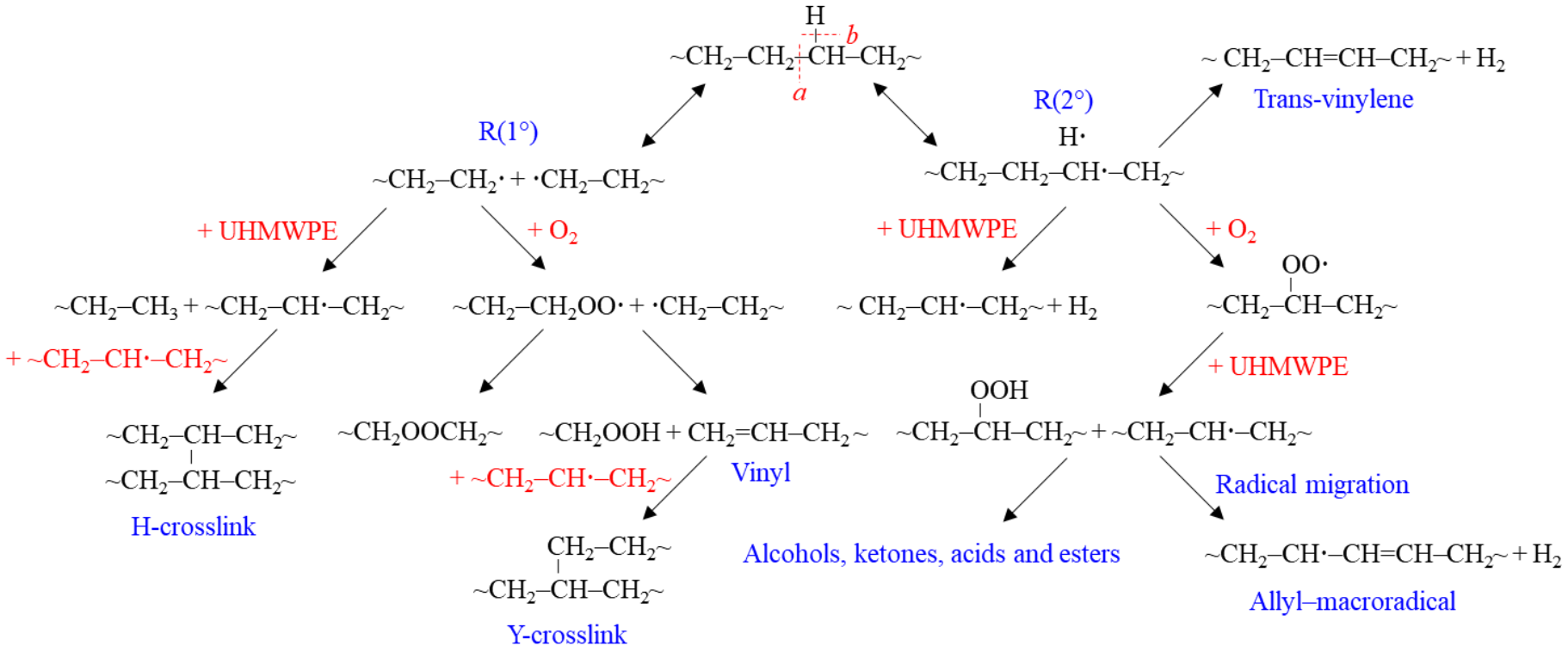


Figure 5. Simplified reaction scheme of the oxidation process of UHMWPE induced by irradiation (Bracco & Oral, 2011).

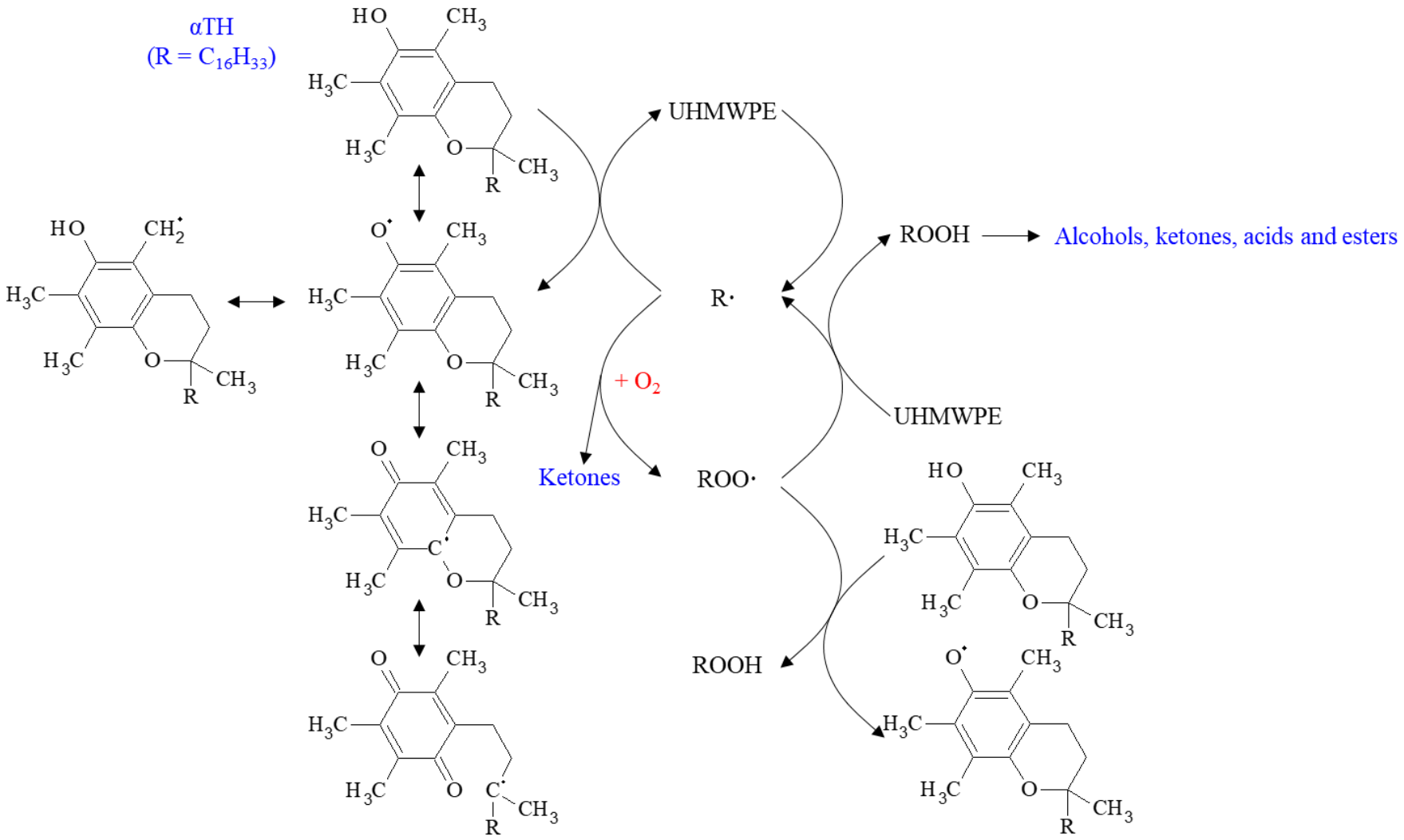


Figure 6. Simplified reaction scheme of the quenching process of αTH in UHMWPE (Shibata et al., 2006).

2.1.4. Biocompatibility of UHMWPE-based biomaterials

To prevent chronic inflammation and subsequent implant failure, it is important that the implant is biocompatible. As discussed in Section 2.1.2., UHMWPE is an chemically/bio-inert material that displays acceptable biocompatibility (Kurtz, 2015). Over its clinical history of over five decades as a biomaterial in TJRs, research has been dedicated to improving the understanding and enhancing the biocompatibility of UHMWPE-based biomaterials during its lifetime inside the body as discussed in Section 2.1.1. Implantation initiates a series of events that may result in (chronic) inflammation and/or other complications (Davenport Huyer et al., 2020; Rahmati et al., 2020). As a result, the biocompatibility of UHMWPE-based biomaterials changes over time, as surface oxidation will take place once the material is implanted. As discussed in Sections 2.1.1-3, oxidation of the material further negatively influences the implant performance and increases the possibility of implant failure – due to an increased degradation rate and subsequent debris formation at the implant surface (Baena et al., 2015; Kurtz, 2015). Surface oxidation can be further accelerated due to degradation induced by both mechanical stress (i.e., from the tensile load of the UHMWPE acetabular socket onto the metal or ceramic femoral head) and attacks from microorganisms in the periprosthetic tissue (i.e., tissue in close contact with the implant) (Hallab & Jacobs, 2020).

More specifically, when the biomaterial is implanted, a foreign body response (FBR) is triggered (Kämmerling et al., 2021; Martin & García, 2021). The FBR involves the interaction of the implant with blood, formation of a protein layer on the implant, the creation of a temporary protein scaffold, the recruitment of immune cells, and the occurrence of (both acute and chronic) inflammation. The host immune system includes both innate immune cells (i.e., cells with a non-specific immune response, like neutrophils, macrophages, dendritic cells, and natural killer cells) and adaptive immune cells (i.e., cells with a targeted immune response that generate long-lasting memory, such as T-cells and B-cells) (Kämmerling et al., 2021). The

immune cells detect tissue injuries through pattern recognition receptors (PRRs) and respond to damage-associated molecular patterns (DAMPs) or pathogen-associated molecular patterns (PAMPs) (Dellacherie et al., 2019). DAMPs are released from stressed, damaged, or dying cells, while PAMPs originate from invading microbes. Antigen presenting cells (APCs; i.e., macrophages and B cells) possess PRRs that can bind to PAMPs, leading to the activation of inflammatory signalling pathways that further activates the innate immune system (Yatim et al., 2017).

When the host's blood meets the implant, serum proteins such as fibrinogen, the von Willebrand factor, immunoglobulin G, and other immunomodulatory proteins adhere and are absorbed onto the surface of the implant (Kizhakkedathu & Conway, 2022; Rahmati & Mozafari, 2018). The immune response to this tissue damage begins with the arrival of platelets and neutrophils, which play a crucial role in hemostasis (i.e., the physiological process that stops bleeding through platelet aggregation, blood vessel constriction, and clot formation) and eliminating foreign substances/particles (i.e., via phagocytosis, degranulation, and/or the formation of neutrophil extracellular traps), respectively (Rosales, 2018). Phagocytosis is a process where the cells engulf substances/particles with their plasma membrane, form an internal compartment known as a phagosome, “digest” the substances/particles using enzymes, and discharge the digested particles as residual waste/antigens (James et al., 1999; Renò et al., 2003). Degranulation is a process where intracellular granules fuse with the plasma membrane and release the contents of their granules into the surrounding extracellular space, these granules contain various biologically active molecules (e.g., enzymes, inflammatory mediators, and signalling molecules) (Othman et al., 2022). The formation of neutrophil extracellular traps (NETs) is a unique cell death process where the neutrophil's nuclear membrane disintegrates, its chromatin is expelled into the extracellular space and forms a meshwork that is able to immobilize/trap pathogens, ultimately preventing their spread and promoting their degradation

by antimicrobial proteins contained within the NETs (Rosales, 2018). Neutrophils have a quick turnover rate, phagocytosis-induced cell death and subsequent clearance of the dead cells by other immune cells is crucial for resolving the inflammatory response, allowing the healing process to proceed (McCracken & Allen, 2014).

Macrophages also play a central role in the FBR, and they can exhibit either a pro-inflammatory (M1-like) or anti-inflammatory (M2-like) phenotype depending on the stage of tissue repair (Kämmerling et al., 2021; Martin & García, 2021). M1-like macrophages attempt to break down the substance/particle by releasing ROS and degradative enzymes. If the particle is too large to be internalised, macrophages aggregate to create foreign body giant cells (FBGCs; i.e., non-cancerous inflammatory masses, also known as pseudotumors), enhancing their phagocytic ability (James et al., 1999; Renò et al., 2003). During the early stages of the FBR, macrophages display an M1 phenotype, but as they fuse into FBGCs, they typically switch to an M2 phenotype due to factors like interleukin (IL) 4 cytokine (i.e., small peptides and/or proteins that facilitate cell-to-cell communication) secretion from activated T cells (Kämmerling et al., 2021). The FBGCs secrete factors that attract fibroblasts, leading to the formation of a collagenous fibrotic capsule around the biomaterial. In some cases, uncontrolled fibroblast activation can result in excessive collagen deposition and tissue fibrosis. The formation of this fibrotic capsule can prevent proper implant-tissue integration and lead to implant failure. Particle-stimulated macrophages will also increase bone resorption-related cytokine production, accelerating various potential degradative mechanisms (Ingham & Fisher, 2005). This is since osteoclasts (i.e., cells responsible for bone resorption) originate from the same progenitors (i.e., un/partially-differentiated cells yet to develop into specialized cell types) as macrophages, and at least some macrophages within the periprosthetic tissue can differentiate into osteoclasts – both mechanisms will lead to periprosthetic osteolysis (Ingham & Fisher, 2005; Stessuk et al., 2021).

In parallel to the activation of macrophages, the release of TNF-α (i.e., a pro-inflammatory cytokine) and other cytokines induced by the immune response leads to the recruitment and migration of osteoclast precursors (N. Yang & Liu, 2021). Osteoclast precursors are bone-resorbing cells that contribute to bone remodelling. At the implant site, these precursors differentiate into mature osteoclasts through a process mediated by RANKL (Tanaka et al., 2005; Teitelbaum, 2000). RANKL is produced by various cells including osteoblasts, osteocytes, and activated T-cells, and binds to RANK receptors on osteoclast precursors, promoting their activation and maturation. The activated osteoclasts, initiate the resorption of bone tissue surrounding the implant and results in periprosthetic bone loss (Ingham & Fisher, 2005). Additionally, the activity of osteoclasts releases inflammatory mediators (such as matrix metalloproteinases and ROS), which further contribute to tissue damage and inflammation (X. Ren et al., 2022).

Moreover, the mechanical stress placed on the UHMWPE implant during normal joint movement can cause wear and tear (Sawae, 2017). This mechanical wear generates UHMWPE particles and other debris, which act as additional stimuli for the immune system. As discussed above, macrophages attempt to phagocytose these particles, perpetuating the release of pro-inflammatory cytokines and sustaining the inflammatory response. The chronic inflammation and the presence of wear particles can disrupt the balance between RANKL and OPG (i.e., osteoprotegerin, a bone resorption inhibitor which binds to RANKL and prevents the activation of osteoclast precursor cells, thereby preventing excessive bone loss), resulting in an increased RANKL/OPG ratio. The increased ratio promotes further activation of osteoclasts and is said to aggravate bone resorption (Massaccesi et al., 2019). Overall, the persistent release of pro-inflammatory cytokines, ongoing osteoclast activity, and the presence of wear particles sustain chronic inflammation around the implant. This chronic inflammation can lead to long-term complications, including bone loss, implant loosening, and impaired implant function.

Costa *et al.* provided an extensive study on the biodegradation of 62 clinically-retrieved UHMWPE tibial plateaux and acetabular cup inserts, sterilised with either γ-ray irradiation or ethylene oxide diffusion, which were retrieved due to a variety of medical reasons (e.g., wear, loosening, or sepsis) (Costa et al., 1998b). These authors confirmed that *in-vivo* degradation and subsequent oxidation increased the debris generation due to decreased abrasion/wear resistance, it was also shown that the oxidation was more significant in γ-ray irradiated samples than observed with the ethylene oxide samples. Next to that, it was observed that the shearing deformation (i.e., the stress experienced by the material during activities such as walking) at the articulating surface is the main area of the degradation and accelerates the delamination, breakage, and debris generation, resulting in increased osteolysis and subsequent implant loosening. This study showed, yet again, the importance of incorporating an antioxidant in the UHMWPE-based biomaterials to minimise oxidation and delamination, extent the implants' lifetime inside the body, and prevent implant failure.

Next to a decrease in oxidation, the incorporation of αTH showed no negative impact on the biocompatibility. By counting the viable cells (i.e., those showing metabolic/ mitochondrial activity) using a XTT cell viability assay, Wolf *et al.* demonstrated that the incorporation of αTH in LDPE did not affect the cell proliferation of L929 mouse fibroblasts (i.e., not cytotoxic) or their membrane integrity (Wolf et al., 2002). After the cytotoxicity testing, αTH and its transformation products formed during processing (in this case, extrusion) were extracted with heptane from the LDPE samples and showed no signs of genotoxicity following an Ames-test (i.e., an assay used to test if a given chemical can cause DNA mutations). Although there was no sign of direct cell toxicity, hemalum staining revealed that the cell adhesion on the αTH-doped LDPE was reduced to 37% relative to the control (i.e., an empty polystyrene well in the culture plate). Additionally, the L929 cells were smaller in diameter and had a more rounded morphology when compared to the control – likely due to

the hydrophobicity of αTH. A reduction in adhesion was also observed by Banche *et al.* with bacteria commonly involved in periprosthetic joint infections (e.g., *Staphylococcus epidermidis, Staphylococcus aureus* and *Escherichia coli*) (Banche et al., 2011, 2014, 2015). Standard, αTH-doped, and oxidised UHMWPE were suspended and incubated in bacterial suspensions for two days, after which the bound bacteria were quantified through the Miles and Misra method after sonication (Banche et al., 2011). With the *Staphylococcus epidermidis* adhesion assays, αTH-doped UHMWPE demonstrated ~12% and ~20% less bacterial adherence when compared to regular and oxidised UHMWPE, respectively. This indicated that the incorporation αTH changed the cell/bacterial adhesion process and may (partially) decrease the risk of infection. Next to that, confirmed by corresponding analysis with FTIR, it was observed that surface oxidation facilitated bacterial adhesion. In another study, Wolf *et al.* investigated the cytotoxicity of standard and αTH-doped UHMWPE towards HF-SAR and GSJO human fibroblasts (Wolf et al., 2007). The cytotoxicity was evaluated following a WST-1 cell viability assay over one week, which remained similar between the UHMWPE samples. Contrary to the mouse fibroblasts, the spreading, adherence, and morphology of the human fibroblasts were not changed relative to the control.

The incorporation of αTH may also reduce the occurrence of inflammation and osteoporosis/osteolysis by preventing the activation of NF-κB (i.e., a transcription factor that binds to DNA and regulates gene expression, cytokine production and cell survival) (Nazrun et al., 2012). For example, Ahmad *et al.* investigated the impact of αTH on the release of bone resorption-related cytokines IL-1 and IL-6 with an oxidative stress model (i.e., the FeNTA model, which uses an iron-containing oxidant) in rats (Ahmad et al., 2005). The results of this study demonstrated that the presence of αTH reduced the levels of interleukin 1 and 6, either by directly quenching ROS/free radicals or by enhancing the native antioxidative enzymes present within the bone. Furthermore, Galliera *et al.* investigated the biological response of

human osteoblast-like cells (i.e., *Saos-2*) to experimentally generated wear debris, from a simulated prosthetic joint for a variety of UHMWPE-based implants (Galliera et al., 2018). The experimentally generated wear debris is more representative of the debris generated *in-vivo* when compared to the use of commercially-purchased particles. The generation of "real" debris for such biological assays is important as the cellular response is dependent on the particle size (Bichara et al., 2014). More specifically, particles smaller than 10 μm undergo phagocytosis by macrophages and consequently produce inflammatory mediators (i.e., promoting an anti-inflammatory response) (Green et al., 2000; Matthews et al., 2000; Shanbhag et al., 1995; Zhang et al., 2001). On the other hand, particles around 0.24–7.2 μm display pro-inflammatory behaviour (i.e., increasing the present inflammation). The cup inserts for which debris was generated included those sterilised following irradiation or ethylene oxide, with and without crosslinking, and with and without αTH doping (Galliera et al., 2018). These authors found that, contrary to UHMWPE that was sterilised following γ-ray/*e*-beam irradiation or ethylene oxide, the wear debris of UHMWPE doped with αTH positively impacted the osteoimmunological response of the human osteoblasts as it suppresses the production of RANKL (i.e., a receptor activator of NF-κB) and consequently reduces the chance of implant loosening induced by wear debris.

Building upon insights gained over the past few decades, most recent work focussed on improving the biocompatibility of UHMWPE-based biomaterials by reducing wear generation and introducing bio-activity (i.e., having a direct impact on biological processes) – for example, by utilizing antioxidants (e.g., vitamin C, polyphenols, etc.), surface plasma treatments, (nano)composites, or a combination of these (Catauro et al., 2020; Chaichi et al., 2019; Hussain et al., 2022; Naresh Kumar et al., 2016; Salari et al., 2019; Turicek et al., 2021; F.Y. Wang et al., 2021). For example, Salari *et al.* demonstrated that the biocompatibility and osteo-conductivity (i.e., the ability of a material to provide a supportive framework and integrate with

surrounding bone tissue) were improved for a UHMWPE-based nanocomposite containing hydroxy apatite (HAp; 10 wt%; i.e., a natural, bio-active form of calcium phosphate, which is known to integrate with surrounding biological tissues and promote the integration of implants) and zirconia (2, 6, and 10 wt%), which was evaluated following a MTT cell viability assay using human MG-63 osteoblast-like cells (i.e., bone forming cells) and by measuring the alkaline phosphatase concentration (ALP; i.e., an enzyme produced by and accelerates the activity of osteoblasts) using an AUDIT-KIT, respectively (Salari et al., 2019). Although the unmodified UHMWPE demonstrated >95% cell viability after one week, the modified samples showed increased cell viability and ALP concentrations. The composite with HAp and 10 wt% zirconia demonstrated the best biocompatibility results, with an increase of ~6.5% in cell proliferation and ~13% in ALP concentrations when compared to unmodified UHMWPE (Salari et al., 2019). In a different study, Catauro *et al.* developed an UHMWPE-based nanocomposite using paraffin oil (2 wt%) and a carbon nano-filler (0.1-2 wt%), which demonstrated increased biocompatibility for murine NIH-3T3 fibroblast cells with a MTT cell viability assay (Catauro et al., 2020). When compared to unmodified UHMWPE, the best nanocomposite was filled with 1 wt% carbon nano-filler, which demonstrated ~10% increase in cell viability and 57% reduction in the specific wear rate as determined in a bovine serum medium. However, achieving a homogeneous dispersion and avoiding filler coalescence remains a concern in the production of these nanocomposites (Catauro et al., 2020). The issues associated with (nano)composites are not experienced by plasma-treated UHMWPE-based components, whilst the treatment inherently serves as a sterilisation method and still allows for the improvement of the biocompatibility and wear resistance. As shown by Chaichi *et al.*, a cold plasma treatment of UHMWPE with a handheld piezoelectric direct discharge (PDD) device in an open air atmosphere improved the tribological wear rate and biocompatibility (Chaichi et al., 2019). When compared to the unmodified UHMWPE, the plasma-treated

UHMWPE sample presented a 60-fold reduction in its wear volume rate using a pin-on-disc setup, and a three-fold increase in the cell viability of human adipose-derived stem cells according to a live/dead cell staining assay.

2.2. Plasma-nitriding of UHMWPE-based surfaces

Plasma-based surface modification is a processing technique used to sterilise, crosslink, or form functional groups on a material surface, predominantly by adsorption/diffusion of plasma (i.e., ionized gas mixtures) onto a material surface. Depending on the working gas from which the plasma is generated, a variety of functional groups can be introduced to the material surface. For example, with plasma-nitriding (i.e., glow-discharge nitriding) using a nitrogen (N_2) and hydrogen (H_2) working gas, nitrogen-based functionalities are introduced (Kaklamani et al., 2010; López-Santos et al., 2011). Subsequently, the introduced functionalities may be used for further surface decoration, as proposed in this work. The use of plasma-nitriding offers several advantages over other nitriding methods, for example, when compared to nitrocarburizing (i.e., salt bath nitriding) of metals using caustic cyanides and gas nitriding using ammonia – as both of these techniques use and/or produce toxic precursors/gases (Davis, 2001; Funatani, 2004; Peng et al., 2010). In contrast, plasma-nitriding allows the direct use of the nitrogen-hydrogen working gas for surface functionalisation and, when compared to nitrocarburizing and gas nitriding, plasma-nitriding uses a relatively small amount of gas to achieve surface functionalisation. In addition, plasma-nitriding also allows for improved control and repeatability over the surface treatment, as the electrical power and working gas ratios used during plasma-nitriding can be readily regulated – resulting in a more uniform treatment of the surface (Mittemeijer & Somers, 2014; Pye, 2003; Z. Xu et al., 1990). In contrast to caustic cyanides/ammonia, the by-products using a nitrogen-hydrogen working gas are non-toxic, which is why plasma-nitriding is considered an environmentally friendly

technology (Bell & Dearnley, 1994; Mittemeijer & Somers, 2014). Due to its non-toxic nature, plasma-nitriding has received increased industrial attention since its introduction (Pye, 2003).

As briefly mentioned in Section 2.1, next to its use in surface functionalisation, plasma has been used for the sterilisation of UHMWPE-based biomaterials and the bombardment of the material surface with the ionized gas mixtures can also remove impurities (e.g., removing dust and/or particles present after polishing) (Burkstrand, 1998). Next to that, the use of plasma (nitriding) offers surface functionalisation and improves mechanical properties, similar to irradiation/chemical-crosslinking, but at faster processing speeds, without the use of wet chemistry, and with reduced environmental impact (Booth et al., 2022). Although the duration of the observed plasma treatments varied a lot, all of the observed treatments were under 60 minutes and most frequently between 5-15 minutes (Chaichi et al., 2019; More et al., 2020; Naresh Kumar et al., 2016; Turicek et al., 2021). On the other hand, irradiation/chemical-crosslinking treatments often take 60 minutes or more – which excludes the time required for annealing afterwards (J. Han et al., 2022; Kurtz, Pruitt, et al., 1999; Wen et al., 2022). Plasma-nitriding of polymers is typically performed under vacuum or ambient atmosphere, the treatment temperature is confined by the melting point of the polymer (Bhat & Upadhyay, 2002; Kaklamani et al., 2010; Kauling et al., 2009). Due to this, plasma modification of most polymers is limited to a penetration depth of a couple of hundred nanometres to a few microns, meaning that the introduced physical and chemical modifications are almost exclusively observed towards the (sub-)surface of the material and generally do not affect the bulk properties (Bhat & Upadhyay, 2002; Chaichi et al., 2019). Many surface properties can be altered, such as biocompatibility, hardness, hydrophilicity, surface charge, surface roughness and wear resistance (Chu et al., 2002; More et al., 2020). Some experimental setups that allow the formation of plasma are presented in Figure 7, all setups consist out of an anode and cathode, and the working gas serves as the conductive medium (Roth, 1995).

Besides the working gas in its neutral and ionised form, the formed plasma will consist out of a mixture of active molecules (e.g., radicals and/or excited atoms), free electrons, and (re)combination products of the ionised working gas (Hirohata et al., 2001; Kambara et al., 2008; Lebedev et al., 2010; Mannella, 2004; Tálský et al., 2017). To stabilise the formation of plasma, it is important to maintain consistent ionisation of the working gas between the anode and cathode. Plasma with a high degree of ionisation is dominated by collisions of active molecules, but plasma with a low degree of ionisation is dominated by collisions of active molecules with neutral molecules. The degree of ionisation is largely dependent on the atmosphere at which the plasma is generated, as this influences the mean free path of the ionised molecules (Massines et al., 2003). At atmospheric pressure the molecules in the working gas will have a relatively small mean free path, limiting the momentum of the molecules and resulting in minimal collusions of molecules. At low pressures around 0.01 Pa, the mean free path of the molecules is relatively large, but this also limits the collisions of the molecules due to the large distance between the neighbouring molecules. In both of these cases (i.e., at atmospheric and very low pressure), it is difficult to maintain consistent ionisation of

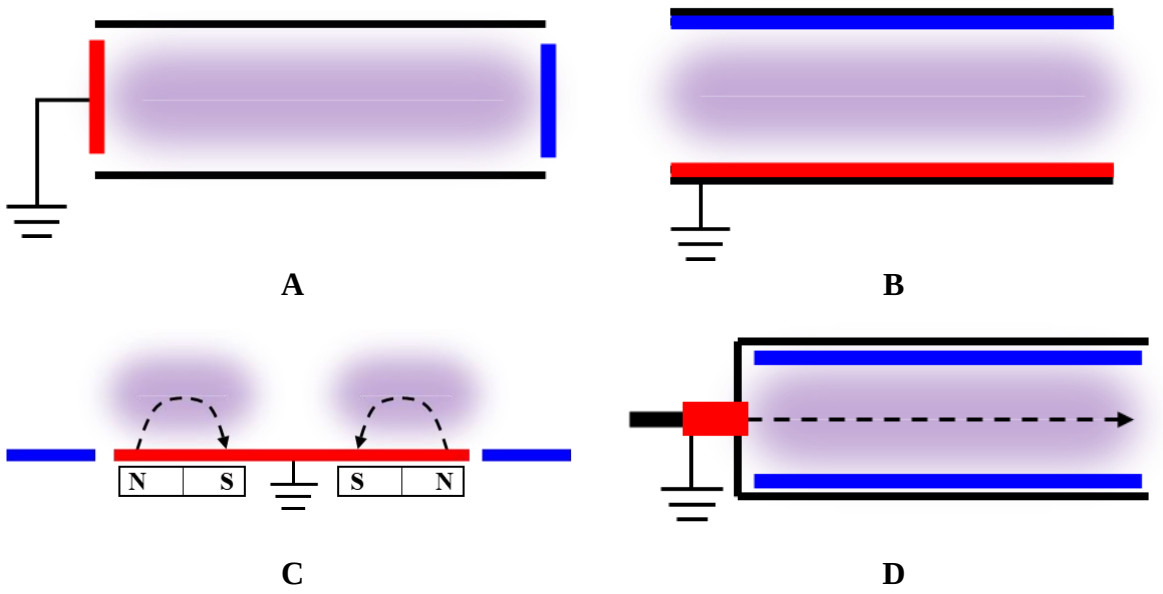


Figure 7. Simplified schematic of DC plasma setups, showing (**A**) a discharge tube, (**B**) a parallel plate reactor, (**C**) a co-planar magnetron reactor (N/S is north/south magnetic pole), and (**D**) a co-axial discharge reactor (arrow shows gas direction), displaying the cathode (**red**), anode (**blue**) and the plasma (**purple**) (Roth, 1995).

the working gas between the anode and cathode. Ideally, low pressures around 10 Pa are used so the mean free path of the molecules and the distance between molecules remains large enough for collisions to occur, allowing for the formation of self-sustained plasma.

The ability of plasma to remain self-sustained is known as the Townsend avalanche, a simplified schematic of this is displayed in Figure 8 (Go, 2018). In short, the electric field formed between the anode and cathode accelerates the free electrons. The accelerated free electrons will collide with gas molecules from the working gas and result in secondary electrons being freed. Consequently, the perpetuated collisions between the free electrons and gas molecules will free more and more electrons, this "avalanche" of multiplication grants electrical conduction through the working gas to form and maintain the self-sustained plasma.

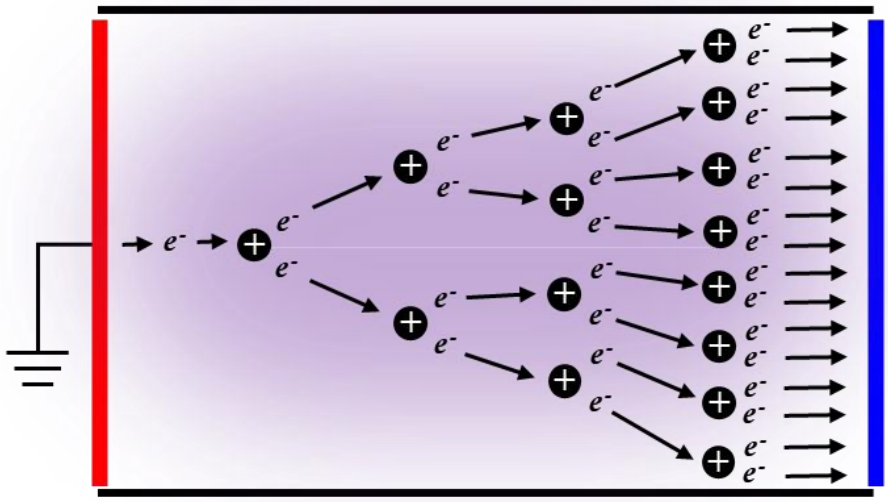


Figure 8. Simplified schematic of an electron avalanche following the Townsend theory, showing the cascading effect of electron-induced ionisation of gas molecules (⊕) and subsequent multiplication of free electrons (e^-), resulting in the formation of plasma (**purple**) between the anode (**blue**) and cathode (**red**) (Go, 2018).

2.2.1. Direct current plasma-nitriding (DCPN)

The original patent for plasma-nitriding using direct current plasma-nitriding (DCPN) was filed in 1932 by Berghaus for the treatment of metallic elements (Berghaus, 1932). In

contrast to the experimental setups presented in Figure 7, with DCPN the metallic samples (or another type of conductive material) itself serve as the cathode and the plasma chamber as the anode – this is also known as direct plasma bombardment. By applying a voltage between the plasma chamber and the metallic samples, plasma is generated from the nitrogen-hydrogen working gas and results in a high nitrogen potential at the sample surface (Hubbard et al., 2010). Further improvements were made to the introduced DCPN setup once Berghaus started collaborating with Wehnheldt, enhancing the stability of the DCPN setup and they ultimately became the first manufacturer of plasma-nitriding equipment under Klöckner Ionon – which equipment was also used in this work (Berghaus, 1932). Unfortunately, despite the advantages of plasma-nitriding mentioned in Section 2.2, DCPN suffers from several drawbacks that may result in the degradation of the material surface and/or an inhomogeneous treatment.

As the samples function as the cathode when using DCPN, this treatment inherently suffers from some drawbacks, such as arcing on the sample surface, inhomogeneous treatment of the samples, the formation of so-called edge effects, and the formation of the hallow cathode effect (Pye, 2003). Edge effects, as implied by the name, are present at the edges/corners of the sample where the exposure of plasma on both sides increases the plasma bombardment density. Consequently, the increased bombardment density also increases the nitrogen diffusion and thermal energy at the edges/corners of the sample, resulting in an inhomogeneous treatment. Next to that, the overlap of plasma exposure also inherently elevates the occurrence of ionisation events, inducing the hollow cathode effect. Traditionally, the denotation “hollow cathode” originates from its formation in hollow cylinder-shaped materials, but this effect is also observed at edges/corners and blind holes/pits and increases the frequency of edge effects.

2.2.2. Active screen plasma-nitriding (ASPN)

To overcome the drawbacks associated with DCPN as mentioned in Section 2.2.1, alternative experimental setups were investigated to allow improved plasma-nitriding. A

modified version of DCPN was patented by Georges in 1999, which is known as active screen plasma-nitriding (ASPN) (Georges, 1999). Contrary to the direct plasma bombardment observed with the use of DCPN, the plasma is formed on an active screen instead which surrounds the samples. A schematic of a conventional ASPN setup is shown in Figure 9. Most commonly, the active screens are made from stainless steel but various other materials have also been used for active screens, such as copper, chromium and titanium to introduce diffusion-layers/deposits of alternative metals onto the sample surface (Li et al., 2002; Nishimoto et al., 2013; Toshioka & Nishimoto, 2020).

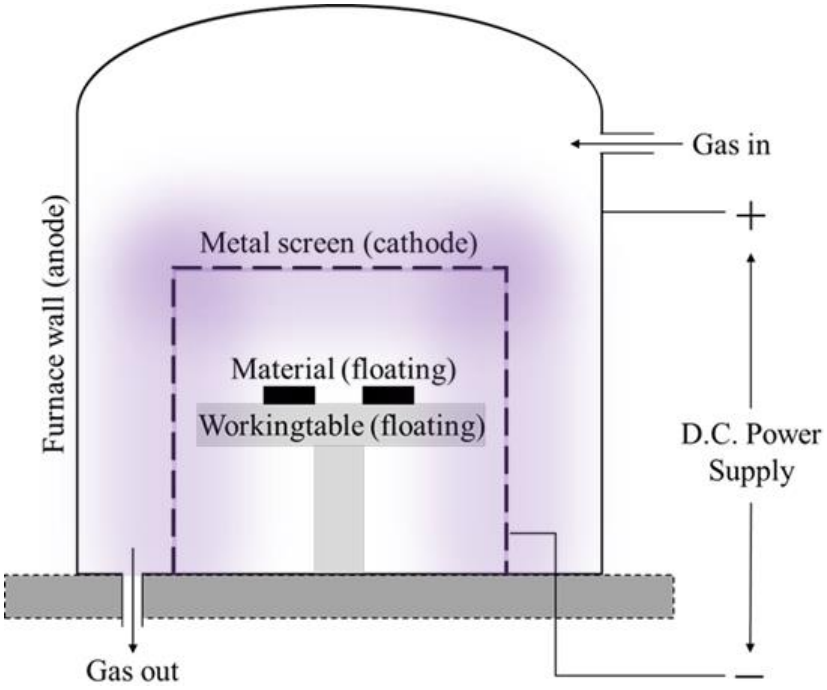


Figure 9. Schematic of conventional active screen plasma-nitriding setup (Kaklamani et al., 2010).

As the active screen functions as the cathode with ASPN, the working table and samples are under a floating potential. Therefore, the drawbacks observed on the samples when using DCPN are now experienced by the active screen instead of the samples (Li, 2010; Zhao et al., 2006). Therefore, the samples will no longer be subjected to the direct arcing and damage to the samples can almost be completely prevented. Next to that, as the plasma is formed on the active screen, the samples do not experience edge effects or the hallow cathode effect, allowing

for a more homogeneous treatment of the samples. Finally, most importantly to this work, ASPN allows for the treatment of non-conducting samples such as polymers (Kaklamani et al., 2010). Despite the prevention of damage and ability to treat polymers, ASPN does suffer from some drawbacks of its own. As the plasma is formed on the active screen, the bombardment experienced by the sample is less intense and this limits the possible surface cleaning. Next to that, the sputtering experienced by the active screen may results in the release of metal ions from the active screen itself and induce sample surface contamination (Biró, 2014).

2.3. Antimicrobial peptides (AMPs) in free-form

Antimicrobial peptides (AMPs) are a class of naturally occurring peptides and are part of the innate immune system for most organisms, protecting them against foreign microorganisms (Huan et al., 2020). AMPs can show antimicrobial activity against bacteria, fungi, parasites, and viruses. The discovery of antibiotics and the subsequent AMPs was initially driven by Alexander Fleming, who discovered the first natural antibiotic lysozyme (i.e., an antimicrobial protein, consisting of a primary polypeptide of 129 amino acid residues) in 1922, progressing the understanding on the modern innate immune system (Fleming, 1932). Since the discovery of lysozyme, the continuous growing concern of antibiotic-resistant microorganisms has resulted in the increased development of therapeutical AMPs (Lewies et al., 2018). Many AMPs show a promising application in a variety of fields, such as agriculture, animal husbandry, aquaculture, food, and medicine (Huan et al., 2020; Kang et al., 2016; Luong et al., 2020). AMPs which have recently been FDA-approved for medical use are *'Oritavancin'* and *'Dalbavancin'*, both of which are from microbial origin, used for bacterial skin (structure) infections, and inhibit bacterial cell wall synthesis (Divyashree et al., 2020). Most current FDA-approved solutions were topical products, primarily due to the susceptibility of AMPs to enzymatic degradation as will be further addressed in the following sections.

2.3.1. Classification of AMPs

Nowadays, the antimicrobial peptide database (APD3) presents a total of 3439 AMPs – the APD3 was last updated on June 30th, 2022 (G. Wang et al., 2016). Besides cataloguing the known AMPs that can be found within the literature, the APD3 database provides information on various commonalities between the wide variety of AMPs, involving their sequence, function, and structure. Most AMPs have a length between 10 and 60 amino acid residues, but the average length of the AMPs presented in the APD3 is 33.13 residues. Most AMPs are cationic (88%), presenting an average net charge of +3.40, although some neutral (6%) and anionic AMPs (6%) also exist (Harris et al., 2009; Lai et al., 2007). When investigating the sequence of the AMPs, most contain the simplest amino acid glycine (G; 11.34%), followed by the cationic amino acid lysine (K; 9.72%), and the hydrophobic side-chain amino acid leucine (L; 8.31%). Most AMPs observed in the APD3 database are antibacterial (84.47%), followed by antifungal (36.57%), and anti-candida (21.11%), but it is worth noting that not all AMPs have their efficiency tested against all types of microorganisms. The structure of the bulk of AMPs remains unknown (60.37%), while most known structures show the presence of disulphide bridges (15.18%) or an α-helical structure (14.45%).

The large variety of AMPs makes it challenging to classify them, the literature separates them based on their source, structure characteristics, sequence composition, or biological function/activity (Agakidou et al., 2022; Huan et al., 2020; Wang et al., 2016). As briefly mentioned in Section 2.3, AMPs are a part of the innate immune system for most organisms, as such, there are bacterial AMPs (i.e., bacteriocins), plant AMPs, and animal AMPs. Animal AMPs can be further separated based on the source of the family name, such as amphibians, fish, insects, mammals, reptiles, etc. The innate immune system is the first line of defence against pathogens, utilizing a set of responses to protect against infections, involving physical barriers (e.g, skin, membranes, etc.), cellular components (e.g., macrophages, etc), and

molecular mechanisms (e.g., AMPs, cytokines, etc.) (Kennedy, 2010). Separation of AMPs based on structural characteristics differentiates between the types of motifs involved with AMPs, the types of structural classes are, linear (which contains neither α-helix or β-sheet), α-helix , β-sheet, a combination of the α-helix and β-sheet (which can be further differentiated by unpacked and packed), and those involving disulphide bridges (Huan et al., 2020). Separation of AMPs based on sequence is characterised by the richness in amino acid residues, in the APD3 this is defined by at least 25% of the same amino acid (G. Wang et al., 2016). Common examples of amino acid-rich peptides are Glycine-rich, Proline-, Arginine-, or Lysine-rich AMPs (Oliveira et al., 2019; Mollica et al., 2017; Qutb et al., 2020; Welch et al., 2020).

Finally, the separation of AMPs based on their biological function/activity is likely the most useful, as it immediately provides information on their mode of action against microorganisms (Agakidou et al., 2022; Huan et al., 2020; Wang et al., 2016). There are three main classes of biological function/activity, including membrane-mediated mechanisms, non-membrane-mediated mechanisms, and other mechanisms that cannot be categorised by the membrane-mediated and/or non-membrane-mediated mechanisms. The membrane-mediated mechanisms are described through several models, including the so-called "carpet" and "pole" models – the "pole" models can be further separated into the "Toroidal pore" model and the "Barrel-stave" model. The non-membrane-mediated mechanisms involve AMPs entering cells by direct penetration or endocytosis (i.e., transporting AMPs/a molecule into the cell by engulfing it with its membrane). Depending on the AMPs' target, non-membrane-mediated mechanisms include the inhibition of biosynthesis (e.g., affecting transcription, translation, or assembly of proteins, enzymes, and effector molecules), inhibition of the cell wall synthesis, or inhibition of cell division (e.g., by preventing DNA replication or DNA damage response). Lastly, the other AMP mechanisms – that cannot be categorised by the membrane-mediated and/or non-membrane-mediated mechanisms – include AMPs that have an anti-biofilm

formation effect (i.e., the ability to prevent the formation of structured communities of microorganisms encased in an extracellular matrix, also known as biofilms) or neutralise the microbial lipopolysaccharide (LPS; i.e., the major component of the outer membrane of Gram-negative bacteria) (Bos & Tommassen, 2004; Dufour et al., 2010). The aforementioned antimicrobial mechanisms of the AMPs are further discussed in the Section 2.3.2.

2.3.2. Antimicrobial mechanisms of AMPs

As mentioned previously, the membrane-mediated mechanisms are described through the "Carpet" model, "Toroidal pore" model and the "Barrel-stave" model – these models are schematically depicted in Figure 10 (Agakidou et al., 2022; Bechinger & Gorr, 2017; Huan et al., 2020; Shai, 2002). With the "Carpet" model (Figure 10A), the AMPs will accumulate parallelly to the membrane, ultimately breaking apart the membrane through the formation of micelles similar to a "detergent" (i.e., as observed when micelles are formed when oil is added to soapy water) (Oren & Shai, 1998). Unfortunately, AMPs that utilise this mechanism (e.g., '*LL-37*' or various AMPs with a *β*-sheet structure) commonly require a high concentration to reach the pore-forming threshold (Corrêa et al., 2019; Shenkarev et al., 2011).

Following the "Toroidal pore" model (Figure 10B), which is also referred to as the "wormhole" model, AMPs will accumulate vertically to the membrane. Once enough AMPs have accumulated, the AMPs bend the membrane to form a ring-like hole with a diameter around 1-2 nm – examples of AMPs that utilise the "Toroidal pore" model are '*Magainin 2*', '*Lacticin Q*' and '*Arenicin*' (Matsuzaki, 2009; Matsuzaki et al., 1996). With the "Barrel-stave" model (Figure 10C), AMPs also accumulate vertically to the membrane. However, in contrast to the "Toroidal pore" model, with the "Barrel-stave" model the AMPs will form multimers within the membrane that results in the formation of holes – initiating the outflow of cytoplasm. Ultimately, at a certain AMP concentration threshold, the membrane collapses and leads to cell lysis (Lohner & Prossnigg, 2009). '*Alamethicin*' and '*Protehrin-1*' are found to use the "Barrel-

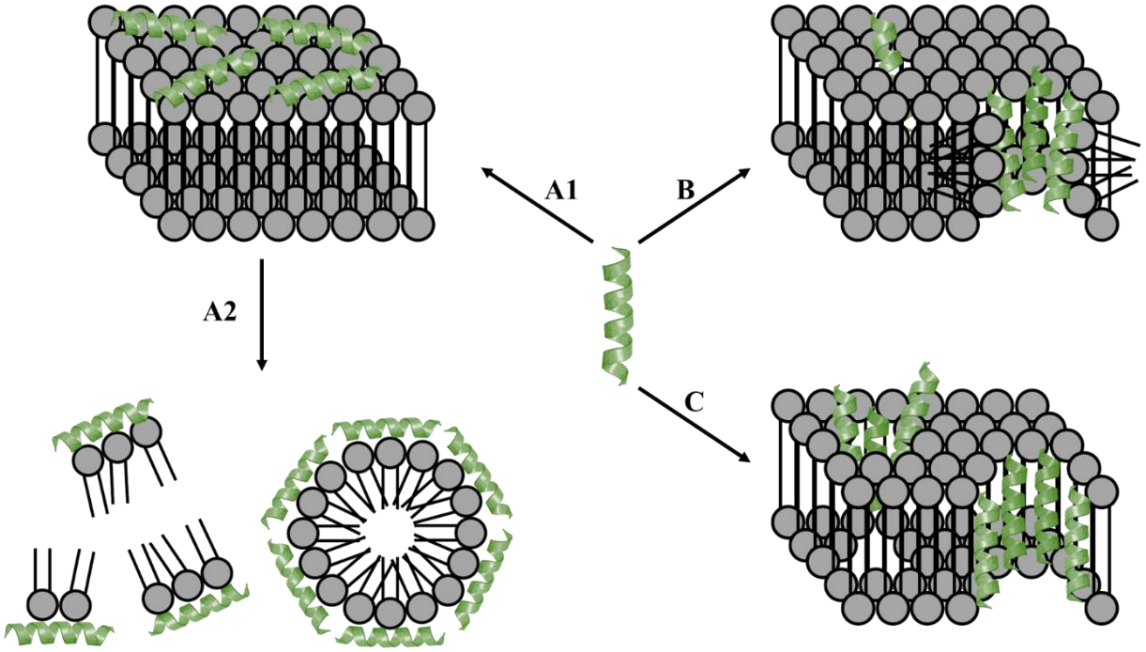


Figure 10. Simplified schematic of membrane-mediated mechanisms of AMPs (green helix), showing (A) the carpet model, where (A1) AMPs accumulate on the membrane (in this case, a phospholipid bilayer; black/grey circles) and (A2) disrupt the membrane through the formation of micelles similar to a "detergent"; (B) the Toroidal pore model, where AMPs embed themselves in the membrane and bend it to form a ring-like hole; and (C) the Barrel-stave model, where AMPs aggregate in multimers and form pores in the membrane (Agakidou et al., 2022; Bechinger & Gorr, 2017; Huan et al., 2020; Shai, 2002).

stave" model, the latter forms so-called β-barrels (i.e., anti-parallel tandem repeats) in a membrane in its octameric form or half β-barrels in its tetrameric form (Lipkin & Lazaridis, 2015; Mihajlovic & Lazaridis, 2012).

On the other hand, the non-membrane-mediated mechanisms of AMPs involve the inhibition biosynthesis, inhibition of the cell wall synthesis, and/or inhibition of cell division. The inhibition of nucleic acid biosynthesis is triggered by AMPs attacking crucial enzymes or degrading nucleic acid molecules. For instance, '*Indolicidin*' is found to either crosslink DNA or inhibit topoisomerase (i.e., an enzyme that assists the replication, transcription, and recombination of DNA, as well as the segregation of chromosomes), resulting in inhibition of nucleic acid biosynthesis (Subbalakshmi & Sitaram, 1998). The inhibition of cell division is caused by inhibiting DNA replication and/or the DNA damage response. '*APP*' is an AMP that was found to penetrate *Candida albicans*, binding to its DNA and provoking a S-phase arrest

(i.e., the inability to duplicate DNA) (Li et al., 2016). Moreover, '*MciZ*' (i.e., mother cell inhibitor) is an AMP that inhibits the division of bacterial cells by hindering the Z-ring formation (i.e., a "ring" that forms around the equator of the cell and acts as a scaffold for the division machinery to assemble on, which includes proteins that will build the cell wall and eventually divide the cell into two daughter cells) (Cruz et al., 2020).

As can be observed from the above-mentioned examples, a wide variety of AMPs are available and these can serve different purposes, depending on the target microorganism. However, with the therapeutical use of AMPs in medicine, cytotoxicity plays a key role in its approval for clinical applications. Preferably, an AMP should show high antimicrobial activity and minimal cytotoxicity. In the simplest terms, this requires the AMP to show high cell selectivity towards (for example) bacterial cells over mammalian cells (e.g., erythrocytes, macrophages, etc.) (Ma et al., 2016). The AMP selected in this work was '*KR-12*', due to its cell-selectivity and low cytotoxicity, which will be discussed in more detail in Section 2.3.3.

2.3.3. LL-37 derivative KR-12 and its analogues

As far as can be observed in literature, Wang was the first to identify the shortest AMP fragment '*KR-12*' from the human cathelicidin '*LL-37*', corresponding to the amino acid residues from position 18 to 29 (i.e., resulting in the peptide sequence KRIVQRIKDFLR-NH_2) (Wang, 2008). The parent peptide, '*LL-37*', is the only cathelicidin AMP found in humans and it plays an important role in our innate immune system (Méndez-Samperio, 2010). '*LL-37*' exhibits a broad antimicrobial spectrum and is expressed in epithelial cells (e.g., in the gastrointestinal tract, the respiratory tract, the skin, etc.) as well as leukocytes (e.g., in monocytes, neutrophils, T cells, etc.) (Dürr et al., 2006). Furthermore, besides its antimicrobial activity, '*LL-37*' was found to be involved in various other immune-modulatory/defensive mechanisms, for example, in regulating inflammatory responses, re-epithelialization, and wound healing (Chereddy et al., 2014; Heilborn et al., 2003).

The same author who identified '*KR-12*' also synthesized eight analogues by various amino acid substitutions (i.e., including alanine, lysine and arginine), the main goal of this was to reveal the functional role of the basic amino acid residues in the antimicrobial activity of '*KR-12*' against *Escherichia coli* (Mishra et al., 2013). These authors found that, almost all the amino acid substitutions by alanine decreased the antimicrobial activity. However, an increase in antimicrobial activity was observed for two of the investigated analogues. Namely, when the arginine (R) on position 6 was replaced by alanine and when the lysine (K) on position 1 and 8 was replaced by arginine, the antimicrobial activity increased by 38% and 47%, respectively. Jacob *et al.* also performed a substitution scan on '*KR-12*', but following systematic substitution of the positively-charged and hydrophobic amino acid residues (Jacob et al., 2013). These authors investigated the antimicrobial activity of '*KR-12*' and the substituted analogues against various clinically relevant bacterial strains (i.e., *Escherichia coli, Pseudomonas aeruginosa, Salmonella typhimurium, Bacillus subtilis, Staphylococcus epidermidis, and Staphylococcus aureus*), and reconfirmed the antimicrobial activity and lack of cytotoxicity towards human cells. The AMPs showed a mean minimum inhibitory concentration (MIC) of <8.3 μM against the bacterial strains, whilst the concentration required to achieve 50% lysis of, in this case, fresh human red blood cells (HC_{50}) was >800 μM – except for analogues 5 and 6 (i.e., the two most hydrophobic analogues due to 2 or 3 substitutions, respectively, with leucine), which showed a HC_{50} of 96 and 22 μM, respectively, instead (Jacob et al., 2013). As seen with the work of Mishra *et al.*, most substitutions resulted in a decrease or no significant difference in antimicrobial activity relative to native '*KR-12*' which displayed a mean MIC of 3.5 μM – although strain-specific differences can be observed, making general comparison challenging. The authors from both above-mentioned works, Mishra *et al.* and Jacob *et al.*, suggested that '*KR-12*' could serve as a tuneable AMP template for the

development of more potent AMPs, which was further attempted using substitution scans by various others in the literature.

For example, the key amino acid residues that are found to be most important for the antimicrobial activity of '*KR-12*' were investigated by Gunasekera *et al.* using both full-sequence alanine and lysine scans (Gunasekera et al., 2018). The analogues prepared during this study were tested on their antimicrobial activity against various clinically relevant pathogens (i.e., *Candida albicans*, *Pseudomonas aeruginosa*, and *Staphylococcus aureus*), and membrane permeabilization by measuring 5(6)-carboxyfluorescein (i.e., 5(6)-FAM) outflow from *Escherichia coli* liposomes. As depicted in Table 4, alanine substitution of practically all amino acid residues in '*KR-12*' resulted in a decrease in antimicrobial activity – except for aspartic acid (D) on position 9. However, the lysine substitution scan showed to increase or make no impact to the antimicrobial activity of '*KR-12*'. When glutamine (Q) on position 5 and aspartic acid (D) on position 9 were substituted for lysine, an eight-fold increase in the antimicrobial activity was observed against the investigated bacteria. Some differences were noted in the cell selectivity towards the various bacterial strains, specifically, through substitution of isoleucine (I) on position 3 and valine (V) on position 4, showing that the cell selectivity was tuneable. None of the prepared analogues from the alanine and lysine scans displayed significant cytotoxicity towards human cells. From this work, it was recognized that the antimicrobial activity of '*KR-12*' was improved when amino acid residues were substituted by cationic residues (in this case, lysine), providing that the amphiphilic character of the AMP was preserved (i.e., the hydrophobic and hydrophilic properties). The impact of amphipathicity on the antimicrobial activity was further supported by Yun *et al*., who showed that '*KR-12*' analogues with a more flawless amphipathic α-helix exhibited a higher antimicrobial activity than regular '*KR-12*' (Yun et al., 2020). Lastly, the membrane permeabilization assays showed

that '*KR-12*' and its analogues exhibit similar leakage kinetics to its parent peptide '*LL-37*' against the liposomes (Gunasekera et al., 2018).

Table 4. Results of the alanine and lysine scans on KR-12, where the colours represent a decrease (**red**), insignificant difference (**yellow**), or increase (**green**) in antimicrobial activity.

KR-12	K	R	I	V	Q	R	I	K	D	F	L	R
Alanine scan												
Lysine scan	-							-				

Next to amino acid substitutions, attempts have also been made to enhance the therapeutical use and/or antimicrobial activity of '*KR-12*' through lipidation. Lipidation involves the covalent modification of lipids (e.g., fatty acids, isoprenoids, or cholesterol) to proteins/peptides, this is a common post-translational modification applied to protein and/or peptides to combat various issues associated with their pharmacokinetics and pharmacodynamics (Menacho-Melgar et al., 2019; Rounds & Straus, 2020). Generally, lipidation improves the half-life time of protein/peptide-based drugs, it reduces the immunogenicity (i.e., immune response induced by the drug), and improves cellular permeabilization/uptake. As demonstrated by Kamysz *et al.*, the conjugation of fatty acids with a length of two to fourteen carbons resulted in an increase in the antimicrobial activity of '*KR-12*' (Kamysz et al., 2020). A conjugation '*KR-12*' to a fatty acid with a chain length of eight carbons showed the lowest MIC against all the so-called '*ESKAPE*' pathogens (i.e., an acronym for *Enterococcus faecium*, *Staphylococcus aureus*, *Klebsiella pneumoniae*, *Acinetobacter baumannii*, *Pseudomonas aeruginosa*, and *Enterobacter*). Next to that, a correlation was observed between the fatty acid chain length and the antimicrobial activity. Based on the self-assembly of the '*KR-12*' analogues studied by nuclear magnetic resonance (NMR) and surface tensiometry, the increased aggregate size observed as the fatty acid chain length increased, resulted in a decrease of the antimicrobial activity. The cytotoxicity also increased similarly to

the antimicrobial activity, despite the increase in cytotoxicity, only when '*KR-12*' was conjugated with a fatty acid chain length of six to ten carbons the MIC against *Staphylococcus aureus* was lower than half maximal inhibitory concentration (IC_{50}) against the human keratinocytes (i.e., the cell type predominantly found in the outermost layers of the skin; HaCaT).

Other efforts to increase the half-life time of peptides have been focused on using substitutes for *L*-amino acids, as natural peptides are more rapidly metabolized (Marr et al., 2006). By substitution of *L*-amino acids by *D*-amino acids and/or the introduction of unnatural peptide bonds, it is possible to drastically increase the stability of AMPs (Gentilucci et al., 2010; Seebach et al., 2004; Tugyi et al., 2005). For example, as concluded by Jia *et al.*, *D*-amino acid analogues of the wasp venom-derived AMP '*polybia-CP*' demonstrated improved stability against two common proteases (i.e., trypsin and chymotrypsin), whilst maintaining its membrane-mediated mechanism and almost the same antimicrobial activity against various bacteria in a broth dilution assay (Jia et al., 2017). For example, regular '*polybia-CP*' displayed a MIC of 8 μM against *S. Aureus* (ATCC 29213), *B. Subtilis* (ATCC 23857), and *S. Epidermidis* (ATCC 12228), whereas the partial/full *D*-amino acid analogues of '*polybia-CP*' (i.e., for the partial analogue, only the *L*-Lysine were replaced by *D*-Lysine) displayed MIC of 64/8, 16/4, and 16/64, respectively (left of diagonal mark are the MIC for the partial *D*-amino acid analogue, the right are for the full *D*-amino acid analogue). Furthermore, specifically the partial *D*-amino acid analogue reduced the hemolytic activity, showing negligible hemolysis up to at least 60 μM. On the other hand, as demonstrated by Frackenpohl *et al.*, based on almost 300 experiments using 15 different proteases (i.e., major classes of peptidases, like serine and aspartic peptidases and metallopeptidases, as well as of different biologically relevant sources, like bacteria, fungi and eukaryotes) on a variety of 50 peptides (e.g., open-chain, cyclic, protected and unprotected, etc.), the cleavage between two homologated amino acids (i.e.,

modified amino acids, including additional CH_2 groups in the backbone of each residue) was never observed and this modification did not impact the antimicrobial activity (Frackenpohl et al., 2001). It was found that the proteases are unable to cleave the bond between the homologated amino acids, as the peptide chains are unable to adjust their conformation required for the proteases to function, which can aid the design of AMPs that remain stable and effective under physiological conditions where proteases are present.

Like its parent peptide '*LL-37*', '*KR-12*' has other positive benefits for therapeutical applications. For example, '*KR-12*' and some of its analogues (i.e., '*KR-12-a5*' and '*KR-12-a4*') were found to enhance the osteogenic differentiation (i.e., improved osteoblast growth, bone forming and regenerating cells), which – considering the main application of UHMWPE in total hip replacements – serves as a major benefit to bone integration, implant anchoring, and the prevention of aseptic loosening (Fu et al., 2020; Li et al., 2018, 2019). Furthermore, as displayed by Liu *et al.*, hyaluronic acid coated on an eggshell membrane which was loaded with '*KR-12*' promoted re-epithelialization and angiogenesis (i.e., the growth of vasculature from pre-existing blood vessels) (Liu et al., 2019). Lastly, '*KR-12*' and some of its analogues are shown to provide anti-inflammatory activity (Fabisiak et al., 2021; Jacob et al., 2013). Jacob *et al*. evaluated the anti-endotoxic activity of '*KR-12*' and some of its analogues, by measuring the inhibition of tumour necrosis factor-α (i.e., a signalling molecule involved in the immune response, which at high concentrations can result in excessive inflammation and tissue damage; TNF-α) production from an LPS-stimulated macrophage cell line. These authors found that some '*KR-12*' analogous (i.e., '*KR-12-a[3-6]*') diminished the TNF-α production (Jacob et al., 2013). Last of all, the use of '*KR-12*' against bowel diseases was tested by Fabisiak *et al.* and these authors demonstrated that '*KR-12*' displayed improved anti-inflammatory activity over its parent peptide '*LL-37*' (Fabisiak et al., 2021).

Despite the increased antimicrobial activity and improved properties achieved with some of the '*KR-12*' analogues and/or modifications, unmodified '*KR-12*' remained the AMP of choice in this work. Using unmodified '*KR-12*' was considered to be the most sensible as it is the most clinically understood AMP, making comparison of the literature on '*KR-12*' versus the experimental results obtained in this work more straightforward. To further increase the half-life time *in-vivo* and reduce the potential cytotoxicity of the AMPs in free-form, AMPs can also be immobilised onto biomaterial surfaces, as proposed in this work. The use of AMP immobilisation on polymeric biomaterial surfaces is further discussed in Section 2.4.

2.4. Immobilisation of AMPs on biomaterials

As discussed in Section 2.1, biofilm formation on the biomaterial surfaces due to bacterial adhesion and colonization is a major contributor to implant-related infections and malfunctions, accounting for about 20% of such incidents (Ben-Shlomo et al., 2022; Grindy et al., 2019). This persistent problem continues to pose significant challenges for healthcare providers, often leading to severe medical and economic consequences (Darouiche, 2001; Percival et al., 2015). Implant-associated infections are typically separated into three main categories, depending on the origin of the infection, namely: immediate superficial infections, immediate deep infections, and late deep infections (Dee et al., 2003). Immediate superficial infections are a result of bacterial colonisation originating from bacteria that are typically present on the skin around the implant-site, e.g., infected sutures. Immediate deep infections are commonly a result of non-sterile implantation, where bacteria from the skin enter and colonise the implant-site after more invasive surgeries (i.e., total joint replacements). Late deep infections will only become visible after a significant amount of time (up to several months, or even years) after surgery, this delayed infection may be a result of low-virulent (i.e., slow onset) bacteria or due to bacteria that were seeded in the sub-surface of the implant.

When a biomaterial is implanted, a layer of (glyco)proteins (e.g., albumin, fibronectin, fibrinogen, etc.) will attach to the biomaterial surface, favouring interplay between the surface and surrounding microorganisms (Dee et al., 2003). The (glycol)proteins present on the biomaterial will initially interact with microbes through secondary attraction forces (i.e., van der Waals interactions and electrostatic charges), as has been demonstrated by (amongst others) the Derjaguin–Landau–Verwey–Overbeek (DLVO) theory (i.e., theoretical model used to describe the interactions between colloidal particles in a liquid medium) (Carvalho, 2008; Hermansson, 1999). The formation of mature biofilms on biomaterials progresses following a sequence of events: microbes will first adhere to the biomaterial, the microbes proliferate and form (micro)colonies, the colonies ultimately produce a surrounding matrix that establishes the biofilm, after maturing microbes will detach from the biofilm and further propagate the infection surrounding the implant-site (Hetrick & Schoenfisch, 2006; Vila et al., 2008). Once the biofilm has matured, it can no longer be simply eradicated using antimicrobial agents, but often requires complete removal of the biomaterial to halt further propagation of the infection.

Fortunately, many of the biomaterials used today can be modified through functionalization or coating of their surfaces, effectively reducing inflammation and the risk of infection before biofilm formation occurs (Zhang et al., 2013). In general, implant-associated infections have been treated by developing materials containing antibiotics and/or biocides (Maillard, 2005; Suhardi et al., 2017). However, the use of antibiotics may result in developing antibiotic-resistance bacteria and the use of biocides comes with the risk of cytotoxicity, raising concern as a potential threat to patient health (Li & Webster, 2018). Due to the issues associated with antibiotics and biocides, alternative antimicrobial agents and/or strategies to prevent infection have been investigated.

An alternative to antimicrobial agents is the use of antifouling coatings, making it possible to prevent attachment of bacteria, proteins, and other microorganisms to the

biomaterial surface (Yebra et al., 2004). However, antifouling coatings prepared on UHMWPE frequently require a pre-treatment to allow further surface decoration (e.g., with SiO_2, "*ECONEA*", etc.), making their development rather time-consuming and potentially costly (Kartal & Sarıışık, 2020; W. Yang et al., 2018). Next to that, although this more passive approach may prevent the risk of cytotoxicity induced by biocides and developing antibiotic-resistance bacteria due to the use of antibiotics, antifouling coatings are not capable of killing already adherent bacteria on the biomaterial surface, which makes it difficult to avoid infection completely during and/or after implantation (Yin & Luan, 2016). Hence, surfaces with antimicrobial properties are desirable in combating the formation of biofilms and minimizing the risk of infection at the implant site (Banerjee et al., 2011; Bruellhoff et al., 2010).

As discussed in Section 2.3, a more recent alternative to the more commonly used antimicrobial agents are AMPs, which are native to the human body and utilise modes-of-action that make it difficult for microbes to become resistant (Wang et al., 2019). However, depending on the target microbe, high AMP concentrations may be required to fully prevent infection (e.g., due to the rapid metabolization of natural AMPs by proteases) which can induce cytotoxicity (Z. Yang et al., 2021). It is crucial to enhance the stability of free-form AMPs against *in vivo* degradation and strengthen the bond between immobilized AMPs and the material surface in order to develop non-toxic and long-lasting antimicrobial surfaces (Bagheri et al., 2009; Chen et al., 2009). Ultimately, by limiting the necessity of implant removal due to implant-associated infections because of AMP inactivity, the negative impact on the patient compliance and the care system can be minimized. Over the past few decades, AMPs have been immobilised on a wide variety of biomaterial surfaces (e.g., ceramics, metals, polymers, etc.), following a broad range of coupling strategies depending on the biomaterial surface composition. Past attempts of AMP immobilisation on biomaterial surfaces are discussed in more detail in Section 2.4.1.

2.4.1. History of AMP immobilisation on biomaterials

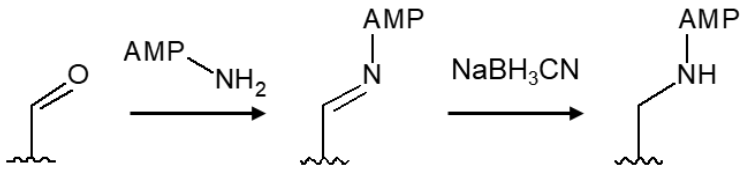
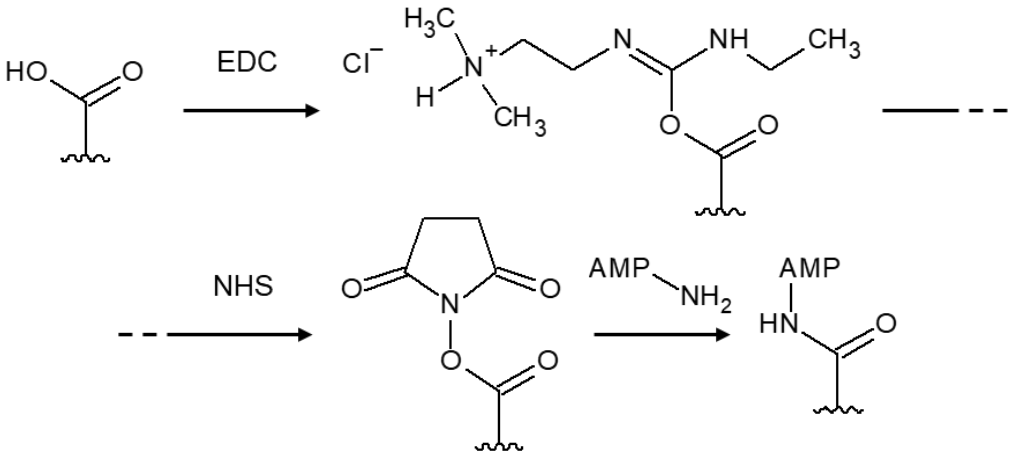
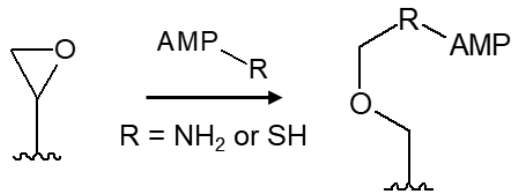
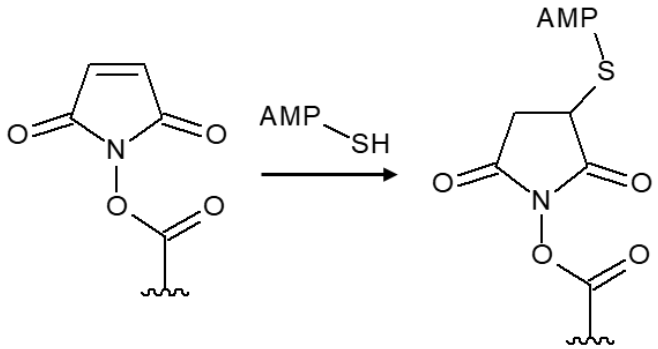
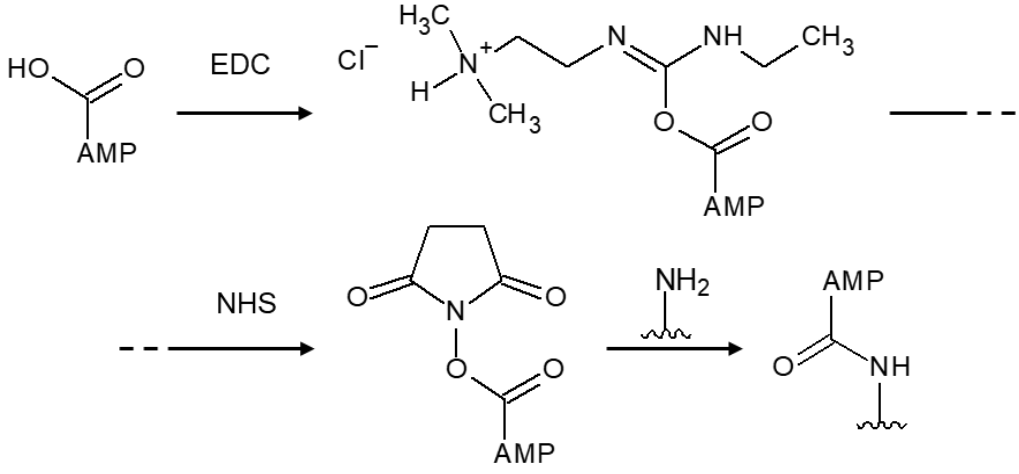
‖ This section presents an advancement on my first-authored published work, specifically from section 4 in (Bruggeman et al., 2019), please see the 'Publications' section. ‖

A variety of polymeric biomaterials have been used for the delivery of AMPs, including but not limited to thermoplastics, resins, hydrogels, polymer-coated metals, etc. (De Zoysa et al., 2020; Small et al., 2018; Trzcińska et al., 2020; Wang & Tang, 2019). It is possible to immobilize AMPs through two main pathways, either physically or chemically. A popular physical method is layer-by-layer assembly, in which AMPs are ‘sandwiched’ between, e.g., two polyionic polymers, making it possible to integrate a controllable loading of AMPs (Boulmedais et al., 2004; Etienne et al., 2004). However, the interspersed AMPs within the polyionic polymer layers are not able to directly interact with the surrounding environment, they will first need to diffuse outwards to utilize their antimicrobial activity. Next to that, although not frequently observed with polymeric biomaterial surfaces, another physical method involves the use of electrostatic interactions between the biomaterial surface and the AMPs. Certain peptide motifs (e.g., RKLDPA) can be conjugated to AMPs to allow electrostatic binding to metallic surfaces such as titanium (Sano & Shiba, 2003). However, following (indirect) physical immobilisation, the AMPs will still suffer from the same issues associated with free-form AMPs once released as discussed in Section 2.3. Therefore, the use of physical immobilization makes it difficult to fully utilize the potency of AMPs and chemical immobilisation following covalent bonds is considered most beneficial.

Covalent-based immobilization of AMPs has significant advantages in comparison to physical immobilization, such as the formation of more stable bonds and thus improvement of their relatively short half-life time, whilst also allowing for minimal undesired leaching of the AMPs (Ferreira & Zumbuehl, 2009). However, when utilising covalent-based immobilisation, there are a variety of (bio)material surface properties to take into consideration. The surface

morphology needs to be well defined, as an undefined/irregular surface could lead to inhibition of attachment of AMPs (Costa et al., 2011). Additionally, depending on the local density of the functional groups that are present or able to be introduced to the biomaterial surface altogether, the number of immobilised AMPs on the material surface can vary significantly across its surface area. Despite that, even though AMP concentration is of importance, it does not always appear to be the most critical criterion for the improvement of antimicrobial activity (Gabriel et al., 2006; Glinel et al., 2009). The antimicrobial activity of covalent-based surface-immobilized AMPs is seen to be mainly dependent on the used coupling chemistries, spacer specifications, AMP orientation, and AMP concentration (Onaizi & Leong, 2011). However, there are certain limits to improving the antimicrobial activity by increasing the AMP concentration, some microbes are insensitive to further AMP concentration increase after reaching a limit in AMP surface density or exposure time (Sun & Sun, 2001).

When functionalizing the biomaterial surface, the orientation of immobilized AMPs can be controlled using chemo-selective (i.e., directed immobilization) coupling chemistries – a variety of commonly observed coupling chemistries are presented in Figure 11. In general, molecules such as 1-ethyl-3-(3-dimethylaminopropyl)-carbodiimide (EDC) and *N*-hydroxy-succinimide (NHS) are found to be widely used as activating agents for the coupling of peptides to surfaces by forming amides, which inhibits the formation of carboxylic salts with an amine (Costa et al., 2011; Onaizi & Leong, 2011). Naturally, there are alternative molecules available to NHS/EDC which can couple the same functional groups. In addition, cysteines or thiols are also found to be frequently used for relatively effortless chemo-selective conjugation of AMPs to various polymeric substrates (Ochtrop & Hackenberger, 2020).

Aldehyde coupling	
Carboxylic acid coupling	
Epoxide coupling	
Maleimide coupling	
Amine coupling	

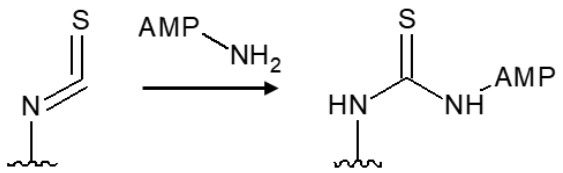
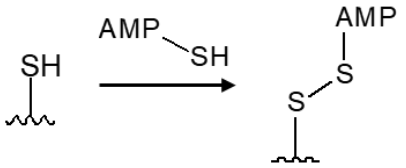
Isothiocyanate coupling	
Thiol coupling	

Figure 11. Simplified reaction schemes of various coupling chemistries used to immobilise AMPs onto (bio)material surfaces (〰) with differing organic functional groups; not drawn to scale or exact structure (Costa et al., 2011; Onaizi & Leong, 2011).

Directly immobilized AMPs

The direct immobilisation of '*Magainin 1*' was achieved on a mixed self-assembled monolayer (SAM) containing mixed thiols, as performed by Humblot et al., to test its antimicrobial activity when immobilised against three gram-positive bacteria (i.e., *Listeria ivanovii*, *Enterococcus faecalis*, and *Staphylococcus aureus*) (Humblot et al., 2009). The thiol-rich SAM consisted of 11-mercaptoundecanoic acid and 6-mercaptohexanol (at a 1:3 ratio, respectively) assembled on gold substrates. In free-form, '*Magainin 1*' is suggested to follow the "Carpet" or "Toroidal pore" model, but in this work it was also found to demonstrate antimicrobial activity when immobilised to the SAM surface. In this work, the orientation of the AMP was not controlled, as the coupling chemistry allowed for any free amine within the AMP to immobilise itself to the mixed thiols on the SAM. Considering '*Magainin 1*' contains five free amine groups, various orientations were likely to be present on the SAM surface. Nonetheless, it was demonstrated that the immobilisation of '*Magainin 1*' reduced the adherence of bacteria by more than 50% relative to AMP-free SAM surfaces, whilst also killing the bacteria that did eventually adhere to the surface. Additionally, no release of the AMP was observed following incubation in bacterial solution for three hours at 37°C and under a slight agitation, the solutions were dried and analysed using a mass spectrometer (Humblot et al.,

2009). In another study, the closely structurally-related AMP '*Magainin 2*' was directly immobilised on ethylenediamine-modified polyamide resin (i.e., '*PepsynK*') by Haynie *et al*., to study its antimicrobial activity against *Escherichia coli* and *Staphylococcus aureus* when immobilised (Haynie et al., 1995). Similar to '*Magainin 1*', '*Magainin 2*' is also suggested to follow the "Toroidal pore" model in free-form. The orientation of the immobilised AMPs was controlled by sequencing the peptide using N-terminal Fmoc-protected amino acid residues (i.e., fluorenylmethyloxycarbonyl protecting groups; Fmoc chemistry), forcing the immobilisation of the C-terminal of the AMP to the resin. This work again confirmed that directly immobilised AMPs can eradicate microbes solely through outer membrane disruption, despite the restricted penetration depth when immobilised.

Next to the stability of the AMP itself, the stability of the biomaterial surface is also of great importance to maintain a long-lasting antimicrobial biomaterial surface. For example, as demonstrated by Xiao *et al.*, a dibromo-maleimide polymer substrate prepared by chemical vapour deposition (CVD) and functionalized with AMPs showed a better antimicrobial stability when compared to the SAM (Xiao et al., 2018). In this work, the AMP consisted of a hybrid sequence between '*Cecropin*' and '*Melittin*' which was modified with a C-terminal cysteine (i.e., excluding the cysteine, the first 18 amino acid residues belonged to '*Melittin*' and the last 8 amino acid residues originate from '*Cecropin*'), the C-terminal cysteine allowed for orientation-controlled conjugation to the polymer substrates. When exposed to air, the DBM polymer substrate showed slower detachment of AMPs when compared to the SAM. These results demonstrated the importance of using a non-degradable material surface to maintain long-lasting bond stability of the immobilised AMPs. For both polymer substrates, the AMP was determined to be in a "standing-up" orientation with respect to the surface and this remained unchanged after exposure to air. However, after the AMP-immobilised polymer substrates were brought into contact with *Escherichia coli*, the orientation of the peptides was

found to change from “standing-up” to “lying-down”. Since directly immobilized AMPs cannot follow their free-form membrane-mediated mechanisms (as those discussed in Section 2.3) due to limited lateral mobility, it is suggested that the charge-charge interaction plays a dominant role in the elimination of microbes (X. Han et al., 2018; Xiao et al., 2018).

Spacer-incorporated immobilized AMPs

Although the AMP orientation can be partly controlled with the use of chemo-selective coupling agents and it is demonstrated that directly immobilized AMPs also show antimicrobial activity without the use of a spacer, a lot of potent developments make use of spacers as direct immobilisation may not provide enough mobility for a high probability of membrane permeabilization (i.e., disruption of cell membrane, allowing the passage of substances into or out of the cell) or polarization (i.e., separation of electrical charge across a cell membrane, creating a voltage potential difference that impacts cellular processes like differentiation, proliferation, etc.) (Semplice et al., 2012). The length (i.e., the distance between the material surface and peptide) of the used spacers are shown to significantly influence the activity of surface-immobilized AMPs, when compared to the AMP surface density (Bagheri et al., 2009). Conversely, the possibility of chain cleavage of the spacer due to polymer degradation reactions could lead to the release of immobilized AMPs. This could be minimized with the use of stabilized, non-degradable polymer spacers (Delaviz et al., 2015). The increased activity seen with the use of spacers is generally attributed to the improved lateral mobility of the AMPs, increasing probability of membrane permeabilization and subsequent microbial cell death. However, this would only be a correct hypothesis assuming that AMPs demonstrate a similar mode of action to that of their free-form counterparts. There are also AMPs that, when immobilised, will depolarize the cytoplasmic membrane and disrupt the electron transport, which subsequently would lead to partial membrane permeabilization and thus cell death (Hilpert et al., 2009; Spindler et al., 2011).

As shown in Figure 12, there are two main types of spacers, stiff and flexible spacers. Stiff spacers (e.g., polyvinyl chloride or polymethyl methacrylate) allow the increase of reach and thus might allow membrane permeabilization, but will restrict sideways mobility by keeping the AMPs pointing in a specific orientation (Onaizi & Leong, 2011). Flexible spacers (e.g., polyethylene glycol; PEG) also allow the increase of reach and can allow sideways mobility; however, the orientation of the AMPs cannot be fixed due to its flexible chains (Holmberg et al., 1992).

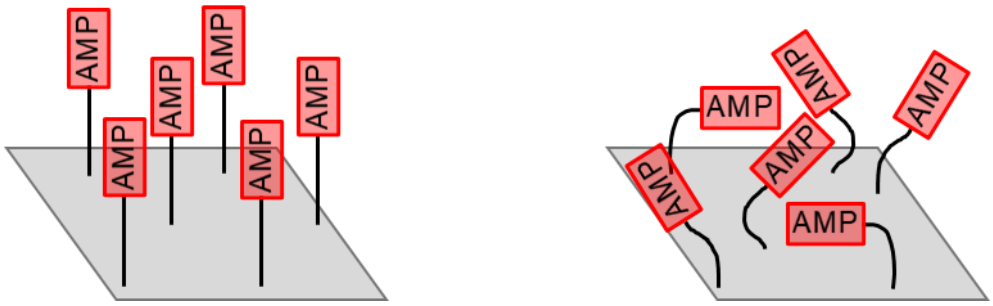


Figure 12. Simplified schematic of spacer-incorporated immobilized AMPs, showing stiff spacers (left) and flexible spacers (right); not drawn to scale or exact structure.

An extensive study performed by Gabriel *et al.* using silanized titanium surfaces demonstrated the importance of spacer specifications and orientation on the antimicrobial activity of '*LL-37*' (Gabriel et al., 2006). In this work, both direct and spacer-incorporated immobilisation (i.e., by introducing PEG-based spacers) to the biomaterial surfaces was investigated through various multi-step coupling chemistries. It was found that direct immobilisation of '*LL-37*' to the silanized titanium surfaces resulted in no observable antimicrobial activity. Next to that, when '*LL-37*' remained inactive when it was linked to a flexible PEG spacer through its C-terminal (i.e., the carboxylic acid end group). However, when '*LL-37*' was conjugated to PEG through its N-terminal, the spacer-incorporated immobilisation demonstrated the ability of killing *Escherichia coli*. As discussed in Section 2.3, considering '*LL-37*' requires access to the microbial membrane, it can be concluded that

this AMP requires lateral freedom to induce its membrane-mediated mechanism, which was only achieved with the use of a long-flexible spacer in a specific orientation. It has also been suggested that the water-swelling property of PEG can aid in maintaining the activity of immobilized peptides (Cho et al., 2007). Additionally, the utilization of PEG as a spacer is found to present other advantages, like its ability to create non-adhesive surfaces due to its anti-fouling characteristics. Lastly, the conjugation of the hydrophilic PEG spacer to a naturally amphiphilic AMP can improve its solubility and stability in water, reducing the chance of aggregation by the hydrophobic regions and protease digestion as the spacer can act as a physical barrier against proteases (Guiotto et al., 2003; Holmberg et al., 1992; Veronese & Pasut, 2005).

Utilising the antifouling properties of the spacers, in addition to the antimicrobial activity of AMPs, is shown to be a promising synergistic approach to prevent biofilm formation. For example, as demonstrated by Glinel *et al.*, anti-fouling polymeric brushes based on 2-(2-methoxyethoxy)ethyl methacrylate (MEO_2MA) and hydroxyl-terminated oligo(ethylene glycol) methacrylate (HOEGMA) were grown on silicon wafers, to allow immobilisation of '*Magainin 1*' (Glinel et al., 2009). Various MEO_2MA:HOEGMA ratios were used (i.e., 100:0, 83:17, 67:33, and 33:67) to produce polymer brushes with different amounts of free hydroxyl groups, allowing for varying AMP surface densities. In this work, the orientation of the AMP was controlled by modifying '*Magainin 1*' with a C-terminal cysteine, which was immobilised to the polymer brushes via a *N*-(p-maleimidophenyl isocyanate) (PMPI) linker. Using the PMPI linker, the isocyanate group conjugates to the free hydroxyl groups of the polymer brushes and its maleimide group conjugates to the C-terminal cysteine of the AMP. To determine the AMP surface density, the N-terminal of the AMP was functionalised with biotin. After immobilisation, the biotin was reacted with a fluorescent tag (i.e., streptavidin-fluorescein isothiocyanate) to allow visualisation under a fluorescent

microscope, which demonstrated a uniform coating. The antimicrobial activity of the spacer-incorporated immobilised '*Magainin 1*' was tested against two gram-positive bacteria (i.e., *Listeria ivanovii* and *Bacillus cereus*), by suspending the decorated silicon wafer in a bacterial solution for three hours. On the AMP-free surfaces, no attachment of bacteria was observed, whereas the surfaces with the immobilised '*Magainin 1*' showed roughly 1% of surface coverage by adherend bacteria – indicating that the interaction of the AMP with the bacterial cell membranes resulted in minor bacterial adhesion. However, from the bacteria that did adhere to the polymer substrate surface, no live bacteria were observed after contact with the spacer-incorporated immobilised '*Magainin 1*'. Even at the lowest surface density of AMPs, achieved with the 83:17 ratio of MEO_2MA:HOEGMA, no live bacteria were observed. Unfortunately, the authors did not evaluate if the endospores (i.e., dormant, highly-resistant structures formed within certain bacteria under unfavourable conditions like heat or exposure to toxic/antimicrobial chemicals, endospores contains a copy of the bacterial DNA for germination once conditions are favourable again) of *Bacillus cereus* remained active, which are generally considered lysis-resistant and known to survive boiling, freezing, and exposure to many disinfectants (Kearney et al., 2018; Thomas et al., 2014).

As can be noted from the wide variety of coupling chemistries, spacer specifications, and assortment of AMPs, there are many different approaches available to develop antimicrobial biomaterial surfaces. The difficulty in the comparison of these developments is the lack of comparable information, since most of the observed antimicrobial activity is found to be specific to the used reactants, type of biomaterial surfaces, and AMPs. Fully understanding the structure-function relationships remains difficult but is important to improve the performance of surface-immobilized AMPs in future developments. Whether degradation of the material and coupling agents is desirable or not, understanding the leaching kinetics is of great importance as the decrease of structural integrity and release of AMPs and/or particles

(i.e., debris) might result in an adverse biological reaction. Nonetheless, there are significant indications that AMPs are suitable candidates to replace conventional biocides and antibiotics to create antimicrobial biomaterial surfaces. Therefore, allowing the development of the next generation of antimicrobial biomaterial surfaces used for medical devices and implants.

2.4.2. Proposed approach of AMP immobilisation

In this work, AMPs were directly immobilised on plasma-treated UHMWPE-based surfaces. As the plasma treatment was performed using a nitrogen-hydrogen working gas, various nitrogen-based functionalities (i.e., amines, amidines, etc.) were expected to form on the UHMWPE-based surfaces. Next to that, as some free radicals were expected to remain on the surface of UHMWPE after the plasma-treatment, oxidation products (i.e., hydroxyl, carboxylic acids, etc.) were also expected to form after contact with air during storage. To accommodate for the different nitrogen/oxygen-based functionalities, three different coupling chemistries were attempted as depicted in Table 5. The coupling chemistries all form a different bond type between the AMP and the plasma-treated surfaces, which were expected to vary in degradation/leaching kinetics. To control the orientation of the AMP, the N-terminal was left protected with a Fmoc protecting group to prevent undesired conjugation to the surfaces. After the AMP immobilisation, the Fmoc protecting group was removed (see Section 3.1.4).

Table 5. Target functionalities and formed bond type of coupling chemistries used for the immobilisation of AMPs to the plasma-treated UHMWPE-based surfaces.

Coupling chemistry (Activator / Base)	Target functionality	Formed bond type
DIC / Oxyma Pure	$–NH_2$	Amide
DCC / DMAP	–OH/–COOH	Ester
CDI / -	$–NH_2$	Carbamate

2.5. Theoretical calculations

‖ This section presents an advancement on my first-authored published work, specifically from section 1 in (Bruggeman et al., 2022), please see the 'Publications' section. ‖

An extensively applied tool to provide additional reference data for spectral interpretation are theoretical calculations, which can be performed in various ways using the Hartree-Fock (HF) molecular orbital (MO) theory (i.e., self-consistent field method; SCF) and Density Functional Theory (DFT) (Viñes et al., 2018). These theories present the approximate, iterative solution to the time-independent Schrödinger equation. When calculating the state of a molecule using computer software, a linear combination of atomic orbitals (LCAO) is used to mathematically represent the MO (i.e., forming a basis set of functions that describe the system) (Huheey et al., 2006). The LCAO scheme attempts to approximate the "true" Hamiltonian by minimizing the total energy of the system through diagonalization of the Fock matrix and the overlap matrix, until the difference between the iterations is below the convergence threshold as depicted in Figure 13 (Callaway, 1974). The Fock matrix describes the total effective potential experienced by each electron in a system of interacting electrons, its diagonalisation determines the eigenvectors and eigenvalues which represent the spatial distribution and energies of the MO, respectively. The overlap matrix represents the overlap between the different AO, providing information on how the AO combine and form MO, its diagonalisation ensures that the resulting MOs are mutually perpendicular and normalized, satisfying the required orthonormality condition for a valid representation of a quantum state.

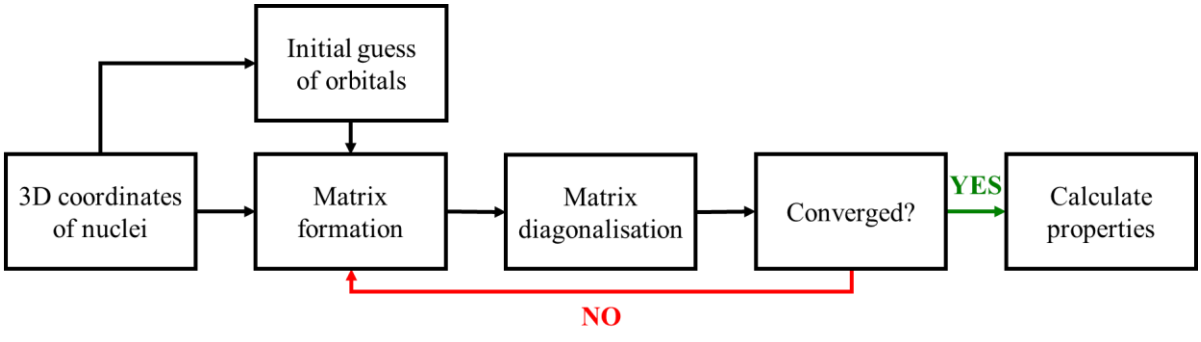


Figure 13. Flowchart of the iterative HF MO method using the LCAO scheme.

Although both HF MO and DFT are used to describe the quantum states of many-body systems, HF MO theory neglects the electron correlation and therefore results in higher energies compared to DFT, which implicitly includes exchange and electron correlation effects (Amusia et al., 2003; Hollister & Sinanoğlu, 1966). A hybrid approach between the two theories also exists, where the exact exchange from the HF theory is "hybridised" with DFT to improve the description of various molecular properties that tend to be poorly described by *ab initio* density functionals (Becke, 1993; Perdew et al., 1996). The main limitations encountered in these theoretical calculations are the required computational effort and the complexity in the subsequent data evaluation. The latter is especially true for those who are not frequent users of computational methods, as in the case of many surface analysts and material scientists. However, due to the development of new and/or more complex material surfaces, as seen in the present work, the need for theoretical calculations and simulations for the interpretation of unidentified spectral features/chemical functionalities increases drastically.

In this work, different types of theoretical calculations were utilized to aid the spectral data analysis for X-ray photoelectron spectroscopy (XPS), Fourier-transform infrared spectroscopy (FTIR), Raman (micro)spectroscopy, and X-ray diffraction spectroscopy (XRD). Core-electron orbital energies were calculated following Koopmans' theorem, further literature on the XPS working principle and *ab initio* orbital calculations are presented in Appendix A1 (Koopmans, 1933). FTIR and Raman spectral calculations were performed using a numerical differentiation procedure established by Komornicki *et al.*, for more information on the working principles and spectral calculations see Appendix A2 and A3, respectively (Barca et al., 2020; Komornicki & McIver, 1979). Lastly, the powder diffraction patterns were calculated following Bragg’s law, the XRD working principle and spectral calculations are further detailed in Appendix A4 (Momma & Izumi, 2008).

Section 3: Materials and Methods

3.1. Sample preparation of UHMWPE-based samples

‖ This section is taken from my first-authored published work, specifically from section 2 in (Bruggeman et al., 2022), please see the 'Publications' section. ‖

3.1.1. Surface polishing of UHMWPE

UHMWPE sheets were purchased at Direct Plastics Ltd (Sheffield, UK) with a thickness of 5 mm. This project served as a proof of concept by utilizing regular UHMWPE instead of GUR®, assuming it would exhibit similar performance characteristics to surgical-grade UHMWPE, with the primary distinction being the absence of processing aids. The UHMWPE sheets were waterjet cut into squares of 10 mm by 10 mm and subsequently polished. The polishing was performed using silicon carbide grinding papers of 400, 800, 1200 and 2000 grit consecutively for two minutes each, after which finished with a 6 μm diamond polishing paste for an additional two minutes. After polishing, the samples were washed with ethanol to remove the polishing paste, left to dry in open air inside a fume hood for approximately 30 minutes, stored in polystyrene Petri dishes, and kept in a small desiccator within a dark cabinet workbench, resulting in undoped and untreated UHMWPE (UD/UT).

3.1.2. α-Tocopherol doping of UHMWPE

α-Tocopherol (αTH; i.e., an orange-coloured viscous fluid with an oily consistency) was purchased at Sigma-Aldrich Ltd (Dorset, UK) with a purity of >96 % (i.e., HPLC grade, the highest grade available apart from pharmaceutical standards/certified reference materials) and kept in a fridge of 5°C during storage. Prior to the doping, the UHMWPE samples were briefly washed with ethanol as αTH is freely soluble in ethanol, and subsequently left to dry in open air inside a fume hood for approximately 30 minutes. Doping of the polished UHMWPE samples was carried out by adding three samples to 50 mL of fresh αTH mixed in a 100 mL round bottom flask at 90°C for 4 hours under stirring and blanketed with nitrogen. The doping temperature of 90°C was chosen as, according to the results of differential scanning calorimetry

(DSC), there was no significant onset of the heating/endothermic peak observed prior to 120°C and the cooling/exothermic peak returned mostly to the baseline at 90°C. As DSC indicated it would have minimal impact on the phase transition of UHMWPE, 90°C was determined to be a 'safe' temperature for the treatments – the DSC diagram of UD/UT and corresponding details are provided in Appendix B1.

The doping duration of 4 hours was chosen based off similar work in the literature, which focussed on the diffusion of αTH in UHMWPE at 100°C for 2 and 8 hours, resulting in a doping depth (i.e., in this work, αTH index = 0.1) of ~1, ~2, and ~4mm, respectively (Oral et al., 2007). Based on the literature, it was assumed that 4 hours of doping would result in a doping depth between 1-2 mm. The doping depth of 1-2 mm was deemed suitable to ensure that the ASPN treatment depth would not surpass this depth and that there would be viable αTH beneath the ASPN layer. After doping, the samples were washed with ethanol to remove any remaining αTH (i.e., until the samples were no longer sticky or visually displaying an orange-coloured fluid), left to dry in open air inside a fume hood for approximately 30 minutes, stored in polystyrene Petri dishes, and kept in a small desiccator within a dark cabinet workbench, resulting in αTH-doped and untreated UHMWPE (D/UT).

3.1.3. Active screen plasma-nitriding of UHMWPE

Plasma-nitriding of the undoped and doped UHMWPE surfaces was performed with a 40 kW DC nitriding unit (Klöckner Ionon, Köln, Germany) in combination with an active screen setup (i.e., ASPN). The active screen mesh cylinder was made of 0.7 mm thick perforated sheet steel, with an average height of 130 mm and a diameter of 120 mm. For each treatment, a total of 36 samples were treated, where half was undoped and the other half doped with αTH. The distance between the sample surface and the active screen was set at 20 mm. A gas mixture of 80% N_2 and 20% H_2 was used with an initial flow rate of 4 NL/h, after which the vacuum pump was adjusted to balance the pressure at 75 Pa. The working gas ratio was

selected as it introduced more nitrogen on the UHMWPE surface after ASPN when compared to the more commonly observed ratio of 25% N_2 and 75% H_2 (i.e., representing the N:H ratio for ammonia, a previously popular gas used for plasma nitriding), as shown with XPS by a former group member (Kaklamani, 2012). Treatments were performed at 90^{o}C (see 3.1.2 for justification on temperature) for a duration of 15, 30 and 60 minutes once the desired temperature was achieved. The ASPN treatment durations of 15, 30 and 60 minutes were chosen as the introduction of nitrogen during ASPN of UHMWPE practically plateaus between 30 and 60 minutes, as shown with XPS by a former group member (Kaklamani, 2012). When completed, the power and inlet gas were switched off so that the plasma chamber was cooled down in the presence of the remaining working gas whilst maintaining the pressure at 75 Pa. When the plasma chamber was cooled down to about 50°C, the vacuum was slowly released, and the samples were removed from the plasma chamber, resulting in undoped plasma-treated and doped plasma-treated UHMWPE (UD/PT# and D/PT#, where # denotes the treatment time of 15, 30, or 60 minutes). The samples were stored in polystyrene Petri dishes with the plasma-treated surface facing upwards, and kept in a small desiccator within a dark cabinet workbench for about two weeks prior to analysis to minimize differences in sample oxidation (i.e., ensuring the radicals can undergo decay/oxidation and reach an equilibrium state, resulting in more stable/representative samples with reduced influence of unstable species).

3.1.4. AMP immobilisation on plasma-treated UHMWPE

Immobilisation of the AMPs and/or amino acids (AAc) on the plasma-treated UHMWPE surfaces was attempted using various coupling chemistries. These attempts include the use of: (1) *N,N′*-diisopropylcarbodiimide (DIC) in combination with ethyl-cyano(hydroxyimino)acetate (i.e., *Oxyma Pure*) to induce peptide-based coupling, purchased at Sigma-Aldrich Ltd (Dorset, UK) with a purity of 99% and CEM Corporation (Matthews, USA) with a purity of >99.5%, respectively; (2) *N,N′*-Dicyclohexylcarbodiimide (DCC) in

combination with *4*-(Dimethyl-amino)pyridine (DMAP) to induce ester-based coupling (i.e., Stiglich esterification), purchased at Sigma-Aldrich Ltd (Dorset, UK) with a purity of 99% and >99%, respectively; and (3) *1,1'*-Carbonyldiimidazole (CDI) to induce carbamate-based coupling, purchased at Sigma-Aldrich Ltd (Dorset, UK) with a purity of >97%. The N-terminal of the AMP/AAc was left Fmoc-protected prior to immobilisation, the AMP/AAc was immobilised to the plasma-treated UHMWPE surface either by conjugation to NH_2-based (e.g., amines, amidine, etc.) or OH-based functionalities (e.g., alcohols, acids, etc.).

In all cases, a concentration of 0.2 M AMP/AAc was used in 50 mL dimethylformamide (DMF) in a 50 mL round-bottom flask under stirring and blanketed with oxygen-free nitrogen gas. Based on preliminary UV spectrophotometry results used to determine the degree of substitution (which were in the nM range), it was assumed that 50 mL of 0.2 M AMP/AAc solution was in the excess of the functionalities present on the plasma-treated UHMWPE surfaces. The activator and activator base equivalence, reaction temperature, and duration used for the above-mentioned coupling procedures, which are presented in Table 6, were taken from reaction conditions observed in the literature (J. M. Collins et al., 2014; Hongmei Li et al., 2011; Neises & Steglich, 1978). After the respective coupling was completed, the samples were taken from the DMF solution and left inside the fume hood to evaporate the last traces of DMF. The samples were briefly stored in polystyrene Petri dishes and kept in a small desiccator within a dark cabinet workbench or used immediately once dried, depending on the analysis.

Table 6. Equivalence of the activator and base, temperature, and duration of the coupling chemistries.

	Activator / Base	**Temperature (°C)**	**Duration**
DIC / Oxyma Pure	1 eq. / 1 eq.	75	30 min
DCC / DMAP	1.1 eq. / 0.11 eq.	0 → RT	5 min → 3 hr
CDI	1.1 eq. / -	RT	4 hr

3.1.5. Sample IDs of UHMWPE-based samples

Throughout this work the UHMWPE-based samples are referred to by their respective sample ID, which depends on the treatment the samples received as were discussed in Section 3.1.1-4. The respective sample IDs of the UHMWPE-based samples are shown in Table 7. If AMPs/AAc were immobilised onto the sample surface, a hyphen is added to the sample ID followed by the AMP/AAc abbreviation, e.g., UD/PT60-(KR-12) or D/PT60-(Gly-Fmoc).

Table 7. Sample IDs of UHMWPE-based samples.

	Untreated (UT)	**Plasma–treated (PT#)**		
		15 min.	**30 min.**	**60 min.**
Undoped (UD)	UD/UT	UD/PT15	UD/PT30	UD/PT60
Doped (D)	D/UT	D/PT15	D/PT30	D/PT60

3.2. Characterisation of the UHMWPE-based surfaces

3.2.1. Scanning electron microscopy (SEM)

Scanning electron microscopy (SEM) was performed either using a JSM-6060LV from JEOL Ltd (Hertfordshire, UK) at a working distance of 10 mm, an acceleration voltage of 5 kV and a spot size of 30; or using a XL-30 Environmental SEM (ESEM) from Philips (Eindhoven, NL) at a working distance of 10 mm, an acceleration voltage of 7 kV and a spot size of 3. Prior to recording the SEM micrographs, the samples were gold-coated using a SC 500 sputter coater from Quorum technologies (Lewes, UK) for 3 minutes at 25 mA – to introduce sample conductivity. SEM micrographs were recorded at a magnification of 500x and 2000x with the JSM-6060LV and at 1000x with the XL-30, for a randomly selected sample from each series. ImageJ (1.53t) was used to enhance the local contrast of the SEM images.

3.2.2. Attenuated total reflectance spectroscopy (ATR-FTIR)

Spectral simulation

To aid the spectral interpretation of the experimental ATR-FTIR spectra, various IR spectra were calculated based on a linear C20 alkane (serving as a model structure for polyethylene), the C20 alkane model structure was modified to reflect the desired chemical functionalities of interest (e.g., containing hydroxyl, amine, etc.). Next to the polyethylene-based model structures, αTH was also investigated. The molecular structures were drawn in 'Avogadro' and pre-optimised using the 'Merck Molecular Force Field' (MMFF94) energy minimisation, the pre-optimised structures were imported in '*Spartan'14*' developed by Wavefunction, Inc. (Irvine, USA). The model structures are shown in Figure 14. Calculations in '*Spartan'14*' were performed using the 6-31G(d) Pople basis set. Prior to the frequency calculations, the molecular structures were further optimised in '*Spartan'14*' using the '*EDF2*' DF and Pulay's DIIS interpolation until they reached a convergence limit of 1.0E-7. After the optimisation, the FTIR spectra were simulated also using the '*EDF2*' DF and Pulay's DIIS interpolation – as displayed in Figure 15. The '*EDF2*' DF was chosen as it was shown to provide a significant improvement in the accuracy of predicted molecular vibrational frequencies, when compared to other more commonly used DFs (i.e., MP2, B3LYP, etc.) and is competitive with the computationally expensive CCSD(T) method (C. Y. Lin et al., 2004).

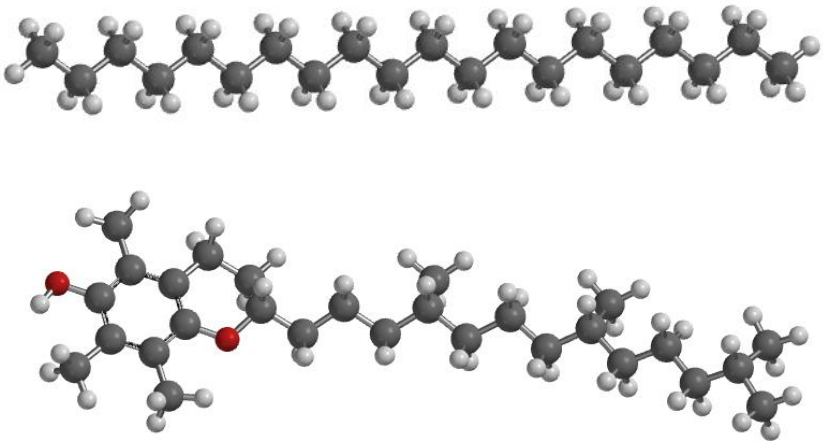


Figure 14. Model structures used for the spectral simulations, showing (top) the C20 alkane and (bottom) αTH.

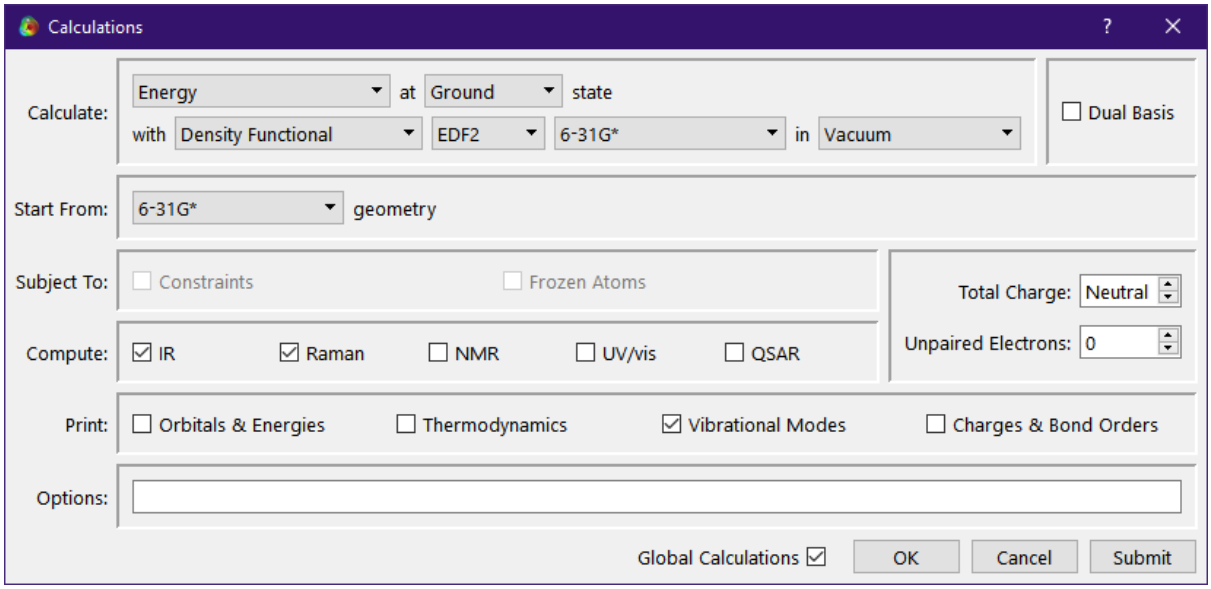


Figure 15. Settings for '*EDF2*' frequency calculations in '*Spartan'14*'.

Spectral acquisition

ATR-FTIR was performed using a Nicolet 8700 FTIR from Thermo Fischer Scientific (Oxford, UK) in combination with a single-reflectance diamond Golden Gate ATR module from Specac (Orpington, UK). The samples were clamped onto the ATR crystal with a force of 60 cNm. After a background measurement of 100 scans prior to each spectral measurement, the spectra were collected at three positions across the sample surface with about 2 mm distance between each point of analysis. All spectra were recorded in absorbance mode by taking 100 scans between 700 – 4000 cm^{-1} with a data spacing of 0.482 cm^{-1}. To allow direct comparison, the same samples used during ATR-FTIR analysis were also used for the Raman analysis.

Spectral processing

The recorded spectra, taken at three positions across the sample surface, were summed to improve the signal-to-noise (S/N) ratio. The individual spectra are presented in Appendix B2. All ATR-FTIR spectra shown in this work were corrected for the penetration depth of the evanescent wave and anomalous dispersion using the advanced ATR correction available in

the Thermo-Fischer OMNIC software (v9.2.86) with the sample's refractive index set at 1.52 – this value was found to be a reasonable estimation for UHMWPE (Kutz et al., 2022).

The advanced ATR correction was used to correct the obtained ATR-FTIR spectra for the angle at which the IR beam strikes the diamond ATR crystal, using the refractive index of the crystal and sample (i.e., convert the spectrum into its expected transmission spectral form). Some of the IR beam light reflects off the crystal surface in contact with the sample, creating an evanescent wave that penetrates the sample. The sample absorbs some of the evanescent wave's energy, which results in the spectrum observed (Nunn et al., 2008). The penetration depth, d_p, of the evanescent wave in the sample can be estimated following:

$$d_p = \frac{\lambda}{2\,\pi\, n_1 \sqrt{sin^2(\theta) - (n_2 / n_1)^2}} \qquad \textit{(Eq. 1)}$$

where λ is the wavelength in nm, θ is the angle of incidence of the IR beam in degrees, n_1 is the refractive index of the ATR crystal, and n_2 is the refractive index of the sample. From Equation 1, plotted for UHMWPE in Figure 16, it is clear that the penetration depth of the evanescent wave in an ATR-FTIR spectra decreased towards higher wavenumbers. The effective penetration, $d(e)$, also plotted in Figure 16, provides an approximate sample thickness required to obtain a similar FTIR spectrum using the Transmission mode set-up when compared to ATR. The effective penetration was estimated by summing the parallel, $d(e)_{\parallel}$, and perpendicular, $d(e)_{\perp}$, polarisation parts of the effective penetration, following:

$$d(e)_{\parallel} = \frac{(n_2 / n_1)\,(\lambda / n_1)\cos(\theta)\,(2\,sin^2(\theta) - (n_2 / n_1)^2)}{\pi\,(1 - (n_2/n_1)^2)\sqrt{sin^2(\theta) - (n_2 / n_1)^2}\,((1 + (n_2/n_1)^2)\,sin^2(\theta) - (n_2 / n_1)^2} \qquad \textit{(Eq. 2)}$$

$$d(e)_{\perp} = \frac{(n_2 / n_1)\,(\lambda / n_1)\cos(\theta)}{\pi\,(1 - (n_2/n_1)^2)\sqrt{sin^2(\theta) - (n_2 / n_1)^2}} \qquad \textit{(Eq. 3)}$$

$$d_e = d(e)_{\parallel} + d(e)_{\perp} \qquad \textit{(Eq. 4)}$$

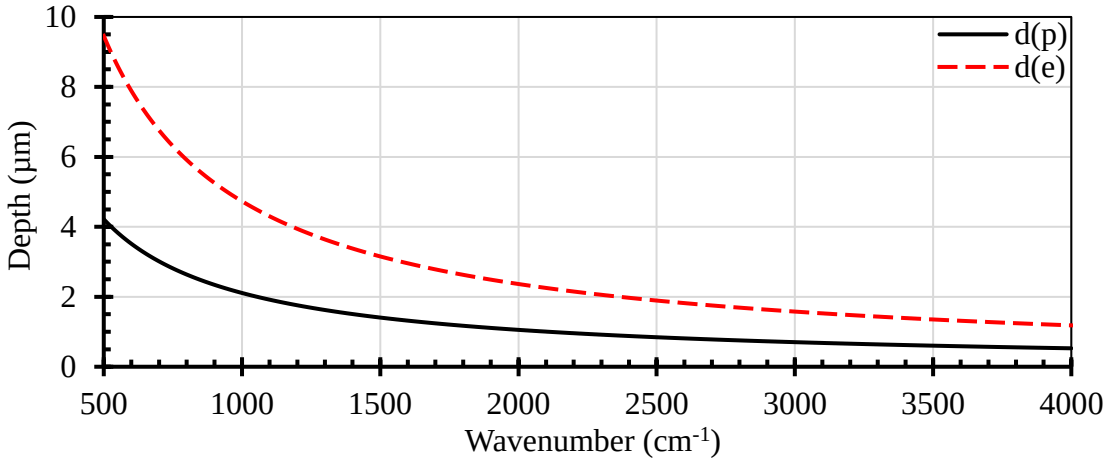


Figure 16. The penetration depth (**black**, solid line) and effective penetration (**red**, dashed line) estimated for UHMWPE (n_2 = 1.52) against a diamond crystal (n_1 = 2.40).

Next to the wavenumber-dependent penetration depth of the evanescent wave, the ATR-FTIR spectra also need to be corrected for the anomalous dispersion (i.e., the change in sample refraction index near an absorption band) which shifts absorption bands to lower frequencies – especially with strong bands. The corrected band intensity is given following:

$$A = (\log_{10} e)\,\frac{n_2}{n_1}\frac{E_0^2}{\cos(\theta)}\frac{d_p}{2}\alpha \qquad \textit{(Eq. 5)}$$

where E_0 and α are the electric fields of the evanescent wave at the boundary and the absorption coefficient per unit thickness of the sample, respectively (Bertie & Eysel, 1985; Spiller, 2010). After the advanced ATR correction, the summed and corrected spectra were imported into the CasaXPS (i.e., Computer-Assisted Spectral Analysis) software for peak fitting.

To fit the spectra accordingly, an appropriate lineshape needed to be determined, which was done following lineshape scans. The ideal lineshape depends on the material, as the spectral lineshape is determined by the sum of the vibrational frequencies, the environment of the molecule (i.e., gas, liquid or solid) which depicts the exact frequency, and the effective relaxation lifetime (τ) of the vibrational population (Bradley, 2007). The relaxation of a vibrational frequency is associated to the lifetime of the excited states (i.e., amplitude

correlation time) when a molecule interacts with IR radiation or a Raman laser, τ_a, and its coherence lifetime, τ_c (i.e., the lifetime of excited molecules vibrating together). Due to this relation, there are two limiting cases within which the spectral lineshapes are defined: $\tau_c >> \tau_a$ or $\tau_c << \tau_a$. As the coherence lifetime diminishes, the intensity of the vibrational frequencies will start to interfere and ultimately cancel each other (i.e., dephasing). In gases, dephasing sets in quickly as the rotations and collisions of molecules occur rapidly (i.e., $\tau_c << \tau_a$), resulting in a dominant Lorentzian lineshape – displaying a sharp centre and long extending wings. Whereas in solids, considering the environment is not in motion, relaxation of the vibrational population sets in before dephasing (i.e., $\tau_c >> \tau_a$), resulting in a dominant Gaussian lineshape – displaying a bell curve shape with short wings. The lineshapes for liquids exist within the two limits, as the environment does not limit the movement of molecules, but the molecules are also not able to display the rapid motion observed in gases.

To achieve the lowest error between the experimental spectra and the synthetic envelope created by the peak fitting, lineshapes are typically a convolution of the Lorentzian and Gaussian lineshape – also known as a pseudo-Voigt lineshape. This is due to, e.g., optical/electrical effects from the instrumental setup resulting in Gaussian broadening or the removal of the extended Lorentzian tails when fitting a background to the experimental spectra. Within CasaXPS, this pseudo-Voigt lineshape (*LA*) is given by:

$$LA(\alpha, \beta, m) = \begin{cases} [L(x)]^{\alpha} & x \leq P \\ [L(x)]^{\beta} & x > P \end{cases}, \qquad \textit{(Eq. 6)}$$

where α and β are the left-hand side and right-hand side asymmetry parameters, respectively, *m* is an integer between 0 and 1400 which defines the width of the Gaussian used to convolute the Lorentzian lineshape, and *L(x)* is the underlying Lorentzian lineshape, following:

$$L(x) = \frac{1}{1 + 4\left(\frac{x - P}{F}\right)^2}, \qquad \textit{(Eq. 7)}$$

where P is the respective position (e.g., in wavenumber, energy, etc.) and F is the full-width-half-maximum (FWHM) of the lineshape (Fairley, 2008). An example of a pure Lorentzian and Gaussian lineshape, as well as various asymmetric lineshapes are shown in Figure 17.

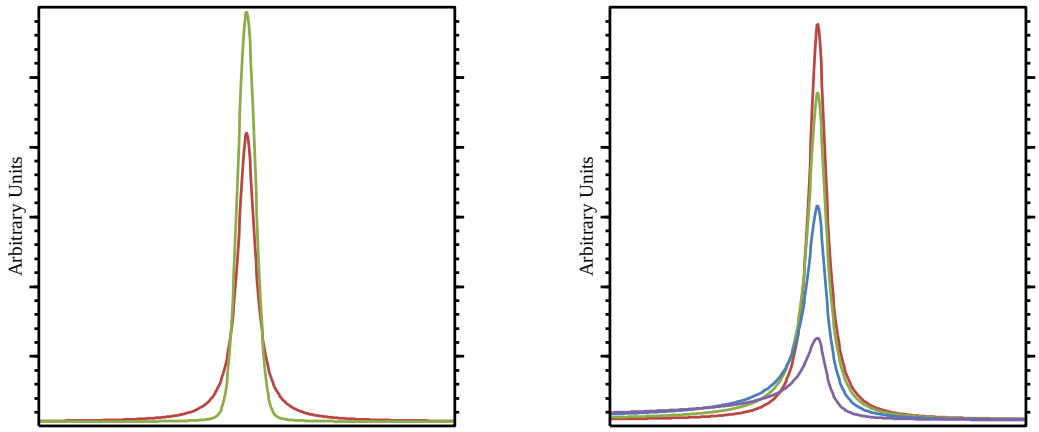


Figure 17. Example lineshapes of (left) a pure (**red**) Lorentzian and (**green**) Gaussian lineshape with the same area and FWHM, and (right) various asymmetric Lorentzian lineshapes with the same area and FWHM, showing (**red**) LA(1,1,0), (**green**) LA(0.8,1,0), (**blue**) LA(0.6,1,0), and (**purple**) LA(0.4,1,0).

In this work, the lineshapes were typically established per region following three lineshape scans and its development was guided by the damped least-squares peak fitting method (i.e., the Levenberg–Marquardt algorithm). An example of a lineshape development is presented in Figure 18. The spectral region was initially fitted with various pure Lorentzian components, after which the Gaussian contribution was determined first by a lineshape scan following LA(1,1,[0,1400]). Subsequently, the symmetric tail extension (α+β) of the lineshape was determined following LA([0.8,2],840). As the area deviation between the experimental spectrum and synthetic envelope was observed on the left side of the spectrum, the left-hand side asymmetric tail extension (α) was determined following LA([0.4,1.6],1.52,840).

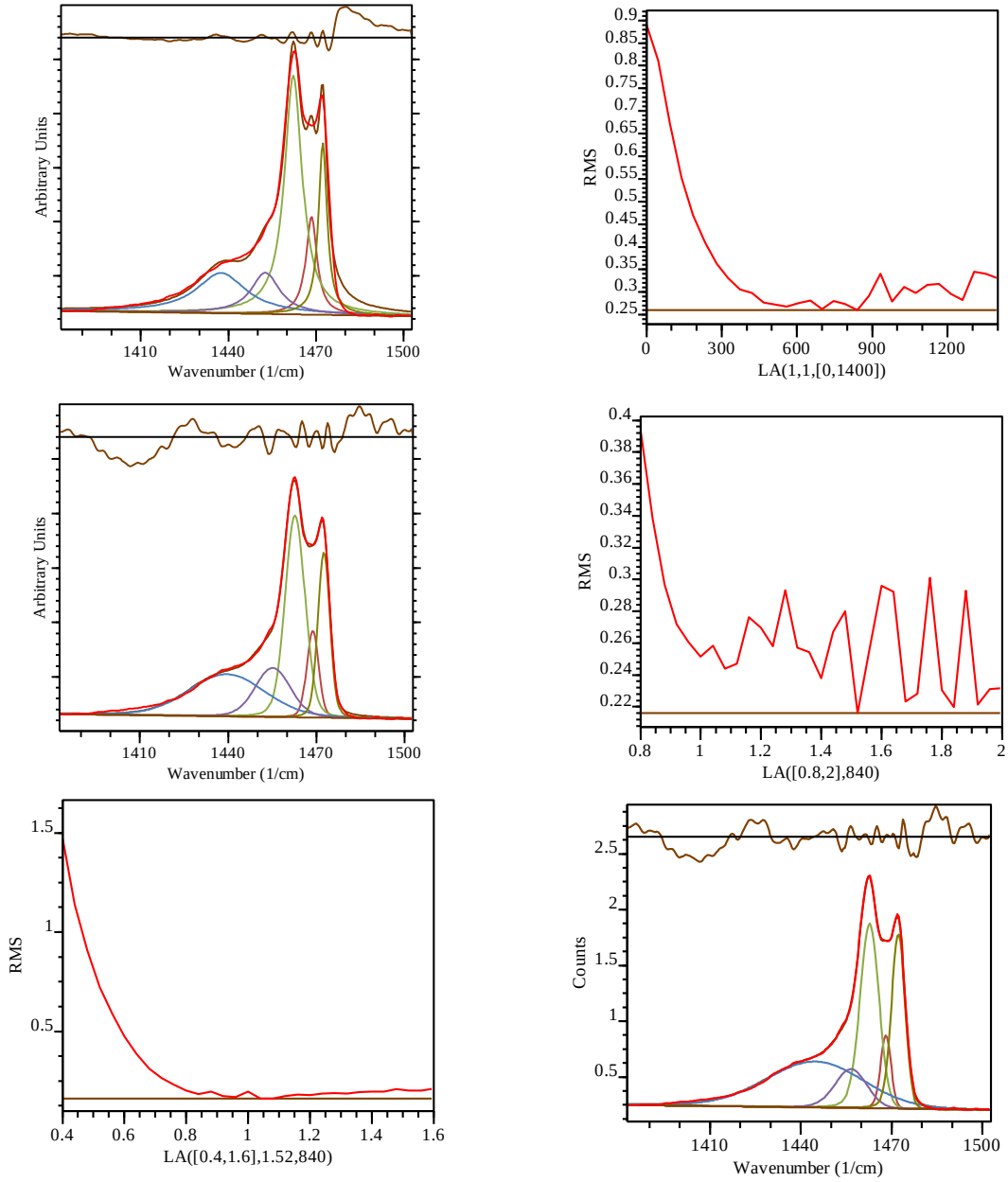


Figure 18. Example of lineshape development in a FTIR spectrum, showing (top-left) the spectral region fitted with LA(1,1,0), (top-right) Gaussian contribution scan LA(1,1,[0,1400]) with min. at 840, (middle-left) spectral region fitted with LA(1,1,840), (middle-right) tail extension scan LA([0.8,2],[0.8,2],840) with min. at 1.52, (bottom-left) asymmetric tail extension scan LA([0.4,1.6],1.52,840) with min. at 1.04, (bottom-right) spectral region fitted with the developed lineshape LA(1.04,1.52,840).

3.2.3. Raman microspectroscopy

Spectral simulation

The Raman spectra were also calculated in '*Spartan'14*' using the 6-31G(d) Pople basis set in combination with the 'EDF2' DF and Pulay's DIIS interpolation, identical to the simulated IR spectra as discussed in Section 3.2.2.

Single-point spectral acquisition

Raman microspectroscopy was performed using a Renishaw inVia Qontor confocal Raman microscope (Gloucestershire, UK) equipped with a Peltier-cooled CCD detector and a RL532C50 laser (i.e., a 532 nm green laser with a maximum power of 50 mW and an excitation wavelength of 532.1 ± 0.3 nm). The laser was not expected to damage UHMWPE, considering laser surface modifications typically require a power around 6-30 W to be effective, and thermal degradation of UHMWPE does not occur (during sintering) until about 400°C (Khalil et al., 2019). All Raman measurements have been recorded with a Leica N PLAN EPI 20x objective (NA = 0.4) and an 1800 l/mm (vis) grating. Next to that, the pinhole was set to 'IN' with a slit opening of 20 μm, the pinhole is used to spatially filter the analysis volume so that the Raman scatter is detected from the desired focal plane only. The laser was set at a relative power of 10% for the single-point spectral acquisition, with an exposure time of 10 seconds. The single-point spectra were collected in extended mode between 700 and 4000 cm^{-1} with a resolution of 1.59 cm^{-1} in high confocality. The single-point spectra were collected at three positions across the sample surface with about 2 mm distance between each point of analysis. Using the laser wavelength (λ), the numerical aperture (NA) of the objective, and the refractive index of the sample (n), the laser spot size (i.e., Airy disc pattern; S), and the diffraction-limited lateral (Φ) and axial (ΔZ) resolution were estimated following Rayleigh criterion:

$$S \approx \frac{1.22 * \lambda}{\mathrm{NA}}, \qquad \textit{(Eq. 8)}$$

$$\Phi \approx \frac{0.61 * \lambda}{\mathrm{NA}}, \qquad \textit{(Eq. 9)}$$

$$\Delta Z \approx \frac{2 * n * \lambda}{\mathrm{NA}^2}, \qquad \textit{(Eq. 10)}$$

(Edinburgh Instruments, 2019; Wallace et al., 2015). When using Equation 8-10 for the above-mentioned instrumental set-up, the laser spot size (S) was estimated at 1.62 μm, and the diffraction-limited lateral (Φ) and axial (ΔZ) resolution were estimated at 0.81 μm and 10.11 μm, respectively. However, these values represent the ideal, the actual resolution will also depend on the power, quality, and alignment of the optics/laser. Next to that, these estimations do not include contributions from scattered light to/from the sample that is analysed.

Point-by-point mapping acquisition

The same instrumental set-up (i.e., laser type, objective, grating, pinhole and slit opening) used for the single-point Raman spectra was also used for the point-by-point mapping, although using different acquisition settings (i.e., laser power, exposure time, and scanning mode). An image of 1 x 1 mm was acquired using a 100 x 100 pixel grid and a step size of 10 μm, resulting in 10000 individual pixel spectra – in this case, undersampling was used to acquire a larger image and ensure each pixel will provide an isolated analysis volume. The exposure time during the point-by-point mapping was set at 100 ms, to compensate for the loss in signal due to the decreased exposure time, the laser power was increased to a relative power of 100% (i.e., 50 mW). The point-by-point maps were collected in static mode centred at 1200 cm^{-1}, resulting in a spectral range between 268 and 2005 cm^{-1}, with a resolution of 1.76 cm^{-1} in high confocality. Next to that, as the signal levels were relatively low due to the short acquisition time used with the mapping, the detector was set to 'high sensitivity, fast readout' mode so it increased the signal gain. After the mapping was completed, the acquired data was processed in the CasaXPS software.

Spectral processing

The recorded single-point spectra were summed to improve the S/N ratio, the individual spectra are presented in Appendix B3. After summing the spectra per sample, the summed

single-point spectra were imported into the CasaXPS software for peak fitting. The appropriate lineshapes were established similarly as described in Section 3.2.1 for FTIR spectra. The point-by-point maps were also imported into the CasaXPS software and PCA-based (i.e., principal component analysis) noise reduction was used to improve the S/N ratio prior to peak fitting the pixel spectra. The PCA-based noise reduction was performed by producing a filter mask of the abstract factors (AFs) that showed spectral features – example pixel spectra and corresponding AFs of UD/UT are displayed in Figure 19. It should be noted that PCA is not a data manipulation technique, it reduces data variability by taking out the AFs that only show noise.

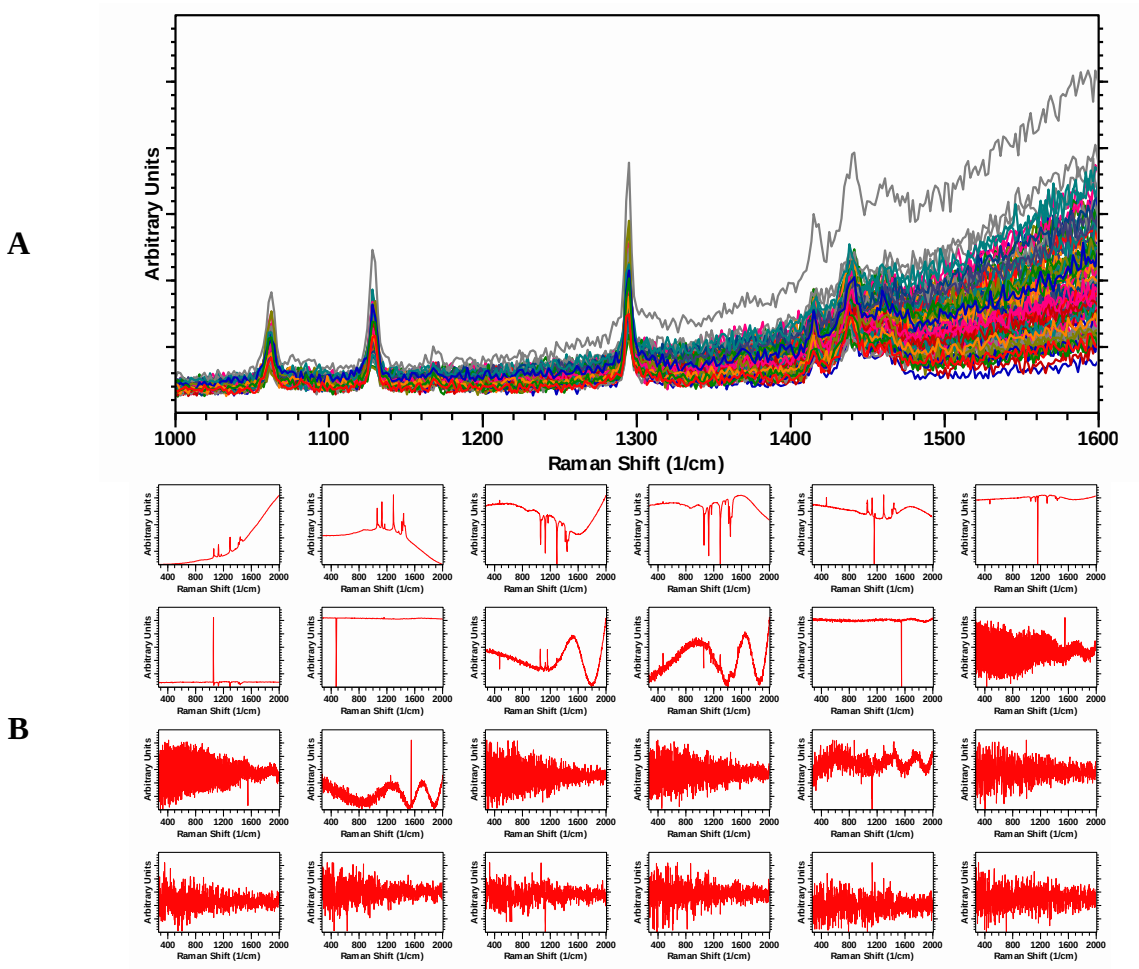


Figure 19. The (A) raw pixel spectra and (B) the corresponding abstract factors (showing the first 24/100).

As can be observed in Figure 19B, spectral features were only present in the first 10 AFs, after which the AFs showed a variety of noise profiles. Using this information, a filter mask was made from the first 12 AFs – although only the first 10 AFs showed spectral features,

two additional AFs were added to ensure that potential "hidden" spectral features were included. Using this filter mask, the noise in the pixel spectra was significantly reduced and the spectral features were more prominent, as shown in Figure 20. Occasionally, small signal artefacts were observed (e.g., at 1550 cm^{-1}) due to the relatively low intensity of the spectra. These artefacts were caused by either cosmic rays present at said location or by the "probe" which scans the spectral intensity during the PCA-based noise reduction.

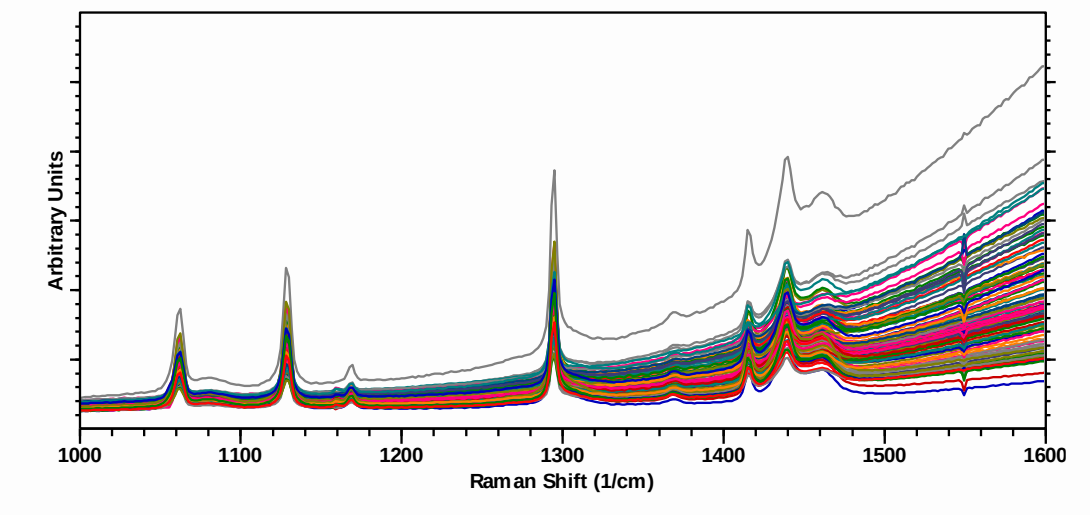


Figure 20. The PCA-based noise reduced spectra of UD/UT using the first 12 AFs as a filter mask.

3.2.4. Wide-Angle X-Ray Diffraction (WXRD)

Spectral simulation

To aid the spectral interpretation of the experimental WXRD spectra, XRD patterns were calculated for the reference-based orthorhombic and monoclinic unit cells of UHMWPE in VESTA (Momma & Izumi, 2008). As discussed in Appendix A4, using the structural parameters and the free atomic scattering factors, the structure factors and thus the XRD patterns were calculated for the PE unit cells. In this work, two crystalline and an amorphous phase were expected to be observed in the UHMWPE-based samples. The two crystalline phases will take form of an orthorhombic (*P n m a*; space group 62) and a meta-stable monoclinic (*A 2/m*; space group 12) unit cell, the reference-based structural parameters of these

unit cells are shown in Table 8 (Bevis & Crellin, 1971; Miao et al., 2001; Olsson et al., 2018; Tasumi & Krimm, 1967). Due to the random chain orientation observed in the liquid-like amorphous phase, it cannot be expressed as a repeating unit cell and its peak position can therefore not be calculated. However, the expected location and peak width of the amorphous halo was determined by Joo *et al.* using variable-temperature XRD, which showed its maximum around 19.5° 2θ with a FWHM of roughly 5° 2θ (Joo et al., 2000).

Table 8. Structure parameters of (left) the drawn PE unit cells and (right) the bonding of the atoms (Bevis & Crellin, 1971; Miao et al., 2001; Olsson et al., 2018; Tasumi & Krimm, 1967).

	Orthorhombic (*P n m a*)	**Monoclinic (*C 2/m*)**
a (Å)	7.42	8.09
b (Å)	4.96	4.79
c (Å)	2.55	2.53
***β* (°)**	90.0	108
***V* (Å^3)**	93.85	93.24

	Bond length (Å)
$r_{C–C}$	1.53
$r_{C–H}$	1.11
	Bond angle (°)
CCC	113.53
CHC	106.06

As depicted in Figure 21, the PE chains in the orthorhombic unit cell are rotated by 45° relative to the a-axis and nearest neighbouring chains are rotated 90° relative to each other, whereas in the monoclinic unit cell the neighbouring chains on the a-axis are rotated by 180°. As briefly mentioned earlier, the monoclinic unit cell is meta-stable and this phase arises due to stress beyond the yield point of PE – resulting in "slippage" of the orthorhombic cell as visualised in Figure 22 (Joo et al., 2000). Despite being unstable at zero pressure, the monoclinic phase remains stable when subjected to compressive transverse deformations that pin the chains due to the closely spaced H atoms and prevent them from wiggling freely, as shown theoretically by Olsson *et al.* (Olsson et al., 2018). This means that the monoclinic unit cell parameters from the literature may not portray that of zero pressure, nonetheless, it was expected that the calculated spectra provided reasonable initial guesses on the peak positions

of this meta-stable phase. To calculate the spectra in VESTA, the X-ray wavelengths for Cu–$K\alpha_1$ and Cu–$K\alpha_2$ were set to 0.15406 nm and 0.15443 nm, respectively.

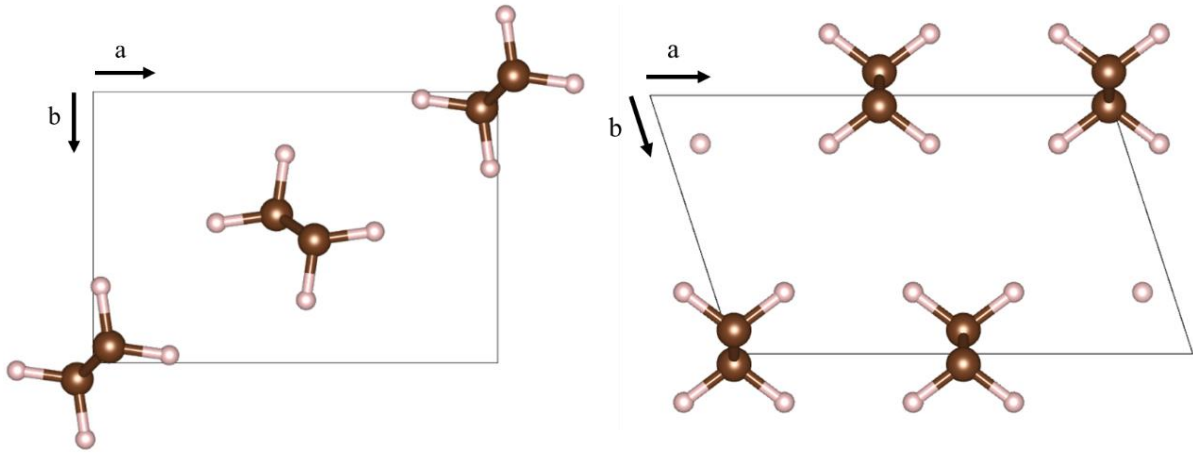


Figure 21. Top-view of (left) the orthorhombic unit cell and (right) the monoclinic unit cell.

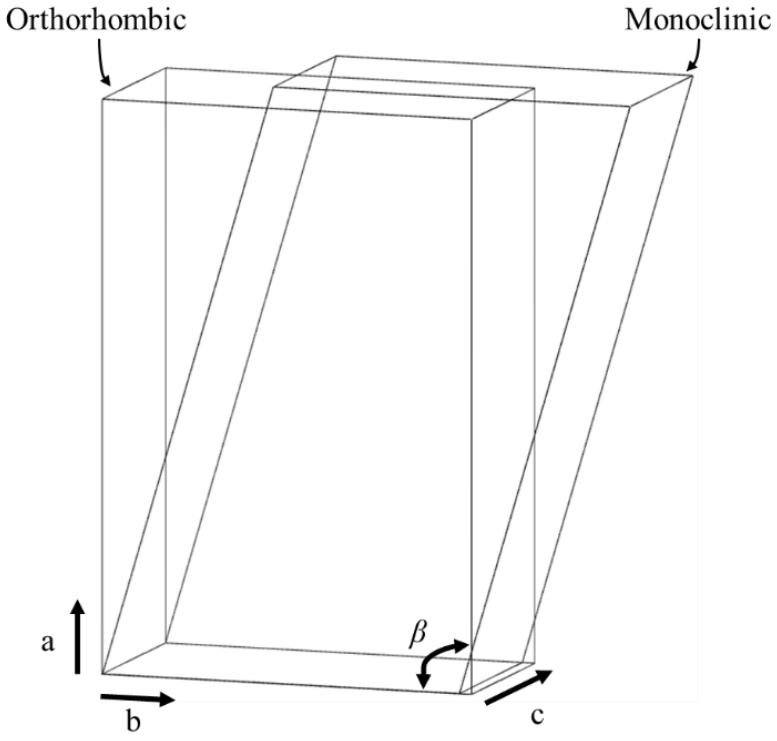


Figure 22. Three-dimensional view of the orthorhombic and monoclinic unit cell.

Spectral acquisition

The WXRD spectra were recorded with a Bruker D8 Advance. Prior to acquiring all sample spectra, various scanning rates were tested to determine the best spectral resolution versus the acquisition speed. A scanning rate of 1.2° per minute was determined to provide the best spectral resolution at a reasonable acquisition speed. The voltage and current of the Cu-Kα X-ray source (0.15406 nm) were set to 40 mA and 40 kV, respectively, providing a power of 160 W. The instrumental broadening of the XRD instrument was corrected for by analysing a corundum (i.e., Al_2O_3) standard (i.e., NIST Standard Reference Material 676a), see Appendix B4 for more information on the performed correction (Cline, 2015; Fawcett et al., 1988). The spectra of the samples were recorded between 5 to 60 2θ using the Bragg-Brentano geometry. Only one sample from each sample type (e.g., UD/UT, D/UT, etc.) was analysed as the spectra showed negligible change when compared to each other, which was expected given that plasma modification of most polymers is often limited to a penetration depth of a couple of hundred nanometers to a few microns (Bhat & Upadhyay, 2002; Chaichi et al., 2019). After the spectral acquisition, the spectra were imported and peak fitted in the CasaXPS software.

Spectral processing

Using the calculated spectra as estimated peak positions (shown in Section 4.1.5, positions were constrained by ± 0.2°), a peak model between 10° and 35° was used to perform lineshape scans to determine the appropriate Gaussian contribution and peak asymmetry (see Section 3.2.2 on lineshape scans) – peak asymmetry towards lower 2θ was induced by the 'transparency effect', which is commonly observed in organic materials containing light elements (e.g., C, H, N, and O) (Cowden, 2021). After the lineshape scan were performed, the respective parameters were adjusted for all crystalline peaks at the same time across the desired interval. As shown in Figure 23A, a 4-knot polynomial was used to separate the crystalline

components from the amorphous halo. The crystalline components, see Figure 23B, are subsequently subtracted from the raw spectrum to reveal the amorphous halo, see Figure 23C. The separation of components allowed for uncomplicated lineshape scans for both phases, once completed, the best-fit lineshapes were used to fit the original spectrum, see Figure 23D.

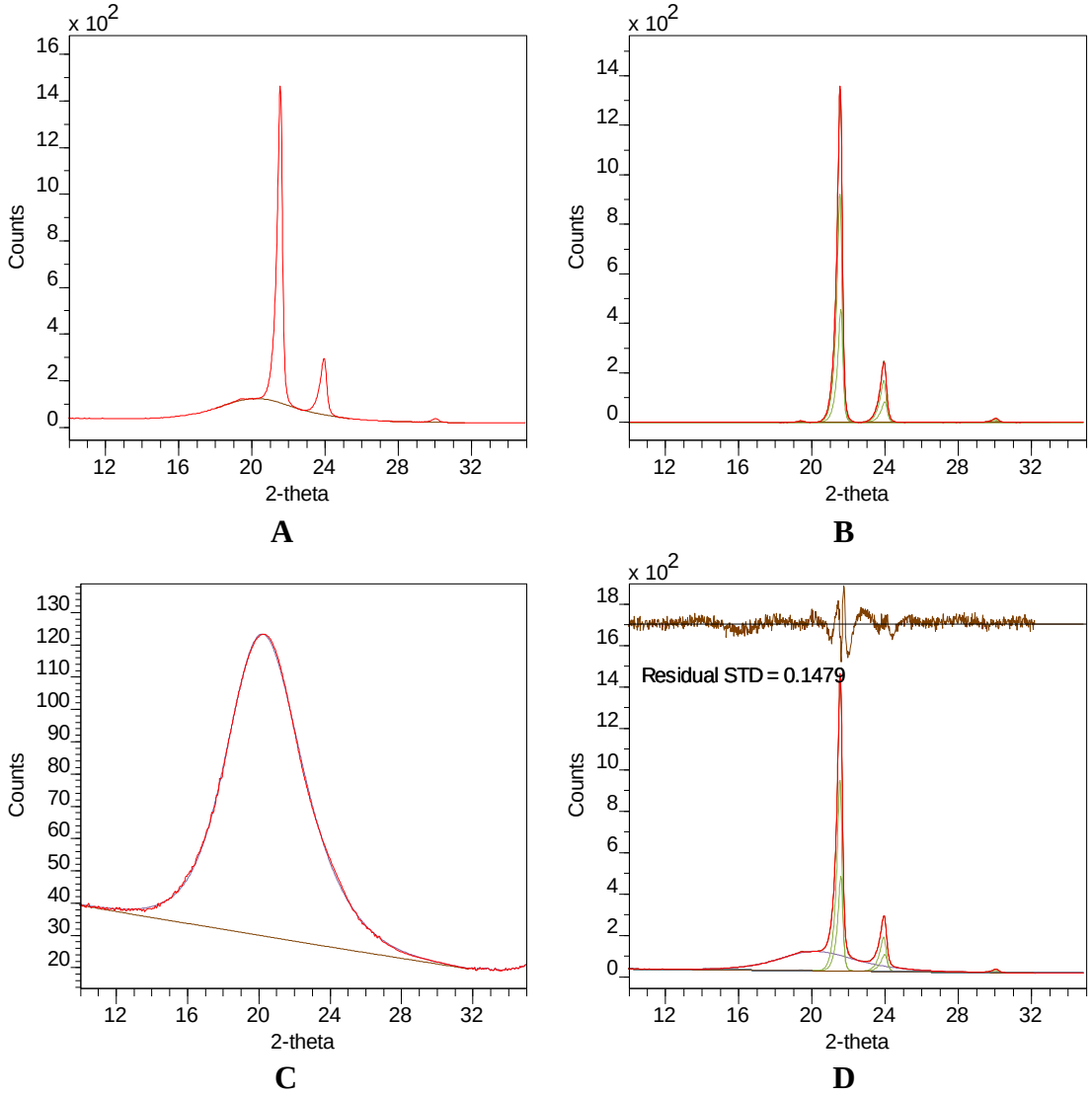


Figure 23. Raw XRD spectrum (**red**) of UD/UT fitted with a 4-knotted polynomial (**brown**) (**A**), separated XRD spectra showing (**B**) the peak-fitted crystalline components (O = **green**, M = **blue**) and (**C**) the peak-fitted amorphous halo (**purple**), and (**D**) the raw XRD spectrum peak-fitted with both components.

3.2.5. X-Ray Photoelectron Spectroscopy (XPS)

‖ This section is taken from my first-authored published work, specifically from section 2 in (Bruggeman et al., 2022), please see the 'Publications' section. ‖

Core-electron binding energy (CEBE) estimations

The investigated model structures were based on a 7-mer PE chain (i.e., $[CH_2–CH_2]_7$), where functionalities were positioned in the centre (C7 or C8) or at the end of the chain (C1 or C14). Next to the model structures, α-tocopherol (αTH) and two by-products that may form during its antioxidative activity (α-tocopheryl quinone, αTQ; and α-tocopheryl hydroquinone, αTHQ) were also evaluated (Yamauchi, 1997b). All structures were drawn in 'Avogadro' and pre-optimised using the 'Merck Molecular Force Field' (MMFF94) energy minimisation, the coordinates of the pre-optimised structures were used to prepare the input files for the quantum chemistry package 'GAMESS' (v2019.R1.P1.pgiblas) (Barca et al., 2020; Hanwell et al., 2012). Calculations in 'GAMESS' were performed using the 6-311++G(d,p) Pople basis set (i.e., a set of primitive Gaussian functions used to describe atomic orbitals, this basis set includes diffuse and polarisation functions to describe electron density far from atomic nuclei and electron correlation between atoms, respectively) and the HF method alone or including the long-range and dispersion-corrected hybrid DF wB97X-D (Chai & Head-Gordon, 2008; Pratt, 1956). The wB97X-D hybrid DF was chosen as it is shown to provide reduced errors in covalent systems compared to more commonly used DFs such as B3LYP-D (Chai & Head-Gordon, 2008). It was also demonstrated that self-interaction errors (i.e., the interaction of an electron with itself which results when exchange-correlation contributions to the total energy are approximated; also referred to as delocalization error) can be greatly reduced by long-range corrected hybrid DFs (Chai & Head-Gordon, 2008). This is of importance as self-interacting electrons are observed in core orbitals and the non-bonding regions of valence 1s orbitals (e.g., in hydrogen) (Tsuneda & Hirao, 2014). The inclusion of a dispersion correction was also found to be beneficial for geometry optimisations, since intramolecular dispersion interactions already affect medium-sized organic molecules (Grimme & Steinmetz, 2013). Cartesian basis functions were used to construct the symmetry-adapted linear combination (SALC) of the basis functions, with a linear dependence threshold of 1.0E-6. Second-order SCF orbital optimisation

was used for the pure HF calculations, and Pulay's DIIS interpolation was used for the hybrid DFT calculations. The molecular geometries were optimised until they reached a convergence limit of 1.0E-5 with the use of Jacobi diagonalisation. Once completed, the model structures were visualised in 'wxMacMolPlt' to inspect and assign the HF/KS orbital energies to the atoms within the model structures. The orbital energies were assigned to the atom with the highest occupant in the atomic orbital coefficient, i.e., the orbital predominantly localized at the atom of interest – for simplicity, from here forth referred to as CEBE. The unrestricted HF (UHF) calculations on the evaluated doublet systems were susceptible to spin contamination, the spin contamination in organic molecules is generally deemed negligible if the total spin ($<S^2>$) deviates less than 10% from s(s+1); where 's' refers to half of the unpaired electrons (Young, 2003). The spin contamination for the carboxylate model structure was shown to be negligible, showing a $<S^2>$ value of 0.760 and 0.755 as calculated by UHF and wB97X-D, respectively. The spin contamination for the centred and end-chain ammonium ion model structures were also negligible, showing a $<S^2>$ value of 0.751 as calculated by both methods. Examples of the GAMESS input files are presented in Appendix B5.

Spectral acquisition

The XPS spectra presented in Section 4.1.3 were recorded at the Queen Mary University of London using a Thermo-Scientific NEXSA Surface Analysis System and a monochromatic Al Kα X-ray source. The samples were mounted using a double-sided scotch tape placed on a glass slide and attached using copper clips to the sample bar. The glass slide ensured the samples were floated from the spectrometer. An electron flood gun was used for charge neutralisation to prevent surface charge build-up. Survey spectra were collected in 25 sweeps at a pass energy of 200 eV, with a dwell time of 10 milliseconds and sweep time of 120 seconds, using a step size of 0.5 eV over the energy range of -10 – 1350 eV. Spectra have been taken before and after brief ion etching, to investigate if the chemical surface compositions

were heterogenous and if any adsorbed carbon/oxygen species were present on the sample surface due to the storage in the Petri dishes. All data was collected at the "magic angle" (i.e., 54.74°) and using a slot aperture resulting in an analysis area of 100 x 100 microns.

The XPS spectra presented in Section 4.3 were recorded at the EPSRC HarwellXPS facility using a Kratos AXIS Supra and a monochromatic Al Kα X-ray source (12 mA × 12 kV = 144 W). The samples were mounted using a double-sided scotch tape placed on a glass slide and attached using copper clips to the sample bar. The glass slide ensured the samples were floated from the spectrometer. To prevent surface charge build-up, charge neutralisation was used with a filament current, filament bias voltage, and charge balance voltage of 0.3 A, 4 V, and 4 V, respectively. The base pressure of the spectrometer was 5×10^{-10} Torr, rising to ca. 1×10^{-9} Torr during the analysis. Survey spectra were collected in a single sweep at a pass energy of 160 eV, with a dwell time of 100 milliseconds and sweep time of 120 seconds, using a step size of 1 eV over the energy range of -5 – 1200 eV. High-resolution spectra were recorded at a pass energy of 20 eV, with a dwell time of 260 milliseconds and sweep time of 60 seconds, using a step size of 0.1 eV over an energy window of 23-26 eV, depending on the element. All data was collected at the "magic angle" (i.e., 54.74°) in the Hybrid mode using a slot aperture resulting in an analysis area of 700 x 300 microns.

Spectral Processing

All peak fitting was performed using the CasaXPS software (v2.3.24rev1.1B). The high-resolution XPS spectra were corrected manually using the relative transmission function as obtained from the respective VAMAS files of the high-resolution spectra. The relative transmission function needed to be applied manually, as the default transmission correction in CasaXPS is otherwise applied after the user's set area constraints – resulting in the erroneous conversion of peak area between elemental regions. The Kratos relative sensitivity factor (RSF)

library was used to define the area constraints between the respective functionality-related components that were present in the different elemental regions. The peak fitting of the survey spectra was performed using both the 'Shirley' or 'Tougaard' backgrounds in separate data processing procedures, whereas the high-resolution spectra were fitted using the 'Shirley' or 'Polymer U Tougaard'. Both background types were used to investigate the influence of the background type on the observed atomic composition. However, as the survey spectra also contained non-polymeric elements, the choice was made to use the regular 'Tougaard' background instead of the 'Polymer U Tougaard' to allow all elements to be fitted with the same background. Unless stated otherwise, all component peaks were described by the symmetric Voight-type lineshape LA(1.53,243), the default lineshape in the version of CasaXPS used to perform the presented peak fits. To account for its vibrational structure, the main [CH_{PE}] component representing the $[CH_2]_n$ of the unmodified UHMWPE was described by the asymmetric Voight-type lineshape LA(4.2,9,4) – this lineshape was established by M.C. Biesinger through peak fitting PE and a C18 alkane (Biesinger, 2015). The higher-order $[CH_2]_n$ carbon shifts, [CH_x], were fitted using the symmetric LA(1.53,243) lineshape, unless stated otherwise. During the high-resolution spectra peak fitting, the component peaks were referenced in position and constrained in FWHM (initial guess: 1 eV; constraint: 0.8–1.8 eV) to a single component per respective elemental region – these may be referred to as "peak model reference components". The peak model reference components consisted of [CH_{PE}] within the C 1s region, [CNH_2] within the N 1s region, and [C=O*] within the O 1s region. The initial position of [CH_{PE}] in the C 1s region, [CNH_2] in the N 1s region, and [C=O*] in the O 1s region were set to 284.8 eV, 399 eV, and 532 eV, respectively, and were constrained between 282–286 eV, 397–401 eV, and 530–534 eV, respectively. Apart from the area% of the contaminants predetermined by the survey spectra, the initial area of all the component peaks in the C 1s region was set to 10E2 and constrained between 0 and 10E6. The area of the

component peaks in the other elemental regions was constrained by the respective RSFs and theoretical composition associated with the evaluated functionalities. The peak fits presented in this work were optimised using the 'Levenberg–Marquardt' algorithm as available in CasaXPS.

3.2.6. Vickers Microhardness (MH_V)

The Vickers microhardness (MH_V) test was performed with an MVK-H1 from Mitutoyo Corp (Kawasaki, JP) using a pyramid-shaped diamond indenter (136º between opposite faces and 22º from each face normal to the sample surface) with a 50 gram-force load applied for 10 seconds at room temperature – Figure 24 depicts the experimental setup. Three random samples from each sample series were indented at three different positions across the sample surface, each indent was at least 2 mm away from the sample edges and other indented positions. The MH_V (in kgf/mm^2) was determined by the ratio of the applied load in kgf (F) and the surface area of the indent in mm^2 (A) of the indentation, the indent surface area was determined following:

$$A = \frac{d^2}{2\sin(\theta/2)}, \qquad \textit{(Eq. 11)}$$

where θ is the angle between the opposite faces (136°) and d is the average length of d_1 and d_2.

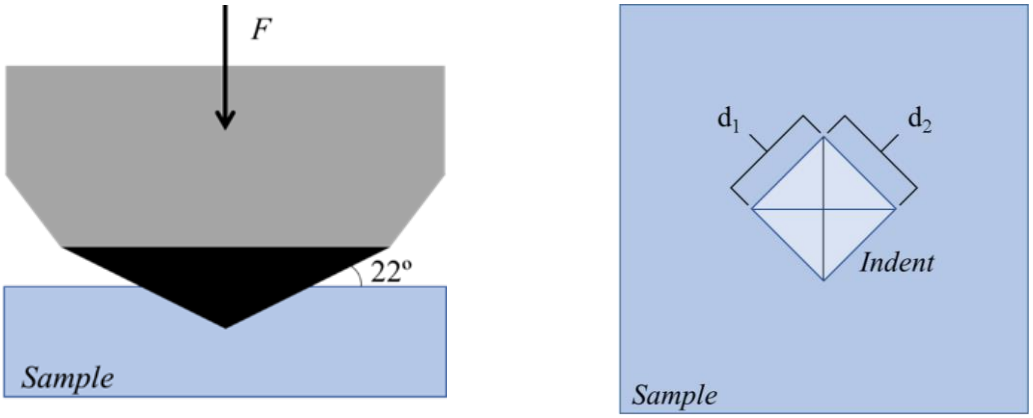


Figure 24. Simplified schematic of (left) a pyramid-shaped diamond indenter indenting a sample from a side-view, showing the direction of the applied load (F); and (right) the top-view of an indent in the sample surface, showing the two impression diagonals (d_1 and d_2).

3.2.7. UV Spectrophotometry

UV spectrophotometry allows for the quantitative analysis of molecules in solution through their absorbance in the near-UV region (i.e., 180-390 nm). Typically, the Beer-Lambert law is used for quantitative analysis with UV spectrophotometry, following:

$$A = \log\left(\frac{I_0}{I}\right) = \epsilon\, l\, c\,, \qquad \textit{(Eq. 12)}$$

where *A* is the total absorbance of the molecule/sample, ϵ is the molar absorbance coefficient, *l* is the path length, and *c* is the concentration of the molecule/sample (Swinehart, 1962). In this work, a SpectraMax M3 Multi-Mode Microplate Reader from Molecular Devices (San Jose, USA) was used to investigate the degree of AMP/AAc substitution on the ASPN treated UHMWPE-based sample surfaces by measuring the Fmoc-adduct after a deprotection cycle – similar to how this is done for Fmoc-protected resins in the literature (Eissler et al., 2017). As demonstrated in the literature, the Fmoc-adduct contains two transitions (i.e., at 289.8 and 301 nm) but its most robust transition (in terms of quantification) was observed at 289.8 nm. The deprotection solutions containing the Fmoc-adduct were measured using a quartz cuvette from StonyLab Scientific (New York, USA) at 290 nm. Using 289.8 nm was not possible as the instrument used in this work only allowed wavelength changed in integers, the expected introduced error on the absorbance value is <1% as determined by the literature.

To validate the literature, a linear correlation of the absorbance versus the concentration was produced to determine the molar absorption coefficient (ε) of the Fmoc-adduct with the used experimental setup. In total, five calibration solutions of 10 mL were prepared in 50 mL falcon tubes, using Fmoc-Glycine-OH (297.32 g/mol; ≥ 99% purity) purchased at CEM Corporation (Matthews, USA) with a starting concentration of 5, 25, 50, 75, and 100 mM. Subsequently, following a three-step 100x dilution series (by pipetting 0.02 mL of the parent solution into 1.98 mL fresh deprotection solution), the final calibration solutions had a

concentration of 5, 25, 50, 75, and 100 nM (i.e., total dilution factor = 10^6). After the deprotection cycle where the AAc solutions were shaken for one hour in an orbital shaker at room temperature, the solutions were centrifuged to pellet the AAc powder and separate it from the deprotection solution containing the Fmoc-adduct. After referencing the absorbance of a fresh deprotection solution as a blank, the separated Fmoc-adduct containing deprotection solutions were measured with the UV spectrophotometer at 290 nm – providing the linear correlation displayed in Figure 25. From the linear correlation, the molar absorption coefficient for the Fmoc-adduct was determined from the slope, i.e., ε = 6112 L mol^{-1} cm^{-1}. When compared to the literature, which presented a molar absorption coefficient for the Fmoc-adduct of 6089 L mol^{-1} cm^{-1}, a negligible difference of 0.38% was noted (Eissler et al., 2017).

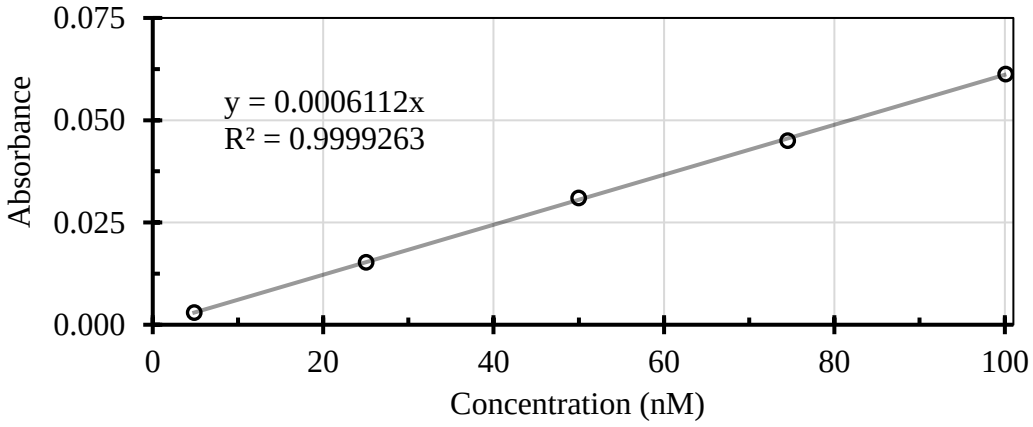


Figure 25. Correlation of the concentration of the calibration solution versus the UV absorbance at 290 nm.

Having obtained the molar absorption coefficient, the degree of substitution of the ASPN-treated UHMWPE-based surfaces was determined similarly. The Fmoc-Glycine-OH was immobilised onto the sample surfaces as specified in Section 3.1.4, after which the samples were put in a falcon tube with 2 mL deprotection solution and shaken for one hour using an orbital shaker at room temperature – three repeats were prepared for each sample type. Assuming all samples have an identical surface area and that all faces (excluding the bottom, which touches the working table) are treated equally during ASPN, the degree of substitution (S; nM/cm^2) per surface area (A; cm^2) could be determined from the absorbance (E) following:

$$S = \frac{E}{\varepsilon A}. \qquad \textit{(Eq. 13)}$$

3.2.8. Wettability

To investigate the surface wettability of the UHMWPE-based samples, contact angle measurements were performed using an Attension Theta Optical Tensiometer from Biolin Scientific (Gothenburg, SE). The sessile drop method was used to measure the equilibrium contact angle (ECA) of 10 µL droplets, at a temperature of 20°C and over a period of 15 seconds once the droplets stabilised. Using the equilibrium contact angles, the surface free energy calculations were performed following the Fowkes theory – where the total surface free energy (γ; SFE) is dissociated into its dispersive (γ^D) and polar (γ^P) components (i.e., $\gamma = \gamma^D + \gamma^P$) (Fowkes, 1964; Rulison, 1999). Combining the Fowkes theory and the Young equation related to a solid-liquid interface (γ_{SL}), the surface free energy components of the surface (γ_S) and liquids (γ_L) can be calculated following:

$$\gamma_{SL} = \gamma_S + \gamma_L - 2\sqrt{\gamma_S^D + \gamma_L^D} - 2\sqrt{\gamma_S^P + \gamma_L^P}, \qquad \textit{(Eq. 14)}$$

(Owens & Wendt, 1969). Deionized water (i.e., purified MilliQ water; DI water) and diiodomethane (CH_2I_2) were selected as probe liquids, the surface energy and polar/dispersive components of the two probe liquids are presented in Table 9 (Owens & Wendt, 1969). Diiodomethane was used as the probe liquid as it exhibits molecular symmetry, a relatively high liquid surface free energy, and it is a fully non-polar liquid (i.e., containing no polar component; $\sigma_L^P = 0$), which made it relatively easy to solve for Equation 14.

Table 9. Liquid surface free energy and polar/dispersive components of water and diiodomethane.

Liquid	$\boldsymbol{\gamma_L}$ **(mJ/m²)**	$\boldsymbol{\gamma_L^D}$ **(mJ/m²)**	$\boldsymbol{\gamma_L^P}$ **(mJ/m²)**
Deionized water	72.8	21.8 ± 0.7	51
Diiodomethane	50.8	50.8	0

3.3. Biological evaluation of the UHMWPE-based surfaces

3.3.1. Bacterial adhesion evaluation

The bacterial growth of the UHMWPE-based surfaces was investigated following an attachment assay, which also provided insight into the anti-bacterial activity on the various surfaces. The attachment assay was performed with *Staphylococcus aureus* (NCTC 10833) and *Staphylococcus epidermidis* (NCTC 11047), as these are two clinically relevant bacteria associated with implant infections due to their natural presence on the skin – the bacterial stocks were kindly supplied by Dr Sarah Kuehne from the School of Dentistry, University of Birmingham (Pandey et al., 2000). The bacterial adhesion assay was carried out in the class II laminar flow hood, where necessary, the consumables/equipment (i.e., agar, broths, slides, filter papers, etc.) sterilised using a steam autoclave at 121°C for 20 minutes or by spraying with 70% ethanol and left to evaporate inside the hood before starting the assay. The obtained results were analysed with one-way ANOVA and post hoc Tukey-Kramer multiple comparison tests to reveal the significant differences (i.e., $p < 0.05$).

Using the bacterial stock, a streak plate was prepared on tryptone soya agar (TSA) from Thermo Fisher scientific (Oxford, UK) in a Petri dish. Care was taken to streak the plate so that single, genetically identical, bacterial colonies were formed (i.e., the quadrant method). Once the inoculum had settled into the agar, the streaked plate was closed, wrapped in clingfilm, and incubated for about 24 hours (37°C; 5% CO_2) in a HERAcell 150i CO_2 incubator from Thermo Fischer scientific (Oxford, UK). After the incubation period, the streaked plate was taken out of the incubator and used to prepare an overnight liquid culture. The overnight liquid culture was prepared by taking 2-3 isolated, single colonies (i.e., to introduce genetic diversity and obtain a "representative" sample) from the streaked plate with a inoculation loop, and resuspending the colonies into a 30 mL culture tube containing 5 mL tryptone soya broth (TSB) from Thermo Fisher scientific (Oxford, UK), and incubate the liquid culture for about 24 hours

(37°C; 5% CO_2) in a shaking incubator. After the incubation period, the overnight liquid culture was diluted with fresh TSB until it displayed an optical density of 0.2 at 600 nm (i.e., as it was found that this is where both bacteria are at the start of their logarithmic/exponential growth phase), the optical density was measured with a Jenway-7315 spectrophotometer from Thermo Fisher scientific (Oxford, UK) (Bansal et al., 2017; L. Wang et al., 2021).

Prior to performing the assay, the UHMWPE-based samples were sterilised by suspending them in 70% ethanol for one hour, leaving them to dry inside the laminar flow hood, and subsequently washing the samples three times with phosphate-buffered saline (PBS) from Sigma-Aldrich (Dorset, UK) to remove any potentially remaining ethanol. Once the UHMWPE-based samples were sterilised, the bacterial adhesion assay was prepared as shown in Figure 26, three repeats were prepared for each sample type. The filter paper was positioned in the centre of the Petri dish and moistened with 600 μL of PBS to prevent the environment from drying out. The microscope slide was positioned on the moistened filter paper in the centre of the Petri dish, and the UHMWPE-based sample was placed in the middle of the microscope slide with sterile forceps to minimize the chance of contamination. Once the sample was positioned, 20 μL of the diluted overnight liquid culture was pipetted in the centre of the sample surface. Subsequently, a square borosilicate glass coverslip (12 mm x 12 mm) was carefully positioned on top of the sample with the droplet of diluted overnight liquid culture, to spread the liquid culture over the entire sample surface. Once the assay was fully set up, the Petri dish was closed, wrapped in clingfilm, and incubated for about 24 hours (37°C; 5% CO_2), care was taken to keep all Petri dishes horizontal to prevent the samples from being disrupted.

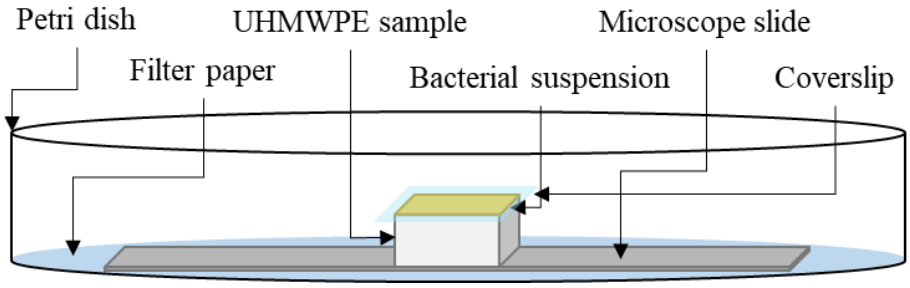


Figure 26. Schematic representation of the bacterial adhesion assay experimental setup.

After the incubation period, the UHMWPE-based sample and its coverslip were transferred into a 30 mL culture tube containing 10 mL PBS. The culture tube containing the PBS solution, sample, and coverslip were vortexed for one minute at 1200 rpm using a Whirlmixer Cyclone Vortex Mixer CM-1 from Thermo Fisher scientific (Oxford, UK). After vortexing, serial dilutions of 200 µL were made from the vortexed PBS solution in a clear polystyrene 96-well plate from Sigma-Aldrich (Dorset, UK), following 10-fold dilutions with fresh PBS down to a $x10^8$ dilution (i.e., following the Miles and Misra method, a technique used to quantify bacterial cell concentrations by diluting samples and plating them on agar plates for colony counting). Two fresh TSA plates were separated into four quadrants and labelled according to its respective dilution factor, three droplets of 20 µL from the $x10^1$ – $x10^8$ dilutions were pipetted into a respective quadrant of the TSA plate – the undiluted PBS solution (i.e., $x10^0$ dilution) was not used as it would be too concentrated. Once the droplets had sunk into the agar, the TSA plates were closed, wrapped in clingfilm, and incubated for about 24 hours (37°C; 5% CO_2). After the incubation period, the number of colony forming units (CFU) in each quadrant of the TSA plates were counted. Lastly, using the respective dilution factors, the CFU/mL was calculated for each sample.

3.3.2. Biocompatibility evaluation

The biocompatibility of the UHMWPE-based surfaces was investigated following a cell viability assay. The cell viability was tested for human osteoblast-like cells (i.e., cells that synthesize bone), more specifically, the *Sarcoma osteogenic* cell line (Saos-2; ATCC HTB-85)

derived from primary osteosarcoma (i.e., bone cancer) – the cell stock was kindly supplied by Lauter Pelepenko from the School of Dentistry, University of Birmingham. It is worth to note that ISO standard 10993-5:2009 on the biological evaluation of medical devices uses murine L929 fibroblast cells, in combination with a MTT/XTT cell viability test to evaluate biocompatibility (ISO, 2009). However, human osteoblast-like *Saos-2* cells are commonly used to specifically determine the biocompatibility of bone-related implant materials, such as total joint replacements as focussed on in this work (Fogh et al., 1977; Galliera et al., 2018; C. Y. Li et al., 2006; Massaccesi et al., 2019). Next to that, the CellTiter-Glo Luminescent cell viability assay from Promega (Madison, USA) was used in this work, as the more commonly used MTT cell viability assay is influenced by antioxidants (like αTH, as present in the UHMWPE-based samples) – the cell viability assay kit was kindly supplied by Dr Melissa Grant from the School of Dentistry, University of Birmingham. The cell viability assay was carried out in the class II laminar flow hood, , where necessary, the consumables/equipment (i.e., PBS, forceps, etc.) were sterilised using an sterilised using a steam autoclave at 121°C for 20 minutes or by spraying with 70% ethanol and left to evaporate inside the hood before starting the assay, and all liquids (i.e., medium, PBS, etc.) were initially left to equilibrate at room temperature prior to their use. The results were analysed with one-way ANOVA and post hoc Tukey-Kramer multiple comparison tests to reveal the significant differences (i.e., $p < 0.05$).

McCoy's 5A medium (containing 1.5 mM L-glutamine and 2200 mg/L sodium bicarbonate) was supplemented with 10 vol% fetal bovine serum (FBS) and 1 vol% Penicillin-Streptomycin solution (5000 units/mL of penicillin and 5000 µg/mL of streptomycin) from Thermo Fisher scientific (Oxford, UK), all media used in this assay was discarded after a week of storage in the fridge. Subsequently, the frozen Saos-2 cell stock was thawed, pipetted into a 15 mL conical Falcon tube, and instantly centrifuged for three minutes at 200 RCF (i.e., the relative centrifugal force for a rotor with a radius of 18 cm at 1000 RPM) to pelletize the cells.

After centrifuging, the supernatant was removed from the Falcon tube and 1 mL of supplemented medium was added into the tube to resuspend the cells. The resuspended cells were pipetted into vented T75 cell culture flask from Thermo Fisher scientific (Oxford, UK), together with another 14 mL of supplemented medium. Care was taken to spread the cells over the T75 flask surface by carefully rocking the flask in all directions, after which the T75 flask was stored in the incubator (37°C; 5% CO_2) until it reached a cell confluency of 80–90%. The confluency was determined with a microscope, by checking the total cell coverage of the flask. After every two/three days the confluency was checked, the medium of the cells was refreshed if the desired confluency was not achieved. Refreshing the medium included removing the old medium, washing the cells twice with 10 mL Dulbecco's PBS (DPBS; i.e., without Ca/Mg), and adding 15 mL of fresh medium to the flask prior to continuing its incubation – care was taken to slowly pipette the liquids into the corner of the flasks whilst holding it sideways (i.e., not directly onto the cells).

Once the desired confluency was achieved, the cells were washed twice with 10 mL DPBS, and trypsinised with 2 mL of Gibco Trypsin-EDTA formulation (i.e., 0.25% trypsin and 0.1% ethylenediamine-tetraacetic acid; EDTA) from Thermo Fisher scientific (Oxford, UK). After five minutes, the T75 flask was inspected under a microscope to check if all cells had detached from the flask surface, if not, the cells were checked again after every additional minute. Once all cells had detached from the flask, the trypsin containing the cells was pipetted into a 15 mL conical Falcon tube containing 5 mL of fresh supplemented medium (so the FBS deactivated the trypsin), which was centrifuged for three minutes at 200 RCF to pelletize the cells. After centrifuging, the medium with trypsin was removed and the cells were resuspended in 1 mL of fresh supplemented medium. From the medium containing the resuspended cells, 10 μL was pipetted into a 2 mL Eppendorf in addition to 10 μL methylene blue cell viability dye in preparation for cell counting (i.e., two-fold dilution), care was taken to properly mix the

solution. The cell counting was performed with an improved Neubauer Bright-Line Hemacytometer from Sigma-Aldrich (Dorset, UK), a specialised glass slide featuring an indentation that creates a "bridge" between two counting chambers with defined volumes. A 10 μL droplet of the methylene-blue-cell mixture was pipetted onto both chambers and covered with a coverslip, to prevent evaporation and spread the cell mixture out across the chambers. Both chambers have a grid pattern etched on the surface, aiding in the cell counting under a microscope. An average cell density (cells/mL) was determined by counting the cells in both chambers, multiplying it by the dilution factor (two-fold), and subsequently dividing the total by the volume of the counted cell mixture (20 μL). Knowing the cell density, the parent cell solution was diluted to achieve a final cell concentration of 500,000 cells/mL for seeding.

Prior to performing the assay, the UHMWPE-based samples were sterilised by suspending them in 70% ethanol for one hour, leaving them to dry inside the laminar flow hood, and subsequently washing the samples three times with DPBS to remove any potentially remaining ethanol. Once the UHMWPE-based samples were sterilised, the cell viability assay was prepared with three repeats for each sample type. To determine the cell viability over time, the decision was made to incubate the seeded UHMWPE-based samples for 1, 4, and 7 days – a polystyrene tissue culture 12-well plate was used to prepare the assay for each incubation period (i.e., 1, 4, or 7 days), as shown in Figure 27, three empty wells for each respective incubation period were also seeded with cells to serve as a positive control. The sterilised UHMWPE-samples were placed in the 12-well plate and 20 μL of the diluted cell solution (500,000 cells/mL) was pipetted onto the centre of the sample, seeding the sample surface with roughly 10,000 cells. Subsequently, the plates were stored in the incubator (37°C; 5% CO_2) for 20 minutes, to allow the cells to adhere to the sample surface. Once adhered, an additional 2 mL of supplemented medium was added to each well – care was taken to slowly add the medium from the bottom of the well and not directly on the sample surface containing the

seeded cells, to prevent detachment of the cells. After every two/three days, if the incubation period for the respective sample was not reached, the medium in the wells was removed and refreshed with 2 mL of fresh supplemented medium.

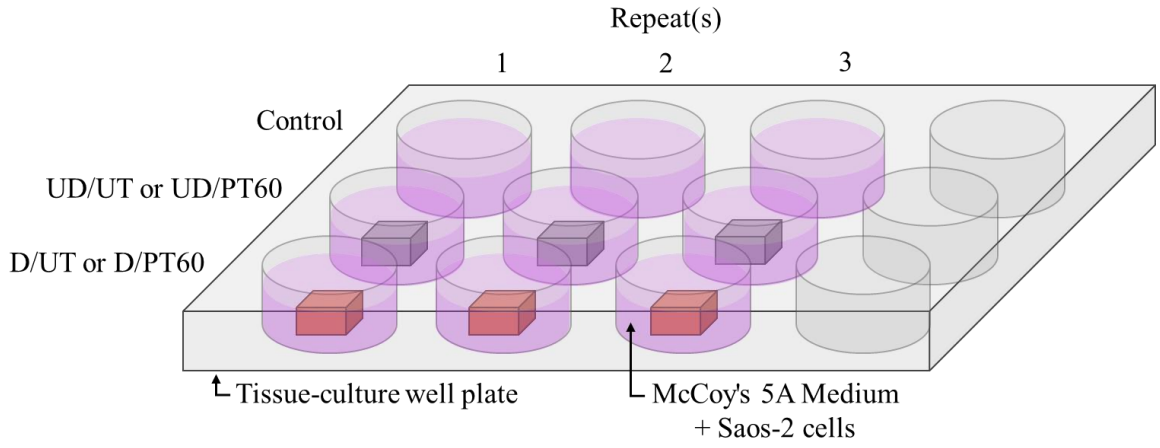


Figure 27. Schematic representation of the cell viability assay experimental setup.

Once the seeded UHMWPE-based samples reached the desired incubation period, the CellTiter-Glo Luminescent cell viability assay was performed. After thawing the CellTiter-Glo buffer and substrate, the buffer was added to the substrate and swirled until fully mixed, forming the CellTiter-Glo reagent. To maintain a 1:1 medium:reagent ratio, 1 mL of medium was removed from each well (leaving 1 mL), after which 1 mL of CellTiter-Glo reagent was added into each well. Subsequently, the plate was mixed for two minutes on a (micro)plate orbital shaker to induce cell lysis and left at room temperature for 10 minutes to stabilise the luminescent signal. After the signal stabilisation, a white polystyrene 96-well plate with a clear flat bottom from Corning Incorporated (New York, USA) was prepared – this type of plate was required to maximize the signal during the luminescence measurements. From each well in the 12-well plate containing the seeded samples with the lysed cells, 200 µL of the solution was pipetted into a well of the white 96-well plate – this was repeated three times for each sample, so it had three wells/data points originating from the same solution. Next to that, three wells

were filled with 200 µL of supplemented medium alone, and three other wells were filled with 200 µL of 1:1 supplemented medium:CellTiter-Glo reagent to serve as a blank.

The luminescence signal of the mixed medium-reagent solutions in the white 96-well plate were measured using a Spark multimode microplate reader from TECAN (Männedorf, CH) with an integration time of one second. As the luminescence signal decreases over time, care was taken to consistently record the luminescence signal at 60 minutes after adding the CellTiter-Glo reagent to the seeded UHMWPE-based samples. Based on the assay protocol, a relative luminescence loss of <15% was expected, but as every solution was measured after the same waiting time the intensity loss cancelled out between the measurements (Promega, 2002).

Section 4: Results and Discussion

The results and discussion section of this thesis presents the findings of research focused on enhancing UHMWPE-based biomaterials used in total joint replacements. The primary aims of this work were to address implant failure/rejection and improve patient outcomes by incorporating αTH for protection against oxidation, implementing ASPN for surface crosslinking and the introduction of chemical functionalities, and utilizing the chemical functionalities to immobilize AMPs to combat infection and reduce the risk of implant failure. To achieve these aims, the project was divided into four key objectives, each contributing to the results section of this thesis. Firstly, the effect of αTH doping in combination with ASPN on UHMWPE was explored using various characterization techniques to uncover changes in chemical and physical properties in Section 4.1. Raman mapping was employed to study the localization of conformational states and other compounds in the untreated and plasma-treated UHMWPE sample surfaces in Section 4.2. XPS was utilized to examine the chemical surface composition of the modified UHMWPE-based samples in Section 4.3, with the development of a theoretical peak model to facilitate a deeper understanding of the spectra. Lastly, the biological response to the UHMWPE-based surfaces was evaluated through bacterial adhesion and cell viability assays in Section 4.4. However, the biological evaluation on the AMP-immobilized UHMWPE-based samples was not completed, as further discussed in Section 4.4.

4.1. Effect of αTH on the ASPN of UHMWPE

4.1.1. ATR-FTIR spectroscopy

ATR-FTIR spectroscopy was used to investigate the effect of αTH doping in combination with ASPN on the chemical composition of the UHMWPE-based samples. The corrected ATR-FTIR spectra allowed for the identification of chemical bonds present within the UHMWPE-based samples at a penetration depth of about 2.11 μm (see Section 3.2.2 for more information on the penetration depth and spectral corrections). FTIR is specifically sensitive to hetero-nuclear vibrations and polar bonds, table 10 depicts the region ranges and

the main chemical bond information that can be evaluated within the respective regions (Socrates, 2004). Where necessary, the amorphous carbon (a-C)/αTH-related components were included during the peak fitting, to differentiate between potentially overlapping components arising from the molecules that were present within the spectra to the best extent possible.

Table 10. FTIR region ranges of interest and the corresponding chemical bond information (Socrates, 2004).

Region (#)	Range (cm^{-1})	Information
1	700-750	C–H
2	900-1000	C=C
3	1000-1200	C–C/O/H
4	1200-1400	C–C/H
5	1400-1500	C–H
6	1500-1800	C=C/N/O
7	2000-3000	C–H
8	3000-3800	OH; NH; O/N---H

Across this section, the area ratios of the regions and/or individual spectral bands were used to calculate indices to reveal the chemical changes occurred during the doping and/or ASPN treatment of UHMWPE. Following ASTM F2381-19 on the determination of the trans-vinylene index and oxidation index in γ-ray irradiated UHMWPE, the area of the region/spectral band was divided by the area of the region from 1330-1380 cm^{-1} (see Region 4) corresponding to the $[CH_x]_{wagging}$ of the methylene units in PE (ASTM, 2019). For example, to determine the trans-vinylene index, the area of the $[CH=CH]_{wagging}$ at 965 cm^{-1} was divided by the area of the $[CH_x]_{wagging}$ region, the normalisation over the $[CH_x]_{wagging}$ region served as an internal standard to account for potential differences in the analysis volume. Each region provided a variety of indices and/or ratios related to the chemical bonds presented in the

respective regions, at the end of this section these indices/ratios were investigated for potential correlations using the Pearson correlation coefficients. For ease of viewing, only the summed spectral peak fits per sample type are shown for each region. However, the corresponding graphs are based on spectral data from the individual peak fits, to provide a confidence interval ($\alpha = 0.05$) for the data mean using a normal distribution. The data obtained from the individual spectral peak fits of the full undoped and doped sample series are presented in Appendix C1.

Region 1 – 700-750 cm^{-1}

Region 1 displayed a doublet with maxima at 719 and 730 cm^{-1}, as depicted in Figure 28, these two peaks are typically assigned to the $[CH_2]_{rocking}$ modes of the amorphous and crystalline phase of UHMWPE, respectively. The calculated IR spectrum of the C20 alkane model structure as depicted in Section 3.2.2, showed the $[CH_2]_{rocking}$ mode at 722 cm^{-1} and confirmed the validity of the vibrational mode assignment from the literature. Although the main contribution to these peaks is associated with the phase separation, literature on the comparison of DSC curves to the crystallinity of HDPE estimated by FTIR showed this doublet was not useful to determine crystallinity (Pagès, 2005; Zerbi et al., 1989). Instead, when estimating crystallinity, it was recommended to use the doublet around 1465 cm^{-1} as it provided more consistent results. Next to that, this phenomenological relation was only resolved for 100% crystalline HDPE and cannot be transferred to UHMWPE.

Despite this, the area ratio between 730 and 719 cm^{-1} does provide an indication on a potential increase/decrease in crystallinity, Figure 28 shows this ratio for the investigated UHMWPE-based sample series. It can be observed that the ratio for the undoped sample series started at 0.30±0.01 for UD/UT, increased to 0.46±0.04 for UD/PT30 and then declined to 0.39±0.02 for PT60. The doped sample series started at a ratio of 0.47±0.01 for D/UT, it showed a slight increase to 0.49±0.04 at D/PT15, but then decreased to a ratio of 0.44±0.04 for

D/PT60. The fact that the peak ratios of the doped and treated samples were above that of UD/UT indicated an increase in crystallinity, likely due to the increased chain mobility present at the elevated temperatures (i.e., 90 °C) during the αTH doping and ASPN treatments, which may have allowed for the reorganisation of the PE chains into its crystalline form.

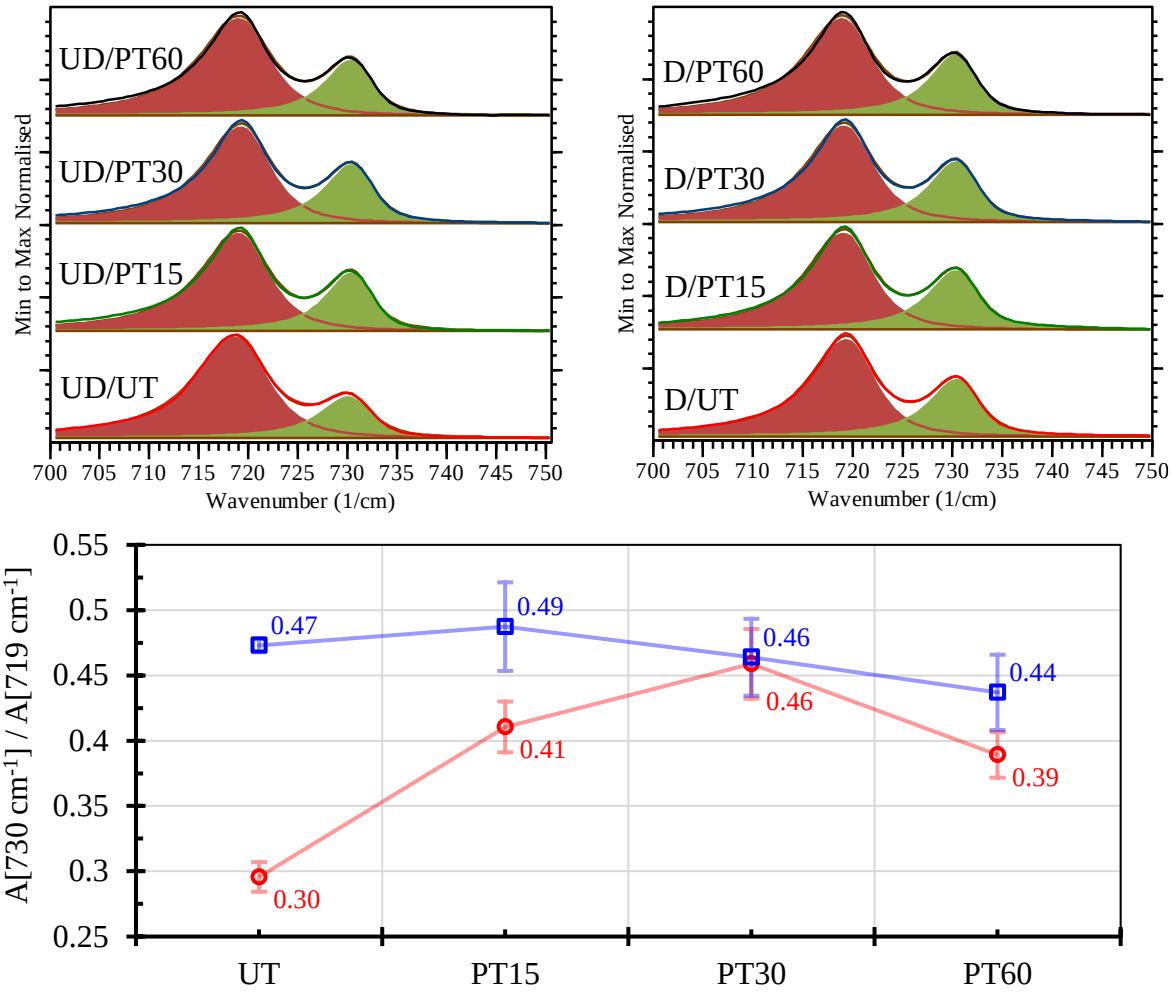


Figure 28. Summed spectral peak fits of the (top-left) undoped and (top-right) doped UHMWPE-based sample series between 700 and 750 cm^{-1}, and (bottom) the corresponding graph displaying the 730:719 cm^{-1} peak area ratios as observed in the individual peak fits of the (**red**, cirlce) undoped and (**blue**, square) doped sample series.

Region 2 – 900-1000 cm^{-1}

Region 2 allowed for the identification of the carbon-carbon double-bonds (i.e., vinyl-based bonds) present in the UHMWPE-based samples. Although a negligible presence of vinyl-based bonds was expected in UD/UT, the effect αTH doping and ASPN treatments were expected to introduce vinyl-based bonds during chain scission and/or crosslinking as was

discussed in Section 2.1.3 (Shibata et al., 2006). Three main types of vinyl-based bonds form in UHMWPE, namely: mono-alkyl vinyl, di-alkyl geminal-vinylidene, and di-alkyl trans-vinylene as schematically presented in Figure 29. The vinyl endcap is predominantly formed as a degradation product during chain scission, although it may subsequently be involved in Y-crosslinking with other alkyl macroradicals. The geminal-vinylidene is an unsaturation product, which was found to be one of the main chemical changes (besides chain scission and crosslinking) in polyethylene and polypropylene when exposed to high-energy radiation (Black & Lyons, 1957). The trans-vinylene is also an unsaturation product, which is formed from an alkyl macroradical due to intermolecular separation of H_2.

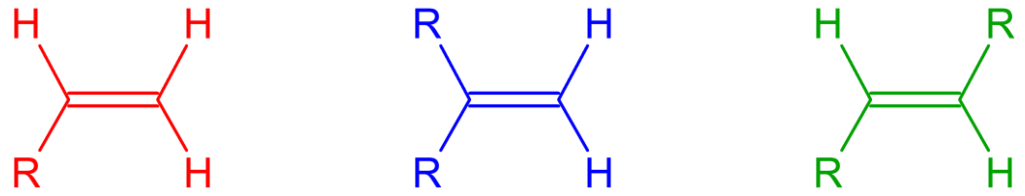


Figure 29. Simplified bond structures of the (left; **red**) mono-alkyl vinyl, (middle; **blue**) di-alkyl geminal-vinylidene, and (right; **green**) di-alkyl trans-vinylene bonds.

Naturally, the three types of vinyl-based bonds have different IR absorption band positions, the assignments found in literature from experimental FTIR and as calculated based on the model structures are presented in Table 11 (W. Collins et al., 2012; Gaston et al., 2016; Pages et al., 1996). The model structures used for the frequency calculations were based on the C20 alkane as described in Section 3.2.2, although modified to reflect the vinyl-based bond structures as presented in Figure 29, resulting in the model structures shown in Figure 30. Unfortunately, the vibrational mode assignments in the literature are often inconclusive, as these are frequently denoted as ‘out-of-plane bending’. However, out-of-plane bending can be separated into wagging or twisting. Therefore, the calculated spectra were used to assign the specific vibrational modes to the corresponding IR absorption wavenumbers. The calculated IR absorption band positions were in reasonable agreement with those from the literature, more

specifically, the sequential order of the four vinyl-based modes was identical and confirmed the validity of the assignments from the literature.

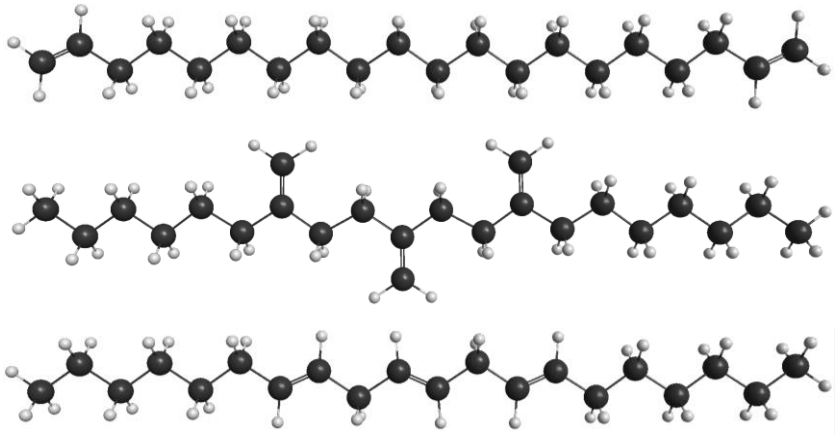


Figure 30. Model structures used to predict the absorption band positions for (top) mono-alkyl vinyl, (middle) di-alkyl geminal-vinylidene, and (bottom) di-alkyl trans-vinylene bonds.

Table 11. Expected FTIR absorption band positions for the various vinyl-based bonds according to the literature and as calculated using the vinyl-based model structures between 900 and 1000 cm^{-1}.

Bond type	**Vibrational mode**	**IR absorption wavenumber (cm^{-1})**	
		Literature	**Calculated**
Vinyl	$[=CH_2]_{wagging}$	~ 910	900
	$[=CH_2]_{twisting}$	~ 990	998
Geminal-vinylidene	$[=CH_2]_{wagging}$	~ 890	883
Trans-vinylene	$[CH=CH]_{wagging}$	~ 965	976

With the vibrational modes confirmed, the spectra were fitted with the beforementioned assignments, as displayed in Figure 31. The absorption band positions for the vinyl endcap, geminal-vinylidene, and trans-vinylene, were observed at 910 and 980 cm^{-1}, 880 cm^{-1}, and 965 cm^{-1}, respectively. The respective peak areas were used to calculate indices (i.e., VI, GVI and TVI), as discussed at the start of Section 4.1.1. During the peak fitting of the doped UHMWPE-based sample series, the components that originated from αTH were constrained in relative

peak area to each other – as the main deviation in peak areas was related to the vinyl-based components from UHMWPE. Next to that, in the corresponding graph in Figure 31, the peak areas from the two vinyl endcap bands at 910 and 980 cm^{-1} were summed.

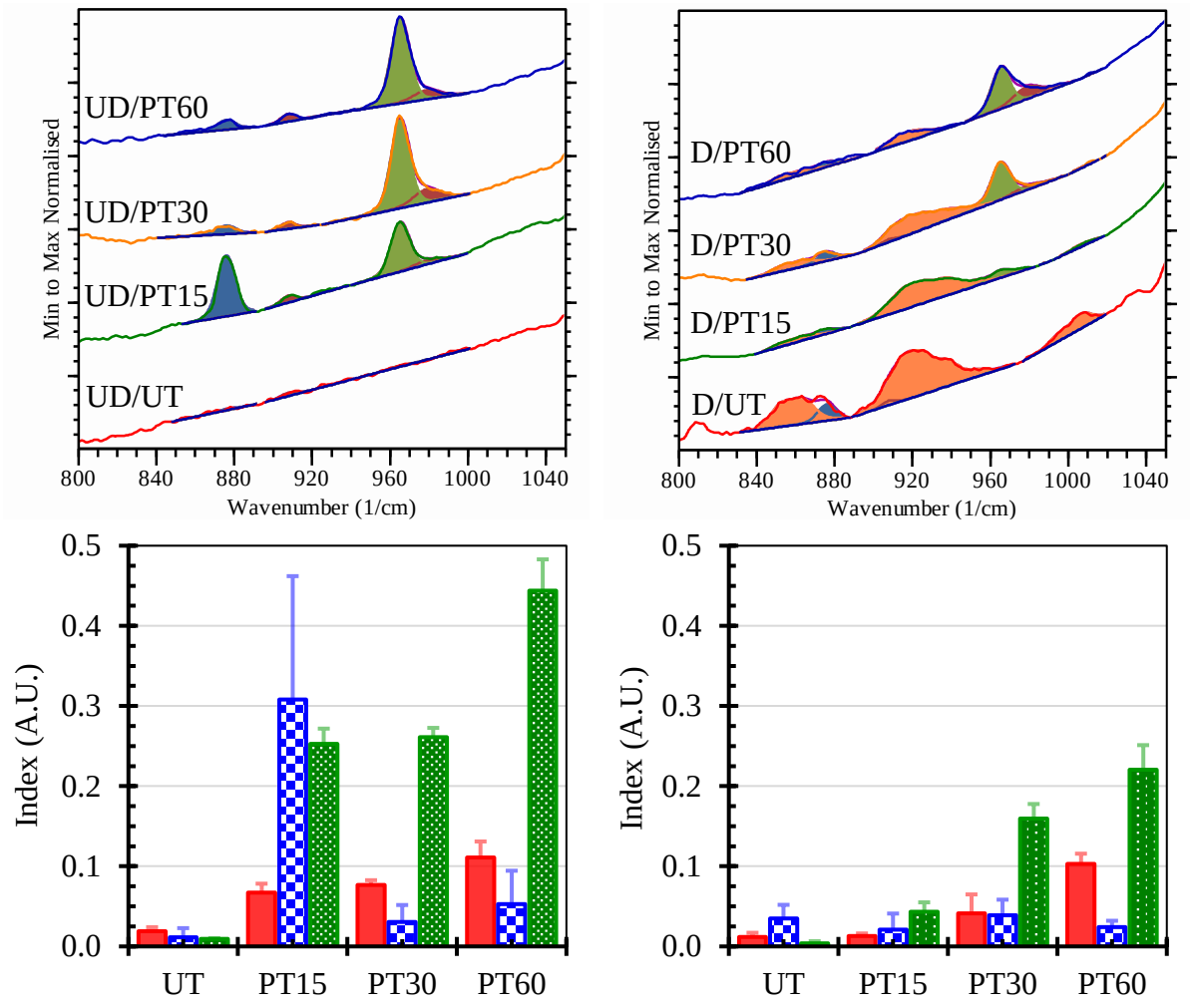


Figure 31. Summed spectral peak fits of the (top-left) undoped and (top-right) doped UHMWPE-based sample series between 800 and 1050 cm^{-1}, displaying the (**red**) vinyl endcap, (**blue**) geminal-vinylidene, (**green**) trans-vinylene, and (**orange**) αTH; and the corresponding graphs for the (bottom-left) undoped and (bottom-right) doped sample series, displaying the (solid, **red**) vinyl endcap, (checkered, **blue**) geminal-vinylidene, and (dotted, **green**) trans-vinylene band indices as observed in the individual peak fits.

As observed in Figure 31, there were clear differences in the vinyl-based bond indices between the undoped and doped UHMWPE-based sample series, evidencing the effect of αTH doping on the ASPN treatment. As expected, UD/UT showed negligible presence of any vinyl-based bonds (i.e., all indices were below 0.02±0.01). A minor, continuous increase was observed for the endcap vinyl index over the ASPN treatment time, starting at 0.02±0.005 with

UD/UT and this increased up to 0.11±0.02 for UD/PT60. However, at UD/PT15 the undoped sample series showed a significant increase of both the geminal-vinylidene and trans-vinylene indices to 0.31±0.15 and 0.25±0.02, respectively. For the undoped samples that were treated longer with ASPN (i.e., UD/PT30 and UD/PT60), notably less geminal-vinylidene was observed (< 0.1) whilst the trans-vinylene index increased up to 0.44±0.04 for UD/PT60.

With the doped UHMWPE-based sample series, it was expected that the presence of the αTH after doping would provide protection against degradative mechanisms, as discussed in Section 2.1.3. D/UT showed negligible presence of any vinyl-based bonds, all indices were below 0.03±0.02. However, where UD/PT15 showed a significant increase in vinyl-based bond indices, almost no change was observed with D/PT15 – apart from a minor increase of the trans-vinylene index to 0.04±0.01, which indicated that the αTH remained abundantly functional during the first 15 minutes of ASPN. A notable four-fold increase for the trans-vinylene index was noted with D/PT30 when compared to D/PT15, as it increased to 0.16±0.02 whilst both the endcap vinyl and geminal-vinylidene indices only increased slightly to 0.04±0.02. This demonstrated that the αTH was getting exhausted by the ASPN treatment, allowing for more degradative mechanisms to occur, although still considerably less than with the undoped sample series. After the full ASPN treatment, D/PT60 showed a further increase of the trans-vinylene and endcap vinyl indices to 0.22±0.03 and 0.10±0.01, respectively. When comparing the overall results between the undoped and doped samples series, the presence of αTH demonstrated to halve the formation of vinyl-based bonds during ASPN.

Region 3 – 1000-1200 cm^{-1}

Region 3 is a spectral range that is frequently ignored in the literature, as it contains various broad and potentially overlapping $[C–C]_{skeletal}$ or $[C–O]_{skeletal}$ modes (e.g., from ethers or secondary alcohols), which makes spectral deconvolution challenging (Charles, 2009;

Gulmine et al., 2002; Guo et al., 2018; Hamzah et al., 2018; Richaud, 2015; Subramani & Sepperumal, 2016). Nonetheless, the IR absorption band assignments from the literature and as calculated based on the C20 alkane and αTH model structures are depicted in Table 12. The αTH model structure was mainly used to provide the $[C–O]_{skeletal}$ band position of its ether group (i.e., around 1090 cm^{-1} according to the literature, 1079 cm^{-1} as calculated). Although some inconsistency remained in the assignments from the literature, the model structures allowed for the confirmation of the presence of the $[C–C/O]_{skeletal}$ and $[CH_2]_{wagging}$ modes.

Table 12. Expected FTIR absorption band positions according to the literature and as calculated using the C20 alkane / αTH model structure between 1000 and 1200 cm^{-1}.

Vibrational mode	**IR absorption wavenumber (cm^{-1})**	
	Literature	**Calculated (C20 / αTH)**
$[C–C]_{skeletal}$ or $[C–O]_{skeletal}$	~ 1040	1048 / 1031
	~ 1090	– / 1079
	~ 1130	1108 / 1133
$[C–C]_{skeletal}$ or $[CH_2]_{wagging}$	~ 1176	1180 / 1160

Based on the area deviations observed between the undoped spectra, Region 3 was peak fitted with four absorption bands positioned at 1040, 1080, 1120 and 1165 cm^{-1}, as displayed in Figure 32. During the peak fitting, the components originating from αTH were constrained in relative peak area to each other and the resulting peak areas were used to calculate the respective indices. The band positions in Table 12 were in close proximity (±20 cm^{-1}) to the band positions noted in the experimental spectra. The separation of the $[C–C]/[C–O]_{skeletal}$ modes was not attempted, as various oxidation products were expected to be present and the overlap of these modes made this practically impossible. Next to that, as will be demonstrated in the subsequent sections, other spectral regions were more appropriate to provide information on the specific presence of oxidation products. Nonetheless, as observed in the corresponding

graphs in Figure 32, some differences were observed between the undoped and doped UHMWPE-based sample series. Most notably, the doped sample series showed a three-fold increase in the 1080 cm^{-1} band after ASPN compared to the undoped sample series, which was assumed to be predominantly related to increased $[C–O]_{skeletal}$ modes due to either increased oxidation of the residual free radicals after ASPN or conjugation of αTH to UHMWPE.

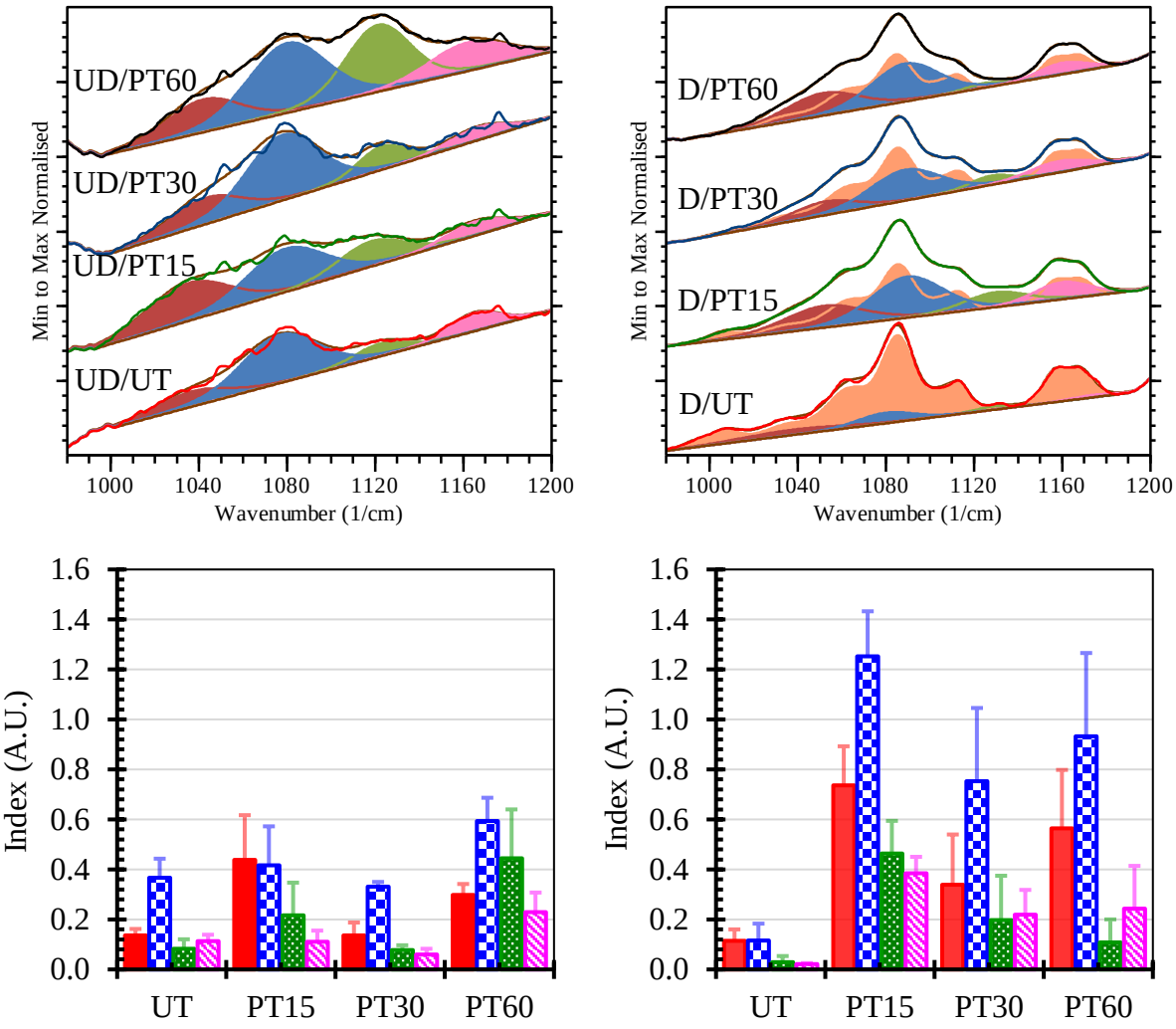


Figure 32. Summed spectral peak fits of the (top-left) undoped and (top-right) doped UHMWPE-based sample series between 1000 and 1200 cm^{-1}; and the corresponding graphs for the (bottom-left) undoped and (bottom-right) doped sample series, displaying the (solid, **red**) 1040 cm^{-1}, (checkered, **blue**) 1080 cm^{-1}, (dotted, **green**) 1120 cm^{-1}, and (striped, **pink**) 1165 cm^{-1} band indices as observed in the individual peak fits.

Region 4 – 1200-1400 cm^{-1}

Region 4 provided insight into the $[CH_2]_{wagging}$ and $[CH_2]_{twisting}$ modes of UHMWPE. The combined peak areas of the $[CH_2]_{wagging}$ modes presented here is what was used to calculate

the various indices presented across this section, as discussed at the start of Section 4.1.1. The IR absorption band assignments found in literature from experimental FTIR and as calculated based on the C20 alkane model structure are presented in Table 13 (Andanson & Kazarian, 2008; Bernstein et al., 2007; Brayton et al., 2017; Charles, 2009; da Silva & Wiebeck, 2018; Ren et al., 2020). Occasionally, the literature makes indiscriminate use of the 'bending' mode notation or assigns both 'wagging' and 'twisting' to the same band positions, therefore, the calculated spectrum of the C20 alkane model structure was used to assign the definitive vibrational modes to the corresponding IR absorption wavenumbers.

Table 13. Expected FTIR absorption band positions according to the literature and as calculated using the C20 alkane model structure between 1200 and 1400 cm^{-1}.

Vibrational mode	**IR absorption wavenumber (cm^{-1})**	
	Literature	**Calculated**
$[CH_2]_{twisting}$	~ 1275	1260
$[CH_2]_{twisting}$	~ 1300	1296
$[CH_2]_{wagging}$	~ 1340	1332
$[CH_2]_{wagging}$	~ 1355	1360
$[CH_{2/3}]_{wagging}$	~ 1370	1384

As can be observed in the spectral peak fits in Figure 33, the $[CH_2]_{twisting}$ bands were experimentally observed at 1275 and 1303 cm^{-1}, and the $[CH_2]_{wagging}$ bands were observed at 1341, 1352, and 1367 cm^{-1}. The values found in the literature closely correspond to the experimentally observed band positions and the calculated values also showed to provide reasonable additional estimates. The $[CH_2]_{wagging}$ showed negligible differences in the undoped sample series indifferent of ASPN treatment time, which allowed these bands to be constrained in terms of peak area relative to each other during the peak fits for the doped sample series, whilst the $[CH_2]_{twisting}$ bands and αTH-related bands were kept unconstrained during peak

fitting. The $[CH_2]_{twisting}$:$[CH_2]_{wagging}$ peak area ratio was investigated, as shown in the corresponding graph in Figure 33. Overall, the undoped sample series showed a notably higher relative presence of $[CH_2]_{twisting}$, but ASPN showed to have a similar effect on the decrease of this ratio over the treatment time as both sample series displayed a similar trend.

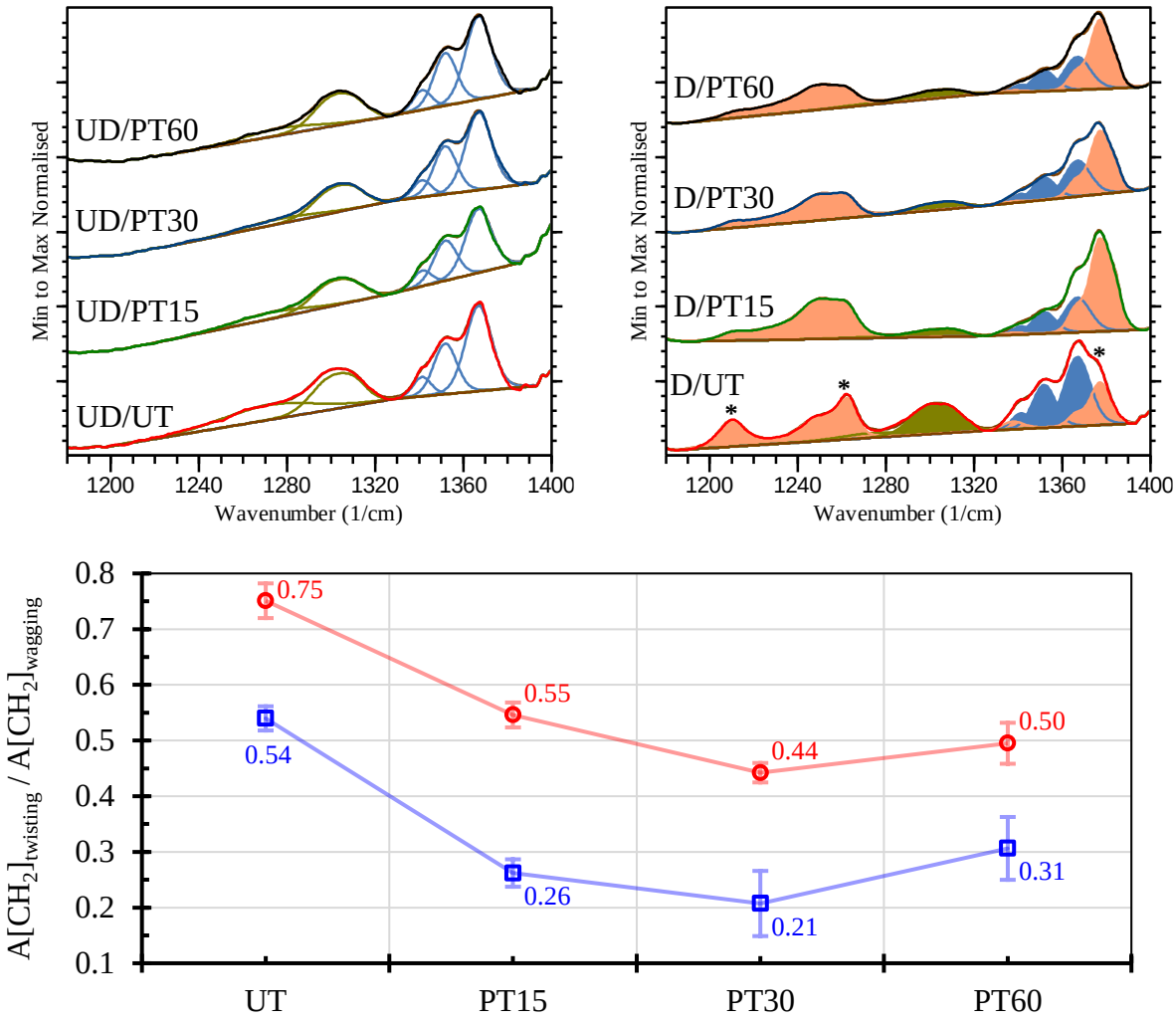


Figure 33. Summed spectral peak fits of the (top-left) undoped and (top-right) doped UHMWPE-based sample series between 1200 and 1400 cm^{-1}, displaying (**blue**) $[CH_2]$wagging, (**green**) $[CH_2]$twisting, and (**orange**) αTH; and (bottom) the corresponding graph displaying the $[CH_2]_{wagging:twisting}$ peak area ratios as observed in the individual peak fits of the (**red**, circle) undoped and (**blue**, square) doped sample series. The asterisks denote the bands of interest related to the αTH components in the doped UHMWPE sample series.

Region 4 also provided information on the chemical changes experienced by the αTH. As denoted by the asterisks in the peak fits of the doped sample series in Figure 33, relative intensity losses were observed at 1210 and 1260 cm^{-1}, whilst a relative increase was noted at

1375 cm^{-1}. The IR absorption band assignments for these positions found in the literature and as calculated based on the αTH model structure are presented in Table 14 (J. Fu et al., 2013; He et al., 2018; Richaud, 2015). The spectra showed a decrease in the $[C–O]_{stretching}$ bands (i.e., 1210 and 1260 cm^{-1}) related to the phenol group of αTH. Within the literature, the $[C–O]_{stretching}$ band at 1260 cm^{-1} is commonly used to calculate the αTH index, providing a measure on the loss of its functioning (Richaud, 2015). As observed in Figure 34, the αTH index started at 0.152±0.010 and showed a negligible reduction for D/PT15 to 0.146±0.019. However, the αTH index showed a three-fold decrease to 0.053±0.016 for D/PT60, indicating loss in functioning as was expected based on the increasing vinyl-based indices calculated in Region 2.

Table 14. Expected FTIR absorption band positions according to the literature and as calculated using the αTH model structure between 1200 and 1400 cm^{-1}.

Vibrational mode	IR absorption wavenumber (cm^{-1})	
	Literature	Calculated
$[C–O]_{str.}$ / $[O–H]_{deform.}$	~ 1210	1211
$[C–O]_{stretching}$	~ 1260	1247
$[CH_{2/3}]_{wagging}$	~ 1375	1381

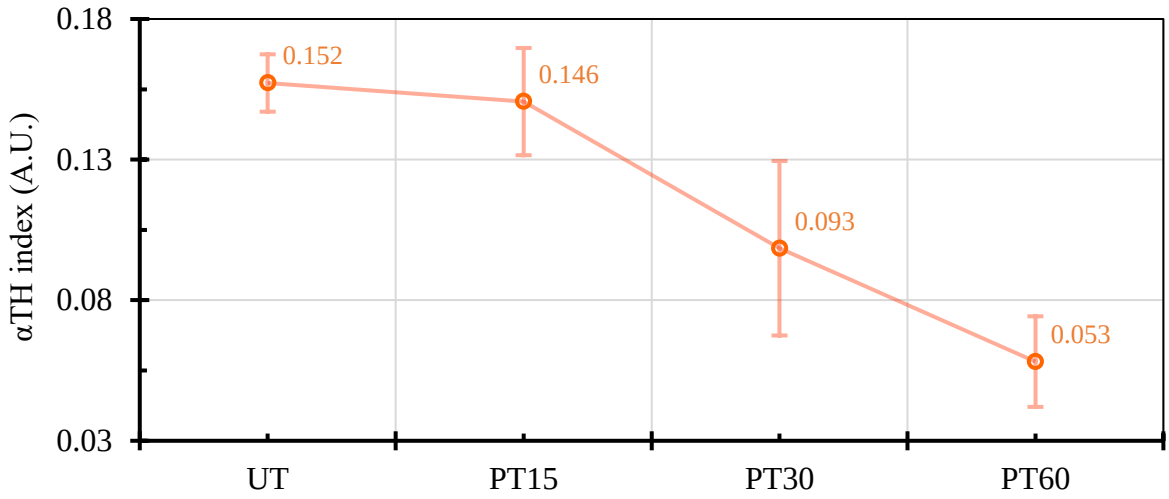


Figure 34. Graph displaying the αTH index as observed in the individual peak fits of the doped sample series.

Region 5 – 1400-1500 cm^{-1}

Region 5 displayed a clear doublet with maxima at 1462 and 1472 cm^{-1}, and a broad additional band at 1442 cm^{-1} as depicted in Figure 35. The IR absorption band assignments found in literature from experimental FTIR and as calculated based on the C20 alkane model structure are presented in Table 15 (Ceppatelli & Bini, 2014; Charles, 2009; A. Xu et al., 2020). The two main peaks (i.e., 1462 and 1472 cm^{-1}) are typically assigned to the $[CH_2]_{scissoring}$ modes of the UHMWPE. According to the literature, the splitting of this doublet is associated with the crystallinity of the PE, although no phenomenological correlations are currently established for UHMWPE using these two bands (Babaghayou et al., 2016). Based on the area deviations observed between the various spectra, peak fitting was performed with two additional components at 1457 and 1468 cm^{-1}, in addition to the bands visually observed at 1462, 1472, and 1442 cm^{-1}. During the peak fitting of the doped UHMWPE-based sample series, the components originating from αTH were constrained in relative peak area to each other. No assignments were found in the literature for the two additional components at 1458 and 1468 cm^{-1}, it was assumed that these were related to the bands at 1462 and 1472 cm^{-1}, respectively, and may be a result of unresolved peak asymmetry. Next to that, the band 1442 cm^{-1} was not observed in the calculated spectrum, according to literature this band is associated with $[CH]_{deformation}$ of the amorphous phase (Chauhan et al., 2008).

Table 15. Expected FTIR absorption band positions according to the literature and as calculated using the C20 alkane model structure between 1400 and 1500 cm^{-1}.

Vibrational mode	**IR absorption wavenumber (cm^{-1})**	
	Literature	**Calculated**
$[CH]_{deformation}$	1442	-
$[CH_2]_{scissoring}$	1462	1467
$[CH_2]_{scissoring}$	1472	1486

The [1472 cm^{-1}]:[1462 cm^{-1}] peak area ratio was investigated, as shown in the corresponding graph in Figure 35. The untreated undoped and doped samples showed the lowest ratio of their respective sample series, starting at 1.08±0.01 and 1.28±0.08, respectively. Both sample series showed a continuous increase in this ratio after the ASPN treatment. Overall, the ratio of the doped samples series showed to be 0.18±0.08 higher when compared to the undoped sample series. More specifically, UD/PT60 ended at a ratio of 1.49±0.11, whilst D/PT60 showed a ratio of 1.75±0.06. When taking the peak area ratio observed in Region 1 into consideration (as this region ratio increased with crystallinity), it can be speculated that the [1472 cm^{-1}]:[1462 cm^{-1}] peak area ratio also demonstrated an increase in crystallinity.

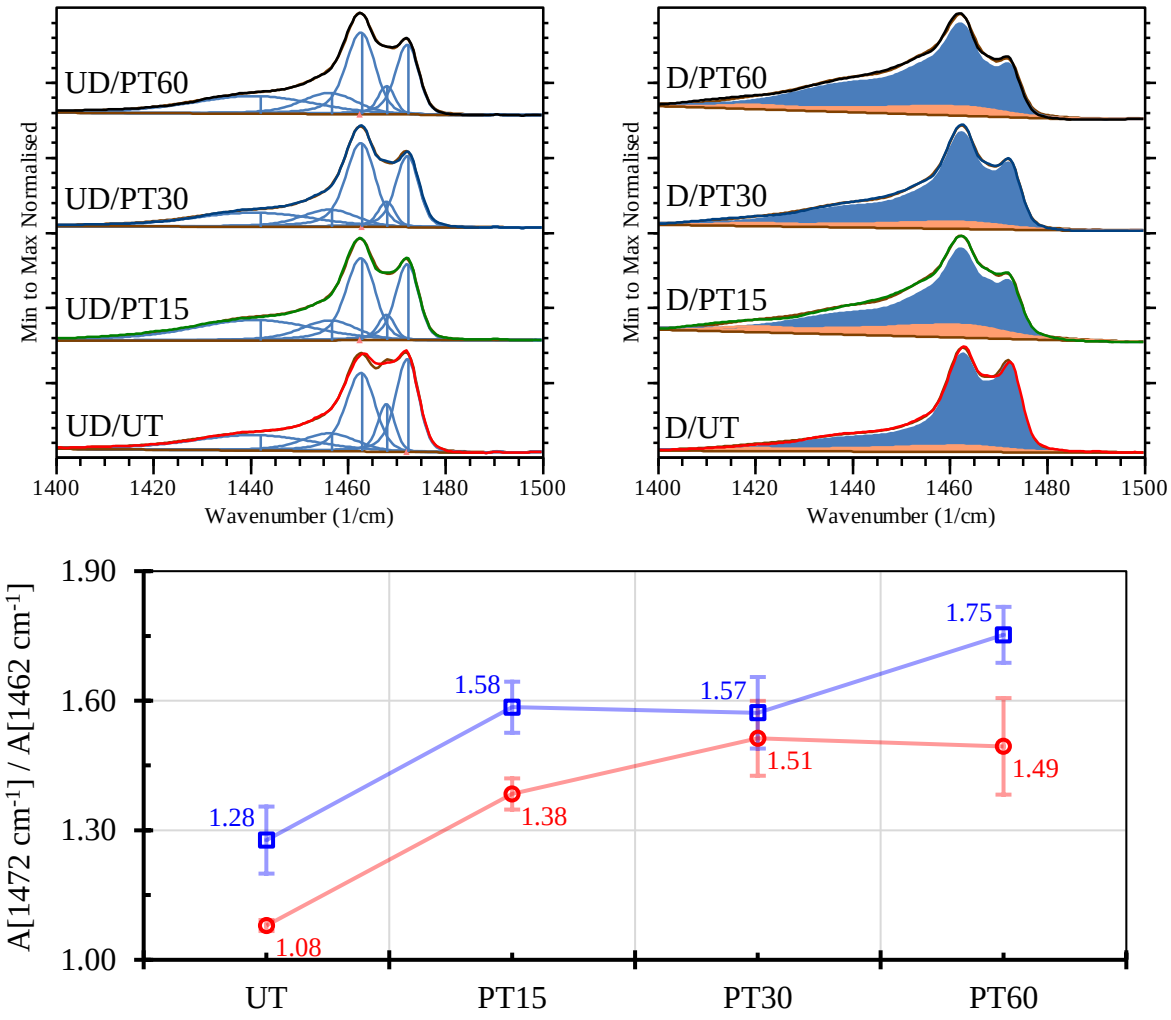


Figure 35. Summed spectral peak fits of the (top-left) undoped and (top-right) doped UHMWPE-based sample series between 1400 and 1500 cm^{-1}, displaying (**blue**) UHMWPE and (**orange**) αTH; and (bottom) the corresponding graph displaying the [1472 cm^{-1}]:[1462 cm^{-1}] peak area ratios as observed in the individual peak fits of the (**red**) undoped and (**blue**) doped sample series.

Region 6 – 1500-1800 cm^{-1}

Region 6 allowed for the identification of various double-bonded functional groups (i.e., [C=C], [C=O], etc.). The IR absorption band assignments found in literature from experimental FTIR and as calculated based on the vinyl-/carbonyl-based model structures are presented in Table 16 – the [C=O]-based model structures are shown in Figure 36 (Benedetti et al., 1998; Norizan & Mohamed, 2013; Reusch, 1980; Santner et al., 2004). It is worth to note that the vinyl-based bonds were rarely characterised in the literature for PE in this region, these values were therefore taken from other materials/molecules to provide a reasonable indication of the expected band positions, although it is unlikely that these are completely accurate for UHMWPE. Next to that, some functionalities (e.g., $[C=O]_{acid}$) showed large variations (up to ±40 cm^{-1}) in the literature due to the structural differences or influences from intermolecular forces like hydrogen bonding. Larger differences were also noted between the literature and calculated band positions. Despite this, a clear difference in the grouping of the [C=C] and [C=O] related band positions was observed, as the $[C=C]_{stretching}$ bonds showed band positions below 1700 cm^{-1} and the $[C=O]_{stretching}$ bonds band positions were above 1700 cm^{-1}.

Table 16. Expected FTIR absorption band positions according to the literature and as calculated using the corresponding vinyl-based and oxygen-based model structures between 1500 and 1800 cm^{-1}.

Vibrational mode	**IR absorption wavenumber (cm^{-1})**	
	Literature	**Calculated**
$[C=C]_{vinyl}$	~ 1645	1708
$[C=C]_{geminal\text{-}vinylidene}$	~ 1653	1674
$[C=C]_{trans\text{-}vinylene}$	~ 1675	1690
$[C=O]_{aldehyde/ketone}$	~ 1730/1715	1772/1745
$[C=O]_{acid}$	~ 1740	1820
$[C=O]_{ester}$	~ 1740	1783

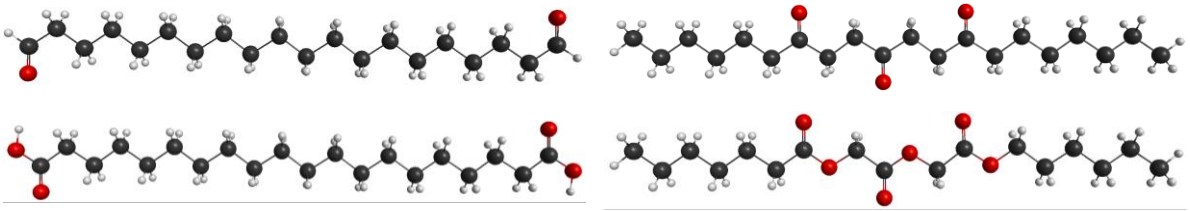


Figure 36. Model structures used to predict the absorption band positions for (top-left) aldehyde, (top-right) ketone, (bottom-left) carboxylic acid, and (bottom-left) ester bonds.

The components from αTH were not included during the peak fitting as these would have had negligible impact on the fitting, considering the $[C=C]_{stretching}$ of its aromatic ring were almost non-existent in FTIR as can be observed from the spectrum of pure αTH in Figure 37. To further aid in the band assignments, the $[C=C]_{stretching}$ from unsaturation in a hydrocarbon system was investigated by recording a spectrum of a-C as shown in Figure 37. The maximum band position for a-C was observed at 1653 cm^{-1} but also showed a shoulder at 1570 cm^{-1}, indicating the presence of various [C=C] bond configurations, although specifically what configurations cannot be confirmed without standard materials. Within the literature, similar band positions for the $[C=C]_{stretching}$ were also observed in polyenes (i.e., poly-unsaturated hydrocarbons, consisting of alternating [C=C] and [C−C] bonds) (Norizan & Mohamed, 2013).

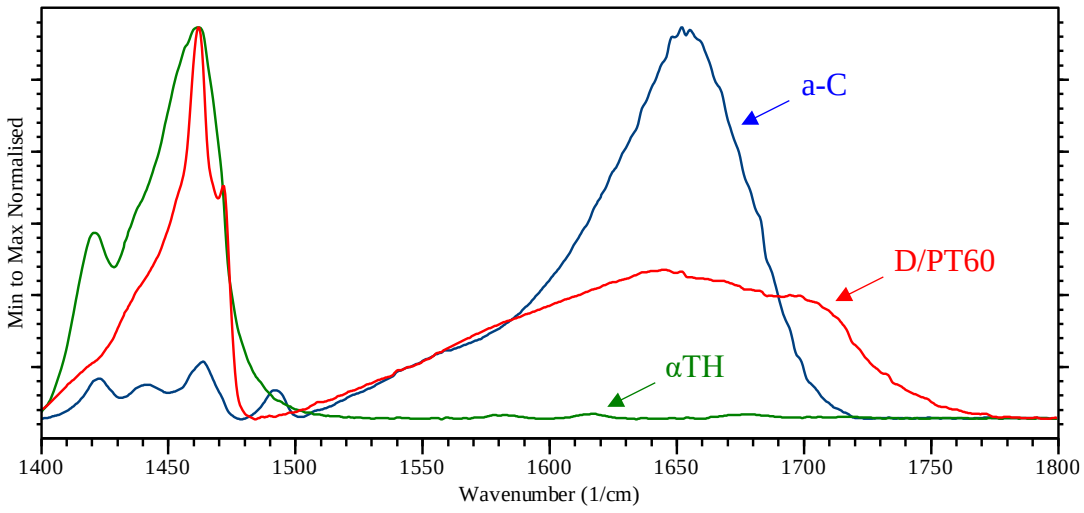


Figure 37. ATR-FTIR spectra of (**red**) D/PT60, (**green**) αTH, and (**blue**) a-C between 1400 and 1800 cm^{-1}.

Based on the area deviations observed between the spectra, peak fitting was performed using four components, as can be observed in Figure 38. Two of the components were related

to $[C=C]_{stretching}$ positioned at 1568 and 1654 cm^{-1} (i.e., $[C=C]_1$ and $[C=C]_2$), the other two components were related to the $[C=O]_{stretching}$ of carbonyls and acids/esters positioned at 1710 and 1749 cm^{-1} (i.e., [C=O] and [O=C−O]), respectively. From the corresponding graph in Figure 38, it can be observed that the untreated samples showed the lowest indices overall. After ASPN, both sample series showed an increase in the $[C=C]_{stretching}$ indices, especially for the doped sample series the $[C=C]_2$ index increased significantly, displaying that hydrocarbon unsaturation increased over the ASPN treatment time. Interestingly, both the undoped and doped sample series showed that a shorter ASPN treatment time (i.e., PT15 and PT30) resulted in a higher presence of [C=O] and [O=C−O] when compared to the PT60 samples.

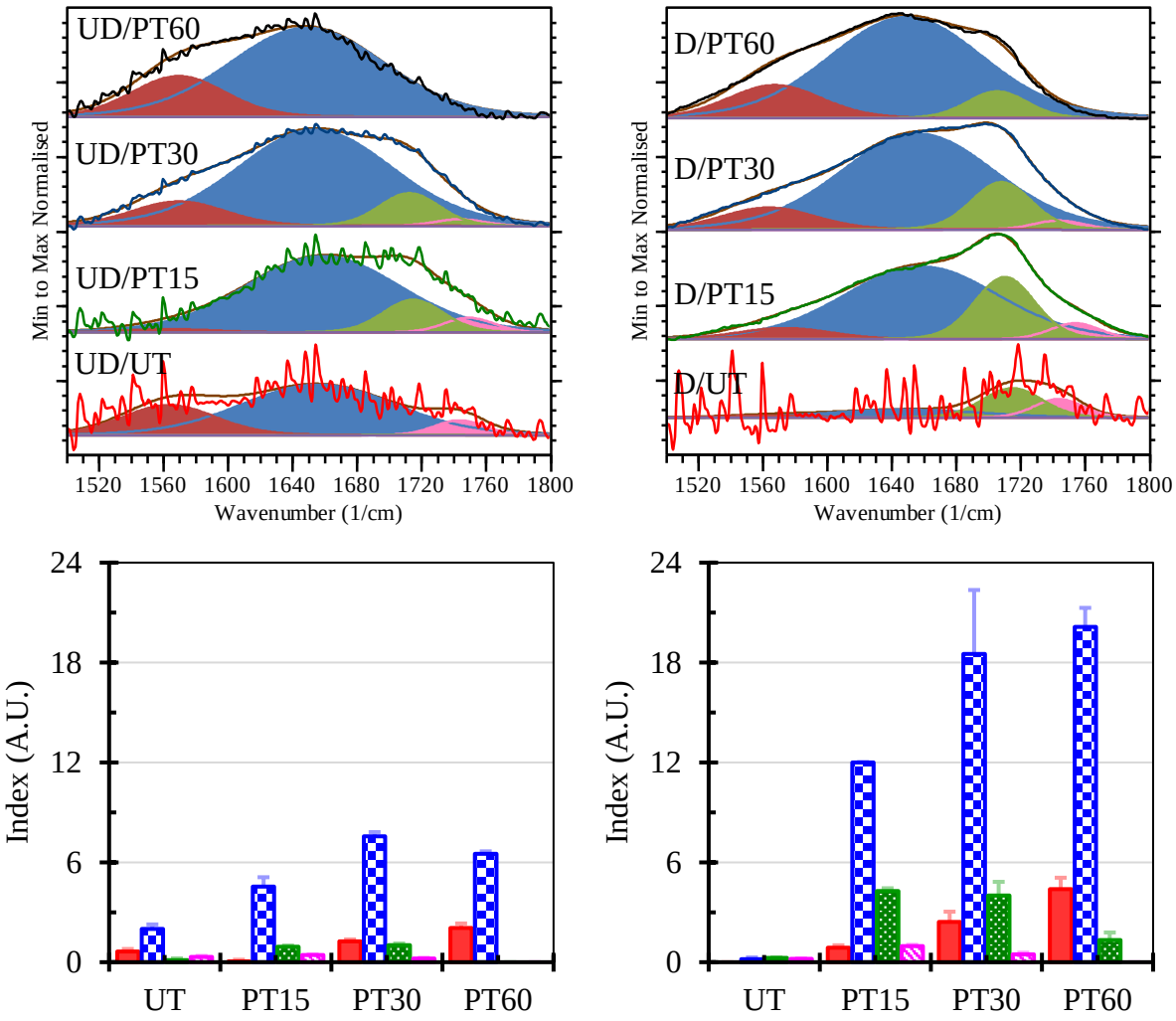


Figure 38. Summed spectral peak fits of the (top-left) undoped and (top-right) doped UHMWPE-based sample series between 1500 and 1800 cm^{-1}; and the corresponding graphs for the (bottom-left) undoped and (bottom-right) doped sample series, displaying the (solid, **red**) $[C=C]_1$, (checkered, **blue**) $[C=C]_2$, (dotted, **green**) [C=O], and (striped, **pink**) [O=C−O] band indices as observed in the individual peak fits.

Region 7 – 2000-3000 cm^{-1}

Region 7 displayed the symmetrical and asymmetrical $[CH_{2/3}]_{stretching}$ bands of UHMWPE, which are typically the most intense bands observed in the FTIR spectra of PE-based materials. The IR absorption band positions found in literature from experimental FTIR and as calculated based on the C20 alkane model structures are presented in Table 17 (da Silva & Wiebeck, 2022; Gaston et al., 2016; Gulmine et al., 2002; Krimm et al., 1956; Öner et al., 2018). The calculated band positions are notably higher than the values from the literature, but the sequential order of the modes is identical and confirms the validity of the assignments from the literature. As it is impossible for the two [C−C] chains within the same crystalline PE lattice to exhibit the same orientation, the asymmetrical:symmetrical $[CH_2]_{stretching}$ peak area ratio is said to be related to the crystallinity – similar to Region 1 and 5 (Yan et al., 2006).

Table 17. Expected FTIR absorption band positions according to the literature and as calculated using the C20 alkane model structure between 2000 and 3000 cm^{-1}.

Vibrational mode	IR absorption wavenumber (cm^{-1})	
	Literature	Calculated
$[CH_2]_{stretching,symmetric}$	~ 2850	2922
$[CH_3]_{stretching,symmetric}$	~ 2875	2933
$[CH_2]_{stretching,asymmetric}$	~ 2920	2969
$[CH_3]_{stretching,asymmetric}$	~ 2955	2998

As displayed in Figure 39, the spectra clearly showed the bands associated with the $[CH_2]_{stretching}$ at 2849 and 2917 cm^{-1}, but no clear peak presence was observed for the $[CH_3]_{stretching}$ bands. Next to the two $[CH_2]_{stretching}$ components, peak fitting was performed with three additional components at 2692, 2821, and 2892 cm^{-1} due to the area deviations observed between the various spectra. No assignments were found in the literature for the additional components, but it was assumed that the components at 2821 and 2892 cm^{-1} were related to

2849 and 2917 cm^{-1}, respectively, and may be a result of unresolved peak asymmetry. The components originating from αTH were constrained in relative peak area to each other during peak fitting. The asymmetrical:symmetrical $[CH_2]_{stretching}$ peak area ratio was investigated, as can be observed in the corresponding graph in Figure 39. The corresponding graph showed that the untreated samples displayed the highest ratio compared their respective sample series, which started at 2.28±0.01 for UD/UT and 2.31±0.03 for D/UT. The ratio for undoped samples series initially decreased but ultimately restored itself to practically the same ratio as UD/UT, ending at 2.22±0.04 for UD/PT60. The ratio of the doped sample series decreased over the ASPN treatment time to 2.06±0.02 for D/PT60.

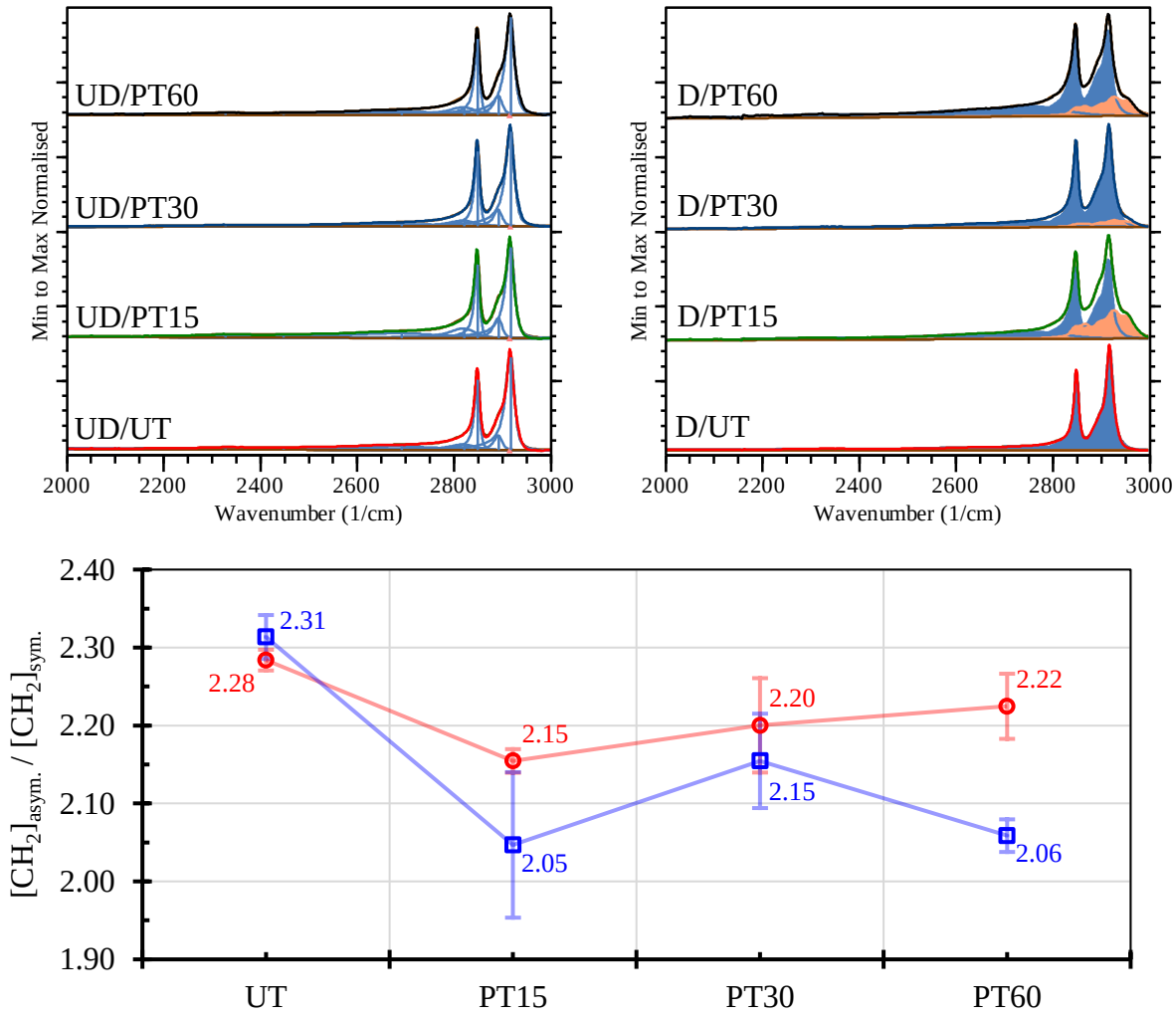


Figure 39. Summed spectral peak fits of the (top-left) undoped and (top-right) doped UHMWPE-based sample series between 2000 and 3000 cm^{-1}, displaying (**blue**) UHMWPE and (**orange**) αTH; and (bottom) the corresponding graph displaying the $[CH_2]_{asymmetrical:symmetrical}$ peak area ratios as observed in the individual peak fits of the (**red**) undoped and (**blue**) doped sample series.

Region 8 – 3000-3800 cm^{-1}

Region 8 displayed broad, overlapping bands related to various bonds, including $[=C-H_x]_{stretching}$, $[O-H]_{stretching}$ of oxygen-related groups (i.e., alcohols, carboxylic acids, etc.), and potentially $[N-H]_{stretching}$ of nitrogen-related groups (i.e., amine, amide, etc.). The IR absorption band positions found in literature from experimental FTIR and as calculated based on various model structures are presented in Table 18 (Borsdorf & Scholz, 1974; Reusch, 1980; Socrates, 2004). The same model structures as presented in Region 6 were used to estimate the $[O\text{-}H]_{stretching}$, the $[N\text{-}H]_{stretching}$ was estimated using the structures presented in Figure 40. It should be noted that the band positions found in the literature show large variations (e.g., up to ±150 cm^{-1} for $[O-H]_{stretching}$), due to structural differences or influences like hydrogen bonding.

Table 18. Expected FTIR absorption band positions according to the literature and as calculated using the vinyl-based, oxygen-based, and nitrogen-based model structures between 3000 and 3800 cm^{-1}.

Vibrational mode	**IR absorption wavenumber (cm^{-1})**		
	Literature	**Calculated**	
$[=CH_x]_{stretching}$	~ 3100	Vinyl	S - 3138 AS - 3209
		Geminal-vinylidene	S - 3068 AS - 3137
		Trans-vinylene	S - 3013 AS - 3026
$[O-H]_{stretching}$	~ 3500	Alcohol	3584
		Acid	3598
		αTH	3642
$[N-H]_{stretching}$	~ 3400	Amine	3357
		Imine	3296
		Amidine	3368
		Amide	3417

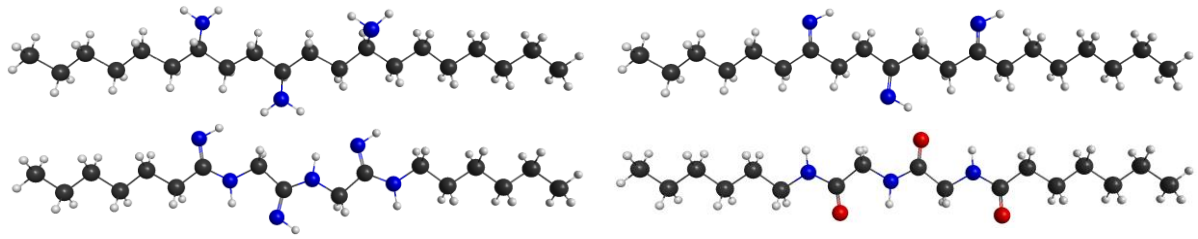


Figure 40. Model structures used to predict the absorption band positions for (top-left) amine, (top-right) imine, (bottom-left) amidine, and (bottom-right) amide bonds.

The large deviation in the $[O\text{-}H]_{stretching}$ bands was also confirmed by the αTH spectrum, depicted in Figure 41, which showed a sharp band at 3631 cm^{-1} for the free $[O\text{-}H]_{stretching}$ and a broad band at 3469 cm^{-1} due to its H-bonded $[O\text{-}H]_{stretching}$. The calculated position for the free $[O\text{-}H]_{stretching}$ of αTH was accurately estimated at 3642 cm^{-1}, but considering the model structures were single molecules, the model structures could only provide the band positions for free $[O/N\text{-}H]_{stretching}$. Based on the area deviations between the various spectra, the peak fitting was performed with four components, namely, at 3055, 3156, 3322, and 3537 cm^{-1}, as shown in Figure 42. It was expected that the components at 3055 and 3156 cm^{-1} were associated with the vinyl-based chemical bonds. Unfortunately, due to the large deviations of the $[O{-}H]_{stretching}$ functionalities, no accurate vibrational assignments could be made between 3200 to 3600 cm^{-1}. However, as there were no strong indications for nitrogen-related bonds in the previous regions, it was assumed that the bands in this region were related to oxygen-based functionalities.

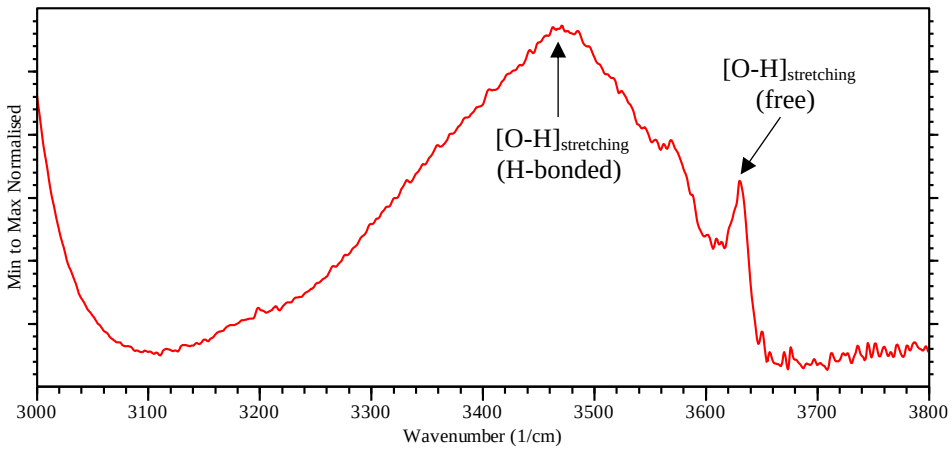


Figure 41. ATR-FTIR spectra of (**red**) αTH between 3000 and 3800 cm^{-1}.

The corresponding graphs in Figure 42 showed a decrease of the $[=C-H_x]_{stretching}$ indices related to 3055 and 3156 cm^{-1} over the ASPN treatment time for the undoped UHMWPE-based sample series, whereas the doped sample series showed an increase of the 3156 cm^{-1} band index over the ASPN treatment time relative to its untreated counterpart. Additionally, the 3322 and 3537 cm^{-1} band indices, which were assumed to be mainly related to $[O-H]_{stretching}$, remained relatively similar for the undoped sample series – apart from the increase observed at UT/PT15. On the other hand, the doped sample series showed the lowest indices from all samples at D/UT, but these increased roughly by five-fold at D/PT60. The 3322 and 3537 cm^{-1} band indices for both the undoped and doped sample series roughly increased or decreased in unison.

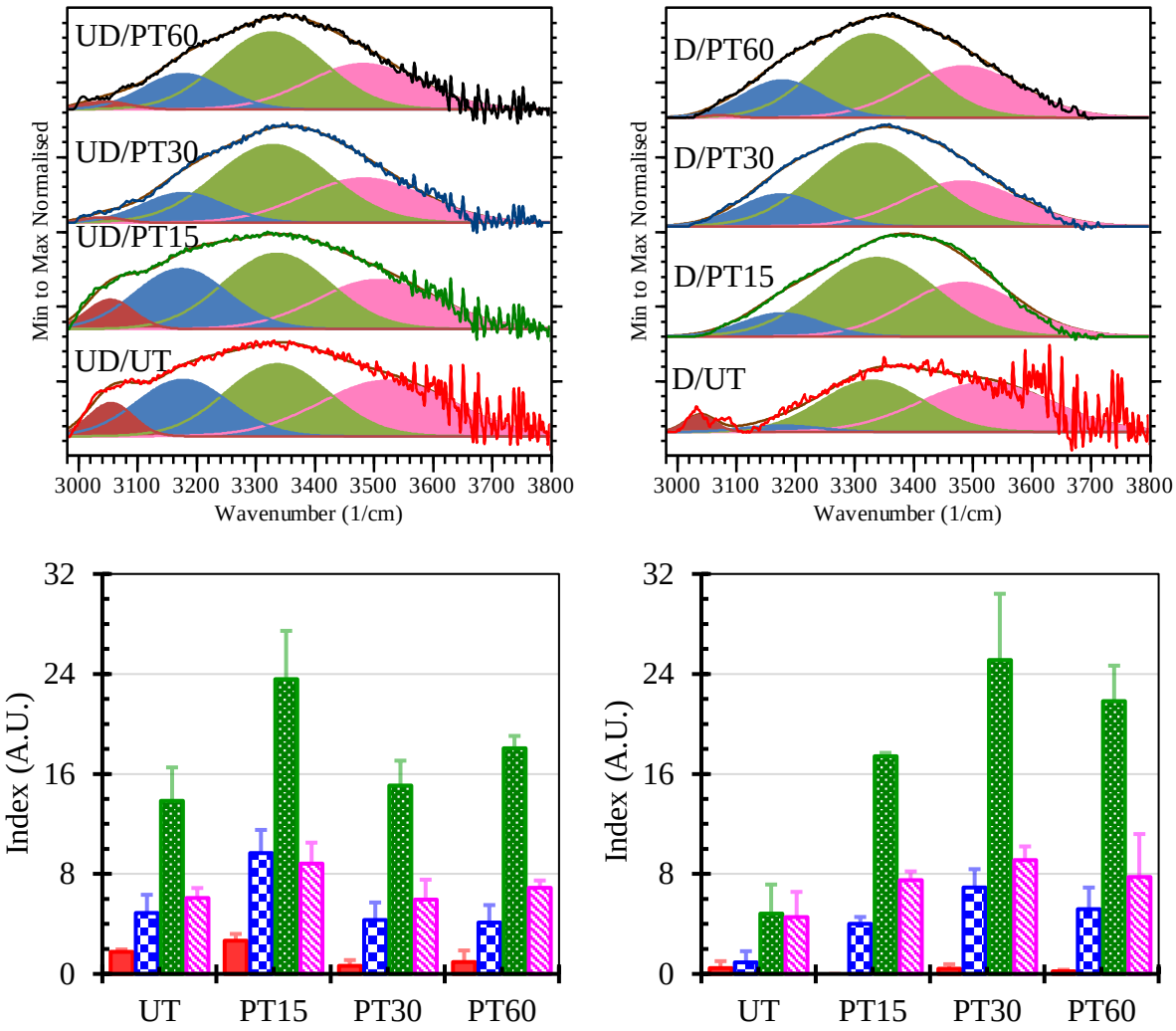


Figure 42. Summed spectral peak fits of the (top-left) undoped and (top-right) doped UHMWPE-based sample series between 1500 and 1800 cm^{-1}; and the corresponding graphs for the (bottom-left) undoped and (bottom-right) doped sample series, displaying the (solid, **red**) 3055 cm^{-1}, (checkered, **blue**) 3156 cm^{-1}, (dotted, **green**) 3322 cm^{-1}, and (striped, **pink**) 3537 cm^{-1} band indices as observed in the individual peak fits.

Summary and correlations

This section presented a systematic investigation into the FTIR spectra of the undoped and doped UHMWPE-based samples treated with ASPN. Aided by the calculations, the investigated spectral regions provided for the identification of most chemical bonds present within the UHMWPE-based samples. However, despite various nitrogen-related bonds were investigated, no strong indications for nitrogen-related bands were observed in the ASPN treated UHMWPE-based spectra. It was assumed that this is likely due to the relatively small treatment depth of ASPN, resulting in the IR signal from the nitrogen-related groups being lost in the noise as, due the relatively large penetration depth of FTIR relative to the treatments depth, the analysis volume would predominantly consist of the UHMWPE/αTH components.

To further explore the obtained absorption band indices/ratios, the strength of the correlation between the calculated indices/ratios was investigated using the Pearson correlation coefficients (r_p). For ease of viewing, Table 19 presents the correlation where $-0.75 > r_p > 0.75$ (i.e., only showing the highly correlated pairs) – the full Pearson correlation matrix is presented in Appendix C2. As can be observed, a total of 15 highly positive correlated pairs and 14 highly negative correlated pairs were noted.

For example, Regions 1 ($[CH_2]_{rock.}$), 4 ($[CH_2]_{twist./wag.}$), 5 ($[CH_2]_{scis.}$), and 7 ($[CH_2]_{str.}$) were all involved in the crystallinity of PE according to the literature, these four regions also showed to be strongly correlated. In addition, the $[C=C]_{str.,2}$ and $[C=O]_{str.}$ indices (from Region 6) also showed to be correlated to the four $[CH_2]$-related regions. As can be observed in Figure 43, the $[CH_2]_{twist.:wag.}$ ratio showed a negative correlation to the other indices/ratios – except for the $[A_{2917}:A_{2849}]$ ratio (i.e., asym.:sym. $[CH_2]_{str.}$). Therefore, a decrease in the $[CH_2]_{twist.:wag.}$ ratio indicated a reduction in crystallinity, as the $[A_{730}:A_{719}]$ ratio (i.e., $[CH_2]_{rock.}$ modes) increased concurrently to the crystallinity of PE (see Region 1). Next to that, this implied that

the other negatively correlated indices related to the chemical changes (i.e., unsaturation/oxidation) increased over the crystallinity (i.e., chemicrystallization). This effect was also observed for the thermal oxidation of PE where the oxidation process increased crystallinity by lamellar thickening, this resulted in a decrease of the interlamellar amorphous phase and increased embrittlement of the material (Fayolle et al., 2008; Reano et al., 2018).

Table 19. Pearson correlations where -0.75 > r_p > 0.75 as observed between the indices and ratios from the individual FTIR spectral peak fits of the undoped and doped UHMWPE-based samples.

Positive correlation			**Negative correlation**		
Array 1	**Array 2**	r_p	**Array 1**	**Array 2**	r_p
1165 cm^{-1}	1080 cm^{-1}	0.97	αTH	$[C=C]_{str.,1}$	-0.99
3540 cm^{-1}	3320 cm^{-1}	0.97	αTH	TVI	-0.99
αTH	A_{730}:A_{719}	0.92	αTH	VI	-0.96
GVI	TVI	0.92	A_{2917}:A_{2849}	1040 cm^{-1}	-0.92
1040 cm^{-1}	1080 cm^{-1}	0.91	A_{2917}:A_{2849}	1080 cm^{-1}	-0.89
1165 cm^{-1}	1040 cm^{-1}	0.86	A_{1300}:A_{1370}	A_{1472}:A_{1462}	-0.88
$[C=C]_{str.,2}$	A_{1472}:A_{1462}	0.86	A_{1300}:A_{1370}	$[C=C]_{str.,2}$	-0.86
3540 cm^{-1}	3155 cm^{-1}	0.85	αTH	$[C=C]_{str.,2}$	-0.84
$[C=C]_{str.,2}$	$[C=C]_{str.,1}$	0.84	A_{1300}:A_{1370}	[C=O]	-0.82
3320 cm^{-1}	3155 cm^{-1}	0.85	A_{2917}:A_{2849}	A_{1472}:A_{1462}	-0.82
1165 cm^{-1}	1120 cm^{-1}	0.78	αTH	A_{1472}:A_{1462}	-0.80
GVI	3055 cm^{-1}	0.78	A_{2917}:A_{2849}	$[C=C]_{str.,2}$	-0.79
$[C=O]_{str.}$	$[O=C-O]_{str.}$	0.76	A_{2917}:A_{2849}	1165 cm^{-1}	-0.78
A_{1300}:A_{1370}	A_{2917}:A_{2849}	0.76	A_{1300}:A_{1370}	A_{730}:A_{719}	-0.78
$[C=O]_{str.}$	1080 cm^{-1}	0.75			

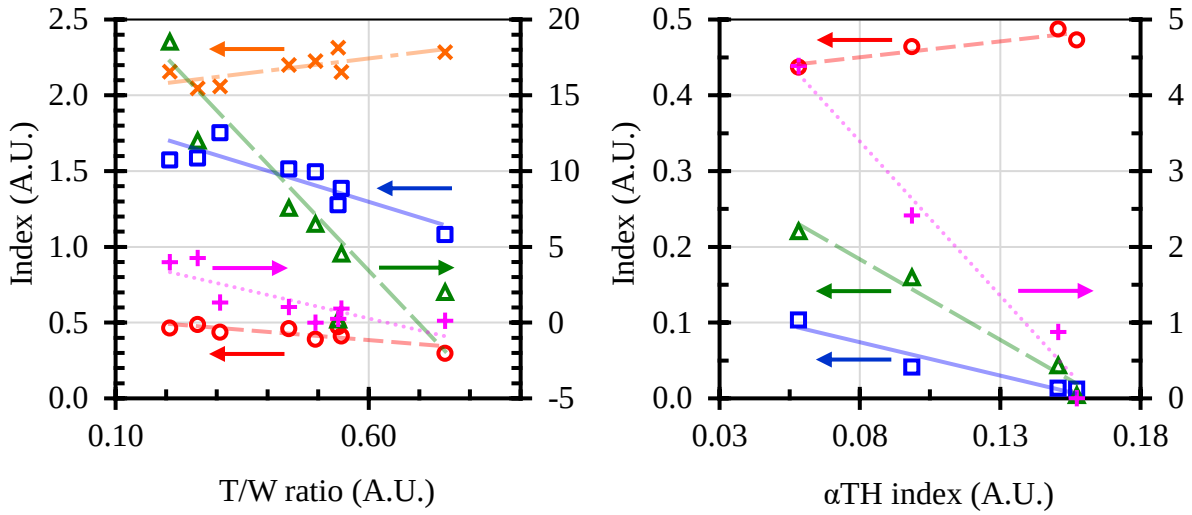


Figure 43. Linear correlations graphs of (left) the [A_{1300}:A_{1370}] ratio versus the (**red**, circle) [A_{730}:A_{719}], (**blue**, square) [A_{1472}:A_{1462}], (**green**, triangle) [C=C]$_2$, (**pink**, plus signs) [C=O], and (**orange**, crosses) [A_{2917}:A_{2849}]; and (right) the αTH index versus the (**red**, circle) [A_{730}:A_{719}], (**blue**, square) vinyl, (**green**, triangle) trans-vinylidene, and (**pink**, plus signs) [C=C]$_1$. The colours of the arrows correspond to its respective series, the direction of the arrows determines the appropriate y-axis.

Additionally, as was expected, various strong correlations (-0.9 > r_p > 0.9) were observed for the αTH index in Table 19. The αTH index was positively correlated with the [A_{730}:A_{719}] ratio but negatively correlated with the vinyl, trans-vinylidene, and [C=C]$_{str.,1}$ index, the linear correlations of these pairs are presented in Figure 43. In short, doping UHMWPE with αTH showed to initially increase its crystallinity (as was expected during the peak fitting in Region 1), but the subsequent treatment with ASPN reduced the functioning of αTH, slightly reduced the crystallinity, and increased the [C=C]-related bonds (i.e., vinyl, trans-vinylidene and [C=C]$_1$ unsaturation) of the UHMWPE-based samples.

Other notable correlations from Table 19 were related to the [A_{2917}:A_{2849}] ratio, which was negatively correlated with the 1080, 1140 and 1165 cm^{-1} band indices, as well as the 3320 and 3540 cm^{-1} band indices (r_p = -0.68 for both band indices, see Appendix C2). This enforced the assumption made in Region 3, i.e., that the increase in the respective indices was most likely related to increased [C–O]$_{skeletal}$/[O–H]$_{stretching}$ modes. Finally, the geminal-vinylidene index showed to be positively correlated to the 3055 cm^{-1} band index, which indicated that the 3055 cm^{-1} band was associated with [=C−H_x]$_{stretching}$ as was hypothesized in Region 8.

4.1.2. Raman microspectroscopy

Raman microspectroscopy was used to investigate the effect of αTH doping in combination with ASPN on the chemical composition, crystallinity, molecular orientation, and stress of the UHMWPE-based samples. The Raman spectra allowed for the identification of chemical bonds present within the UHMWPE samples at a penetration depth of about 10.11 μm (see Section 3.2.3 for more information on the axial resolution following Rayleigh criterion). Contrary to FTIR, Raman is sensitive to homo-nuclear molecular bonds, allowing more accurate distinction of, e.g., [C–C] or [C=C] bonds (Exline, 2013). The Raman spectra were separated into two regions, with 'Region 1' between 1000 and 1800 cm^{-1} and 'Region 2' between 2800 and 3000 cm^{-1}. Where necessary, the a-C/αTH-related components were included during the peak fitting, to differentiate between potentially overlapping components arising from the molecules that were present within the spectra to the best extent possible.

The peak fitting of the spectra provided a variety of band indices related to the chemical bonds that were present in the two regions, at the end of this section the band indices were investigated for potential correlations using the Pearson correlation coefficients. Next to that, as the same samples were investigated by both Raman and FTIR (Section 4.1.1), potential correlations between the two techniques were also investigated. For ease of viewing, only the summed spectral peak fits per sample type are shown for each region. However, the corresponding graphs were based on spectral data from the individual peak fits, to provide a confidence interval ($\alpha = 0.05$) for the data mean using a normal distribution. The data obtained from the individual spectral peak fits of the full undoped and doped sample series are presented in Appendix C3.

Region 1 – 1000-1800 cm^{-1}

Region 1 presented the most interesting portion of the Raman spectra from the UHMWPE-based sample series, as it allowed for the identification of a large variety of carbon-based bonds that were mostly inactive in the previously discussed FTIR spectra. The Raman band assignments found in literature from experimental Raman and as calculated based on the C20 alkane model structure are presented in Table 20 (Affatato et al., 2013; Pezzotti, 2017). The model structure could not provide information related to the phase-specific band positions as it was a single molecule, but the calculated Raman band positions were in reasonable agreement with those from the literature and confirmed the vibrational assignments. The low-intensity band at 1270 cm^{-1} was expected to be related to $[CH_2]_{twisting}$, the literature notes its presence but did not provide a definitive assignment (Keresztury & Földes, 1990; Medel et al., 2009). The Raman spectra were also peak fitted between 750 and 1000 cm^{-1}, but this range is not discussed as there was no literature on assignments – the calculated C20 spectrum presented a band at 876 cm^{-1} due to $[C\text{-}CH_3]_{stretching}$ but further assignments would be speculation.

Table 20. Expected Raman band positions according to the literature and as calculated using the C20 alkane model structure between 1000 and 1800 cm^{-1}; the crystalline (C), amorphous (A), or combined (C+A) origin of the respective bands is denoted in the parentheses.

Vibrational mode	**Raman shift (cm^{-1})**	
	Literature	**Calculated**
$[C–C]_{stretching,AS}$ (C+A)	~ 1060	1043
$[C–C]_{stretching}$ (A)	~ 1080	1079
$[C–C]_{stretching,S}$ (C+A)	~ 1130	1118
$[CH_2]_{rocking}$ (C+A)	~ 1170	1169
$[CH_2]_{twisting}$ (C)	~ 1295	1285
$[CH_2]_{twisting}$ (A)	~ 1305	
$[CH_2]_{wagging}$ (C+A)	~ 1370	1382

$[CH_2]_{scissoring}$ (C)	~ 1415	1462
$[CH_2]_{scissoring}$ ($A_{interphase}$)	~ 1440	
$[CH_2]_{scissoring}$ (A)	~ 1460	

Next to the UHMWPE components, it was important to account for the a-C/αTH-related components, especially considering their presence was confirmed prior with FTIR. The overlayed spectra of D/PT60, a-C, and αTH are presented in Figure 44, the position of the $[C=C]_{stretching}$ bands around 1600 cm^{-1} showed to be nearly identical across the spectra. However, it is important to understand the difference in origin of the $[C=C]_{stretching}$ bands related to a-C and αTH, as it the respective band shapes and this information aids in the assignment for the UHMWPE-based samples. The $[C=C]_{stretching}$ bands in αTH are related to the aromatic "ring breathing" modes of its phenol group which were experimentally observed at 1585 and 1616 cm^{-1}, and calculated to be present at 1583 and 1614 cm^{-1}, respectively. Whereas the $[C=C]_{stretching}$ band around 1600 cm^{-1} for a-C originates from any [C=C] bond (i.e., aliphatic and/or aromatic) within the hydrocarbon system. As the $[C=C]_{stretching}$ band for a-C included contributions of various differing bond orientations, its band was significantly broader than that for a "pure" aromatic system (i.e., αTH) – the band for D/PT60 was more like that of a-C.

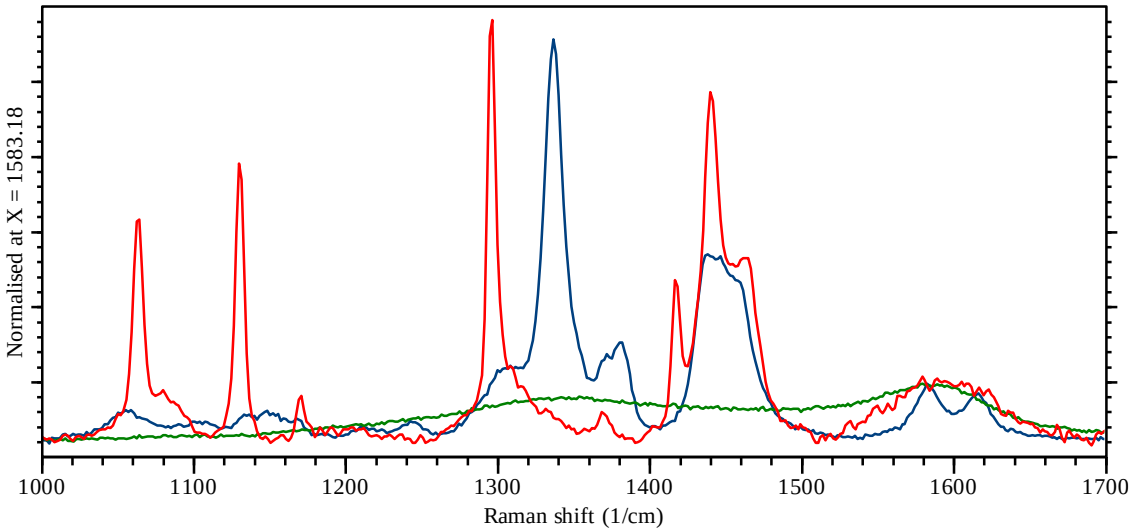


Figure 44. Overlayed spectra of (**red**) D/PT60, (**green**) a-C, and (**blue**) αTH, between 1000 and 1700 cm^{-1}.

The experimental spectrum of αTH was peak fitted with the minimal components required to obtain a residual STD around unity, which indicated an appropriate fit was achieved as can be observed in Figure 45. The band assignments found in literature from experimental Raman and as calculated based on the αTH alkane model structure are presented in Table 21 (Beattie et al., 2007; Cai et al., 2012; Feng et al., 2013; K. Wang et al., 2018). As most literature was related to visualisation/localisation of αTH in a variety of samples, the literature did not attempt to fully resolve the Raman bands associated with αTH and typically left many bands out of consideration (Beattie et al., 2007; Feng et al., 2013; K. Wang et al., 2018). Fortunately, Cai *et al.* also calculated a Raman spectrum for αTH, using the 6-31+G(d) Pople basis set with the B3LYP DF, and compared this with its experimental spectrum which confirmed the assignments in the calculated spectrum from this work (Cai et al., 2012).

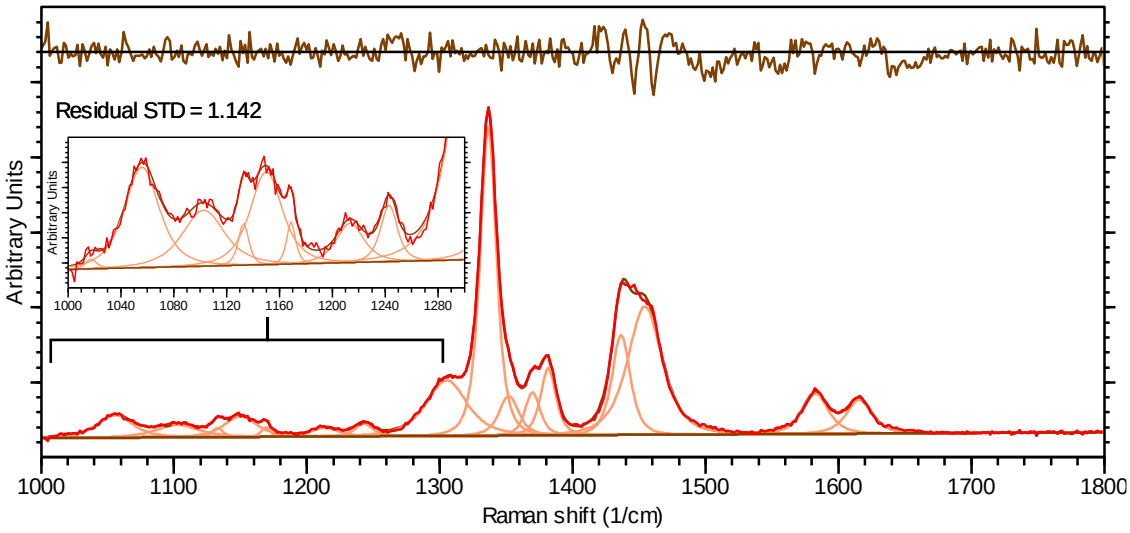


Figure 45. Summed spectral peak fit of αTH, see the band identification presented in Table 21.

Table 21. Raman band positions for αTH as observed in the spectral peak fit (Figure 45) and assignments according to the literature and as calculated using the αTH model structure between 1000 and 1800 cm^{-1}.

Vibrational mode	**Raman shift (cm^{-1})**	
	Experimental (Fig. 43)	**Calculated**
$[C–C]_{deformation}$	1018	1021

$[C–C]_{str.}$ / $[CH_x]_{twist.}$	1056	1054
$[C–C]_{deformation}$	1103	1111
$[C–C]_{stretching}$	1133	1032
$[C–C]_{str.}$ / $[CH_x]_{deform.}$	1150	1144
$[CH_x]_{deformation}$	1169	1163
$[CH_x]_{wag./twist./deform.}$	1213	1218
$[Phe]_{deformation}$	1243	1247
$[CH_x]_{twisting}$	1305	1298
$[CH_x]_{wagging}$	1337	1338
$[CH_x]_{wag./deform.}$	1352	1345
$[CH_x]_{wag./deform.}$	1370	1374
$[CH_x]_{deformation}$	1382	1385
$[CH_x]_{scissoring}$	1436	-
$[CH_x]_{scissoring}$	1454	1457
$[Phe]_{stretching}$	1583	1583
$[Phe]_{stretching}$	1616	1614

To further aid in the vibrational assignments of hydrocarbon unsaturations, a spectrum of a-C was investigated, as presented Figure 46. Based on the area deviations observed in the individual spectra, the spectra of a-C were peak fitted with six components, the corresponding band assignments found in literature from experimental Raman are presented in Table 22 (Eliseyev et al., 2021; Ferrari & Robertson, 2001; Hong & Winter, 2005; Paraschuk et al., 2002; Sadezky et al., 2005). Both the ‘G’ and ‘D’ bands arise due to the presence of [C=C] bonds, but the ‘G’ band is a result of the stretching of [C=C] bonds in both aromatic and aliphatic systems, whereas the ‘D’ peak arises due to disorder in the π-stacking of aromatic

systems. Consequently, when no ‘D’ peak is observed, it is reasonable to assume that there is little to no aromaticity present. The ‘A’, ‘X’, and ‘Y’ bands were found to be related to polyenes (i.e., *trans*-polyacetylene), which were typically observed at the grain boundaries of aromatics.

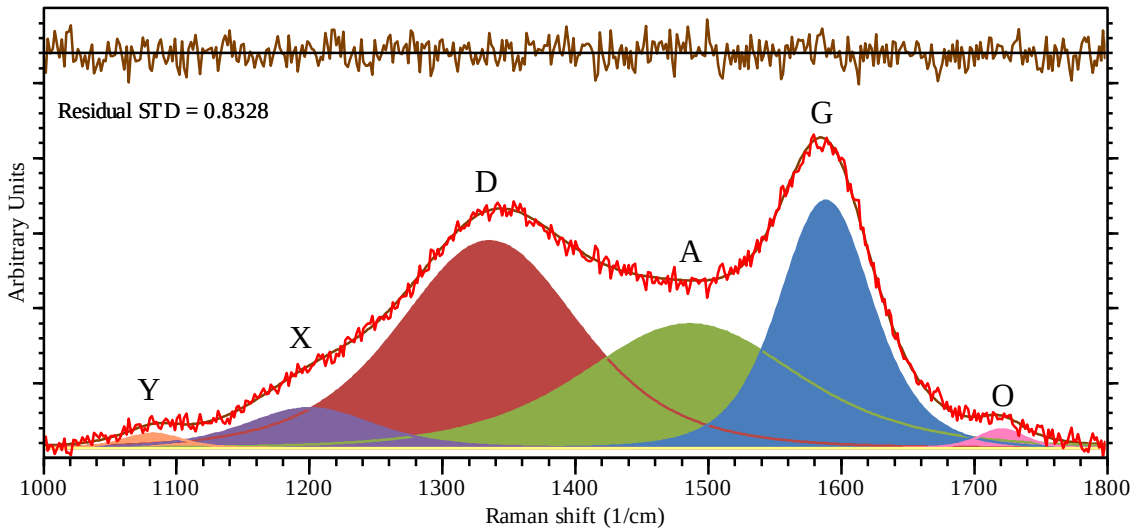


Figure 46. Summed spectral peak fit of a-C, see the band identification presented in Table 22.

Table 22. Expected Raman band positions for a-C according to the literature between 1000 and 1800 cm^{-1}.

ID	Vibrational mode	Origin	Raman shift (cm^{-1})
O	$[C=O]_{stretching}$	Oxidation	~1720
G	$[C=C]_{stretching}$	Graphitic (ideal) / Mixed sp^2 carbons	~1590
A	$[C=C]_{stretching}$	Polyene	~1485
D	$[C=C]_{stretching}$	Graphitic (disordered)	~1330
X	$[C–C]_{str.}$ / $[CH_2]_{wag.}$	Polyene	~1200
Y	$[C–C]_{stretching}$	Polyene	~1080

To confirm the origin of the vibrational assignments from a-C in Table 22, the correlation between the various bands associated with each other (i.e., the graphitic-like and polyene band groups) were investigated as displayed in Figure 47. Although a correlation does not confirm a connection, the signal of the associated bands should increase concurrently if connected as the spectra were taken of the same sample. There were strong positive linear

correlations for both the graphitic-like and polyene band groups, which provided additional validation that these bands were indeed related. No correlations were noted for the 'O' band, indicating that oxidation of a-C was not specific to either the graphitic-like or polyene phase.

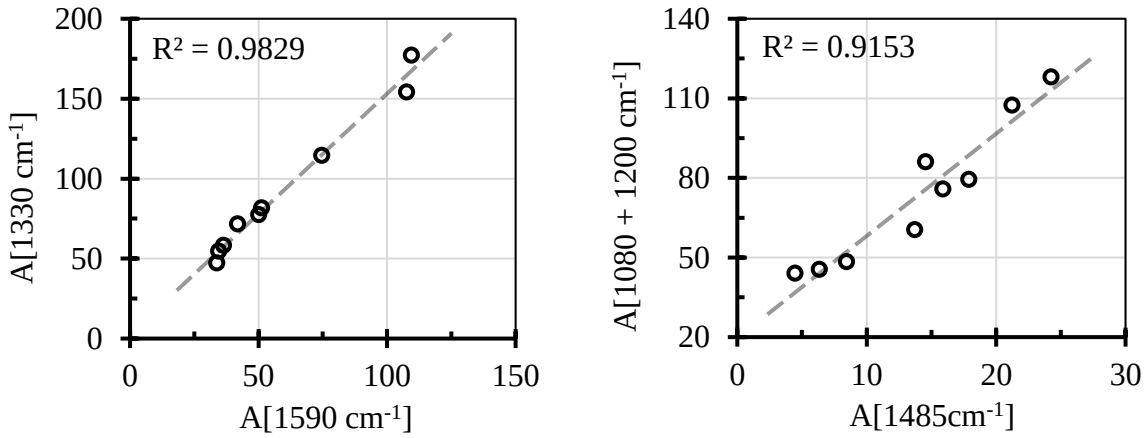


Figure 47. Linear correlation of the component area at (x-axis**)** 1485 cm^{-1} (A) and (y-axis) 1080 + 1200 cm^{-1} (X+Y), as observed in the individual peak fits of a-C; for clarity, the numbers at the axis are divided by 1000.

With the assignments for αTH and a-C fully resolved, these bands were implemented in the peak fitting of the UHMWPE-based samples (in addition to the UHMWPE bands presented in Table 20) as displayed in Figure 48. During the peak fitting, the components that originated from a-C were not constrained in relative peak area to each other, as its components may arise from different types of bonds. Additionally, the component of a-C at 1080 cm^{-1} (Y) was excluded during peak fitting, as it showed direct overlap with the $[C–C]_{stretching}$ of the amorphous phase for UHMWPE. During the peak fitting of the doped UHMWPE-based sample series, the components that originated from αTH were constrained in relative peak area to each other, as the main deviation in peak areas was related to the UHMWPE components.

From the spectral peak fits, various properties related to the UHMWPE-based samples were investigated. As widely demonstrated in the literature, the structure and corresponding changes in the crystallinity of PE can be estimated using the spectral peak fits (Affatato et al., 2013; Glotin & Mandelkern, 1982; Medel et al., 2009; Rull et al., 1993; Strobl & Hagedorn, 1978). This is possible as the $[CH_2]_{scissoring}$ band at 1415 cm^{-1} is related to the crystallinity of

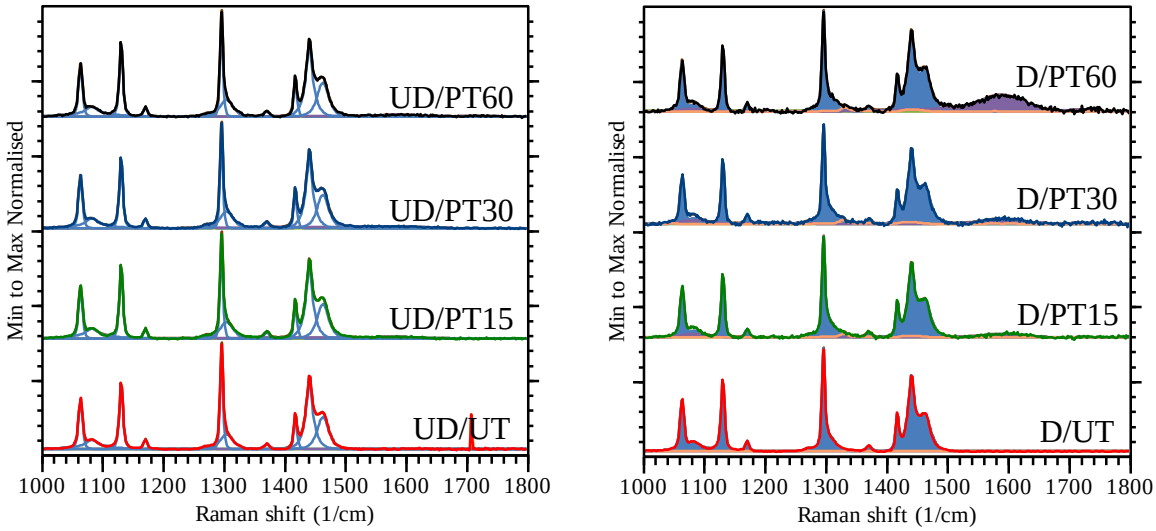


Figure 48. Summed spectral peak fits of the (left) undoped and (right) doped UHMWPE-based sample series between 1000 and 1800 cm^{-1}, displaying (**blue**) UHMWPE, (**orange**) αTH, and (**purple**) a-C.

PE (mostly the orthorhombic phase but may include other polymorphs), the $[C–C]_{stretching}$ band at 1080 cm^{-1} is associated with its amorphicity, and the $[CH_2]_{twisting}$ region (i.e., the bands at 1270, 1295 and 1305 cm^{-1}) shows an independent intensity relative to the crystalline and amorphous phase and can serve as an internal standard. From these five bands, the fractions of the crystalline (α_c), amorphous (α_a), interfacial (α_b) phase content were estimated following:

$$\alpha_c = \frac{I_{1415}}{0.46\, I_T} \qquad \textit{(Eq. 15)}$$

$$\alpha_{a_S} = \frac{I_{1415}}{0.79\, I_T} \text{ OR } \alpha_{a_T} = \frac{I_{1305}}{I_T} \qquad \textit{(Eq. 16)}$$

$$\alpha_a = \frac{1}{2}(\alpha_{a_S} + \alpha_{a_T}) \qquad \textit{(Eq. 17)}$$

$$\alpha_b = 1 - (\alpha_c + \alpha_a) \qquad \textit{(Eq. 18)}$$

where I_{1415} is the component area of the $[CH_2]_{scissoring}$ band at 1415 cm^{-1}, I_{1305} is the component area of the $[CH_2]_{twisting}$ at 1305 cm^{-1}, and I_T is the total component area of the $[CH_2]_{twisting}$ region. As can be observed in Equation 17, the amorphous fraction (α_a) was determined by averaging the amorphous fraction calculated based on the stretching (α_{a_S}) and twisting (α_{a_T}) related

components. The interfacial phase (α_b) represents the anisotropic disordered content between the crystalline and amorphous content, which predominantly arises from chains that originate from the crystallites and "dissipate" into the amorphous phase (Flor, 1962; Strobl & Hagedorn, 1978). As the hydrocarbon chains are spatially inhibited to directly dissipate into the amorphous phase, an anisotropic disordered interfacial phase is formed.

The phase content of the UHMWPE-based samples determined by Equation 15-18 is displayed in Figure 49. As can be observed, the undoped samples series showed an increase of 3.7% in the crystalline phase over the total ASPN treatment time, which started at 45.8% for UD/UT and increased up to 49.5% at UD/PT60. Additionally, the interfacial phase showed a decrease of 5.6% over the total ASPN treatment time, it was assumed that the increased chain mobility in the interfacial phase (due to the ASPN treatment temperature) allowed for recrystallisation. This was deemed most likely as most of the transformed phase content was observed for the crystalline phase, the amorphous phase only showed a minor increase over the total ASPN treatment time (< 2% when comparing UD/UT to UD/PT60). On the other hand, the doped sample series started with a notably higher crystallinity and decreased 2.8% over the total ASPN treatment time, which started at 49.5% for D/UT and decreased to 46.7% at D/PT60. Despite this decrease, all doped samples showed a higher crystallinity than UD/UT. Next to that, a notable increase of 8.1% in the interfacial phase was observed, which started at 5.2% for D/UT and increased up to 13.3% for D/PT60. Most of the gained interfacial phase content could be attributed to the decreased amorphous content which, after showing a minor increase from 45.3% at D/UT to 46.7% at D/PT30, decreased to 40% at D/PT60.

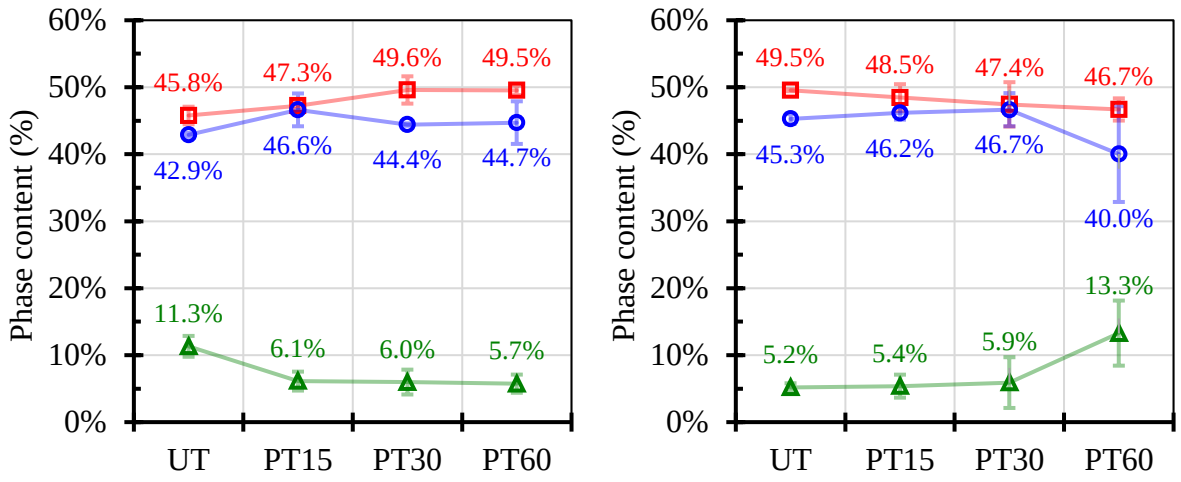


Figure 49. Graph displaying the phase content of the (**red**, squares) crystalline, (**blue**, circles) amorphous, and (**green**, triangles) interfacial phase in the (left) undoped and (right) doped UHMWPE-based sample series, as determined by Equation 15-18 and the individual peak fits; the three phases stack up to a total of 100%.

Next to the phase contents, the molecular orientation of the PE chains can be investigated by evaluating numerous ratios between the Raman bands, following: (Ratio I) $\frac{I_{1415}}{I_{1440}+I_{1460}}$, (Ratio II) $\frac{I_{1415}}{I_{1295}}$, and (Ratio III) $\frac{I_{1130}}{I_{1080}}$, and (Ratio IV) $\frac{I_{1130}}{I_{1060}}$ (Affatato et al., 2013; Kurelec et al., 2000; Pigeon et al., 1991; Reggiani et al., 2006). Ratios I and II evaluate the ordering of the PE chains due to lamellar (re)orientation, these ratios were shown to increase when UHMWPE experienced mechanical stress or pressure but decreased due to wear, the decrease in these ratios were found to be related to a phase transformation of the orthorhombic phase into the monoclinic phase (or at elevated temperatures and high pressures, the hexagonal phase) (Kurelec et al., 2000; Reggiani et al., 2006). However, Ratio I does not always provide an appropriate solution to evaluate this phase transition, as the band intensities at 1440 and 1460 cm^{-1} may be influenced by Fermi resonance (FR; i.e., when two or more vibrational modes have a similar frequency and interact with each other, leading to the energy transfer of one mode to the other mode, resulting in a change in the intensity or frequency), potential overtones (OTs; i.e., a multiple of the fundamental frequency that occurs when a molecule interacts with radiation in a way that creates a secondary vibration), and changes in setting angle of the hydrocarbon chains in the PE unit cell under stress/strain (Pezzotti, 2017). Ratio

II (i.e., $[CH_2]_{scissoring}$:$[CH_2]_{twisting}$ (C)) was found to be more appropriate to evaluate the change in the orthorhombic phase, as the band at 1295 cm^{-1} is independent to the PE chain conformation (Kurelec et al., 2000). Furthermore, Ratio III (i.e., $[C–C]_{stretching}$ (A):$[C–C]_{stretching,AS}$ (C+A)) was used to investigate the orientation in the amorphous phase, this ratio increases with the amount of *trans-gauche* defects (i.e., chain kinks, displaying rotations of ~120° relative to the *all-trans* zig-zag orientation) and was also found to decrease upon the formation of the hexagonal phase (Pigeon et al., 1991; Serra et al., 2002). Lastly, Ratio IV (i.e., $[C–C]_{stretching,S}$:$[C–C]_{stretching,AS}$ (C+A)) is typically investigated with respect to the draw direction of the machine during the polymer production, this ratio was found to increase upon strain/wear due to chain (re)orientation in both the crystalline and amorphous phase, and also increases concurrently with the Young's modulus (Affatato et al., 2013; Kurelec et al., 2000; S. Lu et al., 1998; Pigeon et al., 1991). Ratios I-IV as determined following the individual peak fits of the UHMWPE-based samples are shown in Figure 50.

As can be observed in Figure 50, Ratio I showed an inverse trend between the UHMWPE-based sample series, with a maximum change of about 10% over the total ASPN treatment time. The undoped sample series showed to increase over the ASPN treatment time from 0.114 at UD/UT to 0.123 at UD/PT60, and the doped sample series showed to decrease from 0.121 at D/UT to 0.108 at D/PT60, indicating an increase and loss of the orthorhombic content, respectively. However, due to the potential issues with the mixed band intensities discussed previously, the validity of this ratio remained unknown. Ratio II showed to increase for both sample series, although notably more for the undoped sample series which started at 0.368 for UD/UT and increased to 0.427 at UD/PT60. On the other hand, the doped sample series only showed a minor increase over the total ASPN treatment time, which started at 0.415 at D/UT and increased to 0.426 for D/PT60. The increase in Ratio II indicated an increase in

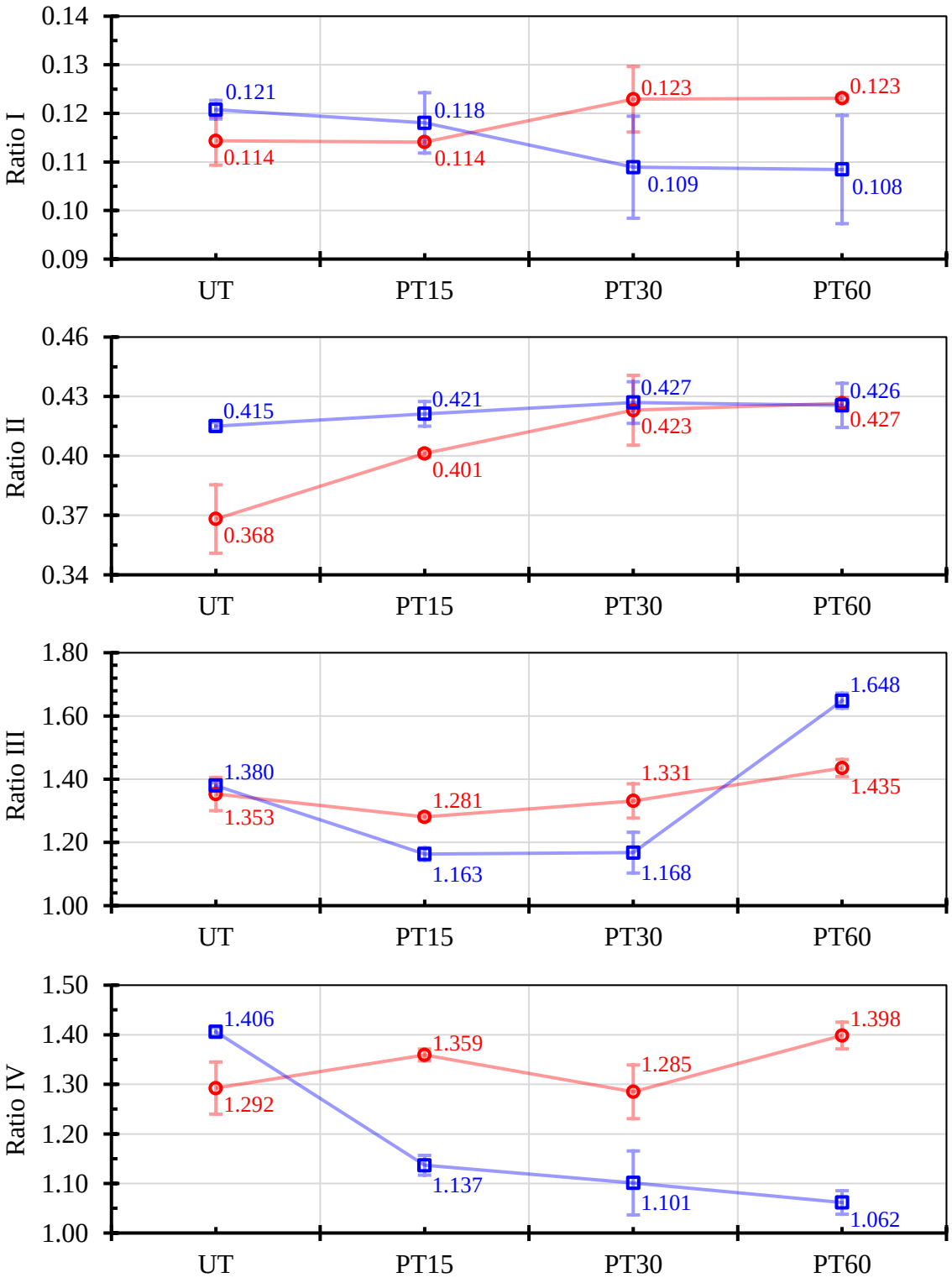


Figure 50. Ratios I-IV as determined by the individual peak fits of the (**red**, circles) undoped and (**blue**, squares) doped UHMWPE-based samples.

the orthorhombic content, this contradicted the results observed with Ratio I, but Ratio II is considered to be more suitable to investigate this phase change (Kurelec et al., 2000).

Ratio III was found to increase for both sample series over the total ASPN treatment time, after initially decreasing at PT15-30, indicating an increase in the amount of *trans-gauche* defects within the amorphous phase when comparing UT to PT60. Although a decrease of Ratio III is also associated with the formation of the hexagonal phase, the treatment conditions (temperature and pressure) in this work did not meet the minimum requirements for the hexagonal phase to form (i.e., at 3.6 kbar and 210°C) (Kurelec et al., 2000). Therefore, it was assumed that Ratio III solely provided information on the amount of *trans-gauche* defects in the amorphous phase. The undoped and doped sample series started off at roughly the same ratio, 1.353 and 1.380, respectively. The undoped series showed an increase over the total ASPN treatment time to 1.435 at UD/PT60, whilst the doped sample series showed a three-fold higher relative increase to 1.648 at D/PT60. Finally, Ratio IV showed an inverse trend between the undoped and doped UHMWPE-based sample series. The undoped sample series showed an increase from 1.292 at UD/UT to 1.398 at UD/PT60, but the doped sample series showed a decrease from 1.406 at D/UT to 1.062 at D/PT60, which indicated a gain and loss in the Young's modulus, respectively.

The relative elasto-plastic strain (ε) in PE was evaluated by analysing the change in the FWHM of the symmetric $[C–C]_{stretching}$ (C+A) band at 1130 cm^{-1}, which is commonly investigated for UHMWPE-based acetabular cups inserts (Affatato et al., 2013; Kumakura et al., 2009; Kyomoto et al., 2007). The samples in this work had not experienced any external load, so the strain observed in the samples was mainly considered to be residual internal stress introduced during the drawing process. As displayed in Figure 51, the strain in the UHMWPE-based samples was determined relative to UD/UT. Interestingly, UD/UT showed the highest strain from the UHMWPE-based samples, the other samples showed a decrease in strain. The undoped samples showed a relative decrease of about 3% in its strain at UD/PT60 relative to UD/UT. The doped sample series displayed a 3.5% decrease in strain at D/UT relative to

UD/UT, which continually decreased over the total ASPN treatment time to -9.01% at D/PT60. It is worth to note that the doped ASPN-treated samples displayed a relatively high deviation in the FWHM of the 1130 cm^{-1} band between the evaluated samples, deviating around 4-6% for ε depending on the sample. Based on the decreased strain in the UHMWPE-based samples, it was assumed that both treatments (i.e., αTH doping and ASPN) resulted in a reduction in residual internal stress, most likely due to the increased mobility of the PE chains at the elevated treatment temperatures which allowed for their reorganization.

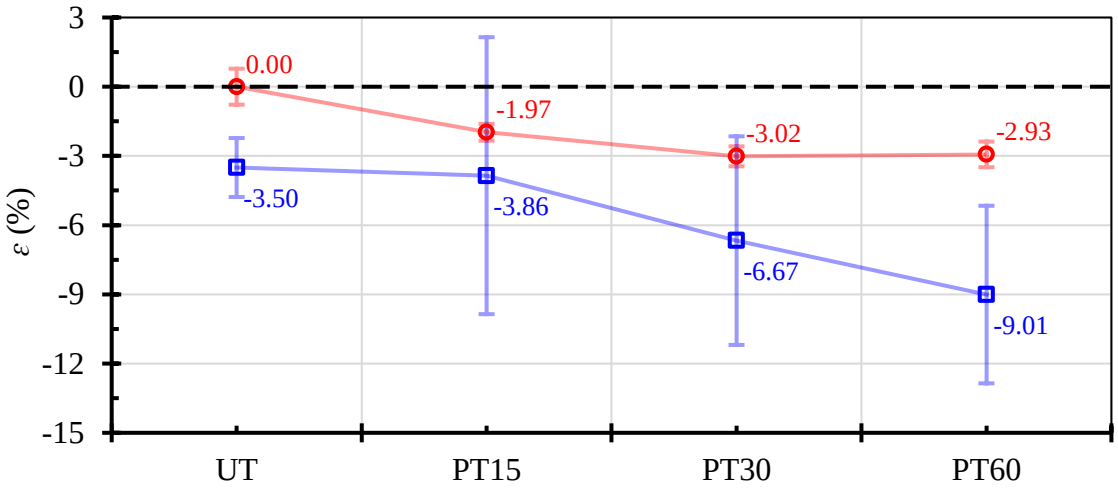


Figure 51. Relative elasto-plastic strain (ε) of the (**red**, circles) undoped and (**blue**, squares) doped UHMWPE-based samples, determined by ΔFWHM of the 1130 cm^{-1} band relative to UD/UT.

Besides the UHMWPE-related properties, the fitted a-C and αTH components were also investigated by calculating an index relative to the $[CH_2]_{twisting}$ region (i.e., the bands at 1270, 1295 and 1305 cm^{-1}; I_T), the same region that served as an internal standard during the crystallinity calculations. As can be observed in Figure 52, both sample series showed an increase in the a-C index over the ASPN treatment time. The undoped sample series initially showed an increase from 0.01 at UD/UT to 0.26 for UD/PT15, and ultimately increased to 0.36 at UD/PT60. However, as was expected based on the FTIR results in Section 4.1.1 (Region 6), the doped sample series displayed a significantly higher presence of the 'a-C'-like components when compared to the undoped sample series. The doped samples series started off at 0.07 and

continually increased over the ASPN treatment time to 2.22 at D/PT60, it is worth to note that this series showed a deviation of ±40% for D/PT30 and D/PT60. The αTH index for the doped sample series showed to increase over the ASPN treatment time from 0.08 at D/UT to 0.44 at D/PT60, a deviation of about ±45% was noted across this index. The increase in the αTH index indicated that either αTH migrated towards the surface during the ASPN treatment or that the relative signal of the UHMWPE components was reduced. Contrary to the αTH index that was determined based on the phenol $[O–H]_{str.}$ band with FTIR (see Section 4.1.1, Region 4), the αTH index determined with Raman spectra did not provide information on its functioning as the observed bands were all $[C–C]/[CH_2]$-related bands (see Table 21).

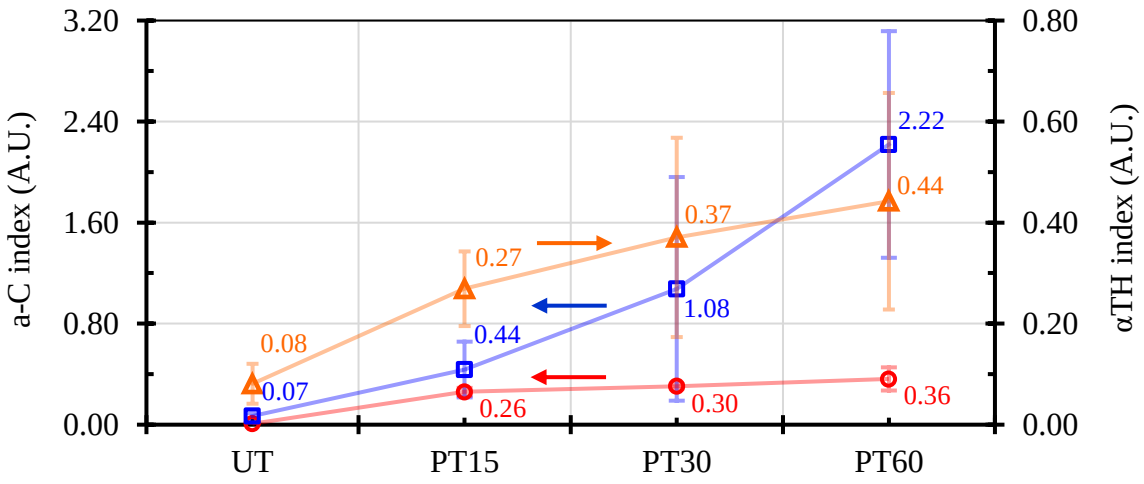


Figure 52. a-C index as observed in the individual peak fits of the (**red**, circles) undoped and (**blue**, squares) doped UHMWPE-based samples, and the (**orange**, triangles) αTH index of the doped sample series. The colours of the arrows correspond to its respective series, the direction of the arrows determines the appropriate y-axis.

As discussed with the peak fitting of a-C, the lack of a 'D' peak indicated there was little to no aromaticity present (Ferrari & Robertson, 2004). In this work, the 'D' peak only showed a minor presence in 7 out of the 24 samples, the averaged I_D/I_G ratio was 0.09±0.07. Thus, it was concluded that the [C=C] bonds were almost exclusively aliphatic or, if aromatic, the π-bonds were insufficiently delocalised over the aromatic rings (Casiraghi et al., 2005).

Region 2 – 2800-3000 cm^{-1}

Region 2 in the Raman spectra allowed for the evaluation of the $[CH_x]_{stretching}$ bands. However, before discussing the peak fitted spectral regions, it is worth to note the difference in the background signal of the spectra as displayed in Figure 53. More specifically, the doped UHMWPE-based sample series showed a continuous increase in its fluorescence and/or (photo)luminescence background over the ASPN treatment time, which reduced the relative signal of the PE components. The overlayed spectra of D/PT60 and a-C as presented in Figure 54 further indicated an 'a-C'-like compound was present, as the (filter) rippling was not present in the UT samples. Based on the increased background signal, there were also indications that it likely entailed a hydrogenated form of a-C (i.e., a-C:H), as the photoluminescence for a-C compounds grows over the wavenumber with increasing H-content (Casiraghi et al., 2005).

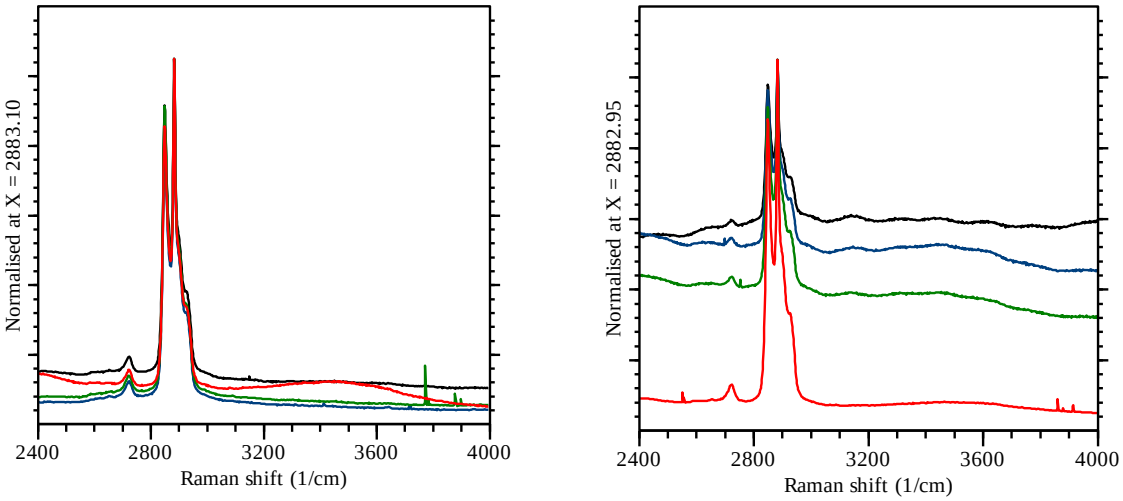


Figure 53. Summed spectra of the (left) undoped and (right) doped UHMWPE-based sample series, showing (**red**) UT, (**green**) PT15, (**blue**) PT30, and (**black**) PT60, showing the increase in background signal.

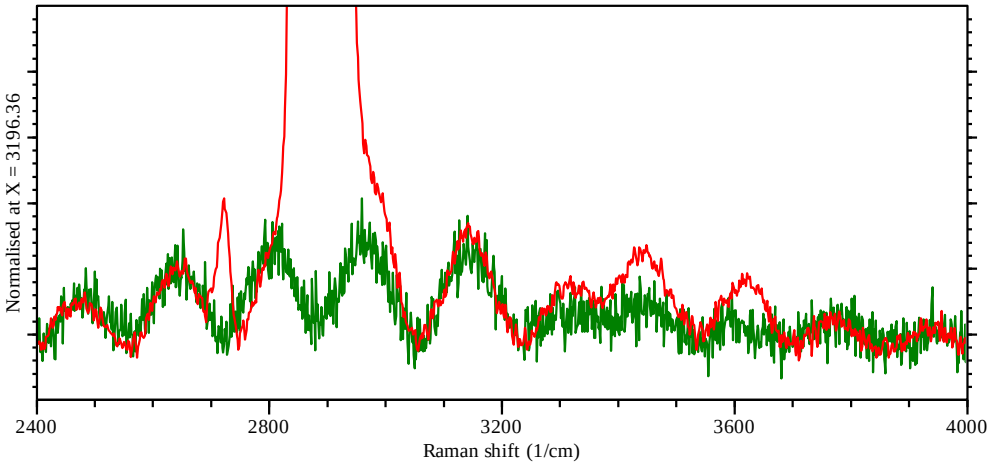


Figure 54. Overlayed spectra of (**red**) D/PT60 and (**green**) a-C, zoomed-in to display the overlap in bands.

Although the spectra were peak fitted between 2400 and 4000 cm^{-1}, only the bands between 2800 and 3000 cm^{-1} will be discussed. This is because the bands between 2400 and 2800 cm^{-1} almost exclusively consist out of a variety of OTs and these were not deemed interesting in terms of quantification (Gall et al., 1972; Tomba et al., 2019). Based on the investigated literature, no definitive assignments were made for the low-intensity bands between 3000 and 4000 cm^{-1}. Next to that, quantification would remain challenging due to the strong overlap of these broad bands. The region between 2800 and 3000 cm^{-1} also included the FR of the $[CH_x]_{stretching}$ bands and various OTs, which are predominantly present near the $[CH_3]_{stretching}$ bands (da Silva & Wiebeck, 2019). Despite this, the Raman band assignments for $[CH_{2/3}]_{stretching}$ found in literature from experimental Raman were investigated and calculated based on the C20 alkane model structure, as presented in Table 23 (Berg et al., 2013; Craig, 2002; da Silva & Wiebeck, 2019; Ferraro, 1994; Fowler, 2018; Prinsloo et al., 2004; Snyder et al., 1978; Socrates, 2004; Wool et al., 1986). The calculated band positions were notably higher than the values from the literature, but the sequential order of the modes was identical and supported the assignments from the literature – the calculated spectra C20 did not provide information on the FR-active bands or OTs.

Table 23. Expected Raman band positions according to the literature and as calculated using the C20 alkane model structure between 2800 and 3000 cm^{-1}.

Vibrational mode	**Raman shift (cm^{-1})**	
	Literature	**Calculated**
$[CH_2]_{stretching,symmetric}$	~ 2850	2906
$[CH_3]_{str.,S}$ / FR+OTs	~ 2870	2919
$[CH_2]_{stretching,asymmetric}$	~ 2885	2933
$[CH_3]_{str.,AS}$ / FR+OTs	~ 2950	2998

Based on the area deviations observed between the various spectra, peak fitting was performed with six components as shown in Figure 55. The two sharp bands at 2848 and 2883 cm^{-1} were likely related to the symmetric and asymmetric $[CH_2]_{stretching}$, respectively, as these positions were identical to those observed in the literature. Unfortunately, the wide bands at 2857, 2894, 2931 cm^{-1} are typically assigned to various FR bands or OTs and strongly overlap with the expected positions of the $[CH_3]_{stretching}$ bands, making their accurate distinction challenging (Gall et al., 1972; R. Lu et al., 2005; Tomba et al., 2019). Considering the FTIR results already provided an appropriate insight into the $[CH_3]_{stretching}$ bands, these were not further investigated within the Raman spectra. Lastly, the spectra displayed a broad band at 2969 cm^{-1}, which showed a more prominent increase for the doped UHMWPE-based samples over the ASPN treatment time. Therefore, it was assumed that this band was related to a-C, being the main component that was found to increase over the ASPN treatment time in Region 1. According to the literature on carbon-like materials, the band at 2969 cm^{-1} is typically assigned to the second order phonon band and associated with increased graphitization (Baldan et al., 2007; Sheka et al., 2020; Shimada et al., 2005). Alternatively, this band could also be associated to $[=C-H_x]_{stretching}$ of vinyl-based bonds (Socrates, 2004). Indices were calculated for the six fitted components relative to I_T, as shown in the corresponding graphs in Figure 55. It was noted that most bands increased or decreased collectively, apart from the bands at 2883 and 2969 cm^{-1}. Excluding the 2969 cm^{-1} band index, the indices for the undoped and doped sample series showed a mean average deviation of ~11% and ~21% across the total ASPN treatment time, respectively. The doped sample series showed more changes in its band indices than the undoped sample series, but the exact changes remained unclear due to the inability to assign individual vibrational modes to all bands. The 2969 cm^{-1} band index for the undoped sample series initially showed an increase from 1.03 at UD/UT to 1.97 at UD/PT15 but

decreased to 1.43 at UT/PT60. The doped sample series showed a continuous increase in the 2969 cm^{-1} band index over the ASPN treatment time, from 0.85 at D/UT to 7.62 for D/PT60.

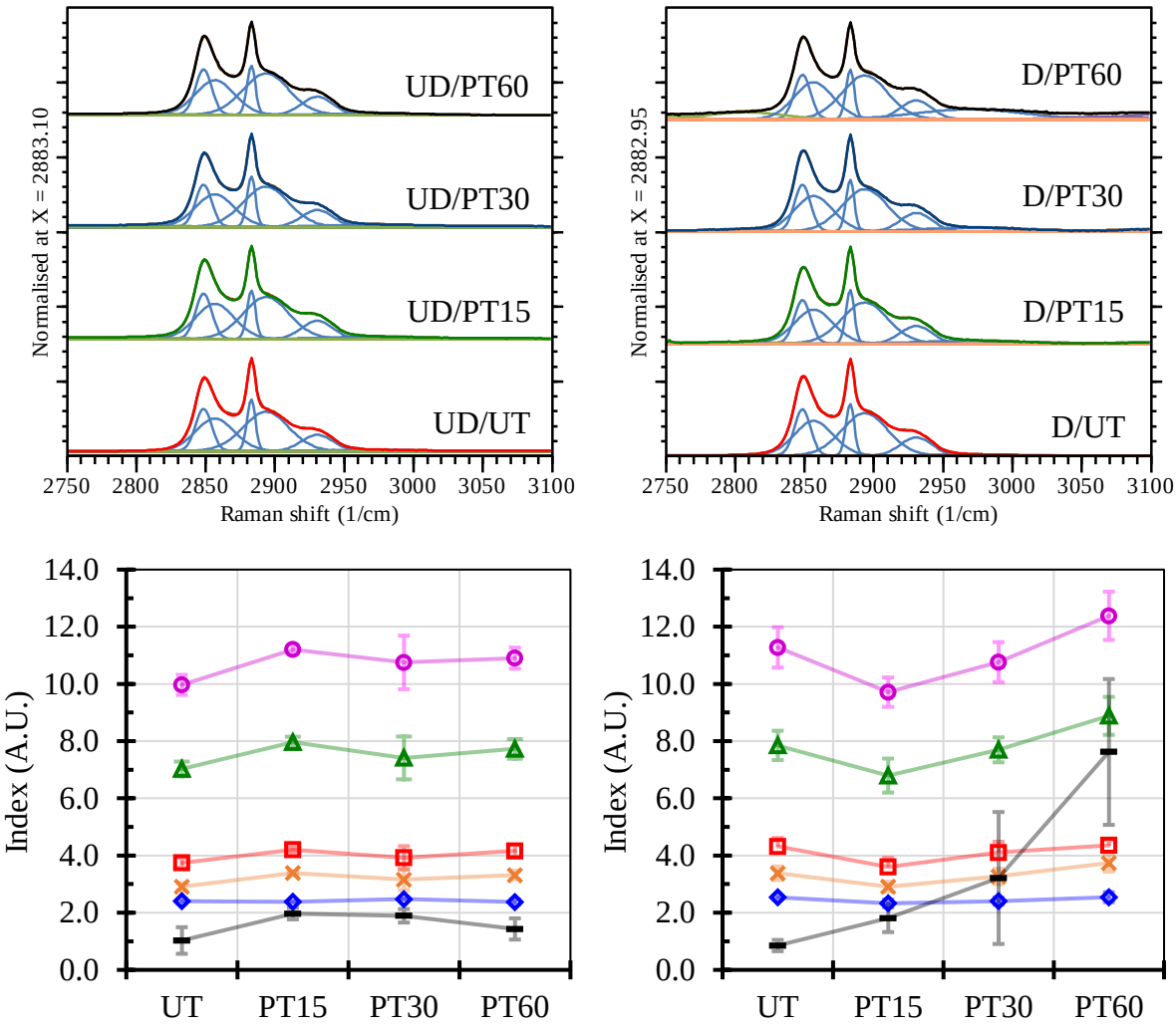


Figure 55. Summed spectral peak fits of the (top-left) undoped and (top-right) doped UHMWPE-based sample series between 2750 and 3100 cm^{-1}; and the corresponding graphs for the (bottom-left) undoped and (bottom-right) doped sample series, displaying the (**red**) 2848 cm^{-1}, (**blue**) 2857 cm^{-1}, (**green**) 2883 cm^{-1}, (**pink**) 2894 cm^{-1}, (**orange**) 2931 cm-1 and (**black**) 2969 cm^{-1} band indices as observed in the individual peak fits.

Summary and correlations

This section presented a systematic investigation into the Raman spectra of the undoped and doped UHMWPE-based samples treated with ASPN. Aided by the calculations, the investigated spectral regions provided for the identification of most chemical bonds present within the UHMWPE-based samples. To further explore the obtained Raman band indices/ratios, the strength of the linear correlation between all the calculated indices/ratios was

investigated using the Pearson correlation coefficients (r_p). For ease of viewing, Table 24 only presents the correlations where -0.75 > r_p > 0.75 – the full Pearson correlation matrix is presented in Appendix C4. As can be observed in Table 26, a total of 12 highly positive correlated pairs and 7 highly negative correlated pairs were noted.

Most positive correlations were related to the band indices originating from Region 2 (i.e., between 2800 and 3000 cm^{-1}), which was expected as Figure 55 already displayed that most of these bands increased or decreased collectively. However, perhaps the most interesting positive correlation was that between the a-C index and the 2969 cm^{-1} band index. It was established that in the literature the band at 2969 cm^{-1} is typically related to increased graphitisation or $[=C-H_x]_{str.}$ of vinyl-based bonds, which was corroborated by the strong Pearson correlation coefficient of 0.98. It was not surprising to observe a positive correlation (0.82) between α_c and Ratio I (related to the phase transformation of the orthorhombic phase), considering these were both related to the 1415 cm^{-1} band. The a-C index and αTH index also showed to be positively correlated with a correlation coefficient of 0.85. However, the αTH index determined by Raman was only related to its [C–C]/[CH_2] presence and not its functioning as with FTIR determined from its relative phenol $[O-H]_{str.}$ presence. It was assumed that the ASPN treatment, next to the formation of the 'a-C'-like compound, resulted in the migration of αTH towards the surface due to the treatment conditions.

Table 24. Pearson correlations where -0.75 > r_p > 0.75 as observed between the indices and ratios from the individual Raman spectral peak fits of the undoped and doped UHMWPE-based samples.

Positive correlation			**Negative correlation**		
Array 1	**Array 2**	r_p	**Array 1**	**Array 2**	r_p
2857 cm^{-1}	2931 cm^{-1}	0.99	Strain	a-C index	-0.93
2857 cm^{-1}	2894 cm^{-1}	0.99	Ratio IV	αTH index	-0.91
2894 cm^{-1}	2931 cm^{-1}	0.99	α_a	α_b	-0.90

a-C index	2969 cm^{-1}	0.98	Strain	αTH index	-0.90
2848 cm^{-1}	2857 cm^{-1}	0.93	α_a	Ratio III	-0.88
2848 cm^{-1}	2894 cm^{-1}	0.91	Strain	2969 cm^{-1}	-0.86
2848 cm^{-1}	2931 cm^{-1}	0.90	Ratio IV	a-C index	-0.78
a-C index	αTH index	0.85			
α_c	Ratio I	0.82			
αTH index	2969 cm^{-1}	0.78			
2857 cm^{-1}	2969 cm^{-1}	0.76			
Ratio III	2894 cm^{-1}	0.75			

The negative correlations also provided some interesting insights, especially with regards to the strain (ε ; i.e., residual internal stress). The a-C, αTH, and 2969 cm^{-1} band indices showed a strong negative correlation to the strain, displaying a Pearson correlation coefficient of -0.93, -0.90, and -0.86, respectively. It was already hypothesized that the αTH doping and ASPN treatments may have reduced the residual internal stress due to the increased chain mobility at the treatment temperatures. Nonetheless, it was notable to observe the correlations as it would be reasonable to observe a reduction in residual internal stress as UHMWPE transforms into an 'a-C'-like compound. Next to that, the αTH index showed to be negatively correlated with Ratio IV (related to the Young's modulus), which demonstrated that the PE chains preferred asymmetric over symmetric to $[C–C]_{stretching}$ as the αTH index increased. Lastly, the amorphous content (α_a) showed a strong negative correlation with the interfacial phase content (α_b) and Ratio III (related to amorphous *trans-gauche* defects), displaying a Pearson correlation coefficient of -0.90, and -0.88, respectively. It was somewhat expected that the interfacial phase content showed to be correlated with the amorphous phase content, considering the interfacial phase content was directly estimated from the crystalline and

amorphous phase content (i.e., $\alpha_b = 1 - (\alpha_c + \alpha_a)$). However, the fact that the amorphous content also displayed a strong negative correlation with Ratio III substantiated the fact that the amount of amorphous *trans-gauche* defects increased as the amorphous phase content transformed into the interfacial phase.

As the same samples were investigated by Raman and FTIR (Section 4.1.1.), correlations between the two techniques were also investigated. It is worth to recognise the difference in penetration depth for Raman (~10.11 μm) and FTIR (~2.11 μm), which drastically impacted the total analysis volume and thus band intensities. The correlation matrix between the Raman and FTIR indices/ratios displayed 10 strong positive correlations and 9 strong negative correlations, the Pearson correlation matrix is presented in Appendix C5 but only the most relevant correlations will be discussed. The strain, a-C, αTH, and 2969 cm^{-1} band indices from Raman showed a strong correlation with the combined $[C=C]_{str.}$ index from FTIR, displaying a Pearson correlation coefficient of -0.89, 0.91, 0.89, and 0.85, respectively, which further supported that the FTIR bands at 1568 and 1654 cm^{-1} were indeed associated to a-C/hydrocarbon unsaturation. Ratio II from Raman showed a strong correlation with the $[A_{730}:A_{719}]$, $[A_{1472}:A_{1462}]$, and $[CH_2]_{twist.:wag.}$ ratios from FTIR, displaying a Pearson correlation coefficient of 0.81, 0.85, and -0.81, respectively, which confirmed the previously discussed connection of these FTIR bands to the crystallinity of UHMWPE.

4.1.3. X-ray photoelectron spectroscopy (XPS) survey

X-ray photoelectron spectroscopy (XPS) was mainly used to investigate the effect of αTH doping in combination with ASPN on the chemical surface composition of the UHMWPE-based samples, but also to provide information on the surface contaminants and treatment homogeneity. The XPS survey spectra allowed for the investigation of the elemental surface composition of the UHMWPE-based samples in the upper few nanometers (Watts, 1998). The XPS survey spectra were recorded before and after ion etching to investigate if the

elemental surface compositions were heterogenous, the spectra of the undoped and doped UHMWPE-based samples are displayed in Figure 56 and 57, respectively. Here, the XPS survey spectra were not peak fitted, as Section 4.3 provides an in-depth peak fitted interpretation of the UHMWPE-based samples using high-resolution XPS spectra. Instead, the assignments in this section were from the NIST XPS BE database based on the BE region maxima (NIST, 2008).

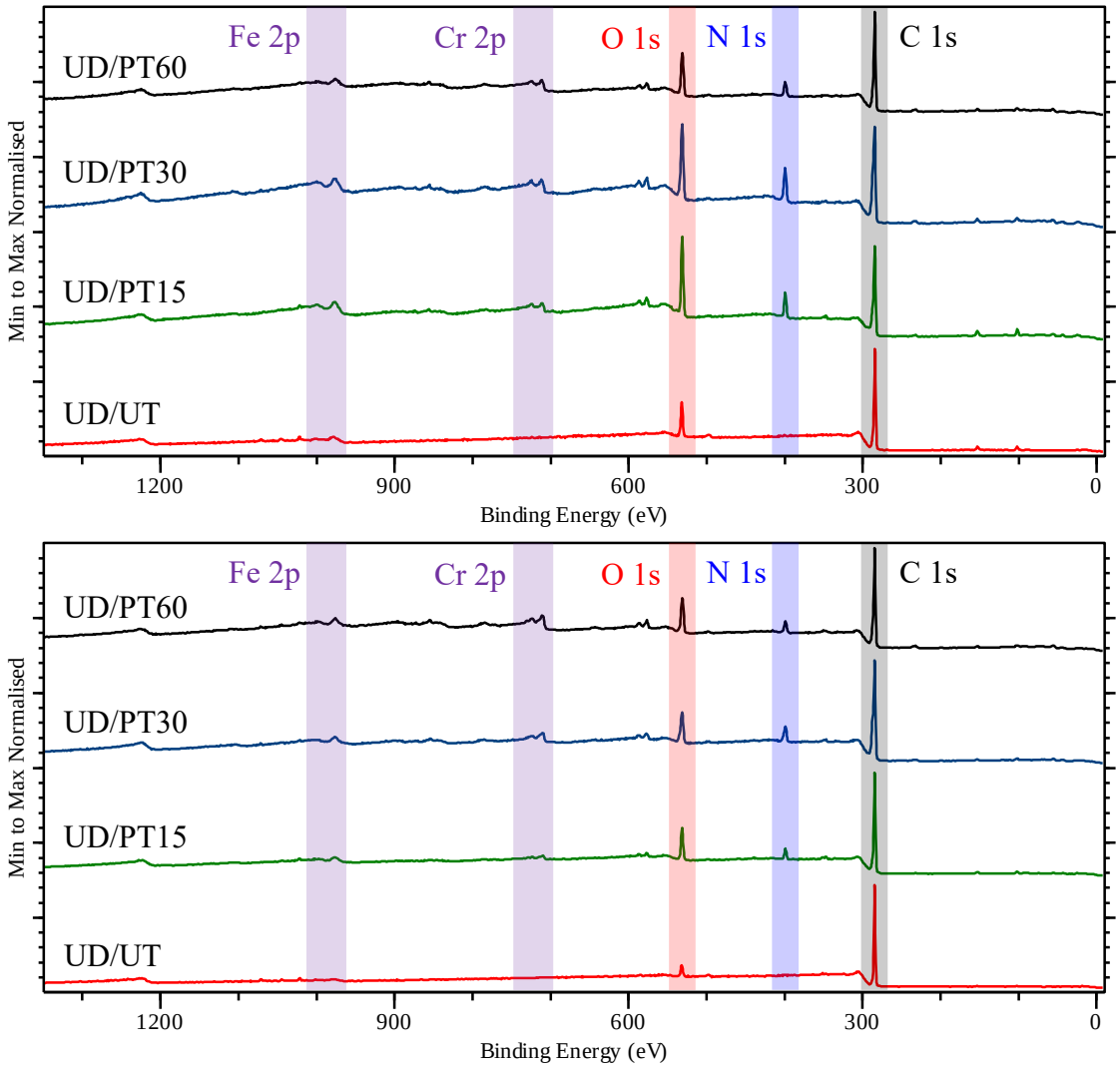


Figure 56. XPS survey spectra of the undoped UHMWPE-based sample series (top) before and (bottom) after ion etching, the most prominent elements are highlighted and labelled with the corresponding orbital shell.

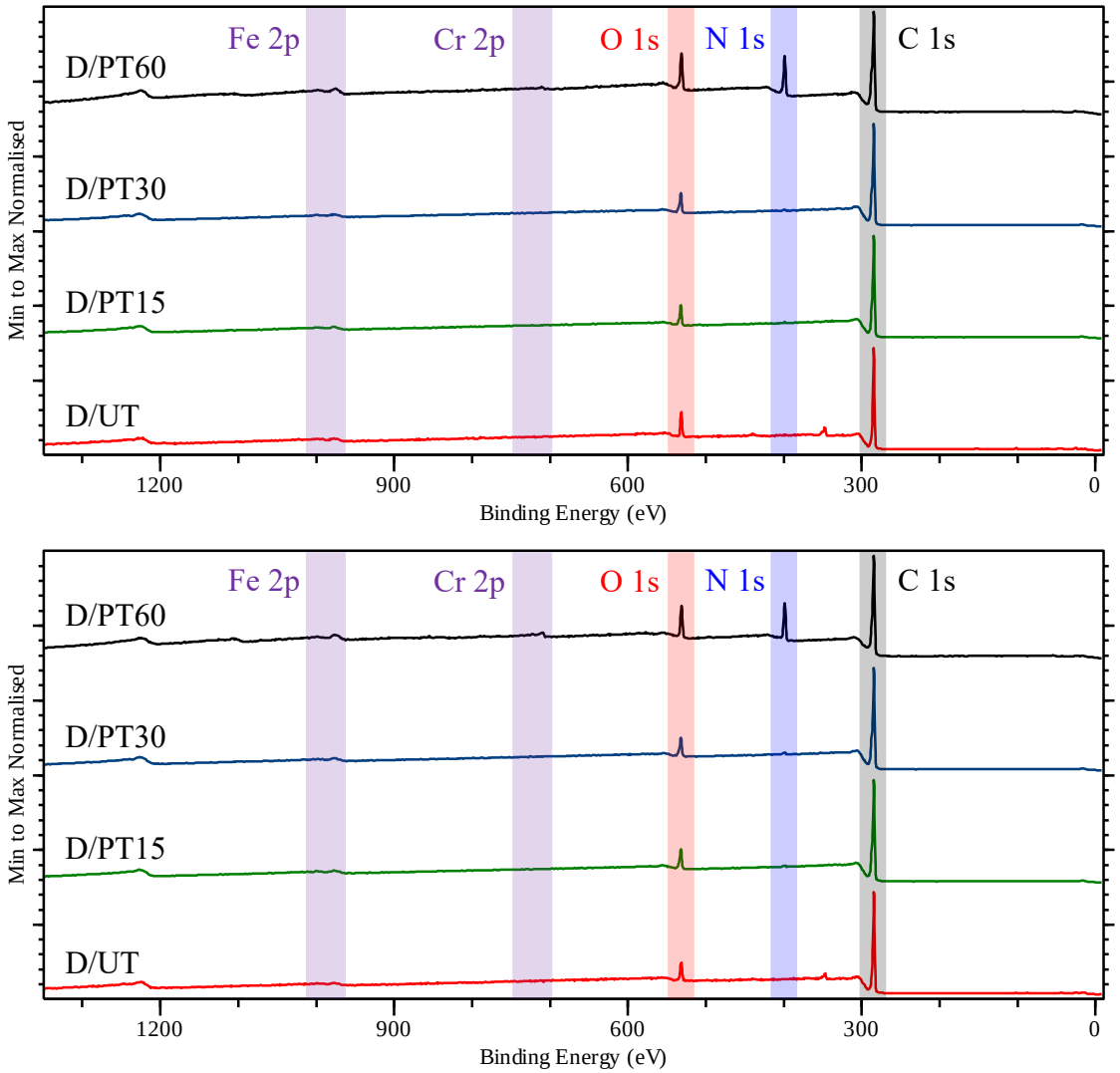


Figure 57. XPS survey spectra of the doped UHMWPE-based sample series (top) before and (bottom) after ion etching, the most prominent elements are highlighted and labelled with the corresponding orbital shell.

As observed in the spectra, the material surfaces clearly showed a notable elemental presence of nitrogen after the ASPN treatment. Which confirmed that the ASPN-treated layer thickness was likely within the nanometer range, as the penetration depth with Raman (~10.11 μm) and FTIR (~2.11 μm) was too large to observe any nitrogen-based components at all. Additionally, all samples showed the same elemental components before and after ion etching, albeit in somewhat different quantities. The observed elemental surface composition of the samples is displayed in Figure 58, the deviation shown is the difference in composition before and after ion etching. For ease of viewing, the contaminants were grouped in Figure 58, but the full elemental composition determined by the survey spectra is shown in Table 25.

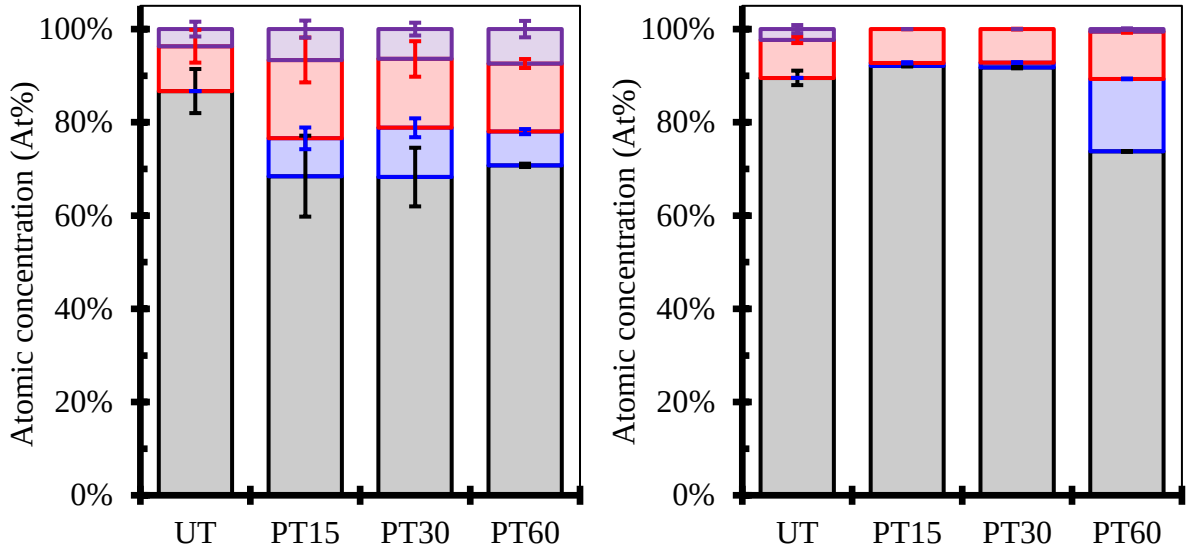


Figure 58. Elemental surface composition of the (left) undoped and (right) doped UHMWPE-based sample series, showing the At% of the (**black**) C 1s, (**blue**) N 1s, (**red**) O 1s, and (**purple**) summed contaminants.

As is evident from Table 27, the undoped UHMWPE-based samples showed a significant reduction in the [N 1s] and [O 1s] presence after the ion etching. The UD/PT15 and UD/PT30 samples showed an average reduction for both elements of 41 At%, whilst the UD/PT60 displayed an average reduction of 13 At%. On the other hand, the doped samples displayed almost no change in elemental composition after ion etching, with an average reduction of < 5 At% across all elements. This indicated that the ASPN layer formed on the undoped sample surfaces was more fragile/less heterogeneous, as it was easily removed/altered by the ion etching in contrast to the ASPN layer formed on the doped sample surfaces.

The undoped UHMWPE-based samples displayed an [O 1s] presence of 9.62±3.52 At% at UD/UT. However, it is worth to note that UD/UT showed 2.44±1.35 At% of [Si 2p] (due to the surface polishing of the UHMWPE-based samples with SiC polishing papers), the [Si 2p] was identified as [$Si(CH_3)_2O$] based on its BE of ~102 eV and would have contributed to the [O 1s] presence (NIST, 2008). Nonetheless, the [O 1s] presence further increased after the ASPN treatment to 16.82±4.82 At% for UD/PT15 but subsequently displayed a decrease to 14.76±3.81 and 14.61±0.96 At% for UD/PT30 and UD/PT60, respectively. The undoped

Table 25. Elemental surface composition of the undoped and doped UHMWPE-based samples before and after ion etching.

ID	Etching	Atomic concentration (At%)											
		C 1s	N 1s	O 1s	Fe 2p	Cr 2p	Zn 2p	Mo 3d	Mn 2p	Si 2p	Ca 2p	Na 1s	Cl 2p
UD/UT	Before	81.98	-	13.14	-	-	0.51	-	-	3.78	-	0.38	0.21
	After	91.43	-	6.10	-	-	0.82	-	-	1.09	-	0.47	0.08
UD/PT15	Before	59.78	10.44	21.63	1.22	1.19	0.14	0.17	0.15	4.43	0.70	0.05	0.12
	After	77.15	5.78	12.00	0.96	0.75	0.31	0.11	0.08	1.89	0.78	0.08	0.11
UD/PT30	Before	61.97	12.60	18.57	1.38	1.31	0.16	0.24	0.13	2.95	0.30	0.16	0.23
	After	74.55	8.55	10.95	1.89	1.07	0.13	0.19	0.11	1.46	0.54	0.33	0.23
UD/PT60	Before	70.41	7.78	15.57	1.49	0.91	0.20	0.29	0.19	2.44	0.29	0.12	0.29
	After	71.13	6.68	13.65	3.01	1.41	0.55	0.37	0.31	1.84	0.53	0.20	0.32
D/UT	Before	87.98	-	8.84	-	-	-	-	-	1.00	2.18	-	-
	After	91.08	-	7.47	-	-	-	-	-	-	1.44	-	-
D/PT15	Before	92.20	0.53	7.26	-	-	-	-	-	-	-	-	-
	After	91.98	0.81	7.21	-	-	-	-	-	-	-	-	-
D/PT30	Before	91.59	1.15	7.26	-	-	-	-	-	-	-	-	-
	After	91.93	0.99	7.09	-	-	-	-	-	-	-	-	-
D/PT60	Before	73.77	15.48	10.37	0.28	-	-	-	-	-	-	-	0.10
	After	73.74	15.65	9.89	0.58	-	-	0.02	-	-	-	-	0.12

ASPN-treated samples also showed the same [Si 2p] contamination as UD/UT, as well as [Fe 2p], [Cr 2p], [Mo 3d], and [Mn 2p] contamination from the ASPN stainless steel active screen. Based on the observed BE of [Fe 2p] at ~711 eV, [Cr 2p] at ~576.6 eV, [Mo 3d] at ~232.2 eV, and [Mn 2p] at 643.7 eV, these elements were assigned to [Fe_2O_3], [Cr_2O_3], [MoO_x], and [MnO_2], respectively (NIST, 2008). Naturally, the observed metal oxides also impacted the total [O 1s] presence. The minor contaminants present on the surface were [Zn 2p] at ~1021.8 eV, [Ca 2p] at ~347.5 eV, [Na 1s] at ~1071 eV, and [Cl 2p] at ~198.4 eV, these elements were assigned to [ZnO], [$CaO/Ca(OH)_2$] and [$Na^+ Cl^-$], respectively. Although the definitive origin of [Zn/Ca] remains unknown, Zinc stearate (50-500 ppm) and Calcium stearate (30-50 ppm) are commonly used as flow modifiers during the production of UHMWPE (Fink, 2010; Z. Liu et al., 2022; Walkenhorst, 2022). As was expected, the undoped samples treated with ASPN showed a notable increase in their [N 1s] presence, although this was not a continuous increase over the ASPN treatment time. The [N 1s] showed a presence of 8.11±2.33 At% at UD/PT15, which increased to 10.58±2.03 At% at UD/PT30, but then decreased to 7.23±0.55 At% for UD/PT60. It was surprising to observe that the sample treated with ASPN for the longest duration (i.e., UD/PT60) showed the lowest [N 1s] At%.

The doped samples series showed an [O 1s] presence of 8.16±0.69 At% at D/UT and this did not change significantly until D/PT60 to 10.13±0.24 At%, which indicated that the αTH prevented further oxidation during storage. Next to that, the doped samples series showed almost no [N 1s] presence at D/PT15 (0.67±0.14 At%) and D/PT30 (1.07±0.08 At%), whilst this suddenly increased to 15.57±0.09 At% at D/PT60 – more than twice the amount as observed with UD/PT60. This indicated that αTH was at least functional during the first 30 minutes of the ASPN treatment, but was exhausted somewhere between 30 and 60 minutes of ASPN as it ultimately allowed for the ASPN surface functionalisation. Next to that, the doped sample series displayed almost no contaminants. More specifically, D/UT showed most

contamination (i.e., 0.50±0.50 At% of [Si 2p] and 1.81±0.37 At% of [Ca 2p]), whilst D/PT15 and D/PT30 showed no contaminants at all, and D/PT60 only showed a minor presence of 0.43±0.15 At% of [Fe 2p] and 0.11±0.01 At% of [Cl 2p]. It appeared that the αTH protected the doped samples from almost all metal-based contamination from the ASPN screen and reduced the extent of surface oxidation. It remained unclear exactly how αTH prevented the metal-based contamination, the doped samples darkened in colour after the ASPN (although the yellow tint is introduced by the doping with αTH) and the working table only showed metal oxide rings around the doped samples. As shown in Figure 59 (right), the colours of the oxide rings indicated the presence of [α/γ-Fe_2O_3] (i.e., red brown/yellow brown) and [α/γ-FeOOH] (i.e., yellow brown/orange) (Scheinost & Schwertmann, 1999).

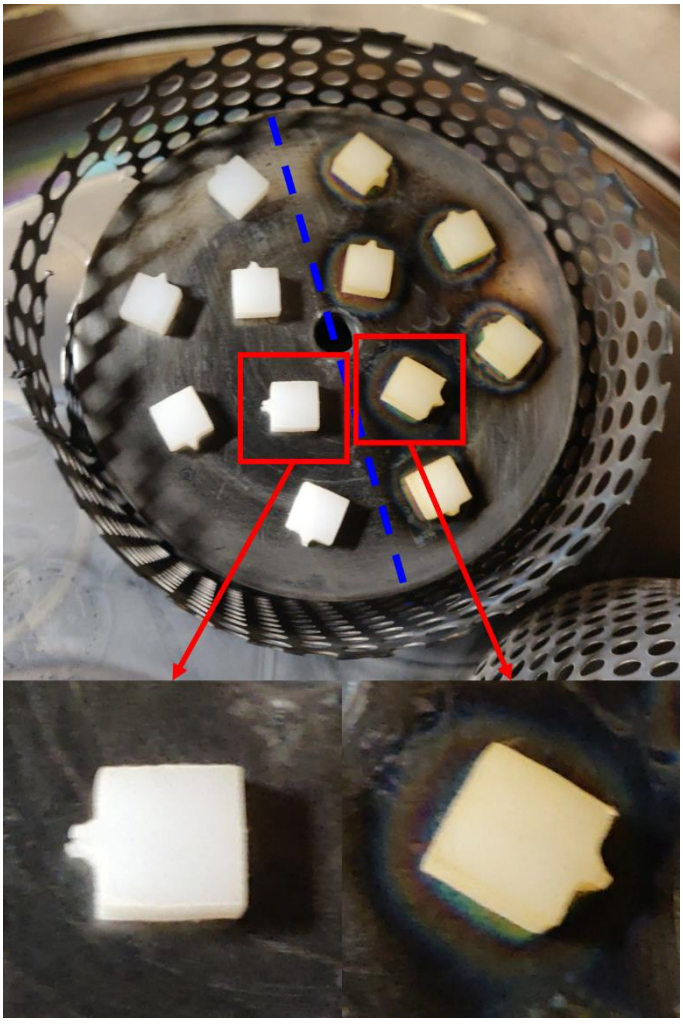


Figure 59. Picture of ASPN working table after a 60-minute treatment of the (left) undoped and (right) doped UHMWPE-based samples, showing the formation of metal oxide rings around the doped samples.

4.1.4. UV spectrophotometry

UV spectrophotometry was used to investigate the degree of AAc substitution on the ASPN treated UHMWPE-based sample surfaces by measuring the Fmoc-adduct after a deprotection cycle. This approach was chosen as it provided the degree of substitution of directly immobilised AAc, not solely free-amine/hydroxyl content. Here, Fmoc-Glycine-OH was immobilised on the ASPN-treated surfaces instead of the AMP itself (i.e., '*KR-12*'), due to the costs associated with the AMP synthesis. As mentioned in Section 2.4.2 and 3.1.4, three types of coupling chemistries were investigated, namely: (I) DIC/Oxyma Pure to form an amide bond between the AAc with surface amine-related groups (i.e., amine, amidine, etc.), (II) DCC/DMAP to form an ester bond between the AAc with surface hydroxyl-related groups (i.e., primary alcohol, carboxylic acid, etc.), and (III) CDI to form a carbamate bond between the AAc with surface amine-related groups.

Using the molar absorption coefficient for the Fmoc-adduct that was established in Section 3.2.7 (i.e., ε = 6112 L mol^{-1} cm^{-1}) and assuming all samples have an identical surface area (i.e., 3 cm^2), the degree of substitution (S; nM/cm^2) was determined following:

$$S = \frac{E}{\varepsilon\, A}. \qquad \textit{(Eq. 19)}$$

where A is the sample surface area in cm^2 and E is the measured UV absorbance at 290 nm. As the doped sample series only showed the presence of nitrogen at D/PT60, as was observed by XPS in Section 4.1.3, it was decided to only investigate the PT60 samples (i.e., UD/PT60 and D/PT60). To determine if the samples would leach/release debris and influence the results, UV measurements of the samples were also taken after a deprotection cycle without prior surface immobilisation of the AAc. Three repeats were prepared for each sample type, the UV absorbance and substitution degree are presented in Table 26. The individual UV absorbance, calculated concentrations and substitutions of the samples are presented in Appendix C6.

Table 26. UV measurements at 290 nm for UD/PT60 and D/PT60, showing the absorbance (*E*) outside the parentheses and the degree of substitution (*S*; nM/cm^2) inside the parentheses, where applicable.

	Deprotection cycle only	**Coupling chemistry**		
		(I) DIC/Oxyma	**(II) DCC/DMAP**	**(III) CDI**
UD/PT60	0.008±0.004 (N/A)	0.039±0.004 (20.819±2.194)	0.019±0.007 (10.230±3.599)	0.041±0.004 (21.896±1.869)
D/PT60	0.445±0.064 (N/A)	0.117±0.010 (N/A)	-	-

The UD/PT60 samples showed a relatively low UV absorbance intensity after the deprotection cycle without surface-immobilised AAc (i.e., 0.008±0.004), this was thought to be the result of some minor debris particles releasing into the deprotection solution – despite the fact the samples were washed with both ethanol and DMF prior to this experiment. Nonetheless, the UD/PT60 sample with surface-immobilised AAc (i.e., UD/PT60-[Gly]) showed a considerably higher UV absorbance intensity, which indicated that the Fmoc deprotection procedure and prior AAc surface immobilisation were successful. The presented absorbance values were not corrected as the observed error for UD/PT60 in deprotection solution alone showed that the "leaching" was somewhat sample-dependent, so the results for the AAc surface-immobilised samples may include some influence from the leaching/debris as was observed for the UD/PT60 in deprotection solution alone.

The two coupling chemistries which targeted surface amine-related groups (i.e., (I) DIC/Oxyma Pure and (III) CDI) displayed the highest degree of substitution and showed almost identical results (about 5% difference), displaying a degree of substitution of 20.819±2.194 and 21.896±1.869 nM/cm^2. The similarity in results also indicated that both coupling chemistries were able to bond to a comparable amount of surface amine-related groups. In terms of experimental practicality, the CDI coupling chemistry would be favourable

as it requires less chemicals, does not necessarily require an oxygen-free environment, and has the potential to be performed solvent-free (i.e., without the use of expensive and toxic DMF) which should also reduce the reaction time to ~5 minutes (Verma et al., 2012). However, to keep the coupling conditions similar, the solvent-free approach was not attempted in this work. The coupling chemistry that targeted surface hydroxyl-related groups (i.e., (II) DCC/DMAP) showed lowest UV absorbance intensity for the undoped ASPN-treated sample, displaying a degree of substitution of 10.230±3.599 nM/cm^2 and was about half of that observed with the other two coupling chemistries. Based on the XPS results which showed notably more [O 1s] At% than [N 1s] At% this was somewhat surprising, but it is worth to note that this coupling chemistry is only susceptible to free hydroxyl groups and not, e.g., secondary alcohols or carbonyl groups which would also contribute to the [O 1s] At%.

Unfortunately, the doped samples clearly showed a considerable amount of leaching for D/PT60 after the deprotection cycle without prior AAc surface immobilisation (i.e., 0.445±0.064), which was likely due to the leaching of αTH from the polymer matrix. Although it was initially thought that this could be corrected for after the AAc surface immobilisation, the results after the attempted surface immobilisation with (I) DIC/Oxyma Pure displayed a three-fold lower absorbance than that without the surface immobilisation (i.e., 0.117±0.010) – likely as most αTH already leached during the AAc surface immobilisation itself. Due to the issues associated with the doped ASPN-treated samples, the experiments with the other two coupling chemistries (i.e., (II) DCC/DMAP and (III) CDI) were discontinued.

Altogether, the UV measurements have shown that the surface immobilisation with the AAc worked for the undoped ASPN-treated sample (i.e., UD/PT60). However, the results were not optimal due to some potential debris particles/leaching influencing the UV absorbance intensities. An alternative approach/method might have been more suitable to determine the degree of substitution, which is further discussed in the recommendations in Section 5.2.1.

4.1.5. Wide-angle X-ray diffraction (WXRD)

Wide-angle X-ray diffraction (WXRD) was used to investigate the effect of αTH doping in combination with ASPN on the crystallinity, unit cell parameters, crystallite size, and lattice strain of the UHMWPE-based samples at a penetration depth of about 1059 μm, see Appendix C7 for more information on the X-ray penetration depth. The calculated spectra associated with the orthorhombic and monoclinic PE unit cells are depicted in Figure 60A, the spectra were calculated between 0° and 60° 2θ as these reflect the experimental conditions. The first four diffraction peaks of each phase in the spectra are highlighted in the top-view of the respective unit cells, as displayed in Figure 60B. For the orthorhombic phase, the three most intense diffraction peaks were the (1 1 0), (2 0 0) and the (0 2 0) planes at 21.53°, 23.97°, and 36.19°, respectively. Whereas for the monoclinic phase, the (0 1 0), (2 0 0) and the (-2 1 0) planes showed the highest intensity at 19.51°, 23.10°, and 25.27°, respectively.

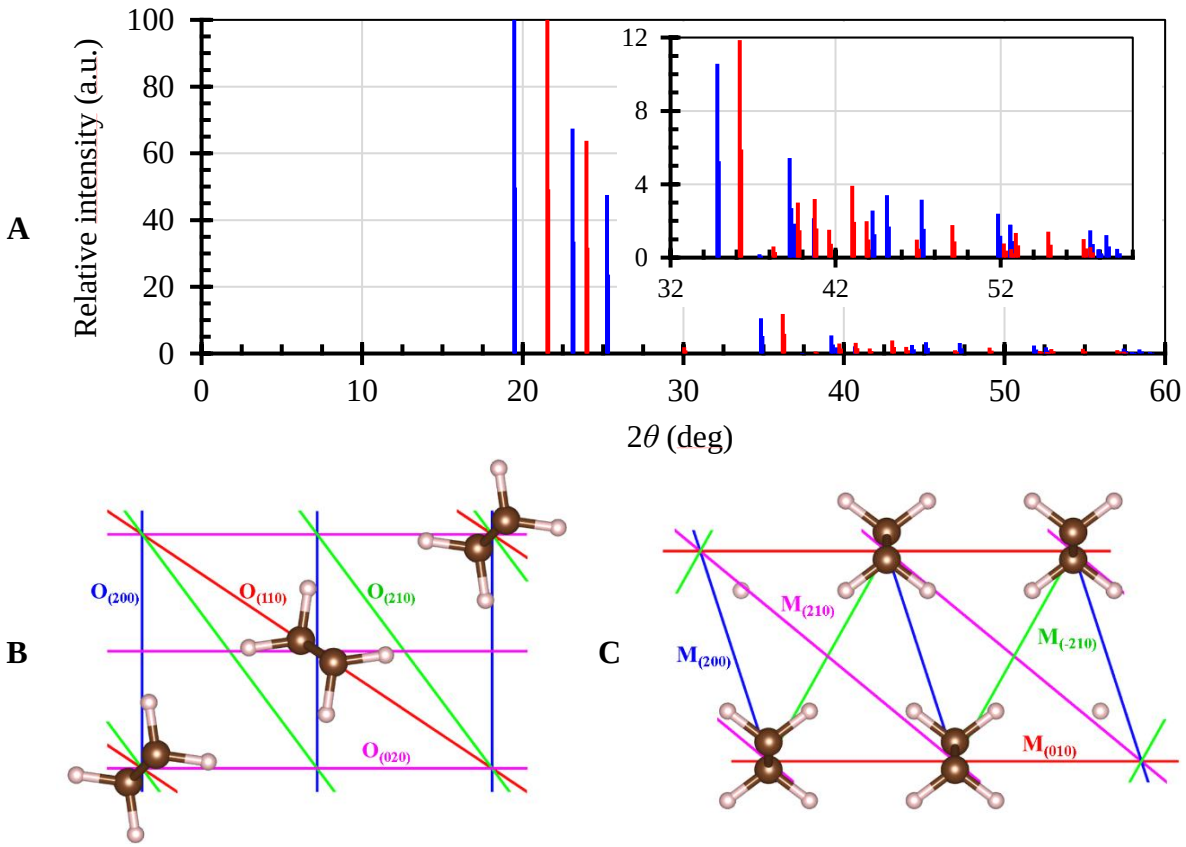


Figure 60. Calculated XRD spectra (**A**) of the (**red**) orthorhombic and (**blue**) monoclinic PE unit cells, and the corresponding top-view of (**B**) the orthorhombic unit cell and (**C**) the monoclinic unit cell including the diffraction planes that are highlighted in the calculated spectra.

After performing the lineshape scans (see Section 3.2.4), the experimental WXRD of the samples were fitted with the best-fit lineshape parameters, the peak-fitted spectra of the undoped and doped ASPN-treated UHMWPE-based samples are shown in Figure 61.

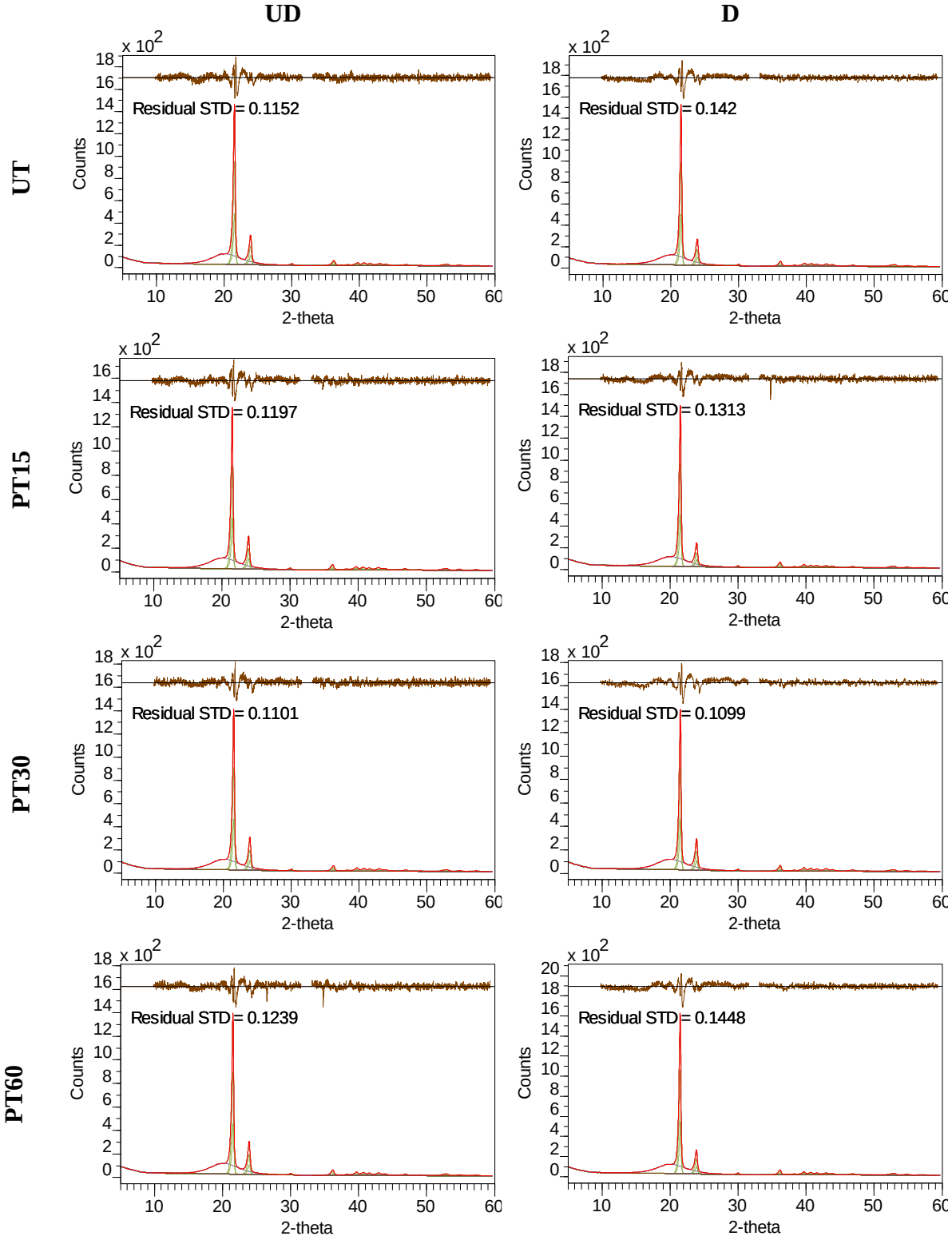


Figure 61. Peak fitted WXRD spectra of the (left) undoped and (right) doped UHMWPE-based sample series.

The observed $K\alpha_1$ diffraction peak positions for the undoped and doped sample series are shown in Table 27 and 28, respectively, including the mean average error (MAE) and maximum absolute error (MAX) versus the calculated $K\alpha_1$ diffraction peak positions. It can be observed that the calculated peak positions provided reasonable initial guesses for the experimental positions, showing a MAE of ≤0.06 2θ. The maximum error was consistently observed for the $O_{(122)}$ diffraction peak, deviating between 0.10-0.16 2θ for all samples.

Table 27. Observed diffraction peak positions of the undoped sample series.

Lattice vector			Observed position (2θ)				Calc.	ΔCalc.–Obs.			
h	**k**	**L**	**UT**	**PT15**	**PT30**	**PT60**	**(2θ)**	**UT**	**PT15**	**PT30**	**PT60**
0	1	1	21.54	21.53	21.54	21.53	21.53	-0.01	0.00	0.00	0.00
0	0	2	23.94	23.92	23.92	23.92	23.97	0.03	0.04	0.04	0.04
0	1	2	30.06	30.04	30.04	30.04	30.06	0.00	0.02	0.01	0.02
0	2	0	36.23	36.24	36.24	36.23	36.19	-0.04	-0.04	-0.05	-0.04
0	2	1	38.25	38.25	38.25	38.25	38.23	-0.02	-0.02	-0.02	-0.02
1	1	0	39.73	39.71	39.71	39.71	39.71	-0.02	0.00	0.00	0.00
0	1	3	40.71	40.69	40.70	40.69	40.73	0.02	0.04	0.03	0.04
1	1	1	41.60	41.59	41.59	41.59	41.61	0.01	0.02	0.02	0.02
1	0	2	42.96	42.96	42.95	42.95	43.01	0.05	0.05	0.06	0.06
0	2	2	43.91	43.90	43.89	43.90	43.88	-0.03	-0.02	-0.02	-0.02
1	1	2	46.90	46.89	46.89	46.89	46.92	0.02	0.03	0.03	0.03
0	0	4	49.03	48.99	49.01	49.00	49.07	0.04	0.08	0.06	0.07
0	2	3	52.23	52.22	52.20	52.19	52.19	-0.04	-0.03	-0.01	0.00
1	2	1	52.94	52.93	52.92	52.92	52.92	-0.03	-0.01	-0.01	0.00
1	1	3	54.83	54.83	54.83	54.83	54.88	0.05	0.05	0.05	0.05
0	3	1	57.05	57.04	57.03	56.99	57.02	-0.03	-0.02	-0.01	0.03
1	2	2	57.29	57.32	57.31	57.33	57.43	0.14	0.11	0.12	0.10
							MAE	0.03	0.03	0.03	0.03
							MAX	0.14	0.11	0.12	0.10

Table 28. Observed diffraction peak positions of the doped sample series.

Lattice vector			Observed position (2θ)				Calc.	ΔCalc.–Obs.			
h	**k**	**l**	**UT**	**PT15**	**PT30**	**PT60**	**(2θ)**	**UT**	**PT15**	**PT30**	**PT60**
0	1	1	21.52	21.52	21.51	21.49	21.53	0.01	0.01	0.02	0.04
0	0	2	23.92	23.92	23.91	23.88	23.97	0.05	0.05	0.06	0.08
0	1	2	30.04	30.03	30.02	30.00	30.06	0.02	0.02	0.04	0.06
0	2	0	36.20	36.20	36.20	36.17	36.19	-0.01	-0.01	-0.01	0.02
0	2	1	38.25	38.24	38.22	38.19	38.23	-0.01	-0.01	0.01	0.04
1	1	0	39.71	39.71	39.70	39.67	39.71	0.00	0.01	0.01	0.04
0	1	3	40.69	40.69	40.68	40.65	40.73	0.04	0.04	0.06	0.08
1	1	1	41.59	41.59	41.58	41.56	41.61	0.01	0.02	0.03	0.05
1	0	2	42.95	42.96	42.93	42.92	43.01	0.06	0.05	0.07	0.08
0	2	2	43.88	43.88	43.87	43.86	43.88	-0.01	0.00	0.01	0.02
1	1	2	46.89	46.88	46.87	46.86	46.92	0.03	0.04	0.04	0.06
0	0	4	49.03	48.96	48.98	48.94	49.07	0.04	0.12	0.10	0.13
0	2	3	52.22	52.22	52.19	52.19	52.19	-0.03	-0.03	0.00	0.00
1	2	1	52.94	52.92	52.91	52.90	52.92	-0.03	0.00	0.00	0.02

1	1	3	54.82	54.83	54.81	54.80	54.88	0.06	0.05	0.08	0.08
0	3	1	57.02	56.99	56.99	56.95	57.02	0.00	0.03	0.03	0.07
1	2	2	57.30	57.29	57.28	57.27	57.43	0.13	0.14	0.15	0.16
							MAE	0.03	0.04	0.04	0.06
							MAX	0.13	0.14	0.15	0.16

The phase compositions determined by the peak fitted WXRD spectra are shown in Figure 62. As can be observed, almost no monoclinic phase was observed in any of the samples, showing less than 0.30% across the complete sample series, which was expected considering it is a meta-stable phase which is almost exclusively present when the material is under stress. Because of this, only the first three components of the monoclinic phase were included in the peak model during the peak fitting procedures, as the intensity of the diffraction peaks at higher 2θ would be insignificant and might have erroneously influenced the orthorhombic components (see peak ratios in the calculated spectra). Naturally, the overall crystalline content would be the summation of the orthorhombic and monoclinic components. The orthorhombic and amorphous phase content showed little variance across both sample series, all samples showed between 57-58% of the orthorhombic phase and between 41.8-43% of the amorphous phase. A minor decrease was noted for the undoped sample series, which showed 57.91% of orthorhombic content for UD/UT to 57.52% for UD/PT60. Whereas a minor increase was noted for the doped sample series, which showed 57.03% of orthorhombic content for D/UT to 57.45% for D/PT60. Altogether, the XRD results showed that the αTH doping and ASPN treatment did not significantly impact the bulk crystallinity of the UHMWPE-based samples, in contrast to the increase in the (sub-)surface crystallinity after doping and ASPN relative to UD/UT as observed with Raman in Section 4.1.2.

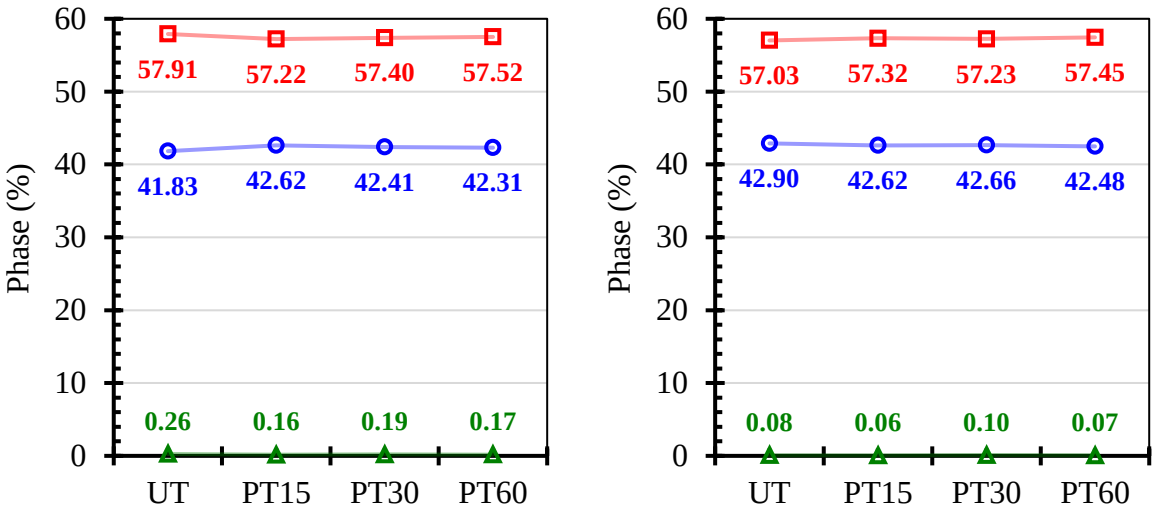


Figure 62. Phase composition of the peak-fitted WXRD spectra of the (left) undoped and (right) doped samples, showing the percentage of the (squares, **red**) orthorhombic, (triangles, **green**) monoclinic, and (circles, **blue**) amorphous phase.

Using the peak-fitted XRD spectra, the observed/experimental unit cell parameters were determined following unit cell refinement, see Appendix C8 for more details on this procedure (Holland & Redfern, 1997). After indexing the XRD spectra to a list of (*h k l)* and 2θ values, the unit cell parameters were refined by a non-linear least-squares fitting procedure, using the 'UnitCell' software package. The refined unit cell parameters as obtained from the 'UnitCell' software package are shown in Figure 63, showing the length of the unit cell parameters (i.e., 'a', 'b', and 'c') and the unit cell volume (V). The unit cell parameters 'a' and 'b' (i.e., the plane perpendicular to the chain direction) are strongly affected by non-bonded interactions between the chains, typically also by the degree of branching for other PE types but UHMWPE is non-branching. The unit cell parameters 'a' and 'b' increased over the total ASPN treatment time (i.e., PT60) relative to their untreated counterpart (i.e., UT). The unit cell parameter 'c' (i.e., following the chain direction) is mainly determined by the length/angle of the *all-trans* zig-zag [C–C] chains, which showed negligible change across the total ASPN treatment time but was slightly higher for the undoped samples when compared to the doped samples. As can be noted from the unit cell volumes, an inverse trend between the undoped and doped sample series unit cells was observed.

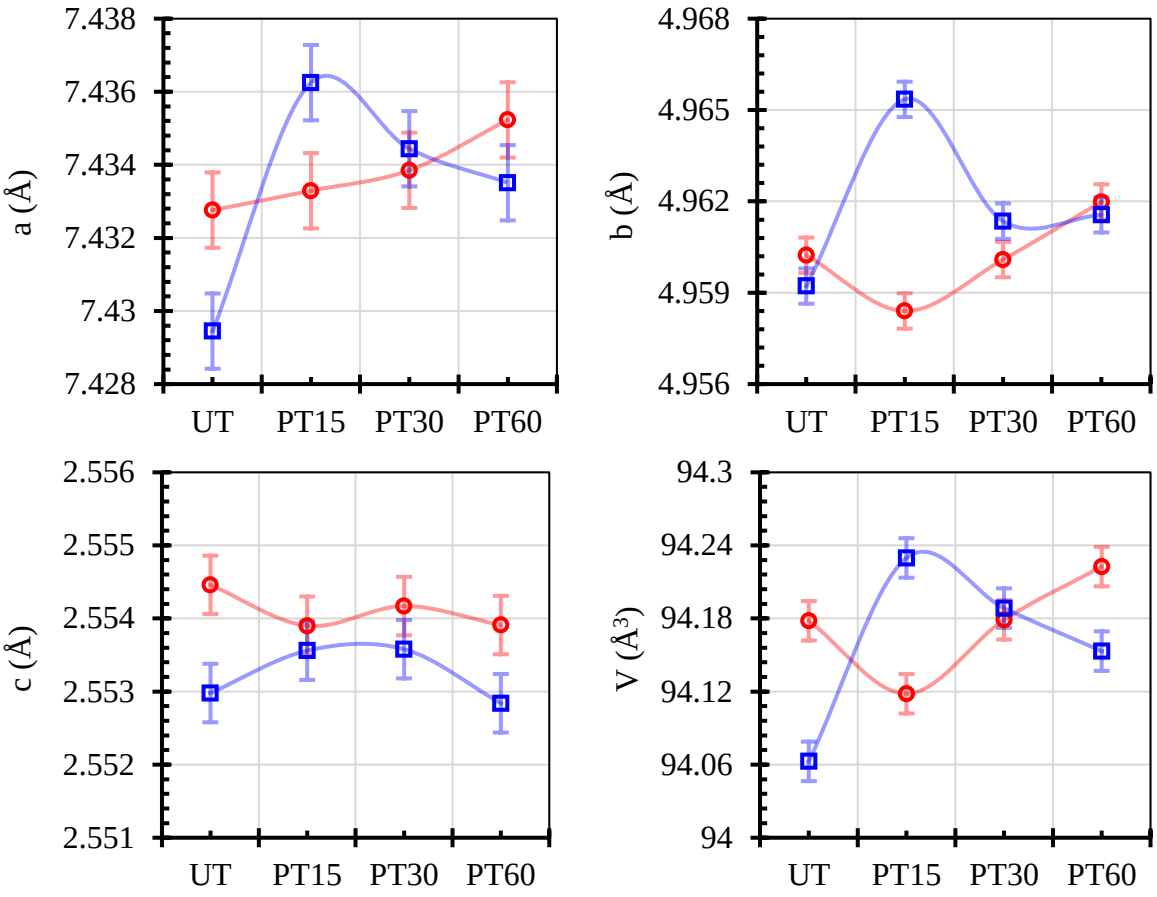


Figure 63. Unit cell parameters as obtained from the refinement in 'UnitCell', showing the length of the unit cell parameters (top-left) a, (top-right) b, and (bottom-left) c, and (bottom-right) the unit cell volume of the (**red**, circles, solid line) undoped and (**blue**, squares, dotted line) doped sample series.

Finally, the average crystallite size (L) was determined using the Scherrer equation:

$$L = \frac{K\,\lambda}{\beta\,cos(\theta)}, \qquad \textit{(Eq. 20)}$$

where λ is the Cu–Kα_1 X-ray wavelength in nm (0.15405 nm), K is a dimensionless shape factor (without detailed shape information, K = 0.9 is generally considered a suitable approximation), β is the FWHM of the diffraction peak in radians, and θ is the angle in radians (Holzwarth & Gibson, 2011). Within the literature, either the most-intense diffraction peak or all diffraction peaks are used to determine the average crystallite size. The Scherrer equation is only valid for crystallite sizes up to about 100–200 nm, above this it is difficult to separate the 'crystallite size'-induced peak broadening from the experiment-induced peak broadening (Holzwarth & Gibson, 2011). Assuming L, K, and λ are fixed, it would be reasonable to assume $\beta * cos(\theta)$

is a fixed multiple between 0° < θ < 90° but at higher θ this would result in unphysical FWHM. Due to these limitations, a modified Scherrer equation has been established, which plots ln β against ln $\frac{1}{cos(\theta)}$ to provide a value of intercept for ln $\frac{K\,\lambda}{L}$, as shown in Figure 64. Theoretically, the regression line must show a slope of 45° (as tan(45°) = 1) but due to experimental errors this is not the case, as can be observed in the modified Scherrer equation plots for the UHMWPE-based sample series shown in Appendix C9.

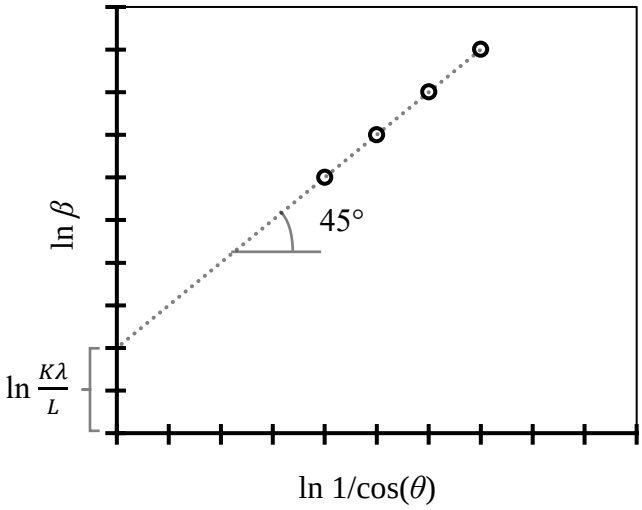


Figure 64. Schematic representation of the plot used for the modified Scherrer equation.

The crystallite sizes estimated with the Scherrer equation using (A) the most intense diffraction peak (i.e., $O_{(110)}$) and (B) all diffraction peaks, and (C) with the modified Scherrer equation are shown in Figure 65; including the corresponding lattice strain (ε) relative to the crystallite size of the undoped and untreated sample (UD/UT), following:

$$\varepsilon = \frac{L - L_0}{L_0}, \qquad \textit{(Eq. 21)}$$

where L_0 is the crystallite size of UD/UT and L is the size of the respective sample.

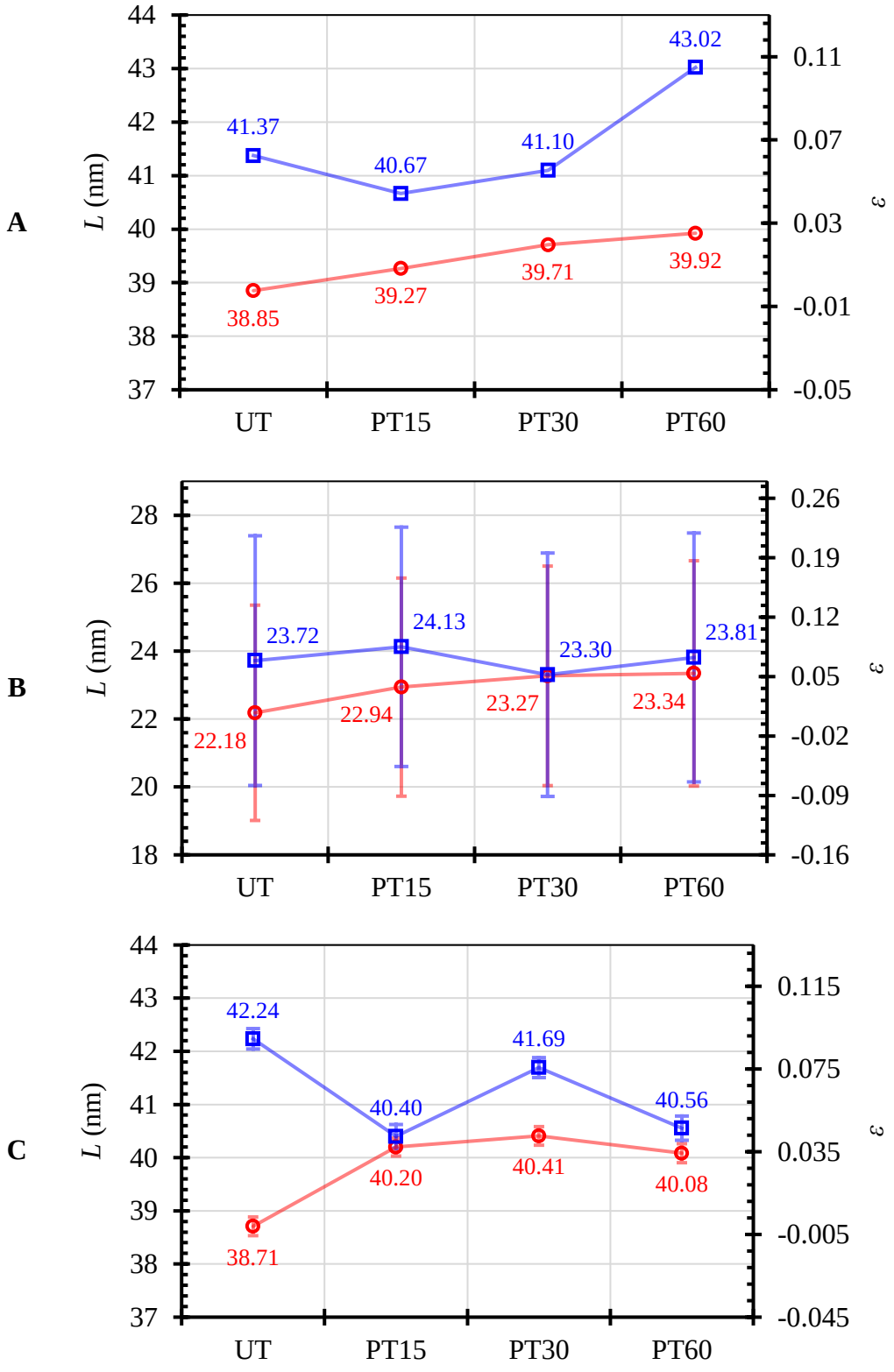


Figure 65. Crystallite size (L) and lattice strain (ε) estimated for the (**red**, circles) undoped and the (**blue**, squares) doped sample series with (A) the Scherrer equation and the most-intense diffraction peak (i.e., $O_{(110)}$) or (B) all diffraction peaks (the error bars depict a confidence interval of $\alpha = 0.05$ with $n = 16$), and (C) the modified Scherrer equation (the error bars depict the root-mean-square of the linear regression fit).

As presented in Figure 65, all methods used to estimate the average crystallite size showed the smallest value for UD/UT. Next to that, the average crystallite sizes and corresponding lattice strain for the doped sample series was consistently larger than for the undoped sample series. The crystallite sizes estimated using (A) the Scherrer equation and the most-intense diffraction peak (i.e., $O_{(110)}$) showed a significantly higher estimation than when (B) using all diffraction peaks. However, the crystallite sizes estimated using (C) the modified Scherrer equation were within the same range as those observed with (A) the Scherrer equation and the most-intense diffraction peak. The error observed when (B) using the Scherrer equation and all diffraction peaks was about ±3.5 nm (i.e., about 15%) for each of the samples. However, using (C) the modified Scherrer equation, the observed error was minimised to about ±0.19 nm (i.e., about 0.5%) for each of the samples. It was expected that the crystallite sizes determined using (C) the modified Scherrer equation provided the most reliable estimations, as it was the most "up-to-date" formula. Typically, an increase in the crystallinity and decrease in the unit cell parameter 'a' are associated with lamellar (crystallite) thickening (Schwartz et al., 1994). Here, unit cell parameter 'a' increased for both series after ASPN but the crystallinity slightly decreased for the undoped series and slightly increased for the doped series. As shown by the correlation of the crystallinity and crystallite size in Figure 66, smaller crystallites may have disappeared, which decreased the total crystallinity but increased the average crystallite size.

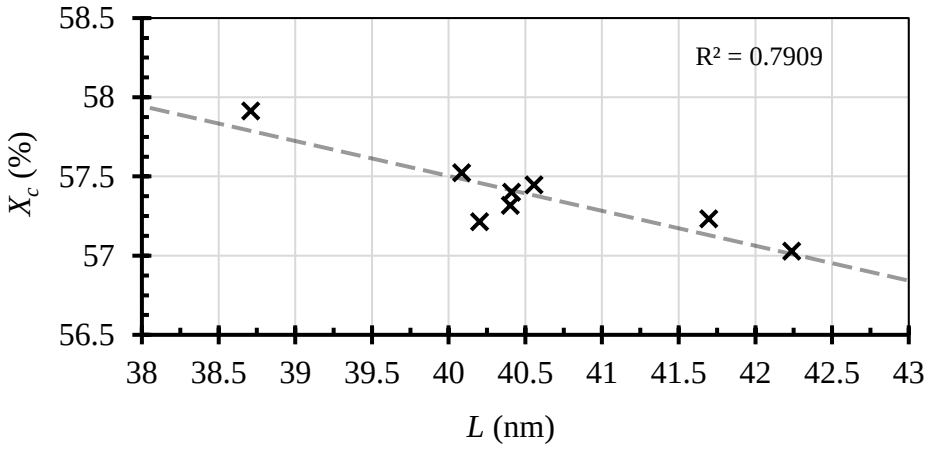


Figure 66. Linear correlation between the crystallite size and crystallinity of the UHMWPE-based samples.

4.1.6. Scanning electron microscopy (SEM)

The SEM micrographs allowed for the investigation of the surface morphology of the UHMWPE-based samples, which revealed surface irregularities and/or delamination as a result of the αTH doping and ASPN treatments. Surface irregularities and/or delamination were important to investigate as these are associated with decreased implant performance (Popoola et al., 2010). To provide a semi-quantitative insight into the surface irregularities and/or delamination, the SEM micrographs were further investigated with ImageJ by determining the average size and area coverage of the cavities/gaps (i.e., the black pixels). In short, a histogram threshold was manually set so the SEM micrographs were practically transformed into a mask that only showed the black pixels. From there, the average "particle" size (only >1 pixels^2 were counted, ignoring single pixel dots) and the percentual area coverage of the black pixels was determined, providing a semi-quantitative insight into the surface irregularities and/or delamination of the UHMWPE-based sample surfaces. An example image of D/PT15 displaying the histogram threshold and resulting mask overlayed on top of the original SEM micrograph is shown in Figure 67, the results from this procedure for all undoped and doped UHMWPE-based samples are presented in Figure 68. The SEM micrographs for the undoped and doped UHMWPE-based samples are shown in Figure 69 and 70, respectively.

As can be observed in the SEM micrographs of the undoped sample series, UD/UT displays the stacked flake-like structure which is typically associated with an UHMWPE surface (G. Liu et al., 2004). UD/UT also displayed the lowest black pixel area coverage at 1.34%, indicating it showed the least amount of surface defects/delamination from all the UHMWPE-based samples. The undoped ASPN-treated samples clearly showed an increase in delamination when compared to UD/UT. The delamination first became apparent at UD/PT15 and notably increased at UD/PT30, which was supported by the increasing black pixel area coverage from 2.91% to 5.35%, respectively. Fortunately, the delamination subsequently

decreased at UD/PT60, which showed to exhibit a much smoother surfaces compared to the shorter ASPN-treated samples (i.e., UD/PT15 and UD/PT30). Next to that, UD/PT60 displayed a reduced black pixel area coverage of 1.74%, which was much closer to that of UD/UT but the flake-like structure associated with UD/UT was no longer visible. It was assumed that the reduction in delamination observed for UD/PT60 is related to the reduced oxidation when compared to UD/PT15 and UD/PT30 as was determined by FTIR (Region 6) and XPS.

As can be observed in the SEM micrographs of the doped sample series, D/UT showed little structural defects but the flake-like structure looked more separated than with UD/UT, which was substantiated by the fact that D/UT showed a black pixel area coverage of 2.83%. A significant increase in the formation of gaps in-between the UHMWPE “flakes” was noted for D/PT15, this sample also displayed the highest black pixel area coverage from all the UHMWPE-based samples at 9.25%. However, no delamination was noted for D/PT15 when compared to its untreated counterpart (i.e., UD/PT15), which was expected to be due to the plasticising effect of αTH. At longer ASPN treatments times (i.e., PT30 and PT60), the doped samples showed the formation of bubble-like clusters, which first became apparent at D/PT30 and these clusters seemed to spread out at D/PT60. The bubble-like clusters looked to be at a slightly higher elevation than the UHMWPE flake-like surface itself, as if the clusters "grew” up/outwards. However, it did not look like the bubble-like clusters were fully separated from the UHMWPE flake-like surface as these two phases appeared to dissipate/flow into each other. The gaps observed at D/PT15 almost completely disappeared at longer ASPN treatment times, showing a black pixel area coverage of 3.80% at D/PT30 and this further decreased to 3.06% at D/PT60. Once again, no delamination was noted for D/PT30 and D/PT60 when compared to their undoped counterparts. To better visualise the presence of the bubble-like clusters, an attempt was made to highlight the separation of the UHMWPE flake-like surface and the bubble-like clusters using colours, as shown in Figure 71 with D/PT30 serving as an example

– the highlighting was done manually, so the phase separation is not perfect. As the surface coverage of these bubble-like clusters showed to increase over the ASPN treatment time, it was expected that these structures are the 'a-C'-like compound which also increased over the ASPN treatment time as was observed with FTIR and Raman. SEM micrographs of a-C presented in the literature also display bubble-like clusters, although the pure a-C samples in the literature showed a more "perfect" circular shape when compared to the clusters observed in this work (Czarnecka et al., 2020; Raev et al., 2015; Sen & Puri, 2004).

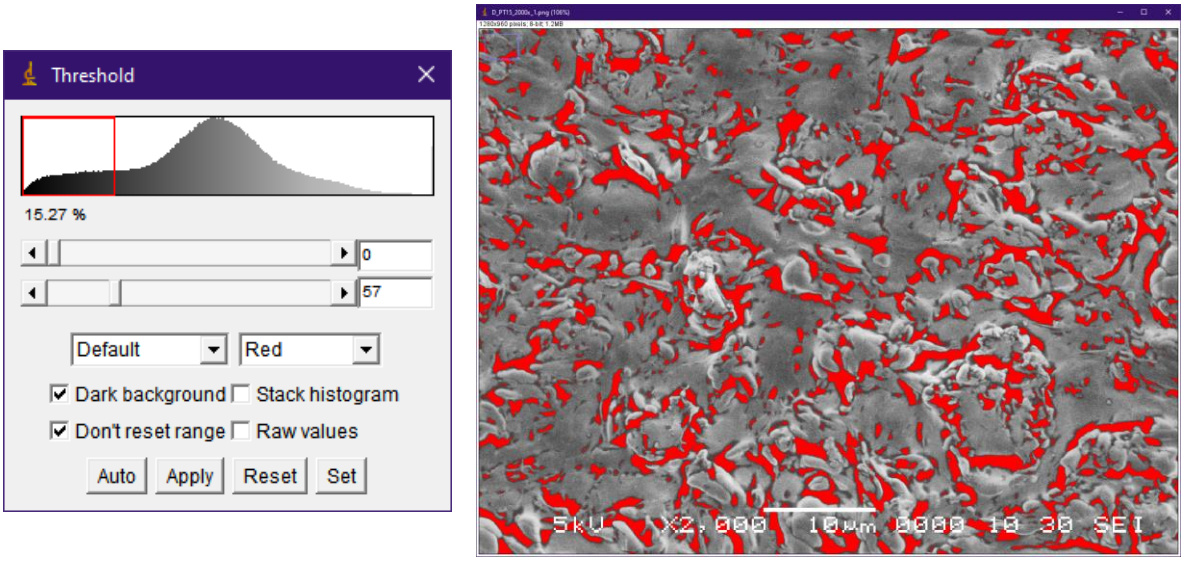


Figure 67. Example of (left) histogram threshold and (right) resulting binary image of the black pixels overlayed on the original SEM micrograph of D/PT15 in ImageJ.

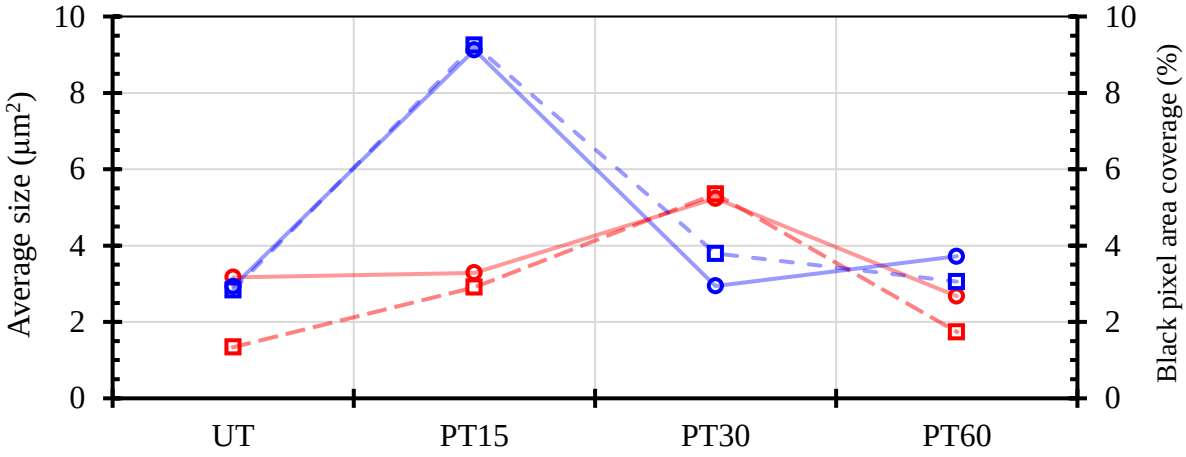


Figure 68. Graph displaying the average size of the black pixels observed in the SEM micrographs of (**red**, circles, solid line) undoped and (**blue**, circles, solid line) doped samples; and corresponding percentual area coverage of the (**red**, squares, dotted line) undoped and (**blue**, squares, dashed line) doped samples.

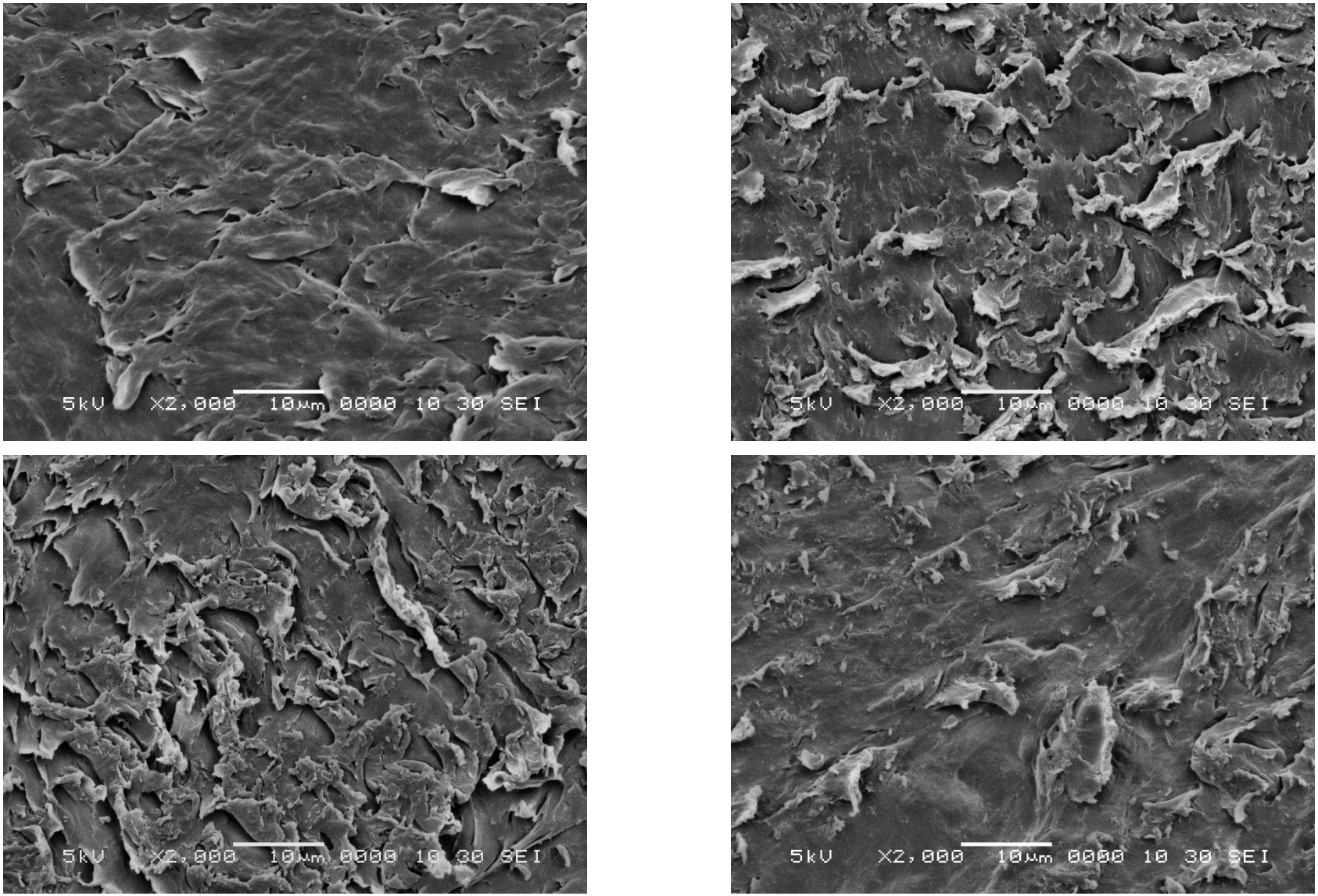


Figure 69. SEM micrographs of (top-left) UD/UT, (top-right) UD/PT15, (bottom-left) UD/PT30 and (bottom-right) UD/PT60, at a 2000x magnification.

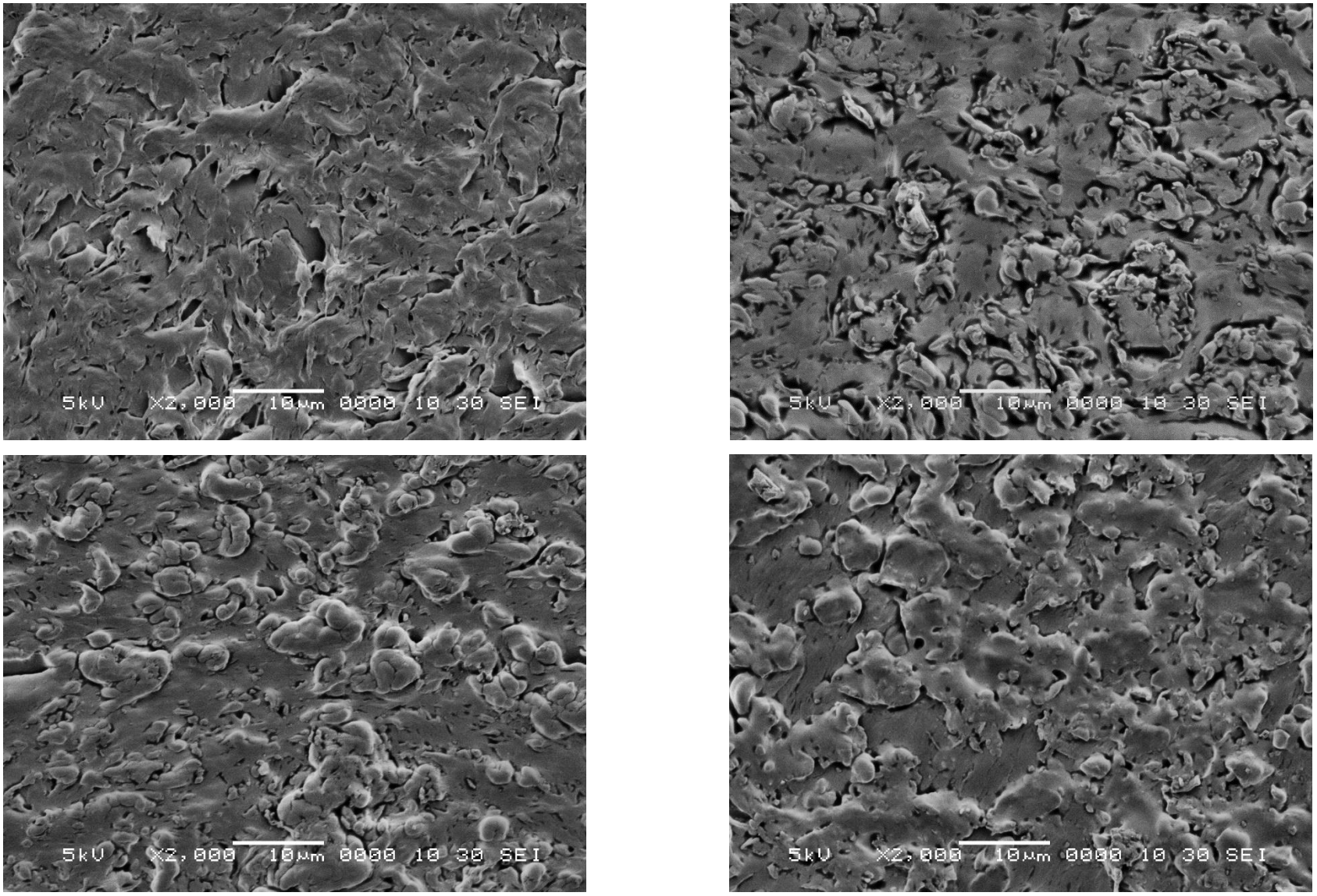


Figure 70. SEM micrographs of (top-left) D/UT, (top-right) D/PT15, (bottom-left) D/PT30 and (bottom-right) D/PT60, at a 2000x magnification.

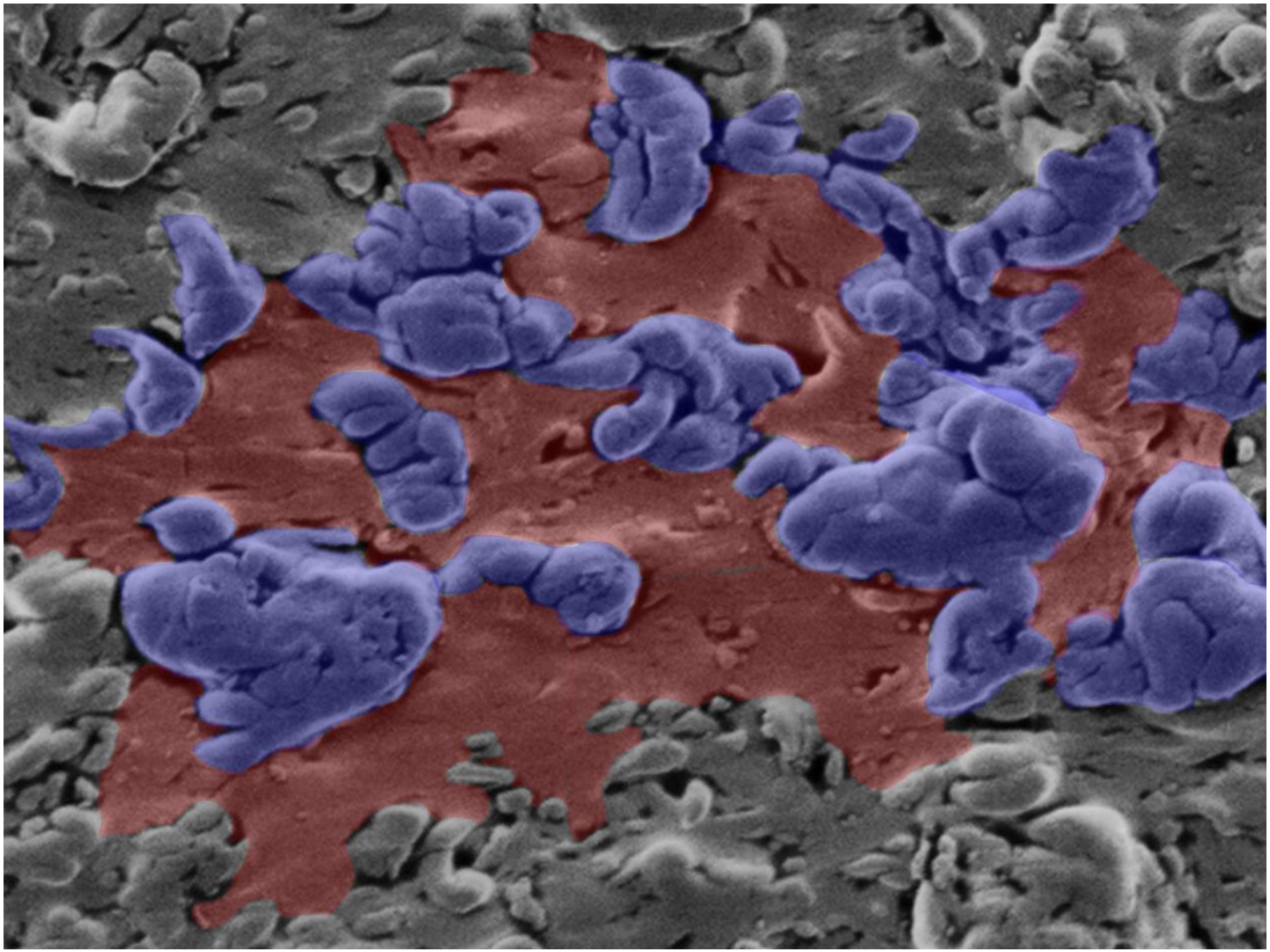


Figure 71. Zoomed-in SEM micrograph of D/PT30 with randomly highlighted sections of the (**red**) UHMWPE flake-like surface and the (**blue**) bubble-like clusters.

4.1.7. Vickers microhardness (MH_V) test

The Vickers microhardness test was used to investigate the effect of αTH doping in combination with ASPN on the surface microhardness of the UHMWPE-based samples at an indentation depth (t) of about 200 µm. The indentation depth was estimated following $t = \frac{d}{2\sqrt{2}\tan\frac{\theta}{2}}$ for the pyramid-shaped indenter, see Section 3.2.6 for more information. Three random samples from each sample type were indented at three different positions across the sample surface, the averaged results from the Vickers microhardness test are displayed in Figure 82. The Vickers microhardness also displays a correlation with the elastic modulus (E) as demonstrated by, e.g., the Tabor relation and the Struik model (Zamfirova et al., 2003). This correlation allowed for the estimation of the elastic modulus for samples where the sample size did not allow common approaches (e.g., tensile testing) to determine this property, as in this work. Using the values provided by Zamfirova *et al.* and Lorenzo *et al.*, who established the logarithmic dependence between the Vickers microhardness and the elastic modulus using LLDPE, LDPE, HDPE, and UHMWPE, the averaged elastic modulus for the UHMWPE-based samples in this work was estimated as shown in Figure 72 (Lorenzo et al., 1989; Zamfirova et al., 2003). The Vickers microhardness and corresponding elastic modulus of the individual samples is presented in Appendix C10.

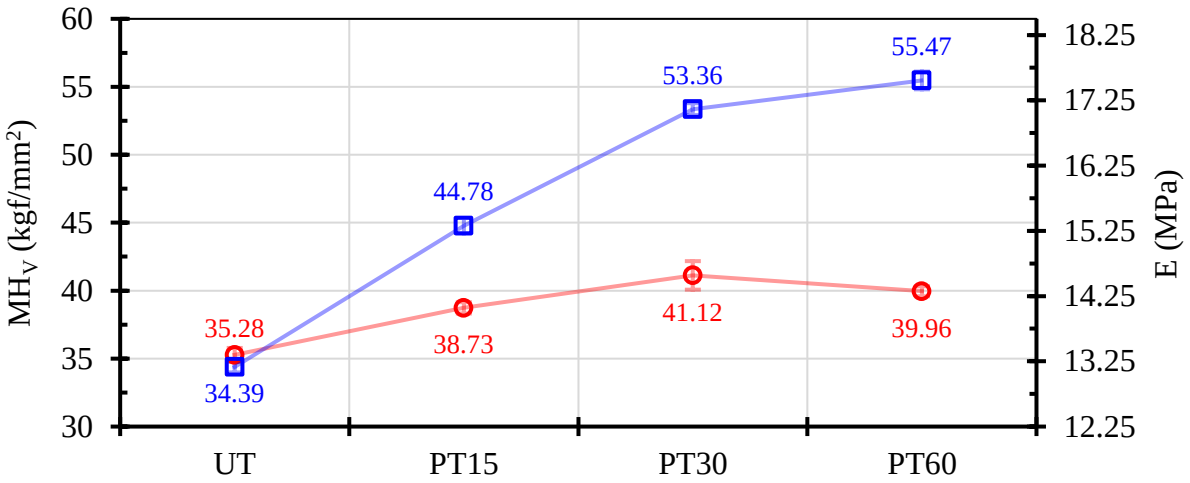


Figure 72. Vickers microhardness for the (**red**, circles) undoped and (**blue**, squares) doped UHMWPE-based sample series, including the elastic modulus as determined by the logarithmic correlation from the literature.

The untreated UHMWPE-based samples (i.e., UD/UT and D/UT) showed the lowest Vickers microhardness across their respective sample series. Additionally, D/UT (34.39±0.40) showed a slightly lower Vickers microhardness when compared to UD/UT (35.28±0.51), which was expected considering αTH also acts as a plasticiser (Zhu et al., 2014). The ASPN treatment showed to increase the Vickers microhardness for both sample series. The undoped sample series initially showed a notable increase of ~9.8% at UD/PT15 (38.78±0.42) but did not increase much over the total ASPN treatment time, showing a total increase of ~13% at UD/PT60 (39.96±0.37). However, a significantly higher increase was observed for the doped sample series, where the Vickers microhardness continuously increased over the ASPN treatment time and ultimately displayed an increase of ~61% at D/PT60 (55.47±0.65). The results displayed that the doped sample series showed an almost five-fold higher increase in Vickers microhardness when compared to the undoped sample series.

In the literature, the Vickers microhardness is often related to the increase in the TVI, oxidation index (i.e., the combined presence of the [C=O] and [O=C−O] band indices), or the crystallinity (Fulin et al., 2014). However, in this work, the TVI (FTIR), oxidation index (FTIR), and crystallinity (Raman) did not show a strong correlation with the Vickers microhardness, displaying a Pearson correlation coefficient of 0.19, -0.27, and 0.55, respectively. In contrast, as was observed by FTIR in Section 4.1.1 (Region 2), the undoped ASPN-treated samples displayed a two-fold higher TVI index when compared to the doped ASPN-treated sample series but showed a roughly ~28% lower Vickers microhardness.

Instead, in this work, a strong Pearson correlation coefficient between the combined $[C=C]_{stretching}$ index determined with FTIR and the Vickers microhardness was observed (i.e., r_p = 0.99), the corresponding linear correlation is shown in Figure 73. The linear correlation also displayed a strong regression coefficient (R^2) of 0.99, confirming the strong correlation between the $[C=C]_{stretching}$ index and the Vickers microhardness.

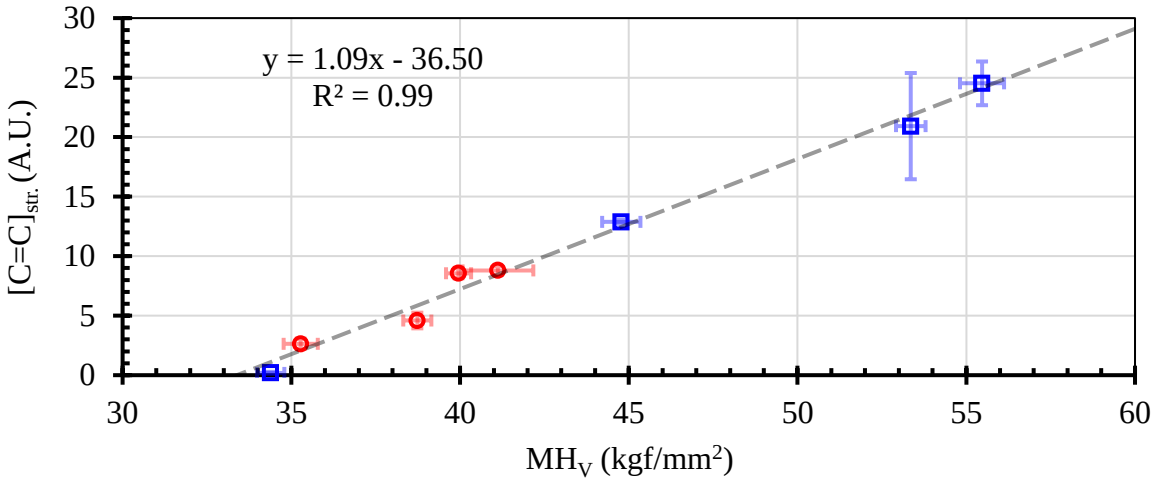


Figure 73. Linear correlation between Vickers microhardness and the $[C=C]_{str.}$ band index from FTIR, showing the data points related to the (**red**, circles) undoped and (**blue**, squares) doped UHMWPE-based sample series.

Next to that, the a-C index determined with Raman in Section 4.1.2 (Region 1) also displayed a strong Pearson correlation coefficient with the Vickers microhardness (i.e., r_p = 0.91), the corresponding linear correlation is shown in Figure 74. The linear correlation also displayed a relatively high regression coefficient (R^2) of 0.83, confirming the correlation between the a-C index determined with Raman and the Vickers microhardness. However, both the Pearson and regression correlation coefficients for the a-C index were notably lower than those observed for the $[C=C]_{stretching}$ index. It was assumed that the lower coefficients for the a-C index were due to the difference in penetration depth of the spectroscopic techniques, as FTIR (~2.11 μm) measurements were closer to the sample surface than Raman (~10.11 μm).

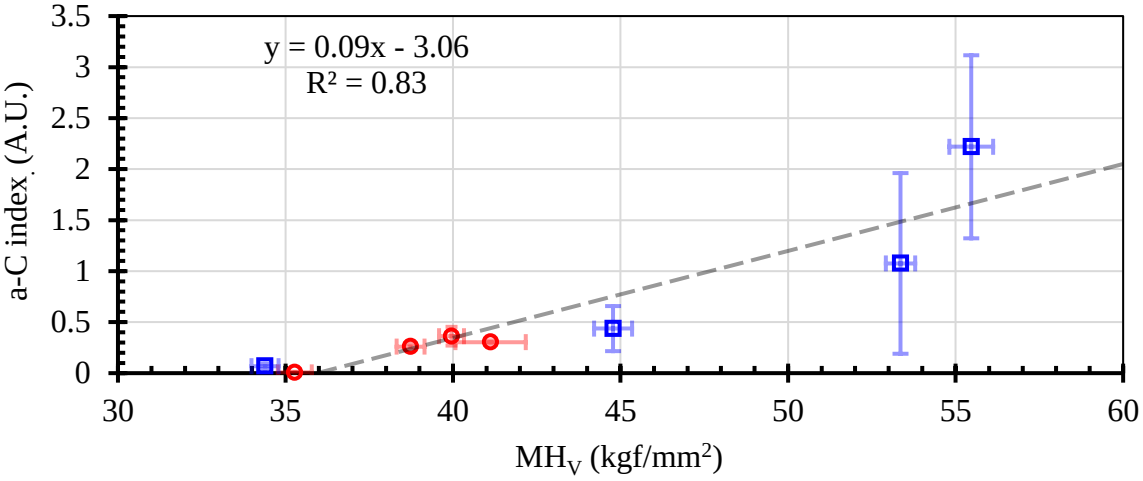


Figure 74. Linear correlation between Vickers microhardness and the a-C index from Raman, showing the data points related to the (**red**, circles) undoped and (**blue**, squares) doped UHMWPE-based sample series.

4.1.8. Wettability

Contact angle (CA) measurements were used to investigate the wettability of the UHMWPE-based sample surfaces after αTH doping, the ASPN treatment (after 60 minutes) and immobilisation of '*KR-12*'. Three repeats were measured for each sample type, the averaged equilibrium contact angles (ECA) as observed for the undoped and doped UHMWPE-based sample series are presented in Figure 75 and 76, respectively. The ECA of the individual samples are presented in Appendix C11. The UD/UT samples showed a relatively high ECA for DI water of 113.68° and considerably lower ECA for diiodomethane of 65.63°, indicating the surface was mostly hydrophobic as was expected for a material consisting out of non-polar methylene units like UHMWPE. After the ASPN treatment, the DI water CA for UD/PT60 did not decrease much, which was surprising considering the increased [O 1s] and [N 1s] At% that was observed with XPS (see Section 4.1.3). However, UD/PT60 did show a notable decrease to 44.64° for the diiodomethane ECA, which could be attributed to the formation of the 'a-C'-like compound as was observed with FTIR and Raman (see Section 4.1.1 and 4.1.2, respectively). After the attempted immobilisation of '*KR-12*' onto the surface of UD/PT60 with DCC/Oxyma Pure, the ECA of the DI water dropped significantly to 32.74°, whilst the diiodomethane ECA increased to 62.38°. The major decrease in the DI water ECA (and thus increased hydrophilicity) indicated that immobilisation of '*KR-12*' was successful, which could be attributed to the H-bonding of the many amine and amide bonds present in the AMPs. The successful immobilisation of '*KR-12*' was also in agreement with the results observed during the degree of substitution measurements (see Section 4.1.4). The D/UT samples showed a notably lower DI water and diiodomethane ECA (i.e., 86.23° and 13.13°, respectively) when compared to UD/UT. The decrease in the diiodomethane ECA of D/UT was due to the doping with αTH as it is a part-polar molecule, whilst the decrease in the DI water ECA was likely due to the H-bonding with the phenol group of αTH. After ASPN the DI water and diiodomethane

ECA for D/PT60 increased to 106.50° and 56.67°, respectively, which was expected to be due to the exhaustion of the αTH (as was observed by FTIR) and the formation of the ASPN layer. After the attempted immobilisation of '*KR-12*' to D/PT60, only minor changes were observed in the DI water and diiodomethane ECA (i.e., 105.74° and 54.11°, respectively), which indicated that the immobilisation of '*KR-12*' was unsuccessful. Unfortunately, it was expected this might occur after the leaching of αTH was observed during the degree of substitution measurements, it was assumed that the free-form presence of αTH inhibited the immobilisation of '*KR-12*' during the coupling reaction.

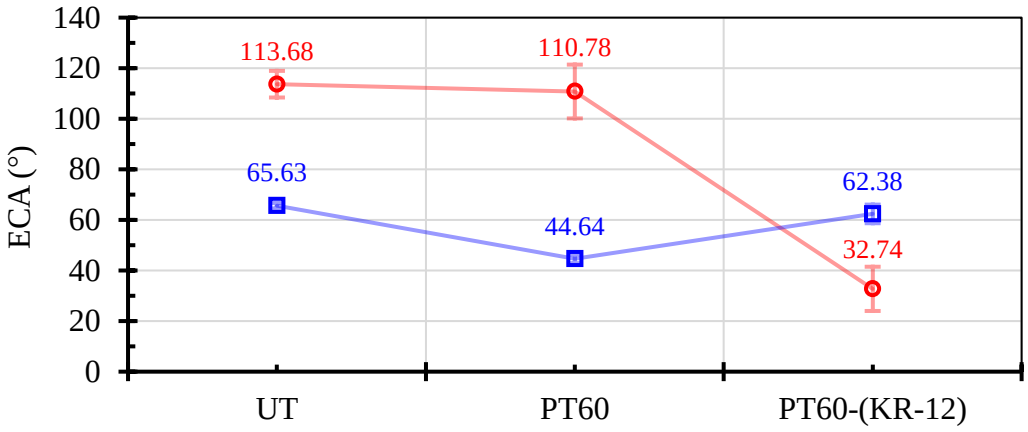


Figure 75. ECA of (**red**, circles) DI water and (**blue**, squares) diiodomethane for the undoped samples.

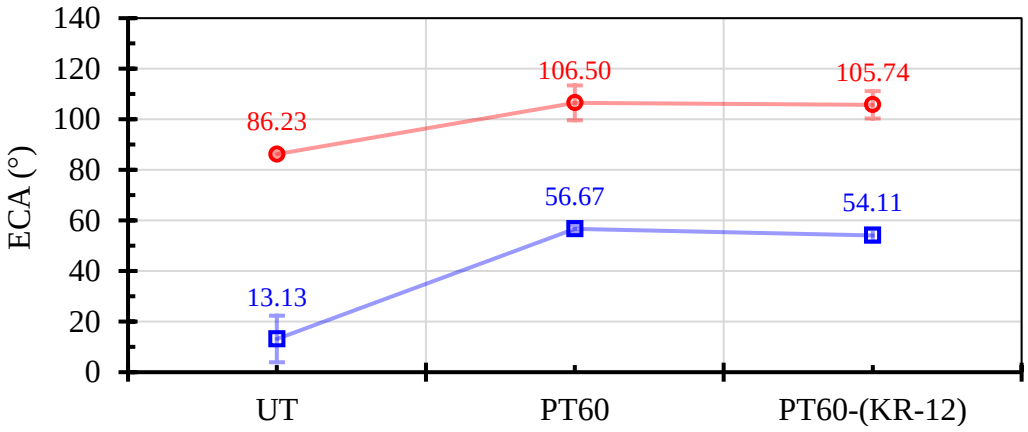


Figure 76. ECA of (**red**, circles) DI water and (**blue**, squares) diiodomethane for the doped samples.

As discussed, the ASPN treatment introduced a notable presence of nitrogen (up to 15.57 At%) to the UHMWPE-based surfaces, as determined with XPS survey in Section 4.1.3. In general, it would be expected that the introduction of nitrogen-containing functional groups

would increase the hydrophilicity when compared to untreated UHMWPE. Since nitrogen-containing functional groups are generally polar due to the electronegativity difference between nitrogen and hydrogen, carbon, and oxygen, as well as due to the presence of its lone pair of electrons, which allow for hydrogen bonding and dipole-dipole interactions. For example, Jokinen *et al.* studied the hydrophilicity of plasma-treated HDPE, using either pure O_2 or N_2 gas in a microwave plasma batch reactor for 1 and 10 minutes (Jokinen et al., 2012). The ECA for DI water on the untreated HDPE surface was the highest at ~90°, whereas the 10-minute nitrogen plasma treatment resulted in the most hydrophilic HDPE surface with an ECA of ~30°. The samples plasma-treated for one minute or with the oxygen plasma, displayed ECAs around 40-50°. Next to that, the hydrophobic recovery of the polymers in dry air storage was also investigated, this partial recovery stabilised after 18 days and the ECA recovered to 60-70° (Jokinen et al., 2012). Hydrophobic recovery is likely caused by the reorientation/reptation of polymeric chains at the surface during ageing, resulting in the reorganization of polar groups into the bulk of the material, as shown by Kotál *et al.* by comparison of new and aged Ar^+ plasma-treated PET (Kotál et al., 2007). In this work, the ECA of DI water on UD/UT was barely reduced after ASPN, considering the ECA for UD/PT60 only decreased by 2.9°. López-Santos *et al.* observed a similar result for LDPE plasma-nitrided with low-pressure microwave and atmospheric-pressure DBD plasma, treated for one minute at a pressure of 40 Pa with a working gas of both N_2 or a mixture of argon with NH_3 (López-Santos et al., 2011). These authors also found that the decrease in the ECA of DI water could not be attributed to the introduction of nitrogen, but instead to the increased presence of oxygen-containing functional groups. In this work, the XPS survey results (Section 4.1.3) revealed that there was an increase in the atomic presence of oxygen after ASPN, UD/PT60 showed an increase of ~5 At% and D/PT60 increased by ~2 At%, when compared to UD/UT. Despite the increased oxygen presence, the ECA of DI water did not notably decrease for either plasma-treated samples.

However, the metal-oxide contamination on UD/PT60 also contributed to the total At% of oxygen. Next to that, as shown with Raman in Section 4.1.2, ASPN formed an 'a-C'-like compound on the surface which likely consisted of polyene and some aromatic bonds. The formation of this 'a-C'-like compound could explain why there was no significant reduction in the ECA of DI water after ASPN, despite the notable introduction of nitrogen. The π-electrons in the carbon-carbon double bonds can move freely along the conjugated system, which results in a resonance structure where the π-electrons are delocalized (Batsanov, 2022; Wei et al., 2016). This delocalization of electrons leads to a relatively uniform distribution of electron density, and this diminishes the dipole moment. Thus, although oxygen/nitrogen-containing functional groups generally introduce polarity, the impact is typically more pronounced in aliphatic compounds where the electron density is not spread out across a conjugated system. Therefore, the a-C formed by ASPN may have prevented the expected hydrophilization of the surface from the introduced polar functional groups.

Using the ECAs, the solid surface free energy (γ_S; i.e., the summation of the polar and dispersive solid surface free energy components) was calculated using the Owens–Wendt method, which builds upon the Fowkes theory and the Young equation as discussed in Section 3.2.8. Using the Owens–Wendt method, the solid polar (γ_S^P) and dispersive (γ_S^D) surface free energy components were determined following:

$$\sqrt{\gamma_S^D} = \frac{\gamma_{L2}(\cos\theta_{L2}+1) - \sqrt{\gamma_{L2}^P/\gamma_{L1}^P}\gamma_{L1}(\cos\theta_{L1}+1)}{2\left(\sqrt{\gamma_{L2}^D} - \sqrt{\gamma_{L2}^P(\gamma_{L1}^P/\gamma_{L1}^P)}\right)}, \qquad \textit{(Eq. 22)}$$

$$\sqrt{\gamma_S^P} = \frac{\gamma_{L1}(\cos\theta_{L1}+1) - 2\sqrt{\gamma_S^D/\gamma_{L1}^D}}{2\sqrt{\gamma_{L1}^P}}, \qquad \textit{(Eq. 23)}$$

where $\gamma_{L1/L2}$ refers to the liquid surface free energy components of the DI water and diiodomethane, respectively, as previously presented in Section 3.2.8; and $\theta_{L1/L2}$ refers to the ECA of the DI water and diiodomethane, respectively (Rudawska & Jacniacka, 2009).

Equation 22 needed to be performed first to determine γ_S^D before equation 23 could be performed, the results are displayed in Figure 77. As can be observed, the total solid surface free energy of the undoped samples increased with each subsequent treatment. At UD/UT and UD/PT60, the total solid surface free energies were almost entirely composed of the dispersive solid surface free energy components (i.e., for 99.77% and 98.70%, respectively), displaying a total solid surface free energy of 25.34 and 37.20, respectively. After the immobilisation of '*KR-12*' onto the UD/PT60 sample surface, the solid surface free energy showed a roughly two-fold increase to 62.90 and was predominantly composed of the polar solid surface free energy component (i.e., for 56.75%). On the other hand, the total solid surface free energy of the doped samples decreased after the ASPN treatment, showing a reduction from 50.17 at D/UT to 30.49 at D/PT60. Similar to the undoped samples, the solid surface free energy was almost entirely composed of the dispersive solid surface free energy component, only showing 1.39% contribution of the polar solid surface free energy component at D/UT and 0% for the other two samples (i.e., D/PT60 and D/PT60-(KR-12)). As was established previously, the immobilisation of 'KR-12' was not successful on D/PT60 and the solid surface free energy also remained almost identical, displaying a total solid surface free energy of 31.95.

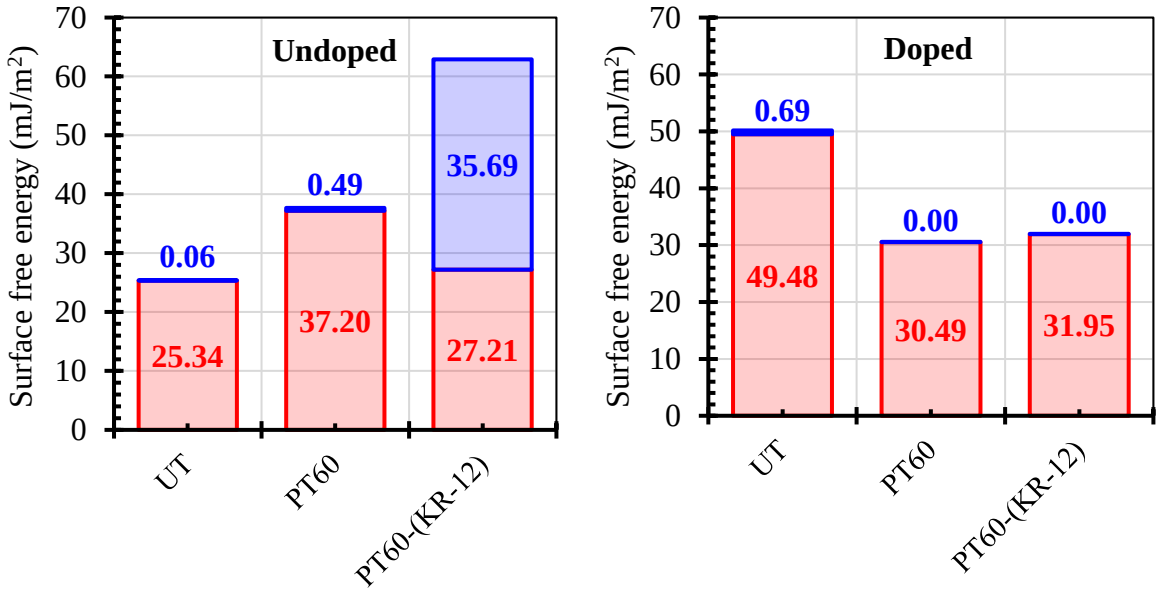


Figure 77. Surface free energy for the (left) undoped and (right) doped sample series, showing the separated (**red**) dispersive and (**blue**) polar surface energy components which stack to form total the surface free energy.

Next to the surface free energy values itself, the corresponding wettability envelopes following the Owens–Wendt method were also plotted (Owens & Wendt, 1969). The wettability envelopes provide a 2D visual representation of the polar and dispersive components rewritten in a polar coordinate system, following:

$$\gamma_L^D = R\ \cos\Phi\,, \qquad \textit{(Eq. 24)}$$

$$\gamma_L^P = R\ \sin\Phi\,, \qquad \textit{(Eq. 25)}$$

$$R = \left[\left(\frac{2}{1+\cos\theta}\right)\left(\frac{\sqrt{\gamma_S^P\ \sin\Phi} + \sqrt{\gamma_S^D\cos\Phi}}{\cos\Phi + \sin\Phi}\right)\right]^2, \qquad \textit{(Eq. 26)}$$

where R is the radial coordinate calculated over the angle (Φ) from 0° to 90°, θ can be any given theoretical CA to produce the respective isoline (Nanoscience Instrument, 2020). By repeating this calculation for various contact angles, a wetting envelope contour plot can be generated. The wetting envelope contour plots for the UHMWPE-based sample surfaces investigated in this work are shown in Figure 78. Next to that, various commonly observed probing liquids were also plotted in the wetting envelopes, to predict the corresponding ECA on the UHMWPE-based sample surfaces (Nanoscience Instrument, 2020).

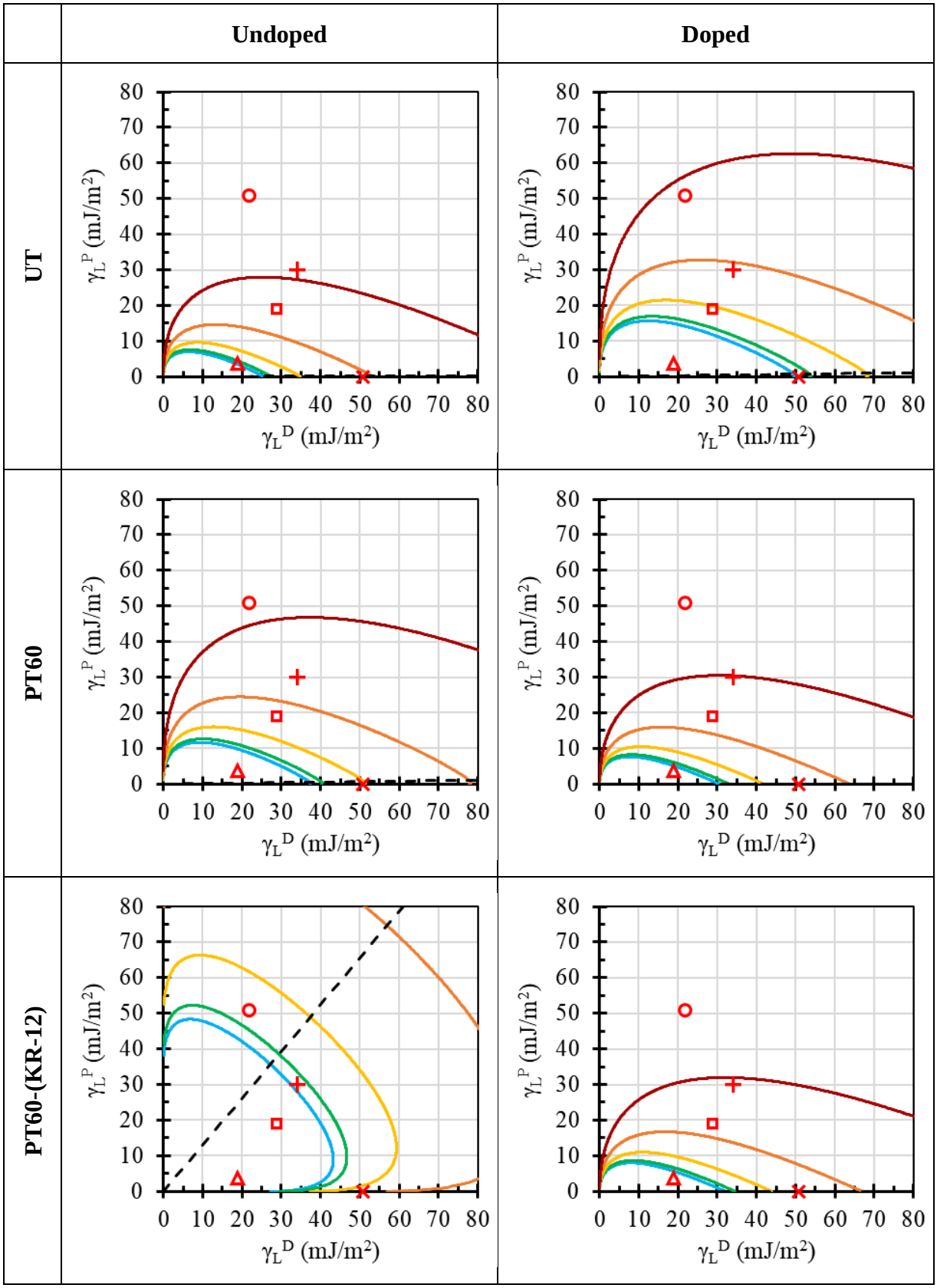


Figure 78. Wettability envelopes for the (left) undoped and (right) doped samples, the solid isolines depict the contact angles of (**blue**) 0°, (**green**) 22.5°, (**yellow**) 45°, (**orange**) 67.5°, and (**red**) 90°; the symbols represent various commonly used probing liquids, namely: (**circle**) DI water, (**square**) ethylene glycol, (**triangle**) ethanol, (**cross**) diiodomethane, and (**plus**) glycerol – the dashed black line depicts the P/D ratio (i.e., $\gamma_L^P/\gamma_L = \gamma_S^P/\gamma_S$).

4.2. Raman mapping of UHMWPE-based samples

Raman mapping was used to determine the spatial distribution/localisation of the crystallinity, ratios related to the molecular orientations, and component presence (i.e., a-C and αTH indices) as previously done in Section 4.1.2 for the single-point spectra. Due to the substantially lower signal-to-noise ratio observed with the short acquisition time, PCA-based noise reduction was used to improve the spectral quality as was demonstrated in Section 3.2.3. The image-related pixel spectra were fitted with the previously established peak models from Section 4.1.2, throughout the peak fitting of the pixel spectra, the αTH components were kept area-constrained to each other but the UHMWPE and a-C components were kept unconstrained. To calculate the properties/ratios, the components from the peak fitted pixel spectra were transformed into component-based images and used for further calculations, an example for the UHMWPE components within the UD/UT image is shown in Figure 79. All presented Raman images are 1 x 1 mm measured with a 100 x 100 pixel grid, see section 3.2.3.

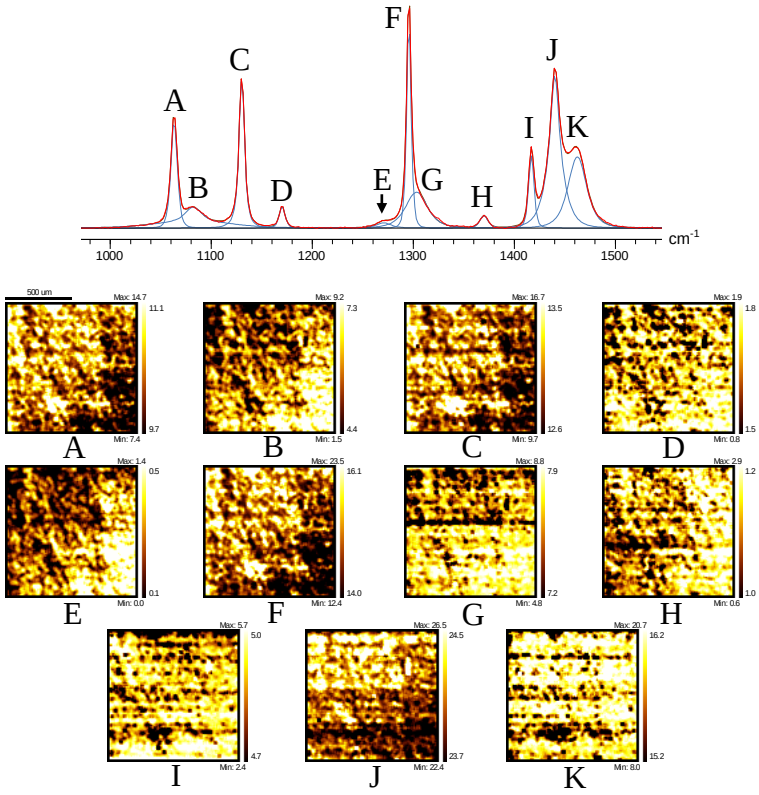


Figure 79. Example of (top) UD/UT spectral peak fit and (bottom) component-based Raman images.

Prior to discussing the results of the Raman mapping, it is worth to recognise that the shorter acquisition time impacted the observed results (i.e., 100 ms was used for the image-related pixel spectra, 10,000 ms was used for the single-point spectra). The reduction of the acquisition time also reduced the laser penetration depth as it had less time to penetrate the sample, reducing the total analysis volume and the corresponding observed signal intensities. The exact penetration depth with the imaging was not known, but clearly less than estimated previously for the single-point spectra (i.e., <10.11 μm). Where applicable, the results were compared to those from the single-point spectra, see Section 4.1.2 for more information.

4.2.1. Crystallinity maps

The crystalline, amorphous, and interfacial fractional phase contents of the UHMWPE-based samples were estimated with Equations 15-18, the same equations that were used for the single-point spectra as shown in Section 4.1.2 (Affatato et al., 2013; Glotin & Mandelkern, 1982; Medel et al., 2009; Rull et al., 1993; Strobl & Hagedorn, 1978). The observed phase contents based on the Raman images for all the UHMWPE-based samples are shown in Figure 80. The corresponding Raman images of the individual phase contents for the undoped and doped sample series are shown in Figure 81 and 82, respectively.

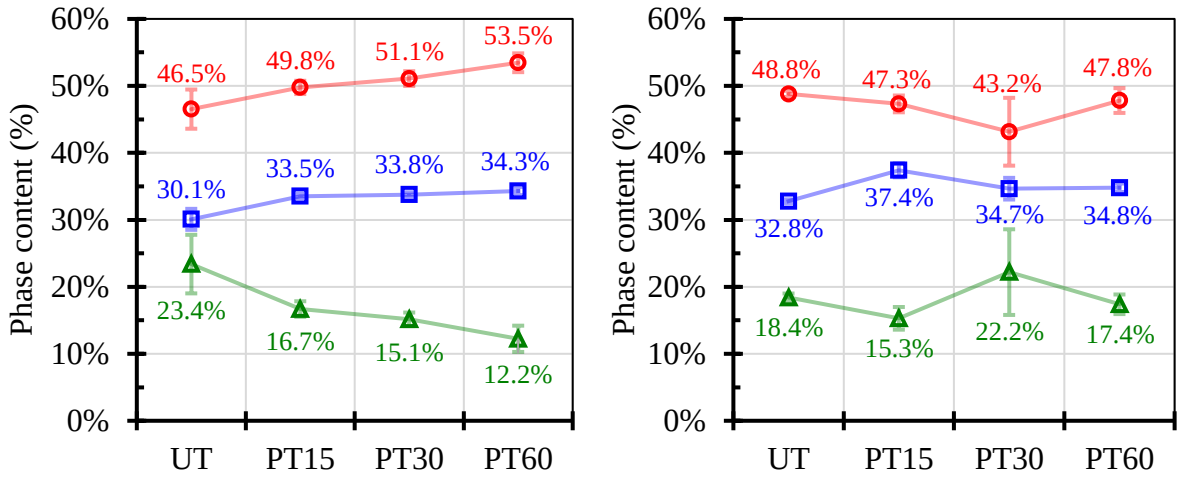


Figure 80. Graph displaying the phase content of the (**red**, squares) crystalline, (**blue**, circles) amorphous, and (**green**, triangles) interfacial phase in the (left) undoped and (right) doped UHMWPE-based sample series, as determined by the individual peak fits; the three phases stack up to a total of 100%.

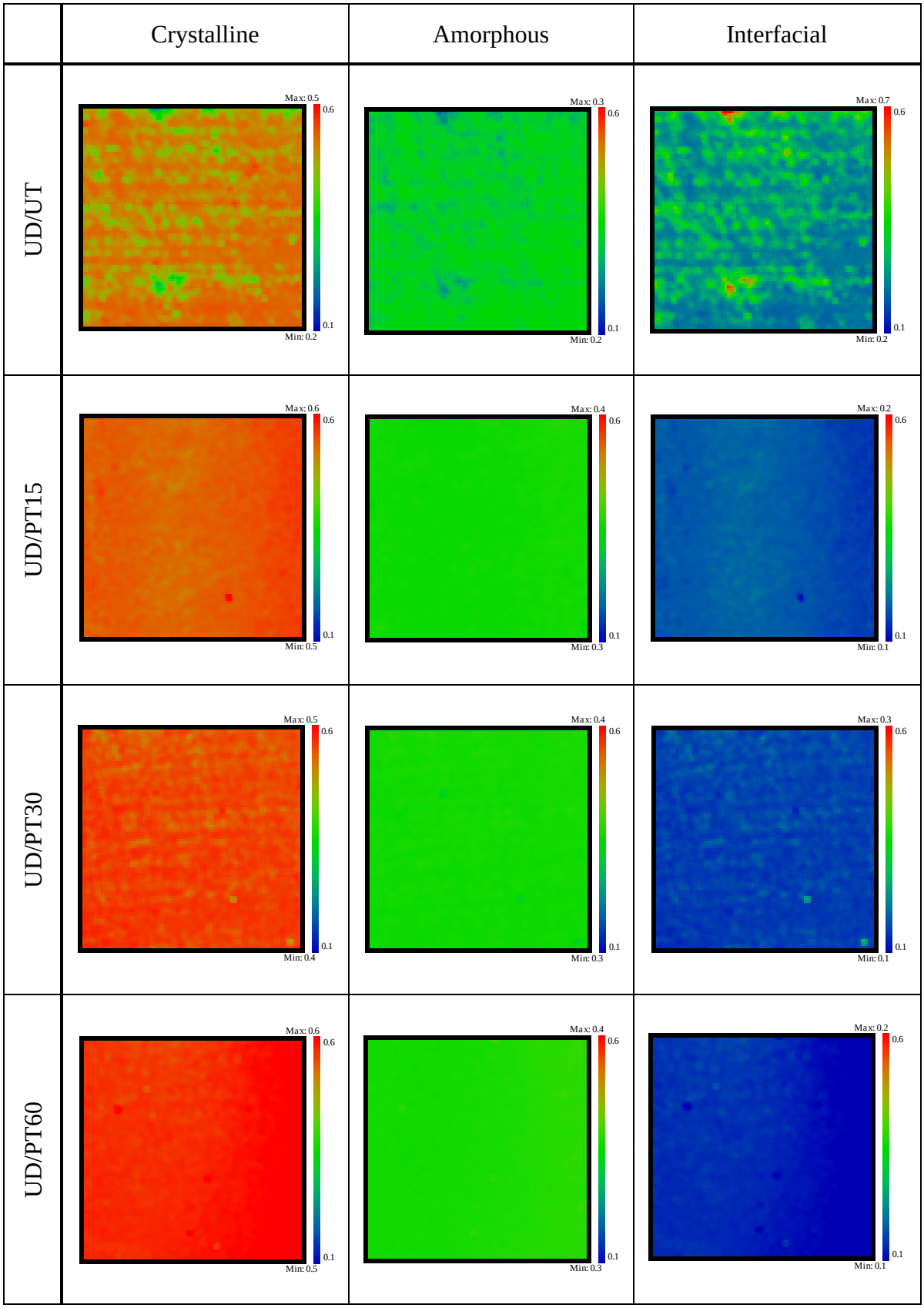


Figure 81. Raman images of the crystalline, amorphous, and interfacial fractional phase content for the undoped sample series. The presented colour scale was the same for every image, displaying the respective fractional phase content between 0.1 and 0.6.

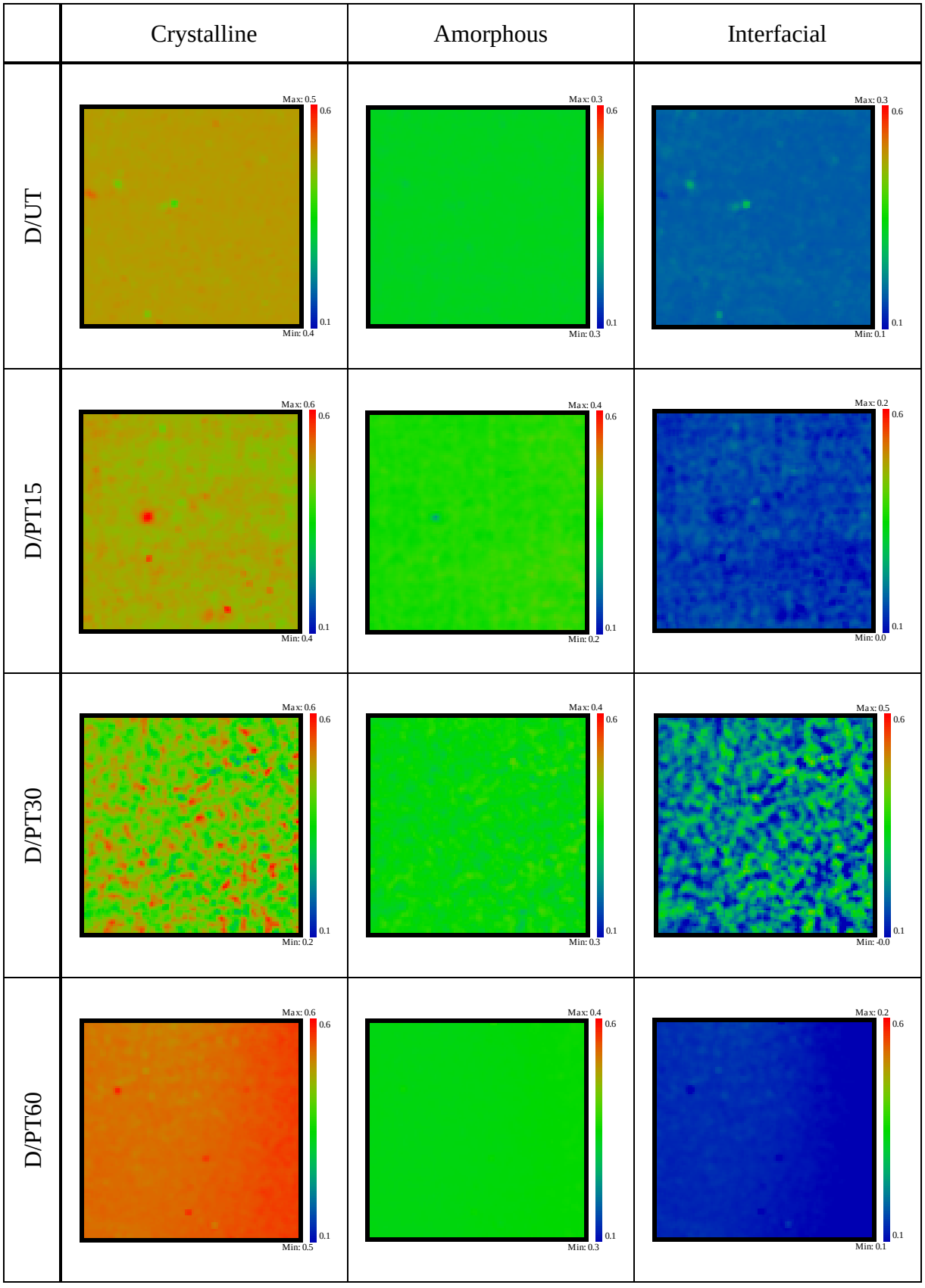


Figure 82. Raman images of the crystalline, amorphous, and interfacial fractional phase content for the doped sample series. The presented colour scale was the same for every image, displaying the respective fractional phase content between 0.1 and 0.6.

The crystallinity determined with the Raman images displayed a larger range than the single-point spectra, the images showed a crystalline phase content between 43 to 53% whilst the single-point spectra ranged between 46 and 50%. However, similar to what was observed with the single-point spectra, the crystallinity showed to increase for the undoped UHMWPE-based samples and slightly decreased for the doped sample series. Regarding the undoped sample series, the crystalline phase content showed a presence of 46.5% at UD/UT and continually increased over the ASPN treatment time to 53.5% at UD/PT60. On the other hand, the doped sample series started with a crystalline phase content of 48.8% at D/UT and initially decreased to 43.2% at D/PT30 but increased again to 47.8% for D/PT60. However, it is worth to note that D/PT30 showed the highest deviation, ranging between a minimum of 20.8% and a maximum 60.4% crystalline phase content across the individual image pixel spectra.

The amorphous phase content showed the least amount of change in the Raman images but was notably lower than with the single-point spectra, the images showed an amorphous phase content between 30 to 37% whilst the single-point spectra ranged between 40 and 47%. The undoped sample series displayed an increase of about 4% in the amorphous phase content, which started at 30.1% for UD/UT and increased to 34.3% for UD/PT60. The amorphous phase content for the doped sample series remained similar, showing 32.8% at D/UT and increased to 34.8% at D/PT60. Due to the relatively low amount of amorphous phase content, the Raman images showed significantly more presence of the interfacial phase content when compared to the single-point spectra. The interfacial phase content ranged between 12 to 23% with the images whereas the single-point spectra this was between 5 to 13%. For the undoped sample series, the interfacial phase content decreased over the ASPN treatment time from 23.4% at UD/UT to 12.2% at UD/PT60, which was mostly attributed to the increased crystallinity. In contrast, the interfacial phase content for the doped sample series was more comparable over the treatment time, which started at 18.4% at D/UT and decreased to 17.4% at D/PT60.

4.2.2. Molecular orientation

The four ratios related to the molecular orientation of UHMWPE were estimated the same as was done for the single-point spectra, see Section 4.1.2 for the respective ratios. As a reminder, Ratios I and II evaluated the increasing ordering of the PE chains due to crystalline lamellar (re)orientation, Ratio III provided insight into the orientation of the amorphous phase, and Ratio IV evaluated overall chain (re)orientation (in both the crystalline and amorphous phase) (Affatato et al., 2013; Kurelec et al., 2000; Pigeon et al., 1991; Reggiani et al., 2006). The observed ratios based on the Raman images for all the UHMWPE-based samples are shown in Figure 83. The Raman images of the individual ratios for the undoped and doped sample series are shown in Figure 84 and 85, respectively.

Ratio I showed to increase over the total ASPN treatment time for both UHMWPE-based sample series. The undoped sample series increased from 0.123 at UD/UT to 0.133 at UD/PT60 and the doped sample series from 0.116 at D/UT to 0.123 at D/PT60, both indicated an increase in orthorhombic content. However, it is worth to remember that the bands used for Ratio I (i.e., 1440 and 1460 cm^{-1}) may be influenced by FR. Ratio II also showed an increasing trend over the total ASPN treatment time for both sample series, but the increase was notably higher for the undoped sample series. The undoped sample series increased from 0.327 at UD/UT to 0.425 at UD/PT60 and the doped sample series from 0.378 at D/UT to 0.413 at D/PT60, showing an increase in the orthorhombic content like was observed with Ratio I.

Ratio III was found to decrease for both sample series over the total ASPN treatment time, although this was more notable for the undoped sample series. The undoped sample series decreased from 2.290 at UD/UT to 1.186 at UD/PT60, whilst the doped sample series decreased from 1.373 at D/UT to 1.103 at D/PT60, which indicated a decrease in the amount of *trans-gauche* defects within the amorphous phase. Finally, Ratio IV remained practically the same for the undoped sample series and slightly decreased for the doped series over the total ASPN

treatment time. The undoped sample series increased from 1.253 at UD/UT to 1.275 at UD/PT60 and the doped sample series decreased from 1.320 at D/UT to 1.245 at D/PT60, which indicated a potential gain and loss in the Young's modulus, respectively.

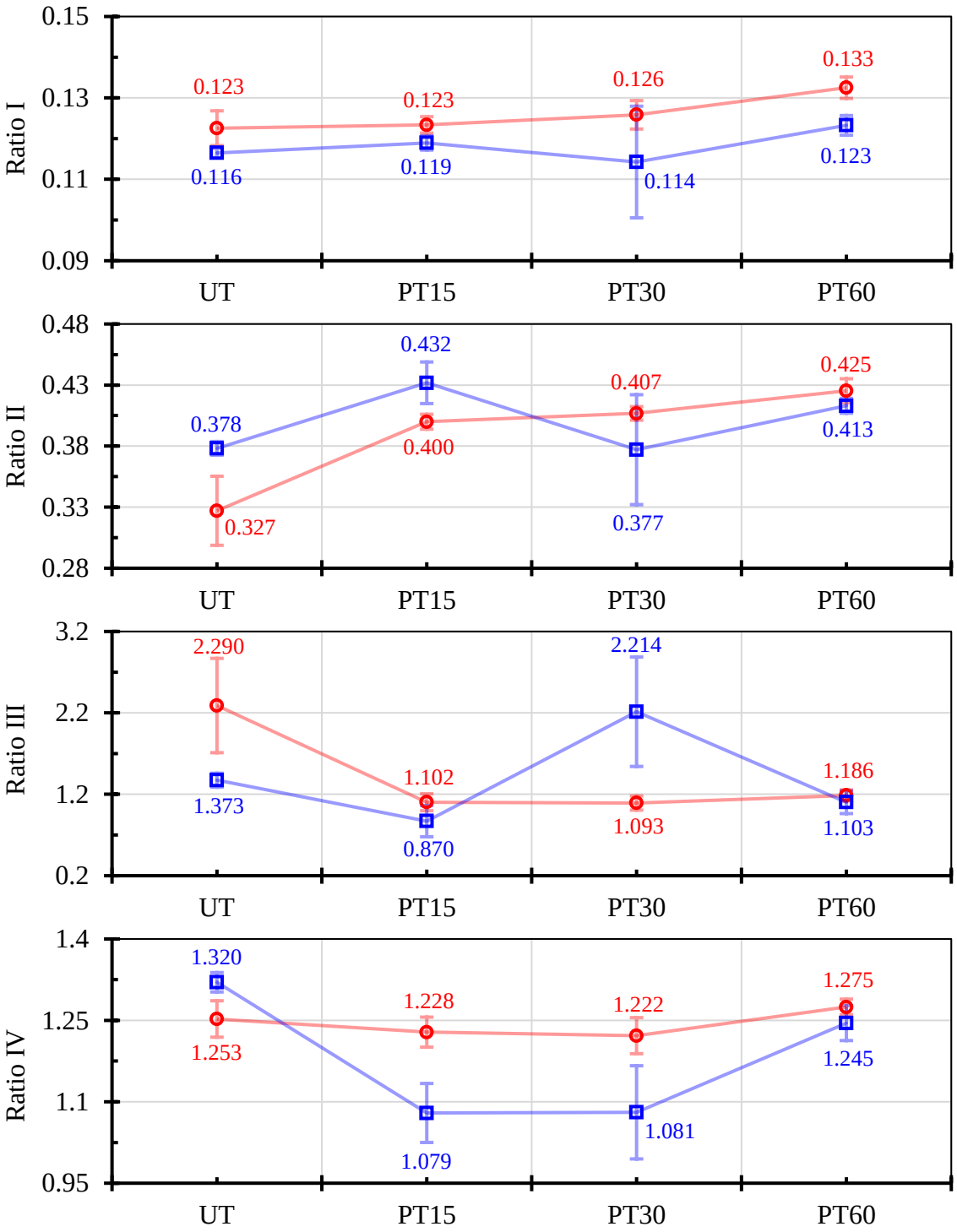


Figure 83. Ratios I-IV as determined by the individual peak fits of the (**red**, circles) undoped and (**blue**, squares) doped UHMWPE-based samples.

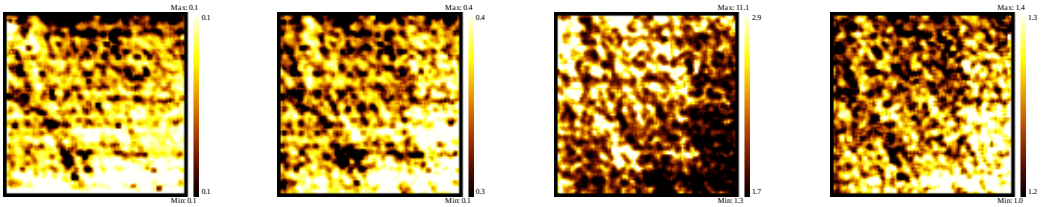
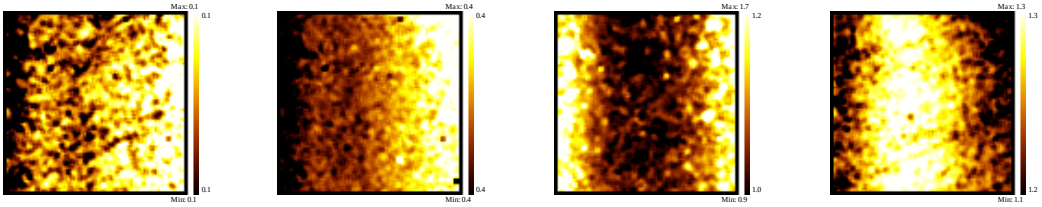
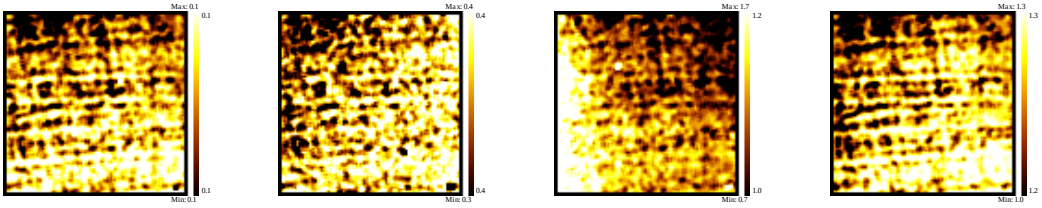
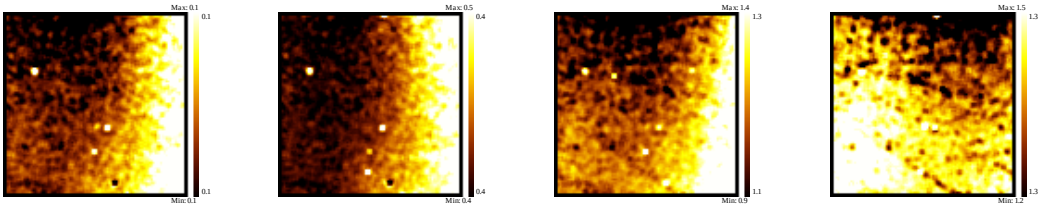
	Ratio I	Ratio II	Ratio III	Ratio IV
UD/UT				
UD/PT15				
UD/PT30				
UD/PT60				

Figure 84. Raman images of the ratios related to the molecular orientation for the undoped sample series. The colour scales are auto-scaled to display the highest amount of contrast, the intensities are not comparable.

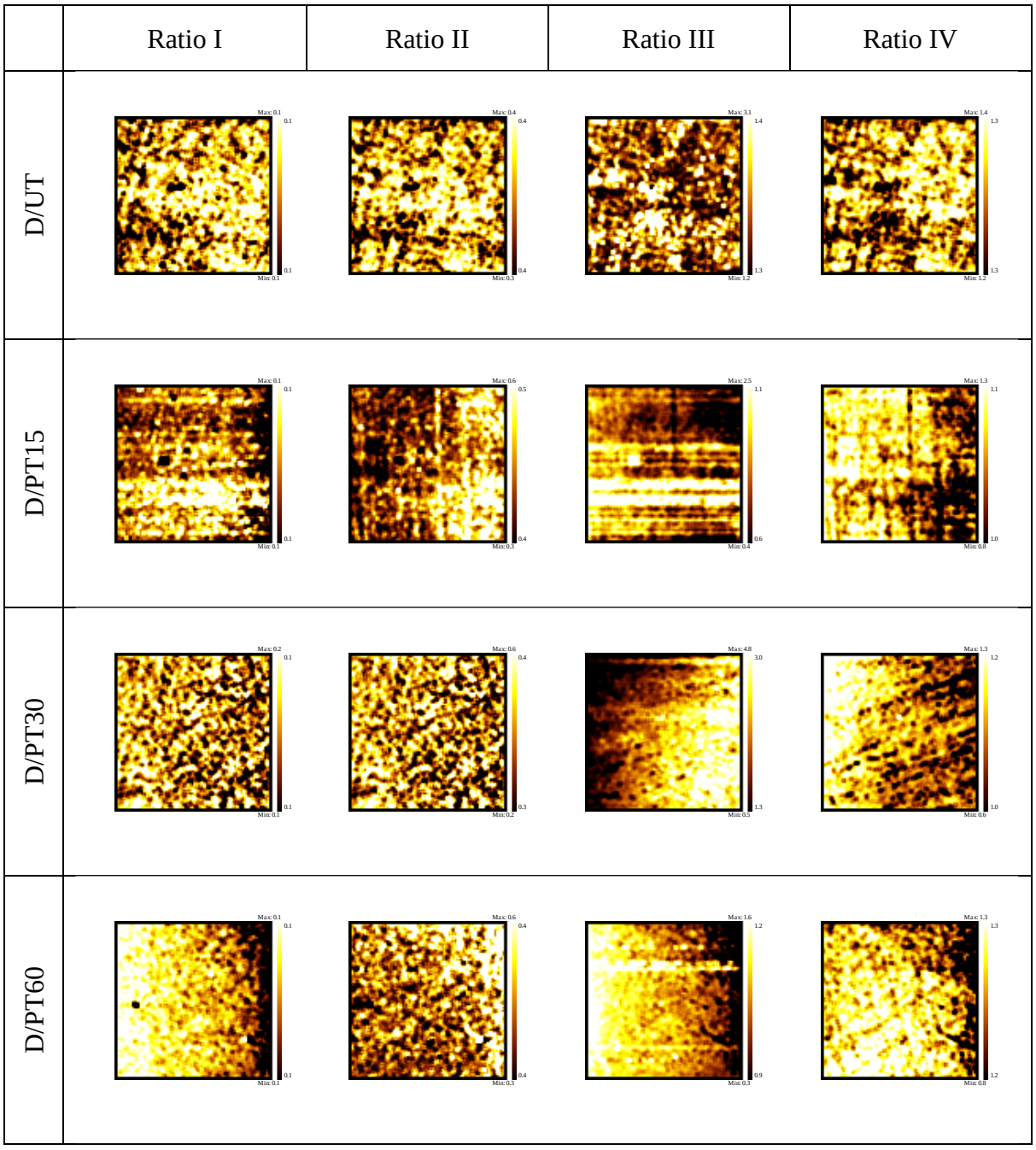


Figure 85. Raman images of the ratios related to the molecular orientation for the doped sample series. The colour scales are auto-scaled to display the highest amount of contrast, the intensities are not comparable.

4.2.3. Presence and localisation of αTH and a-C in the UHMWPE matrix

The Raman images displayed a prominent presence of the a-C components, likely as a higher amount of a-C was formed closer towards the surface which was revealed by the shorter laser penetration depth. The 'D' band at 1335 cm^{-1} of a-C was not observed in the single-point spectra (see Section 4.1.2), which initially indicated that no aromaticity was present. However, as can be observed in Figure 86, the summed pixel spectra of the doped sample series clearly showed the presence of the 'D' band. When overlaying the synthetic envelope of the peak fitted 'a-C'-like components within D/PT60 with the spectrum of a-C itself (normalised over the 'G' band at 1588 cm^{-1}), the relative band intensities for the formed 'a-C'-like components in D/PT60 were lower at (X) 1200, (D) 1335, and (O) 1721 cm^{-1} and slightly higher at (A) 1486 cm^{-1}. These results confirmed that the ASPN introduced π-stacked aromatic systems (partially disordered, as evident from the 'D' band), but only closer towards the surface. Next to that, in some pixel spectra, a low-intensity band was observed at 1640 cm^{-1} in addition to the a-C components (not shown here). In the literature, the band at 1640 cm^{-1} is ascribed to mixed sp^2/sp^3 olefinic defects in carbon-rich systems (i.e., damaged diamond-like carbon or graphite), which likely arose due to the transformation of the PE chains to a-C (Khomich et al., 2019).

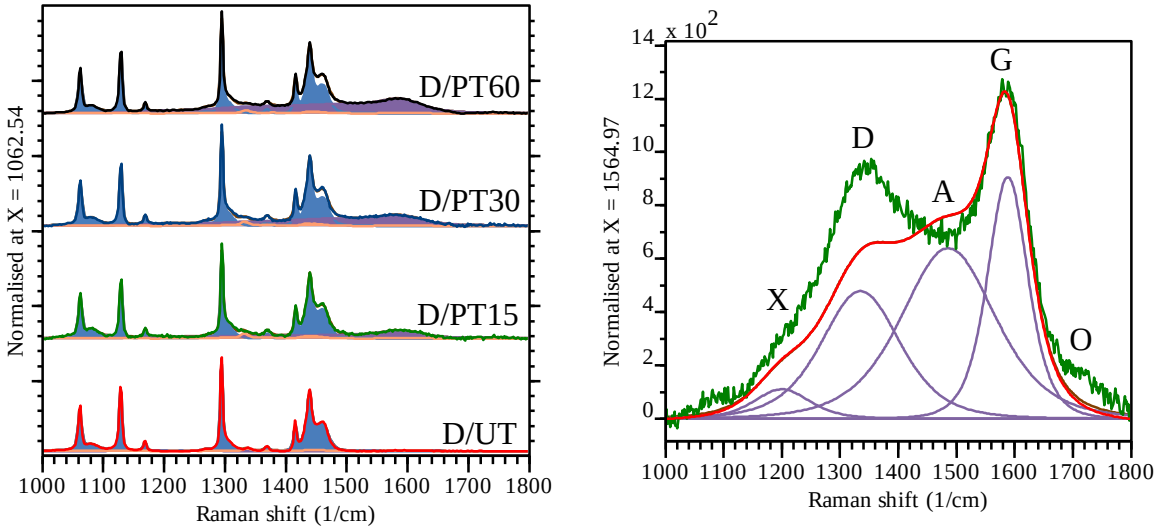


Figure 86. The (left) peak fitted summed pixel spectrum of the undoped sample series, showing the (**blue**) UHMWPE, (**orange**) αTH, and (**purple**) a-C components; and (right) the (**red**) synthetic envelope of the a-C components within the D/PT60 summed pixel spectrum overlayed with the unfitted spectrum of (**green**) a-C.

Next to the a-C and αTH indices that were calculated as was shown previously in Section 4.1.2, an oxidation/wear-related index (OI) was also established following:

$$OI = e^{(1.19 \tan\left(14.26\left(\frac{I_{1416}}{I_T} - 0.26\right)\right) - 0.13)}, \qquad \textit{(Eq. 27)}$$

this equation is the result of a phenomenological relationship established through FTIR and Raman analysis of a series of oxidized UHMWPE samples (Kumakura et al., 2009). The observed a-C, αTH and OI indices based on the Raman images for all the UHMWPE-based samples are shown in Figure 87. The corresponding Raman images of the individual indices for the undoped and doped sample series are shown in Figure 88 and 89, respectively.

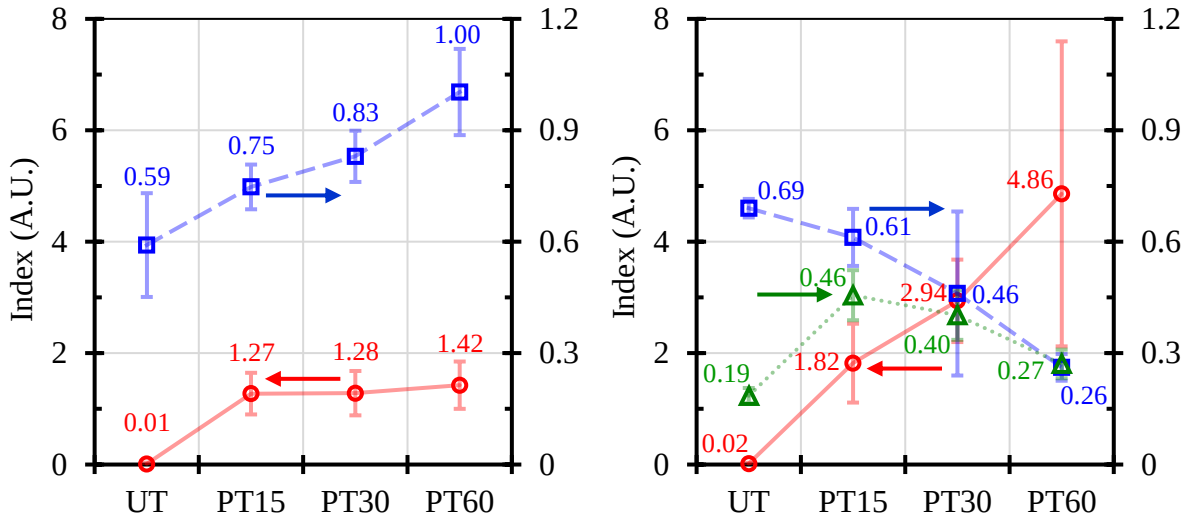


Figure 87. The (**red**, circles) a-C, (**blue**, squares) oxidation, and (**green**, triangles) αTH indices for the (left) undoped and (right) doped sample series.

As was already established from the spectra in Figure 86, the presence of a-C in the image-based pixel spectra was notably higher than what was observed in the single-point spectra. Following the calculated a-C index, the undoped sample series initially increased from 0.01 at UD/UT to 1.27 at UD/PT15 but subsequently only showed a minor increase over the remaining ASPN treatment time to 1.42 at UD/PT60. In contrast, the doped sample series showed a continuous increase over the ASPN treatment time, starting at 0.02 for D/UT and displayed a significant increase to 4.86 at D/PT60. Although the a-C indices for the undoped

and doped sample series were notably higher in the image-based pixel spectra, identical trends were observed with the single-point spectra.

The oxidation index showed an inverse trend between the undoped and doped sample series. The undoped sample series started at 0.59 for UD/UT and continually increased over the total ASPN treatment time to 1.00 for UD/PT60, whilst the doped sample series showed a continuous decrease over the total ASPN treatment time from 0.69 at D/UT to 0.26 for D/PT60. The decrease in the oxidation index observed with the doped sample series was attributed to the presence of αTH, especially as the undoped sample series did display an increase in the oxidation index. Lastly, the αTH index evaluated for the doped sample series showed a slight increase over the total ASPN treatment time, from 0.19 at D/UT to 0.27 for D/PT60. The αTH index determined from the image-based pixel spectra showed a smaller relative increase when compared to the single-point spectra (see Section 4.1.2).

As the 'D' band related to a-C was observed in the pixel spectra, the measure of disorder within the formed a-C as a result of amorphization and/or defects was evaluated as well. To determine the measure of disorder/amorphization, the area ratio between the 'D' and 'G' bands (i.e., I_{1335}/I_{1588}; I_D/I_G) was calculated, which is commonly done for carbon-rich systems as noted in the literature (Ferrari & Robertson, 2004). Typically, the disorder in (ordered) graphite increases as it transforms into nano-crystalline graphite, increasing the I_D/I_G ratio and corresponding position of the 'G' band from ~1580 to ~1600 cm^{-1}. Subsequently, as nano-crystalline graphite transforms into a-C, the I_D/I_G ratio decreases, as well as the corresponding position of the 'G' band from ~1600 to ~1520 cm^{-1}. Next to that, as nano-crystalline graphite transforms into a-C, the degree of amorphization and associated sp^3 content increases up to ~20%. Any higher amount of sp^3 content in a-C (i.e., between 20-80%) would indicate the formation of (ta-C) instead, this would also result in the disappearance of the 'D' band and an increase in the 'G' band position from ~1520 to ~1580 cm^{-1}.

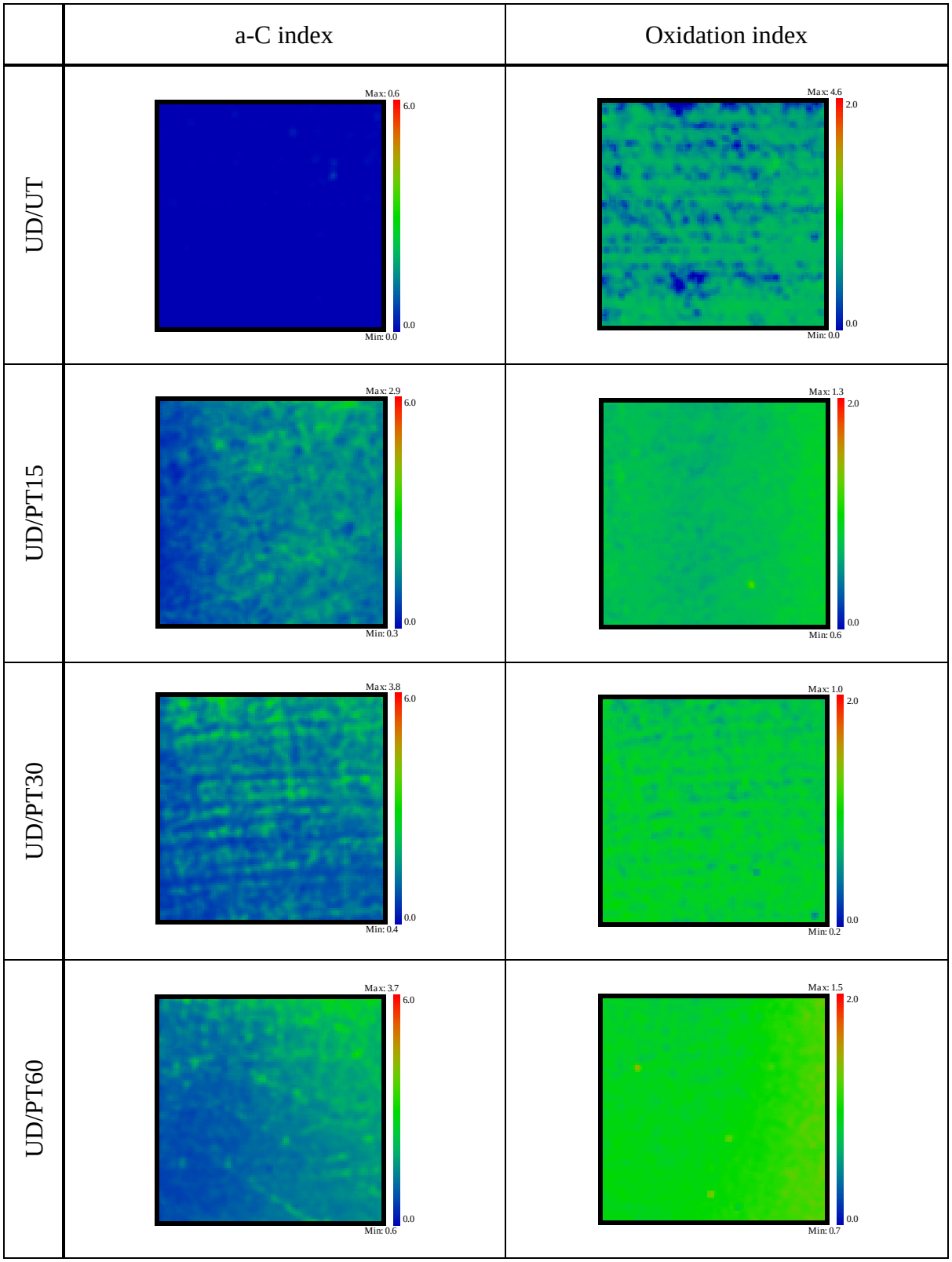


Figure 88. Raman images of the a-C index and oxidation index for the undoped sample series. The colour scale for the a-C index is between 0 and 6 and for the oxidation index between 0 and 2.

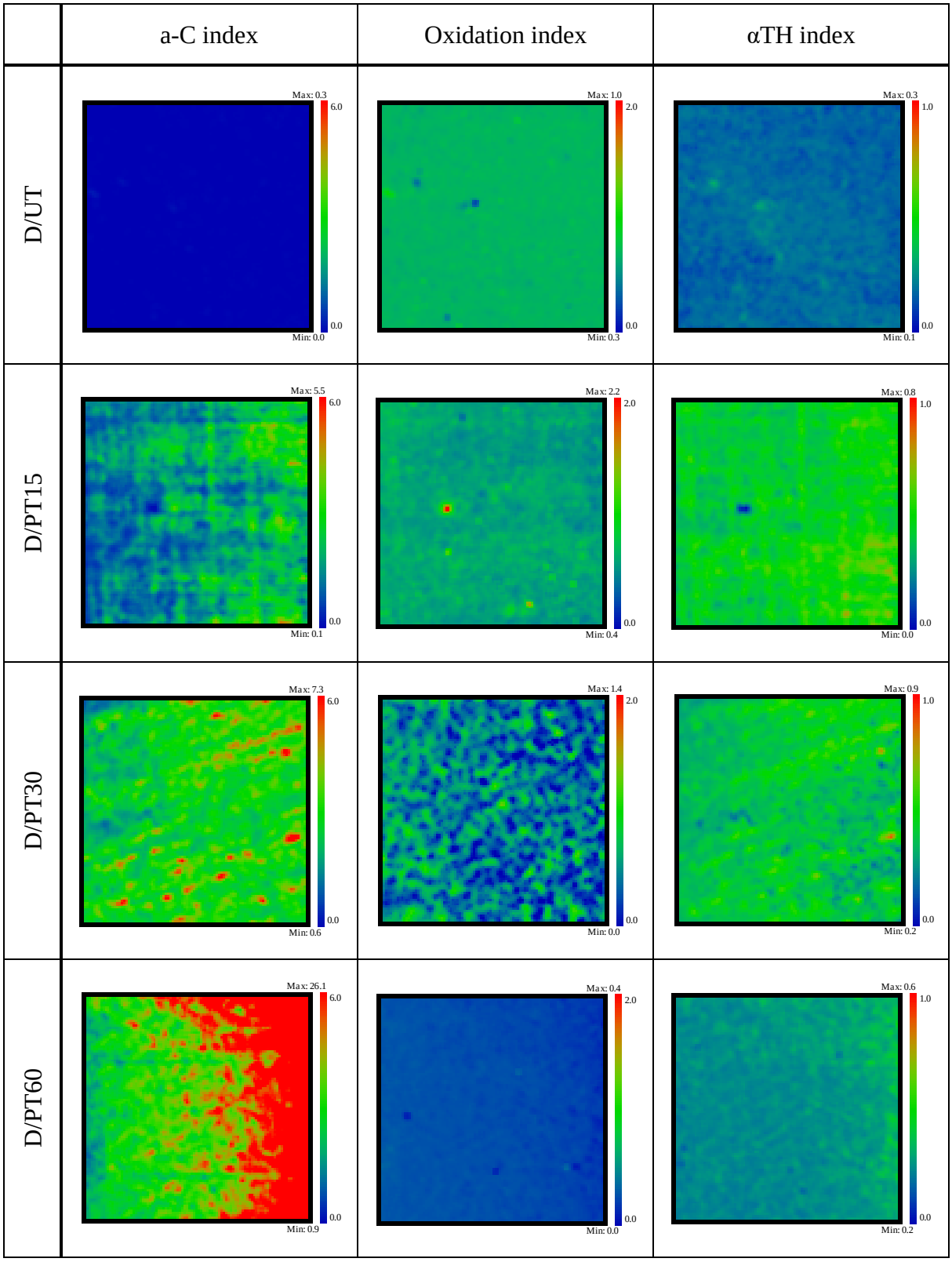


Figure 89. Raman images of the a-C index, oxidation index, and αTH index for the doped sample series. The colour scale for the a-C index is between 0 and 6, for the oxidation index between 0 and 2, and for the αTH index between 0 and 1.

Furthermore, the ratio between the graphitic (i.e., $I_{1335} + I_{1588;}\ I_{(D+G)}$) and polyene-related bands (i.e., $I_{1200} + I_{1486;}\ I_{(A+X)}$) was also evaluated (i.e., $I_{(A+X)}/I_{(D+G)}$), to investigate the ratio between aliphatic and aromatic [C=C] bonds. The calculated I_D/I_G and $I_{(A+X)}/I_{(D+G)}$ ratios for the UHMWPE-based sample series are shown in Figure 90. When evaluating these two ratios, it is worth to recognize the a-C index as previously presented in Figure 87. The I_D/I_G ratio for the undoped sample series started at 0.51 for UD/UT and increased to 1.75 for UD/PT60, whilst the doped sample series started at 0.16 for D/UT and increased to 1.03 for D/PT60. The higher ratio observed for the undoped sample series indicates it displayed a higher amount of disorder than the doped sample series. For the $I_{(A+X)}/I_{(D+G)}$ ratios, the undoped sample series started at 0.51 for UD/UT and increased to 3.36 for UD/PT60, whereas the doped sample series started at 0.00 for D/UT and increased to 2.62 for D/PT60. From this ratio, it was concluded that the undoped sample series showed a higher relative presence of aliphatic [C=C] bonds over aromatic [C=C] bonds, when compared to the doped sample series. Based on the literature and considering the I_D/I_G ratios, the 'G' band position at 1588 cm^{-1}, and the fact that the 'D' band was observed, the formed 'a-C'-like compound in this work appeared to be most likely a mixture of polyene, a-C, and aromatics (Ferrari & Robertson, 2004). However, this assumption neglects the influence of potential non-carbon substitutions.

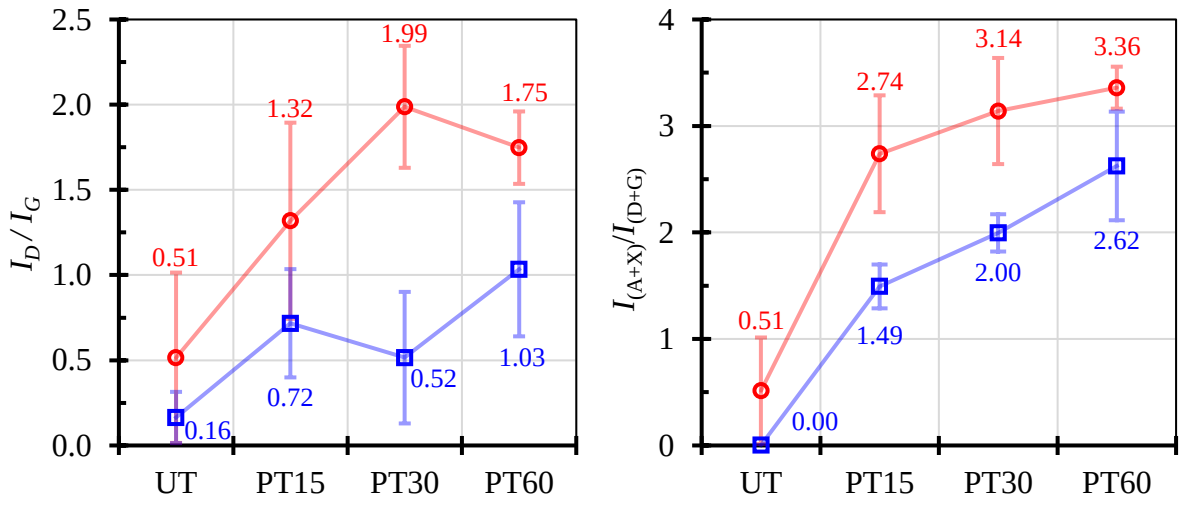


Figure 90. The (left) I_D/I_G and (right) $I_{(A+X)}/I_{(D+G)}$ ratios for the (**red**, circles) undoped and (**blue**, squares) doped sample series.

The formation of diamond-like carbon (DLC; i.e., the overarching category for a-C, ta-C, etc.) was also observed in the literature for UHMWPE, although in this case it was treated with nitrogen plasma immersion ion implantation (PIII) instead of ASPN (Marcondes et al., 2004). The PIII treatment was performed at 0.068 Pa, using pulses of 10 μs and at a frequency of 100 Hz, with a plasma density of 10^9 cm^{-3} and a plasma temperature of 5.0 eV for 30 minutes. These authors hypothesized that the crosslinking allows for reconstruction and/or reorientation of the crystalline lamellae, allowing the formation of the DLC layer, although no evidence was provided for this. Based on the results observed in this work, it was thought that the presence of the di-alkyl trans-vinylene bonds (as noted with FTIR, Section 4.1.1) allowed for the formation of the aromatic rings, which is also observed in the literature on the formation of zigzag-edged graphene nanoribbons from *trans*-polyacetylene (i.e., a polyene) (Jiang et al., 2009). This is similar to mechanisms like the Diels-Alder reactions observed for the formation of alkyl aromatics from olefins produced by thermal degradation of alkanes (Cypres, 1987).

Although the presence of a-C and αTH was established, it remained unknown which phase most likely allowed the formation of a-C and in what phase αTH was localised. To investigate this, the derivative of the UHMWPE phase content images and the a-C/αTH index images were overlayed, displaying the difference in the rate-of-change between the images. In short, the resulting images should display overlap if the phase/index changed concurrently or no overlap if they phase/index changed alternatively. As it was expected that a-C was formed from the PE chains, one would expect a reduction in the UHMWPE-related phase content as the a-C index increased and depleted another phase during its formation. Therefore, the image that displayed no/the least overlap was assumed to be the phase that a-C originated from. In contrast, αTH was freely present within the polymer matrix and its presence should have changed concurrently with the phase it was present in. Thus, the image that displayed the most overlap was the likely the phase αTH was present in. The overlayed derivative images related

to a-C for the undoped and doped sample series are shown in Figure 91 and 92, respectively, the derivative images related to αTH for the doped sample series are shown in Figure 93.

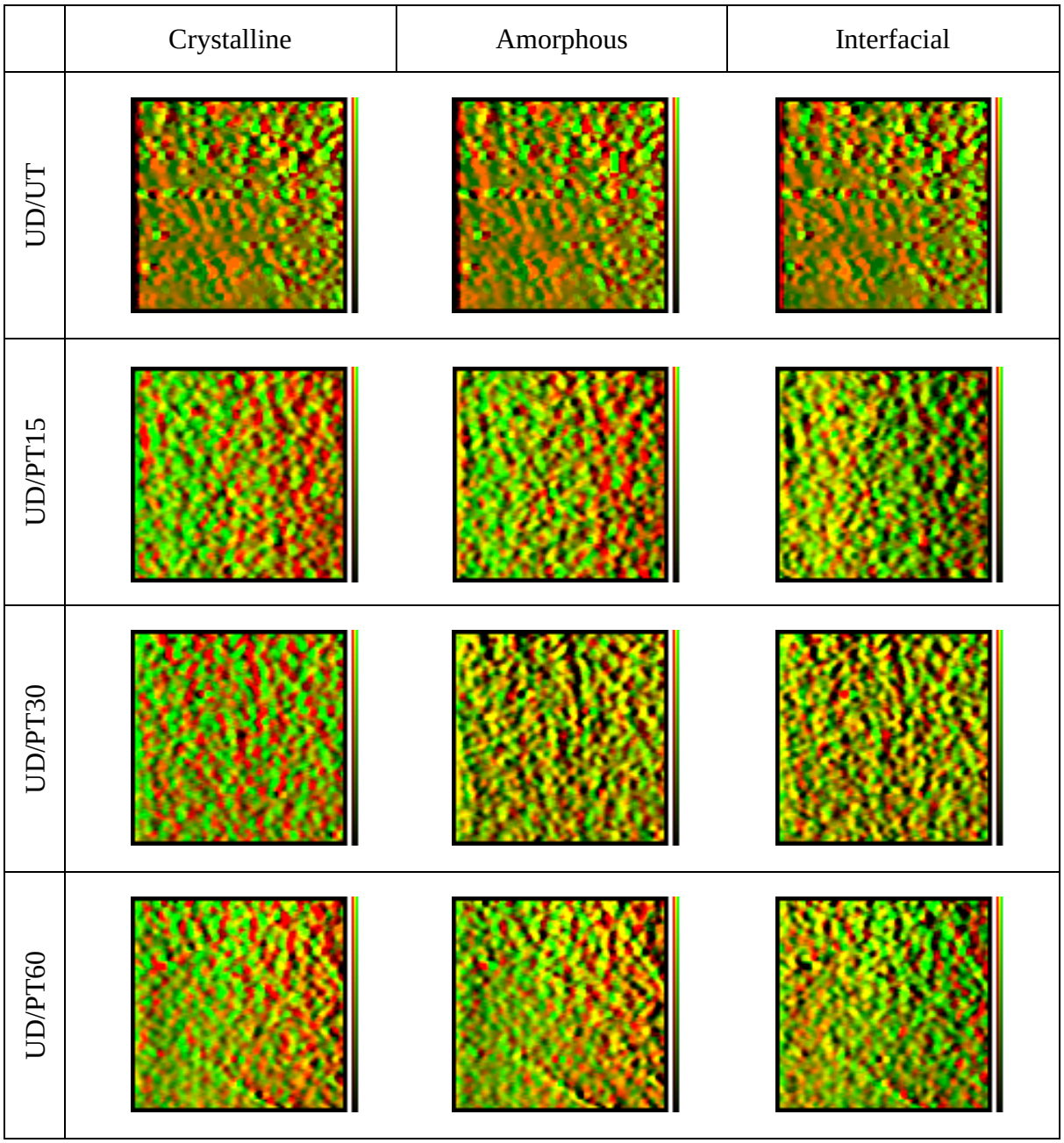


Figure 91. Derivative Raman images of the (**red**) respective UHMWPE-related phase contents overlayed with the (**green**) a-C index for the undoped sample series, overlap is observed by the yellow colour.

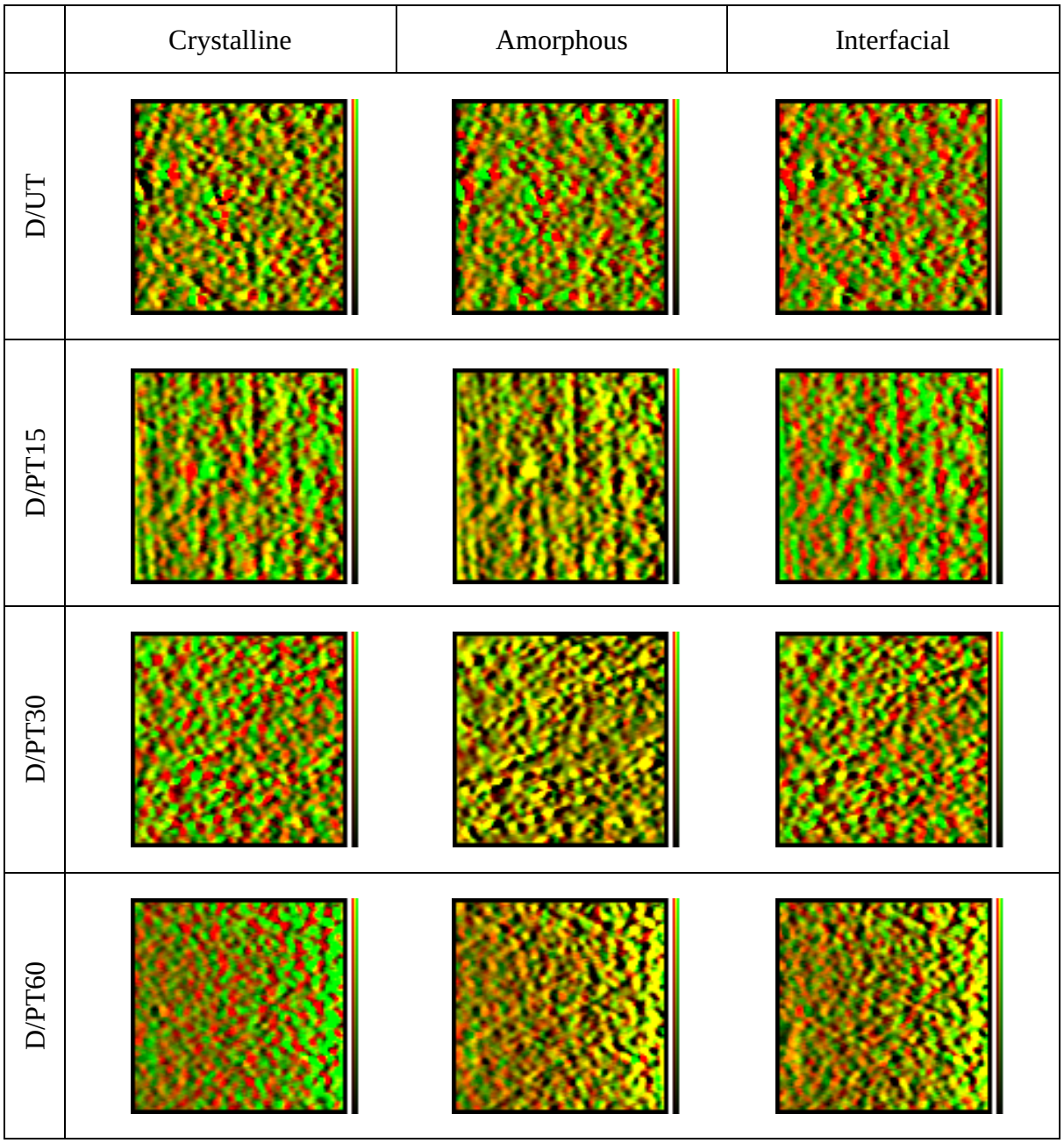


Figure 92. Derivative Raman images of the (**red**) respective UHMWPE-related phase contents overlayed with the (**green**) a-C index for the doped sample series, overlap is observed by the yellow colour.

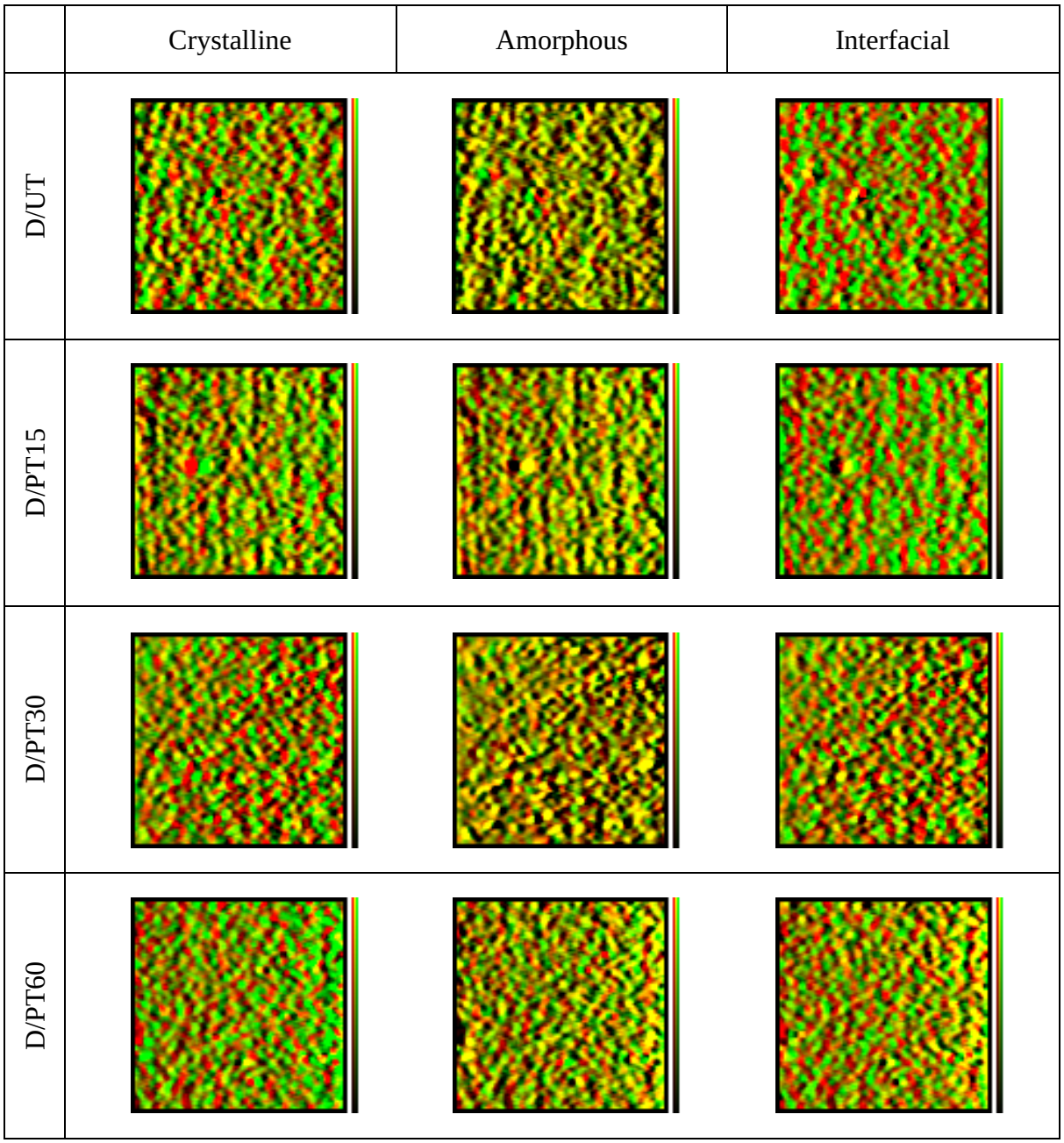


Figure 93. Derivative Raman images of the (**red**) respective UHMWPE-related phase contents overlayed with the (**green**) αTH index for the doped sample series, overlap is observed by the yellow colour.

To quantify the overlap between the derivative images, the yellow pixels from Figure 91 to 91 were counted in ImageJ (like how this was done for the SEM micrographs in Section 4.1.6), which provided insight into the overlap between the respective indices and the phase contents. When evaluating the overlap in the derivative images, it is important to be aware of the a-C/αTH indices as calculated in Figure 87, and of the fact that the derivative images may show overlap when 'y = 0' (i.e., a maximum in the original data). The fractional overlap related to a-C for the undoped and doped sample series are shown in Figure 94 and 95, respectively, the fractional overlap related to αTH for the doped sample series are shown in Figure 96.

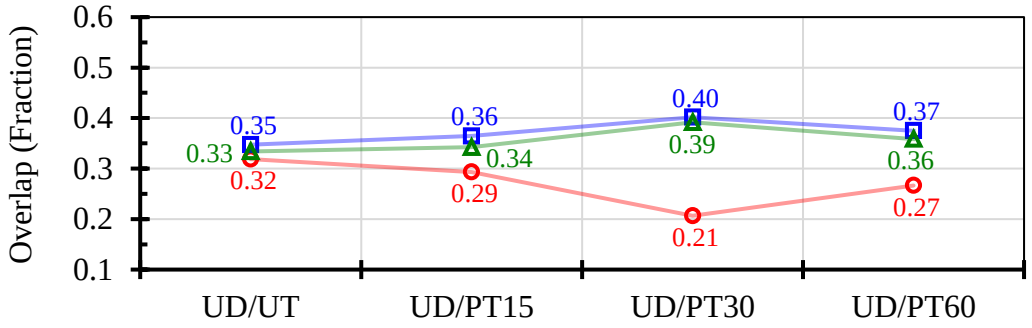


Figure 94. Fractional derivative overlap of the a-C index with the (**red**, circles) crystalline, (**blue**, squares) amorphous, and (**green**, triangles) interfacial phase content, for the undoped sample series.

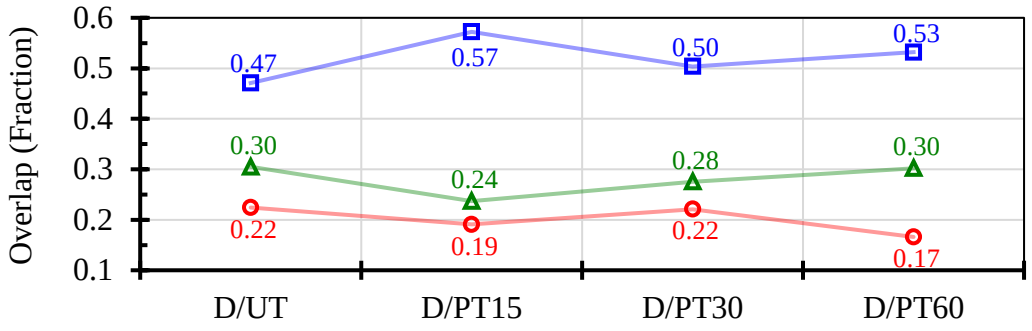


Figure 95. Fractional derivative overlap of the a-C index with the (**red**, circles) crystalline, (**blue**, squares) amorphous, and (**green**, triangles) interfacial phase content, for the doped sample series.

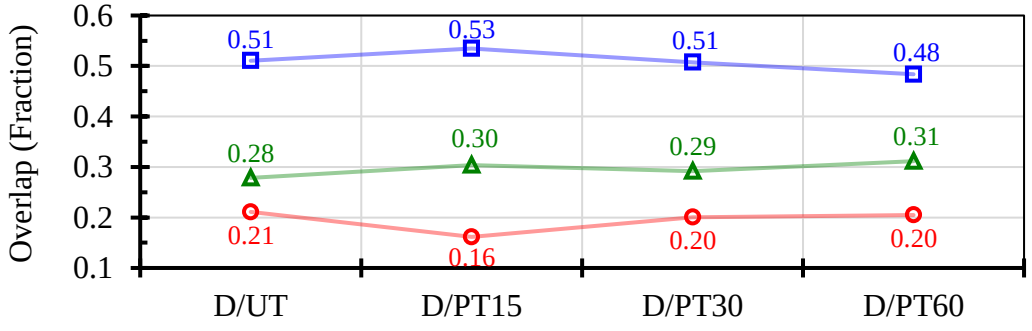


Figure 96. Fractional derivative overlap of the αTH index with the (**red**, circles) crystalline, (**blue**, squares) amorphous, and (**green**, triangles) interfacial phase content, for the doped sample series.

As can be observed in Figure 94 and 95, the derivative overlap of the a-C index for the undoped and doped sample series showed the most overlap with the amorphous phase and second-most with the interfacial phase. Therefore, all the derivative Raman images displayed the least amount of overlap between the a-C index and the crystalline phase. As discussed before, this indicated that the observed 'a-C'-like compound was most likely formed from the crystalline phase – assuming it would show a decrease in the crystalline phase content as it transformed into a-C and increased its corresponding index. As discussed previously, that the 'a-C'-like compound originated from the crystalline phase was also suggested in the literature on DLC formed on the UHMWPE surface after nitrogen PIII, but the derivative Raman images in this work provided more evidence on this (Marcondes et al., 2004).

The localisation of αTH in the doped samples was determined by evaluating the overlap between the derivative images of the αTH index with the UHMWPE-related phase contents, as displayed in Figure 96. The derivative of the αTH index showed minimal overlap with the crystalline phase, but a clear overlap was noted with the amorphous phase, and a partial overlap with the interfacial phase. This indicated that αTH was almost exclusively present within the amorphous phase of UHMWPE, which was expected considering it would have been improbable that a molecule the size of αTH would have been able to insert itself in the crystalline lamellae of UHMWPE without disrupting its tightly ordered structure. It has previously been hypothesized in the literature that αTH was retained within the amorphous phase of (UHMW)PE based on this assumption (Strandberg, 2006). However, this work visually displayed this phenomenon based on data with the use of Raman mapping.

4.3. Interpretation of complex UHMWPE-based surfaces using XPS

‖ This section is taken from my first-authored published work, specifically from section 3 in (Bruggeman et al., 2022), please see the 'Publications' section. ‖

The interpretation of XPS spectra of complex material surfaces, such as those obtained after surface plasma treatment of polymers, is typically confined by the available references. The limited understanding of the chemical surface composition may impact the ability to determine suitable coupling chemistries used for surface decoration or assess surface-related properties like biocompatibility. In this section, XPS was used to investigate the chemical composition of the various UHMWPE-based surfaces. Through *ab initio* orbital calculations and by employing Koopmans' theorem, the core-electron binding energies (CEBEs) were evaluated for a substantial number of possible chemical functionalities positioned on PE-based model structures. The calculated ΔCEBEs were used to develop a material-specific peak model suitable for the interpretation of merged high-resolution C 1s, N 1s and O 1s XPS spectra of PE-based materials.

4.3.1. Functionality evaluation

The functionalities considered during peak fitting of nitrogen and/or oxygen plasma-treated polymers vary in the literature but typically include: hydroxyl, ether/epoxide, carbonyl, acid/ester, amine, imine, nitrile, amide, and imide functional groups (Foerch et al., 1991; Grace et al., 2003; Kaklamani et al., 2010; Kauling et al., 2009; Paynter, 2000; Yasuda, 1976). However, this is not an exhaustive list of all the possible functionalities since the peak identification is based on comparison to the available reference materials and cannot always provide conclusive results. Furthermore, functionalities showing overlapping/closely positioned BEs are often grouped in the C 1s spectrum (e.g., assigning a single peak between 1-1.6 eV above the main hydrocarbon peak to all [C-O/N]-based functionalities) and are most often not further investigated by peak fitting the areas of their corresponding elemental regions.

Unfortunately, plasma-polymer surface reactions are not as well understood as pure plasma gas chemistries. Especially in the case of ASPN, where plasma is formed on the active screen instead of directly on the sample, the sample surfaces are mainly subjected to ion bombardment. Consequently, the ion bombardment of the surface can lead to electron-induced fragmentation and low-energy (i.e., ≤ 50 eV) electron-induced surface reactions (Arumainayagam et al., 2010). As ASPN was originally introduced as a treatment for metals, there is also little literature available on ASPN of polymers (C. X. Li, 2010). Additionally, the available literature focusses on changing surface-related physical/biological properties rather than determining the surface-related chemical changes that have occurred during the ASPN treatment (Kaklamani et al., 2010; C. X. Li & Bell, 2005). Therefore, a range of additional functionalities were evaluated to encompass more possible functionalities that may have formed during the plasma-chemical reactions – considering the presence of the polymer ($[CH_2]_n$) and at least three different gases (oxygen diffused within the polymer and the nitrogen-hydrogen working gas). The complete list of 50 different functionalities, their IDs, and additional visual structural information is available in Appendix D1.

4.3.2. Peak model assembly

To assemble the calculated peak model that was used during the high-resolution peak fitting, the calculated CEBEs were calibrated over the lowest observed CEBE per model structure, which showed an average of 304.97 ± 0.08 eV as calculated by HF and 279.45 ± 0.07 eV as calculated by wB97X-D ($\alpha = 0.0001$; $n = 50$). From here on, considering UHMWPE chains contain an average of 125,000 to 263,000 [CH_2] repeating units, all carbon shifts were considered relative to the averaged [CH_2] of the PE model structure ΔCEBE (i.e., [CH_{PE}]) as it was expected to be the most abundant functionality (Kurtz, 2015). Examples of various centred and end-chain model structures and their corresponding carbon ΔCEBEs are displayed in Figure 97, showing the structural differences in the model structures with an increasing number

of non-carbon atoms included. The calculated primary carbon shifts, nitrogen and oxygen shifts, and higher-order carbon shifts covering the full PE-based model structures are presented in Appendix D2, D3, and D4, respectively. On occasion, asymmetry in the estimated ΔCEBEs of the PE backbone in model structures with centred functionalities can be observed, this effect is due to long-range effects of the evaluated functionalities and is further discussed in Section 4.3.4. The simplified chemical structures and corresponding ΔCEBEs of the tocopherol-like components ([αTH], [αTQ], and [αTHQ]), are shown in Appendix D5.

4.3.3. Effect of functional group positioning

The effect of the functionality positioning on the calculated ΔCEBEs was investigated by taking the difference between the ΔCEBEs of end-chain and centred model structures. Within the literature, the effect of functionality positioning is rarely investigated during XPS analysis of modified polymers, and these structural differences are most often grouped during conventional peak fitting despite the clear differences in theoretical composition. Within the Beamson and Briggs reference database, a few experimentally observed ΔCEBE deviations due to a difference in functionality positioning were observed. As presented in Table 29, a comparison between the calculated (this work, as available in Appendix D2) and experimental (Beamson and Briggs reference database) ΔCEBEs of esters and carboxylic acids, as well as primary and secondary amides, show clear differences in the ΔCEBEs due to the functionality positioning. Both the calculated and experimental primary carbon ΔCEBEs were found to increase when the functionalities were in the end-chain positioning (i.e., carboxylic acid and primary amide) when compared to centred positioning (i.e., ester and secondary amide), showing a ΔCEBE increase of roughly 0.30 eV regardless of the functionality. The experimental ΔCEBEs showed a slightly higher deviation between the primary and secondary amide positioning when compared to the calculated ΔCEBEs. However, the calculated deviation for this functionality was still within the experimentally observed ΔCEBE range.

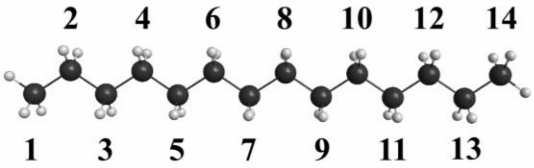
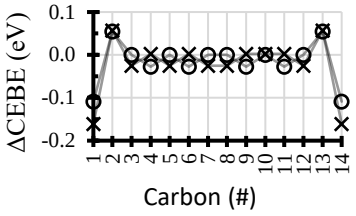
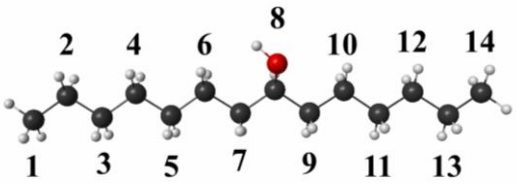
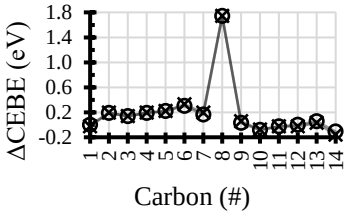
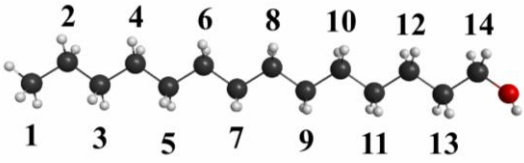
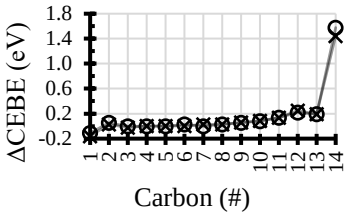
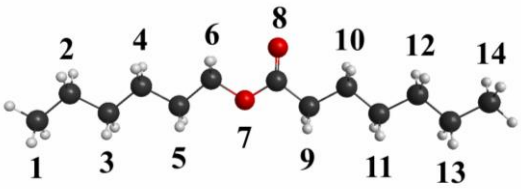
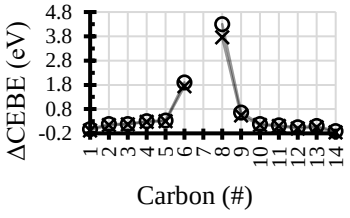
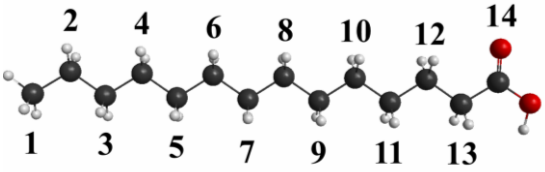
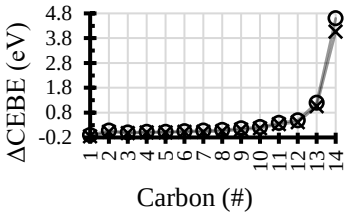
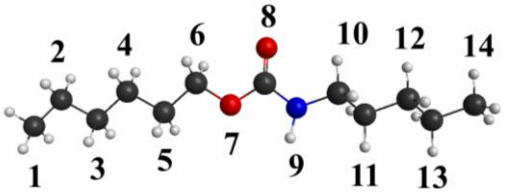
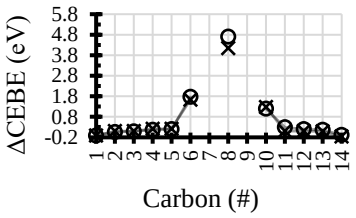
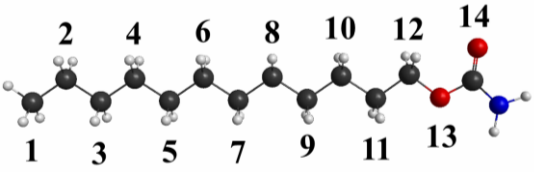
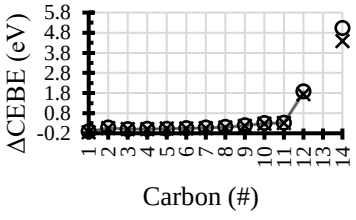
ID	3D Model structure	Carbon ΔCEBEs
CH_2 & CH_3*		
COH		
COH*		
O=COC		
O=COH*		
COC(=O)NHC		
COC(=O)NH_2*		

Figure 97. Examples of 3D model structures showing carbon (**black**), oxygen (**red**), nitrogen (**blue**), and hydrogen (light grey) atoms. The numbers refer to the plotted carbon ΔCEBEs relative to [CH_{PE}], as calculated by HF (circles) and wB97X-D (crosses).

At least one of the calculated ΔCEBEs involved in each functionality exceeds the resolution of state-of-the-art XPS instruments (i.e., > 0.1 eV) as shown in Appendix D6. Therefore, the calculated ΔCEBE differences were expected to be significant enough to allow differentiation between the positioning of functionalities during the high-resolution spectra peak fitting – especially in the case of functionalities with more than one non-carbon atom.

Table 29. Comparison between the calculated and mean experimental primary carbon CEBE deviations observed for esters/acids and primary/secondary amides in the literature (Hantsche, 1993). 'R' represents the different atom present in the centred or end-chain functionality, C or H, respectively.

	HF (eV)		**wB97X-D (eV)**		**Experimental (eV)**	
	O=COR	**O=CNHR**	**O=COR**	**O=CNHR**	**O=COR**	**O=CNHR**
Centred	4.30	3.41	3.76	2.91	3.99 ± 0.30	3.00 ± 0.02
End-chain	4.60	3.70	4.06	3.21	4.26 ± 0.10	3.45 ± 0.15
$\Delta_{\text{end-centred}}$	0.30	0.29	0.30	0.30	0.27	0.45
$\Delta_{\text{calc-exp}}$	0.03	0.16	0.03	0.15		

4.3.4. Long-range effects of functional groups

The PE model structures also allowed investigation into the ΔCEBEs of neighbouring carbon atoms present in the model structures, which are susceptible to so-called "long-range" effects (i.e., chemical shifts in the XPS spectra due to the presence of a functionality that is not the first nearest neighbour of the functional group under consideration). These long-range effects have been investigated and observed for other polymers, such as trifluoroacetic anhydride and polyvinyl trifluoroacetate (Kröner et al., 2011; Pippig et al., 2009). However, there is a lack of literature on the secondary and higher-order carbon shifts (i.e., binding energy shifts exerted on carbons that are positioned two or more carbons away from the functionality) as seen in functionalised (UHMW)PE-based material surfaces.

In this work, higher-order carbon shifts were expected to be of importance for several reasons. Excluding this fine structure can result in the erroneous estimation of functionalities, especially those close to the main hydrocarbon peak, such as single-bonded oxygen/nitrogen functionalities. Additionally, by including the higher-order carbon shifts, the theoretical composition of an otherwise unknown chemical surface composition can be estimated during peak fitting (i.e., by constraining the component peak areas by the expected C/N/O ratios of the evaluated functionalities) and component stability (i.e., the observed change in component presence with the inclusion of its associated higher-order carbon shifts) can be evaluated. As ASPN is known for its homogenous treatment of materials, even in the case of complex geometries/morphologies, an even spatial distribution of the functionalities on the polymer surface was assumed (Kaklamani et al., 2010). Using this assumption, increasingly higher-order carbon shifts were introduced to the peak model until the introduced theoretical composition resulted in [CH_x] overestimation in the C 1s region, or underestimation of the components within the N 1s and O 1s regions.

The assignment of the higher-order carbon shifts and the mean influence of carbon-oxygen and carbon-nitrogen functionalities on the ΔCEBEs of the PE carbon backbone are shown in Figure 98 – separated by atom type and bond type, as calculated by wB97X-D. The mean values calculated by HF are shown in Appendix D7, and graphs showing the individual carbon shifts as calculated by HF and wB97X-D per functionality are displayed in Appendix D8 and D9, respectively. As the calculated database in this work only contained two model structures containing a carbonyl group, all model structures with double-bonded oxygen were grouped (i.e., carbonyls, esters, acids, etc.). As seen in Figure 98, the secondary carbon shift for single-bonded oxygen was ~0.14 eV, for double-bonded oxygen ~0.69 eV, for single-bonded nitrogen ~0.12 eV, and for double-bonded nitrogen ~0.40 eV. Typically, the average deviation between the functionalities was roughly ±0.11 eV and continuously decreased

towards higher-order carbon shifts. It can be clearly observed that double-bonded functionalities influenced the ΔCEBEs of [CH_2] more than single-bonded functionalities. Additionally, the difference between the primary and secondary carbon shift was most prominent; this difference decreased considerably when the functional group was situated further away from the primary carbon. Around the quinary carbon shift, most functionalities showed no significant (≤ 0.1 eV) long-range effects on the ΔCEBEs of the PE carbon backbone. Within the reference database of Beamson and Briggs, only four mean secondary carbon shifts were reported that relate to oxygen-based functionalities (Hantsche, 1993). The reported secondary carbon shift for single-bonded oxygen was ~0.2 eV, for carbonyl oxygen ~0.4 eV and for ester/acid-like functionalities ~0.4 to ~0.7 eV. The mean calculated and experimental oxygen-based secondary carbon ΔCEBEs were similar although not identical. Differences in the ΔCEBEs were also most likely affected by energy referencing/material-specific differences. It is worth to note the higher-order carbon shifts can be small (as shown in Figure 98, for 3° or above typically <0.30 eV) and within the range of experimental errors of around 0.20–0.30 eV, but only through their inclusion the self-consistency of the peak model can be maintained. The inclusion of the higher-order carbon shifts should reduce the erroneous estimation of functionalities close to the hydrocarbon peak during high-resolution peak fitting.

In the present work, the higher-order carbon shifts were introduced as individual component peaks per respective functionality during peak fitting. This was done to maintain the stoichiometry of the present elements and to account for the occasional asymmetry observed in the carbon ΔCEBEs of the PE backbone in the model structures with centred functionalities as was observed in Figure 97. The observed charge distribution in the model structures, which were clearly asymmetrically affected by the orientation of the centred functional groups in cases such as [COH] but symmetric in cases such as [COC_α] and [C=O], gave rise to inequivalent or equivalent carbon sites, respectively. The origin of the asymmetry

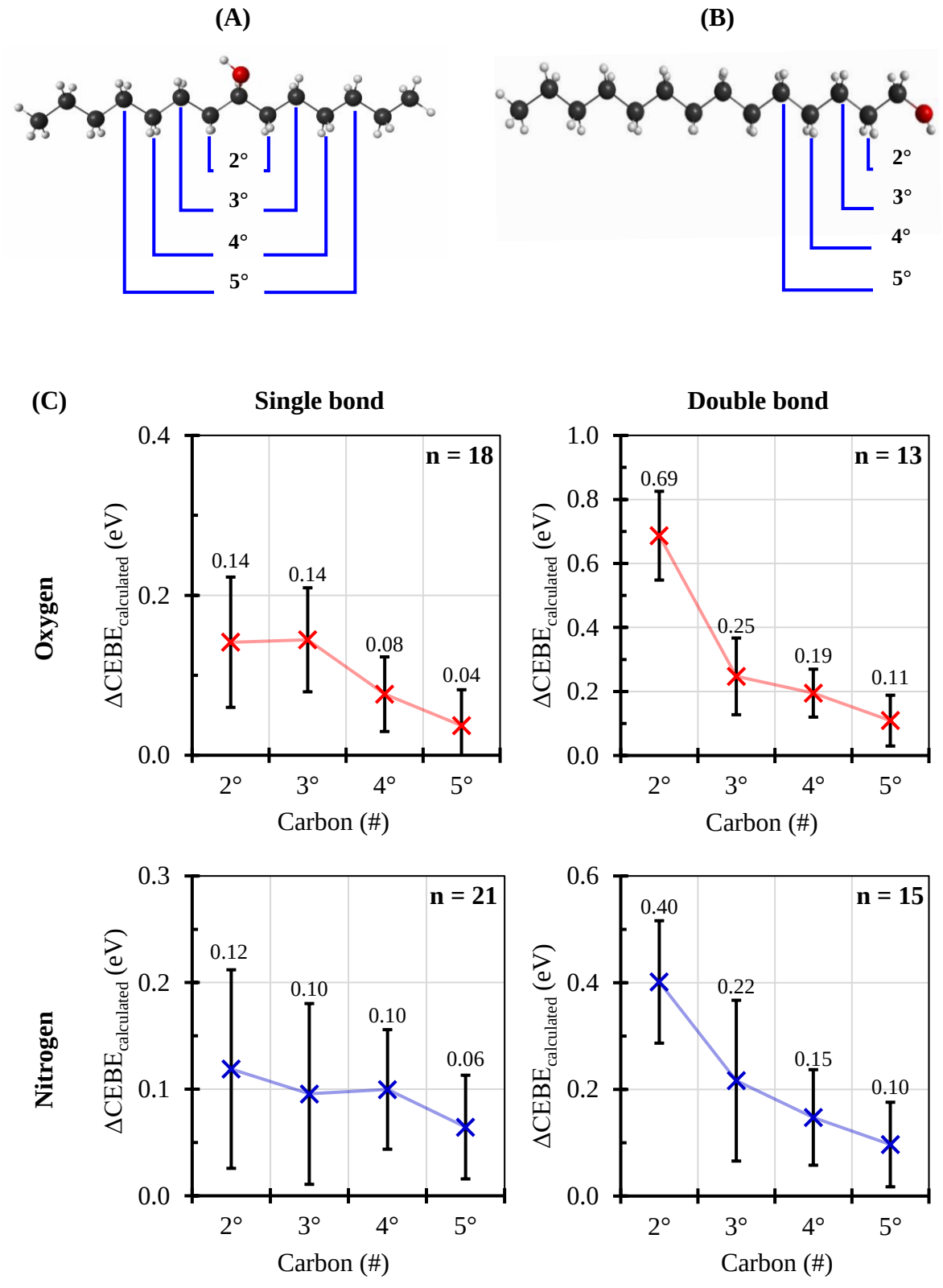


Figure 98. Assignment of higher-order carbon shifts (i.e., [CH_x]) in the centred (A) and end-chain (B) model structures, with the [COH] model structure serving as an example. The graphs (C) depict the mean secondary (2°), tertiary (3°), quaternary (4°) and quinary (5°) ΔCEBEs for [CH_2] groups in the vicinity of carbon-oxygen and carbon-nitrogen functionalities, calculated with 'wB97X-D' relative to [CH_{PE}]. Values are separated by atom type (i.e., oxygen or nitrogen) and bond type (i.e., single or double bond), confidence interval of $\alpha = 0.01$ with n as shown per group within the respective graphs.

in the ΔCEBEs of the PE backbone was illustrated by the 2D molecular electrostatic potential contour maps of the model structures, examples of [COH], [COC_{α}], and [C=O] are depicted in Appendix D10. This showed that despite the alkyl segments on both sides of the centred functionalities were chemically equivalent, electrostatic effects introduced by the functionalities had an impact on the observed ΔCEBEs in the carbon backbone and were dependent on the orientation of the functionality. The influence of electrostatic effects arising from chemical functionalities positioned in hydrocarbon backbones was reported in the literature for molecules in a self-assembled monolayer theoretically and experimentally (Cabarcos et al., 2008; Taucher et al., 2016). These authors showed that functional groups exert long-range effects on the alkyl segments regardless of chain length, which resulted in asymmetry in the CEBEs of the carbons in the alkyl segments (Cabarcos et al., 2008; Taucher et al., 2016). This work highlighted that electrostatic effects significantly contribute to the shifts observed in CEBEs, which was in agreement with our observations (Taucher et al., 2016).

4.3.5. Comparison and validation of peak models

To assess the peak model quality, the calculated ΔCEBEs and experimental ΔCEBEs from the Beamson and Briggs database were compared by linear correlation (Hantsche, 1993). A difficulty in the comparison of calculated ΔCEBEs versus experimental ΔCEBEs was introduced by energy referencing. When comparing the same material of a known composition that displays a XPS spectrum with a clear separation of components, energy referencing the C 1s region has little to no impact on the relative shifts. However, this is not valid when the aliphatic hydrocarbon peak cannot be clearly identified, as is the case with complex samples where introduced functionalities have peak positions near the aliphatic hydrocarbon peak (e.g., C-O/N) as was frequently observed in the literature of plasma-treated polymers (Foerch et al., 1991; Grace et al., 2003; Kaklamani et al., 2010; Kauling et al., 2009; Paynter, 2000; Yasuda, 1976). Within the reference database, the XPS spectra for aliphatic polymers are typically

calibrated to 284.8 or 285 eV, but this neglects the fact that different polymers may have a difference in their C 1s region maximum. Because of this, energy referencing can result in data misinterpretation and has received substantiated criticism over the past decades (Greczynski & Hultman, 2020). Furthermore, averaged experimental ΔCEBEs are often used for the assignment of functional groups, most of which originate from various materials and occasionally show relatively large material-specific deviations in their ΔCEBE.

To allow one-to-one comparison, the ΔCEBEs in the linear correlations were compared from the lowest experimental CEBE available per respective region – the hydrocarbon in the C 1s region, the secondary amine in the N 1s region and the secondary amide in the O 1s region. The linear correlation graphs and corresponding statistical analysis are displayed in Figure 99 and Table 30, respectively. The origin of the experimental reference data within the Beamson and Briggs database is shown in Appendix D11. The individual (Δ)CEBEs per functionality as used in the linear correlation fits are shown in Appendix D12-14.

Table 30. Statistical analysis showing the slope (a), offset (b) and regression coefficient (R^2) of the linear fits, as well as the Pearson correlation coefficient (r_p), the mean absolute error (MAE), and the maximum absolute deviation (MAX) between the experimental and calculated ΔCEBE datasets.

		Slope (a)	**Offset (b; eV)**	**R^2**	**r_p**	**MAE (eV)**	**MAX (eV)**
HF	**C 1s**	0.92	20.07	1.00	1.00	0.22	0.45
	N 1s	0.68	23.53	0.99	0.99	0.36	0.53
	O 1s	0.99	26.28	0.98	0.97	0.16	0.44
wB97X-D	**C 1s**	1.04	-5.39	1.00	1.00	0.14	0.48
	N 1s	0.72	-6.86	0.97	0.97	0.30	0.49
	O 1s	1.01	-9.11	0.98	0.98	0.15	0.41

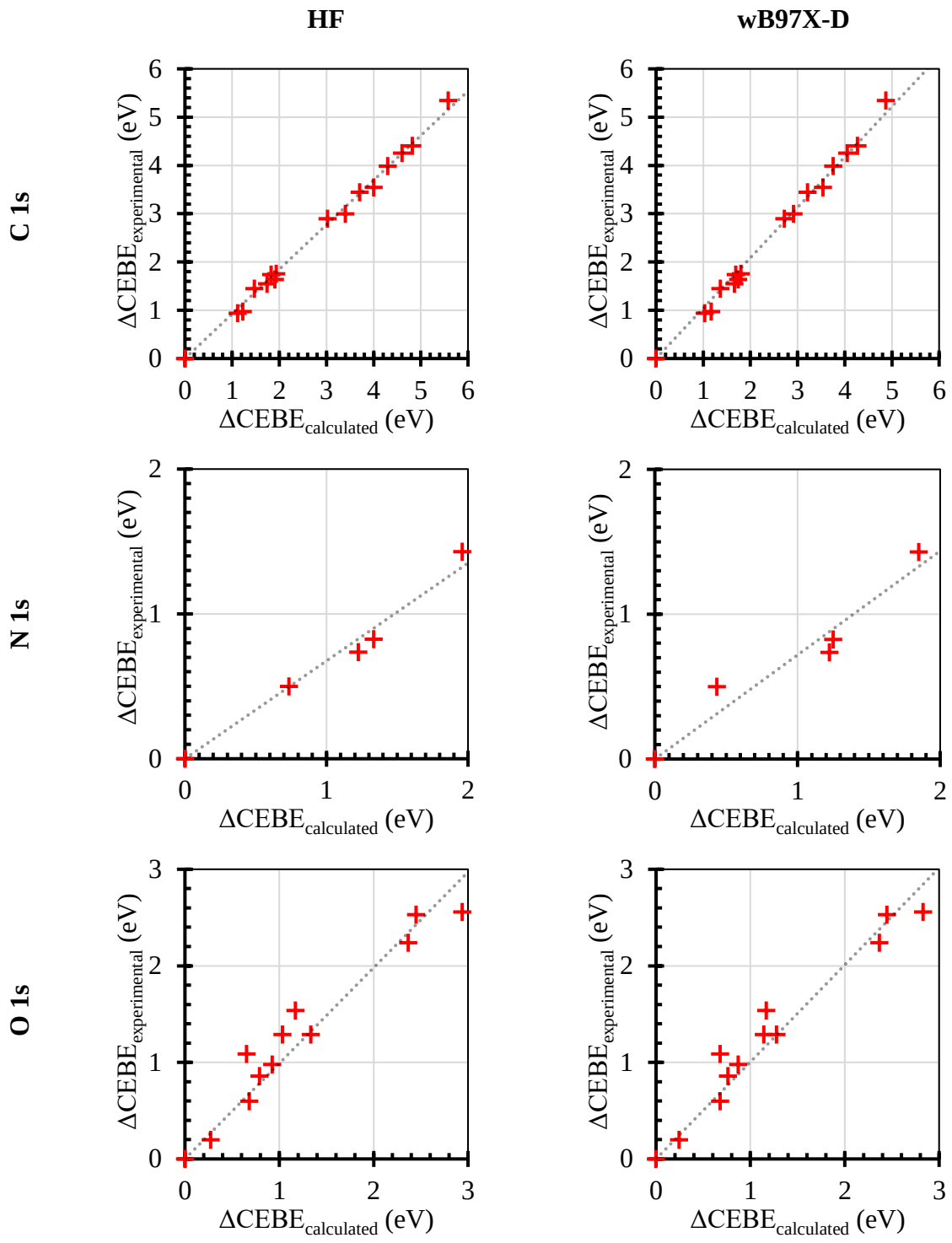


Figure 99. Linear correlation fits of the HF (left) and wB97X-D (right) calculated ΔCEBEs versus the experimental ΔCEBEs, relative to the lowest experimental CEBE per elemental region. The C 1s values are relative to the hydrocarbon, the N 1s shifts are relative to the centred secondary amine, and the O 1s shifts are relative to the centred secondary amide.

The C 1s ΔCEBEs were reasonably well estimated by HF, but the linear correlation was notably improved after the introduction of wB97X-D with a reduction of the mean absolute error from 0.22 eV to 0.14 eV. The observed mean absolute error and maximum absolute error when involving DFT in this work (0.14 eV and 0.48 eV, respectively) showed to be smaller than those observed in the simulated C 1s spectra of organic monolayers by Giesbers et al. (0.30 eV and 0.67 eV, respectively; compared to the average error based on the methods that used a Pople basis set) (Giesbers et al., 2013). A direct comparison with the C 1s simulated spectra of Giesbers et al. was also performed, the observed differences in the estimated ΔCEBEs compared to this work are shown in Appendix D15 (Giesbers et al., 2013). The mean absolute difference of the C 1s ΔCEBEs between this work and the work of Giesbers et al. was 0.2 eV and 0.1 eV for HF and wB97X-D, respectively (Giesbers et al., 2013). There are methodological and structural differences between this work and the work of Giesbers *et al.* (i.e., Giesbers *et al.* used a smaller basis set, different DF, and silicon clusters, whereas this work made use of a PE backbone) and the values provided by Giesbers *et al.* were only available up to the first decimal place, limiting the extent to which conclusions can be drawn.

The calculated N 1s ΔCEBEs were overestimated by both HF and wB97X-D when compared to the experimental N 1s ΔCEBEs and showed an increased mean absolute error of 0.36 eV and 0.30 eV, respectively. Compared to our results, almost identical errors in calculated N 1s CEBEs were reported in the literature, where organic monolayers on silicon and metal-based model structures were investigated, although the literature values show a linear correlation that was closer to unity when compared to our work (Giesbers et al., 2013; J. Zhao et al., 2017). The N 1s CEBEs estimated by Zuilhof *et al.* (using B3LYP/ 6-311+G(d,p)) showed a mean absolute error of 0.40 eV and a maximum absolute error of 0.54 eV, whereas Zhao *et al.* (also using B3LYP/ 6-311+G(d,p)) showed a mean absolute error of 0.27 eV and maximum absolute error of 0.67 eV. Both above-mentioned articles made use of the

commercially available package 'natural bond orbital (NBO) analysis' to estimate CEBEs. This was not included in this work with the intent to keep our method free-of-charge. The similarity of the mean absolute errors between the estimated and experimental CEBEs in our work and that reported in the literature showed that the quality of estimation was comparable. Zuilhof *et al.* and Zhao *et al.* compared their estimated CEBEs to experimental data acquired at various laboratories including their own for their small-molecule-based monolayers. This work solely compared the calculated CEBEs to the Beamson and Briggs polymer database, as this database was built from data acquired from polymer-based samples which was more appropriate for our PE-based surfaces. Lastly, the observed mean absolute error in the O 1s region was relatively small, showing an error of 0.16 eV with HF and 0.15 eV with wB97X-D.

Altogether, a comparison of the calculated ΔCEBEs to the mean experimental ΔCEBEs indicated a strong correlation. Both methods demonstrated a regression coefficient (R^2) and a Pearson correlation coefficient (r_p) of 0.97 or higher for all the investigated regions, indicating that the experimental and calculated values linearly correlated with each other. The overestimation of the ΔCEBEs in the N 1s region as observed by the linear correlation slope was noted as a concern. However, this error may be (partially) introduced by energy referencing/material-specific differences. Despite that, the calculated ΔCEBEs were in reasonable agreement to the experimental ΔCEBEs, with those obtained by wB97X-D consistently exhibiting a lower error compared to those obtained by HF. Therefore, the wB97X-D-based peak model was used during the high-resolution peak fitting.

4.3.6. XPS analysis

Survey XPS spectra

The XPS survey spectra of the various UHMWPE samples are available in Appendix D16, showing the polymer undoped and untreated (A; UD/UT), undoped and plasma-treated

(B; UD/PT60), doped and untreated (C; D/UT), and doped and plasma-treated (D; D/PT60). The region maxima, after energy referencing the C 1s region maximum to 284.8 eV (to allow comparison with the literature) are presented in Appendix D17. To quantify the elemental regions both the 'Shirley' or the 'Tougaard' background were used, in separate data processing procedures, to inspect the change in the atomic composition due to the choice of background, as shown in Table 31. Generally, the deviations in the observed atomic composition due to the change in the background are small apart from iron (more specifically, Fe 2p).

For the theoretical peak model to work accordingly during the high-resolution spectra peak fitting, the contaminants needed to be identified as accurately as possible. Across the present sample set, a total of eight elements were identified that were considered contaminants, namely: fluoride (F), chloride (Cl), sodium (Na), silicon (Si), iron (Fe), chromium (Cr), aluminium (Al), and molybdenum (Mo). Due to the sample preparation and the ASPN treatment, the presence of silicon, iron, chromium, and molybdenum was expected. However, the presence of the other contaminants was unexpected, and their true origin is unknown. Fortunately, very few samples are contaminated by these “unexpected” contaminants and are only observed in minor quantities (≤ 1 %) – except for the fluoride observed in sample ‘C1’.

For the identification of the contaminants and their contributions to the C 1s and O 1s peak fits into account, reference BE tables were prepared based on the data available in the NIST database (NIST, 2008). The BEs used to identify the minor contaminants (i.e., fluoride, chloride, sodium, and aluminium) are shown in Appendix D18. The major contaminants (i.e., silicon, chromium and iron) were evaluated using more extensive BE tables, as shown in Appendix D19, D20, and D21, respectively. Lastly, where applicable, the corresponding oxygen and nitrogen BEs of the contaminants are presented separately in Appendix D22. Next to assigning the most likely components based on the observed region maxima, the major contaminants were also investigated by means of peak fitting. The survey spectra peak fits of

Table 31. Atomic composition of UHMWPE UD/UT (A1-3), UD/PT60 (B1-3), D/UT (C1-3), and D/PT60 (D1-3), determined by the survey spectra fitted with a Shirley/(Tougaard) background.

	Atomic concentration ± St.Dev. (%)				
	C 1s	**N 1s**	**O 1s**	**Contaminants**	
A1	91.46 ± 0.07 (91.59 ± 0.08)	0.64 ± 0.05 (0.50 ± 0.07)	5.92 ± 0.04 (5.94 ± 0.03)	Si 2p	1.72 ± 0.02 (1.67 ± 0.02)
				F 1s	0.27 ± 0.03 (0.31 ± 0.04)
A2	98.24 ± 0.05 (98.33 ± 0.07)	–	1.76 ± 0.05 (1.67 ± 0.07)	–	
A3	89.20 ± 0.05 (89.14 ± 0.11)	0.83 ± 0.03 (0.88 ± 0.11)	7.74 ± 0.04 (7.72 ± 0.04)	Si 2p	2.23 ± 0.03 (2.25 ± 0.02)
B1	64.28 ± 0.10 (61.56 ± 0.09)	15.55 ± 0.09 (16.15 ± 0.08)	16.42 ± 0.07 (16.86 ± 0.07)	Fe 2p	2.10 ± 0.05 (3.63 ± 0.03)
				Cr 2p	0.98 ± 0.03 (1.40 ± 0.03)
				Mo 3d	0.08 ± 0.01 (0.06 ± 0.01)
				Na 1s	0.32 ± 0.03 (0.18 ± 0.02)
				Cl 2p	0.27 ± 0.01 (0.16 ± 0.01)
B2	64.50 ± 0.09 (61.98 ± 0.07)	16.37 ± 0.08 (16.39 ± 0.07)	16.28 ± 0.05 (16.34 ± 0.06)	Fe 2p	1.34 ± 0.06 (3.50 ± 0.03)
				Cr 2p	1.03 ± 0.03 (1.37 ± 0.03)
				Mo 3d	0.07 ± 0.01 (0.06 ± 0.01)
				Na 1s	0.23 ± 0.02 (0.22 ± 0.02)
				Cl 2p	0.19 ± 0.01 (0.15 ± 0.01)
B3	84.39 ± 0.07 (83.88 ± 0.07)	5.47 ± 0.06 (5.79 ± 0.07)	9.66 ± 0.04 (9.86 ± 0.05)	Si 2p	0.49 ± 0.02 (0.47 ± 0.02)
C1	90.55 ± 0.05 (90.61 ± 0.05)	–	6.03 ± 0.04 (6.09 ± 0.04)	F 1s	2.75 ± 0.03 (2.61 ± 0.04)
				Si 2p	0.66 ± 0.02 (0.69 ± 0.02)
C2	90.91 ± 0.06 (90.83 ± 0.06)	–	6.50 ± 0.05 (6.64 ± 0.05)	Si 2p	2.18 ± 0.03 (2.11 ± 0.03)
				Al 2p	0.41 ± 0.01 (0.42 ± 0.02)
C3	95.38 ± 0.08 (95.27 ± 0.08)	–	4.11 ± 0.08 (4.40 ± 0.07)	Si 2p	0.51 ± 0.02 (0.34 ± 0.02)
D1	77.59 ± 0.09 (77.01 ± 0.09)	11.00 ± 0.08 (11.36 ± 0.08)	11.41 ± 0.06 (11.63 ± 0.06)	**D1-3**†	
D2	79.90 ± 0.08 (79.45 ± 0.07)	10.42 ± 0.08 (10.88 ± 0.06)	9.68 ± 0.04 (9.67 ± 0.04)	Fe 2p	0.32 ± 0.02 (0.34 ± 0.02)
D3	81.55 ± 0.08 (81.20 ± 0.08)	8.95 ± 0.07 (9.06 ± 0.07)	9.50 ± 0.05 (9.73 ± 0.05)	Cr 2p	0.33 ± 0.01 (0.36 ± 0.01)

†Averaged presence as determined in the summed spectrum; intensity was too low in individual spectra to determine the component area.

the Si 2p, Cr $2p_{(3/2)}$ and Fe $2p_{(3/2)}$ regions are presented in Appendix D23, D24, and D25, respectively. The observed component concentrations of the fits are depicted in Appendix D26, D27, and D28, respectively; these are also tabulated per peak fit individually in Appendix D29 and D30.

Apart from aluminium, minor contaminants were only found in samples 'B1' and 'B2' (i.e., after ASPN of undoped UHMWPE). The observed presence of molybdenum (≤ 0.07 At%) was considered negligible and therefore disregarded during peak fitting of the high-resolution O 1s spectra. Despite its relatively low presence, to prevent misidentification with S 2s, the assignment of Mo 3d was confirmed by orbital splitting (~3 eV, limited by XPS resolution in survey spectra) and a 3**:**2 peak area ratio between the $3d_{5/2}$ and $3d_{3/2}$ orbital peaks. Furthermore, it was assumed that the sodium and chloride in 'B1' and 'B2' were solely present as [Na^+ Cl^-], considering a roughly 1:1 At% ratio of these two elements was observed in the survey spectra. This was supported by comparison of their BE region maxima with the reference BE tables. A small amount of aluminium was observed in 'C2', with its $2p_{3/2}$ region maximum at 73.8 eV and 2s region maximum at 118.8 eV, Al_2O_3 was found to be the most probable assignment.

Fluoride was observed in both 'A1' and 'C1', although its presence in 'A1' was very low and displayed a high uncertainty. With both samples the F 1s showed its region maximum at 688.8 eV. Additionally, the high-resolution O 1s of 'C1' indicated the inclusion of oxygen to the fluoride-based compound with a newly observed peak around 536.3 eV. Based on the NIST database, a compound such as trifluoroethanol was thought to be the most likely assignment, but the C 1s assignments for this (as well as all other fluoride/oxygen-based compounds within the NIST database) were too high for the observed C 1s region which ends at ~290.5 eV as seen in Appendix D31. Therefore, despite the available references, no assignment could be made regarding the fluoride contamination. Nonetheless, during the high-resolution fitting, the new peak observed in the O 1s was fitted regardless including a

corresponding area-constrained peak in the C 1s between 289-292 eV, to reduce the influence of the fluoride-based contamination on the peak model.

Silicon was found in most reference samples, the observed Si 2p, Si 2s, and O 1s region maxima were similar as those observed for polydimethylsiloxane (PDMS) in the Beamson and Briggs database – when keeping the difference in energy referencing in mind. Throughout all samples that showed silicon contamination, no deviation in the Si 2p and Si 2s region maxima were noted. In addition to the minor contaminants present in 'B1' and 'B2', iron and chromium were also observed in more abundance. All region maxima of the two elements were the same for these samples and allowed assignment of the same components to the respective region maxima. The Fe $2p_{3/2}$ and 3p region maxima were noted at 710.8 eV and 55.5 eV, respectively, allowing the assignment of Fe_2O_3 in both cases. Next to that, the region maxima of Cr $2p_{3/2}$ and 3p were observed at 576.8 eV and 43.8 eV, respectively, leading to conclude that Cr_2O_3 was most likely present.

Next to assigning the most likely components based on the observed region maxima, the major contaminants were also investigated by means of peak fitting. The Si 2p regions were fitted using the Si $2p_{3/2}$ BEs as observed in the reference BE table, after which a Si $2p_{1/2}$ peak was introduced for each component with an orbital splitting of 0.61 eV as was observed for PDMS in the Beamson and Briggs database. The chromium and iron regions are known to contain many overlapping species and/or potential satellites were significantly more complex to fit. Therefore, to fit the metallic regions, peak models as provided by Biesinger *et al.* were used (Biesinger et al., 2011). No changes were made to the relative peak positions, FWHMs or relative Area% per component peak model, but both constrained and unconstrained peak fits were evaluated by relaxing the constrained component models with the respective average deviation observed in the reference BE tables. Furthermore, the $2p_{1/2}$ were fitted by copying the $2p_{3/2}$ component peak models and introducing an orbital splitting of 9.3 eV and 13.1 eV for

chromium and iron, respectively, and a 1:2 area ratio. Unfortunately, no component peak model for FeN currently exists, but its presence should be considered when Fe(0) is found considering the slightly lower BE of FeN relative to Fe(0).

The Si 2p peak fits did not show a significant difference after relaxing the position constraints and confirmed the assignment of PDMS as the major component in all survey peak fits, together with some minor presence of SiC and potentially SiO_2-like species. The metallic elements showed large differences between the constrained and unconstrained fits, as expected due to the overlapping peaks within these regions and the relatively low-resolution spectra. With the Cr 2p survey peak fits, a presence of $FeCr_2O_4$ was only noted after relaxing the position constraints but this may be due to the proximity of the component model to the Cr_2O_3. The presence of $FeCr_2O_4$ was negligible in the Fe 2p fits and therefore, the above assignment in the Cr 2p peak fits seemed less likely and was disregarded. The area fitted as $FeCr_2O_4$ was ascribed to Cr_2O_3 instead, which might have influenced the presence of the metal-based contaminants within the high-resolution O 1s spectra slightly. The Fe 2p survey peak fits mainly displayed an interplay between FeO and Fe_2O_3 species of about 15-30 area%, as was seen by the increase in Fe_2O_3 after relaxing the position constraints. Nonetheless, the presence of both Cr_2O_3 and Fe_2O_3 were confirmed by the peak fits, but also indicated a notable presence of CrN and FeO species. Fe(0) was only observed in minor quantities – it was therefore thought to be unlikely that any FeN was present in the high-resolution N 1s spectra.

In preparation for the high-resolution peak fitting, a conversion table was prepared to account for the expected presence of the silicon- and metal-based contaminants in the high-resolution spectra as determined by the survey peak fits, available in Appendix D32 and D33, respectively. To allow conversion, the components were assumed to uphold their assigned theoretical composition. It was expected that this would introduce the least amount of error, considering the different survey peak fits identified the same components, albeit in somewhat

different quantities. The conversion tables contain those that will be included in the high-resolution fits, apart from an unidentified fluoride-based component in 'C1' and aluminium identified as Al_2O_3 in 'C2' – which was expected to make up ([0.41 $At\%_{Al2p} * \frac{3}{2}$] / 6.50 $At\%_{O1s}$ =) 9.46 area% of the 'C2' its O 1s region.

High-resolution XPS spectra

The high-resolution XPS spectra of UHMWPE UD/UT (A1-3), UD/PT60 (B1-3), D/UT (C1-3), and D/PT60 (D1-3) are available in Appendix D31. The C 1s region maximum was referenced to 284.8 eV to allow comparison of the peak positions to the literature. Both the 'Shirley' or the 'Universal Polymer Tougaard' background were used, in separate data processing procedures, to fit the high-resolution spectra to inspect the difference in the atomic composition due to the background change as shown in Appendix D34. After introducing the peaks associated with the contaminants, constraining their position as determined by the BE reference tables, and constraining their area% as was established by the survey spectra peak fits, the high-resolution spectra were fitted using the peak model as calculated by wB97X-D. One of the UHMWPE-based high-resolution spectra fitted using the 'Shirley' background was selected from each of the sample series, namely: 'A2' (as it was the least oxidised/contaminated UHMWPE reference sample), 'B1', 'C3' (as it indicated the presence of α-tocopheryl quinone, [αTQ], similarly to 'D1-3'), and 'D1'.

The tables depicting the component concentrations (predetermined contaminants established with the survey spectra were omitted) as obtained from the individual high-resolution peak fits of UHMWPE UD/UT (A1-3), UD/PT60 (B1-3), D/UT (C1-3), and D/PT60 (D1-3), using a 'Shirley' background and the wB97X-D-based peak model including the respective higher-order carbon shifts are presented in Appendix D35-38. When comparing the component tables, it can be observed that the introduction of the higher-order carbon shifts had

minimal effect on the type of functionalities identified by the peak model, but it did influence the estimated presence or positioning (i.e., centred or end-chain). This is due to the positional constraints set for the peak model reference components (see Section 2.4), as the peak models could move freely within the set BE ranges per elemental region, the influence of energy referencing in terms of component identification was prevented (as the ΔCEBEs relative to the peak model reference component remain constrained). As shown in Appendix D39, energy referencing still introduced a deviation in the observed absolute CEBEs between sample series (A, B, etc.). It was observed that the untreated samples (A and C) showed the [CH_{PE}] component at about 284.7 eV whilst the plasma-treated samples (B and D) showed the [CH_{PE}] component at about 284.5 eV – this may be caused by the C1s region maximum shifting upwards as the newly introduced functionalities form photoelectron peaks close to the main hydrocarbon peak. Apart from samples series 'B1-3', the peak model reference components in the showed a similar positioning between the samples of the same series (D1, D2, etc.).

The high-resolution peak fits of the UHMWPE UD/UT and D/UT samples ('A2' and 'C3') allowed a reasonable fit of the C 1s region using the LA(4.2,9,4) lineshape for the [CH_{PE}] peak model reference component, as presented in Appendix D40 and D41, respectively. The introduction of the higher-order carbon shifts had negligible influence on the peak fits of 'A2', only a small improvement in the residual standard deviation (STD) was noted from 1.747 to 1.634 – which was expected considering the low degree of oxidation components that are associated with the higher-order carbon shifts. A minor [$\pi-\pi^*$] presence was observed in the C 1s region of 'A2', likely due to some contamination originating from the polystyrene Petri dishes used for sample storage − which was accounted for by introducing an additional position-constrained component to the peak model between 291−292 eV. Based on ATR-FTIR peak fits of UHMWPE D/UT, the expected presence of the tocopherol-like components was between 9-22% as shown in Appendix D42. It is worth to note that the sampling depth of ATR-

FTIR (several microns) is much higher than for XPS (several nanometres), making it difficult to compare the observed chemical composition between these two techniques. However, the estimation of the tocopherol-like components present in the polymer matrix was necessary to guide the model when overestimation of the tocopherol-like components was expected. The introduction of the higher-order carbon shifts to 'C3' only slightly increased the presence of [αTQ], when comparing the composition observed with the 1° and 4° carbon peak model it increased from 14.9%$_{[\alpha TQ]}$ to about 17.7%$_{[\alpha TQ]}$, respectively, the estimated presence of the tocopherol-like components matches closely to that observed by ATR-FTIR (ranging from 9% to 22%). Further addition of the higher order carbon shifts had a negligible impact on the composition as seen in Appendix D37, which indicated that the peak model reached a "stable" component estimation**.**

From the peak fits of UHMWPE UD/PT60 (B1-3) it was established that the wB97X-D-based peak model including the 3° carbon shifts was most suitable for fitting the high-resolution XPS spectra of the plasma-treated UHMWPE surfaces evaluated in this work. As can be observed in the fitted spectra of 'B1' shown in Appendix D43, the introduction of the higher-order carbon shifts improved the residual STD of the spectra fits from 1.671 to 1.492 until the introduction of the 4° carbon shifts (residual STD = 3.311). Following the incorporation of the 4° carbon shifts, the peak model suffered from [CH_x] overestimation in the C 1s region and underestimation of the components within the N 1s and O 1s regions. This also indicated that, although lineshapes designed from unmodified polymers were suitable to fit their reference spectra, a single unconstrained asymmetric peak was not sufficient to estimate the hydrocarbon presence in the modified PE-based surfaces due to the long-range effects arising from the newly introduced functional groups affecting the [CH_2] ΔCEBEs of the polymer backbone. It was thought that the increase of the C 1s region FWHM, as observed in Appendix D31, forced the [CH_{PE}] peak to broaden (average FWHM$_{[CH]}$ in A1-3 was 1.07 eV;

average $FWHM_{C1s}$ in B1-3 was 1.17 eV) and resulted in increased tailing towards higher BEs with the asymmetric lineshape used for the [CH_{PE}] component peak.

The high-resolution peak fits of the combined system, UHMWPE D/PT60 (D1), using the higher-order carbon shift models are presented in Figure 100 and its corresponding component graph in Figure 101. Using the ATR-FTIR peak fits discussed previously (showing 9-22% tocopherol-like products), and the UHMWPE D/UT (C3) model system (showing ~78% [$CH_{PE/x}$] and ~16% tocopherol-like products), the presence of the tocopherol-like components in the high-resolution peak fits of 'D1' using the 1° carbon peak model appeared drastically overestimated (showing ~19% [$CH_{PE/x}$] and ~44% tocopherol-like products). When comparing the high-resolution spectra of sample series 'C' and 'D' in Appendix D31, this overestimation was expected to be the result of spectral broadening introduced after plasma-treatment of doped UHMWPE. The broadened spectra made it more complicated for the 1° and 2° carbon peak models to distinguish between the [$CH_{PE/x}$] associated with the UHMWPE carbon backbone or the tocopherol-like components. The inclusion of the higher-order carbon shifts forced the reduction of the tocopherol-like components, but the peak model consistently identified [αTQ] throughout the peak fits. Similarly, as it was established during the peak fitting of UHMWPE UD/PT60 (B1), the 3° carbon peak model seemed most suitable for fitting the high-resolution XPS spectra of the UHMWPE D/PT60 surfaces evaluated in this work. As it can be observed in Figure 100, most of the residual area was situated at the higher binding energies (288–291 eV) in the C 1s region and may be a result of unresolved loss events, neglected peak asymmetry, or a minor error in the RSFs used as peak area constraints between the elemental regions – as Kratos RSFs are related to homogeneous materials, which excludes homogeneous materials with surface contamination. The corresponding high-resolution peak fit of the N 1s and O 1s region for ‘D1’ are presented in Appendix D44. The high-resolution peak fit of ‘D1’ using the 3° carbon peak model is presented in more detail with labelling in Figure 102.

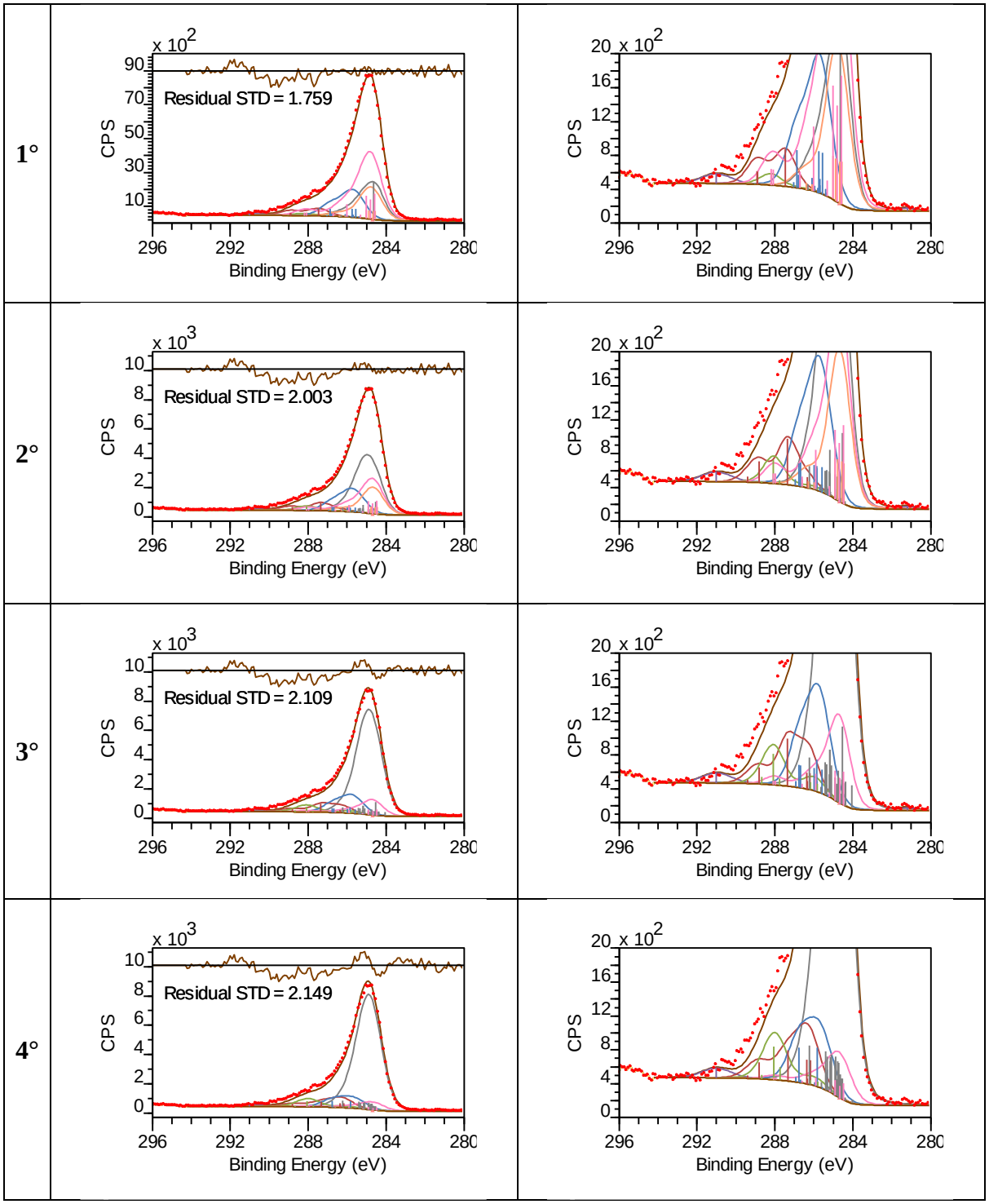


Figure 100. High-resolution C 1s spectra peak fits of UHMWPE D/PT60 (D1) using a 'Shirley' background and the wB97X-D-based peak model, including the respective symmetric higher-order carbon shifts. The spectra display the recorded experimental data (**red**, dotted) and the summed peak model envelope (**brown**, solid). The colours represent the various component groups: [CH] (**grey**), [CO] (**dark red**), [CN] (**blue**), [CNO] (**green**), [αTH] (**orange**), [αTQ] (**pink**), [αTHQ] (**yellow**), and contaminants (**purple**).

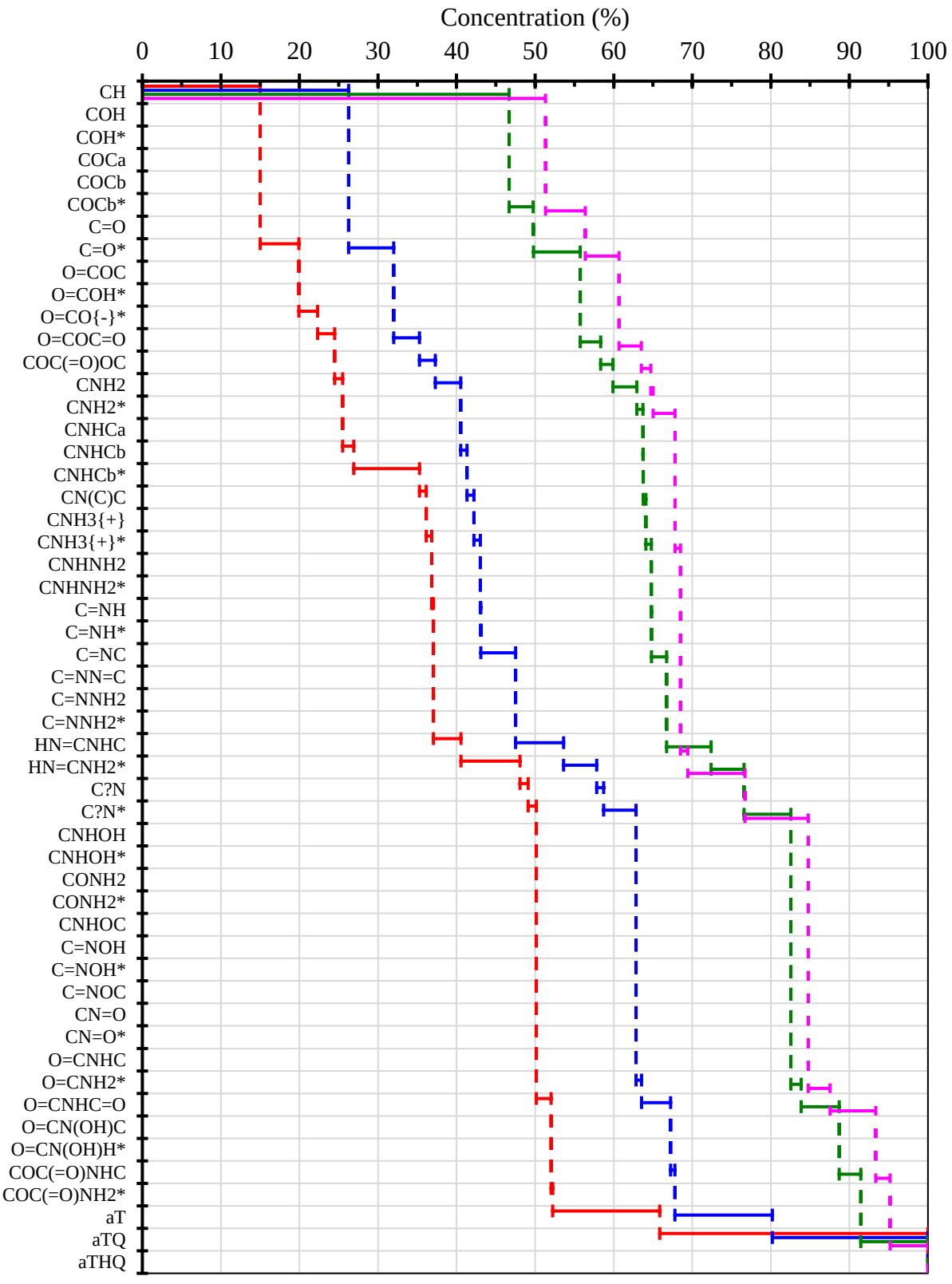


Figure 101. Composition of UHMWPE D/PT60 (D1) determined by the high-resolution spectra peak fits using a 'Shirley' background and the wB97X-D-based peak model including the 1° (**red**), 2° (**blue**), 3° (**green**), and 4° (**pink**) symmetric higher-order carbon shifts. The bars depict the component presence, stacking up to a total of 100%.

The peak fits indicated that the inclusion of the higher-order carbon shifts prevented the overestimation of the tocopherol-like components incorporated within the polymer matrix. The component graph of the high-resolution peak fits, displaying the observed component concentrations of the above-discussed samples' high-resolution peak fits (i.e., 'A2', 'B1', 'C3', and 'D1') using the 3° carbon peak model, is shown in Figure 103. As it can be observed in the component graph, the components identified by the peak model in the combined system (UHMWPE D/PT60) generally agreed to those identified from the respective model systems (UHMWPE UD/UT, UD/PT60, and D/UT). The high-resolution peak fits of the untreated reference samples, UHMWPE UD/UT (A2) and D/UT (C3), both showed the presence of [C=O*]. However, only the peak fit of UHMWPE UD/UT (A2) showed some minor additional oxidation products (i.e., [O=COH*] and [O=COC=O]) and UHMWPE D/UT (C3) showed the presence of [αTQ]. When comparing the high-resolution peak fits of the functionality-rich samples obtained after ASPN treatment of the reference samples, UHMWPE UD/PT60 (B1) and D/PT60 (D1), the presence of [C=O*], [O=COC=O], [$CNH_2^{(*)}$], [$O=CNH_2$*] [O=CNHC=O], and [HN=CNHR] were observed in both plasma-treated sample series – where 'R' represents the atom present in the centred or end-chain functionality, C or H, respectively. However, only the peak fit of UHMWPE UD/PT60 (B1) showed the presence of [CNHNH2*] and [C=NH*], and only with UHMWPE D/PT60 (D1) the presence of [$C{\equiv}N^{(*)}$] was noted. As it can be observed in Appendix D35-38, the components identified in the 'B' sample series correspond more often to functionalities in their end-chain positioning when the samples also showed metal-contamination (i.e., Fe and Cr) in their corresponding survey spectra (i.e., 'B1' and 'B2'; see Section 3.2.1). Whereas the samples showing little to no sign of metal-contamination (i.e., 'B3' and 'D1–3'), predominantly showed the presence of functionalities in their centred positioning.

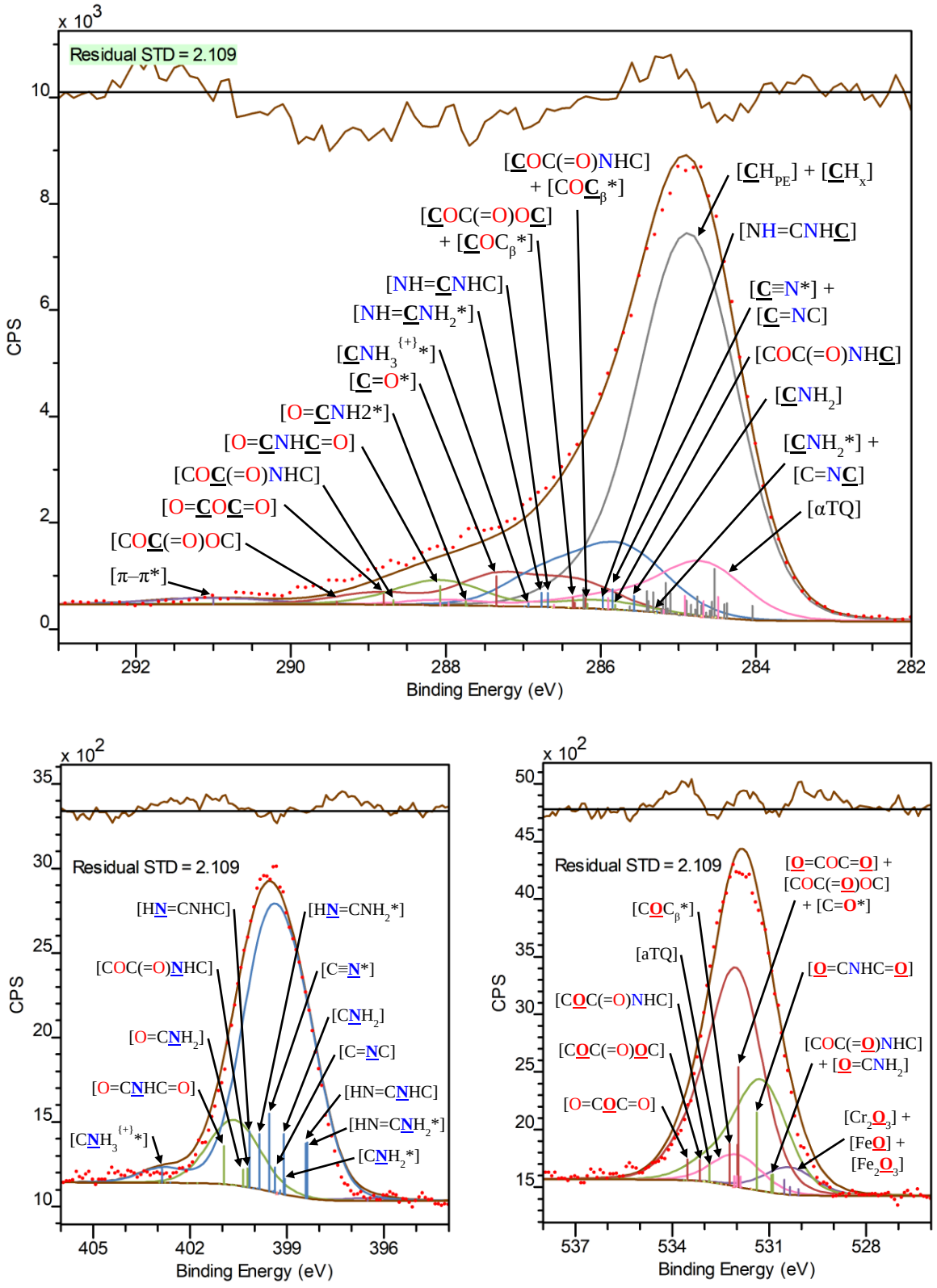


Figure 102. High-resolution C 1s, N 1s and O 1s spectra peak fit of UHMWPE D/PT60 (D1) using a 'Shirley' background and the wB97X-D peak model with the 3° symmetric higher-order carbon shifts. The spectra display the experimental data (**red**, dotted) and the summed peak model envelope (**brown**, solid). The colours represent the various component groups: [CH] (**grey**), [CO] (**dark red**), [CN] (**blue**), [CNO] (**green**), [αTQ] (**pink**), and contaminants (**purple**). The labels denote the component IDs, with the evaluated atom **bold** and underlined.

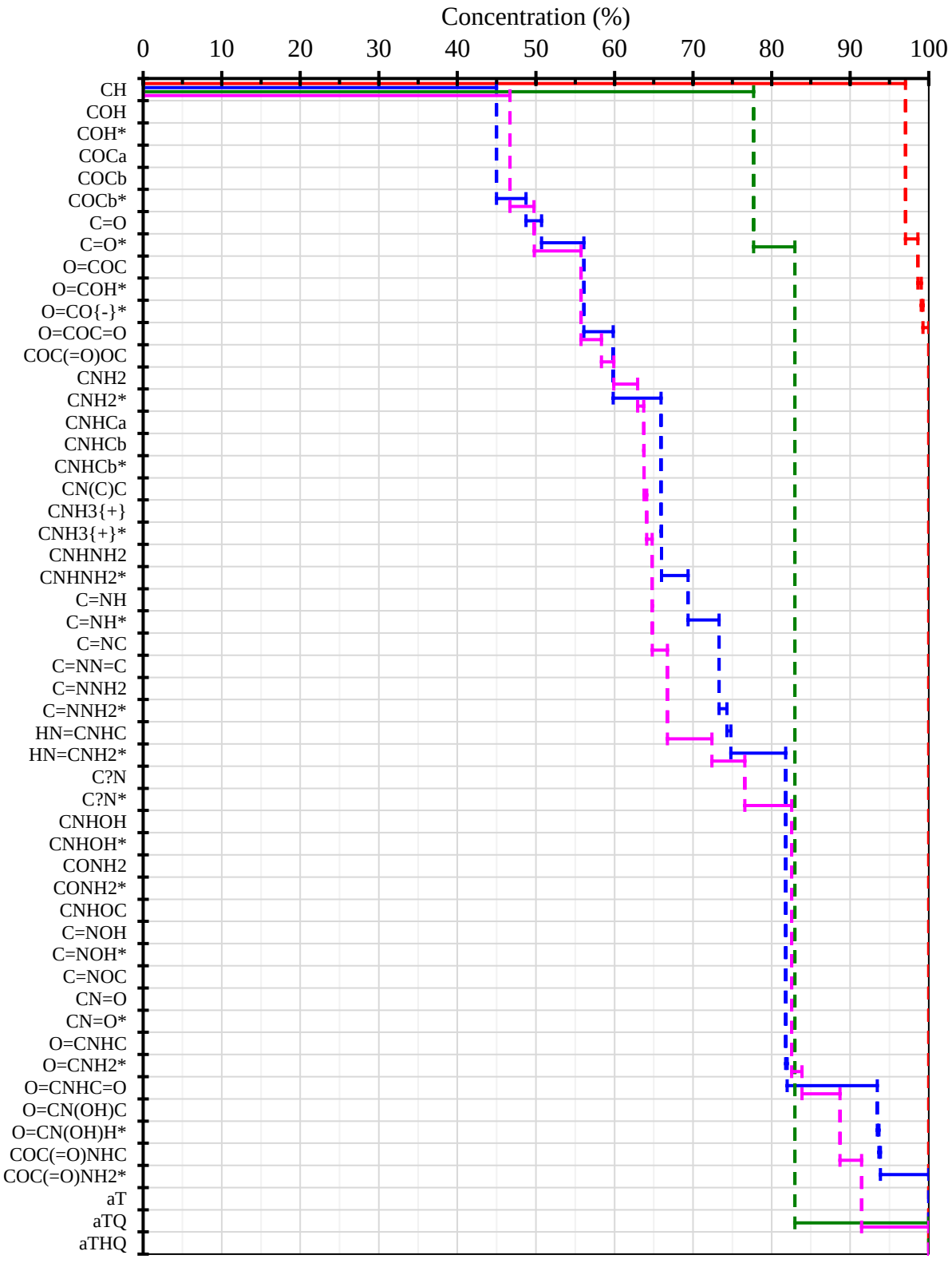


Figure 103. Composition of UHMWPE UD/UT (A2, **red**), UD/PT60 (B1, **blue**), D/UT (C3, **green**), and D/PT60 (D1, **pink**), determined by the high-resolution spectra peak fits using a 'Shirley' background and the wB97X-D-based peak model including the 3° symmetric higher-order carbon shifts. The bars depict the component presence, stacking up to a total of 100%.

The high-resolution spectra of selected samples (i.e., 'B1', and 'D1') were also further investigated by using the 'Universal Polymer Tougaard' background during peak fitting with the 3° carbon peak model, to observe the difference in peak model response due to a change in background. In addition to that, the use of the asymmetric lineshape LA(4.2,9,4) was also tested for all [CH_x] components instead of solely for the [CH_{PE}] component; to investigate the influence of increased peak asymmetry on the peak model response. As presented in Appendix D45, the change in the background and peak asymmetry had a negligible impact on the peak fits of 'B1' and 'D1' when using the 3° carbon peak model. When using the asymmetric lineshape for the higher-order [CH_x] components, only minor variation was observed in the presence of some components. The peak fits involving 'B1' showed a maximum average deviation of 2.55 At% for [$COC(=O)NH_2$*]. The peak fits involving 'D1' showed a maximum average deviation of 4.98 At% for [αTH] and 4.58 At% for [CH], the [αTH] component was only present in the fits including the asymmetric higher-order [CH_x] components. The minimal changes observed when changing the background type or introducing peak asymmetry indicates that the peak model is robust, especially in terms of component identification.

Comparison to reference-based peak fitting

To demonstrate the improved detail which was achieved when using the developed multi-region peak model for the interpretation of the complex system (UHMWPE D/PT60, D1), a comparison was made with (i) conventional reference-based peak fitting (i.e., area-unconstrained peak fitting of the C 1s region; informed but not computationally connected to the N 1s and O 1s regions) and (ii) advanced reference-based peak fitting (i.e., area-constrained multi-region peak fitting of the C 1s, N 1s and O 1s regions). The C 1s spectra peak fits of the comparison between the various peak fitting approaches are presented in Figure 104. The corresponding N 1s and O 1s spectra peak fits are shown in Appendix D46. Positional constraints were based on the mean ΔCEBEs from the Beamson and Briggs database as used

in the linear correlations; available in Appendix D12-14. With the reference-based peak fitting (i and ii), the considered functionalities were those typically seen with the XPS spectral interpretation of plasma-treated polymeric surfaces (Foerch et al., 1991; Grace et al., 2003; Kaklamani et al., 2010; Kauling et al., 2009; Paynter, 2000; Yasuda, 1976). The evaluated functionalities and chemical compositions as obtained after peak fitting are tabulated in Table 32; the components that showed no presence after peak fitting using the wB97X-D-based peak model were omitted for readability but are depicted in Appendix D38.

With the conventional reference-based peak fitting, a C 1s region peak model was used to identify the present components. The observed presence of the components was informed by the observed peak shifts and magnitude of the peak ratios of the corresponding peak fits of the N 1s and O 1s regions. However, as the peak areas of the components within each elemental region are unconstrained, the peak fits are individual least-square solutions and therefore hard to control – often resulting in subjective interpretation due to manual influence from the spectral analyst. Nonetheless, as it can be observed in the N 1s and O 1s peak fits of the conventional reference-based peak fits in Appendix D46, both regions were fitted with three components. The N 1s region was fitted with a component to reflect carbon single- bonded nitrogen ([C–NX]), carbon triple-bonded nitrogen ([C≡N]), and oxygen double-bonded to a carbon single-bonded nitrogen ([O=C–N]), whereas the corresponding O 1s region was fitted with components presenting carbon single-bonded oxygen ([C–OX), carbon double bonded oxygen ([C=O]), and oxygen double-bonded to a carbon single-bonded nitrogen ([O=C-N]). Altogether, this minimal interpretation of the N 1s and O 1s provided sufficient rationale to consider the major functionalities that are typically peak fitted with plasma-treated polymeric surfaces to the C 1s region peak model (Foerch et al., 1991; Grace et al., 2003; Kaklamani et al., 2010; Kauling et al., 2009; Paynter, 2000; Yasuda, 1976). The subsequent peak fit of the C 1s region, where effort was made for the peak fit to reflect the peak ratios of the above-

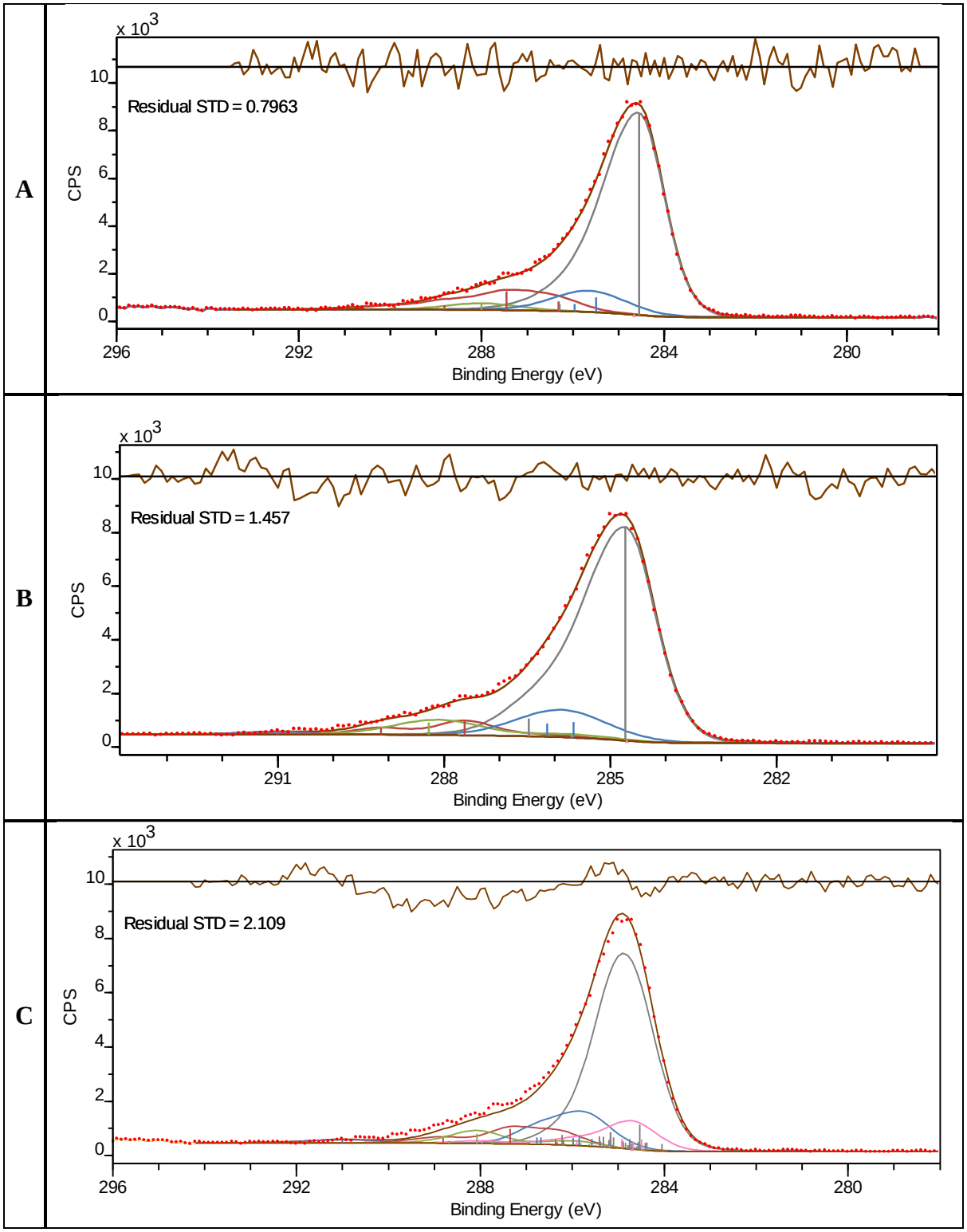


Figure 104. High-resolution C 1s spectra peak fits of UHMWPE D/PT60 (D1) using a 'Shirley' background following (A) conventional reference-based peak fitting, (B) advanced reference-based peak fitting and (C) the wB97X-D-based peak fitting using the 3° symmetric higher-order carbon shifts. The spectra display the experimental data (**red**, dotted) and the summed peak model envelope (**brown**, solid). The colours represent the various component groups: [CH] (**grey**), [CO] (**dark red**), [CN] (**blue**), [CNO] (**green**), [αTQ] (**pink**), and contaminants (**purple**).

Table 32. Composition of the high-resolution spectra peak fits of UHMWPE D/PT60 (D1) using a 'Shirley' background following (A) conventional peak fitting, (B) reference-based advanced peak fitting, and (C) the wB97X-D-based peak fitting using the 3° higher-order carbon shifts. Presenting the individual component presence (based on the combined presence of all corresponding atoms related to the respective IDs), and the summed presence of the various component groups as grouped in the peak fits: [CH], [CO], [CN], and [CNO]. For ease of comparison, the atomic composition determined with the conventional reference-based peak fitting of the C 1s region (A), was adjusted to reflect the inclusion of the corresponding [N and O] atoms. Additionally, as the reference-based peak fitting did not include the tocopherol-like components, the summed [CH] presence in 'C' represents the combined presence of [CH] and [αTQ].

ID	A (At%)	B (At%)	ID	C (At%)
CH	57.5	59.9	CH	46.7
C-OX	0.00	0.91	COC_{β}*	3.06
C=O	8.97	5.59	C=O	0.04
			C=O*	5.95
O=COC	2.85	0.02	O=COC	0.00
O=COH*	1.16	0.00	O=COH*	0.00
O=COC=O	0.95	3.15	O=COC=O	2.60
COC(=O)OC	7.06	0.22	COC(=O)OC	1.57
C-NX	9.56	9.31	CNH_2	3.04
			CNH_2*	1.57
			$CNHC_{\beta}$	0.04
			CN(C)C	0.34
			$CNH_3^{\{+\}}$*	0.69
C=NX or HN=C-NX	Not evaluated.		C=NC	1.93
			HN=CNHC	5.66
			$HN=CNH_2$*	4.19
C≡N	5.07	7.95	C≡N*	5.96
O=CNHC	1.15	3.66	O=CNHC	0.00
$O=CNH_2$*	5.26	0.00	$O=CNH_2$*	1.31
O=CNHC=O	0.50	9.28	O=CNHC=O	4.84
COC(=O)NHC	Not evaluated.		COC(=O)NHC	2.75
aTQ	Not evaluated.		aTQ	8.55

ID	A (At%)	B (At%)	C (At%)
CH	57.5	59.9	55.2
CO	21.0	9.90	13.2
CN	14.6	17.3	22.6
CNO	6.91	12.9	8.90

discussed components fitted within the N 1s and O 1s regions, showed a major presence (>5 %) of [C=O], [COC(=O)OC], [C–NX], [C≡N], and [O=CNH$_2$].

Despite that the conventional reference-based peak fitting provided strong indications of the present component groups (i.e., [C–OX], [C–NX], [O=C–N] etc.), the area-unconstrained peak fits did not provide a detailed interpretation, remained hard to control, and were prone to arbitrary interpretation. Therefore, advanced reference-based peak fitting was also explored, where a reference-based multi-region peak model was used to interpret the merged high-resolution spectra. Similarly, as with the high-resolution peak fitting performed using the developed theoretical peak model, the areas of the component peaks in the N 1s and O 1s regions were constrained to the C 1s region components with the respective RSFs and theoretical composition associated with the evaluated functionalities. In contrast to the area-unconstrained reference-based peak fit, a significantly larger presence of [O=CNHC=O] was noted instead of [O=CNH$_2$*]. The presence of the [CO] components showed a decrease from 21.0% to 9.90%, the [CN] components showed an increase from 14.6% to 17.3%, and the [CNO] components showed an increase from 6.91% to 12.9% between the reference-based area-unconstrained and multi-region peak fits, respectively.

Altogether, little change was observed in the [CH] presence, and the main interplay of the component's presence was noted between the other component groups (i.e., [CO], [CN], and [CNO]). The main difference observed when switching from the reference-based multi-region peak model (Model B) to the developed multi-region peak model (Model C) was an increase in [CO] and [CN], most likely as significantly more nitrogen-based functionalities were evaluated which were not included within the Beamson and Briggs database. However, despite the inclusion of the additional functionalities in the developed peak model, various similarities between the reference-based and developed multi-region peak fits were also recognised. For example, both multi-region peak fits showed a notable presence of [C=O],

[C≡N], and [O=CNHC=O]. However, where the reference-based peak fit showed a major presence of [C-NX], this seemed to have shifted in the wB97X-D-based peak fit to the newly introduced [HN=CNHR] components – where 'R' represents the atom present in the centred or end-chain functionality, C or H, respectively. The inclusion of the carbon double-bonded nitrogen functionalities with the developed peak model increased the presence of nitrogen and reduced that of [O=CNHC=O] compared to the reference-based multi-region peak fit.

The residual STD increased when comparing the conventional reference-based peak fitting to the advanced reference-based peak fitting and to the wB97X-D-based peak fitting (0.7963, 1.457, and 2.109, respectively), which was to be expected as the peak model became increasingly more constrained. Most of the residual in both the reference-based and developed multi-region peak models was noted at the higher binding energies in the C 1s region (i.e., 288–291 eV), and likely a result of unresolved loss events, neglected peak asymmetry, or a minor error in the RSFs used as peak area constraints between the elemental regions (i.e., as RSFs are related to homogeneous materials, which excludes homogeneous materials with surface contamination). However, as was observed with the reference-based peak fits, it was difficult to identify functionalities that extend outside the reference database. More specifically, various functionalities that contain more than one ΔCEBE within an elemental region (i.e., amidine, carbamate, etc.) were seldomly evaluated within the reference database – which limited the ability of detailed spectral interpretation. This is where conventional peak fitting becomes more subjective when involving other references or prone to personal experience or bias in terms of component identification.

Another difficulty of using the conventional reference database, to construct a peak model for the interpretation of complex, high-resolution XPS spectra arises from the fact that the observed ΔCEBEs will originate from a variety of materials. As a result of the latter, common evaluated component groups such as [C-NX] display broad BE ranges (> 0.8 eV) in

the reference database. Additionally, as discussed previously, there are indications that energy referencing the C 1s region maximum to 284.8 eV is not suitable when comparing the XPS spectra of the unmodified and modified UHMWPE surfaces – as the functionalities closely positioned to the main hydrocarbon peak influence the C 1s region maximum. However, contrary to reference-based peak fitting, this issue was resolved by using the developed multi-region peak model and with positional constraints for the peak model reference components (see Section 3.2.5) that were flexible enough to overcome the influence of the functionalities near the main hydrocarbon peak.

Using conventional peak fitting, the typical generalisations observed to improve peak fitting convenience (e.g., assigning a single peak to describe all [C-O]/[C-N]-based functionalities, or grouping differences in functionality positioning despite the variation in the theoretical composition of, e.g., centred and end-chain functionalities) limited the ability to establish a detailed spectral interpretation. As was shown previously in Section 4.3.3, a comparison of the calculated ΔCEBE database to the experimental ΔCEBEs showed that the deviation introduced by the change in functionality positioning was significant enough to allow differentiation during the high-resolution XPS spectra peak fitting. Ultimately, the developed approach allowed the identification of a small number of functional groups (out of a larger number of possible functionalities) whose presence could not readily be predicted or 'guessed' otherwise using conventional XPS peak fitting. Biomolecules incorporated within the polymer matrix were able to be distinguished by the peak model – which was not possible with reference-based peak fitting due to a lack of available references in the literature.

Furthermore, as the long-range effects of the evaluated functionalities on the carbon backbone are not considered with reference-based peak fitting, component stability (i.e., the observed change in component presence with the inclusion of its associated higher-order carbon shifts) cannot be evaluated through spectral processing. When peak fitting

functionality-rich polymeric surfaces, such as those obtained after plasma-treatment of polymers, peak fitting based on the nearest-neighbour analysis is insufficient to establish the full hydrocarbon presence and may result in data misinterpretation. Instead, using the higher-order carbon shifts included within the developed peak model, the theoretical composition of the otherwise unknown chemical surface composition can be estimated during peak fitting (i.e., by the area constraints set on the component peaks with the respective RSFs and theoretical composition of the evaluated functionalities).

As with any theoretical model, there are limitations to the peak model due to its highly constrained nature, the observed outcome may deviate if a different method was used to estimate the (Δ)CEBEs or the positional and/or FWHM constraints were set differently/relaxed. Furthermore, in the present work, vibrational and configurational effects on the ΔCEBEs were neglected. However, the developed peak model provided a material-specific solution for PE-based surfaces and highly reproducible peak fits. Based on comparison to the reference-based peak fitting and the fact that many if not most of the components included in the developed peak model had peak areas at or close to zero indicated that the model and data were able to handle the input of functionalities in the model that were, or were not, present on the surface. Using the developed theoretical peak model, manual input and personal bias (in terms of component identification) from the spectral analyst becomes negligible – apart from when establishing the presence of contaminants and setting the positional constraints of the peak model reference components.

4.4. Biological evaluation of UHMWPE-based surfaces*

The biological response to the UHMWPE-based surfaces was evaluated through bacterial adhesion and cell viability assays. Unfortunately, the experiments on the UHMWPE-based samples with immobilised AMPs were unable to be completed (see footnote).

4.4.1. Bacterial adhesion assay

A bacterial adhesion assay was used to evaluate the bacterial growth on the UHMWPE-based surfaces, which provided insight into potential antibacterial activity. The bacterial adhesion assay was performed with *Staphylococcus aureus* (NCTC 10833) and *Staphylococcus epidermidis* (NCTC 11047), see Section 3.3.1 for more information on the performed assay and how the bacterial concentrations (CFU/mL) were determined using the Miles and Misra method. By comparing the bacterial concentration of the respective UHMWPE-based sample surfaces to the positive control (i.e., a TSA plate), the relative bacterial growth was determined following:

$$\text{Bacterial growth (\%)} = \frac{N - N_0}{N_0} * 100 \qquad \textit{(Eq. 28)}$$

where N_0 is the bacterial concentration of the control and N is the bacterial concentration for the respective UHMWPE-based sample surfaces. Three repeats were prepared for each sample type, the raw data showing the individual counted CFUs, dilution factor (mL) and resulting bacterial concentrations are shown in Appendix E1. Next to that, additional statistic results from the one-way ANOVA and Tukey-Kramer post-hoc analysis on the bacterial concentrations are available in Appendix E2 (i.e., group-wise variance, individual *p* values between pairs, etc.). The observed bacterial concentration and relative bacterial growth for the two bacterial strains on the UHMWPE-based sample surfaces are shown in Figure 105.

* The results for this section are not complete, please see the declaration of disruption to planned research.

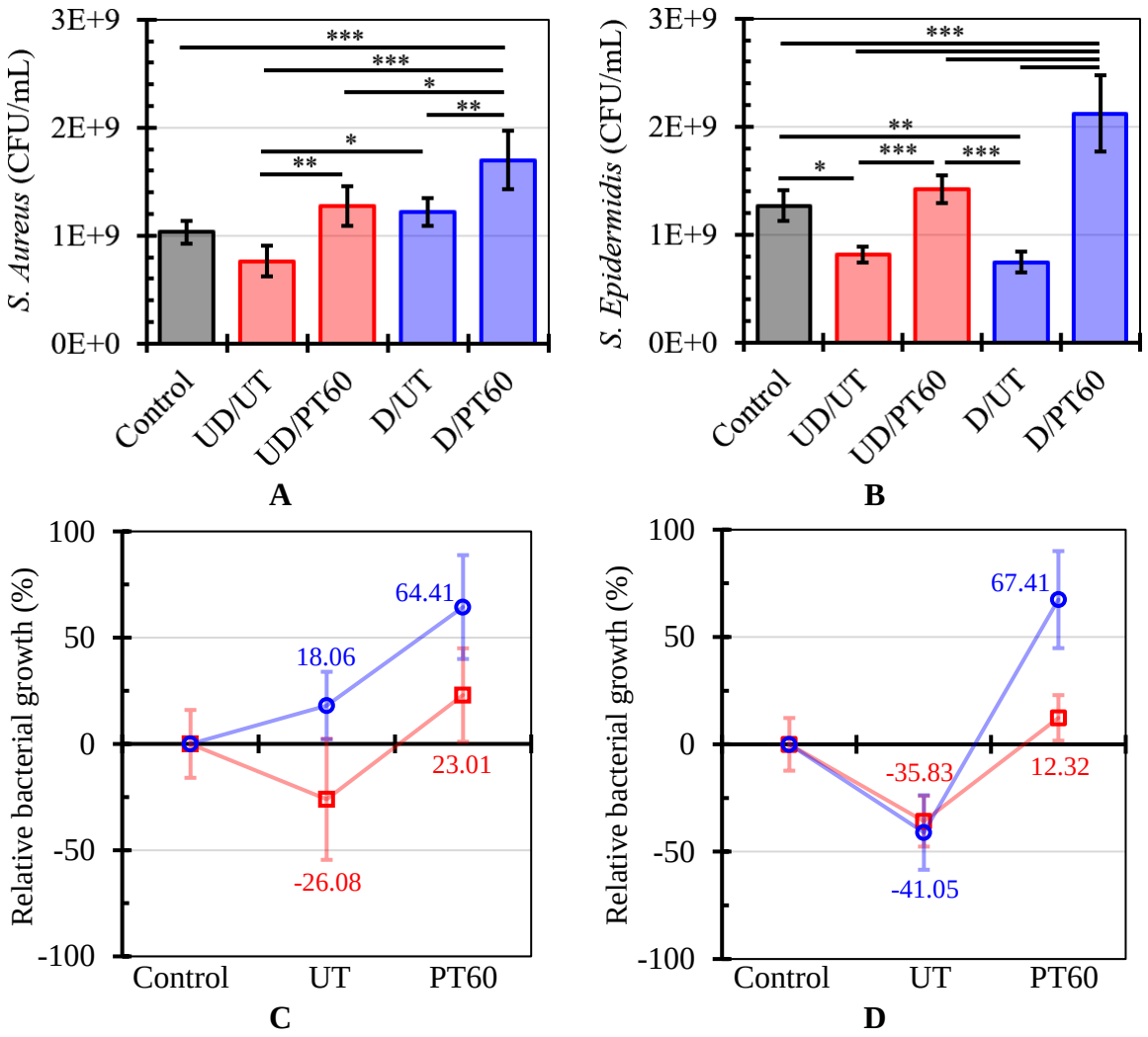


Figure 105. One-way ANOVA with Tukey-Kramer post-hoc analysis on the **b**acterial concentrations (CFU/mL) for (**A**) *S. aureus* and (**B**) *S. epidermidis* on the control (PS-TC) and undoped and untreated (UD/UT), undoped and plasma-treated (UD/PT60), doped and untreated (D/UT), and doped and plasma-treated (D/PT60) UHMWPE (the bars with asterisks indicate the *p*-value, showing *p<0.05, **p<0.01, and ***p<0.001 – when there is no bar between a pair, their difference is insignificant, i.e., p>0.05); and the bacterial growth (%) for (**C**) *S. aureus* and (**D**) *S. epidermidis* with the (**red**) undoped and (**blue**) doped sample series, relative to the positive control – errors bars show confidence internal with α = 0.05.

As shown in Figure 105A, the bacterial growth control of *Staphylococcus Aureus* only showed a significant difference to D/PT60 (p < 0.001). However, although not showing a significant difference to the control, UD/UT showed a significant difference to UD/PT60 (p < 0.01) and D/UT (p < 0.05), which indicated the treatments used to modify UHMWPE (i.e., αTH doping or ASPN) increased the bacterial growth of *Staphylococcus aureus*. Next to that, the difference between D/UT and D/PT60 was also significant (p < 0.01), demonstrating that both treatments sequentially increased the bacterial growth of *Staphylococcus aureus* on

UHMWPE. For example, as shown in Figure 105C after αTH doping or ASPN, the bacterial growth relative to the control significantly increased from –26.08% at UD/UT to +23.01% and +18.06% at UD/PT60 and D/UT, respectively (i.e., a relative increase of 49.09% and 44.14%, respectively). Subsequently, after the ASPN of D/UT, the relative bacterial growth increased from +18.06% at D/UT to +64.41% at D/PT60 (i.e., an increase of 46.35%). The bacterial growth control of *Staphylococcus epidermidis* showed a significant difference to all samples apart from UD/PT60 ($p > 0.05$), as shown in Figure 105B. Most notably, as seen with *Staphylococcus aureus*, the ASPN treatment significantly increased the bacterial growth of *Staphylococcus epidermidis* when comparing UD/UT to UD/PT60 ($p < 0.001$). However, in this case, there was no significant difference in bacterial growth for D/UT (i.e., after αTH doping) when compared to UD/UT. After the ASPN of D/UT, a significant increase was observed for D/PT60 when compared to UD/PT60. As shown in Figure 105D, both untreated samples UD/UT and D/UT showed a significant ($p < 0.01$) reduction in the bacterial growth of –35.83% and –41.05%, respectively, relative to the control for *Staphylococcus epidermidis*. The bacterial growth was restored after ASPN and UD/PT60 showed to be similar (i.e., not significantly different, $p > 0.05$) to the control. However, when compared to UD/UT, UD/PT60 did show a significant increase in relative bacterial growth of *Staphylococcus epidermidis* from –35.83% at UD/UT to +12.32% at UD/PT60 (i.e., an increase of 48.15%) – a similar increase (49.09%) was also noted between UD/UT to UD/PT60 with *Staphylococcus aureus*. From all samples, D/PT60 showed the highest increase in relative bacterial growth at +67.41%, which was also the case with *Staphylococcus aureus*.

According to a comprehensive review by Hartmann *et al.* of *in-vivo*/*in-vitro* studies (i.e., in laboratory settings or in living organisms, respectively) published between 2010 and 2020 using αTH, αTH showed promising results to aid/enhance antimicrobial agents (Hartmann et al., 2020). For example, αTH showed the ability to counteract the resistance-

mechanism induced by various Gram-negative and multi-drug-resistant bacterial species (e.g., *Burkholderia cenocepacia* [K56-2], *Pseudomonas aeruginosa* [PAO1], etc.) that produce the bacterial lipocalin protein (BcnA; i.e., a protein that induces resistance by binding to antibiotics in the extracellular space) (El-Halfawy et al., 2017; Naguib & Valvanoa, 2018). Due to the higher binding affinity of αTH to the lipocalin tunnel (i.e., according to docking analysis, its alkyl chain is buried within the tunnel and the cyclic head is positioned near the entrance), *Galleria mellonella* larva showed ~45% increased survival after 200 minutes in an *in-vivo* infection model using *Acinetobacter baumannii*, due to increased antibiotic effectiveness of ceftazidime and norfloxacin (El-Halfawy et al., 2017). In another study, Andrade *et al.* showed that addition of αTH in sub-inhibitory concentrations (i.e., MIC/8, MIC/4, and MIC/2) to antibiotic aminoglycosides (i.e., amikacin, neomycin, gentamicin) resulted in a mean MIC reduction of 41%, 75%, and 80%, respectively, when compared to the MIC of the antibiotic alone against three clinical multi-drug-resistant bacteria (i.e., *Pseudomonas aeruginosa* [ATCC 15442], *Escherichia coli* [ATCC 10536], and *Staphylococcus aureus* [ATCC 25923]) in a broth microdilution assay (Andrade et al., 2014). Next to that, these authors also reported that αTH alone did not exhibit antimicrobial effects (i.e., MIC of >1024 μg/mL was observed for all bacteria) or directly impact the antibiotic effects of aminoglycosides apart from acting as a lipocalin binding inhibitor. Furthermore, Williams *et al.* studied the biofilm formation of a clinical isolate of methicillin-resistant *Staphylococcus aureus* (MRSA) on UHMWPE that was either compression moulded, crosslinked, or αTH-doped and crosslinked (Williams et al., 2015). The UHMWPE-based samples were evaluated through incubation in a flow cell, containing a bacterial solution of 10^5 CFU/mL pumped through at 4.5 mL/hour. These authors also demonstrated that αTH doping of UHMWPE did not prevent or reduce the attachment/formation of bacterial biofilms on the material surface. Based off the literature,

αTH doping does not provide antibacterial activity but (depending on the bacterial strain) may improve the efficiency of antimicrobial agents by acting as a lipocalin binding inhibitor.

In this work, the incorporation of αTH showed mixed results with the bacterial adhesion assay. When compared to UD/UT, D/UT displayed a significant increase in bacterial growth with *Staphylococcus aureus* but not with *Staphylococcus epidermidis*, as shown in Figure 105A-B. In other words, the presence of αTH in D/UT did not display antibacterial activity when compared to UD/UT – which was expected based off the previously discussed literature. However, when comparing the relative bacterial growth of D/UT to UD/UT, *Staphylococcus aureus* displayed ~59% more relative bacterial growth than *Staphylococcus epidermidis*. According to a bacterial adherence assay performed by Gómez-Barrena *et al*., D/UT showed a reduction of 20% and 80% in bacterial adhesion relative to UD/UT, as determined using the Miles and Misra method following incubation of the UHMWPE-based samples in 10^8 CFU/mL solutions of *Staphylococcus aureus* (15981) and *Staphylococcus epidermidis* (ATCC 35984), respectively (Gómez-Barrena et al., 2011). Although no reduction in bacterial adhesion was observed for D/UT in this work, Gómez-Barrena *et al*. did also observe a lower bacterial adhesion of ~43% with *Staphylococcus epidermidis* on D/UT when compared to *Staphylococcus aureus* – like in this work, which also displayed a lower relative bacterial growth for *Staphylococcus epidermidis*. Next to that, these authors also demonstrated that different clinical strains of the same bacterial species (i.e., strains isolated directly from different prosthetic joint infections) displayed a difference in bacterial adherence and that the αTH only affected the adherence of some inter-species strains (Gómez-Barrena et al., 2011).

Both UD/PT60 and D/PT60 showed a significant increase in the bacterial growth for both bacteria relative to their untreated counterpart, as shown in Figure 105A-B, which indicated that ASPN positively impacted the bacterial growth. Moreover, D/PT60 always showed a significant increase relative to UD/PT60 and the highest bacterial growth overall. To

provide some insight into what is most likely to have resulted in this increase, the bacterial concentrations were correlated to various indices from FTIR, Raman, XPS and CA measurements (see Section 4.1.1, 4.1.2, 4.1.3, and 4.1.5, respectively), to obtain Pearson and linear regression coefficients (i.e., r_p and R^2, respectively). It is important to keep in mind that there are only four data points in each array used in the correlations, which limits the extent to which conclusions can be drawn. However, there are two sets of correlations being considered, given the use of two different bacterial strains. Although the overall sample size is still small, analysing the correlations from both strains together was thought to provide valuable insights into potential relationships. As can be observed in Table 33, various strong correlations ($-0.75 > r_p > 0.75$) were observed between the bacterial growths and the analysis results. Most notable positive correlations are the [C=C] (r_p = 0.82/0.98**)** and [C=O] indices (r_p = 0.78/0.79**)** from FTIR, the [a-C] index (r_p = 0.86/0.94**)** from Raman, and the [N 1s] At% (r_p = 0.87/1.00**)** from XPS, which indicated that the bacterial growth may have increased due to ASPN. However, it cannot be determined whether this increased due to introduction of nitrogen, a-C, or both. Next to that, it was found that the bacterial growths showed a negative correlation with the [O=C–O] index (r_p = -0.85/-0.85**)** from FTIR and the [C 1s] At% (r_p = -0.61/-0.83**)** from XPS. The negative correlation of [C 1s] At% from XPS is likely related to the introduction of nitrogen. The negative correlation of the bacterial growths with the [O=C–O] index would indicate that bacterial growth was more effective on hydrophobic surfaces than on hydrophilic surfaces.

Table 33. Pearson and linear regression coefficients between bacterial concentration of *S. Aureus* and *S. Epidermidis* to various results obtained by FTIR, Raman, XPS and CA measurements.

		***S. Aureus* (CFU/mL)**		***S. Epidermidis* (CFU/mL)**	
		r_p	R^2	r_p	R^2
FTIR (A.U.)	**VI**	0.69	0.47	0.87	0.75
	GWI	0.33	0.11	0.13	0.02

	TVI	0.46	0.22	0.61	0.37
	αTH	0.26	0.07	-0.26	0.07
	C=C$_{(1+2)}$	0.82	0.68	0.98	0.97
	C=O	0.78	0.61	0.79	0.63
	O=C–O	-0.85	0.73	-0.85	0.72
Raman (A.U.)	α_c	0.21	0.04	-0.18	0.03
	α_a	-0.48	0.23	-0.75	0.57
	α_b	0.18	0.03	0.53	0.28
	a-C	0.86	0.74	0.94	0.88
XPS (At%)	**C 1s**	-0.61	0.37	-0.83	0.68
	N 1s	0.87	0.76	1.00	1.00
	O 1s	0.13	0.02	0.36	0.13
ECA (°)	**DI water**	-0.2	0.04	0.34	0.11
	Diiodomethane	-0.15	0.02	0.39	0.15

The correlation between bacterial growth and surface hydrophobicity is also observed in the literature, for example, Gottenbos *et al.* investigated the adhesion and surface growth of *Staphylococcus epidermidis* (HBH_2 102) and *Pseudomonas aeruginosa* (AK1) on various polymers (i.e., PE, PP, PET, etc.) using a parallel plate flow chamber pumping through bacterial solutions of 3 * 10^8 CFU/mL at 0.025 mL/s over 48 hours (Gottenbos et al., 2000). These authors, as well as others, found that the bacterial growth positively correlated with hydrophobicity and negatively correlated with surface charge (Cordeiro et al., 2019; Gottenbos et al., 2000; Higashi et al., 1998). The hydrophobicity and surface charge were therefore considered two of the most important surface-related properties to facilitate the adsorption of

nutrients and proteins required for the biofilm adhesion. However, no correlation was observed between the bacterial growth and the ECA of DI water (Gottenbos et al., 2000). In this work, there was also no strong correlation observed between the bacterial growth of *Staphylococcus aureus* and *Staphylococcus epidermidis* with the ECA of DI water or diiodomethane.

Although it cannot be fully excluded that changes in the surface roughness influenced the bacterial growth, this is generally not deemed a significant factor for bacterial growth on polymers. For example, Kinnari *et al.* showed that increased surface roughness of UHMWPE did not significantly affect the bacterial adhesion of *Staphylococcus aureus* (15981) and *Staphylococcus epidermidis* (ATCC 35984), as determined with the Miles and Misra method after sonication of the UHMWPE-based samples incubated overnight in bacterial solutions of 10^8 CFU/mL (Kinnari et al., 2010). Surface roughness was introduced by polishing UHMWPE with 360, 600 and 2500 grit paper, prior to a low-pressure nitrogen (99.9%) plasma treatment, which resulted in a roughness arithmetic average of 1.93, 0.80 and 0.27 μm, respectively. However, it is worth to note that in this research article the surface was notably more hydrophilic (i.e., ECA of DI water of ~40°), when compared to this work (i.e., ECA of DI water of ~104 ± 9°), which impacts the bacterial growth. Almaguer-Flores *et al.* tested the bacterial adhesion on smooth and rough a-C coatings, following the Miles and Misra method after sonication of samples incubated for 24 hours in bacterial solutions (10^6 CFU/mL) of various bacteria (e.g., *Campylobacter rectus* (332838), *Streptococcus sanguinis* (10556), etc.) (Almaguer-Flores et al., 2010). Some bacteria displayed better general adhesion overall to rougher a-C surfaces (e.g., *Streptococcus sanguinis*), whilst others preferred smooth surfaces (e.g., *Prevotella intermedia*). However, at times this preference would change depending on the incubation media, e.g., *Fusobacterium nucleatum* showed a two-fold increase in growth on a smooth a-C surface in human saliva relative to a rough a-C surface, but a three-fold increase in growth on a rough a-C surface in mycoplasma medium relative to a smooth a-C surface.

However, it was also shown that the results in well-controlled culture media were more reliable, as "natural" media like saliva differed in composition (Almaguer-Flores et al., 2010).

Finally, it is worth noting that the experimental set-up (Section 3.3.1) presented some issues which may have influenced the observed results. Due to the hydrophobicity of some of the sample surfaces, the inoculum did not "like" to spread on the sample surface and had the tendency to retract. When placing the glass coverslip on the droplet of inoculum pipetted on the UHMWPE-based surface, the droplet tended to "escape" from in-between the hydrophobic microscope slide and sample it was placed upon. Because of this issue, it might be favourable to add additional PBS to the filter paper to prevent the inoculum from drying out, instead of placing glass slides on top of the droplet of the inoculum.

4.4.2. Cell viability assay

A cell viability assay was used to evaluate the biocompatibility of the UHMWPE-based surfaces, which was performed with the human *Sarcoma osteogenic* cell line (*Saos-2*; ATCC HTB-85), see Section 3.3.2 for more information on the performed assay. From the recorded luminescence intensity of the CellTiter-Glo reagent and using its correlation to the standard curve available in the assay manual, the resulting cell count was determined (Promega, 2002). The cell viability assay for the UT samples was performed with cell passage 34 and for the PT60 samples with cell passage 32, three repeats were prepared for each sample type. The recorded luminescence, standard curve, and resulting cell count, are available in Appendix E3. As the assays for the UT and PT60 samples used different cell passages, these each had a separate control (i.e., a polystyrene tissue culture plate). The '*Saos-2*' cell count for the respective controls and on the UHMWPE-based sample surfaces determined after one, four and seven days, are shown in Figure 106. The one-way ANOVA and Tukey-Kramer post-hoc analysis was performed between pairs from the same day (i.e., day 1, 4, and 7) – additional

statistic results are available in Appendix E4. The cell count assesses the direct/immediate effects experienced on the overall health and survival of cells relative to the control or other samples of interest. As can be observed in Figure 106, only three significant (i.e., $p < 0.05$) pair-wise differences were observed. Namely, at day 4 between the control and D/UT ($p = < 0.05$), and at day 1 between the control and UD/PT60 ($p = < 0.001$), as well as D/PT60 ($p < 0.01$). The error observed in the cell counts of an already relatively small number of the repeats (3), resulted in relatively high *p*-values and minimized the number of significant differences. Next to that, although the cell count between the two controls looked notably different, one-way ANOVA with Tukey-Kramer post-hoc analysis between their cell counts (not shown here) revealed that there was only a significant difference at day 4 ($p = 0.0097$), but not at day 1 ($p = 0.1460$) and day 7 ($p = 0.1215$).

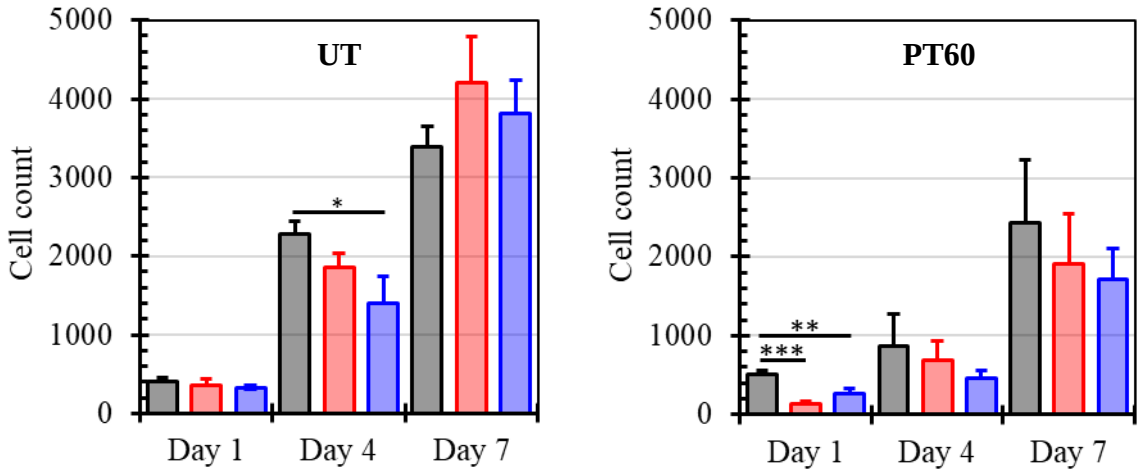


Figure 106. One-way ANOVA with Tukey-Kramer post-hoc analysis on the cell count for *Saos-2* on (left) untreated (UT) and (right) plasma-treated (PT60), (**red**) undoped and (**blue**) doped UHMWPE-based samples (the bars with asterisks indicate the *p*-value, showing *p<0.05, **p<0.01, and ***p<0.001; when there is no bar between a pair, their difference is insignificant, i.e., p>0.05) – errors bars show confidence internal with α=0.05.

The cell growth rates (CGR) were estimated by taking the slope (a) from the linear regression fits ($y = a\,x + b$) of the cell count from the samples (y) over the incubation period in days (x), the results are shown in Table 34. The estimated CGR assess the overall cell proliferation, related to the long-term metabolic activity and biomass accumulation within the cell population. The highest CGR (i.e., steepest slope) presented in Table 34 was from UD/UT

at 642 cells/day, whereas the lowest CGR was from D/PT60 at 241 cells/day. The linear regression fits of the relative CGR showed strong correlation coefficients, with a R^2 of 0.98, 0.95, 0.95, and 0.85 for UD/UT, UD/PT60, D/UT and D/PT60, respectively.

Table 34. Relative cell growth rate (*a*; CGR) of *Saos-2* estimated by the linear regression fits ($y = ax + b$) on the cell count of the control and samples (y) over the incubation period (x), including the regression coefficient (R^2).

	UT			**PT60**		
Sample (*y*)	**Control**	**UD/UT**	**D/UT**	**Control**	**UD/PT60**	**D/PT60**
Slope (*a*; CGR)	497	642	582	322	293	241
Offset (*b*)	+33	-452	-488	-17	-260	-152
R^2	0.98	0.98	0.95	0.89	0.95	0.85

Various indices from FTIR, Raman, XPS and CA measurements were correlated to the cell count and CGR of *Saos-2*, to obtain Pearson and linear regression coefficients (i.e., r_p and R^2, respectively). Both the cell count at different days and the CGR were evaluated, as both provide distinct insights on the behaviour of the cell population as discussed before. Although the cell counts did not display many significant differences individually (at least, at a significance level of $p < 0.05$), analysing these correlations together was thought to provide some valuable insights into potential relationships with the cell growth. As can be observed in Table 35, the correlations from the cell counts at different days showed similar coefficients throughout, as well as with the CGR. Focussing on the CGR, as this assessed the overall cell proliferation over time, seven strong correlations ($-0.75 > r_p > 0.75$) were observed with the indices. The two positive correlations with the CGR were with the [C 1s] At% ($r_p = 0.94$**)** from XPS and the [O=C–O] index ($r_p = 0.98$**)** from FTIR, which indicated that the cell growth rate was higher on the untreated surfaces or those that contained more carboxylic acid groups. It is worth to note that, there was no strong correlation observed with the [αTH] index ($r_p = 0.26$) from FTIR or the ECA from DI water ($r_p = -0.27$) and diiodomethane ($r_p = -0.19$). On the other

hand, there were five negative correlations, with the [C=C] (r_p = -0.84), [VI] (r_p = -0.97) and [TVI] (r_p = -0.84) indices from FTIR, the [a-C] index (r_p = -0.76) from Raman, and the [N 1s] At% (r_p = -0.93) from XPS. The negative correlations with these indices indicated again that the CGR was higher on untreated surfaces, instead of plasma-treated surfaces. However, it cannot be determined whether the cell growth decreased due to the introduction of nitrogen, a-C, carbon-carbon double bonds, or their combined effect. Interestingly, there was a contrast in the strong Pearson correlation coefficients (i.e., a shift from negative to positive correlation or vice versa, with the [O=C–O], [C=C], [a-C], [C 1s], and [N 1s] indices) observed between the CGR of *Saos-2* cells and the bacterial concentrations of *S. Aureus* and *S. Epidermidis* in Section 4.4.1. This contrast may be attributed to the different preferences in surface hydrophobicity by these cells, as bacteria tend to prefer hydrophobic surfaces but human cells generally thrive on more hydrophilic surfaces (Geckeler et al., 2003; Gottenbos et al., 2000).

Table 35. Pearson and linear regression coefficients between the cell count at day 1, 4, and 7, and the cell growth rate (CGR) of *Saos-2* to indices obtained by FTIR, Raman, XPS and CA measurements.

		Cell count						**CGR**	
		Day 1		**Day 4**		**Day 7**			
		r_p	R^2	r_p	R^2	r_p	R^2	r_p	R^2
FTIR (A.U.)	**VI**	-0.85	0.94	-0.92	0.94	-0.98	0.94	-0.97	0.94
	GWI	-0.88	0.24	-0.54	0.24	-0.53	0.24	-0.49	0.24
	TVI	-0.97	0.71	-0.78	0.71	-0.86	0.71	-0.84	0.71
	αTH	0.32	0.07	0.08	0.07	0.26	0.07	0.26	0.07
	$C{=}C_{(1+2)}$	-0.33	0.70	-0.81	0.70	-0.81	0.70	-0.84	0.70
	C=O	0.08	0.30	-0.58	0.30	-0.51	0.30	-0.55	0.30
	O=C–O	0.85	0.96	0.99	0.96	0.99	0.96	0.98	0.96
Raman	α_c	-0.58	0.03	-0.27	0.03	-0.20	0.03	-0.16	0.03

	α_a	-0.16	0.20	0.39	0.20	0.41	0.20	0.45	0.20
	α_b	0.37	0.03	-0.10	0.03	-0.15	0.03	-0.18	0.03
	a-C	-0.19	0.58	-0.76	0.58	-0.73	0.58	-0.76	0.58
XPS (At%)	**C 1s**	0.86	0.89	0.87	0.89	0.95	0.89	0.94	0.89
	N 1s	-0.49	0.86	-0.91	0.86	-0.91	0.86	-0.93	0.86
	O 1s	-0.90	0.38	-0.52	0.38	-0.65	0.38	-0.62	0.38
ECA (°)	**DI water**	-0.24	0.08	-0.10	0.08	-0.28	0.08	-0.27	0.08
	Diiodomethane	0.06	0.04	-0.03	0.04	-0.17	0.04	-0.19	0.04

More specifically regarding *Saos-2*, Geckeler *et al.* investigated the *Saos-2* (ATCC HTB-85; the same cell line as used in this work) cell viability on 18 different polymers and determined the cell viability relative to polystyrene tissue culture plates (PS-TC; similar to those used in this work as a control), following a MTT cell viability assay after seven days of incubation (Geckeler et al., 2003). The reported results from the cell viability on the various tested polymers were compiled and displayed in Figure 107. As can be observed, all polymers showed reduced cell viability relative to PS-TC (reduction varied from 25-98%), the deviation between the evaluated polymers was high within the same group (e.g., see [CO] or [CNO]). When comparing the relative cell viability, the polymers containing only [C] (i.e., HDPE and regular PS) generally showed similar cell viability or outperformed those containing [CO] and [CNO] – apart from epoxy resin (MY) which showed the highest cell viability at 75% relative to the PS-TC control. The same authors also correlated the cell viabilities with the advancing and receding CAs for DI water, the optimal cell viability was achieved at 80° and 20°, respectively (Geckeler et al., 2003). The conversion formula established by Tadmor was used to approximate the ECA using the provided advancing/receding CAs from Geckeler *et al.*, to allow comparison to this work, which showed the optimal DI water ECA for *Saos-2* cell

viability was ~35° (Geckeler et al., 2003; Tadmor, 2004). The optimal ECA for DI water (~35°) is significantly lower than the ECA of ~104 ± 9° observed in this work, which could (to some extent) explain the lack of increase in CGR on the plasma-treated UHMWPE-based surfaces.

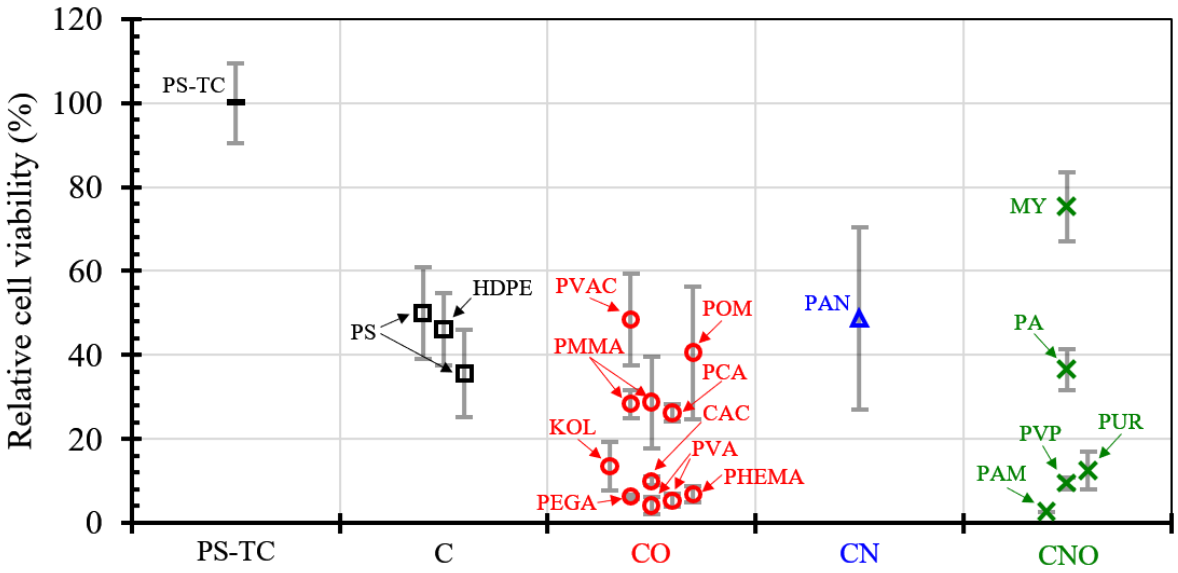


Figure 107. *Saos-2* cell viability (%) from various polymers relative to the PS-TC control, polymers are separated by their atomic composition, containing [C] (**black**, square), [CO] (**red**, circle), [CN] (**blue**, triangle), or [CNO] atoms (**green**, cross) – data plotted in this graph was taken from (Geckeler et al., 2003).

Next to that, based on the results presented by Geckeler *et al.*, simply the introduction of polar functional groups did not necessarily increase the cell viability relative to [C]-containing polymers (Geckeler et al., 2003). More specifically, HDPE displayed a moderate relative cell viability of 46.1±8.6%, whereas polyvinyl alcohol (PVA) and polyacrylamide (PAM) showed the lowest cell viability from all investigated polymers at 4.1±1.5% and 2.5±0.0%, respectively. PVA and PAM both consist of an aliphatic carbon backbone like HDPE, but contain a primary hydroxyl or amide substituent, respectively, on alternating carbons. Both hydroxyl and amide groups are polar and were found to be present on the surface of the ASPN-treated UHMWPE-based samples in this work, following high-resolution XPS analysis as shown in Section 4.3. Next to that, various other functional groups (at >1 At%) observed on the ASPN-treated UHMWPE-based samples are also present in the investigated polymers by Geckeler *et al.* – although the actual surface composition of the samples produced

in this work will be significantly different from these other polymers, comparisons were made to allow discussion on the potential effects of the present functionalities on the cell viability (Geckeler et al., 2003). For example, polycarbonate (PCA) contains a carbonate ester group attached to an aromatic ring on both sides, the cell viability for this polymer was 26.2±2.0% – slightly above half of the cell viability observed for HDPE. Next to that, polyacrylonitrile (PAN) consists of an aliphatic carbon backbone with a nitrile substituent on alternating carbons, which showed a cell viability like HDPE but had a very high standard deviation at 48.7±21.7%. Lastly, polyurethane (PUR) contains two carbamate groups in its subunit and displayed a cell viability of 12.4±4.5% – almost a fourth of the cell viability observed for HDPE (Geckeler et al., 2003). Altogether, this meant at least five different functional groups found on the surface of the ASPN-treated UHMWPE-based samples in this work (i.e., hydroxyl, amide, carbonate ester, nitrile, and carbamate), were found to result in reduced *Saos-2* cell viability in their "native polymeric forms" (i.e., PVA, PAM, PCA, PAN, and PUR, respectively) relative to HDPE – which also may (to some extent) explain the decreased CGR after the ASPN of UHMWPE when compared to the untreated samples (Geckeler et al., 2003). Additionally, Geckeler *et al.* displayed there was a strong correlation with the *Saos-2* cell viability and the Hoy's solubility parameter (HSP; i.e., the molar water attraction constant divided by the molar volume of the polymer subunits), as well as CA hysteresis (i.e., the difference in advancing and receding CA) (Geckeler et al., 2003). In general, the polymers with a lower HSP of around 17-19 (e.g., HDPE and PS) displayed a relative cell viability of ~50%, whereas those with a high HSP of about 21-26 (e.g., PUR, PVA, PAM, etc.) displayed a cell viability ~10%. Next to that, a CA hysteresis of about 62° as seen with PS-TC control resulted in the highest cell viability from all investigated polymers. This work used the sessile drop method which only determined the ECA, but the CA hysteresis for the HDPE samples from Geckeler *et al.* was about 25°

(Geckeler et al., 2003). CA hysteresis is generally found to increase due to surface roughness, chemical heterogeneities, and surface deformation (Eral et al., 2013).

Investigating the effect of αTH, Massaccesi *et al.* demonstrated the difference of wear debris from unmodified, αTH-doped, and αTH-doped and irradiation-crosslinked UHMWPE generated using a simulated prosthetic joint, on cell viability, oxidative stress response, and osteoimmunological response (i.e., the interplay between the immune system and bone tissue) of *Saos-2* cells (Massaccesi et al., 2019). The generated wear debris was diluted in growth media at a concentration of 1:1, seeded with 10^3 of *Saos-2* cells/mL, and incubated for 96 hours (37°C and 5% CO_2). Cell viability was assessed quantitatively using an Alamar Blue® cell viability assay. The cell viability was expressed as a percentage of reduced Alamar Blue® (%AB) between the samples and the control (i.e., medium and Alamar Blue®), there were no significant differences observed in %AB between the control and/or samples. The expression of osteoimmunological biomarkers (i.e., RANKL and osteoprotegerin/OPG) were evaluated by ELISA assays in *Saos-2* supernatant. More specifically, RANKL was measured using an ELISA Duo Set assay, while OPG was measured with an ELISA Quantikine colorimetric sandwich assay. Next to that, O-GlcNAC levels were determined using a western blot with CTD110.6 antibody. O-GlcNAC is a post-translational modification involved in a cellular defence mechanism known as 'dynamic O-GlcNAcylation', this modification can alter protein function, cellular processes, and stress responses, ultimately promoting cell survival and adaptation when facing physiological/environmental challenges like oxidative stress (Massaccesi et al., 2019). The results from the performed assays indicated that *Saos-2* cells on the αTH-doped UHMWPE displayed an enhanced response to oxidative stress by increased activation of dynamic O-GlcNAcylation and an improved osteoimmunological response by promoting the secretion of bone-protective factors like OPG (reducing the RANKL/OPG ratio),

but the incorporation of αTH itself did not increase the cell growth relative to undoped UHMWPE – the latter was also observed in this work (Massaccesi et al., 2019).

In another study, Reznickova *et al.* investigated the cell growth of murine L929 fibroblast cells (NCTC 85103115) on UHMWPE plasma-treated between 20 to 480 seconds with direct glow/diode Ar^+ plasma (at a flow rate of 0.3 l/s and a pressure of 10 Pa), using a WST-1 cell viability assay after one and three days of incubation (Reznickova et al., 2015). Directly after the Ar^+ plasma treatment, the UHMWPE samples showed an ECA for DI water between 10-20°. However, once the hydrophobic recovery for plasma-treated UHMWPE stabilised after ~24 hours, samples treated with longer durations (>60 seconds) displayed higher ECA (105-120°) than untreated UHMWPE (~95°). The L929 cell count on the plasma-treated UHMWPE surfaces following staining and fluorescence microscopy showed to be almost quadrupled, when compared to PS-TC and the untreated UHMWPE (Reznickova et al., 2015). However, the opposite was observed with the metabolic activity of the L929 cells according to the WST-1 cell viability assay, as the plasma-treated UHMWPE showed a significant decrease, reaching only 15-40% relative cell viability to the PS-TC control, whereas unmodified UHMWPE displayed 58-66%. These results also highlighted that visual cell counting alone is not enough to evaluate the biocompatibility, cell viability assays must also be performed. This paper demonstrated similar ECAs (95-120°) after the plasma treatment of UHMWPE as observed in this work (104 ± 9°), but it is worth to recognize that an Ar^+ plasma working gas predominantly results in the formation of [O]-containing functional groups upon the exposure of the reactive surface to the ambient conditions (Reznickova et al., 2015). Nonetheless, this paper also demonstrated that, like this work, the plasma-treatment of UHMWPE reduced the cell viability when compared to untreated UHMWPE despite the introduction of polar functionalities.

Finally, it is worth to note that the experimental set-up (Section 3.3.2) presented some issues which may have influenced the observed results. For example, due to the density of UHMWPE, it had the tendency to float in the medium. Although this was mostly counteracted by not overfilling the wells with too much medium, it could not be fully prevented. Alternatively, the use of a sticker (e.g., carbon adhesive tape, as used with SEM) or polystyrene rings fitted around the samples to restrict them at the bottom of the wells, would be optimal to prevent any undesired floating. Next to that, although the seeded cells were initially incubated for 20 minutes to allow adherence to the sample surface, it cannot be fully excluded that cells would detach and continue growing in the well itself instead of solely on the sample surface. Naturally, this would impact the observed results when performing the cell viability assay using the CellTiter-Glo reagent, as the polystyrene wells are always biocompatible. Next to that, the well plates had to be transported from the Institute of Inflammation and Ageing to the School of Dentistry to have access to a photoluminescence spectrometer, which reduced the luminescence signal over time. Although this was accounted by measuring the luminescence signal after the same waiting time, it was not practical. Lastly, the assays were performed with an already relatively high passage number, and this may have influenced the results. According to the literature, it would be beneficial to perform such assays with a fresh cell line and keep the passage number to a minimum (Mouriaux et al., 2016).

Section 5: Conclusions and Future Perspectives

5.1. Conclusions

The overarching aim of this work was to improve the current state-of-the-art of UHMWPE-based biomaterials as used in total joint replacements. In order to achieve this, αTH doping of UHMWPE was used to provide protection against oxidation and wear debris generation, ASPN was used to induce surface functionalisation and improve mechanical properties, and AMPs were immobilised to the introduced functionalities in order to prevent infection and subsequent implant failure. Prior to this work, the combination of αTH doping and ASPN of UHMWPE was not yet reported within the literature, but this combination has been extensively investigated and showed promising results. Although the overarching aim of this work was not fully realized, most objectives were achieved. The presented results have improved the understanding of the performed treatments and/or analysis with regards to the developed UHMWPE-based samples, the findings of which can be summarised as follows:

1. The doping of UHMWPE with αTH resulted in the reduction of the vinyl-based bond formations after the ASPN treatment but, when comparing the doped sample series to the undoped sample series, the overall (non-vinyl) hydrocarbon unsaturation increased over the ASPN treatment time.
2. It was revealed that the unsaturated carbon-based compound formed on the UHMWPE surface after ASPN was likely a depth-dependent mixture of polyene, amorphous carbon, and aromatics – where most aromaticity was observed closer towards the sample surface.
3. The ‘a-C’-like compound likely originated from the orthorhombic crystalline phase of UHMWPE, whereas the αTH was found to be almost exclusively retained in the amorphous phase of UHMWPE.

4. The doped sample series displayed a minor decrease in (sub-)surface crystallinity over the ASPN treatment time, in contrast to the undoped samples which showed a minor increase in crystallinity.
5. The ASPN treatment was initially inhibited by the presence of αTH in the UHMWPE polymer matrix. However, the doped samples showed a higher presence of nitrogen (about two-fold) and reduced presence of oxygen (about one-third less) after 60 minutes when compared to the undoped sample series.
6. The doped sample series displayed a practically negligible amount of surface contamination originating from the active screen, whereas the undoped samples displayed various contaminants. The ASPN layer of the doped sample series also showed to be less fragile/more heterogeneous.
7. The surface immobilisation of glycine onto the undoped sample series was successful using all three proposed coupling chemistries, but DIC/Oxyma and CDI allowed a two-fold increased substitution compared to DCC/DMAP. The doped sample series displayed leaching of αTH, which inhibited the surface immobilisation of glycine.
8. There were practically no changes in the bulk crystallinity of UHMWPE. However, there were indications that smaller crystallites may have disappeared, which decreased the total crystallinity but increased the average crystallite size.
9. The doped sample series showed no delamination, in contrast to the notable delamination observed with the undoped sample series. Instead, the doped sample series displayed the formation of bubble-like clusters on top of the UHMWPE flake-like surface, which seemed to further spread out across the surface over the ASPN treatment time.

10. The doped sample series showed a major additional increase in microhardness when compared to the undoped sample series. The increased microhardness was attributed to the increased presence of the ‘a-C’-like compound, as it displayed a strong positive linear correlation.
11. The material-specific theoretical ΔCEBE peak model allowed for a more detailed interpretation of the high-resolution XPS spectra of the UHMWPE-based samples when compared to conventional peak fitting. More specifically, several (nitrogen-based) functionalities were identified that were not able to be readily identified using the conventional XPS reference databases or any of other characterisation techniques used in this work.
12. The UHMWPE-based samples displayed increased bacterial growth of *Staphylococcus aureus* and *Staphylococcus epidermidis* on the plasma-treated samples when compared to their untreated counterparts. On the other hand, the *Saos-2* cell proliferation showed the inverse, as the untreated samples demonstrated increased cell growth when compared to the plasma-treated samples. Thus, ASPN alone may not be ideal in terms of modifying UHMWPE for use in total joint replacements, highlighting the need for the immobilisation of AMPs onto the material surface – creating an interface that should be able to eliminate microbes and increase the surface hydrophilicity to improve the biological response towards human cells.

5.2. Future perspectives

The results within this work presented a broad investigation into the modified UHWPE-based samples using various characterisation techniques, which revealed changes experienced in its chemical, physical, and biological material- and/or surface-related properties. However, some of the performed experiments/analysis presented certain limitations and/or a degree of

uncertainty inevitable with the use of the respective techniques/instruments. In this section, the limitations experienced during the completion of this work are discussed and recommendations were formulated to benefit the future development of this project. Next to that, additional proposed future work that was unable to be completed or would be beneficial to expand upon for the understanding of the developed UHMWPE-based samples was also evaluated.

5.2.1. Limitations and recommendations

The XPS analysis (Section 4.1.3 and 4.3) and the degree of substitution measurements (Section 4.1.4) were used to reveal potential possible coupling chemistries and the success thereof by AAc immobilisation, respectively. Although the presented results showed to be (partially) successful with respect to the established aims, developing theoretical CEBE peak models and dealing with an unknown quantity of leaching products was not practical. Instead, it would be more ideal to use, e.g., chemical derivation using XPS. Using chemical derivation, it is possible to directly quantify the amount of functional groups across the spot size by immobilisation of a chemical containing an element that is not typically present on the material surface. For example, the chemical derivation of hydroxyl or amino groups on polymeric surfaces is frequently done with trifluoroacetic anhydride, which allows direct derivation of the investigated functional groups by the elemental ratio of fluoride (Pippig et al., 2009).

SEM (Section 4.1.6) was used investigate surface morphology of the UHMWPE-based samples, which demonstrated surface delamination and the formation of bubble-like clusters. However, as it was assumed that ASPN deposited a relatively fragile layer within the nanometre-scale, it is important to consider that the gold sputtering used to introduce conductivity to the sample surface may result in an altered morphology (Juhász et al., 2021). In this work, attempts were made to use an ESEM but, unfortunately, the environmental mode was not functional. It is therefore recommended that additional SEM micrographs are recorded using the environmental mode when available. This would allow one to observe the “true”

surface morphology, without potential modification induced by the gold sputtering, and evaluate any introduced differences by comparing the micrographs in this work.

Finally, as was demonstrated by the degree of substitution and CA measurements (Section 4.1.8), αTH doping of UHMWPE inhibited the immobilisation of '*KR-12*'. This was unfortunate considering the immobilisation of '*KR-12*' was ultimately the goal within this work. However, based on the increased Vickers microhardness and negligible surface contamination observed by XPS, the αTH doping prior to ASPN still showed to be a promising route for the surface modification of UHMWPE. Clearly, the αTH gets mostly exhausted by ASPN after 60 minutes as it eventually allowed surface functionalisation, but not enough to permit the subsequent immobilisation of '*KR-12*'. It might be worth to investigate if covering the bottom face of the sample prevents leaching or if longer ASPN treatment times are able to fully exhaust the αTH at which it would allow the immobilisation of '*KR-12*'.

5.2.2. Proposed future work

Although the SEM micrographs provided some insight into the visual surface roughness and delamination, it would be beneficial to analyse the surface roughness with, e.g., an atomic force microscope (AFM) or profilometer. More specifically, it would be interesting to investigate the shape and size of the bubble-like clusters (as was observed with SEM) formed on the D/PT# sample series in more detail. When using an AFM, the atomic force adhesion of the UHMWPE-based surfaces can also be evaluated, which especially after the formation of the 'a-C'-like compound is expected to reveal more interesting results.

Next to the surface roughness, no wear testing was performed on the UHMWPE-based sample surfaces. The Vickers microhardness showed a clear difference between the undoped and doped sample series, but that is solely based on a load applied perpendicular to the sample surface. When it comes to UHMWPE-based biomaterials, wear testing is typically performed

with a ball-on-disc tribometer or, preferably, with a knee simulator (Haider & Baykal, 2015; Tsukamoto et al., 2006). Naturally, a knee simulator would require full-scale implant, whereas a tribometer could be used for samples similar to those used within this work.

As discussed in Section 4.4, the biological evaluation of the AMP-immobilised UHMWPE-based sample could not be completed. Naturally, completing these biological evaluations would be important to complete the aims proposed in this work. However, when completing these biological evaluations, it will be important to further improve the experimental setups of the assays and consider limitations and/or incorporate the recommendations provided in Section 5.2.1. Lastly, it would be of interest to compare the biological evaluation of the surface-immobilised '*KR-12*' to that of its free-form counterpart, to determine the change in its antimicrobial activity once immobilised.

After evaluating the anti-bacterial activity and biocompatibility of the UHMWPE-based surfaces with the immobilised '*KR-12*', it is important to investigate the stability of the coupling chemistries. It was demonstrated that all the coupling chemistries used in this work allowed immobilisation of '*KR-12*', which each formed a different bond with the surface. Next to that, the linear backbone of peptides inherently consists out of amide bonds as well. Once the UHMWPE-based implant resides in the body, it will be in a constant humid/wet environment. Even when not directly placed in water, the water molecule is a frequent reactant or product formed by the general internal/external metabolism cycle of tissues, organisms, and cells (Testa & Mayer, 2006). Next to water, enzymes are abundantly present in the surrounding tissues, which will also accelerate the degradation of both the implant and the surface-immobilised AMPs, e.g., due to creating strong oxidative environments (Fiorito et al., 2001). The typical pH of blood and synovial fluid in/around the knees is about 7.4 (i.e., slightly alkaline), which is important to consider with regards to the AMP bond stability (Cummings & Nordby, 1966; Schwalfenberg, 2012). To investigate the bond stability and/or degradation

of immobilised AMPs, simulated body fluid (SBF) is a good substitute to investigate this, which can be combined with high-performance liquid chromatography to evaluate the AMP degradation/leaching kinetics (Trzcińska et al., 2020).

References

Affatato, S., Modena, E., Carmignato, S., & Taddei, P. (2013). The use of Raman spectroscopy in the analysis of UHMWPE uni-condylar bearing systems after run on a force and displacement control knee simulators. *Wear*, *297*(1–2), 781–790. https://doi.org/10.1016/j.wear.2012.10.002

Agakidou, E., Agakidis, C., Kontou, A., Chotas, W., & Sarafidis, K. (2022). Antimicrobial Peptides in Early-Life Host Defense, Perinatal Infections, and Necrotizing Enterocolitis—An Update. In *Journal of Clinical Medicine* (Vol. 11, Issue 17, p. 5074). Multidisciplinary Digital Publishing Institute. https://doi.org/10.3390/jcm11175074

Ahmad, N. S., Khalid, B. A. K., Luke, D. A., & Ima Nirwana, S. (2005). Tocotrienol offers better protection than tocopherol from free radical-induced damage of rat bone. *Clinical and Experimental Pharmacology & Physiology*, *32*(9), 761–770. https://doi.org/10.1111/j.1440-1681.2005.04264.x

Almaguer-Flores, A., Ximénez-Fyvie, L. A., & Rodil, S. E. (2010). Oral bacterial adhesion on amorphous carbon and titanium films: Effect of surface roughness and culture media. *Journal of Biomedical Materials Research - Part B Applied Biomaterials*, *92*(1), 196–204. https://doi.org/10.1002/jbm.b.31506

Alves, C., Araújo, O. F., & Sousa, M. de R. R. (2013). Comparison of Plasma-Assisted Nitriding Techniques. *Encyclopedia of Tribology*, 402–410. https://doi.org/10.1007/978-0-387-92897-5_716

Amusia, M. Y., Msezane, A. Z., & Shaginyan, V. R. (2003). Density Functional Theory versus the Hartree–Fock Method: Comparative Assessment. *Physica Scripta*, *68*(6), C133–C140. https://doi.org/10.1238/physica.regular.068ac0133

Andanson, J.-M., & Kazarian, S. G. (2008). In situ ATR-FTIR spectroscopy of poly (ethylene terephthalate) subjected to high-temperature methanol. *Macromolecular Symposia*, *265*(1), 195–204.

Andrade, J. C., Morais-Braga, M. F. B., Guedes, G. M. M., Tintino, S. R., Freitas, M. A., Menezes, I. R. A., & Coutinho, H. D. M. (2014). Enhancement of the antibiotic activity of aminoglycosides by alpha-tocopherol and other cholesterol derivates. *Biomedicine & Pharmacotherapy*, *68*(8), 1065–1069. https://doi.org/https://doi.org/10.1016/j.biopha.2014.10.011

Arumainayagam, C. R., Lee, H. L., Nelson, R. B., Haines, D. R., & Gunawardane, R. P. (2010). Low-energy electron-induced reactions in condensed matter. *Surface Science Reports*, *65*(1), 1–44. https://doi.org/10.1016/j.surfrep.2009.09.001

ASTM. (2019). Standard Test Method for Evaluating Trans-Vinylene Yield in Irradiated Ultra-High Molecular Weight Polyethylene Fabricated Forms Intended for Surgical Implants by Infrared Spectroscopy. In *ASTM Volume 13.01: Medical And Surgical Materials And Devices (I): E667–F2477*. https://doi.org/10.1520/F2381-19

ASTM. (2021). Standard Specification for Ultra-High-Molecular-Weight Polyethylene Powder and Fabricated Form for Surgical Implants. In *ASTM Volume 13.01: Medical And Surgical Materials And Devices (I): E667–F2477* (pp. 1–9). https://doi.org/10.1520/F0648-21

Babaghayou, M. I., Mourad, A.-H. I., Lorenzo, V., de la Orden, M. U., Urreaga, J. M., Chabira, S. F., & Sebaa, M. (2016). Photodegradation characterization and heterogeneity evaluation of the exposed and unexposed faces of stabilized and unstabilized LDPE films. *Materials \& Design*, *111*, 279–290.

Baena, J. C., Wu, J., & Peng, Z. (2015). Wear performance of UHMWPE and reinforced UHMWPE composites in arthroplasty applications: A review. *Lubricants*, *3*(2), 413–436. https://doi.org/10.3390/lubricants3020413

Bagheri, M., Beyermann, M., & Dathe, M. (2009). Immobilization reduces the activity of surface-bound cationic antimicrobial peptides with no influence upon the activity spectrum. *Antimicrobial Agents and Chemotherapy*, *53*(3), 1132–1141. https://doi.org/10.1128/AAC.01254-08

Baldan, M. R., Almeida, E. C., Azevedo, A. F., Gonçalves, E. S., Rezende, M. C., & Ferreira, N. G. (2007). Raman validity for crystallite size L a determination on reticulated vitreous carbon with different graphitization index. *Applied Surface Science*, *254*(2), 600–603. https://doi.org/10.1016/j.apsusc.2007.06.038

Banche, G., Allizond, V., Bracco, P., Bistolfi, A., Boffano, M., Cimino, A., Brach Del Prever, E. M., & Cuffini, A. M. (2014). Interplay between surface properties of standard, vitamin E blended and oxidised ultra high molecular weight polyethylene used in total joint replacement and adhesion of Staphylococcus aureus and Escherichia coli. *Bone and Joint Journal*, *96 B*(4), 497–501. https://doi.org/10.1302/0301-620X.96B4.32895

Banche, G., Bracco, P., Allizond, V., Bistolfi, A., Boffano, M., Cimino, A., Brach del Prever, E. M., & Cuffini, A. M. (2015). Do Crosslinking and Vitamin E Stabilization Influence Microbial Adhesions on UHMWPE-based Biomaterials? *Clinical Orthopaedics and Related Research*, *473*(3), 974–986. https://doi.org/10.1007/s11999-014-4024-9

Banche, G., Bracco, P., Bistolfi, A., Allizond, V., Boffano, M., Costa, L., Cimino, A., Cuffini, A. M., & Del Prever, E. M. B. (2011). Vitamin e blended Uhmwpe may have the potential to reduce bacterial adhesive ability. *Journal of Orthopaedic Research*, *29*(11), 1662–1667. https://doi.org/10.1002/jor.21432

Banerjee, I., Pangule, R. C., & Kane, R. S. (2011). Antifouling coatings: Recent developments in the design of surfaces that prevent fouling by proteins, bacteria, and marine organisms. *Advanced Materials*, *23*(6), 690–718. https://doi.org/10.1002/adma.201001215

Bansal, D. R., Pathak, R., Kumar, B., Gautam, H., & Kumar, P. (2017). Enhanced antimicrobial activity of amphiphilic cationic polymers against a broad range of bacterial strains and skin microbes. *Colloid and Polymer Science*, *295*, 1177–1185. https://doi.org/10.1007/s00396-017-4106-9

Barca, G. M. J., Bertoni, C., Carrington, L., Datta, D., De Silva, N., Deustua, J. E., Fedorov, D. G., Gour, J. R., Gunina, A. O., Guidez, E., Harville, T., Irle, S., Ivanic, J., Kowalski, K., Leang, S. S., Li, H., Li, W., Lutz, J. J., Magoulas, I., … Gordon, M. S. (2020). Recent developments in the general atomic and molecular electronic structure system. *Journal of Chemical Physics*, *152*(15), 154102. https://doi.org/10.1063/5.0005188

Barnes, L., & Cooper, I. (2014). *Biomaterials and medical device-associated infections*. Elsevier.

Barron, D., & Birkinshaw, C. (2008). Ultra-high molecular weight polyethylene - Evidence

for a three-phase morphology. *Polymer*, *49*(13–14), 3111–3115. https://doi.org/10.1016/j.polymer.2008.05.004

Bartczak, Z., & Galeski, A. (2010). Plasticity of semicrystalline polymers. *Macromolecular Symposia*, *294*(1), 67–90.

Bassett, D. C., Block, S., & Piermarini, G. J. (1974). A high-pressure phase of polyethylene and chain-extended growth. *Journal of Applied Physics*, *45*(10), 4146–4150. https://doi.org/10.1063/1.1663028

Batsanov, S. S. (2022). Energy Electronegativity and Chemical Bonding. In *Molecules* (Vol. 27, Issue 23). https://doi.org/10.3390/molecules27238215

Bauer, T. W., & Zhang, Y. (2016). Implants and implant reactions. *Diagnostic Histopathology*, *22*(10), 384–396. https://doi.org/10.1016/J.MPDHP.2016.09.001

Beattie, J. R., Maguire, C., Gilchrist, S., Barrett, L. J., Cross, C. E., Possmayer, F., Ennis, M., Elborn, J. S., Curry, W. J., McGarvey, J. J., & Schock, B. C. (2007). The use of Raman microscopy to determine and localize vitamin E in biological samples. *The FASEB Journal*, *21*(3), 766–776. https://doi.org/10.1096/fj.06-7028com

Bechinger, B., & Gorr, S.-U. (2017). Antimicrobial peptides: mechanisms of action and resistance. *Journal of Dental Research*, *96*(3), 254–260.

Becke, A. D. (1993). A new mixing of Hartree-Fock and local density-functional theories. *The Journal of Chemical Physics*, *98*(2), 1372–1377. https://doi.org/10.1063/1.464304

Bell, T., & Dearnley, P. A. (1994). Environmental issues in surface engineering and related industrial sectors. *Surface Engineering*, *10*(2), 123–128.

Ben-Shlomo, Y., Blom, A., Boulton, C., Brittain, R., Clark, E., Dawson-Bowling, S., Deere, K., Esler, C., Espinoza, O., Evans, J., & others. (2022). *The National Joint Registry 19th Annual Report 2022*.

Benedetti, E., Catanorchi, S., D'Alessio, A., Vergamini, P., Ciardelli, F., & Pracella, M. (1998). FTIR microspectroscopy and DSC analysis of blends of poly(vinylidene fluoride) with isotactic and syndiotactic poly(methyl methacrylate). *Polymer International*, *45*(4), 373–382. https://doi.org/10.1002/(sici)1097-0126(199804)45:4<373::aid-pi948>3.3.co;2-q

Berg, C. M., Lagutchev, A., & Dlott, D. D. (2013). Probing of molecular adsorbates on Au surfaces with large-amplitude temperature jumps. *Journal of Applied Physics*, *113*(18), 183509. https://doi.org/10.1063/1.4804307

Berghaus, B. (1932). Process for surface treatment of metallic elements. *German Patent DRP*, *668639*.

Bernstein, R., Thornberg, S. M., Assink, R. A., Mowery, D. M., Alam, M. K., Irwin, A. N., Hochrein, J. M., Derzon, D. K., Klamo, S. B., & Clough, R. L. (2007). Insights into oxidation mechanisms in gamma-irradiated polypropylene, utilizing selective isotopic labeling with analysis by GC/MS, NMR and FTIR. *Nuclear Instruments and Methods in Physics Research Section B: Beam Interactions with Materials and Atoms*, *265*(1), 8–17.

Bertie, J. E., & Eysel, H. H. (1985). Infrared Intensities of Liquids - I: Determination of Infrared Optical and Dielectric Constants By Ft-Ir Using the Circle Atr Cell. *Applied Spectroscopy*, *39*(3), 392–401. https://doi.org/10.1366/0003702854248575

Bevis, M., & Crellin, E. B. (1971). The geometry of twinning and phase transformations in crystalline polyethylene. *Polymer*, *12*(11), 666–684. https://doi.org/10.1016/0032-3861(71)90083-8

Bhat, N. V., & Upadhyay, D. J. (2002). Plasma-induced surface modification and adhesion enhancement of polypropylene surface. *Journal of Applied Polymer Science*, *86*(4), 925–936. https://doi.org/10.1002/APP.11024

Bhateja, S. K., Duerst, R. W., Aus, E. B., & Andrews, E. H. (1995). Free radicals trapped in polyethylene crystals. *Journal of Macromolecular Science, Part B*, *34*(3), 263–272.

Bichara, D. A., Malchau, E., Sillesen, N. H., Cakmak, S., Nielsen, G. P., & Muratoglu, O. K. (2014). Vitamin E-diffused highly cross-linked UHMWPE particles induce less osteolysis compared to highly cross-linked virgin UHMWPE particles in vivo. *Journal of Arthroplasty*, *29*(9 SUPPL.), 232–237. https://doi.org/10.1016/j.arth.2014.03.044

Biesinger, M.C. (2015). *Polyethylene Surfaces*. http://www.xpsfitting.com/2015/11/polyethylene-surfaces.html

Biesinger, Mark C., Payne, B. P., Grosvenor, A. P., Lau, L. W. M., Gerson, A. R., & Smart, R. S. C. (2011). Resolving surface chemical states in XPS analysis of first row transition metals, oxides and hydroxides: Cr, Mn, Fe, Co and Ni. *Applied Surface Science*, *257*(7), 2717–2730. https://doi.org/10.1016/j.apsusc.2010.10.051

Biró, A. S. (2014). Active Screen Plasma Nitriding State of the Art. *Production Processes and Systems*, *7*(1), 103–114.

Bistolfi, A., Giustra, F., Bosco, F., Sabatini, L., Aprato, A., Bracco, P., & Bellare, A. (2021). Ultra-high molecular weight polyethylene (UHMWPE) for hip and knee arthroplasty: The present and the future. *Journal of Orthopaedics*, *25*, 98–106.

Black, R. M., & Lyons, B. J. (1957). Effect of high-energy radiation on polypropylene. *Nature*, *180*(4598), 1346–1347.

Bleß, H.-H., & Kip, M. (2017). *White Paper on Joint Replacement: Status of Hip and Knee Arthroplasty Care in Germany*.

Booth, J.-P., Mozetic, M., Nikiforov, A. Y., & Oehr, C. (2022). Foundations of plasma surface functionalisation of polymers for industrial and biological applications. *Plasma Sources Science and Technology*. https://doi.org/10.1088/1361-6595/AC70F9

Borsdorf, R., & Scholz, M. (1974). Spektroskopische Methoden in der organischen Chemie. In *Spektroskopische Methoden in der organischen Chemie*. Georg Thieme Verlag. https://doi.org/10.1515/9783112596685

Bos, M. P., & Tommassen, J. (2004). Biogenesis of the Gram-negative bacterial outer membrane. *Current Opinion in Microbiology*, *7*(6), 610–616. https://doi.org/https://doi.org/10.1016/j.mib.2004.10.011

Boulmedais, F., Frisch, B., Etienne, O., Lavalle, P., Picart, C., Ogier, J., Voegel, J. C., Schaaf, P., & Egles, C. (2004). Polyelectrolyte multilayer films with pegylated polypeptides as a new type of anti-microbial protection for biomaterials. *Biomaterials*, *25*(11), 2003–2011. https://doi.org/10.1016/j.biomaterials.2003.08.039

Bracco, P., Bellare, A., Bistolfi, A., & Affatato, S. (2017). Ultra-high molecular weight polyethylene: influence of the chemical, physical and mechanical properties on the wear

behavior. A review. *Materials*, *10*(7), 791. https://doi.org/10.3390/ma10070791

Bracco, P., Brunella, V., Zanetti, M., Luda, M. P., & Costa, L. (2007). Stabilisation of ultra-high molecular weight polyethylene with Vitamin E. *Polymer Degradation and Stability*, *92*(12), 2155–2162. https://doi.org/10.1016/j.polymdegradstab.2007.02.023

Bracco, P., & Oral, E. (2011). Vitamin E-stabilized UHMWPE for total joint implants: A review. *Clinical Orthopaedics and Related Research*, *469*(8), 2286–2293. https://doi.org/10.1007/s11999-010-1717-6

Brach del Prever, E. M., Bistolfi, A., Bracco, P., & Costa, L. (2009). UHMWPE for arthroplasty: Past or future? *Journal of Orthopaedics and Traumatology*, *10*(1), 1–8. https://doi.org/10.1007/s10195-008-0038-y

Bradley, M. (2007). Curve Fitting in Raman and IR Spectroscopy : Basic Theory of Line Shapes and Applications. *Thermo Fisher Scientific Application Note*, *50733*, AN50733. https://doi.org/10.1002/2015JG003204.Received

Brayton, A. L., Yeh, I.-C., Andzelm, J. W., & Rutledge, G. C. (2017). Vibrational analysis of semicrystalline polyethylene using molecular dynamics simulation. *Macromolecules*, *50*(17), 6690–6701.

Bruellhoff, K., Fiedler, J., Möller, M., Groll, J., & Brenner, R. E. (2010). Surface coating strategies to prevent biofilm formation on implant surfaces. *International Journal of Artificial Organs*, *33*(9), 646–653. https://doi.org/10.1177/039139881003300910

Bruggeman, M., Ijakipour, H., & Stamboulis, A. (2019). Defensin-Like Peptides and Their Antimicrobial Activity in Free-Form and Immobilized on Material Surfaces. *Peptide Synthesis*. https://doi.org/10.5772/intechopen.85508

Bruggeman, M., Zelzer, M., Dong, H., & Stamboulis, A. (2022). Processing and interpretation of core-electron XPS spectra of complex plasma-treated polyethylene-based surfaces using a theoretical peak model. *Surface and Interface Analysis*, *54*(9), 986–1007. https://doi.org/10.1002/SIA.7125

Burkstrand, J. M. (1998). Electron spectroscopic study of oxygen-plasma-treated polymer surfaces. *Journal of Vacuum Science and Technology*, *15*(2), 223. https://doi.org/10.1116/1.569484

Cabarcos, O. M., Shaporenko, A., Weidner, T., Uppili, S., Dake, L. S., Zharnikov, M., & Allara, D. L. (2008). Physical and electronic structure effects of embedded dipoles in self-assembled monolayers: Characterization of mid-chain ester functionalized alkanethiols on Au{111}. *Journal of Physical Chemistry C*, *112*(29), 10842–10854. https://doi.org/10.1021/jp801618j

Cai, T., Gu, H., Liu, F., & Xie, M. (2012). A combined normal Raman, surface-enhanced Raman scattering (SERS), and theoretical calculation (DFT and PED) study of alpha-tocopherol. *Applied Spectroscopy*, *66*(1), 114–121. https://doi.org/10.1366/11-06423

Callaway, J. (1974). *Quantum theory of the solid state*. Academic press.

Carvalho, C. C. C. R. (2008). Biofilms: Recent Developments on an Old Battle. *Recent Patents on Biotechnology*, *1*(1), 49–57. https://doi.org/10.2174/187220807779813965

Casiraghi, C., Ferrari, A. C., & Robertson, J. (2005). Raman spectroscopy of hydrogenated amorphous carbons. *Physical Review B - Condensed Matter and Materials Physics*,

72(8), 85401. https://doi.org/10.1103/PhysRevB.72.085401

Catauro, M., Scolaro, C., Dal Poggetto, G., Pacifico, S., & Visco, A. (2020). Wear Resistant Nanocomposites Based on Biomedical Grade UHMWPE Paraffin Oil and Carbon Nano-Filler: Preliminary Biocompatibility and Antibacterial Activity Investigation. *Polymers*, *12*(4). https://doi.org/10.3390/polym12040978

Ceppatelli, M., & Bini, R. (2014). Light-Induced Catalyst and Solvent-Free High Pressure Synthesis of High Density Polyethylene at Ambient Temperature. *Macromolecular Rapid Communications*, *35*(8), 787–793. https://doi.org/10.1002/MARC.201300919

Chai, J. Da, & Head-Gordon, M. (2008). Long-range corrected hybrid density functionals with damped atom-atom dispersion corrections. *Physical Chemistry Chemical Physics*, *10*(44), 6615–6620. https://doi.org/10.1039/b810189b

Chaichi, A., Prasad, A., Kootta Parambil, L., Shaik, S., Hemmasian Ettefagh, A., Dasa, V., Guo, S., Osborn, M. L., Devireddy, R., Khonsari, M. M., & Gartia, M. R. (2019). Improvement of Tribological and Biocompatibility Properties of Orthopedic Materials Using Piezoelectric Direct Discharge Plasma Surface Modification. *ACS Biomaterials Science & Engineering*, *5*(5), 2147–2159. https://doi.org/10.1021/acsbiomaterials.9b00009

Charles, J. (2009). Qualitative analysis of high density polyethylene using FTIR spectroscopy. *Asian Journal of Chemistry*, *21*(6), 4477.

Chauhan, R. S., Singh, A., Shrivastava, A. R., Singh, L., & Pant, S. C. (2008). Photo-induced Structural Changes in Polyolefin-nanoclay Composite. *Defence Science Journal*, *58*(6), 778.

Chen, R., Cole, N., Willcox, M. D. P., Park, J., Rasul, R., Carter, E., & Kumar, N. (2009). Synthesis, characterization and in vitro activity of a surface-attached antimicrobial cationic peptide. *Biofouling*, *25*(6), 517–524. https://doi.org/10.1080/08927010902954207

Chereddy, K. K., Her, C. H., Comune, M., Moia, C., Lopes, A., Porporato, P. E., Vanacker, J., Lam, M. C., Steinstraesser, L., Sonveaux, P., Zhu, H., Ferreira, L. S., Vandermeulen, G., & Préat, V. (2014). PLGA nanoparticles loaded with host defense peptide LL37 promote wound healing. *Journal of Controlled Release : Official Journal of the Controlled Release Society*, *194*, 138–147. https://doi.org/10.1016/J.JCONREL.2014.08.016

Chhetri, S., & Bougherara, H. (2021). A comprehensive review on surface modification of UHMWPE fiber and interfacial properties. *Composites Part A: Applied Science and Manufacturing*, *140*, 106146. https://doi.org/10.1016/j.compositesa.2020.106146

Chikkali, S., Ambade, A. V, de Bruin, B., & Shaver, M. (2017). *Metal-catalyzed polymerization: fundamentals to applications*. CRC Press.

Cho, W. M., Joshi, B. P., Cho, H., & Lee, K. H. (2007). Design and synthesis of novel antibacterial peptide-resin conjugates. *Bioorganic and Medicinal Chemistry Letters*, *17*(21), 5772–5776. https://doi.org/10.1016/j.bmcl.2007.08.056

Chu, P. K., Chen, J. Y., Wang, L. P., & Huang, N. (2002). Plasma-surface modification of biomaterials. *Materials Science and Engineering: R: Reports*, *36*(5–6), 143–206. https://doi.org/10.1016/S0927-796X(02)00004-9

Clegg, D. W., & Collyer, A. A. (1991). *Irradiation effects on polymers*. Elsevier Applied Science.

Cline, J. P. (2015). *NIST: Standard Reference Material 676a*. https://www-s.nist.gov/srmors/certificates/676A.pdf

Collins, J. M., Porter, K. A., Singh, S. K., & Vanier, G. S. (2014). High-Efficiency Solid Phase Peptide Synthesis (HE-SPPS). *Organic Letters*, *16*(3), 940–943. https://doi.org/10.1021/ol4036825

Collins, W., Seelenbinder, J., & Higgins, F. (2012). *Determination of the vinyl content of polyethylene resins*. Agilent Technologies. https://www.agilent.com/cs/library/applications/5991-0458EN_AnalyticalMethod_630_Vinyl.pdf

Combs, G. F., & McClung, J. P. (2017). The Vitamins: Fundamental Aspects in Nutrition and Health. In *The Vitamins: Fundamental Aspects in Nutrition and Health*. Academic press. https://doi.org/10.1016/B978-0-12-802965-7.01001-7

Cordeiro, A. L., Rückel, M., Bartels, F., Maitz, M. F., Renner, L. D., & Werner, C. (2019). Protein adsorption dynamics to polymer surfaces revisited—A multisystems approach. *Biointerphases*, *14*(5). https://doi.org/10.1116/1.5121249

Corrêa, J. A. F., Evangelista, A. G., de Melo Nazareth, T., & Luciano, F. B. (2019). Fundamentals on the molecular mechanism of action of antimicrobial peptides. *Materialia*, *8*, 100494.

Costa, F., Carvalho, I. F., Montelaro, R. C., Gomes, P., & Martins, M. C. L. (2011). Covalent immobilization of antimicrobial peptides (AMPs) onto biomaterial surfaces. *Acta Biomaterialia*, *7*(4), 1431–1440. https://doi.org/10.1016/j.actbio.2010.11.005

Costa, L., Carpentieri, I., & Bracco, P. (2009). Post electron-beam irradiation oxidation of orthopaedic Ultra-High Molecular Weight Polyethylene (UHMWPE) stabilized with vitamin E. *Polymer Degradation and Stability*, *94*(9), 1542–1547. https://doi.org/10.1016/j.polymdegradstab.2009.04.023

Costa, L., Luda, M. P., Trossarelli, L., Brach Del Prever, E. M., Crova, M., & Gallinaro, P. (1998a). Oxidation in orthopaedic UHMWPE sterilized by gamma-radiation and ethylene oxide. *Biomaterials*, *19*(7–9), 659–668. https://doi.org/10.1016/S0142-9612(97)00160-9

Costa, L., Luda, M. P., Trossarelli, L., Brach Del Prever, E. M., Crova, M., & Gallinaro, P. (1998b). In vivo UHMWPE biodegradation of retrieved prosthesis. *Biomaterials*, *19*(15), 1371–1385. https://doi.org/10.1016/S0142-9612(98)00013-1

Cowden, C. (2021). *Personal communication: Instrumental broadening on Bruker D8 Advance*. Bruker UK Limited.

Craig, R. L. (2002). Applications of Raman Microspectroscopy to the Study of Atmospheric Aerosol Particles. In *Mycological Research* (Vol. 106, Issue 11).

Cruz, G. F., de Araujo, I., Torres, M. D. T., de la Fuente-Nunez, C., Oliveira, V. X., Ambrosio, F. N., Lombello, C. B., Almeida, D. V, Silva, F. D., & Garcia, W. (2020). Photochemically-generated silver chloride nanoparticles stabilized by a peptide inhibitor of cell division and its antimicrobial properties. *Journal of Inorganic and Organometallic Polymers and Materials*, *30*(7), 2464–2474.

Cummings, N. A., & Nordby, G. L. (1966). Measurement of synovial fluid pH in normal and arthritic knees. *Arthritis & Rheumatism*, *9*(1), 47–56. https://doi.org/10.1002/art.1780090106

Cypres, R. (1987). Aromatic hydrocarbons formation during coal pyrolysis. *Fuel Processing Technology*, *15*(C), 1–15. https://doi.org/10.1016/0378-3820(87)90030-0

Czarnecka, J., Wisniewski, M., Forbot, N., Bolibok, P., Terzyk, A. P., & Roszek, K. (2020). Cytotoxic or not? Disclosing the toxic nature of carbonaceous nanomaterials through nano-bio interactions. *Materials*, *13*(9), 2060. https://doi.org/10.3390/MA13092060

da Silva, D. J., & Wiebeck, H. (2018). CARS-PLS regression and ATR-FTIR spectroscopy for eco-friendly and fast composition analyses of LDPE/HDPE blends. *Journal of Polymer Research*, *25*(5), 1–9.

da Silva, D. J., & Wiebeck, H. (2019). Predicting LDPE/HDPE blend composition by CARS-PLS regression and confocal Raman spectroscopy. *Polimeros*, *29*(1). https://doi.org/10.1590/0104-1428.00218

da Silva, D. J., & Wiebeck, H. (2022). ATR-FTIR Spectroscopy Combined with Chemometric Methods for the Classification of Polyethylene Residues Containing Different Contaminants. *Journal of Polymers and the Environment*, *30*(7), 3031–3044. https://doi.org/10.1007/s10924-022-02396-3

Darouiche, R. O. (2001). Device-associated infections: A macroproblem that starts with microadherence. *Clinical Infectious Diseases*, *33*(9), 1567–1572. https://doi.org/10.1086/323130

Davenport Huyer, L., Pascual-Gil, S., Wang, Y., Mandla, S., Yee, B., & Radisic, M. (2020). Advanced Strategies for Modulation of the Material–Macrophage Interface. *Advanced Functional Materials*, *30*(44), 1909331. https://doi.org/https://doi.org/10.1002/adfm.201909331

Davis, J. R. (2001). *Surface engineering for corrosion and wear resistance*. ASM international.

De Jesus Oliveira, T., De Oliveira, U. C., & Da Silva Junior, P. I. (2019). Serrulin: A Glycine-Rich Bioactive Peptide from the Hemolymph of the Yellow Tityus serrulatus Scorpion. *Toxins*, *11*(9). https://doi.org/10.3390/TOXINS11090517

De Zoysa, G. H., Wang, K., Lu, J., Hemar, Y., & Sarojini, V. (2020). Covalently Immobilized Battacin Lipopeptide Gels with Activity against Bacterial Biofilms. *Molecules 2020, Vol. 25, Page 5945*, *25*(24), 5945. https://doi.org/10.3390/MOLECULES25245945

Dee, K. C., Puleo, D. A., & Bizios, R. (2003). *An introduction to tissue-biomaterial interactions*. John Wiley \& Sons.

Delaviz, Y., Santerre, J. P., & Cvitkovitch, D. G. (2015). Infection resistant biomaterials. *Biomaterials and Medical Device-Associated Infections*, *11*, 223–254.

Dellacherie, M. O., Seo, B. R., & Mooney, D. J. (2019). Macroscale biomaterials strategies for local immunomodulation. *Nature Reviews Materials*, *4*(6), 379–397. https://doi.org/10.1038/s41578-019-0106-3

DIN. (2023). Requirements for terminally sterilized medical devices. In *Sterilization of*

medical devices - Requirements for medical devices to be designated "STERILE" - Part 1: DIN EN 556-1 (pp. 1–30).

Divyashree, M., Mani, K. M., Reddy, D., Kumavath, R., Ghosh, P., Azevedo, V., & Barh, D. (2020). Clinical Applications of Antimicrobial Peptides (AMPs): Where do we Stand Now? In *Protein & Peptide Letters* (Vol. 27, Issue 2, pp. 120–134). https://doi.org/http://dx.doi.org/10.2174/0929866526666190925152957

Dufour, D., Leung, V., & Lévesque, C. M. (2010). Bacterial biofilm: structure, function, and antimicrobial resistance. *Endodontic Topics*, *22*(1), 2–16. https://doi.org/https://doi.org/10.1111/j.1601-1546.2012.00277.x

Dumbleton, J. H., Wang, A., Sutton, K., & Manley, M. T. (2009). Highly Crosslinked and Annealed UHMWPE. *UHMWPE Biomaterials Handbook*, 205–219. https://doi.org/10.1016/B978-0-12-374721-1.00014-6

Dürr, U. H. N., Sudheendra, U. S., & Ramamoorthy, A. (2006). LL-37, the only human member of the cathelicidin family of antimicrobial peptides. *Biochimica et Biophysica Acta*, *1758*(9), 1408–1425. https://doi.org/10.1016/J.BBAMEM.2006.03.030

Edidin, A. A., & Kurtz, S. M. (2000). Influence of mechanical behavior on the wear of 4 clinically relevant polymeric biomaterials in a hip simulator. *Journal of Arthroplasty*, *15*(3), 321–331. https://doi.org/10.1016/S0883-5403(00)90647-8

Edidin, A. A., Pruitt, L., Jewett, C. W., Crane, D. J., Roberts, D., & Kurtz, S. M. (1999). Plasticity-induced damage layer is a precursor to wear in radiation- cross-linked UHMWPE acetabular components for total hip replacement. *Journal of Arthroplasty*, *14*(5), 616–627. https://doi.org/10.1016/S0883-5403(99)90086-4

Edinburgh Instruments. (2019). *Laser spot size in a microscope*. https://www.edinst.com/blog/laser-spot-size-in-a-microscope/

Eissler, S., Kley, M., Bächle, D., Loidl, G., Meier, T., & Samson, D. (2017). Substitution determination of Fmoc-substituted resins at different wavelengths. *Journal of Peptide Science*, *23*(10), 757–762. https://doi.org/10.1002/psc.3021

El-Halfawy, O. M., Klett, J., Ingram, R. J., Loutet, S. A., Murphy, M. E. P., Martín-Santamaría, S., & Valvanoa, M. A. (2017). Antibiotic capture by bacterial lipocalins uncovers an extracellular mechanism of intrinsic antibiotic resistance. *MBio*, *8*(2), 10.1128/mbio.00225-17. https://doi.org/10.1128/mBio.00225-17

Eliseyev, I. A., Smirnov, A. N., Davydov, V. Y., Platonov, A. V., Yavsin, D. A., & Gurevich, S. A. (2021). Raman studies of amorphous nanocarbon obtained by laser sputtering. *Journal of Physics: Conference Series*, *2103*(1), 12093. https://doi.org/10.1088/1742-6596/2103/1/012093

Eral, H. B., 't Mannetje, D. J. C. M., & Oh, J. M. (2013). Contact angle hysteresis: a review of fundamentals and applications. *Colloid and Polymer Science*, *291*(2), 247–260. https://doi.org/10.1007/s00396-012-2796-6

Etienne, O., Picart, C., Taddei, C., Haikel, Y., Dimarcq, J. L., Schaaf, P., Voegel, J. C., Ogier, J. A., & Egles, C. (2004). Multilayer polyelectrolyte films functionalized by insertion of defensin: A new approach to protection of implants from bacterial colonization. *Antimicrobial Agents and Chemotherapy*, *48*(10), 3662–3669. https://doi.org/10.1128/AAC.48.10.3662-3669.2004

Evans, J. T., Evans, J. P., Walker, R. W., Blom, A. W., Whitehouse, M. R., & Sayers, A. (2019). How long does a hip replacement last? A systematic review and meta-analysis of case series and national registry reports with more than 15 years of follow-up. *The Lancet*, *393*(10172), 647–654.

Exline, D. (2013). *Comparison of Raman and FTIR Spectroscopy: Advantages and Limitations*. Gateway Analytical. http://www.gatewayanalytical.com/blog/comparison-of-raman-and-ftir-spectroscopy-advantages-and-limitations/

Fabisiak, N., Fabisiak, A., Chmielowiec-Korzeniowska, A., Tymczyna, L., Kamysz, W., Kordek, R., Bauer, M., Kamysz, E., & Fichna, J. (2021). Anti-inflammatory and antibacterial effects of human cathelicidin active fragment KR-12 in the mouse models of colitis: a novel potential therapy of inflammatory bowel diseases. *Pharmacological Reports*, *73*(1), 163–171. https://doi.org/10.1007/s43440-020-00190-3

Fairley, N. (2008). Lorentzian Asymmetric Lineshape. In *CasaXPS Software*.

Fawcett, T. G., Crowder, C. E., Brownell, S. J., Zhang, Y., Hubbard, C., Schreiner, W., Hamill, G. P., Huang, T. C., Sabino, E., Langford, J. I., Hamilton, R., & Louër, D. (1988). Establishing an Instrumental Peak Profile Calibration Standard for Powder Diffraction Analyses: International Round Robin Conducted by the JCPDS-ICDD and the U.S. National Bureau of Standards†. *Powder Diffraction*, *3*(4), 209–218. https://doi.org/10.1017/S0885715600013506

Fayolle, B., Richaud, E., Colin, X., & Verdu, J. (2008). Review: Degradation-induced embrittlement in semi-crystalline polymers having their amorphous phase in rubbery state. *Journal of Materials Science*, *43*(22), 6999–7012. https://doi.org/10.1007/s10853-008-3005-3

Feng, S., Gao, F., Chen, Z., Grant, E., Kitts, D. D., Wang, S., & Lu, X. (2013). Determination of α-tocopherol in vegetable oils using a molecularly imprinted polymers-surface-enhanced Raman spectroscopic biosensor. *Journal of Agricultural and Food Chemistry*, *61*(44), 10467–10475. https://doi.org/10.1021/jf4038858

Ferrari, A. C., & Robertson, J. (2001). Origin of the 1150 − cm−1 Raman mode in nanocrystalline diamond. *Physical Review B - Condensed Matter and Materials Physics*, *63*(12), 121405. https://doi.org/10.1103/PhysRevB.63.121405

Ferrari, Andrea Carlo, & Robertson, J. (2004). Raman spectroscopy of amorphous, nanostructured, diamond-like carbon, and nanodiamond. *Philosophical Transactions of the Royal Society A: Mathematical, Physical and Engineering Sciences*, *362*(1824), 2477–2512. https://doi.org/10.1098/rsta.2004.1452

Ferraro, J. R. (1994). Introductory Raman Spectroscopy. In *Introductory Raman Spectroscopy*. Elsevier. https://doi.org/10.1016/c2009-0-21238-4

Ferreira, L., & Zumbuehl, A. (2009). Non-leaching surfaces capable of killing microorganisms on contact. *Journal of Materials Chemistry*, *19*(42), 7796–7806. https://doi.org/10.1039/b905668h

Fink, J. K. (2010). Ultra High Molecular Weight Poly(ethylene). In *Handbook of Engineering and Specialty Thermoplastics* (pp. 75–107). Google Patents. https://doi.org/10.1002/9780470881712.ch3

Fiorito, S., Goze, C., Adrey, J., Magrini, L., Goalard, C., & Bernier, P. (2001). Increase in

free radicals on UHMWPE hip prostheses components due to inflamed synovial cell products. *Journal of Biomedical Materials Research*, *57*(1), 35–40. https://doi.org/10.1002/1097-4636(200110)57:1<35::AID-JBM1138>3.0.CO;2-B

Fleming, A. (1932). *Lysozyme*. SAGE Publications.

Flor, P. J. (1962). On the Morphology of the Crystalline State in Polymers. *Journal of the American Chemical Society*, *84*(15), 2857–2867. https://doi.org/10.1021/ja00874a004

Foerch, R., Izawa, J., & Spears, G. (1991). A Comparative Study of the Effects of Remote Nitrogen Plasma, Remote Oxygen Plasma, and Corona Discharge Treatments on the Surface Properties of Polyethylene. *Journal of Adhesion Science and Technology*, *5*(7), 549–564. https://doi.org/10.1163/156856191X00747

Fogh, J., Fogh, J. M., & Orfeo, T. (1977). One hundred and twenty seven cultured human tumor cell lines producing tumors in nude mice. *Journal of the National Cancer Institute*, *59*(1), 221–226. https://doi.org/10.1093/jnci/59.1.221

Fowkes, F. M. (1964). Attractive Forces At Interfaces. *Industrial & Engineering Chemistry*, *56*(12), 40–52. https://doi.org/10.1021/ie50660a008

Fowler, J. E. (2018). *Multi-Technique Characterizations of Natural and Biomimetic Adhesives*.

Frackenpohl, J., Arvidsson, P. I., Schreiber, J. V., & Seebach, D. (2001). The outstanding biological stability of β- and γ-peptides toward proteolytic enzymes: An in vitro investigation with fifteen peptidases. *ChemBioChem*, *2*(6), 445–455. https://doi.org/10.1002/1439-7633(20010601)2:6<445::aid-cbic445>3.3.co;2-i

Fu, J., Ghali, B. W., Lozynsky, A. J., Oral, E., & Muratoglu, O. K. (2011). Wear resistant UHMWPE with high toughness by high temperature melting and subsequent radiation cross-linking. *Polymer*, *52*(4), 1155–1162. https://doi.org/https://doi.org/10.1016/j.polymer.2011.01.017

Fu, J., Shen, J., Gao, G., Xu, Y., Hou, R., Cong, Y., & Cheng, Y. (2013). Natural polyphenol-stabilised highly crosslinked UHMWPE with high mechanical properties and low wear for joint implants. *Journal of Materials Chemistry B*, *1*(37), 4727–4735.

Fu, L., Jin, P., Hu, Y., Lu, H., & Su, L. (2020). KR-12-a6 promotes the osteogenic differentiation of human bone marrow mesenchymal stem cells via BMP/SMAD signaling. *Molecular Medicine Reports*, *21*(1), 61–68. https://doi.org/10.3892/mmr.2019.10843

Fulin, P., Pokorny, D., Slouf, M., Nevoralova, M., Vackova, T., Dybal, J., & Pilar, J. (2014). Quantification of structural changes of UHMWPE components in total joint replacements. *BMC Musculoskeletal Disorders*, *15*(1), 1–8. https://doi.org/10.1186/1471-2474-15-109

Funatani, K. (2004). Low-Temperature Salt Bath Nitriding of Steels. *Metal Science and Heat Treatment 2004 46:7*, *46*(7), 277–281. https://doi.org/10.1023/B:MSAT.0000048834.48163.2E

Gabriel, M., Nazmi, K., Veerman, E. C., Amerongen, A. V. N., & Zentner, A. (2006). Preparation of LL-37-grafted titanium surfaces with bactericidal activity. *Bioconjugate Chemistry*, *17*(2), 548–550. https://doi.org/10.1021/bc050091v

Gall, M. J., Hendra, P. J., Peacock, O. J., Cudby, M. E. A., & Willis, H. A. (1972). The laser-Raman spectrum of polyethylene. The assignment of the spectrum to fundamental modes of vibration. *Spectrochimica Acta Part A: Molecular Spectroscopy*, *28*(8), 1485–1496. https://doi.org/10.1016/0584-8539(72)80118-1

Galliera, E., Ragone, V., Marazzi, M. G., Selmin, F., Banci, L., & Corsi Romanelli, M. M. (2018). Vitamin E-stabilized UHMWPE: Biological response on human osteoblasts to wear debris. *Clinica Chimica Acta*, *486*, 18–25. https://doi.org/10.1016/j.cca.2018.07.012

Gaston, F., Dupuy, N., Marque, S. R. A., Barbaroux, M., & Dorey, S. (2016). One year monitoring by FTIR of $γ$-irradiated multilayer film PE/EVOH/PE. *Radiation Physics and Chemistry*, *125*, 115–121.

Geckeler, K., Wacker, R., Martini, F., Hack, A., & Aicher, W. (2003). Enhanced Biocompatibility for SAOS-2 Osteosarcoma Cells by Surface Coating with Hydrophobic Epoxy Resins. *Cellular Physiology and Biochemistry*, *13*(3), 155–164. https://doi.org/10.1159/000071866

Gencur, S. J., Rimnac, C. M., & Kurtz, S. M. (2003). Failure micromechanisms during uniaxial tensile fracture of conventional and highly crosslinked ultra-high molecular weight polyethylenes used in total joint replacements. *Biomaterials*, *24*(22), 3947–3954. https://doi.org/10.1016/S0142-9612(03)00277-1

Gentilucci, L., De Marco, R., & Cerisoli, L. (2010). Chemical Modifications Designed to Improve Peptide Stability: Incorporation of Non-Natural Amino Acids, Pseudo-Peptide Bonds, and Cyclization. *Current Pharmaceutical Design*, *16*(28), 3185–3203. https://doi.org/10.2174/138161210793292555

Georges, J. (1999). *Nitriding process and nitriding furnace therefor*. Google Patents.

Giesbers, M., Marcelis, A. T. M., & Zuilhof, H. (2013). Simulation of XPS C1s spectra of organic monolayers by quantum chemical methods. *Langmuir*, *29*(15), 4782–4788. https://doi.org/10.1021/la400445s

Glinel, K., Jonas, A. M., Jouenne, T., Leprince, J., Galas, L., & Huck, W. T. S. (2009). Antibacterial and antifouling polymer brushes incorporating antimicrobial peptide. *Bioconjugate Chemistry*, *20*(1), 71–77. https://doi.org/10.1021/bc800280u

Glotin, M., & Mandelkern, L. (1982). A Raman spectroscopic study of the morphological structure of the polyethylenes. *Colloid & Polymer Science*, *260*(2), 182–192. https://doi.org/10.1007/BF01465438

Go, D. B. (2018). Gaseous ionization processes. In *Ionization and Ion Transport* (pp. 4–11). Morgan & Claypool Publishers. https://doi.org/10.1088/978-1-6817-4601-2ch4

Goldman, M., & Pruitt, L. (1998). Comparison of the effects of gamma radiation and low temperature hydrogen peroxide gas plasma sterilization on the molecular structure, fatigue resistance, and wear behavior of UHMWPE. *Journal of Biomedical Materials Research*, *40*(3), 378–384. https://doi.org/10.1002/(SICI)1097-4636(19980605)40:3<378::AID-JBM6>3.0.CO;2-C

Gómez-Barrena, E., Esteban, J., Molina-Manso, D., Adames, H., Martínez-Morlanes, M. J., Terriza, A., Yubero, F., & Puértolas, J. A. (2011). Bacterial adherence on UHMWPE with vitamin E: an in vitro study. *Journal of Materials Science: Materials in Medicine*,

22(7), 1701–1706. https://doi.org/10.1007/s10856-011-4340-5

Gottenbos, B., van der Mei, H. C., & Busscher, H. J. (2000). Initial adhesion and surface growth of Staphylococcus epidermidis and Pseudomonas aeruginosa on biomedical polymers. *Journal of Biomedical Materials Research: An Official Journal of The Society for Biomaterials, The Japanese Society for Biomaterials, and The Australian Society for Biomaterials and the Korean Society for Biomaterials*, *50*(2), 208–214.

Grace, J. M., Zhuang, H. K., Gerenser, L. J., & Freeman, D. R. (2003). Time-resolved investigation of the surface chemical modification of poly(ethylene naphthalate) by nitrogen plasma treatment. *Journal of Vacuum Science & Technology A: Vacuum, Surfaces, and Films*, *21*(1), 37–46. https://doi.org/10.1116/1.1521960

Greczynski, G., & Hultman, L. (2020). Compromising Science by Ignorant Instrument Calibration—Need to Revisit Half a Century of Published XPS Data. *Angewandte Chemie - International Edition*, *59*(13), 5002–5006. https://doi.org/10.1002/anie.201916000

Green, T. R., Fisher, J., Bridget Matthews, J., Stone, M. H., & Ingham, E. (2000). Effect of size and dose on bone resorption activity of macrophages by in vitro clinically relevant ultra high molecular weight polyethylene particles. *Journal of Biomedical Materials Research*, *53*(5), 490–497. https://doi.org/10.1002/1097-4636(200009)53:5<490::AID-JBM7>3.0.CO;2-7

Grimme, S., & Steinmetz, M. (2013). Effects of London dispersion correction in density functional theory on the structures of organic molecules in the gas phase. *Physical Chemistry Chemical Physics*, *15*(38), 16031–16042. https://doi.org/10.1039/c3cp52293h

Grindy, S. C., Gil, D., Suhardi, J. V, Muratoglu, O. K., Bedair, H., & Oral, E. (2019). Delivery of bupivacaine from UHMWPE and its implications for managing pain after joint arthroplasty. *Acta Biomaterialia*, *93*, 63–73.

Grobbelaar, C. J., Du Plessis, T. A., & Marais, F. (1978). The radiation improvement of polyethylene prostheses. A preliminary study. *Journal of Bone and Joint Surgery - Series B*, *60 B*(3), 370–374. https://doi.org/10.1302/0301-620x.60b3.681412

Guiotto, A., Pozzobon, M., Canevari, M., Manganelli, R., Scarin, M., & Veronese, F. M. (2003). PEGylation of the antimicrobial peptide nisin A: Problems and perspectives. *Farmaco*, *58*(1), 45–50. https://doi.org/10.1016/S0014-827X(02)01301-0

Gulmine, J. V, Janissek, P. R., Heise, H. M., & Akcelrud, L. (2002). Polyethylene characterization by FTIR. *Polymer Testing*, *21*(5), 557–563.

Gunasekera, S., Muhammad, T., Strömstedt, A. A., Rosengren, K. J., & Göransson, U. (2018). Alanine and Lysine Scans of the LL-37-Derived Peptide Fragment KR-12 Reveal Key Residues for Antimicrobial Activity. *ChemBioChem*, *19*(9), 931–939. https://doi.org/10.1002/CBIC.201700599

Guo, Y. C., Cai, C., & Zhang, Y. H. (2018). Observation of conformational changes in ethylene glycol–water complexes by FTIR–ATR spectroscopy and computational studies. *AIP Advances*, *8*(5), 055308. https://doi.org/10.1063/1.4995975

Haider, H., & Baykal, D. (2015). Wear Assessment of UHMWPE with Pin-on-Disc Testing. In *UHMWPE Biomaterials Handbook: Ultra High Molecular Weight Polyethylene in Total Joint Replacement and Medical Devices* (pp. 553–578). Elsevier.

https://doi.org/10.1016/B978-0-323-35401-1.00030-2

Hallab, N. J., & Jacobs, J. J. (2020). Orthopedic Applications. In W. R. Wagner, S. E. Sakiyama-Elbert, G. Zhang, & M. J. Yaszemski (Eds.), *Biomaterials Science (Fourth Edition)* (Fourth Edi, pp. 1079–1118). Academic Press. https://doi.org/https://doi.org/10.1016/B978-0-12-816137-1.00070-2

Hamzah, M., Khenfouch, M., Rjeb, A., Sayouri, S., Houssaini, D. S., Darhouri, M., & Srinivasu, V. V. (2018). Surface chemistry changes and microstructure evaluation of low density nanocluster polyethylene under natural weathering: A spectroscopic investigation. *Journal of Physics: Conference Series*, *984*(1), 012010. https://doi.org/10.1088/1742-6596/984/1/012010

Han, J., Duan, W., Xia, Q., & Song, D. (2022). Diffusion behavior of vitamin-E in irradiation cross-linked GO/UHMWPE composites. *Polymer Bulletin*, *79*(6), 3649–3664. https://doi.org/10.1007/s00289-021-03652-7

Han, X., Zheng, J., Lin, F., Kuroda, K., & Chen, Z. (2018). Interactions between Surface-Immobilized Antimicrobial Peptides and Model Bacterial Cell Membranes. *Langmuir*, *34*(1), 512–520. https://doi.org/10.1021/acs.langmuir.7b03411

Handa, T., Nagashima, T., & Ebihara, N. (1982). Synergistic action of Sb2O3 with bromine-containing flame retardant in polyolefins: 3—The relationship between certain combustion variables. *Fire and Materials*, *6*(1), 1–6. https://doi.org/10.1002/fam.810060102

Hantsche, H. (1993). High resolution XPS of organic polymers. The scienta database. *Analytica Chimica Acta*, *276*(2), 469–470. https://doi.org/10.1016/0003-2670(93)80419-l

Hanwell, M. D., Curtis, D. E., Lonie, D. C., Vandermeerschd, T., Zurek, E., & Hutchison, G. R. (2012). Avogadro: An advanced semantic chemical editor, visualization, and analysis platform. *Journal of Cheminformatics*, *4*(8), 17. https://doi.org/10.1186/1758-2946-4-17

Harris, F., Dennison, S., & Phoenix, D. (2009). Anionic Antimicrobial Peptides from Eukaryotic Organisms. *Current Protein & Peptide Science*, *10*(6), 585–606. https://doi.org/10.2174/138920309789630589

Hartmann, M. S., Mousavi, S., Bereswill, S., & Heimesaat, M. M. (2020). Vitamin E as promising adjunct treatment option in the combat of infectious diseases caused by bacterial including multi-drug resistant pathogens - Results from a comprehensive literature survey. *European Journal of Microbiology & Immunology*, *10*(4), 193–201. https://doi.org/10.1556/1886.2020.00020

Haynie, S. L., Crum, G. A., & Doele, B. A. (1995). Antimicrobial activities of amphiphilic peptides covalently bonded to a water-insoluble resin. *Antimicrobial Agents and Chemotherapy*, *39*(2), 301–307. https://doi.org/10.1128/AAC.39.2.301

He, J., Shi, H., Huang, S., Han, L., Zhang, W., & Zhong, Q. (2018). Core-shell nanoencapsulation of $α$-tocopherol by blending sodium oleate and rebaudioside A: Preparation, characterization, and antioxidant activity. *Molecules*, *23*(12), 3183.

Heilborn, J. D., Frohm Nilsson, M., Kratz, G., Weber, G., Sørensen, O., Borregaard, N., & Ståhle-Bäckdahl, M. (2003). The cathelicidin anti-microbial peptide LL-37 is involved in re-epithelialization of human skin wounds and is lacking in chronic ulcer epithelium.

The Journal of Investigative Dermatology, *120*(3), 379–389. https://doi.org/10.1046/J.1523-1747.2003.12069.X

Hermansson, M. (1999). The DLVO theory in microbial adhesion. *Colloids and Surfaces B: Biointerfaces*, *14*(1), 105–119. https://doi.org/https://doi.org/10.1016/S0927-7765(99)00029-6

Hetrick, E. M., & Schoenfisch, M. H. (2006). Reducing implant-related infections: Active release strategies. *Chemical Society Reviews*, *35*(9), 780–789. https://doi.org/10.1039/b515219b

Higashi, J. M., Wang, I., Shlaes, D. M., Anderson, J. M., & Marchant, R. E. (1998). Adhesion of Staphylococcus epidermidis and transposon mutant strains to hydrophobic polyethylene. *Journal of Biomedical Materials Research: An Official Journal of The Society for Biomaterials, The Japanese Society for Biomaterials, and the Australian Society for Biomaterials*, *39*(3), 341–350.

Hilpert, K., Elliott, M., Jenssen, H., Kindrachuk, J., Fjell, C. D., Körner, J., Winkler, D. F. H., Weaver, L. L., Henklein, P., Ulrich, A. S., Chiang, S. H. Y., Farmer, S. W., Pante, N., Volkmer, R., & Hancock, R. E. W. (2009). Screening and Characterization of Surface-Tethered Cationic Peptides for Antimicrobial Activity. *Chemistry and Biology*, *16*(1), 58–69. https://doi.org/10.1016/j.chembiol.2008.11.006

Hirohata, Y., Tsuchiya, N., & Hino, T. (2001). Effect of mixing of hydrogen into nitrogen plasma. *Applied Surface Science*, *169–170*, 612–616. https://doi.org/10.1016/S0169-4332(00)00799-6

Holland, T. J. B., & Redfern, S. A. T. (1997). Unit cell refinement from powder diffraction data: the use of regression diagnostics. *Mineralogical Magazine*, *61*(404), 65–77. https://doi.org/10.1180/minmag.1997.061.404.07

Hollister, C., & Sinanoğlu, O. (1966). Molecular Binding Energies. *Journal of the American Chemical Society*, *88*(1), 13–21. https://doi.org/10.1021/ja00953a003

Holmberg, K., Bergström, K., & Stark, M.-B. (1992). Immobilization of Proteins via PEG Chains. In *Poly(Ethylene Glycol) Chemistry* (pp. 303–324). Springer. https://doi.org/10.1007/978-1-4899-0703-5_19

Holzwarth, U., & Gibson, N. (2011). The Scherrer equation versus the "Debye-Scherrer equation." *Nature Nanotechnology*, *6*(9), 534. https://doi.org/10.1038/nnano.2011.145

Hong, S.-H., & Winter, J. (2005). Micro-Raman spectroscopy on a-C: H nanoparticles. *Journal of Applied Physics*, *98*(12), 124304.

Huan, Y., Kong, Q., Mou, H., & Yi, H. (2020). Antimicrobial Peptides: Classification, Design, Application and Research Progress in Multiple Fields. *Frontiers in Microbiology*, *11*, 2559. https://doi.org/10.3389/FMICB.2020.582779/XML/NLM

Hubbard, P., Dowey, S. J., Partridge, J. G., Doyle, E. D., & McCulloch, D. G. (2010). Investigation of nitrogen mass transfer within an industrial plasma nitriding system II: Application of a biased screen. *Surface and Coatings Technology*, *204*(8), 1151–1157. https://doi.org/10.1016/J.SURFCOAT.2009.08.030

Huddleston, J. I., Harris, A. H. S., Atienza, C. A., & Woolson, S. T. (2010). Hylamer vs Conventional Polyethylene in Primary Total Hip Arthroplasty: A Long-Term Case-Control Study of Wear Rates and Osteolysis. *Journal of Arthroplasty*, *25*(2), 203–207.

https://doi.org/10.1016/j.arth.2009.02.006

Huheey, J. E., Keiter, E. A., Keiter, R. L., & Medhi, O. K. (2006). *Inorganic chemistry: principles of structure and reactivity*. Pearson Education India.

Humblot, V., Yala, J. F., Thebault, P., Boukerma, K., Héquet, A., Berjeaud, J. M., & Pradier, C. M. (2009). The antibacterial activity of Magainin I immobilized onto mixed thiols Self-Assembled Monolayers. *Biomaterials*, *30*(21), 3503–3512. https://doi.org/10.1016/J.BIOMATERIALS.2009.03.025

Hussain, O., Sheikh, S. S., & Ahmad, B. (2022). Fabrication and tribological behavior of novel UHMWPE/vitamin-C/graphene nanoplatelets based hybrid composite for joint replacement. *Industrial Lubrication and Tribology*, *74*(8), 956–963. https://doi.org/10.1108/ILT-02-2021-0033

IMCD. (2022). *Selecting materials for medical device sterilisation*. https://www.imcdgroup.com/en/business-groups/advanced-materials/new-frontiers-knowledge-center/selecting-materials-for-medical-device-sterilization

Ingham, E., & Fisher, J. (2005). The role of macrophages in osteolysis of total joint replacement. *Biomaterials*, *26*(11), 1271–1286. https://doi.org/https://doi.org/10.1016/j.biomaterials.2004.04.035

ISO. (2009). *ISO 10993-5: 2009-Biological evaluation of medical devices-Part 5: Tests for in vitro cytotoxicity*. ISO Geneva.

ISO. (2019). Implants for surgery — Ultra-high-molecular-weight polyethylene — Part 1: Powder form. *Implants for Surgery, Prosthetics and Orthotics*.

Jacob, B., Park, I. S., Bang, J. K., & Shin, S. Y. (2013). Short KR-12 analogs designed from human cathelicidin LL-37 possessing both antimicrobial and antiendotoxic activities without mammalian cell toxicity. *Journal of Peptide Science*, *19*(11), 700–707. https://doi.org/10.1002/PSC.2552

James, S. P., Lee, K. R., Beauregard, G. P., Rentfrow, E. D., & McLaughlin, J. R. (1999). Clinical wear of 63 ultrahigh molecular weight polyethylene acetabular components: Effect of starting resin and forming method. *Journal of Biomedical Materials Research*, *48*(3), 374–384. https://doi.org/10.1002/(SICI)1097-4636(1999)48:3<374::AID-JBM23>3.0.CO;2-O

Jia, F., Wang, J., Peng, J., Zhao, P., Kong, Z., Wang, K., Yan, W., & Wang, R. (2017). D-amino acid substitution enhances the stability of antimicrobial peptide polybia-CP. *Acta Biochimica et Biophysica Sinica*, *49*(10), 916–925. https://doi.org/10.1093/ABBS/GMX091

Jiang, D., Chen, X.-Q., Luo, W., & Shelton, W. A. (2009). From trans-polyacetylene to zigzag-edged graphene nanoribbons. *Chemical Physics Letters*, *483*(1–3), 120–123.

Jokinen, V., Suvanto, P., & Franssila, S. (2012). Oxygen and nitrogen plasma hydrophilization and hydrophobic recovery of polymers. *Biomicrofluidics*, *6*(1), 16501. https://doi.org/10.1063/1.3673251

Joo, Y. L., Han, O. H., Lee, H. K., & Song, J. K. (2000). Characterization of ultra high molecular weight polyethyelene nascent reactor powders by x-ray diffraction and solid state NMR. *Polymer*, *41*(4), 1355–1368. https://doi.org/10.1016/S0032-3861(99)00272-4

Juhász, L., Moldován, K., Gurikov, P., Liebner, F., Fábián, I., Kalmár, J., & Cserháti, C. (2021). False morphology of aerogels caused by gold coating for sem imaging. *Polymers*, *13*(4), 1–12. https://doi.org/10.3390/polym13040588

Kaklamani, G. (2012). *The effect of active screen plasma nitriding on the cellular compatibility of polmeric biomaterials*. University of Birmingham.

Kaklamani, G., Mehrban, N., Chen, J., Bowen, J., Dong, H., Grover, L., & Stamboulis, A. (2010). Effect of plasma surface modification on the biocompatibility of UHMWPE. *Biomedical Materials*, *5*(5), 054102. https://doi.org/10.1088/1748-6041/5/5/054102

Kambara, S., Kuriyama, R., Osakabe, T., & Yukimura, K. (2008). Hydrogen oxidation in H2/O2/N2 gas mixture by pulsed DBD at atmospheric pressure. *International Journal of Hydrogen Energy*, *33*(22), 6792–6799. https://doi.org/10.1016/j.ijhydene.2008.07.024

Kämmerling, L., Fisher, L. E., Antmen, E., Simsek, G. M., Rostam, H. M., Vrana, N. E., & Ghaemmaghami, A. M. (2021). Mitigating the foreign body response through 'immune-instructive' biomaterials. *Journal of Immunology and Regenerative Medicine*, *12*, 100040. https://doi.org/https://doi.org/10.1016/j.regen.2021.100040

Kamysz, E., Sikorska, E., Jaśkiewicz, M., Bauer, M., Neubauer, D., Bartoszewska, S., Barańska-Rybak, W., & Kamysz, W. (2020). Lipidated Analogs of the LL-37-Derived Peptide Fragment KR12—Structural Analysis, Surface-Active Properties and Antimicrobial Activity. *International Journal of Molecular Sciences*, *21*(3). https://doi.org/10.3390/IJMS21030887

Kang, H. K., Kim, C., Seo, C. H., & Park, Y. (2016). The therapeutic applications of antimicrobial peptides (AMPs): a patent review. *Journal of Microbiology 2017 55:1*, *55*(1), 1–12. https://doi.org/10.1007/S12275-017-6452-1

Kartal, G. E., & Sarıışık, A. M. (2020). Modifying of UHMWPE fishing nets with layer-by-layer deposition method for antifouling properties. *Journal of Coatings Technology and Research 2020 18:1*, *18*(1), 163–171. https://doi.org/10.1007/S11998-020-00392-7

Kauling, A. P., Soares, G. V., Figueroa, C. A., de Oliveira, R. V. B., Baumvol, I. J. R., Giacomelli, C., & Miotti, L. (2009). Polypropylene surface modification by active screen plasma nitriding. *Materials Science and Engineering C*, *29*(2), 363–366. https://doi.org/10.1016/j.msec.2008.07.002

Kearney, S. M., Gibbons, S. M., Poyet, M., Gurry, T., Bullock, K., Allegretti, J. R., Clish, C. B., & Alm, E. J. (2018). Endospores and other lysis-resistant bacteria comprise a widely shared core community within the human microbiota. *The ISME Journal*, *12*(10), 2403–2416. https://doi.org/10.1038/s41396-018-0192-z

Kennedy, M. A. (2010). A brief review of the basics of immunology: the innate and adaptive response. *Veterinary Clinics: Small Animal Practice*, *40*(3), 369–379.

Keresztury, G., & Földes, E. x. (1990). On the Raman spectroscopic determination of phase distribution in polyethylene. *Polymer Testing*, *9*(5), 329–339. https://doi.org/10.1016/0142-9418(90)90004-W

Khalifa, A. A., & Bakr, H. M. (2021). Updates in biomaterials of bearing surfaces in total hip arthroplasty. *Arthroplasty*, *3*(1), 32.

Khalil, Y., Hopkinson, N., Kowalski, A., & Fairclough, J. P. (2019). Characterisation of UHMWPE Polymer Powder for Laser Sintering. In *Materials* (Vol. 12, Issue 21).

https://doi.org/10.3390/ma12213496

Khomich, A. A., Averin, A. A., Poklonskaya, O. N., Bokova-Sirosh, S. N., Dzeraviaha, A. N., Khmelnitsky, R. A., Vlasov, I. I., Shenderova, O., Poklonski, N. A., & Khomich, A. V. (2019). Features of the 1640 cm-1 band in the Raman spectra of radiation-damaged and nano-sized diamonds. *Journal of Physics: Conference Series*, *1400*(4), 44017. https://doi.org/10.1088/1742-6596/1400/4/044017

Kinnari, T. J., Esteban, J., Zamora, N., Fernandez, R., López-Santos, C., Yubero, F., Mariscal, D., Puertolas, J. A., & Gomez-Barrena, E. (2010). Effect of surface roughness and sterilization on bacterial adherence to ultra-high molecular weight polyethylene. *Clinical Microbiology and Infection : The Official Publication of the European Society of Clinical Microbiology and Infectious Diseases*, *16*(7), 1036–1041. https://doi.org/10.1111/j.1469-0691.2009.02995.x

Kizhakkedathu, J. N., & Conway, E. M. (2022). Biomaterial and cellular implants: foreign surfaces where immunity and coagulation meet. *Blood*, *139*(13), 1987–1998. https://doi.org/10.1182/blood.2020007209

Komornicki, A., & McIver, J. W. (1979). An efficient ab initio method for computing infrared and Raman intensities: Application to ethylene. *The Journal of Chemical Physics*, *70*(4), 2014–2016. https://doi.org/10.1063/1.437627

Koopmans, T. (1933). Ordering of wave functions and eigenenergies to the individual electrons of an atom. *Physica*, *1*, 104–113.

Kotál, V., Švorčík, V., Slepička, P., Sajdl, P., Bláhová, O., Šutta, P., & Hnatowicz, V. (2007). Gold Coating of Poly(ethylene terephthalate) Modified by Argon Plasma. *Plasma Processes and Polymers*, *4*(1), 69–76. https://doi.org/https://doi.org/10.1002/ppap.200600069

Krimm, S., Liang, C. Y., & Sutherland, G. B. B. M. (1956). Infrared spectra of high polymers. II. Polyethylene. *The Journal of Chemical Physics*, *25*(3), 549–562. https://doi.org/10.1063/1.1742963

Kröner, D., Ehlert, C., Saalfrank, P., & Holländer, A. (2011). Ab initio calculations for XPS chemical shifts of poly(vinyl- trifluoroacetate) using trimer models. *Surface Science*, *605*(15–16), 1516–1524. https://doi.org/10.1016/j.susc.2011.05.021

Kumakura, T., Puppulin, L., Yamamoto, K., Takahashi, Y., & Pezzotti, G. (2009). In-depth oxidation and strain profiles in UHMWPE acetabular cups non-destructively studied by confocal raman microprobe spectroscopy. *Journal of Biomaterials Science, Polymer Edition*, *20*(12), 1809–1822. https://doi.org/10.1163/156856208X386417

Kurelec, L., Rastogi, S., Meier, R. J., & Lemstra, P. J. (2000). Chain mobility in polymer systems: On the borderline between solid and melt. 3. Phase transformations in nascent ultrahigh molecular weight polyethylene reactor powder at elevated pressure as revealed by in situ Raman spectroscopy. *Macromolecules*, *33*(15), 5593–5601. https://doi.org/10.1021/ma9911187

Kurtz, S. M. (2009). Composite UHMWPE Biomaterials and Fibers. *UHMWPE Biomaterials Handbook*, 249–258. https://doi.org/10.1016/B978-0-12-374721-1.00017-1

Kurtz, S. M. (2015). The UHMWPE Handbook: Ultra-High Molecular Weight Polyethylene in Total Joint Replacement. In *The UHMWPE Handbook: Ultra-High Molecular Weight*

Polyethylene in Total Joint Replacement (3rd ed.). Elsevier. https://doi.org/10.1016/C2013-0-16083-7

Kurtz, S. M. (2016). The Origins of UHMWPE in Total Hip Arthroplasty. *UHMWPE Biomaterials Handbook: Ultra High Molecular Weight Polyethylene in Total Joint Replacement and Medical Devices: Third Edition*, 33–44. https://doi.org/10.1016/B978-0-323-35401-1.00004-1

Kurtz, S. M., Cooper, C., Siskey, R., Allen, M., & Hubbard, N. (2003). Effects of Dose Rate and Thermal Treatment on the Physical and Mechanical Properties of Highly Crosslinked UHMWPE Used in Total Joint Replacements. *49th Annual Meeting of the Orthopaedic Research Society*, *28*, 9–13.

Kurtz, S. M., Dumbleton, J., Siskey, R. S., Wang, A., & Manley, M. (2009). Trace concentrations of vitamin E protect radiation crosslinked UHMWPE from oxidative degradation. *Journal of Biomedical Materials Research - Part A*, *90*(2), 549–563. https://doi.org/10.1002/jbm.a.32122

Kurtz, S. M., Muratoglu, O. K., Evans, M., & Edidin, A. A. (1999). Advances in the processing, sterilization, and crosslinking of ultra-high molecular weight polyethylene for total joint arthroplasty. *Biomaterials*, *20*(18), 1659–1688. https://doi.org/10.1016/S0142-9612(99)00053-8

Kurtz, S. M., Pruitt, L. A., Jewett, C. W., Foulds, J. R., & Edidin, A. A. (1999). Radiation and chemical crosslinking promote strain hardening behavior and molecular alignment in ultra high molecular weight polyethylene during multi-axial loading conditions. *Biomaterials*, *20*(16), 1449–1462.

Kutz, J., Liebermeister, L., Vieweg, N., Wenzel, K., Kohlhaas, R., & Naftaly, M. (2022). A Terahertz Fast-Sweep Optoelectronic Frequency-Domain Spectrometer: Calibration, Performance Tests, and Comparison with TDS and FDS. *Applied Sciences (Switzerland)*, *12*(16). https://doi.org/10.3390/app12168257

Kyomoto, M., Miwa, Y., & Pezzotti, G. (2007). Strain in UHMWPE for orthopaedic use studied by Raman microprobe spectroscopy. *Journal of Biomaterials Science, Polymer Edition*, *18*(2), 165–178. https://doi.org/10.1163/156856207779116685

Lai, Y., Villaruz, A. E., Li, M., Cha, D. J., Sturdevant, D. E., & Otto, M. (2007). The human anionic antimicrobial peptide dermcidin induces proteolytic defence mechanisms in staphylococci. *Molecular Microbiology*, *63*(2), 497–506. https://doi.org/10.1111/J.1365-2958.2006.05540.X

Lebedev, Y. A., Shakhatov, V. A., & Epstein, I. L. (2010). Kinetic models of nonequilibrium nitrogen and hydrogen plasma for diagnostics of gas discharges. *Journal of Physics: Conference Series*, *207*(1), 012001. https://doi.org/10.1088/1742-6596/207/1/012001

Lerf, R., Zurbrügg, D., & Delfosse, D. (2010). Use of vitamin E to protect cross-linked UHMWPE from oxidation. *Biomaterials*, *31*(13), 3643–3648. https://doi.org/10.1016/j.biomaterials.2010.01.076

Lewies, A., Du Plessis, L. H., & Wentzel, J. F. (2018). Antimicrobial Peptides: the Achilles' Heel of Antibiotic Resistance? *Probiotics and Antimicrobial Proteins 2018 11:2*, *11*(2), 370–381. https://doi.org/10.1007/S12602-018-9465-0

Li, B., & Webster, T. J. (2018). Bacteria antibiotic resistance: New challenges and

opportunities for implant-associated orthopedic infections. *Journal of Orthopaedic Research®*, *36*(1), 22–32. https://doi.org/10.1002/JOR.23656

Li, C. X. (2010). Active screen plasma nitriding - An overview. *Surface Engineering*, *26*(1–2), 135–141. https://doi.org/10.1179/174329409X439032

Li, C. X., & Bell, T. (2005). Potential of plasma nitriding of polymer for improved hardness and wear resistance. *Journal of Materials Processing Technology*, *168*(2), 219–224. https://doi.org/10.1016/j.jmatprotec.2004.10.018

Li, C. X., Bell, T., & Dong, H. (2002). A study of active screen plasma nitriding. *Surface Engineering*, *18*(3), 174–181. https://doi.org/10.1179/026708401225005250

Li, C. Y., Gao, S. Y., Terashita, T., Shimokawa, T., Kawahara, H., Matsuda, S., & Kobayashi, N. (2006). In vitro assays for adhesion and migration of osteoblastic cells (Saos-2) on titanium surfaces. *Cell and Tissue Research*, *324*(3), 369–375. https://doi.org/10.1007/s00441-005-0153-5

Li, Hongmei, Chen, C. Y., & Balsells Padros, J. (2011). Highly efficient carbamate formation from alcohols and hindered amino acids or esters using N, N′-disuccinimidyl carbonate (DSC). *Synlett*, *2011*(10), 1454–1458. https://doi.org/10.1055/s-0030-1260584

Li, Hui, Zhang, S., Nie, B., Du, Z., Long, T., & Yue, B. (2018). The antimicrobial peptide KR-12 promotes the osteogenic differentiation of human bone marrow stem cells by stimulating BMP/SMAD signaling. *RSC Advances*, *8*(28), 15547. https://doi.org/10.1039/C8RA00750K

Li, Hui, Zhang, S., Nie, B., Long, T., Qu, X., & Yue, B. (2019). KR-12-A5 reverses adverse effects of lipopolysaccharides on HBMSC osteogenic differentiation by influencing BMP/Smad and p38 MAPK signaling pathways. *Frontiers in Pharmacology*, *10*(JUN), 639. https://doi.org/10.3389/fphar.2019.00639

Li, L., Sun, J., Xia, S., Tian, X., Cheserek, M. J., & Le, G. (2016). Mechanism of antifungal activity of antimicrobial peptide APP, a cell-penetrating peptide derivative, against Candida albicans: intracellular DNA binding and cell cycle arrest. *Applied Microbiology and Biotechnology*, *100*(7), 3245–3253.

Li, S. (2001). Ultra high molecular weight polyethylene: From charnley to cross-linked. *Operative Techniques in Orthopaedics*, *11*(4), 288–295. https://doi.org/10.1016/S1048-6666(01)80044-6

Lin, C. Y., George, M. W., & Gill, P. M. W. (2004). EDF2: A density functional for predicting molecular vibrational frequencies. *Australian Journal of Chemistry*, *57*(4), 365–370. https://doi.org/10.1071/CH03263

Lin, L., & Argon, A. S. (1994). Structure and plastic deformation of polyethylene. *Journal of Materials Science*, *29*(2), 294–323. https://doi.org/10.1007/BF01162485

Lipkin, R. B., & Lazaridis, T. (2015). Implicit membrane investigation of the stability of antimicrobial peptide $β$-barrels and arcs. *The Journal of Membrane Biology*, *248*(3), 469–486.

Liu, G., Chen, Y., & Li, H. (2004). Study on processing of ultrahigh molecular weight polyethylene/ polypropylene blends. *Journal of Applied Polymer Science*, *94*(3), 977–985. https://doi.org/10.1002/app.20679

Liu, M., Liu, T., Zhang, X., Jian, Z., Xia, H., Yang, J., Hu, X., Xing, M., Luo, G., & Wu, J. (2019). Fabrication of KR-12 peptide-containing hyaluronic acid immobilized fibrous eggshell membrane effectively kills multi-drug-resistant bacteria, promotes angiogenesis and accelerates re-epithelialization . *International Journal of Nanomedicine*, *14*, 3345–3360. https://doi.org/10.2147/IJN.S199618

Liu, X., Zhang, S., Xu, X. J., Zhang, Z., Zhou, L., & Zhang, G. (2013). Study on the creep and recovery behaviors of UHMWPE/CNTs composite fiber. *Fibers and Polymers*, *14*(10), 1635–1640. https://doi.org/10.1007/s12221-013-1635-9

Liu, Z., Du, Y., Li, J., Kang, D., Ye, C., & Zhao, S. (2022). Mechanism of calcium stearate deteriorating the wear resistance of UHMWPE: structure–property relationship. *Journal of Polymer Research*, *29*(10), 1–13. https://doi.org/10.1007/s10965-022-03283-0

Lohner, K., & Prossnigg, F. (2009). Biological activity and structural aspects of PGLa interaction with membrane mimetic systems. *Biochimica et Biophysica Acta (BBA)-Biomembranes*, *1788*(8), 1656–1666.

López-Santos, C., Yubero, F., Cotrino, J., & González-Elipe, A. R. (2011). Nitrogen plasma functionalization of low density polyethylene. *Surface and Coatings Technology*, *205*(11), 3356–3364. https://doi.org/10.1016/j.surfcoat.2010.11.038

Lorenzo, V., Pereña, J. M., & Fatou, J. M. G. (1989). Relationships between mechanical properties and microhardness of polyethylenes. *Die Angewandte Makromolekulare Chemie*, *172*(1), 25–35. https://doi.org/10.1002/apmc.1989.051720103

Lu, R., Gan, W., Wu, B. H., Zhang, Z., Guo, Y., & Wang, H. F. (2005). C-H stretching vibrations of methyl, methylene and methine groups at the vapor/Alcohol (n = 1-8) interfaces. *Journal of Physical Chemistry B*, *109*(29), 14118–14129. https://doi.org/10.1021/jp051565q

Lu, S., Russell, A. E., & Hendra, P. J. (1998). The Raman spectra of high modulus polyethylene fibres by Raman microscopy. *Journal of Materials Science*, *33*(19), 4721–4725. https://doi.org/10.1023/A:1004489104344

Luong, H. X., Thanh, T. T., & Tran, T. H. (2020). Antimicrobial peptides – Advances in development of therapeutic applications. *Life Sciences*, *260*, 118407. https://doi.org/10.1016/J.LFS.2020.118407

Lustiger, A., & Markham, R. L. (1983). Importance of tie molecules in preventing polyethylene fracture under long-term loading conditions. *Polymer*, *24*(12), 1647–1654. https://doi.org/10.1016/0032-3861(83)90187-8

Ma, Z., Yang, J., Han, J., Gao, L., Liu, H., Lu, Z., Zhao, H., & Bie, X. (2016). Insights into the Antimicrobial Activity and Cytotoxicity of Engineered α-Helical Peptide Amphiphiles. *Journal of Medicinal Chemistry*, *59*(24), 10946–10962. https://doi.org/10.1021/ACS.JMEDCHEM.6B00922

Machado Rodrigues, M., Kerstner Baldin, E. K., Fontoura, C. P., Leidens, L. M., Barbieri, R. A., Frassini, R., De Fraga Malfatti, C., Roesch-Ely, M., Figueroa, C. A., & Aguzzoli, C. (2020). Overview of sterilization methods for UHMWPE through surface analysis. *Materials Advances*, *1*(9), 3243–3255. https://doi.org/10.1039/d0ma00772b

Maillard, J.-Y. (2005). Antimicrobial biocides in the healthcare environment: efficacy, usage, policies, and perceived problems. *Therapeutics and Clinical Risk Management*, *1*(4),

307–320.

Man, K., Jiang, L.-H., Foster, R., & Yang, X. (2017). Immunological Responses to Total Hip Arthroplasty. *Journal of Functional Biomaterials*, *8*(3), 33. https://doi.org/10.3390/jfb8030033

Mannella, G. G. (2004). Reaction of Nitrogen and Hydrogen in a Low-Temperature Plasma. *The Journal of Chemical Physics*, *37*(3), 678. https://doi.org/10.1063/1.1701401

Marcondes, A. R., Ueda, M., Kostov, K. G., Beloto, A. F., Leite, N. F., Gomes, G. F., & Lepienski, C. M. (2004). Improvements of ultra-high molecular weight polyethylene mechanical properties by nitrogen plasma immersion ion implantation. *Brazilian Journal of Physics*, *34*(4 B), 1667–1672. https://doi.org/10.1590/S0103-97332004000800029

Marr, A. K., Gooderham, W. J., & Hancock, R. E. (2006). Antibacterial peptides for therapeutic use: obstacles and realistic outlook. *Current Opinion in Pharmacology*, *6*(5), 468–472. https://doi.org/10.1016/j.coph.2006.04.006

Martin, K. E., & García, A. J. (2021). Macrophage phenotypes in tissue repair and the foreign body response: Implications for biomaterial-based regenerative medicine strategies. *Acta Biomaterialia*, *133*, 4–16. https://doi.org/https://doi.org/10.1016/j.actbio.2021.03.038

Massaccesi, L., Ragone, V., Papini, N., Goi, G., Corsi Romanelli, M. M., Galliera, E., Romanelli, M. M. C., & Galliera, E. (2019). Effects of Vitamin E-stabilized ultra high molecular weight polyethylene on oxidative stress response and osteoimmunological response in human osteoblast. *Frontiers in Endocrinology*, *10*(APR), 203. https://doi.org/10.3389/fendo.2019.00203

Massines, F., Ségur, P., Gherardi, N., Khamphan, C., & Ricard, A. (2003). Physics and chemistry in a glow dielectric barrier discharge at atmospheric pressure: diagnostics and modelling. *Surface and Coatings Technology*, *174–175*, 8–14. https://doi.org/10.1016/S0257-8972(03)00540-1

Matsuzaki, K. (2009). Control of cell selectivity of antimicrobial peptides. *Biochimica et Biophysica Acta - Biomembranes*, *1788*(8), 1687–1692. https://doi.org/10.1016/j.bbamem.2008.09.013

Matsuzaki, K., Murase, O., Fujii, N., & Miyajima, K. (1996). An antimicrobial peptide, magainin 2, induced rapid flip-flop of phospholipids coupled with pore formation and peptide translocation. *Biochemistry*, *35*(35), 11361–11368. https://doi.org/10.1021/bi960016v

Matthews, J. B., Besong, A. A., Green, T. R., Stone, M. H., Wroblewski, B. M., Fisher, J., & Ingham, E. (2000). Evaluation of the response of primary human peripheral blood mononuclear phagocytes to challenge with in vitro generated clinically relevant UHMWPE particles of known size and dose. *Journal of Biomedical Materials Research*, *52*(2), 296–307. https://doi.org/10.1002/1097-4636(200011)52:2<296::AID-JBM8>3.0.CO;2-9

McCracken, J. M., & Allen, L.-A. H. (2014). Regulation of Human Neutrophil Apoptosis and Lifespan in Health and Disease. *Journal of Cell Death*, *7*, JCD.S11038. https://doi.org/10.4137/JCD.S11038

Medel, F. J., Rimnac, C. M., & Kurtz, S. M. (2009). On the assessment of oxidative and

microstructural changes after in vivo degradation of historical UHMWPE knee components by means of vibrational spectroscopies and nanoindentation. *Journal of Biomedical Materials Research - Part A*, *89*(2), 530–538. https://doi.org/10.1002/jbm.a.31992

Menacho-Melgar, R., Decker, J. S., Hennigan, J. N., & Lynch, M. D. (2019). A review of lipidation in the development of advanced protein and peptide therapeutics. *Journal of Controlled Release*, *295*, 1–12. https://doi.org/10.1016/J.JCONREL.2018.12.032

Méndez-Samperio, P. (2010). The human cathelicidin hCAP18/LL-37: A multifunctional peptide involved in mycobacterial infections. *Peptides*, *31*(9), 1791–1798. https://doi.org/10.1016/J.PEPTIDES.2010.06.016

Miao, M. S., Zhang, M. L., Van Doren, V. E., Van Alsenoy, C., & Martins, J. L. (2001). Density functional calculations on the structure of crystalline polyethylene under high pressures. *Journal of Chemical Physics*, *115*(24), 11317–11324. https://doi.org/10.1063/1.1420404

Mihajlovic, M., & Lazaridis, T. (2012). Charge distribution and imperfect amphipathicity affect pore formation by antimicrobial peptides. *Biochimica et Biophysica Acta - Biomembranes*, *1818*(5), 1274–1283. https://doi.org/10.1016/j.bbamem.2012.01.016

Mikić, Z. D. j., & Lesić, A. R. (2013). 50 years of total hip prosthesis--a tribute to Prof. Sir John Charnley. *Acta Chirurgica Iugoslavica*, *60*(1), 9–13.

Mishra, B., Epand, R. F., Epand, R. M., & Wang, G. (2013). Structural location determines functional roles of the basic amino acids of KR-12, the smallest antimicrobial peptide from human cathelicidin LL-37. *RSC Advances*, *3*(42), 19560–19571. https://doi.org/10.1039/C3RA42599A

Mittemeijer, E. J., & Somers, M. A. J. (2014). *Thermochemical surface engineering of steels*. Woodhead Publishing Cambridge.

Mollica, A., Macedonio, G., Stefanucci, A., Costante, R., Carradori, S., Cataldi, V., Giulio, M. Di, Cellini, L., Silvestri, R., Giordano, C., Scipioni, A., Morosetti, S., Punzi, P., & Mirzaie, S. (2017). Arginine- and Lysine-rich Peptides: Synthesis, Characterization and Antimicrobial Activity. *Letters in Drug Design & Discovery*, *15*(3). https://doi.org/10.2174/1570180814666170213161341

Momma, K., & Izumi, F. (2008). VESTA: A three-dimensional visualization system for electronic and structural analysis. *Journal of Applied Crystallography*, *41*(3), 653–658. https://doi.org/10.1107/S0021889808012016

More, S. E., Dave, J. R., Makar, P. K., Bhoraskar, S. V, Premkumar, S., Tomar, G. B., & Mathe, V. L. (2020). Surface modification of UHMWPE using ECR plasma for osteoblast and osteoclast differentiation. *Applied Surface Science*, *506*, 144665. https://doi.org/https://doi.org/10.1016/j.apsusc.2019.144665

Mouriaux, F., Zaniolo, K., Bergeron, M. A., Weidmann, C., De La Fouchardière, A., Fournier, F., Droit, A., Morcos, M. W., Landreville, S., & Guérin, S. L. (2016). Effects of long-term serial passaging on the characteristics and properties of cell lines derived from uveal melanoma primary tumors. *Investigative Ophthalmology and Visual Science*, *57*(13), 5288–5301. https://doi.org/10.1167/iovs.16-19317

Naguib, M. M., & Valvanoa, M. A. (2018). Vitamin E Increases Antimicrobial Sensitivity by

Inhibiting Bacterial Lipocalin Antibiotic Binding. *MSphere*, *3*(6). https://doi.org/10.1128/mSphere.00564-18

Nanoscience Instrument. (2020). Surface Tension, Surface Free Energy, and Wettability. In *Nanoscience.Com*.

Naresh Kumar, N., Yap, S. L., Bt Samsudin, F. N. D., Khan, M. Z., & Pattela Srinivasa, R. S. (2016). Effect of Argon Plasma Treatment on Tribological Properties of UHMWPE/MWCNT Nanocomposites. *Polymers*, *8*(8). https://doi.org/10.3390/polym8080295

Nazrun, A. S., Norazlina, M., Norliza, M., & Nirwana, S. I. (2012). The anti-inflammatory role of vitamin e in prevention of osteoporosis. *Advances in Pharmacological Sciences*, *2012*. https://doi.org/10.1155/2012/142702

Neises, B., & Steglich, W. (1978). Simple Method for the Esterification of Carboxylic Acids. *Angewandte Chemie International Edition in English*, *17*(7), 522–524. https://doi.org/https://doi.org/10.1002/anie.197805221

NHS. (2022). *National schedule of NHS costs*. https://www.england.nhs.uk/wp-content/uploads/2023/04/2_National_schedule_of_NHS_costs_FY21-22_v3.xlsx

Niki, E. (2014). Role of vitamin e as a lipid-soluble peroxyl radical scavenger: In vitro and in vivo evidence. *Free Radical Biology and Medicine*, *66*, 3–12. https://doi.org/10.1016/j.freeradbiomed.2013.03.022

Nishimoto, A., Bell, T. E., & Bell, T. (2013). Feasibility study of active screen plasma nitriding of titanium alloy. *Https://Doi.Org/10.1179/026708409X12454193831760*, *26*(1–2), 74–79. https://doi.org/10.1179/026708409X12454193831760

NIST. (2008). NIST Standard Reference Database, National Institute of Standards and Technology. In *NIST X-ray Photoelectron Spectroscopy Database* (p. [27/05/2018]).

Norizan, M. N., & Mohamed, R. (2013). FTIR Characterisation and Conductivity Studies of Undoped and Doped Conductive Polyene From PVC Recycle With Sustainable Epoxidised Oil Coating Resin. *Australian Journal of Basic and Applied Sciences*, *8*(5), 313–318. https://doi.org/10.2991/iccnce.2013.180

Nortje, B. D. (2021). *Feasibility of Additive Manufacturing for Patient-Specific Knee Replacements.*

Novo, E., & Parola, M. (2008). Redox mechanisms in hepatic chronic wound healing and fibrogenesis. *Fibrogenesis and Tissue Repair*, *1*(1). https://doi.org/10.1186/1755-1536-1-5

Ochtrop, P., & Hackenberger, C. P. R. (2020). Recent advances of thiol-selective bioconjugation reactions. *Current Opinion in Chemical Biology*, *58*, 28–36. https://doi.org/10.1016/J.CBPA.2020.04.017

Office for National Statistics. (2021). *National life tables--life expectancy in the UK: 2018 to 2020*.

Olsson, P. A. T., Hyldgaard, P., Schröder, E., Jutemar, E. P., Andreasson, E., & Kroon, M. (2018). Ab initio investigation of monoclinic phase stability and martensitic transformation in crystalline polyethylene. *Physical Review Materials*, *2*(7), 75602. https://doi.org/10.1103/PhysRevMaterials.2.075602

Onaizi, S. A., & Leong, S. S. J. (2011). Tethering antimicrobial peptides: Current status and potential challenges. *Biotechnology Advances*, *29*(1), 67–74. https://doi.org/10.1016/j.biotechadv.2010.08.012

Öner, M., Kızıl, G., Keskin, G., Pochat-Bohatier, C., & Bechelany, M. (2018). The effect of boron nitride on the thermal and mechanical properties of poly(3-hydroxybutyrate-co-3-hydroxyvalerate). *Nanomaterials*, *8*(11), 940. https://doi.org/10.3390/nano8110940

Oral, E., Ghali, B. W., & Muratoglu, O. K. (2011). The elimination of free radicals in irradiated UHMWPEs with and without vitamin e stabilization by annealing under pressure. *Journal of Biomedical Materials Research - Part B Applied Biomaterials*, *97 B*(1), 167–174. https://doi.org/10.1002/jbm.b.31799

Oral, E., Godleski, C., Malhi, A., & Muratoglu, O. (2006). Cross-linking is not necessary to decrease wear of UHMWPE: A Super-tough and low-wear UHMWPE. *Transactions of the 52nd Annual Meeting of the Orthopaedic Research Society*, 659.

Oral, E., Greenbaum, E. S., Malhi, A. S., Harris, W. H., & Muratoglu, O. K. (2005). Characterization of irradiated blends of α-tocopherol and UHMWPE. *Biomaterials*, *26*(33), 6657–6663. https://doi.org/10.1016/j.biomaterials.2005.04.026

Oral, E., Kurtz, S. M., & Muratoglu, O. K. (2011). Ultrahigh molecular weight polyethylene total joint implants. *Comprehensive Biomaterials*, *6*, 29–49. https://doi.org/10.1016/b978-0-08-055294-1.00199-9

Oral, E., Malhi, A. S., & Muratoglu, O. K. (2006). Mechanisms of decrease in fatigue crack propagation resistance in irradiated and melted UHMWPE. *Biomaterials*, *27*(6), 917–925.

Oral, E., & Muratoglu, O. K. (2011). Vitamin E diffused, highly crosslinked UHMWPE: A review. *International Orthopaedics*, *35*(2), 215–223. https://doi.org/10.1007/s00264-010-1161-y

Oral, E., & Muratoglu, O. K. (2016). Highly Cross-Linked UHMWPE Doped with Vitamin E. *UHMWPE Biomaterials Handbook: Ultra High Molecular Weight Polyethylene in Total Joint Replacement and Medical Devices: Third Edition*, 307–325. https://doi.org/10.1016/B978-0-323-35401-1.00018-1

Oral, E., Rowell, S. L., & Muratoglu, O. K. (2006). The effect of α-tocopherol on the oxidation and free radical decay in irradiated UHMWPE. *Biomaterials*, *27*(32), 5580–5587. https://doi.org/10.1016/j.biomaterials.2006.07.017

Oral, E., Wannomae, K. K., Hawkins, N., Harris, W. H., & Muratoglu, O. K. (2004). α-Tocopherol-doped irradiated UHMWPE for high fatigue resistance and low wear. *Biomaterials*, *25*(24), 5515–5522. https://doi.org/10.1016/j.biomaterials.2003.12.048

Oral, E., Wannomae, K. K., Rowell, S. L., & Muratoglu, O. K. (2007). Diffusion of vitamin E in ultra-high molecular weight polyethylene. *Biomaterials*, *28*(35), 5225–5237.

Oren, Z., & Shai, Y. (1998). Mode of action of linear amphipathic $α$-helical antimicrobial peptides. *Peptide Science*, *47*(6), 451–463.

OrthopaedicSpecialists. (2022). *Hip Replacement*. https://www.orthopaedicspecialists.com/contents/services-more/hip-replacement-more

Othman, A., Sekheri, M., & Filep, J. G. (2022). Roles of neutrophil granule proteins in

orchestrating inflammation and immunity. *The FEBS Journal*, *289*(14), 3932–3953. https://doi.org/https://doi.org/10.1111/febs.15803

Owens, D. K., & Wendt, R. C. (1969). Estimation of the surface free energy of polymers. *Journal of Applied Polymer Science*, *13*(8), 1741–1747. https://doi.org/10.1002/app.1969.070130815

Pagès, P. (2005). Characterization of polymer materials using FT-IR and DSC techniques. *Universidade Da Coruña*.

Pages, P., Carrasco, F., Saurina, J., & Colom, X. (1996). FTIR and DSC study of HDPE structural changes and mechanical properties variation when exposed to weathering aging during Canadian winter. *Journal of Applied Polymer Science*, *60*(2), 153–159. https://doi.org/10.1002/(sici)1097-4628(19960411)60:2<153::aid-app2>3.0.co;2-r

Pandey, R., Berendt, A. R., Athanasou, N. A., & Group), O. C. S. (2000). Histological and microbiological findings in non-infected and infected revision arthroplasty tissues. *Archives of Orthopaedic and Trauma Surgery*, *120*, 570–574.

Pandiyaraj, K. N., Selvarajan, V., Deshmukh, R. R., & Bousmina, M. (2008). The effect of glow discharge plasma on the surface properties of Poly (ethylene terephthalate) (PET) film. *Surface and Coatings Technology*, *202*(17), 4218–4226. https://doi.org/10.1016/j.surfcoat.2008.03.015

Paraschuk, D. Y., Golovnin, I. V., Smekhova, A. G., & Kobryanskii, V. M. (2002). Anomalously high Raman scattering cross section for carbon-carbon vibrations in trans-nanopolyacetylene. *JETP Letters*, *76*(9), 572–574. https://doi.org/10.1134/1.1538292

Parth, M., Aust, N., & Lederer, K. (2002). Studies on the effect of electron beam radiation on the molecular structure of ultra-high molecular weight polyethylene under the influence of α-tocopherol with respect to its application in medical implants. *Journal of Materials Science: Materials in Medicine*, *13*(10), 917–921. https://doi.org/10.1023/A:1019892004830

Patil, N. A., Njuguna, J., & Kandasubramanian, B. (2020). UHMWPE for biomedical applications: Performance and functionalization. *European Polymer Journal*, *125*, 109529. https://doi.org/10.1016/j.eurpolymj.2020.109529

Paynter, R. W. (2000). XPS studies of the ageing of plasma-treated polymer surfaces. *Surface and Interface Analysis*, *29*(1), 56–64. https://doi.org/10.1002/(SICI)1096-9918(200001)29:1<56::AID-SIA693>3.0.CO;2-2

Peng, D. Q., Kim, T. H., Chung, J. H., & Park, J. K. (2010). Development of nitride-layer of AISI 304 austenitic stainless steel during high-temperature ammonia gas-nitriding. *Applied Surface Science*, *256*(24), 7522–7529. https://doi.org/10.1016/J.APSUSC.2010.05.100

Percival, S. L., Suleman, L., Vuotto, C., Donelli, G., Darouiche, R. O., Barnes, L., Cooper, I., Hetrick, E. M., & Schoenfisch, M. H. (2015). Healthcare-Associated infections, medical devices and biofilms: Risk, tolerance and control. *Journal of Medical Microbiology*, *64*(4), 323–334. https://doi.org/10.1099/jmm.0.000032

Perdew, J. P., Ernzerhof, M., & Burke, K. (1996). Rationale for mixing exact exchange with density functional approximations. *Journal of Chemical Physics*, *105*(22), 9982–9985. https://doi.org/10.1063/1.472933

Pezzotti, G. (2017). Raman spectroscopy of biomedical polyethylenes. *Acta Biomaterialia*, *55*, 28–99. https://doi.org/10.1016/j.actbio.2017.03.015

Pigeon, M., Prud'homme, R. E., & Pezolet, M. (1991). Characterization of Molecular Orientation in Polyethylene by Raman Spectroscopy. *Macromolecules*, *24*(20), 5687–5694. https://doi.org/10.1021/ma00020a032

Pippig, F., Sarghini, S., Holländer, A., Paulussen, S., & Terrvn, H. (2009). TFAA chemical derivatization and XPS. Analysis of OH and NHx polymers. *Surface and Interface Analysis*, *41*(5), 421–429. https://doi.org/10.1002/sia.3043

Popoola, O. O., Yao, J. Q., Johnson, T. S., & Blanchard, C. R. (2010). Wear, delamination, and fatigue resistance of melt-annealed highly crosslinked UHMWPE cruciate-retaining knee inserts under activities of daily living. *Journal of Orthopaedic Research*, *28*(9), 1120–1126. https://doi.org/10.1002/jor.21104

Pratt, G. W. (1956). Unrestricted Hartree-Fock method. *Physical Review*, *102*(5), 1303–1307. https://doi.org/10.1103/PhysRev.102.1303

Prinsloo, L. C., Du Plooy, W., & Van Der Merwe, C. (2004). Raman spectroscopic study of the epicuticular wax layer of mature mango (Mangifera indica) fruit. *Journal of Raman Spectroscopy*, *35*(7), 561–567. https://doi.org/10.1002/jrs.1185

Promega. (2002). *CellTiter-Glo ® Luminescent Cell Viability Assay Cell Viability Assay*. https://www.promega.co.uk/-/media/files/resources/protocols/technical-bulletins/0/celltiter-glo-luminescent-cell-viability-assay-protocol.pdf?rev=0d95c232094b41daa06d0c110d1d916f&sc_lang=en

Pye, D. (2003). *Practical nitriding and ferritic nitrocarburizing*. ASM international.

Qutb, A. M., Wei, F., & Dong, W. (2020). Prediction and Characterization of Cationic Arginine-Rich Plant Antimicrobial Peptide SM-985 From Teosinte (Zea mays ssp. mexicana). *Frontiers in Microbiology*, *11*, 1353. https://doi.org/10.3389/FMICB.2020.01353/BIBTEX

Raev, M. B., Khramtsov, P. V., & Bochkova, M. S. (2015). Investigation into size distribution of carbon nanoparticles covalently functionalized with proteins. *Nanotechnologies in Russia*, *10*(1–2), 140–148. https://doi.org/10.1134/S1995078015010152

Rahmati, M., & Mozafari, M. (2018). Protein adsorption on polymers. *Materials Today Communications*, *17*, 527–540. https://doi.org/https://doi.org/10.1016/j.mtcomm.2018.10.024

Rahmati, M., Silva, E. A., Reseland, J. E., A. Heyward, C., & Haugen, H. J. (2020). Biological responses to physicochemical properties of biomaterial surface. *Chemical Society Reviews*, *49*(15), 5178–5224. https://doi.org/10.1039/D0CS00103A

Reano, A. F., Guinault, A., Richaud, E., & Fayolle, B. (2018). Polyethylene loss of ductility during oxidation: Effect of initial molar mass distribution. *Polymer Degradation and Stability*, *149*, 78–84. https://doi.org/10.1016/j.polymdegradstab.2018.01.021

Reggiani, M., Tinti, A., Taddei, P., Visentin, M., Stea, S., De Clerico, M., & Fagnano, C. (2006). Phase transformation in explanted highly crystalline UHMWPE acetabular cups and debris after in vivo wear. *Journal of Molecular Structure*, *785*(1–3), 98–105. https://doi.org/10.1016/j.molstruc.2005.09.029

Ren, X., Liu, H., Wu, X., Weng, W., Wang, X., & Su, J. (2022). Reactive Oxygen Species (ROS)-Responsive Biomaterials for the Treatment of Bone-Related Diseases. *Frontiers in Bioengineering and Biotechnology*, *9*. https://doi.org/10.3389/fbioe.2021.820468

Ren, Y., Wang, F. Y., Chen, Z. J., Lan, R. T., Huang, R. H., Fu, W. Q., Gul, R. M., Wang, J., Xu, J. Z., & Li, Z. M. (2020). Antibacterial and anti-inflammatory ultrahigh molecular weight polyethylene/tea polyphenol blends for artificial joint applications. *Journal of Materials Chemistry B*, *8*(45), 10428–10438. https://doi.org/10.1039/d0tb01677b

Ren, Y., Wang, Z. Y., Wei, X., Xu, L., Gul, R. M., Huang, S. S., Xu, J. Z., & Li, Z. M. (2020). Insights into Oxidation of the Ultrahigh Molecular Weight Polyethylene Artificial Joint Related to Lipid Peroxidation. *ACS Applied Bio Materials*, *3*(1), 547–553. https://doi.org/10.1021/acsabm.9b00960

Ren, Y., Wei, X., Wei, S.-T., Wang, F. Y., Wang, J., Xu, J. Z., Xu, L., Gul, R. M., & Li, Z. M. (2019). High oxidation stability of tea polyphenol-stabilized highly crosslinked UHMWPE under an in vitro aggressive oxidative condition. *Clinical Orthopaedics and Related Research*, *477*(8), 1947.

Renò, F., Sabbatini, M., & Cannas, M. (2003). Surface oxidation of UHMWPE for orthopedic use increases apoptosis and necrosis in human granulocytes. *Journal of Materials Science: Materials in Medicine*, *14*(3), 241–245. https://doi.org/10.1023/A:1022832707221

Reusch, W. (1980). *Virtual Textbook of Organic Chemistry*. https://www2.chemistry.msu.edu/faculty/reusch/VirtTxtJml/intro1.htm

Reznickova, A., Novotna, Z., Kolska, Z., Kasalkova, N. S., Rimpelova, S., & Svorcik, V. (2015). Enhanced adherence of mouse fibroblast and vascular cells to plasma modified polyethylene. *Materials Science and Engineering: C*, *52*, 259–266. https://doi.org/https://doi.org/10.1016/j.msec.2015.03.052

Richaud, E. (2015). Stabilization of Irradiated Polyethylene by Introduction of Antioxidants (Vitamin E). *Polyethylene Based Blends, Composites, and Nanocomposities*, 41–91. https://doi.org/10.1002/9781118831328.ch3

Rosales, C. (2018). Neutrophil: A Cell with Many Roles in Inflammation or Several Cell Types? *Frontiers in Physiology*, *9*. https://doi.org/10.3389/fphys.2018.00113

Roth, J. R. (1995). Industrial Plasma Engineering : Volume 1: Principles. *Industrial Plasma Engineering*. https://doi.org/10.1201/9780367802615

Rounds, T., & Straus, S. K. (2020). Lipidation of Antimicrobial Peptides as a Design Strategy for Future Alternatives to Antibiotics. *International Journal of Molecular Sciences*, *21*(24), 1–15. https://doi.org/10.3390/IJMS21249692

Rudawska, A., & Jacniacka, E. (2009). Analysis for determining surface free energy uncertainty by the Owen-Wendt method. *International Journal of Adhesion and Adhesives*, *29*(4), 451–457. https://doi.org/10.1016/j.ijadhadh.2008.09.008

Rulison, C. (1999). Models for Surface Free Energy Calculation. *Kruss USA Technical Note 306*, *49*(40), 1–16.

Rull, F., Prieto, A. C., Casado, J. M., Sobron, F., & Edwards, H. G. M. (1993). Estimation of crystallinity in polyethylene by Raman spectroscopy. *Journal of Raman Spectroscopy*, *24*(8), 545–550. https://doi.org/10.1002/jrs.1250240813

Sadezky, A., Muckenhuber, H., Grothe, H., Niessner, R., & Pöschl, U. (2005). Raman microspectroscopy of soot and related carbonaceous materials: Spectral analysis and structural information. *Carbon*, *43*(8), 1731–1742. https://doi.org/10.1016/j.carbon.2005.02.018

Sakoda, H., Osaka, Y., Uetsuki, K., Okamoto, Y., & Haishima, Y. (2019). Evaluating the durability of UHMWPE biomaterials used for articulating surfaces of joint arthroplasty using delamination tests. *Journal of Biomedical Materials Research - Part B Applied Biomaterials*, *107*(1), 65–72. https://doi.org/10.1002/jbm.b.34095

Salari, M., Mohseni Taromsari, S., Bagheri, R., & Faghihi Sani, M. A. (2019). Improved wear, mechanical, and biological behavior of UHMWPE-HAp-zirconia hybrid nanocomposites with a prospective application in total hip joint replacement. *Journal of Materials Science*, *54*(5), 4259–4276. https://doi.org/10.1007/s10853-018-3146-y

Sano, K. I., & Shiba, K. (2003). A Hexapeptide Motif that Electrostatically Binds to the Surface of Titanium. *Journal of the American Chemical Society*, *125*(47), 14234–14235. https://doi.org/10.1021/JA038414Q/SUPPL_FILE/JA038414QSI20031015_085141.PDF

Santner, H. J., Korepp, C., Winter, M., Besenhard, J. O., & Möller, K. C. (2004). In-situ FTIR investigations on the reduction of vinylene electrolyte additives suitable for use in lithium-ion batteries. *Analytical and Bioanalytical Chemistry*, *379*(2), 266–271. https://doi.org/10.1007/s00216-004-2522-4

Sawae, Y. (2017). Wear of UHMWPE for Joint Prosthesis. In *Handbook of Polymer Tribology* (pp. 81–109). WORLD SCIENTIFIC. https://doi.org/doi:10.1142/9789813227798_0003

Scheinost, A. C., & Schwertmann, U. (1999). Color Identification of Iron Oxides and Hydroxysulfates. *Soil Science Society of America Journal*, *63*(5), 1463–1471. https://doi.org/10.2136/sssaj1999.6351463x

Schwalfenberg, G. K. (2012). The alkaline diet: Is there evidence that an alkaline pH diet benefits health? *Journal of Environmental and Public Health*, *2012*. https://doi.org/10.1155/2012/727630

Schwartz, K. B., Cheng, J., Reddy, V. N., Fone, M., & Fisher, H. P. (1994). Crystallinity and Unit Cell Variations in Linear High-Density Polyethylene. *Advances in X-Ray Analysis*, *38*, 495–502. https://doi.org/10.1154/s0376030800018152

Seebach, D., Beck, A. K., & Bierbaum, D. J. (2004). The world of β- And γ-Peptides comprised of homologated proteinogenic amino acids and other components. *Chemistry and Biodiversity*, *1*(8), 1111–1239. https://doi.org/10.1002/cbdv.200490087

Semplice, M., Veglio, A., Naldi, G., Serini, G., & Gamba, A. (2012). A bistable model of cell polarity. *PloS One*, *7*(2), e30977.

Sen, S., & Puri, I. K. (2004). Flame synthesis of carbon nanofibres and nanofibre composites containing encapsulated metal particles. *Nanotechnology*, *15*(3), 264–268. https://doi.org/10.1088/0957-4484/15/3/005

Serra, S., Iarlori, S., Tosatti, E., Scandolo, S., Righi, M. C., & Santoro, G. E. (2002). Self-trapping vs. non-trapping of electrons and holes in organic insulators: Polyethylene. *Chemical Physics Letters*, *360*(5–6), 487–493. https://doi.org/10.1016/S0009-

2614(02)00832-1

Shai, Y. (2002). Mode of action of membrane active antimicrobial peptides. *Biopolymers - Peptide Science Section*, *66*(4), 236–248. https://doi.org/10.1002/bip.10260

Shanbhag, A. S., Jacobs, J. J., Black, J., Galante, J. O., & Glant, T. T. (1995). Human monocyte response to particulate biomaterials generated in vivo and in vitro. *Journal of Orthopaedic Research*, *13*(5), 792–801. https://doi.org/10.1002/jor.1100130520

Sheka, E. F., Golubev, Y. A., & Popova, N. A. (2020). Raman Scattering by sp2 Amorphous Carbons. *ArXiv*.

Shen, J., Gao, G., Liu, X., & Fu, J. (2015). Natural polyphenols enhance stability of crosslinked UHMWPE for joint implants. *Clinical Orthopaedics and Related Research®*, *473*(3), 760–766.

Shen, J., Liu, X., & Fu, J. (2014). Effect of squalene absorption on oxidative stability of highly crosslinked UHMWPE stabilized with natural polyphenols. *Polymer Degradation and Stability*, *110*, 113–120.

Shenkarev, Z. O., Balandin, S. V, Trunov, K. I., Paramonov, A. S., Sukhanov, S. V, Barsukov, L. I., Arseniev, A. S., & Ovchinnikova, T. V. (2011). Molecular mechanism of action of $β$-hairpin antimicrobial peptide arenicin: oligomeric structure in dodecylphosphocholine micelles and pore formation in planar lipid bilayers. *Biochemistry*, *50*(28), 6255–6265.

Shibata, N., Kurtz, S. M., & Tomita, N. (2006). Recent Advances of Mechanical Performance and Oxidation Stability in Ultrahigh Molecular Weight Polyethylene for Total Joint Replacement: Highly Crosslinked and .ALPHA.-Tocopherol Doped. *Journal of Biomechanical Science and Engineering*, *1*(1), 107–123. https://doi.org/10.1299/jbse.1.107

Shibata, N., & Tomita, N. (2005). The anti-oxidative properties of α-tocopherol in γ-irradiated UHMWPE with respect to fatigue and oxidation resistance. *Biomaterials*, *26*(29), 5755–5762. https://doi.org/10.1016/j.biomaterials.2005.02.035

Shimada, T., Sugai, T., Fantini, C., Souza, M., Cançado, L. G., Jorio, A., Pimenta, M. A., Saito, R., Grüneis, A., Dresselhaus, G., Dresselhaus, M. S., Ohno, Y., Mizutani, T., & Shinohara, H. (2005). Origin of the 2450 cm-1 Raman bands in HOPG, single-wall and double-wall carbon nanotubes. *Carbon*, *43*(5), 1049–1054. https://doi.org/10.1016/j.carbon.2004.11.044

Shintani, H., Sakudo, A., Burke, P., & McDonnell, G. (2010). Gas plasma sterilization of microorganisms and mechanisms of action. *Experimental and Therapeutic Medicine*, *1*(5), 731–738. https://doi.org/10.3892/etm.2010.136

Side, D. D., Alifano, P., Nassisi, V., Talà, A., Tredici, S. M., & Velardi, L. (2013). Enhancing UHMWPE Antibacterial Properties Through Ion Implantation. In *3rd Workshop-Plasmi, Sorgenti, Biofisica ed Applicazioni* (pp. 143–148).

Small, M., Faglie, A., Craig, A. J., Pieper, M., Narcisse, V. E. F., Neuenschwander, P. F., & Chou, S. F. (2018). Nanostructure-Enabled and Macromolecule-Grafted Surfaces for Biomedical Applications. *Micromachines 2018, Vol. 9, Page 243*, *9*(5), 243. https://doi.org/10.3390/MI9050243

Snyder, R. G., Hsu, S. L., & Krimm, S. (1978). Vibrational spectra in the CH stretching

region and the structure of the polymethylene chain. *Spectrochimica Acta Part A: Molecular Spectroscopy*, *34*(4), 395–406. https://doi.org/10.1016/0584-8539(78)80167-6

Sobieraj, M. C., & Rimnac, C. M. (2009). Ultra high molecular weight polyethylene: mechanics, morphology, and clinical behavior. *Journal of the Mechanical Behavior of Biomedical Materials*, *2*(5), 433–443.

Socrates, G. (2004). *Infrared and Raman characteristic group frequencies: tables and charts*. John Wiley \& Sons. https://doi.org/10.1007/s00396-004-1164-6

Spiller, E. (2010). Optical Constants. *Soft X-Ray Optics*, 5–22. https://doi.org/10.1117/3.176482.ch2

Spindler, E. C., Hale, J. D. F., Giddings, T. H., Hancock, R. E. W., & Gill, R. T. (2011). Deciphering the mode of action of the synthetic antimicrobial peptide bac8c. *Antimicrobial Agents and Chemotherapy*, *55*(4), 1706–1716. https://doi.org/10.1128/AAC.01053-10

Stessuk, T., Husch, J., Hermens, I. A. T., Hofmann, S., & van den Beucken, J. J. J. P. (2021). Osteogenic differentiation driven by osteoclasts and macrophages. *Journal of Immunology and Regenerative Medicine*, *12*, 100044. https://doi.org/https://doi.org/10.1016/j.regen.2021.100044

Strandberg, C. (2006). *Long-Term Properties of Polyethylene Films – Efficiency of a Natural Antioxidant*. KTH.

Strobl, G. R., & Hagedorn, W. (1978). Raman Spectroscopic Method for Determining the Crystallinity of Polyethylene. *AIP Conf Proc*, *16*(7), 1181–1193. https://doi.org/10.1002/pol.1978.180160704

Subbalakshmi, C., & Sitaram, N. (1998). Mechanism of antimicrobial action of indolicidin. *FEMS Microbiology Letters*, *160*(1), 91–96.

Subramani, M., & Sepperumal, U. (2016). FTIR analysis of bacterial mediated chemical changes in polystyrene foam. *Ann. Biol. Res*, *7*(5), 55–61.

Suhardi, V. J., Bichara, D. A., Kwok, S. J. J., Freiberg, A. A., Rubash, H., Malchau, H., Yun, S. H., Muratoglu, O. K., & Oral, E. (2017). A fully functional drug-eluting joint implant. *Nature Biomedical Engineering*, *1*(6). https://doi.org/10.1038/s41551-017-0080

Sun, Y., & Sun, G. (2001). Surface modification of poly(styrene) by the attachment of an antimicrobial peptide. *Journal of Applied Polymer Science*, *81*(3), 609–616. https://doi.org/10.1002/app.1476

Swinehart, D. F. (1962). The beer-lambert law. *Journal of Chemical Education*, *39*(7), 333.

Tadmor, R. (2004). Line energy and the relation between advancing, receding, and young contact angles. *Langmuir*, *20*(18), 7659–7664.

Tálský, A., Štec, O., Pazderka, M., & Kudrle, V. (2017). Kinetic Study of Atmospheric Pressure Nitrogen Plasma Afterglow Using Quantitative Electron Spin Resonance Spectroscopy. *Journal of Spectroscopy*, *2017*. https://doi.org/10.1155/2017/5473874

Tam, T., & Bhatnagar, A. (2016). High-performance ballistic fibers and tapes. *Lightweight Ballistic Composites: Military and Law-Enforcement Applications: Second Edition*, 1–

39. https://doi.org/10.1016/B978-0-08-100406-7.00001-5

Tanaka, S., Nakamura, K., Takahasi, N., & Suda, T. (2005). Role of RANKL in physiological and pathological bone resorption and therapeutics targeting the RANKL–RANK signaling system. *Immunological Reviews*, *208*(1), 30–49. https://doi.org/https://doi.org/10.1111/j.0105-2896.2005.00327.x

Tanoira, R. P. (2019). *" Race for the Surface": Competition between Bacteria and Host Cells in Implant Colonization Process*.

Tasumi, M., & Krimm, S. (1967). Crystal vibrations of polyethylene. *The Journal of Chemical Physics*, *46*(2), 755–766. https://doi.org/10.1063/1.1840736

Taucher, T. C., Hehn, I., Hofmann, O. T., Zharnikov, M., & Zojer, E. (2016). Understanding Chemical versus Electrostatic Shifts in X-ray Photoelectron Spectra of Organic Self-Assembled Monolayers. *Journal of Physical Chemistry C*, *120*(6), 3428–3437. https://doi.org/10.1021/acs.jpcc.5b12387

Teitelbaum, S. L. (2000). Bone Resorption by Osteoclasts. *Science*, *289*(5484), 1504–1508. https://doi.org/10.1126/science.289.5484.1504

Testa, B., & Mayer, J. M. (2006). Hydrolysis in drug and prodrug metabolism: Chemistry, biochemistry, and enzymology. In *Hydrolysis in Drug and Prodrug Metabolism: Chemistry, Biochemistry, and Enzymology*. John Wiley \& Sons. https://doi.org/10.1002/9783906390444

Thomas, P., Sekhar, A. C., & Mujawar, M. M. (2014). Vulnerability of Bacillus spores and of related genera to physical impaction injury with particular reference to spread-plating. *Journal of Applied Microbiology*, *117*(5), 1358–1372.

Thorn, L., Lamagni, T., Harrington, P., Wloch, C., Rusell, H., & Colin, B. (2022). *Surgical site infections (SSI) surveillance: NHS hospitals in England*.

Tomba, J. P., Silva, L. I., García Genga, M., Barrera Galland, G., & Perez, C. J. (2019). Characterizing chemical composition of polyolefin-based copolymers from spectral features in the C═H stretching region. *Journal of Raman Spectroscopy*, *50*(4), 576–586. https://doi.org/10.1002/jrs.5554

Tomita, N., Kitakura, T., Onmori, N., Ikada, Y., & Aoyama, E. (1999). Prevention of fatigue cracks in ultrahigh molecular weight polyethylene joint components by the addition of vitamin E. *Journal of Biomedical Materials Research*, *48*(4), 474–478. https://doi.org/10.1002/(SICI)1097-4636(1999)48:4<474::AID-JBM11>3.0.CO;2-T

Toshioka, N., & Nishimoto, A. (2020). Surface-Modified Layer Formed by Plasma Nitriding Using Chromium Screen. *MATERIALS TRANSACTIONS*, *61*(6), H-M2020815. https://doi.org/10.2320/MATERTRANS.H-M2020815

Trzcińska, Z., Bruggeman, M., Ijakipour, H., Hodges, N. J., Bowen, J., & Stamboulis, A. (2020). Polydopamine linking substrate for AMPs: Characterisation and stability on Ti6Al4V. *Materials*, *13*(17), 3714. https://doi.org/10.3390/MA13173714

Tsukamoto, R., Chen, S., Asano, T., Ogino, M., Shoji, H., Nakamura, T., & Clarke, I. (2006). Improved wear performance with crosslinked UHMWPE and zirconia implants in knee simulation. *Acta Orthopaedica*, *77*(3), 505–511. https://doi.org/10.1080/17453670610046479

Tsuneda, T., & Hirao, K. (2014). Self-interaction corrections in density functional theory. *Journal of Chemical Physics*, *140*(18), 18A513. https://doi.org/10.1063/1.4866996

Tugyi, R., Uray, K., Iván, D., Fellinger, E., Perkins, A., & Hudecz, F. (2005). Partial D-amino acid substitution: Improved enzymatic stability and preserved Ab recognition of a MUC2 epitope peptide. *Proceedings of the National Academy of Sciences of the United States of America*, *102*(2), 413–418. https://doi.org/10.1073/pnas.0407677102

Turicek, J., Ratts, N., Kaltchev, M., & Masoud, N. (2021). Surface treatment of ultra-high molecular weight polyethylene (UHMWPE) by cold atmospheric plasma (CAP) for biocompatibility enhancement. *Applied Sciences*, *11*(4), 1703.

Vasconcellos, L. A., Blando, E., Souto, A. A., Oliveira, M. G., Woitchunas, G. F. P., & Hübler, R. (2007). Study of mechanical degradation of UHMWPE acetabular components due to clinical X-ray procedures. *Journal of Materials Science: Materials in Medicine*, *18*(8), 1659–1663. https://doi.org/10.1007/s10856-007-3034-5

Verma, S. K., Ghorpade, R., Pratap, A., & Kaushik, M. P. (2012). Solvent free, N,N'-carbonyldiimidazole (CDI) mediated amidation. *Tetrahedron Letters*, *53*(19), 2373–2376. https://doi.org/10.1016/j.tetlet.2012.01.125

Veronese, F. M., & Pasut, G. (2005). PEGylation, successful approach to drug delivery. *Drug Discovery Today*, *10*(21), 1451–1458. https://doi.org/10.1016/S1359-6446(05)03575-0

Vila, J., Soriano, A., & Mensa, J. (2008). Molecular basis of microbial adherence to prosthetic materials. Role of biofilms in prosthesis-associated infection. *Enfermedades Infecciosas y Microbiologia Clinica*, *26*(1), 48–54.

Viñes, F., Sousa, C., & Illas, F. (2018). On the prediction of core level binding energies in molecules, surfaces and solids. In *Physical Chemistry Chemical Physics* (Vol. 20, Issue 13, pp. 8403–8410). Royal Society of Chemistry. https://doi.org/10.1039/c7cp08503f

Walkenhorst, R. (2022). *Personal communication: Contamination in GUR (UHMWPE)*. Celanese Corporation.

Wallace, W., Schaefer, L., & Swedlow, J. (2015). *Deconvolution in Optical Microscopy: Resolution Criteria and Performance Issues*. https://micro.magnet.fsu.edu/primer/digitalimaging/deconvolution/deconresolution.html

Wang, F.-Y., Ren, Y., Lan, R.-T., Fu, W.-Q., Chen, Z.-J., Huang, S., Gul, R. M., Wang, J., Xu, J.-Z., & Li, Z.-M. (2021). Controlled bacteriostasis of tea polyphenol loaded ultrahigh molecular weight polyethylene with high crosslink density and oxidation resistance for total joint replacement. *Materials Science and Engineering: C*, *124*, 112040. https://doi.org/https://doi.org/10.1016/j.msec.2021.112040

Wang, G. (2008). Structures of human host defense cathelicidin LL-37 and its smallest antimicrobial peptide KR-12 in lipid micelles. *Journal of Biological Chemistry*, *283*(47), 32637–32643. https://doi.org/10.1074/jbc.M805533200

Wang, G., Li, X., & Wang, Z. (2016). APD3: The antimicrobial peptide database as a tool for research and education. *Nucleic Acids Research*, *44*(D1), D1087–D1093. https://doi.org/10.1093/nar/gkv1278

Wang, G., Watson, K. M., & Buckheit, R. W. (2008). Anti-Human Immunodeficiency Virus Type 1 Activities of Antimicrobial Peptides Derived from Human and Bovine Cathelicidins. *Antimicrobial Agents and Chemotherapy*, *52*(9), 3438–3440.

https://doi.org/10.1128/aac.00452-08

Wang, J., Dou, X., Song, J., Lyu, Y., Zhu, X., Xu, L., Li, W., & Shan, A. (2019). Antimicrobial peptides: Promising alternatives in the post feeding antibiotic era. *Medicinal Research Reviews*, *39*(3), 831–859. https://doi.org/10.1002/med.21542

Wang, K., Sun, D. W., Wei, Q., & Pu, H. (2018). Quantification and visualization of α-tocopherol in oil-in-water emulsion based delivery systems by Raman microspectroscopy. *Lwt*, *96*, 66–74. https://doi.org/10.1016/j.lwt.2018.05.017

Wang, L., Huang, B., Duan, X., Jiang, G., Xiong, Y., Zhong, S., Wang, J., & Liao, X. (2021). The development of three ruthenium-based antimicrobial metallodrugs: Design, synthesis, and activity evaluation against Staphylococcus aureus. *Journal of Chemical Research*, *45*, 174751982110550. https://doi.org/10.1177/17475198211055098

Wang, M., & Tang, T. (2019). Surface treatment strategies to combat implant-related infection from the beginning. *Journal of Orthopaedic Translation*, *17*, 42–54. https://doi.org/10.1016/J.JOT.2018.09.001

Wang, Y., Wu, K., Cubero, D., Mackernan, D., Coker, D., & Quirke, N. (2013). Electron trapping in polyethylene. *2013 IEEE International Conference on Solid Dielectrics (ICSD)*, 19–22.

Watts, J. F. (1998). Surface analysis of polymers by XPS and static SIMS. In *Surface Engineering* (Vol. 14, Issue 4). Cambridge University Press. https://doi.org/10.1179/sur.1998.14.4.290

Wei, S., Chu, L., Lau, J., Blaber, M., & Chieh, C. (2016). *Valence Bond Theory*. https://chem.libretexts.org/Bookshelves/Physical_and_Theoretical_Chemistry_Textbook_Maps/Supplemental_Modules_(Physical_and_Theoretical_Chemistry)/Chemical_Bonding/Valence_Bond_Theory

Welch, N. G., Li, W., Hossain, M. A., Separovic, F., O'Brien-Simpson, N. M., & Wade, J. D. (2020). (Re)Defining the Proline-Rich Antimicrobial Peptide Family and the Identification of Putative New Members. *Frontiers in Chemistry*, *8*. https://doi.org/10.3389/fchem.2020.607769

Wen, X., Li, Z., Yang, C., Yan, K., Wu, G., & Wang, D. (2022). Electron beam irradiation assisted preparation of UHMWPE fiber with 3D cross-linked structure and outstanding creep resistance. *Radiation Physics and Chemistry*, *199*, 110370. https://doi.org/https://doi.org/10.1016/j.radphyschem.2022.110370

Williams, D. L., Vinciguerra, J., Lerdahl, J. M., & Bloebaum, R. D. (2015). Does vitamin E-blended UHMWPE prevent biofilm formation? *Clinical Orthopaedics and Related Research®*, *473*, 928–935.

Wolf, C., Lederer, K., & Müller, U. (2002). Tests of biocompatibility of α-tocopherol with respect to the use as a stabilizer in ultrahigh molecular weight polyethylene for articulating surfaces in joint endoprostheses. *Journal of Materials Science: Materials in Medicine*, *13*(7), 701–705. https://doi.org/10.1023/A:1015750112343

Wolf, C., Lederer, K., Pfragner, R., Schauenstein, K., Ingolic, E., & Siegl, V. (2007). Biocompatibility of ultra-high molecular weight polyethylene (UHMW-PE) stabilized with α-tocopherol used for joint endoprostheses assessed in vitro. *Journal of Materials Science: Materials in Medicine*, *18*(6), 1247–1252. https://doi.org/10.1007/s10856-006-

0098-6

Wool, R. P., Bretzlaff, R. S., Li, B. Y., Wang, C. H., & Boyd, R. H. (1986). Infrared and raman spectroscopy of stressed polyethylene. *Journal of Polymer Science Part B: Polymer Physics*, *24*(5), 1039–1066. https://doi.org/10.1002/polb.1986.090240508

Xiao, M., Jasensky, J., Foster, L., Kuroda, K., & Chen, Z. (2018). Monitoring Antimicrobial Mechanisms of Surface-Immobilized Peptides in Situ. *Langmuir*, *34*(5), 2057–2062. https://doi.org/10.1021/acs.langmuir.7b03668

Xu, A., Roland, S., & Colin, X. (2020). Physico-chemical characterization of the blooming of Irganox 1076® antioxidant onto the surface of a silane-crosslinked polyethylene. *Polymer Degradation and Stability*, *171*, 109046. https://doi.org/10.1016/J.POLYMDEGRADSTAB.2019.109046

Xu, Z., Fang, B. H., Zheng, W. N., Wang, C. Z., & Tang, B. (1990). A novel plasma surface metallurgy: Xu-Tec process. *Surface and Coatings Technology*, *43*, 1065–1073.

Yamauchi, R. (1997a). Free Radical-Scavenging Reactions of α-Tocopherol During the Peroxidation of Unsaturated Lipids. *Food Factors for Cancer Prevention*, 483–487. https://doi.org/10.1007/978-4-431-67017-9_95

Yamauchi, R. (1997b). Vitamin E: Mechanism of Its Antioxidant Activity. *Food Science and Technology International, Tokyo*, *3*(4), 301–309. https://doi.org/10.3136/fsti9596t9798.3.301

Yan, C., Zhang, J., Shen, D., & Yan, S. (2006). Structure characterization of melt drawn polyethylene ultrathin films. *Chinese Science Bulletin*, *51*(23), 2844–2850. https://doi.org/10.1007/s11434-006-2166-1

Yang, N., & Liu, Y. (2021). The Role of the Immune Microenvironment in Bone Regeneration. *International Journal of Medical Sciences*, *18*(16), 3697–3707. https://doi.org/10.7150/ijms.61080

Yang, W., Liu, C., & Chen, Y. (2018). Stability of Polydopamine Coatings on Gold Substrates Inspected by Surface Plasmon Resonance Imaging. *Langmuir*, *34*(12), 3565–3571. https://doi.org/10.1021/acs.langmuir.7b03143

Yang, Z., He, S., Wu, H., Yin, T., Wang, L., & Shan, A. (2021). Nanostructured Antimicrobial Peptides: Crucial Steps of Overcoming the Bottleneck for Clinics. *Frontiers in Microbiology*, *12*. https://doi.org/10.3389/fmicb.2021.710199

Yasuda, H. (1976). Plasma for Modification of Polymers. *Journal of Macromolecular Science: Part A - Chemistry*, *10*(3), 383–420. https://doi.org/10.1080/00222337608061190

Yatim, N., Cullen, S., & Albert, M. L. (2017). Dying cells actively regulate adaptive immune responses. *Nature Reviews Immunology*, *17*(4), 262–275. https://doi.org/10.1038/nri.2017.9

Yebra, D. M., Kiil, S., & Dam-Johansen, K. (2004). Antifouling technology—past, present and future steps towards efficient and environmentally friendly antifouling coatings. *Progress in Organic Coatings*, *50*(2), 75–104.

Yin, J., & Luan, S. (2016). Opportunities and challenges for the development of polymer-based biomaterials and medical devices. *Regenerative Biomaterials*, *3*(2), 129–135.

https://doi.org/10.1093/RB/RBW008

Young, D. C. (2003). Spin Contamination. In *Computational Chemistry* (pp. 227–230). John Wiley & Sons, Inc. https://doi.org/10.1002/0471220655.ch27

Yun, H., Min, H. J., & Lee, C. W. (2020). NMR structure and bactericidal activity of KR-12 analog derived from human LL-37 as a potential cosmetic preservative. *Journal of Analytical Science and Technology*, *11*(1), 1–9. https://doi.org/10.1186/S40543-020-00213-X/FIGURES/6

Zamfirova, G., Lorenzo, V., Benavente, R., & Pereña, J. M. (2003). On the relationship between modulus of elasticity and microhardness. *Journal of Applied Polymer Science*, *88*(7), 1794–1798. https://doi.org/10.1002/app.11788

Zerbi, G., Gallino, G., Del Fanti, N., & Baini, L. (1989). Structural depth profiling in polyethylene films by multiple internal reflection infra-red spectroscopy. *Polymer*, *30*(12), 2324–2327.

Zhang, H., Porro, G., Orzech, N., Müllen, B., Liu, M., & Slutsky, A. S. (2001). Neutrophil defensins mediate acute inflammatory response and lung dysfunction in dose-related fashion. *American Journal of Physiology - Lung Cellular and Molecular Physiology*, *280*(5 25-5), L947--L954. https://doi.org/10.1152/ajplung.2001.280.5.l947

Zhang, L., Keogh, S., & Rickard, C. M. (2013). Reducing the risk of infection associated with vascular access devices through nanotechnology: A perspective. *International Journal of Nanomedicine*, *8*, 4453–4466. https://doi.org/10.2147/IJN.S50312

Zhang, W., Hu, Z., Zhang, Y., Lu, C., & Deng, Y. (2013). Gel-spun fibers from magnesium hydroxide nanoparticles and UHMWPE nanocomposite: The physical and flammability properties. *Composites Part B: Engineering*, *51*, 276–281. https://doi.org/10.1016/j.compositesb.2013.03.014

Zhao, C., Li, C. X., Dong, H., & Bell, T. (2006). Study on the active screen plasma nitriding and its nitriding mechanism. *Surface and Coatings Technology*, *201*(6), 2320–2325. https://doi.org/10.1016/J.SURFCOAT.2006.03.045

Zhao, J., Gao, F., Pujari, S. P., Zuilhof, H., & Teplyakov, A. V. (2017). Universal Calibration of Computationally Predicted N 1s Binding Energies for Interpretation of XPS Experimental Measurements. *Langmuir*, *33*(41), 10792–10799. https://doi.org/10.1021/acs.langmuir.7b02301

Zhao, Y., Wang, M., Tang, Z., & Wu, G. (2010). ESR study of free radicals in UHMW-PE fiber irradiated by gamma rays. *Radiation Physics and Chemistry*, *79*(4), 429–433.

Zhu, X., Wei, X., & Shen, L. (2014). Effect of tocopherols incorporation on physical properties of LDPE, PP and blend film of LDPE/PP. *Journal of Shanghai Normal University (Natural Sciences)*, *43*(6).

Zingg, J.-M., & Azzi, A. (2012). Non-Antioxidant Activities of Vitamin E. *Current Medicinal Chemistry*, *11*(9), 1113–1133. https://doi.org/10.2174/0929867043365332

Appendices

Appendix A1 – XPS and electron binding energies IV

Appendix A2 – FTIR and vibrational normal modes VIII

Appendix A3 – Raman spectroscopy and scattering intensities XII

Appendix A4 – XRD and atomic scattering factors XIV

Appendix B1 – DSC diagram of UD/UT XVII

Appendix B2 – Individual ATR-FTIR spectra of the UHMWPE-based samples XVIII

Appendix B3 – Individual Raman spectra of the UHMWPE-based samples XX

Appendix B4 – Instrumental broadening correction for WXRD XXII

Appendix B5 – Example of GAMESS input file XXIII

Appendix C1 – FTIR data from the individual spectral peak fits VII

Appendix C2 – Pearson correlation matrix of the FTIR spectral peak fitting data IX

Appendix C3 – Raman data from the individual spectral peak fits X

Appendix C4 – Pearson correlation matrix of the Raman spectral peak fitting data XII

Appendix C5 – Pearson correlation matrix of the FTIR vs. the Raman spectral peak fitting data XIII

Appendix C6 – Degree of substitution data from the individual samples I

Appendix C7 – Cu–Kα X-ray attenuation length for polyethylene II

Appendix C8 – Unit cell refinement procedure III

Appendix C9 – Modified Scherrer equation plots from the individual samples IV

Appendix C10 – Vickers microhardness data from the individual samples V

Appendix C11 – Equilibrium contact angle data from the individual samples VI

Appendix D1 – List of evaluated functionalities for the theoretical peak model VII

Appendix D2 – Calculated primary carbon ΔCEBEs XI

Appendix D3 – Calculated nitrogen and oxygen ΔCEBEs XIV

Appendix D4 – Calculated higher-order carbon ΔCEBEs XVII

Appendix D5 – Calculated ΔCEBEs of the tocopherol-like components XXIII

Appendix D6 – ΔCEBE deviations between centred and end-chain positioning XXV

Appendix D7 – Mean influence of carbon-oxygen/nitrogen functionalities on the ΔCEBEs of the PE carbon backbone calculated with HF XXVI

Appendix D8 – Individual influence of carbon-oxygen/nitrogen functionalities on the ΔCEBEs of the PE carbon backbone calculated with HF XXVII

Appendix D9 – Individual influence of carbon-oxygen/nitrogen functionalities on the ΔCEBEs of the PE carbon backbone calculated with wB97X-D XXVIII

Appendix D10 – Two-dimensional molecular electrostatic potential contour maps XXIX

Appendix D11 – Origin of the reference data within the Beamson and Briggs database .. XXX

Appendix D12 – CEBEs used in the linear correlation fits for the C 1s region XXXI

Appendix D13 – CEBEs used in the linear correlation fits for the N 1s region XXXII

Appendix D14 – CEBEs used in the linear correlation fits for the O 1s region XXXIII

Appendix D15 – Comparison of the calculated C 1s ΔCEBEs to the literature XXXIV

Appendix D16 – XPS survey spectra of the various UHMWPE-based samples XXXV

Appendix D17 – Region maxima in the survey spectra after energy calibration XXXVI

Appendix D18 – Reference-based BEs used to identify the minor contaminants XXXVII

Appendix D19 – Reference-based BEs used to identify the silicon contaminants XXXVIII

Appendix D20 – Reference-based BEs used to identify the chromium contaminants ... XXXIX

Appendix D21 – Reference-based BEs used to identify the iron contaminants XL

Appendix D22 – Reference-based nitrogen/oxygen BEs related to the contaminants XLI

Appendix D23 – XPS survey peak fits of the silicon contaminants XLII

Appendix D24 – XPS survey peak fits of the chromium contaminants XLIV

Appendix D25 – XPS survey peak fits of the iron contaminants XLVIII

Appendix D26 – Averaged atomic composition of the silicon contaminants LII

Appendix D27 – Averaged atomic composition of the chromium contaminants LIII

Appendix D28 – Averaged atomic composition of the iron contaminants LIV

Appendix D29 – Atomic composition of the silicon survey peak fits LV

Appendix D30 – Atomic composition of the chromium and iron survey peak fits LVI

Appendix D31 – High-resolution XPS spectra of UHMWPE-based samples LVII
Appendix D32 – Conversion table of the silicon contaminants for the HR spectra LVIII
Appendix D33 – Conversion table of the Cr and Fe contaminants for the HR spectra LIX
Appendix D34 – Difference in the atomic composition due to the change in background ... LX
Appendix D35 – Component compositions of the UD/UT high-resolution peak fits LXI
Appendix D36 – Component compositions of the UD/PT60 high-resolution peak fits LXII
Appendix D37 – Component compositions of the D/UT high-resolution peak fits LXIII
Appendix D38 – Component compositions of the D/PT60 high-resolution peak fits LXIV
Appendix D39 – Positioning of the reference components within the HR spectra LXV
Appendix D40 – High-resolution XPS spectra peak fits of UD/UT LXVI
Appendix D41 – High-resolution XPS spectra peak fits of D/UT LXVIII
Appendix D42 – Presence of the tocopherol-like components determined by FTIR LXX
Appendix D43 – High-resolution XPS spectra peak fits of UD/PT60 LXXI
Appendix D44 – HR XPS N 1s and O 1s spectra peak fits of D/PT60 LXXIII
Appendix D45 – Change in composition due to the background and peak asymmetry . LXXIV
Appendix D46 – HR XPS N 1s and O 1s spectra of the reference-based peak fits LXXV
Appendix E1 – Bacterial adhesion assay CFUs, dilution factors, and CFUs/mL LXXVI
Appendix E2 – Additional statistic results for bacterial adhesion assay LXXVIII
Appendix E3 – Cell viability assay luminescence data, standard curve, and cell counts . LXXX
Appendix E4 – Additional statistic results for cell viability assay LXXXI
Appendix references LXXXIII

Appendix A1 – XPS and electron binding energies

‖ This section contains content taken from my first-authored published work, specifically from section 2 in (Bruggeman et al., 2022), please see the 'Publications' section. ‖

X-ray photoelectron spectroscopy (XPS; i.e., electron spectroscopy for chemical analysis, ESCA) is a highly surface sensitive spectroscopic technique, allowing quantitative chemical characterisation in the upper few nanometres of the material surface (Watts, 1998). As implied by its name, XPS is based on the photoelectric effect (i.e., the process of emission or ejection of electrons when a material is hit by light/electromagnetic radiation), which is typically induced by irradiating the sample surface with monochromatic X-ray beams. The X-rays are most frequently generated using a cathode-ray tube, the cathode-ray tube contains a cathode that emits electrons when heated, the emitted electrons are subsequently accelerated by a high-potential field. The high-energy electrons are discharged on a metal target, which results in the metal target emitting X-rays distinctive of the target material (e.g., Al, Mg, etc.). A schematic of the characteristic generated X-ray photon lines within a simplified electronic energy diagram are depicted in Figure 13 (Goldstein et al., 2017).

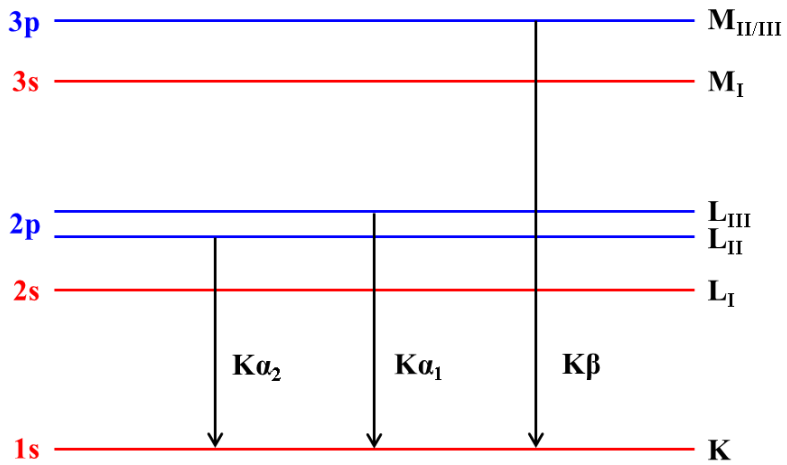


Figure A1. Simplified electronic energy diagram including the characteristic X-ray photon lines.

Typically, the X-rays are passed through a slightly bent monochromator to only preserve the Kα X-rays and focus the beam on the desired focal point, the monochromators are typically made of quartz due to its lattice spacing and accessibility as a single crystal (Watts,

1998). When the X-rays hit the material surface, photoelectrons are emitted, their kinetic energies (*KEs*) are measured using a hemispherical electron energy analyser and counted by an electron detector to provide the resulting XPS spectrum. As the incident X-ray beam energy (*hv*) is known, the binding energy (*BE*) of an electron can be determined, following:

$$BE = hv - (KE + \Phi)\,, \qquad (Eq.\ 3)$$

where Φ is the material-specific work function (Turner and Jobory, 1962; Siegbahn, 1982).

A major advantage with XPS is that, besides the characterisation of the elemental surface composition, it can also provide insight to the chemical states (e.g., oxidation states, ionic charges, etc.) and chemical bonds (i.e., which elements are bonded to each other). When investigating materials with few and/or distinct chemical states and/or bonds, XPS spectra interpretation can be relatively straightforward. However, with an increasing number of chemical functionalities present on the surface, peak fitting becomes more complex and potentially prone to personal bias. Generally, when investigating polymeric materials with unknown functionalities as observed in this work, reference data such as provided by Beamson and Briggs database and the National Institute of Standards and Technology (NIST) database are used for comparison (Hantsche, 1993; NIST, 2008). However, the subsequent peak fitting applied is limited by the available references and therefore, does not always reflect the range of functionalities that may form during the surface treatment. Additionally, specifically in the case of the NIST XPS database, a spread in binding energies (BEs) was noted and this can result in arbitrary spectral interpretation (Greczynski and Hultman, 2020). This is of particular concern in cases where potentially overlapping or unknown chemical functionalities, such as those obtained after surface plasma treatment of polymers, are present.

Using conventional reference databases, the BE assignments used to construct a peak model will originate from various materials. Although some existing reference data can provide

a reasonable initial indication for peak assignments, chemical shifts in XPS are dependent on the electronic structure of the investigated molecule(s), and reference data alone can be insufficient for accurate and detailed XPS peak assignment. Specifically, in complex systems where biomolecules are incorporated within the plasma-treated polymer matrices, no suitable literature reference exists. The inability to establish a detailed interpretation of the spectra limits the understanding of the chemical nature of the surface, which may impact the suitability of coupling chemistries used for surface decoration or evaluation of the relation between the chemical surface composition and biomaterial properties like biocompatibility. In such cases, alternative reference sources are desirable to allow a more in-depth interpretation of the experimental XPS spectra.

Most literature that utilises calculated core-electron binding energies (CEBEs) to interpret experimental XPS spectra make use of simplified model structures, as calculations of solids using periodic conditions as seen in the Projected Augmented Wave (PAW) can be costly and result in the formation of artefacts arising from the periodic unit cells (Schwerdtfeger, 2011; Viñes et al., 2018). The unrestricted generalised transition-state (uGTS) method was one of the earlier methods to provide accurate absolute BEs for small gas molecules, displaying a mean error of 0.2 eV compared to experimental BEs (Chong, 1995). Later, it was found that this accuracy was achieved as a result of consistent error cancellation, but it is occasionally still used in the estimation of BEs (Triguero et al., 1999; Endo et al., 2016). Other approaches, for example, those employing correlation-consistent basis sets or configuration interaction calculations, display a mean error of around 0.15 eV (Cavigliasso and Chong, 1999; Sherrill and Schaefer, 1999). However, the high computational cost limits their applicability for larger structures and use on "average" office-based PCs.

A more forthright approach for the estimation of CEBEs is using Koopmans' theorem (KT), where the negative orbital energy ($-\varepsilon_i$) is equated to the ionisation potential and thereby

provides an estimate for the respective CEBE (Koopmans, 1933). KT allows the estimation of CEBEs without calculating the work function, but these CEBEs only include initial state effects as the structure remains in its neutral ground state. KT neglects the electronic relaxation in response to the formed electron core-hole and the CEBEs estimated with KT are therefore also referred to as frozen orbital (FO) CEBEs. Corrections can be applied to absolute CEBEs to account for the relativistic effects (i.e., Lorentz contraction) and the zero-point energy contribution (i.e., the lowest energy state, at 0 K, as described by the Heisenberg uncertainty principle), but such corrections typically do not influence the CEBE shifts (ΔCEBEs) significantly as the errors are small due to error cancellation effects (Viñes et al., 2018). No differentiation was made between HF orbital energies (ε_{HF}) and Kohn-Sham (KS) orbital energies (i.e., the DFT analogues of HF orbital energies, ε_{KS}), as in both cases, KT is validated in regards to the calculated initial state ΔCEBEs (Bellafont et al., 2015). However, contrary to $\Delta\varepsilon_{HF}$, $\Delta\varepsilon_{KS}$ may not solely be a result of initial state effects due to the included exchange and electron correlation effects with the use of DFT.

The ΔCEBEs obtained through KT are shown to allow satisfying spectral interpretation if the energy offset of the calculated CEBEs, relative to the experimental CEBEs, are constant throughout a set of structures (Kröner et al., 2011; Giesbers et al., 2013; Bagus et al., 2016; Tardio and Cumpson, 2018). Depending on the method and basis set used for the calculations, the mean error of calculated KT ΔCEBEs are typically between 0.2–0.7 eV for atoms in the second row of the periodic table when compared to experimental ΔCEBEs. This approach is utilised extensively in the literature to aid in the interpretation of various elemental regions, but often focussing on one region at a time and with materials of known chemical composition. However, as will be demonstrated in this work, a multi-region fitting approach is also possible.

Appendix A2 – FTIR and vibrational normal modes

Fourier-transform infrared (FTIR) spectroscopy allows for the identification of chemicals bonds based on the absorption or emission of infrared radiation (IR) by the analysed molecule/sample (Griffiths, 1983). FTIR instruments make use of a broadband light source that is shone on a Michelson interferometer, the interferometer is a configuration that splits a beam of light and recombines them, using – at minimum – a stationary mirror, a moving mirror, and a beam splitter (i.e., a half-silvered mirror) (Hariharan and Braun, 1992). When the light is split and recombined again at the beam splitter, the recombined beam is focussed on the to-be analysed sample. Using the moving mirror in the beam splitter, the optical path difference can be varied, recording the signal over the varied optical path difference results in an interferogram. Using a discrete Fourier transformation, the interferogram can be converted into its desired spectral form which displays the IR absorbance of the molecule/sample over the wavelengths of the broadband light source (Herres and Gronholz, 1984). According to the Schrödinger equation for a harmonic oscillator describing atomic vibrations in molecules, the frequency (ν) of absorbance for a molecular vibration depends on the spring constant (k; i.e., the second derivative of the potential energy with respect to the interatomic distance) and the reduced mass (μ) of the atoms, following:

$$\mu = \frac{m_1\, m_2}{m_1 + m_2},$$

$$k = \frac{\partial^2 V(r)}{\partial(\Delta r)^2},$$

$$\nu = \frac{1}{2\pi}\sqrt{\frac{k}{\mu}},$$

where m_1 and m_2 are the atomic masses (amu) of the atoms involved in the vibration, as schematically depicted for a di-atomic molecule in Figure A2a (Steele, 2006). *V* is the potential energy (i.e., the bond energy), and Δr is the extension of the interatomic distance (i.e., $r - r_0$).

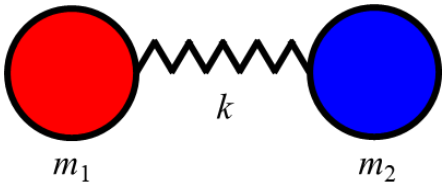


Figure A2a. Simplified schematic of a di-atomic molecule, displaying the origin of the masses of the two atoms (m_1 and m_2) and the spring constant (k) as used in the frequency calculation of a molecular vibration.

IR radiation will only be absorbed by a molecule when it experiences a change in its dipole moment (p; i.e., the charge value, q, multiplied by the separation distance, d, between the positive and negative atomic charges in the molecule) during the vibration or rotation (Harris and Bertolucci, 1989). In addition, when the molecules absorb the IR radiation, the molecules will only vibrate at its corresponding frequencies when the incoming photons have sufficient energy for the vibrational transition (associated with the discrete energy levels for the harmonic oscillator) to take place (i.e., $\Delta E = E_{v+1} - E_v = \hbar\omega$) as schematically depicted in Figure A2b (Griffiths, 2004). Therefore, the band intensity of the IR-active modes (I_{IR}) is related to the electric dipole moment (p) and the normal vibrational coordinates (Q; i.e., a set of coordinates that are used to describe the relative atom displacements of the molecule during vibrations, essentially the replacement for Δr in a three-dimensional space), following:

$$I_{IR} \propto \left|\frac{\partial \vec{p}}{\partial Q}\right|^2 .$$

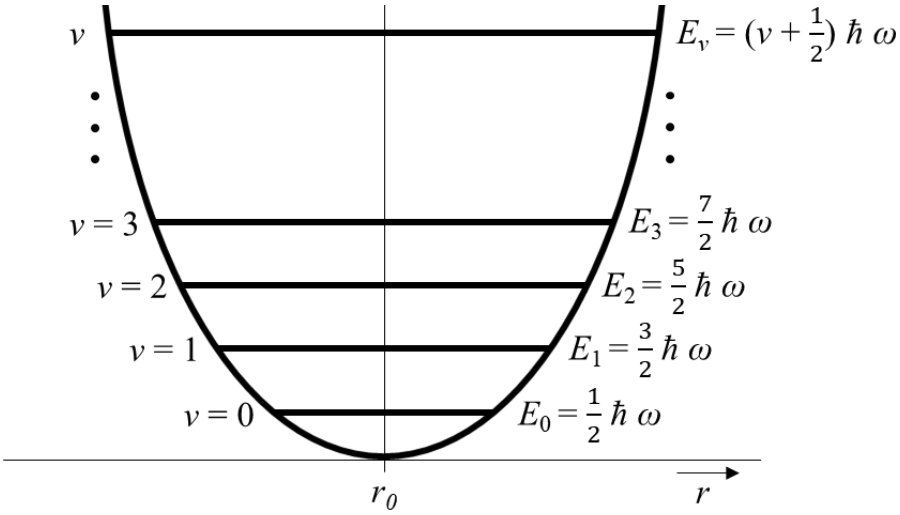


Figure A2b. Simplified schematic of a quantum harmonic oscillator.

The total number of vibrational normal modes (i.e., degrees of freedom) for polyatomic molecules containing a number of atoms (*N*) is given by $3N$, as the atoms are displaced along the x, y, and z coordinates (Mills and Robiette, 1985). From the total degrees of freedom, three degrees are associated with translations of the centre of mass of the molecule. Next to that, two (for linear molecules) or three (for non-linear molecules) degrees are connected to the rotation of the molecule around the centre of mass. Therefore, the degrees of vibrational freedom is $3N - 5$ for linear molecules and $3N - 6$ for non-linear molecules. Molecular vibrations can either change the bond length (stretching) or bond angle (bending) (El-Azazy, 2019). The stretching of bonds can occur in-plane (i.e., symmetric stretching) or out-of-plane (i.e., asymmetric stretching). The bending of bonds can also be in-plane (i.e., scissoring or rocking) or out-of-plane (i.e., wagging or twisting).

After the geometry optimisation of the molecular structure following HF and/or DFT and calculating the Hessian matrix (i.e., the second-order derivative of the molecular potential energy with respect to the nuclear/Cartesian molecular coordinates), the vibrational normal modes (δ) in the computer software are determined following:

$$\delta_{j,k} = \Sigma_a M_a \mathbf{R}_a^j \cdot \mathbf{R}_a^k ,$$

where M is the mass of the atom *a*, $\mathbf{R}_a^{j/k}$ is the vibrational vector (i.e., a vector that is used to describe the vibrational motion associated with a particular normal mode of the molecule) in 3D for atom *a* in mode *j/k* (Barca et al., 2020). Numbers (*j* and *k*) are assigned to the modes in the order of increasing energy (i.e., the vibrational frequencies, ν_j and ν_k, respectively). Finally, the IR intensities for the vibrational normal modes are then calculated through the numerical differentiation of the dipole moment (*p*) as established by Komornicki *et al.*, following:

$$\frac{\partial p}{\partial X_i} = -\frac{\partial}{\partial X_i}\frac{\partial E}{\partial F} = -\frac{\partial}{\partial F}\frac{\partial E}{\partial X_i} = -\frac{\partial g_i}{\partial F},$$

where E is the energy, F is the applied external electric field, X_i represents the nuclear coordinates, and g_i represents the potential energy gradient (Komornicki and McIver, 1979; Barca et al., 2020). Numerical differentiation is useful because it can be used to calculate the derivative of the dipole moment even if an analytical expression for the dipole moment is not known. Typically, the applied external electric field strength is set around 0.002 N/C (i.e., Newton per Coulomb) and applied in various directions towards the molecule to determine the band intensities with respect to different angles (Peters, 2014).

Appendix A3 – Raman spectroscopy and scattering intensities

Raman spectroscopy allows for the identification of chemicals bonds based on the inelastic scattering of photons (i.e., Raman shifts) of the analysed molecule/sample when excited by electromagnetic radiation. Raman instruments typically combine an optical microscope with an excitation laser, a monochromator, various laser rejection filters, and an optical sensitive detector (most commonly, a charge-coupled device; CCD) (Graves and Gardiner, 1989). Raman follows the same theory on the atomic vibrations and vibrational normal modes in molecules as discussed in Section 2.4.2 for FTIR, but the band intensity of the Raman-active modes (I_{Raman}) is related the electric polarizability (α), following:

$$\alpha = \frac{p}{F},$$

$$I_{Raman} \propto \left|\frac{\partial \vec{\alpha}}{\partial Q}\right|^2,$$

where F is the electric field of the light/photon source that induces the dipole moment (p) (McCreery, 2001). Raman modes are only active when the molecule experiences a change in the polarizability during the vibration or rotation. When the photons from the laser interact with the molecule/sample (more specifically, with its molecular vibrations, phonons, etc.) the energy of the photons from the laser will be scattered elastically (i.e., Rayleigh scattering) or inelastically (Hammes, 2005). The inelastic scattering will result in the frequency of the photons to be shifted up (i.e., Stokes shift) or down (anti-Stokes shift), as schematically depicted for a molecule in Figure A3a and in an electronic energy diagram in Figure A3b.

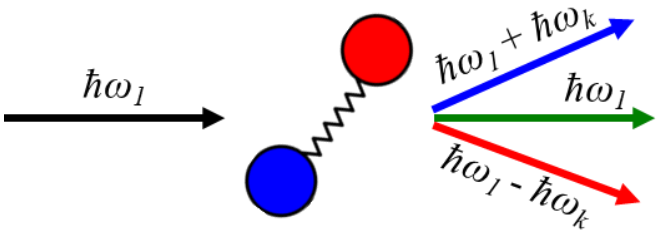


Figure A3a. Simplified schematic of a molecule interacting with photons, displaying the scattering states.

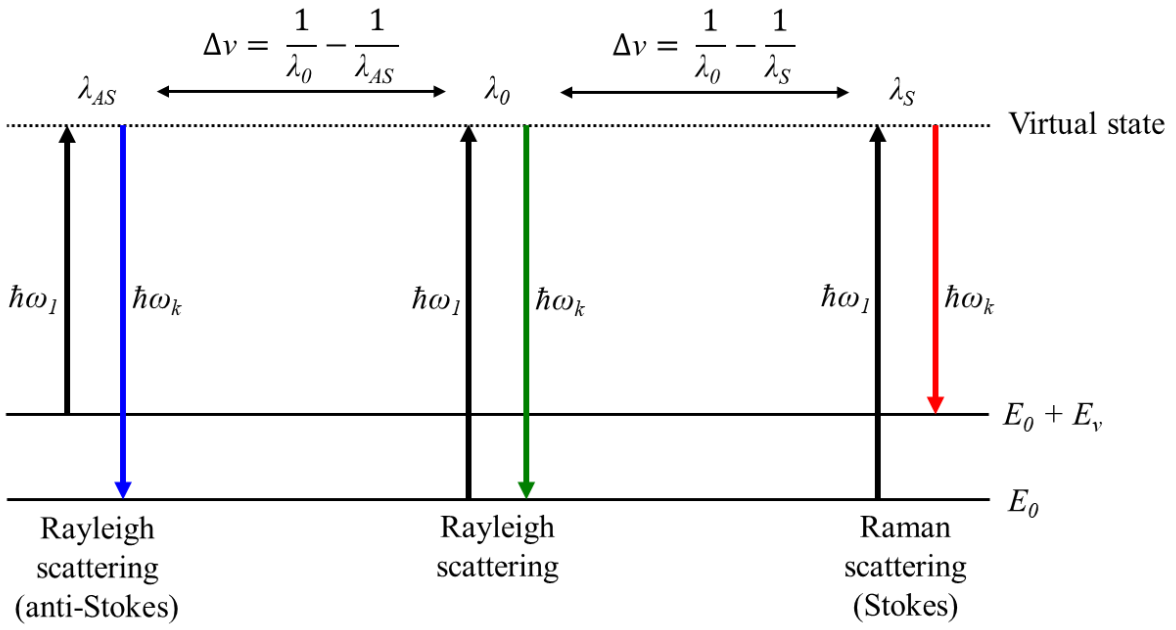


Figure A3b. Simplified electronic energy diagram showing the scattering states involved in Raman.

The Raman intensities for the vibrational normal modes are calculated through a similar numerical differentiation procedure developed by Komornicki *et al.* as was discussed for the IR intensities, but in the case of Raman this is performed for the polarizability (α), following:

$$\frac{\partial \alpha}{\partial X_i} = \frac{\partial}{\partial X_i}\frac{\partial p}{\partial F} = \frac{\partial}{\partial F}\frac{\partial p}{\partial X_i} = -\frac{\partial^{2^2} g_i}{\partial F^2}$$

(Komornicki and McIver, 1979). It is worth to note that, a limitation of this procedure is that the excitation wavelength of the laser is not integrated into the calculations, resulting in some deviations in the calculated and experimental Raman intensities (Peters, 2014).

Appendix A4 – XRD and atomic scattering factors

X-ray diffraction spectroscopy (i.e., X-ray crystallography; XRD) is based on the principle that the spacing of atomic planes in a crystal lattice act as a 3D diffraction grating for monochromatic X-rays, as the separation of atoms in a crystal lattice are of a similar order as X-rays (~10^{-10} m) (Ermrich and Opper, 2013). The generation of the X-rays is similar to that observed in XPS, as discussed in Appendix A1. The interaction of X-rays with a crystalline material produces constructive interference when the conditions satisfy Bragg's law:

$$2\,d\,\sin(\theta) = n\,\lambda\,,$$

where d is the spacing of the planes in Å, θ is the X-ray angle of incidence (i.e., Bragg angle), n is the order of diffraction, and λ is the wavelength of the radiation; destructive interference arises when the two waves cancel each other (which is not observed in the spectra). A simplified schematic of X-rays reflecting inside a crystal lattice is shown in Figure A4a, it can be observed that the constructive interference of the X-rays (see [1] and [2]) will differ by an integer multiple of its wavelength ($n\,\lambda$) when the two X-rays are in-phase. Considering the wavelength of the monochromatic X-ray is fixed and 2θ is measured during the spectral acquisition, the distance between atom planes (d) can be determined.

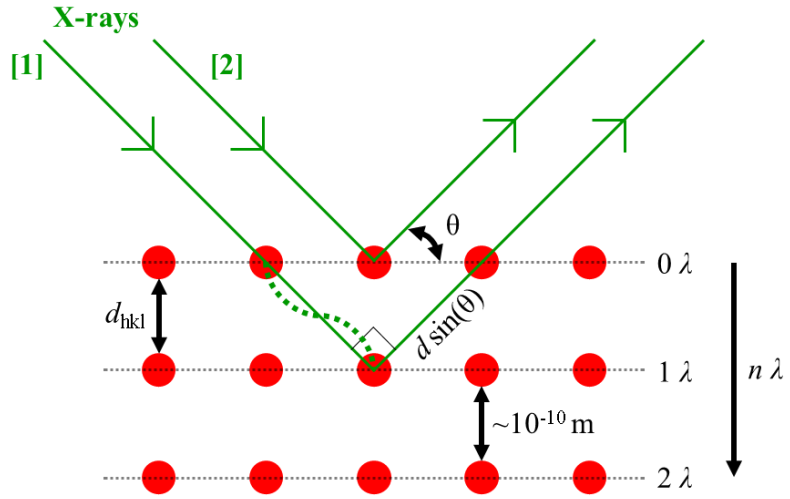


Figure A4a. Schematic overview of X-rays (**green**) reflecting on a crystal lattice (**red**).

The type of atoms and their positions on the atomic planes determines the intensity of light scattered by a crystal, I_{hkl} , following:

$$I_{hkl} \propto |F_{hkl}|^2 ,$$

which is quantified by the structure factor, F_{hkl}, that sums the scattering intensity from all the atoms in the unit cell to form a diffraction peak along the (h k l) planes of atoms:

$$F_{hkl} = \sum_{j=1}^{n} f_j N_j T_j e^{2\pi i(hx_j+ky_j+lz_j)} ,$$

where f_j is the atomic scattering factor (i.e., a measure of the probability that an X-ray photon will be scattered by an atom), $N_j$is the site occupancy factor of atom j (i.e., the probability to find an atom at a specific site), T_j is the Debeye-Waller factor (i.e., the attenuation of X-ray scattering caused by thermal motion), and x_j, y_j, and z_j are the fractional coordinates inside the unit cell (Warren, 1990; Ermrich and Opper, 2013). When accounting for anomalous dispersion, the atomic scattering factor consists out of four components:

$$f(q) = f_0 + f' + if'' + f_{NT},$$

where f_0 is the coherent scattering factor, f' and if'' are the real and imaginary components of the dispersion correction, respectively, and f_{NT} is the nuclear Thomson scattering factor (i.e., a measure of the probability that a charged particle will be scattered by a nucleus). When the effect of X-ray anomalous dispersion is neglected, f', if'' and f_{NT} are zero. The coherent atomic scattering factor, $f_{0(h)}$, is estimated following:

$$f_0\left(\sin\left(\frac{\theta}{\lambda}\right)\right) = \sum_{i=1}^{N} a_i e^{-b_i\left(\sin\left(\frac{\theta}{\lambda}\right)\right)^2} + c ,$$

where $\sin\left(\frac{\theta}{\lambda}\right)$ is typically approximated across the range of $0 < \sin\left(\frac{\theta}{\lambda}\right) < 25$ Å^{-1}, N is the number of Guassians (G) used in the linear combination fit to the scattering factors (e.g., 4 or 5). The set of parameters, a_i, b_i, and c, are atom-specific and their values are taken from the International Tables for Crystallography when using the 4G function or from the values

tabulated by Waasmaier and Kirfel when using the 5G function (Allen et al., 1995; Waasmaier and Kirfel, 1995). The values for f' and if'' are calculated by linear interpolation of the calculated atomic scattering factors. Finally, the mass attenuation coefficient (i.e., the reduction in X-ray radiation intensity as it passes through a substance) is determined by:

$$u / \rho ,$$

where u is the linear attenuation coefficient (cm^{-1}) and ρ is the density (g/cm^3). The values for the set of parameters (a_i, b_i, and c) for carbon (C) and hydrogen (H) are shown in Table A4a, the values for f', if'', and f_{NT} are shown in Table A4b. The corresponding free atomic scattering factors for carbon and hydrogen are calculated and plotted in Figure A4b – it is worth to note that the maxima of $f(q)$ are equal to the atomic number (Z) of the respective atoms.

Table A4a. Parameters of the 4G scattering-factor functions (Allen et al., 1995).

	a_1	a_2	a_3	a_4	c
	b_1	b_2	b_3	b_4	
C	2.31	1.02	1.5886	0.865	0.2156
	20.8439	10.2075	0.5687	51.6512	
H	0.489918	0.262003	0.196767	0.049879	0.001305
	20.6593	7.74039	49.519	2.20159	

Table A4b. X-ray dispersion coefficients for Cu–Kα_1 (i.e., 0.15406 nm; values outside brackets) and Cu–Kα_2 (i.e., 0.15443 nm; values inside brackets).

	f'	if''	f_{NT}	u / ρ
C	1.77875E-2 (1.78642E-2)	9.05508E-3 (9.09998E-3)	-1.64420E-3 (-1.64420E-3)	4.30679 (4.33550)
H	1.00136E-5 (1.00136E-5)	1.07678E-6 (1.08282E-6)	-5.44230E-4 (-5.44230E-4)	3.84218E-1 (3.84157E-1)

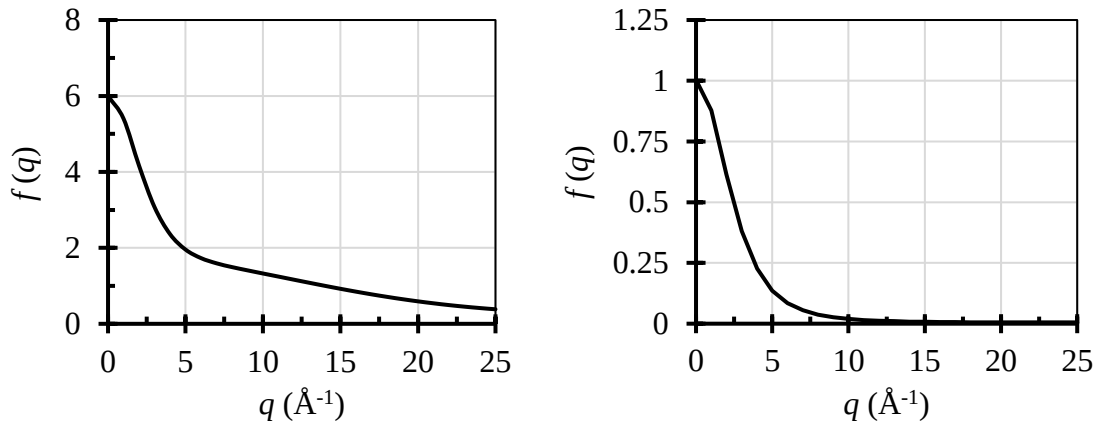


Figure A4b. Atomic scattering factor for carbon (left) and hydrogen (right) calculated using the 4G scattering-factor function with the parameters shown in Table 6.

Appendix B1 – DSC diagram of UD/UT

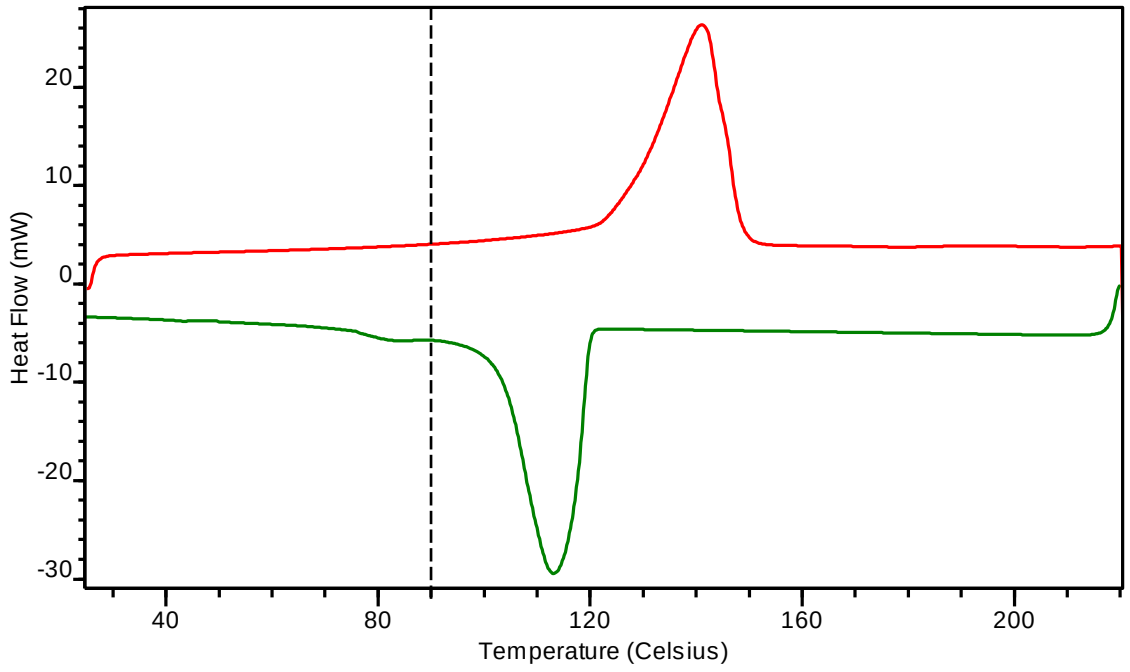


Figure B1. DSC diagram of undoped and untreated UHMWPE (UD/UT) between 25–220ºC at a symmetrical heating-cooling rate of 10ºC/min, recorded with a Mettler Toledo DSC 1 (Greifensee, Switzerland) connected to a Huber TC100 immersion cooler and operated using Mettler Toledo's STARe software (version 16.10) – the dashed line indicates the treatment temperature used during αTH doping and ASPN of UHMWPE.

Appendix B2 – Individual ATR-FTIR spectra of the UHMWPE-based samples

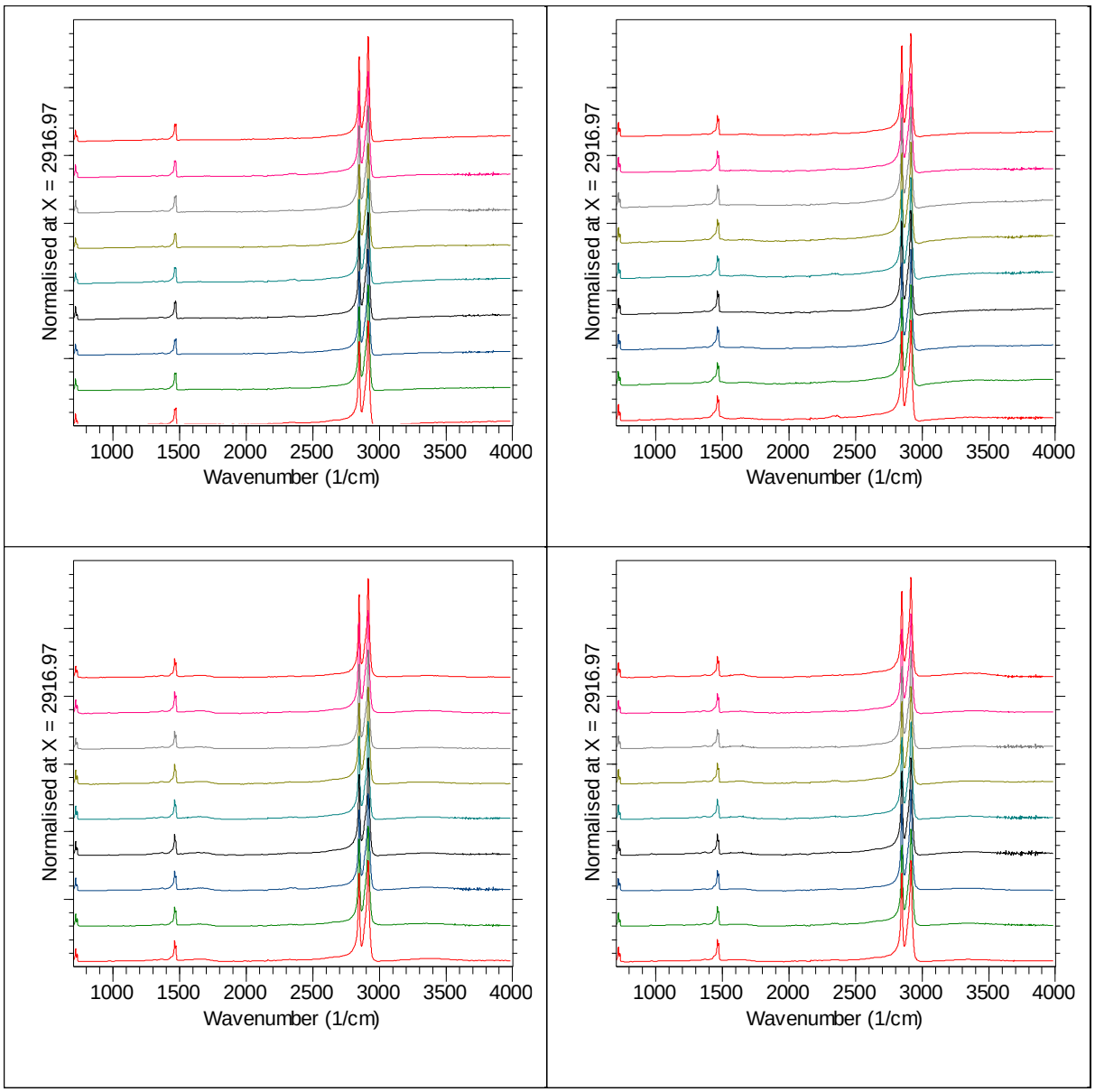


Figure B2a. ATR-FTIR spectra of (top-left) UD/UT, (top-right) UD/PT15, (bottom-left) UD/PT30, and (bottom-right) UD/PT60.

Continued on the next page…

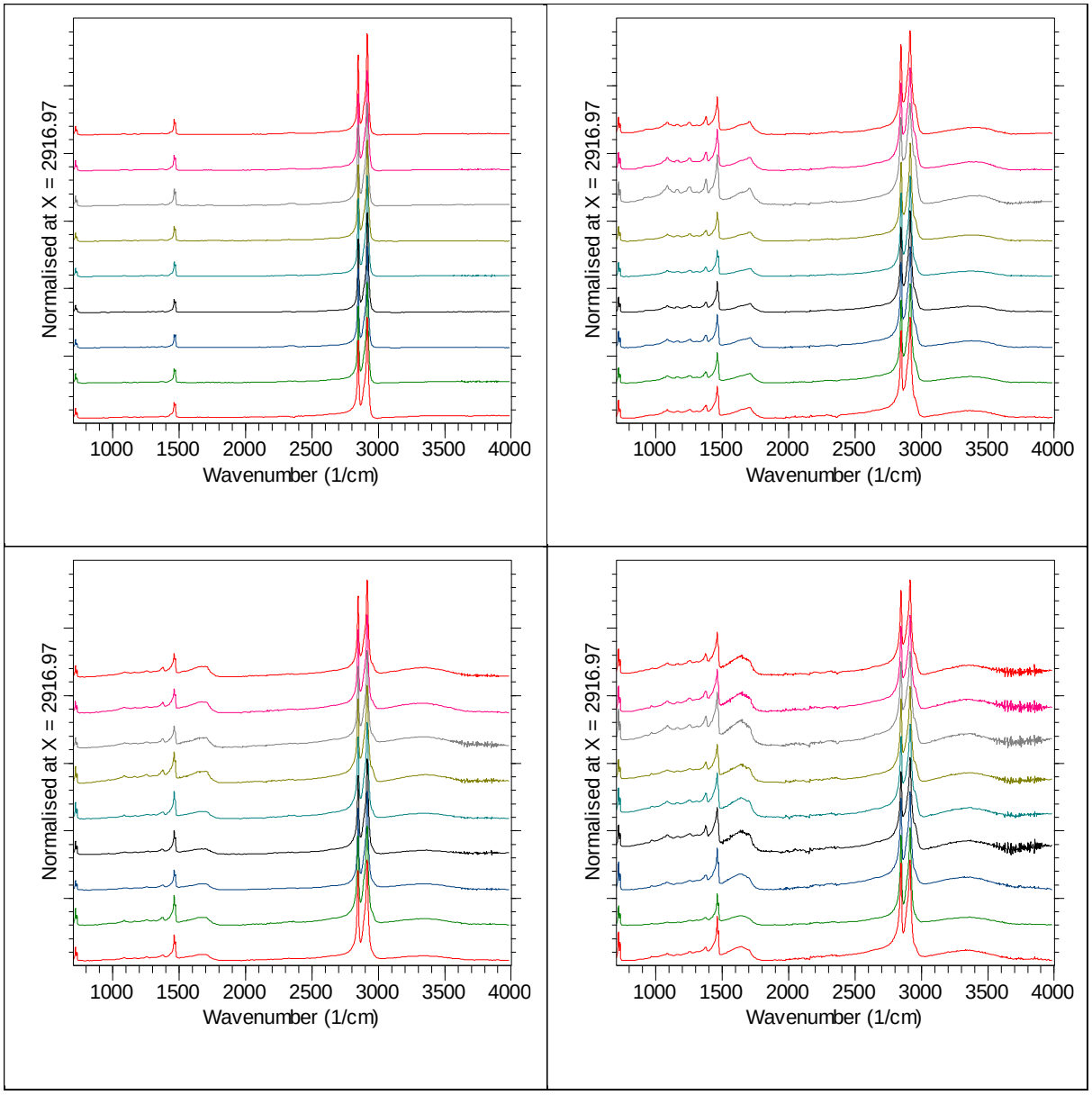


Figure B2b. ATR-FTIR spectra of (top-left) D/UT, (top-right) D/PT15, (bottom-left) D/PT30, and (bottom-right) D/PT60.

Appendix B3 – Individual Raman spectra of the UHMWPE-based samples

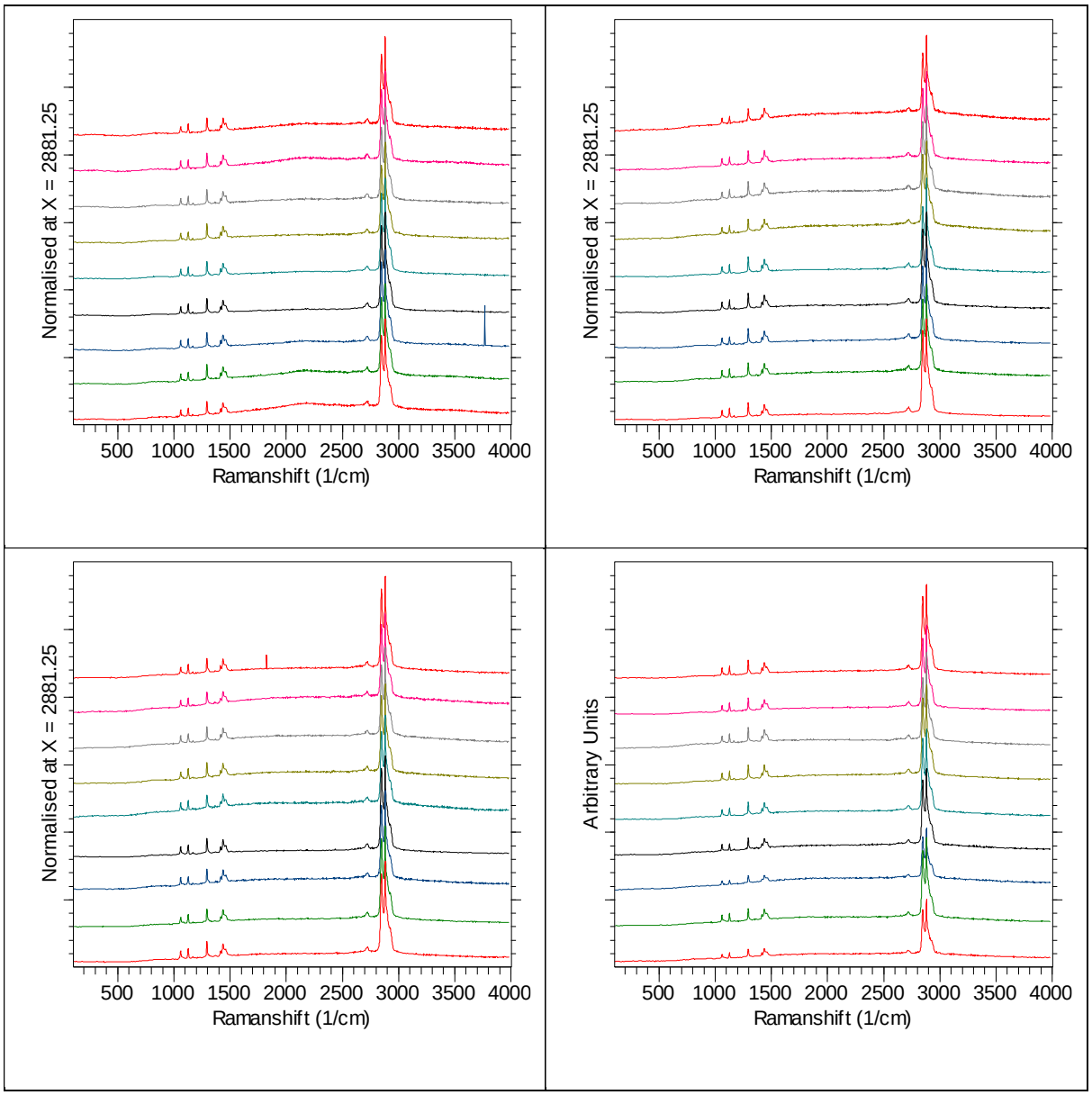


Figure B3a. Raman spectra of (top-left) UD/UT, (top-right) UD/PT15, (bottom-left) UD/PT30, and (bottom-right) UD/PT60.

Continued on the next page…

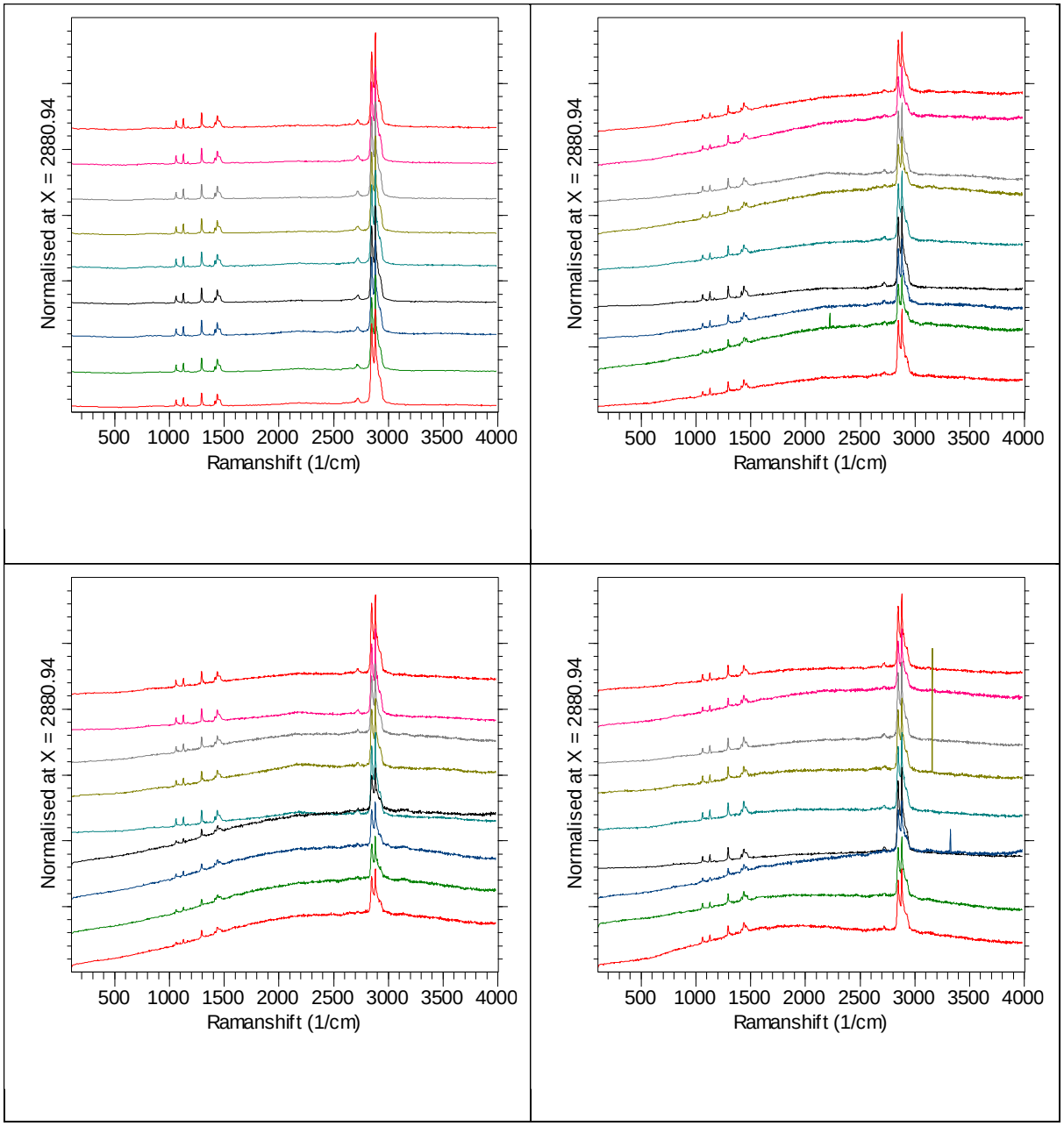


Figure B3b. ATR-FTIR spectra of (top-left) D/UT, (top-right) D/PT15, (bottom-left) D/PT30, and (bottom-right) D/PT60.

Appendix B4 – Instrumental broadening correction for WXRD

Corundum (NIST SRM 676a; 99.02% crystalline alumina powder) was used to determine the instrumental broadening of the XRD instrument (Cline, 2015). The recorded WXRD spectrum is shown in Figure A3a, the subsequent peak fitting was performed with a pseudo-Voight lineshape (98.3% Lorentzian). Following the procedure from the National Bureau of Standards, the FWHM (β) of the $K_{\alpha 1}$ peaks that showed >5% relative intensity were fitted over 2θ with a second-degree polynomial, as shown in Figure A3b (Fawcett et al., 1988). The equation obtained from the second-degree polynomial ($\beta_{instrument}$) was used to correct the FWHM values from the diffraction peaks in the sample spectra (β_{sample}), following:

$$\beta_i = \beta_{sample} - \beta_{instrument} .$$

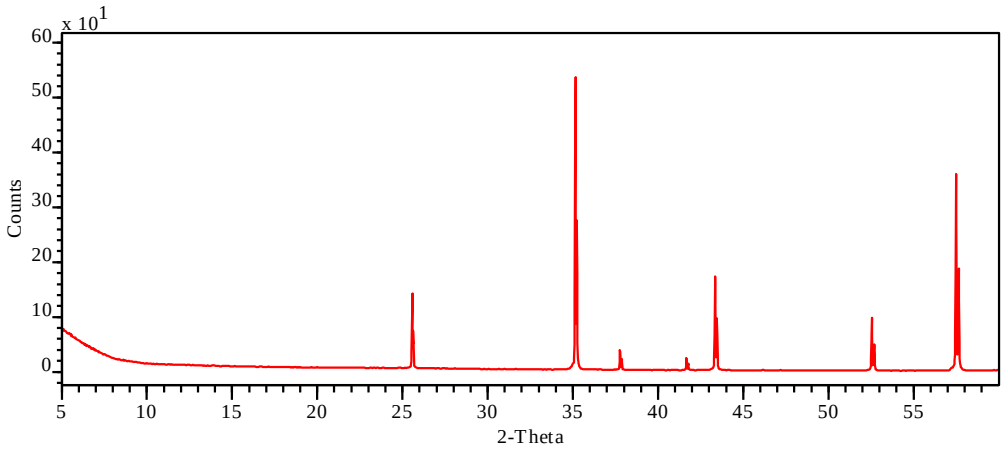


Figure B4a. WXRD spectrum of corundum SRM 676a using a Bruker D8 Advance.

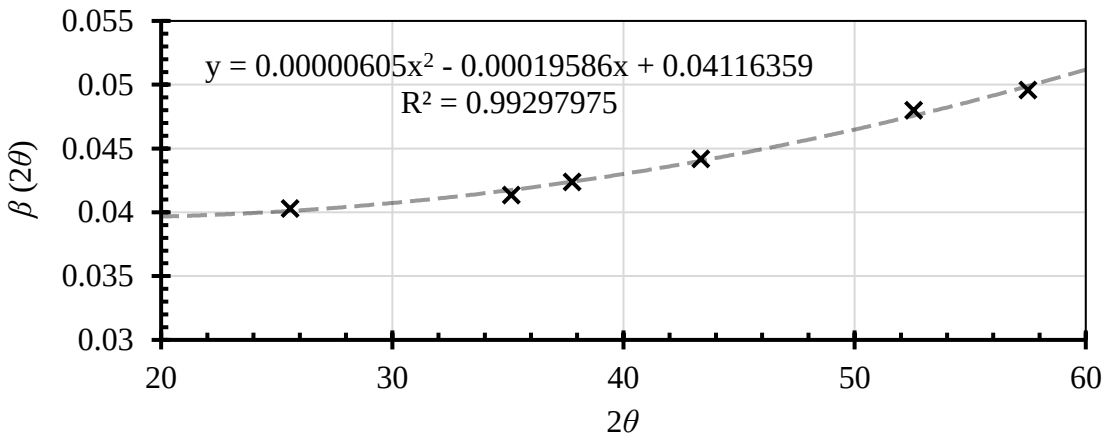


Figure B4b. Second degree polynomial regression fit of the β and 2θ from the corundum diffraction peaks.

Appendix B5 – Example of GAMESS input file

Note: The linear dependence threshold (1.0E-6) and convergence limit (1.0E-5) are default in GAMESS. The empty `{space}` in front of the $-signs are required, for further information on how to prepare GAMESS input files, please see: https://www.msg.chem.iastate.edu/GAMESS/documentation.html.

Example of GAMESS input with HF:

```
 $BASIS GBASIS=N311 NGAUSS=6 NDFUNC=1 NPFUNC=1 DIFFSP=.T. DIFFS=.T.
$END
 $CONTRL SCFTYP=RHF DFTTYP=NONE RUNTYP=OPTIMIZE MOLPLT=.T.
PLTORB=.T. MAXIT=200 $END
 $SCF SOSCF=.T. $END
 $SYSTEM MWORDS=100 MEMDDI=100 PARALL=.T. KDIAG=3 $END
 $ELPOT IEPOT=1 $END
```

Example of GAMESS input with wB97X-D:

```
 $BASIS GBASIS=N311 NGAUSS=6 NDFUNC=1 NPFUNC=1 DIFFSP=.T. DIFFS=.T.
$END
 $CONTRL SCFTYP=RHF DFTTYP=wB97X-D RUNTYP=OPTIMIZE MOLPLT=.T.
PLTORB=.T. MAXIT=200 $END
 $SCF DIIS=.T. $END
 $SYSTEM MWORDS=100 MEMDDI=100 PARALL=.T. KDIAG=3 $END
 $ELPOT IEPOT=1 $END
```

Example of MMFF94 pre-optimized PE model structure:

```
 $DATA
Title
C1
C         6.0  -4.9855999103   0.1100153379  -0.0181484055
C         6.0  -3.6842233697   0.9094283175   0.0365122477
H         1.0  -5.8485825650   0.7701652097   0.0251460356
H         1.0  -5.0535810209  -0.5816730087   0.8175046619
H         1.0  -5.0519133975  -0.4643252391  -0.9385310386
C         6.0  -2.4382126482   0.0275619724  -0.0212352212
H         1.0  -3.6648655211   1.5046149207   0.9482234279
H         1.0  -3.6632112332   1.6206221007  -0.7878651330
C         6.0  -1.1312266145   0.8170647215   0.0327603366
H         1.0  -2.4643005734  -0.5684312454  -0.9329251809
H         1.0  -2.4659409125  -0.6844156926   0.8030133847
C         6.0   0.1138320947  -0.0670563882  -0.0251261812
H         1.0  -1.1094666535   1.4129223431   0.9444340424
H         1.0  -1.1078099131   1.5288898068  -0.7915132723
C         6.0   1.4203098203   0.7237585778   0.0289360763
H         1.0   0.0893398287  -0.6624785651  -0.9368816628
H         1.0   0.0877056142  -0.7784420905   0.7992975063
C         6.0   2.6652588370  -0.1607101936  -0.0289468873
H         1.0   1.4427893086   1.3191314411   0.9406869807
H         1.0   1.4444478409   1.4350698229  -0.7955149111
```

Continued on the next page…

```
C       6.0   3.9716332017   0.6304710075   0.0251136592
H       1.0   2.6419450781  -0.7559619761  -0.9407381985
H       1.0   2.6403101595  -0.8718882852   0.7955748264
C       6.0   5.2165825300  -0.2539996233  -0.0327402138
H       1.0   3.9949353876   1.2257360811   0.9368961541
H       1.0   3.9965951919   1.3416377511  -0.7994172253
C       6.0   6.5230610000   0.5368178993   0.0212678720
H       1.0   5.1940905280  -0.8494077719  -0.9444680576
H       1.0   5.1924572748  -0.9652808836   0.7917365579
C       6.0   7.7681192665  -0.3473092469  -0.0365433837
H       1.0   6.5475448568   1.1322985098   0.9329859308
H       1.0   6.5491970505   1.2481515151  -0.8032002528
C       6.0   9.0751075310   0.4421973832   0.0173537895
H       1.0   7.7463452116  -0.9432454890  -0.9481653702
H       1.0   7.7447148673  -1.0590638271   0.7877911409
C       6.0  10.3211165599  -0.4396783251  -0.0402883760
H       1.0   9.1011940430   1.0382873536   0.9289797056
H       1.0   9.1028398811   1.1540883551  -0.8069694607
C       6.0  11.6224947779   0.3597386799   0.0142512539
H       1.0  10.3017461179  -1.0349735169  -0.9519274734
H       1.0  10.3001119716  -1.1507738048   0.7841756294
H       1.0  11.6904696871   1.0513265563  -0.8214838288
H       1.0  12.4854757374  -0.3004181525  -0.0289542467
H       1.0  11.6888130774   0.9341976612   0.9345627617
 $END
```

Appendix C1 – FTIR data from the individual spectral peak fits

Table C1a. FTIR data from the individual spectral peak fits of the undoped sample series.

Region	Index/Ratio	UD/UT			UD/PT15			UD/PT30			UD/PT60		
		1	2	3	1	2	3	1	2	3	1	2	3
1	730:719	0.31	0.28	0.29	0.39	0.40	0.44	0.41	0.45	0.50	0.41	0.36	0.39
2	VI	0.01	0.02	0.03	0.06	0.08	0.06	0.07	0.08	0.07	0.13	0.09	0.11
	GVI	0.01	0.00	0.02	0.45	0.35	0.12	0.06	0.02	0.02	0.10	0.03	0.02
	TVI	0.01	0.01	0.01	0.26	0.27	0.23	0.27	0.25	0.27	0.49	0.40	0.44
3	1040	0.16	0.10	0.14	0.62	0.46	0.23	0.20	0.12	0.09	0.32	0.24	0.33
	1080	0.44	0.28	0.38	0.61	0.33	0.31	0.32	0.35	0.32	0.60	0.49	0.69
	1120	0.12	0.09	0.04	0.38	0.16	0.11	0.09	0.09	0.05	0.52	0.21	0.61
	1165	0.13	0.12	0.08	0.16	0.06	0.11	0.04	0.09	0.05	0.26	0.13	0.30
4	T:W	0.74	0.73	0.79	0.54	0.57	0.53	0.44	0.43	0.46	0.53	0.50	0.45
5	1472:1462	1.07	1.07	1.10	1.39	1.34	1.42	1.48	1.62	1.44	1.39	1.62	1.47
6	$[C=C]_1$	0.46	0.81	0.63	0.00	0.00	0.17	1.38	1.25	1.11	1.74	2.29	2.15
	$[C=C]_2$	2.02	2.28	1.71	4.80	4.97	3.83	7.88	7.38	7.41	6.38	6.44	6.69
	[C=O]	0.03	0.12	0.24	0.90	1.02	0.85	0.97	1.15	0.95	0.00	0.00	0.00
	[O=C-O]	0.25	0.35	0.36	0.38	0.47	0.43	0.21	0.27	0.17	0.00	0.00	0.00
7	2917:2849	2.30	2.28	2.27	2.17	2.14	2.15	2.18	2.27	2.15	2.18	2.27	2.22
8	3055	1.51	1.82	1.94	2.62	3.26	2.11	0.89	0.96	0.04	0.03	2.03	0.78
	3156	3.10	5.44	6.09	10.45	11.17	7.41	4.73	5.58	2.61	2.42	4.60	5.32
	3322	10.79	14.23	16.53	23.14	27.97	19.63	17.45	14.51	13.24	17.02	19.18	17.93
	3537	6.74	5.11	6.38	8.85	10.63	7.00	7.94	4.92	4.96	6.34	7.60	6.68

Continued on the next page…

Table C1b. FTIR data from the individual spectral peak fits of the doped sample series.

Region	Index/Ratio	D/UT			D/PT15			D/PT30			D/PT60		
		1	2	3	1	2	3	1	2	3	1	2	3
1	730:719	0.47	0.48	0.47	0.44	0.48	0.54	0.51	0.45	0.43	0.48	0.44	0.40
2	VI	0.02	0.01	0.01	0.02	0.01	0.01	0.02	0.07	0.03	0.12	0.11	0.09
	GVI	0.05	0.02	0.03	0.00	0.01	0.05	0.02	0.03	0.06	0.03	0.01	0.03
	TVI	0.01	0.00	0.00	0.05	0.05	0.03	0.16	0.18	0.14	0.26	0.21	0.20
3	1040	0.13	0.06	0.15	0.63	0.64	0.93	0.19	0.23	0.59	0.31	0.82	0.57
	1080	0.03	0.16	0.16	1.16	1.12	1.48	0.54	0.60	1.12	0.67	1.34	0.78
	1120	0.06	0.01	0.02	0.34	0.44	0.62	0.05	0.13	0.41	0.00	0.20	0.13
	1165	0.02	0.02	0.03	0.34	0.35	0.47	0.12	0.19	0.34	0.06	0.43	0.24
4	T:W	0.55	0.56	0.51	0.25	0.29	0.24	0.26	0.23	0.14	0.38	0.27	0.27
	αTH	0.16	0.14	0.16	0.13	0.14	0.17	0.12	0.11	0.06	0.07	0.03	0.06
5	1472:1462	1.18	1.31	1.34	1.61	1.51	1.63	1.55	1.67	1.49	1.70	1.72	1.83
6	$[C=C]_1$	0.31	0.12	0.14	11.99	11.99	12.03	17.49	14.96	23.09	21.51	19.08	19.80
	$[C=C]_2$	0.00	0.00	0.00	1.05	0.78	0.80	2.10	1.95	3.18	5.19	3.72	4.26
	[C=O]	0.28	0.20	0.27	4.06	4.40	4.35	3.76	3.25	4.99	0.81	1.80	1.37
	[O=C-O]	0.23	0.19	0.21	0.94	1.06	0.88	0.60	0.42	0.38	0.00	0.00	0.00
7	2917:2849	2.32	2.34	2.28	2.10	2.11	1.93	2.08	2.21	2.18	2.03	2.08	2.07
8	3055	1.14	0.28	0.00	0.00	0.00	0.00	0.04	0.39	0.82	0.33	0.24	0.08
	3156	2.03	0.23	0.49	4.58	4.04	3.37	6.63	5.48	8.62	7.02	5.26	3.29
	3322	7.62	2.73	4.14	17.55	17.61	17.05	23.54	20.31	31.47	25.01	18.89	21.60
	3537	6.80	2.43	4.39	8.20	6.67	7.61	10.45	8.23	8.67	11.99	6.24	5.00

Appendix C2 – Pearson correlation matrix of the FTIR spectral peak fitting data

Table C2. Pearson correlation matrix of the FTIR spectral peak fitting data.

Index/ Ratio	730: 720	VI	GVI	TVI	1040	1080	1120	1165	T:W	aTH	1472: 1462	C=C1	C=C2	C=O	O=C-O	2917:2849	3055	3156	3322
730:720																			
VI	-0.08																		
GVI	-0.07	0.18																	
TVI	-0.04	0.92	0.29																
1040	0.37	0.09	0.14	0.04															
1080	0.32	0.07	-0.21	0.02	0.91														
1120	0.12	0.16	0.08	0.37	0.62	0.65													
1165	0.22	0.08	-0.21	0.09	0.86	0.97	0.78												
T:W	-0.78	-0.14	0.20	-0.13	-0.64	-0.73	-0.35	-0.64											
αTH	0.92	-0.96	0.06	-0.99	-0.23	-0.29	0.28	-0.18	0.48										
1472:1462	0.64	0.53	-0.11	0.44	0.66	0.69	0.34	0.60	-0.88	-0.80									
C=C1	0.10	0.63	-0.37	0.39	0.35	0.52	0.04	0.45	-0.56	-0.99	0.75								
C=C2	0.40	0.33	-0.24	0.19	0.61	0.75	0.18	0.64	-0.86	-0.84	0.86	0.84							
C=O	0.58	-0.33	-0.15	-0.25	0.64	0.75	0.40	0.69	-0.82	0.04	0.52	0.18	0.66						
O=C-O	0.32	-0.68	0.08	-0.51	0.52	0.50	0.42	0.48	-0.32	0.58	0.00	-0.42	0.08	0.76					
2917:2849	-0.44	-0.25	-0.08	-0.15	-0.92	-0.89	-0.45	-0.78	0.76	0.48	-0.82	-0.53	-0.79	-0.68	-0.40				
3055	-0.64	0.07	0.78	0.16	-0.26	-0.49	-0.12	-0.44	0.69	-0.01	-0.59	-0.48	-0.54	-0.49	-0.09	0.33			
3156	-0.20	0.28	0.74	0.33	0.31	0.16	0.12	0.12	-0.09	-0.70	0.14	0.08	0.28	0.21	0.16	-0.39	0.63		
3322	0.01	0.46	0.39	0.47	0.55	0.54	0.35	0.50	-0.50	-0.73	0.56	0.51	0.70	0.46	0.13	-0.68	0.18	0.85	
3537	0.10	0.27	0.47	0.32	0.62	0.57	0.39	0.53	-0.53	-0.61	0.50	0.37	0.65	0.57	0.30	-0.68	0.19	0.85	0.97

Appendix C3 – Raman data from the individual spectral peak fits

Table C3a. Raman data from the individual spectral peak fits of the undoped sample series.

Region	Index/Ratio	UD/UT			UD/PT15			UD/PT30			UD/PT60		
		1	2	3	1	2	3	1	2	3	1	2	3
1	α_c	0.45	0.47	0.45	0.47	0.47	0.48	0.48	0.52	0.49	0.49	0.50	0.50
	α_{as}	0.47	0.47	0.47	0.54	0.49	0.52	0.47	0.47	0.47	0.50	0.49	0.43
	α_{at}	0.40	0.39	0.38	0.41	0.42	0.42	0.42	0.41	0.42	0.42	0.42	0.42
	α_a	0.43	0.43	0.42	0.48	0.45	0.47	0.45	0.44	0.44	0.46	0.46	0.42
	α_b	0.11	0.10	0.13	0.05	0.08	0.05	0.08	0.04	0.07	0.05	0.05	0.07
	Ratio I	0.11	0.12	0.11	0.11	0.11	0.11	0.12	0.13	0.12	0.12	0.12	0.12
	Ratio II	0.38	0.38	0.35	0.40	0.40	0.40	0.41	0.44	0.42	0.43	0.42	0.43
	Ratio III	1.33	1.41	1.32	1.21	1.32	1.31	1.39	1.35	1.25	1.38	1.35	1.57
	Ratio IV	1.28	1.35	1.24	1.37	1.35	1.36	1.34	1.30	1.22	1.43	1.37	1.40
	Strain	6.96	7.05	7.07	6.91	6.91	6.86	6.78	6.84	6.83	6.81	6.79	6.87
	a-C	0.01	0.01	0.00	0.24	0.24	0.30	0.30	0.29	0.32	0.34	0.47	0.28
2	**2848**	3.61	3.97	3.65	4.20	4.13	4.29	4.43	3.66	3.67	4.11	3.96	4.42
	2857	6.83	7.35	6.91	7.85	7.84	8.20	8.35	6.89	7.01	7.64	7.41	8.14
	2883	2.32	2.46	2.45	2.38	2.36	2.41	2.48	2.45	2.50	2.26	2.45	2.42
	2894	9.59	10.35	9.97	11.17	11.05	11.40	11.93	10.17	10.17	10.59	10.76	11.35
	2931	2.81	3.07	2.84	3.35	3.35	3.46	3.63	2.93	2.93	3.28	3.17	3.49
	2969	0.58	0.92	1.58	1.82	1.87	2.21	2.18	1.81	1.69	1.07	1.86	1.36

Continued on the next page…

Table C3b. Raman data from the individual spectral peak fits of the undoped sample series.

Region	Index/Ratio	UD/UT			UD/PT15			UD/PT30			UD/PT60		
		1	2	3	1	2	3	1	2	3	1	2	3
1	α_c	0.49	0.50	0.50	0.46	0.49	0.51	0.48	0.51	0.44	0.47	0.45	0.48
	α_{as}	0.50	0.50	0.49	0.49	0.49	0.47	0.47	0.46	0.51	0.29	0.30	0.43
	α_{at}	0.40	0.42	0.40	0.44	0.46	0.42	0.43	0.50	0.44	0.44	0.49	0.46
	α_a	0.45	0.46	0.45	0.46	0.48	0.45	0.45	0.48	0.47	0.36	0.39	0.45
	α_b	0.05	0.04	0.06	0.07	0.04	0.05	0.07	0.01	0.09	0.17	0.16	0.07
	Ratio I	0.12	0.12	0.12	0.11	0.12	0.12	0.12	0.11	0.10	0.12	0.09	0.11
	Ratio II	0.41	0.43	0.41	0.40	0.44	0.43	0.41	0.50	0.36	0.42	0.41	0.45
	Ratio III	1.33	1.35	1.47	1.10	1.10	1.29	1.39	1.03	1.09	2.07	1.61	1.26
	Ratio IV	1.34	1.41	1.46	1.08	1.11	1.22	1.33	0.95	1.03	1.19	0.88	1.11
	Strain	6.73	6.73	6.89	7.05	6.97	6.25	6.77	6.19	6.71	6.61	6.10	6.48
	a-C	0.05	0.06	0.10	0.36	0.70	0.24	0.11	2.02	1.09	2.11	3.24	1.31
	αTH	0.03	0.11	0.10	0.26	0.35	0.19	0.27	0.62	0.22	0.26	0.70	0.37
2	**2848**	4.03	4.67	4.25	3.32	3.49	3.98	4.56	3.77	3.99	4.53	4.41	4.13
	2857	7.32	8.43	7.80	6.47	6.38	7.54	8.10	7.18	7.81	9.02	9.53	8.11
	2883	2.50	2.62	2.49	2.47	2.18	2.33	2.51	2.26	2.46	2.60	2.70	2.33
	2894	10.69	12.14	11.01	9.60	9.22	10.32	11.39	9.92	10.98	12.47	13.25	11.43
	2931	3.15	3.66	3.34	2.83	2.77	3.12	3.55	2.97	3.29	3.78	4.05	3.40
	2969	0.67	1.09	0.79	1.98	2.22	1.22	0.59	5.57	3.48	5.63	10.77	6.46

Appendix C4 – Pearson correlation matrix of the Raman spectral peak fitting data

Table C4. Pearson correlation matrix of the FTIR spectral peak fitting data.

Index/ Ratio	α_c	α_c	α_c	Ratio I	Ratio II	Ratio III	Ratio IV	Strain	a-C	αTH	2848	2857	2883	2894	2931
α_c															
α_a	0.38														
α_b	-0.75	-0.90													
Ratio I	0.82	0.27	-0.58												
Ratio II	0.62	0.12	-0.38	0.11											
Ratio III	-0.11	-0.88	0.69	-0.09	0.06										
Ratio IV	0.45	0.30	-0.43	0.71	-0.30	0.01									
Strain	0.06	0.35	-0.28	0.55	-0.70	-0.35	0.74								
a-C	-0.34	-0.58	0.58	-0.69	0.47	0.52	-0.78	-0.93							
αTH	-0.31	-0.27	0.34	-0.71	0.48	0.11	-0.91	-0.90	0.85						
2848	0.11	-0.22	0.11	-0.20	0.36	0.58	0.16	-0.48	0.43	0.16					
2857	-0.13	-0.50	0.42	-0.43	0.36	0.74	-0.16	-0.67	0.72	0.39	0.90				
2883	0.08	-0.58	0.38	-0.10	0.16	0.67	-0.03	-0.43	0.40	0.19	0.64	0.66			
2894	-0.02	-0.50	0.37	-0.32	0.38	0.75	-0.10	-0.64	0.67	0.33	0.91	0.99	0.74		
2931	0.00	-0.42	0.30	-0.34	0.45	0.70	-0.11	-0.67	0.68	0.37	0.93	0.99	0.65	0.99	
2969	-0.40	-0.66	0.66	-0.68	0.38	0.60	-0.73	-0.86	0.98	0.78	0.43	0.76	0.45	0.71	0.70

Appendix C5 – Pearson correlation matrix of the FTIR vs. the Raman spectral peak fitting data

Table C5. Pearson correlation matrix of the FTIR vs. the Raman spectral peak fitting data.

Index/ Ratio		FTIR																		
		730: 720	**VI**	**GVI**	**TVI**	**1040**	**1080**	**1120**	**1165**	**T:W**	**αTH**	**1472: 1462**	**C=C1**	**C=C2**	**C=O**	**O=C-O**	**2917: 2849**	**3055**	**3156**	**3322**	**3540**
Raman	α_c	0.56	0.12	-0.13	0.31	-0.21	-0.20	0.24	-0.14	-0.16	0.24	0.17	*-0.23*	*-0.26*	-0.08	-0.09	0.21	-0.38	-0.53	-0.44	-0.44
	α_a	0.34	-0.41	0.41	-0.04	0.00	-0.08	0.38	0.00	-0.14	0.27	-0.17	*-0.64*	*-0.26*	0.39	0.60	0.10	0.19	0.21	0.06	0.23
	α_b	-0.51	0.24	-0.23	-0.11	0.09	0.15	-0.39	0.06	0.18	-0.31	0.04	*0.57*	*0.31*	-0.25	-0.39	-0.18	0.04	0.10	0.16	0.04
	Ratio I	0.08	0.02	-0.11	0.21	-0.38	-0.38	0.22	-0.27	0.34	-0.07	-0.26	*-0.50*	*-0.65*	-0.39	-0.08	0.46	-0.04	-0.55	-0.63	-0.66
	Ratio II	*0.81*	*0.43*	*-0.16*	*0.46*	*0.35*	*0.39*	*0.33*	*0.36*	*-0.81*	*0.35*	*0.85*	*0.49*	*0.57*	*0.40*	*-0.08*	*-0.46*	*-0.67*	*-0.16*	*0.23*	*0.21*
	Ratio III	-0.25	0.62	-0.16	0.31	-0.08	-0.12	-0.32	-0.16	0.19	-0.30	0.19	*0.57*	*0.11*	-0.62	-0.82	0.03	-0.07	-0.22	-0.11	-0.26
	Ratio IV	-0.32	0.00	0.35	0.18	-0.62	-0.78	-0.06	-0.64	0.75	-0.30	-0.66	*-0.68*	*-0.91*	-0.74	-0.31	0.77	0.54	-0.20	-0.55	-0.54
	Strain	-0.56	-0.35	0.25	-0.14	-0.47	-0.53	0.04	-0.40	0.81	-0.37	-0.84	*-0.83*	*-0.88*	-0.44	0.17	0.61	0.64	-0.02	-0.41	-0.39
	a-C	0.26	0.48	-0.18	0.21	0.50	0.55	-0.07	0.42	-0.64	0.09	0.78	*0.92*	*0.89*	0.30	-0.27	-0.66	-0.44	0.19	0.54	0.47
	αTH	0.47	0.02	-0.33	-0.17	0.62	0.72	0.06	0.60	-0.81	0.52	0.71	*0.72*	*0.90*	0.68	0.18	-0.70	-0.64	0.06	0.44	0.48
	2848	0.17	0.50	0.29	0.38	-0.17	-0.33	-0.35	-0.36	-0.06	-0.03	0.24	*0.34*	*0.11*	-0.39	-0.70	0.13	0.06	0.06	0.07	0.05
	2857	0.14	0.63	0.22	0.39	0.10	-0.05	-0.33	-0.14	-0.20	-0.11	0.46	*0.62*	*0.39*	-0.27	-0.67	-0.20	-0.02	0.18	0.28	0.22
	2883	0.19	0.17	-0.25	-0.11	-0.38	-0.41	-0.79	-0.54	0.04	0.11	0.10	*0.31*	*0.05*	-0.40	-0.64	0.23	-0.27	-0.40	-0.38	-0.46
	2894	0.19	0.61	0.20	0.37	0.02	-0.13	-0.39	-0.23	-0.17	-0.09	0.44	*0.56*	*0.32*	-0.33	-0.70	-0.14	-0.05	0.09	0.17	0.10
	2931	0.24	0.62	0.23	0.42	0.10	-0.06	-0.28	-0.14	-0.25	-0.05	0.49	*0.57*	*0.37*	-0.25	-0.65	-0.19	-0.07	0.13	0.24	0.19
	2969	0.19	0.50	-0.11	0.19	0.48	0.49	-0.15	0.34	-0.53	0.00	0.73	*0.88*	*0.82*	0.20	-0.30	-0.65	-0.33	0.23	0.52	0.43

Appendix C6 – Degree of substitution data from the individual samples

Table C6. Degree of substitution data from the individual samples, showing the UV absorbance (Abs.), resulting Fmoc-adduct concentration (nM) and degree of substitution (*S*), determined with ε = 6112 L $mol^{-1}cm^{-1}$.

Sample	Unit	Repeat	DP only	DIC/ Oxyma	DCC/ DMAP	CDI
UD/PT60	Abs.	1	0.004	0.037	0.015	0.036
		2	0.013	0.035	0.014	0.043
		3	0.009	0.044	0.027	0.043
	nM	1	-	59.764	24.767	58.687
		2	-	57.072	23.152	69.456
		3	-	70.532	44.150	68.917
	S	1	-	19.921	8.256	19.562
		2	-	19.024	7.717	23.152
		3	-	23.511	14.717	22.972
D/PT60	Abs.	1	0.378	0.120	-	-
		2	0.517	0.105	-	-
		3	0.439	0.125	-	-
	nM	1	-	-	-	-
		2	-	-	-	-
		3	-	-	-	-
	S	1	-	-	-	-
		2	-	-	-	-
		3	-	-	-	-

Appendix C7 – Cu–Kα X-ray attenuation length for polyethylene

The penetration depth was based on the X-ray attenuation length, following:

$$T = e^{-n\,\mu_a\,d},$$

where n is the number of atoms per unit volume in the slab, d is the slab thickness, and μ_a is the atomic photo-absorption cross section, the latter was obtained following:

$$\mu_a = 2\,r_0\,\lambda\,\mathrm{i}f'',$$

where r_0 is the classical electron radius, λ is the X-ray wavelength, and $\mathrm{i}f''$ is the imaginary part of the atomic scattering factor (see Appendix A4) (Henke et al., 1993). The full Cu–Kα X-ray attenuation length is presented in Figure C7**,** which plateaus as the grazing angle (2θ) moved towards a perpendicular angle relative to the sample surface (i.e., 90°). Next to that, the penetration depth showed that the results are from the bulk of the UHMWPE-based samples.

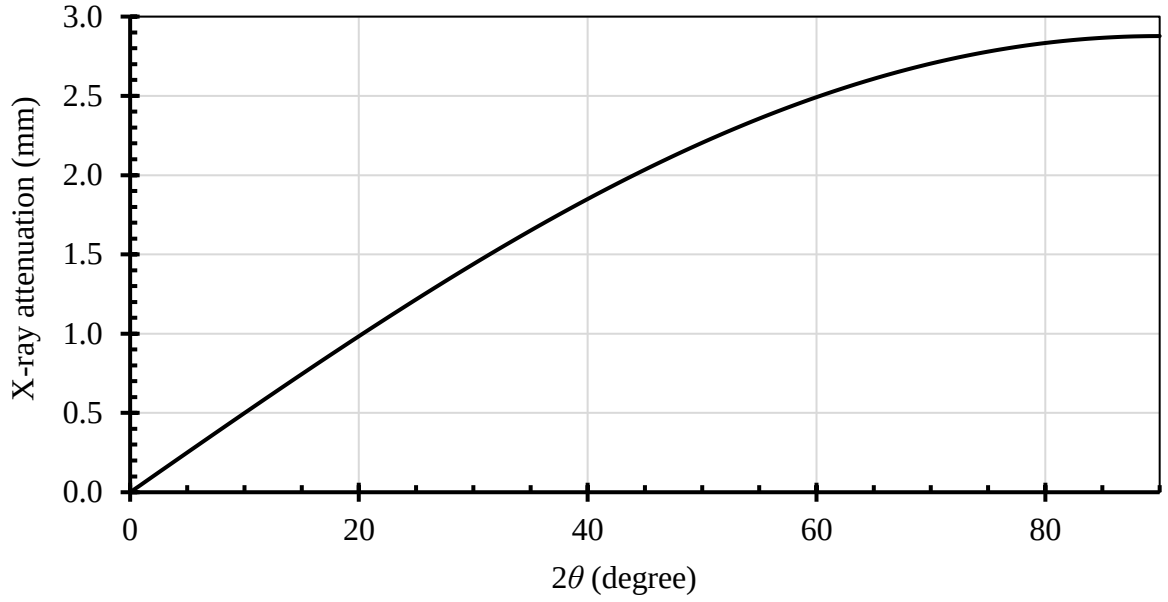


Figure C7. Cu–Kα X-ray attenuation length for polyethylene.

Appendix C8 – Unit cell refinement procedure

Using the peak-fitted XRD spectra, the observed/experimental unit cell parameters were determined following unit cell refinement (Holland and Redfern, 1997). After indexing the XRD spectra to a list of (*h k l)* and 2θ values, the unit cell parameters were refined by a non-linear least-squares fitting procedure, following:

$$\sum_{n=1}^{N} w_n \left(2\theta_{n,\text{obs}} - 2\theta_{n,\text{calc}}\right)^2, \qquad \textit{(Eq. 23)}$$

where w_n is the weight of the observation and $2\theta_n$ is the observed/calculated position for the respective diffraction peak 'n'. The perpendicular distance between the interplanar spacing, d_{hkl}, is given by the inverse of the magnitude of the reciprocal lattice vector, following:

$$d_{hkl} = \frac{1}{|h\mathrm{a}^* + k\mathrm{b}^* + l\mathrm{c}^*|}. \qquad \textit{(Eq. 24)}$$

Since the interplanar angles (α*, β*, γ*) in an orthorhombic system are all equal 90°, the unit cell parameters were determined following:

$$d^2{}_{hkl} = \frac{1}{h^2a^{*2} + k^2b^{*2} + l^2c^{*2}}, \qquad \textit{(Eq. 25)}$$

where $a^* = \frac{1}{a}$, $b^* = \frac{1}{b}$, and $c^* = \frac{1}{c}$ (Kelly and Knowles, 2012). In this work, the software package 'UnitCell' was used to refine the unit cell parameters based on the experimental XRD data (i.e., the indexed diffraction peak positions) (Holland and Redfern, 1997). To prevent adverse effects on the regression results, only the orthorhombic-related Kα_1 diffraction peaks showing an intensity above 0.1% were used, which excluded the $O_{(401)}$ and $O_{(030)}$ diffraction peaks that showed negligible intensity across all of the sample spectra.

Appendix C9 – Modified Scherrer equation plots from the individual samples

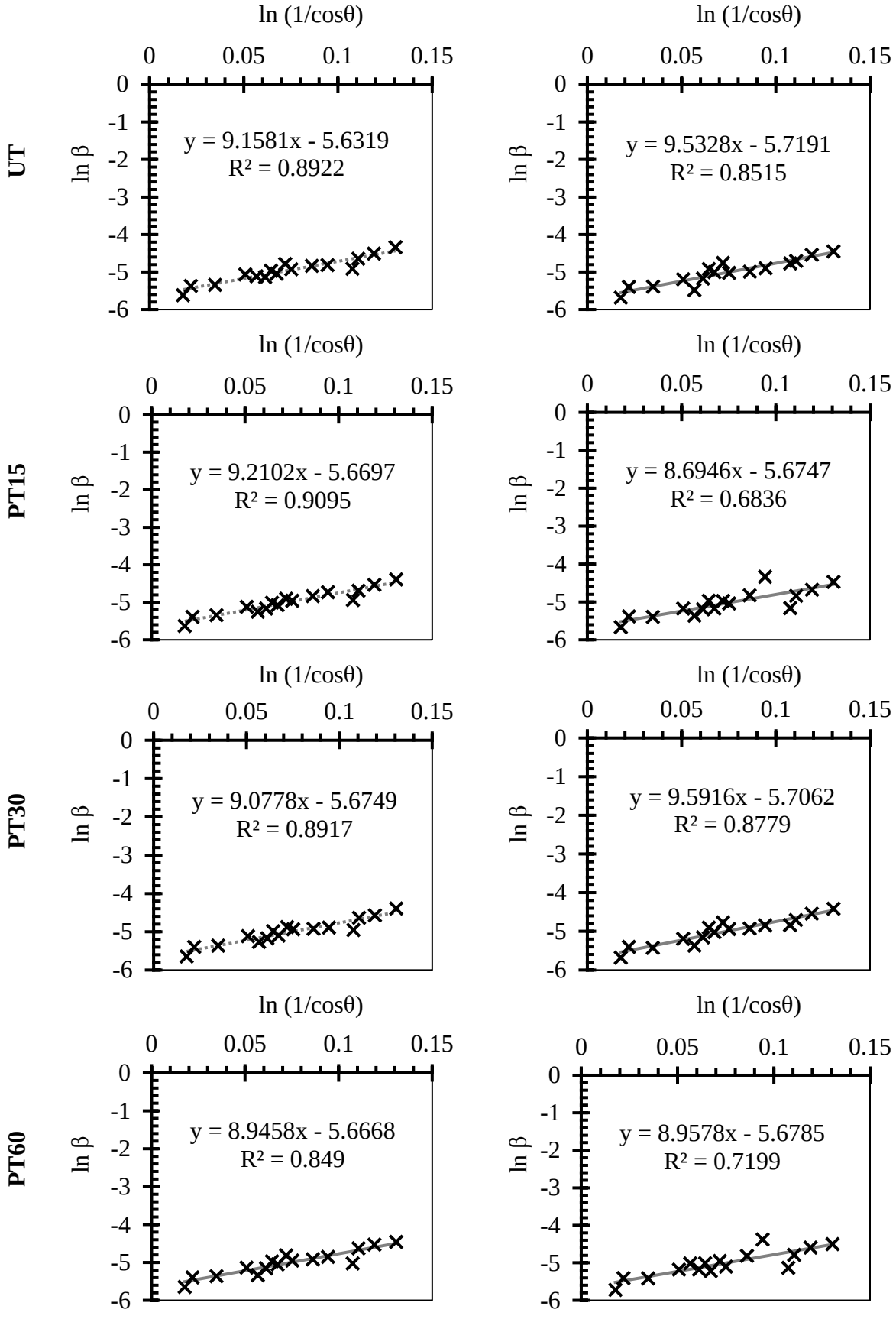


Figure C9. Plots of the modified Scherrer equation for the (left) undoped and (right) doped sample series.

Appendix C10 – Vickers microhardness data from the individual samples

Table C10. Vickers microhardness (MH_V) data from the individual samples and corresponding elastic modulus (E) determined by the logarithmic relation LOG(E)=1.388*LOG(MHv)+0.442 as observed in the literature (Lorenzo et al., 1989; Zamfirova et al., 2003).

	Sample	**1**			**2**			**3**		
	Indent	**1**	**2**	**3**	**1**	**2**	**3**	**1**	**2**	**3**
MH_V (kgf/mm^2)	**UD/UT**	36.30	35.30	34.00	35.90	34.60	35.70	35.50	34.90	35.30
	UD/PT15	39.40	38.50	37.90	38.90	38.20	39.20	38.10	39.00	39.40
	UD/PT30	43.60	40.30	43.50	40.00	40.40	40.90	40.30	39.80	41.30
	UD/PT60	40.20	39.80	40.90	40.10	39.20	39.60	40.40	39.90	39.50
E (MPa)	**UD/UT**	13.56	13.33	13.04	13.47	13.17	13.42	13.38	13.24	13.33
	UD/PT15	14.25	14.05	13.92	14.14	13.98	14.20	13.96	14.16	14.25
	UD/PT30	15.14	14.44	15.12	14.38	14.46	14.57	14.44	14.33	14.66
	UD/PT60	14.42	14.33	14.57	14.40	14.20	14.29	14.46	14.36	14.27
MH_V (kgf/mm^2)	**D/UT**	34.40	34.00	33.60	34.10	35.30	34.60	35.10	33.90	34.50
	D/PT15	45.50	44.50	45.70	45.90	43.80	45.00	44.20	44.50	43.90
	D/PT30	54.50	53.70	53.20	53.80	53.50	52.90	52.80	53.30	52.50
	D/PT60	56.60	54.00	55.10	56.50	54.40	55.40	56.20	55.20	55.80
E (MPa)	**D/UT**	13.13	13.04	12.94	13.06	13.33	13.17	13.29	13.01	13.15
	D/PT15	15.54	15.33	15.58	15.62	15.19	15.44	15.27	15.33	15.21
	D/PT30	17.32	17.17	17.07	17.19	17.13	17.02	17.00	17.09	16.94
	D/PT60	17.72	17.23	17.44	17.70	17.31	17.50	17.65	17.46	17.57

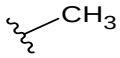
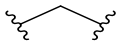
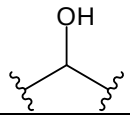
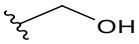
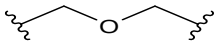
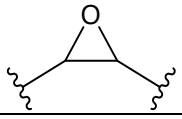
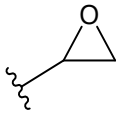
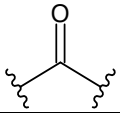
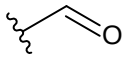
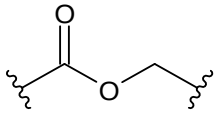
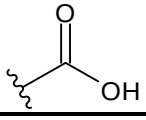
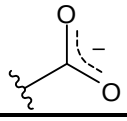
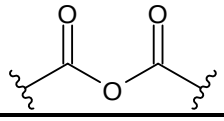
Appendix C11 – Equilibrium contact angle data from the individual samples

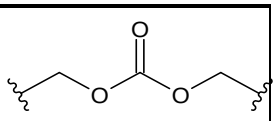
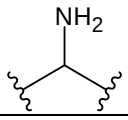
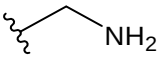
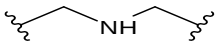
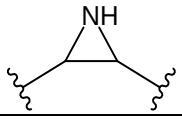
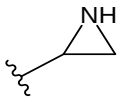
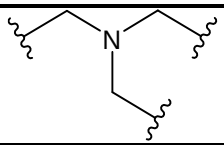
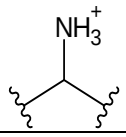
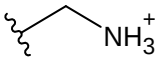
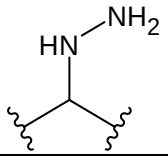
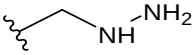
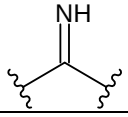
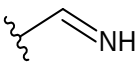
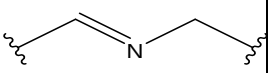
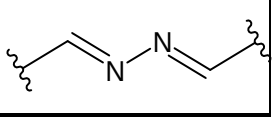
Table C11. Equilibrium contact angle data for DI water and diiodomethane from the individual samples.

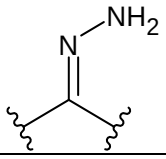
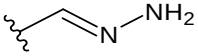
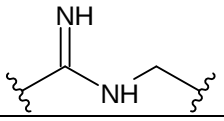
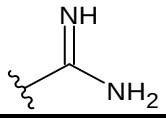
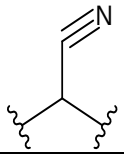
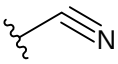
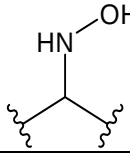
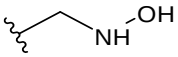
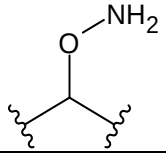
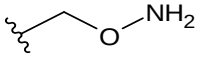
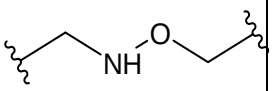
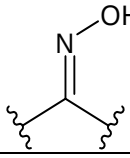
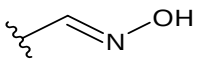
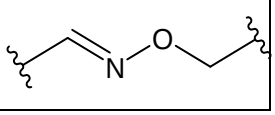
Sample	Repeat	Equilibrium contact angle (°)	
		DI Water	Diiodomethane
UD/UT	1	109.46	66.40
	2	121.57	66.49
	3	110.00	64.00
UD/PT60	1	110.17	47.26
	2	126.74	43.67
	3	95.43	43.00
UD/PT60-(KR-12)	1	44.82	61.07
	2	33.78	67.90
	3	19.62	58.17
D/UT	1	85.19	26.95
	2	86.52	9.39
	3	86.97	3.06
D/PT60	1	107.30	58.73
	2	96.15	55.82
	3	116.06	55.45
D/PT60-(KR-12)	1	113.85	51.32
	2	101.33	53.09
	3	102.03	57.93

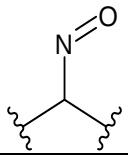
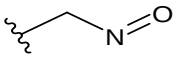
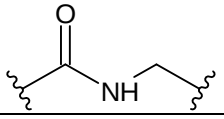
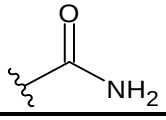
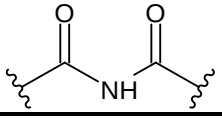
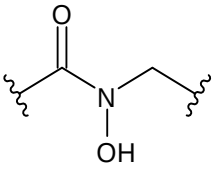
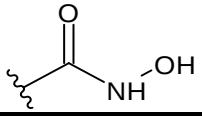
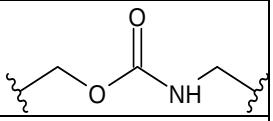
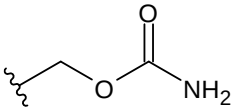
Appendix D1 – List of evaluated functionalities for the theoretical peak model

Table D1. List of evaluated functionalities, including the corresponding IDs, linear structures and simplified chemical structure depicting the functionalities. The functionality is positioned in the centre of the model structure, unless when denoted with an asterisk (*) indicating the functionality is in an end-chain positioning.

Functionality	ID	Linear structure	Structure
Methyl	CH_3*	~CH_3	
Alkane	CH_2	~CH_2~	
Hydroxyl	COH	~CH(−OH)~	
	COH*	~CH_2−OH	
Ether	COC_α	~CH_2−O−CH_2~	
Epoxide	COC_β	~CH(−O−)−CH~	
	COC_β*	~CH(−O−)−CH_2	
Carbonyl	C=O	~C(=O)~	
	C=O*	~CH=O	
Ester	O=COC	~C(=O)−O−CH_2~	
Carboxylic Acid	O=COH*	~C(=O)−OH	
Carboxylate	$O=CO^{\{-\}}$*	~$C(=O)-O^{\{-\}}$	
Anhydride	O=COC=O	~C(=O)−O−C(=O)~	

Carbonate Ester	COC(=O)OC	~C−O−C(=O)−O−C~	
Amine (1°)	CNH_2	~CH(−NH_2)~	
	CNH_2*	~CH_2−NH_2	
Amine (2°)	$CNHC_\alpha$	~CH_2−NH−CH_2~	
Aziridine	$CNHC_\beta$	~CH(−N−)−CH~	
	$CNHC_\beta$*	~CH(−N−)−CH_2	
Amine (3°)	CN(C)C	~ CH_2−N(−CH_2~)−CH_2~	
Ammonium ion	$CNH_3^{\{+\}}$	~CH($NH_3^{\{+\}}$)~	
	$CNH_3^{\{+\}}$*	~CH−$NH_3^{\{+\}}$	
Hydrazide	$CNHNH_2$	~CH(−NH−NH_2)~	
	$CNHNH_2$*	~ CH_2−NH−NH_2	
Imine	C=NH	~C(=NH)~	
	C=NH*	~CH=NH	
	C=NC	~CH=N−CH_2~	
Azine	C=NN=C	~CH=N−N=CH_2~	

Hydrazone	C=NNH$_2$	~C(=N−NH$_2$)~	
	C=NNH$_2$*	~CH=N−NH$_2$	
Amidine	HN=CNHC	~C(=NH)−NH−CH$_2$~	
	HN=CNH$_2$*	~C(=NH)−NH$_2$	
Nitrile	C≡N	~CH(−C≡N)~	
	C≡N*	~C≡N	
Hydroxylamine	CNHOH	~CH$_2$(−NH−OH)~	
	CNHOH*	~CH$_2$−NH−OH	
Aminoxyl	CONH$_2$	~CH$_2$(−O−NH$_2$)~	
	CONH$_2$*	~CH$_2$−O−NH$_2$	
	CNHOC	~CH$_2$−NH−O−CH$_2$~	
Oxime	C=NOH	~C(=N−OH)~	
	C=NOH*	~CH=N−OH	
Iminoxyl	C=NOC	~CH=N−O−CH$_2$~	

Nitroso	CN=O	~CH(−N=O)~	
	CN=O*	~CH_2−N=O	
Amide	O=CNHC	~C(=O)−NH−C~	
	O=CNH_2*	~C(=O)−NH_2	
Imide	O=CNHC=O	~C(=O)−NH−C(=O)~	
Hydroxamic acid	O=CN(OH)C	~C(=O)−N(−OH)−CH_2~	
	O=CN(OH)H*	~C(=O)−NH−OH	
Carbamate	COC(=O)NHC	~CH_2−O−C(=O)−NH−CH_2~	
	COC(=O)NH_2*	~CH_2−O−C(=O)−NH_2	

Appendix D2 – Calculated primary carbon ΔCEBEs

Table D2. Carbon ΔCEBEs relative to the averaged methylene group of the PE model structure. The functionality is positioned in the centre of the model structure, unless when denoted with an asterisk (*) indicating the functionality is in an end-chain positioning. The numbers in the linear structures of the functionalities refer to numbered ΔCEBEs. The ΔCEBEs are calculated by HF (normal) and wB97X-D (*italic*). Relative to CEBE of (a) 304.97 eV and (b) 279.45 eV.

ID	Linear structure	C 1s (Δ_{CH2})		
		1	2	3
CH_3*	~C^1H_3	-0.11		
		-0.16		
CH_2	~C^1H_2~	0[a]		
		0[b]		
COH	~$C^1H(-OH)$~	1.74		
		1.74		
COH*	~C^1H_2-OH	1.58		
		1.44		
COC_α	~$C^1H_2-O-C^2H_2$~	1.47	1.47	
		1.36	*1.36*	
COC_β	~$C^1H(-O-)-C^2H$~	1.77	1.74	
		1.66	*1.64*	
COC_β*	~$C^1H(-O-)-C^2H_2$	1.96	1.80	
		1.83	*1.66*	
C=O	~$C^1(=O)$~	3.02		
		2.72		
C=O*	~$C^1H=O$	3.10		
		2.81		
O=COC	~$C^1(=O)-O-C^2H_2$~	4.30	1.90	
		3.76	*1.74*	
O=COH*	~$C^1(=O)-OH$	4.60		
		4.06		
$O=CO^{\{-\}}$*	~$C^1(=O)-O^{\{-\}}$	4.93		
		4.25		
O=COC=O	~$C^1(=O)-O-C^2(=O)$~	4.82	4.82	
		4.27	*4.27*	
COC(=O)OC	~ $C^2-O-C^1(=O)-O-C^2$~	5.58	1.93	
		4.87	*1.80*	
CNH_2	~$C^1H(-NH_2)$~	1.12		
		1.04		
CNH_2*	~$C^1H_2-NH_2$	0.84		
		0.79		
$CNHC_\alpha$	~$C^1H_2-NH-C^2H_2$~	0.73	0.73	
		0.68	*0.68*	
$CNHC_\beta$	~$C^1H(-N-)-C^2H$~	1.06	1.09	
		1.04	*1.04*	
$CNHC_\beta$*	~$C^1H(-N-)-C^2H_2$	1.14	0.95	
		1.09	*0.90*	

CNCC	~ C^1H_2–N(–C^3H_2~)–C^2H_2~	0.79	0.79	0.76
		0.74	*0.74*	*0.68*
$CNH_3^{\{+\}}$	~C^1H($NH_3^{\{+\}}$)~	2.86		
		2.45		
$CNH_3^{\{+\}}$*	~C^1H–$NH_3^{\{+\}}$	2.86		
		2.40		
$CNHNH_2$	~C^1H(–NH–NH_2)~	1.12		
		1.04		
$CNHNH_2$*	~ C^1H_2–NH–NH_2	0.71		
		0.66		
C=NH	~C^1(=NH)~	1.85		
		1.66		
C=NH*	~C^1H=NH	1.74		
		1.53		
C=NC	~C^1H=N–C^2H_2~	1.50	0.87	
		1.31	*0.79*	
C=NN=C	~C^1H=N–N=CH_2~	1.42	1.42	
		1.25	*1.25*	
C=NNH_2	~C^1H(=N–NH_2)~	1.36		
		1.12		
C=NNH_2*	~C^1H=N–NH_2	1.25		
		1.01		
HN=CNHC	~C^1(=NH)–NH–C^2H_2~	2.53	1.50	
		2.15	*1.44*	
HN=CNH_2*	~C^1(=NH)–NH_2	2.61		
		2.23		
C≡N	~C^1H(–C^2≡N)~	1.80	1.55	
		1.66	*1.15*	
C≡N*	~ C^1H_2–C^2≡N	1.82	1.42	
		1.69	*1.31*	
CNHOH	~C^1H_2(–NH–OH)~	1.12		
		1.06		
CNHOH*	~C^1H_2–NH–OH	0.90		
		0.85		
$CONH_2$	~C^1H_2(–O–NH_2)~	1.47		
		1.39		
$CONH_2$*	~C^1H_2–O–NH_2	1.42		
		1.31		
CNHOC	~C^2H_2–NH–O–C^1H_2~	1.36	0.87	
		1.25	*0.82*	
C=NOH	~C^1(=N–OH)~	1.55		
		1.31		
C=NOH*	~C^1H=N–OH	1.50		
		1.28		
C=NOC	~C^2H=N–O–C^1H_2~	1.50	1.39	
		1.39	*1.12*	
CN=O	~C^1H(–N=O)~	1.36		

		1.25		
CN=O*	~C¹H₂–N=O	1.42		
		1.25		
O=CNHC	~C¹(=O)–NH–C²~	3.40	1.22	
		2.91	*1.17*	
O=CNH₂*	~C¹(=O)–NH₂	3.70		
		3.21		
O=CNHC=O	~C¹(=O)–NH–C²(=O)~	4.00	4.00	
		3.54	*3.54*	
O=CN(OH)C	~C¹(=O)–N(–OH)–C²H₂~	3.73	1.25	
		3.19	*1.23*	
O=CN(OH)H*	~C¹(=O)–NH–OH	4.11		
		3.51		
COC(=O)NHC	~C²H₂–O–C¹(=O)–NH–C³H₂~	4.71	1.77	1.20
		4.14	*1.64*	*1.28*
COC(=O)NH₂*	~C²H₂–O–C¹(=O)–NH₂	5.03	1.88	
		4.38	*1.74*	

Appendix D3 – Calculated nitrogen and oxygen ΔCEBEs

Table D3. Summary of the ΔCEBEs for the N 1s shifts relative to the centred amine and O 1s shifts relative to the centred hydroxyl. The functionality is positioned in the centre of the model structure, unless when denoted with an asterisk (*) indicating the functionality is in an end-chain positioning. The numbers in the linear structures of the functionalities refer to numbered ΔCEBEs. The elements are coloured to represent the respective atom type - nitrogen (blue) and oxygen (red). The ΔCEBEs displayed are calculated by HF (normal) and wB97X-D (*italic*) per functionality. The N 1s ΔCEBEs are relative to the CEBE for CNH_2 of (a) 422.71 eV and (b) 392.21 eV, and the O 1s ΔCEBEs are relative to the CEBE for COH of (c) 559.17 eV and (d) 523.78 eV.

ID	Linear structure	N 1s (Δ_{CNH2})		O 1s (Δ_{COH})	
		1	2	1	2
COH	~CH(−O^1H)~			0[c]	
				0[d]	
COH*	~CH_2−O^1H			0	
				0	
COC_α	~CH_2−O^1−CH_2~			-0.14	
				-0.03	
COC_β	~CH(−O^1−)−CH~			0.16	
				0.16	
COC_β*	~CH(−O^1−)−CH_2			0.38	
				0.35	
C=O	~C(=O^1)~			-0.24	
				-0.30	
C=O*	~CH=O^1			0.14	
				0.08	
O=COC	~C(=O^1)−O^2−CH_2~			-0.38	1.20
				-0.41	*1.20*
O=COH*	~C(=O^1)−O^2H			-0.22	1.61
				-0.27	*1.47*
$O=CO^{\{-\}}$*	~C(=O^1)−$O^{2\{-\}}$			0.24	2.42
				1.28	*1.39*
O=COC=O	~C(=O^1)−O^2−C(=O^1)~			0.16	1.77
				0.11	*1.66*
COC(=O)OC	~ C−O^2−C(=O^1)−O^2−C~			-0.52	1.28
				-0.49	*1.28*
CNH_2	~CH(−N^1H_2)~	0[a]			
		0[b]			
CNH_2*	~CH_2−N^1H_2	-0.05			
		-0.03			
$CNHC_\alpha$	~CH_2−N^1H−CH_2~	-0.11			
		0.00			
$CNHC_\beta$	~CH(−N^1−)−CH~	0.27			
		0.30			
$CNHC_\beta$*	~CH(−N^1−)−CH_2	0.33			
		0.33			
CN(C)C	~ CH_2−N^1(−CH_2~)−CH_2~	0.03			
		0.11			
$CNH_3^{\{+\}}$	~CH($N^1H_3^{\{+\}}$)~	4.14			

		3.51			
$CNH_3^{\{+\}}$*	~CH–$N^1H_3^{\{+\}}$	4.41			
		3.76			
$CNHNH_2$	~CH(–N^2H–N^1H_2)~	1.01	0.95		
		0.95	*0.95*		
$CNHNH_2$*	~ CH_2–N^1H–N^2H_2	0.79	0.76		
		0.82	*0.73*		
C=NH	~C(=N^1H)~	-0.03			
		-0.05			
C=NH*	~CH=N^1H	0.24			
		0.16			
C=NC	~CH=N^1–CH_2~	0.30			
		0.27			
C=NN=C	~CH=N^1–N^2=CH_2~	1.03	1.03		
		0.93	*0.93*		
C=NNH_2	~C(=N^1–N^2H_2)~	1.03	1.06		
		0.95	*1.09*		
C=NNH_2*	~CH=N^2–N^1H_2	1.12	1.42		
		1.20	*1.28*		
HN=CNHC	~C(=N^2H)–N^1H–CH_2~	-0.71	0.95		
		-0.73	*1.06*		
HN=CNH_2*	~C(=N^2H)–N^1H_2	-0.60	0.71		
		-0.68	*0.76*		
C≡N	~CH(–C≡N^1)~	0.79			
		0.35			
C≡N*	~C≡N^1	0.63			
		0.44			
CNHOH	~CH_2(–N^1H–O^1H)~	1.66		0.84	
		1.61		*0.76*	
CNHOH*	~CH_2–N^1H–O^1H	1.66		0.76	
		1.61		*0.71*	
$CONH_2$	~CH_2(–O^1–N^1H_2)~	1.66		0.54	
		1.55		*0.63*	
$CONH_2$*	~CH_2–O^1–N^1H_2	1.66		0.73	
		1.55		*0.73*	
CNHOC	~CH_2–N^1H–O^1–CH_2~	1.52		0.54	
		1.47		*0.60*	
C=NOH	~C(=N^1–O^1H)~	1.80		1.01	
		1.63		*1.01*	
C=NOH*	~CH=N^1–O^1H	2.18		1.14	
		1.99		*1.12*	
C=NOC	~CH=N^1–O^1–CH_2~	2.01		0.90	
		1.80		*1.01*	
CN=O	~CH(–N^1=O^1)~	4.05		1.90	
		3.67		*1.69*	
CN=O*	~CH_2–N^1=O^1	4.25		2.04	

		3.84		*1.77*	
O=CNHC	~C(=O[1])–N[1]H–C~	1.12		-1.17	
		1.22		*-1.17*	
O=CNH$_2$*	~C(=O[1])–N[1]H$_2$	1.22		-0.90	
		1.25		*-0.93*	
O=CNHC=O	~C(=O[1])–N[1]H–C(=O[1])~	1.85		-0.49	
		1.85		*-0.49*	
O=CN(OH)C	~C(=O[1])–N[1](–O[2]H)–CH$_2$~	2.61		-0.68	1.71
		2.67		*-0.76*	*1.69*
O=CN(OH)H*	~C(=O[1])–N[1]H–O[2]H	2.94		-0.27	1.44
		2.97		*-0.38*	*1.39*
COC(=O)NHC	~CH$_2$–O[2]–C(=O[1])–N[1]H–CH$_2$~	0.98		-1.06	0.98
		1.12		*-0.98*	*0.98*
COC(=O)NH$_2$*	~CH$_2$–O[2]–C(=O[1])–N[1]H$_2$	1.22		-0.79	1.25
		1.22		*-0.79*	*1.17*

Appendix D4 – Calculated higher-order carbon ΔCEBEs

Table D4. Carbon ΔCEBEs calculated by HF (normal) and wB97X-D (*italic*) for the investigated functionalities. The functionality is positioned in the centre of the model structure, unless when denoted with an asterisk (*) indicating the functionality is in an end-chain positioning. The numbers represent the carbon position in the structure, non-carbon atoms are omitted, and primary carbon ΔCEBEs are **bold**.

ID	ΔCEBE (eV)													
	1	**2**	**3**	**4**	**5**	**6**	**7**	**8**	**9**	**10**	**11**	**12**	**13**	**14**
CH_2	-0.11	0.05	0.00	-0.03	0.00	-0.03	0.00	0.00	-0.03	0.00	-0.03	0.00	0.05	-0.11
	-0.16	*0.06*	*-0.02*	*0.00*	*-0.02*	*0.00*	*-0.02*	*-0.02*	*0.00*	*0.00*	*0.00*	*-0.02*	*0.06*	*-0.16*
COH	-0.11	0.05	0.00	-0.03	-0.08	0.03	**1.74**	0.16	0.30	0.22	0.19	0.14	0.19	0.00
	-0.16	*0.03*	*-0.02*	*-0.02*	*-0.08*	*0.06*	***1.74***	*0.19*	*0.33*	*0.22*	*0.19*	*0.14*	*0.19*	*-0.02*
COH*	-0.11	0.05	0.00	0.00	0.00	0.03	0.00	0.03	0.05	0.08	0.14	0.22	0.19	**1.58**
	-0.16	*0.03*	*-0.02*	*0.00*	*0.00*	*0.00*	*0.03*	*0.03*	*0.06*	*0.08*	*0.14*	*0.25*	*0.19*	***1.44***
COC_α	-0.11	0.05	0.00	0.03	0.11	-0.03	**1.47**		**1.47**	0.00	0.11	0.03	0.08	-0.11
	-0.16	*0.06*	*0.00*	*0.03*	*0.11*	*0.00*	***1.36***		***1.36***	*0.00*	*0.11*	*0.03*	*0.06*	*-0.13*
COC_β	-0.11	0.08	0.00	0.05	0.08	0.27	**1.74**	**1.77**	0.27	0.27	0.16	0.11	0.14	-0.05
	-0.16	*0.06*	*0.00*	*0.06*	*0.08*	*0.27*	***1.63***	***1.66***	*0.25*	*0.25*	*0.14*	*0.11*	*0.11*	*-0.11*
COC_β*	-0.11	0.08	0.00	0.03	0.03	0.00	0.00	0.03	0.05	0.11	0.16	0.38	**1.96**	**1.80**
	-0.16	*0.06*	*0.00*	*0.00*	*0.00*	*0.00*	*0.03*	*0.03*	*0.06*	*0.11*	*0.17*	*0.36*	***1.83***	***1.66***
C=O	-0.11	0.08	0.03	0.05	0.14	0.14	0.54	**3.02**	0.54	0.14	0.14	0.05	0.11	-0.11
	-0.16	*0.06*	*0.03*	*0.03*	*0.11*	*0.11*	*0.49*	***2.72***	*0.49*	*0.11*	*0.14*	*0.03*	*0.08*	*-0.13*

$CNHC_{\alpha}$		CNH_2*		CNH_2		COC(=O)OC		O=COC=O		O=$CO^{\{-\}}$*		O=COH*		O=COC		C=O*	
-0.16	-0.11	*-0.16*	-0.11	*0.00*	0.08	*-0.16*	-0.11	*-0.16*	-0.11	*-0.16*	-0.11	*-0.16*	-0.11	*-0.08*	-0.03	*-0.16*	-0.11
0.03	0.05	*0.06*	0.05	*0.19*	0.27	*0.08*	0.11	*0.08*	0.11	*0.06*	0.05	*0.03*	0.08	*0.14*	0.19	*0.03*	0.05
0.00	0.00	*-0.02*	0.00	*0.17*	0.22	*0.08*	0.11	*0.08*	0.08	*0.00*	0.00	*-0.02*	0.00	*0.17*	0.19	*0.00*	0.00
0.00	0.00	*0.00*	0.00	*0.19*	0.24	*0.22*	0.24	*0.19*	0.24	*0.03*	0.00	*0.00*	0.03	*0.27*	0.30	*0.00*	0.00
0.06	0.05	*0.00*	0.00	*0.22*	0.27	*0.25*	0.24	*0.30*	0.33	*0.03*	0.03	*0.00*	0.03	*0.30*	0.33	*0.03*	0.03
0.00	0.00	*-0.02*	0.00	*0.14*	0.16	***1.80***	**1.93**	*0.85*	0.90	*0.06*	0.03	*0.03*	0.05	***1.74***	**1.90**	*0.03*	0.05
0.68	**0.73**	*0.00*	-0.03	***1.04***	**1.12**			***4.27***	**4.82**	*0.11*	0.05	*0.03*	0.08			*0.06*	0.05
		0.00	0.00	*0.03*	0.08	***4.87***	**5.58**			*0.14*	0.11	*0.06*	0.11	***3.76***	**4.30**	*0.11*	0.11
0.68	**0.73**	*0.00*	0.03	*-0.16*	-0.11			***4.27***	**4.82**	*0.22*	0.16	*0.11*	0.16	*0.55*	0.65	*0.17*	0.16
0.03	0.00	*0.00*	0.00	*-0.02*	0.00	***1.80***	**1.93**	*0.85*	0.93	*0.30*	0.24	*0.17*	0.22	*0.14*	0.19	*0.22*	0.24
0.06	0.05	*0.03*	0.03	*-0.02*	0.03	*0.25*	0.27	*0.30*	0.35	*0.52*	0.44	*0.33*	0.38	*0.11*	0.14	*0.36*	0.38
0.00	0.00	*0.06*	0.05	*0.00*	0.05	*0.22*	0.24	*0.22*	0.24	*0.76*	0.63	*0.41*	0.49	*0.00*	0.05	*0.63*	0.65
0.06	0.05	*0.00*	0.00	*0.06*	0.14	*0.17*	0.19	*0.11*	0.16	*1.28*	1.33	*1.06*	1.20	*0.06*	0.11	*0.63*	0.68
-0.16	-0.11	***0.79***	**0.84**	*-0.13*	-0.03	*-0.11*	-0.05	*-0.11*	-0.05	***4.25***	**4.93**	***4.06***	**4.60**	*-0.16*	-0.11	***2.81***	**3.10**

C=NH		$CNHNH_2$*		$CNHNH_2$		$CNH_3^{\{+\}}$*		$CNH_3^{\{+\}}$		CN(C)C				$CNHC_\beta$*		$CNHC_\beta$	
-0.16	-0.11	*-0.16*	-0.11	*-0.05*	0.05	*-0.16*	-0.11	*-0.16*	-0.11			*-0.13*	-0.03	*-0.16*	-0.11	*-0.16*	-0.11
0.06	0.08	*0.06*	0.05	*0.14*	0.22	*0.03*	0.08	*0.06*	0.11			*0.06*	0.14	*0.03*	0.05	*0.06*	0.05
-0.02	-0.03	*-0.02*	0.00	*0.06*	0.14	*0.00*	0.03	*0.06*	0.14			*0.00*	0.05	*-0.02*	0.00	*-0.02*	-0.03
0.03	0.03	*0.00*	0.00	*0.00*	0.08	*0.03*	0.03	*0.14*	0.22			*0.03*	0.08	*0.00*	0.00	*0.00*	0.00
-0.08	-0.08	*0.00*	-0.03	*-0.02*	0.03	*0.00*	0.05	*0.33*	0.44			*0.06*	0.11	*0.00*	0.00	*-0.02*	0.00
0.33	0.35	*0.00*	-0.03	*-0.16*	-0.11	*0.06*	0.08	*0.52*	0.68			*-0.02*	0.00	*0.00*	0.00	*0.08*	0.11
1.66	**1.85**	*0.00*	0.00	*-0.13*	-0.08	*0.08*	0.11	*0.90*	1.12			***0.74***	**0.79**	*0.03*	0.03	***1.04***	**1.06**
0.57	0.63	*0.00*	0.00	***1.04***	**1.12**	*0.11*	0.16	***2.45***	**2.86**	*Continued*				*0.06*	0.05	***1.04***	**1.09**
0.52	0.54	*0.00*	0.00	*0.14*	0.16	*0.19*	0.27	*0.90*	1.12	***0.68***	**0.76**	***0.74***	**0.79**	*0.06*	0.08	*0.38*	0.38
0.36	0.35	*0.00*	0.03	*0.41*	0.44	*0.27*	0.38	*0.52*	0.71	*-0.13*	-0.11	*-0.02*	0.00	*0.14*	0.14	*0.25*	0.27
0.27	0.27	*0.03*	0.03	*0.33*	0.38	*0.44*	0.60	*0.33*	0.44	*0.00*	0.05	*0.06*	0.11	*0.17*	0.19	*0.19*	0.19
0.22	0.22	*0.08*	0.08	*0.30*	0.35	*0.68*	0.90	*0.14*	0.22	*-0.02*	0.03	*0.03*	0.08	*0.36*	0.38	*0.14*	0.16
0.22	0.24	*0.06*	0.05	*0.33*	0.41	*1.09*	1.33	*0.11*	0.19	*0.03*	0.11	*0.06*	0.14	***1.09***	**1.14**	*0.17*	0.19
0.00	0.05	***0.66***	**0.71**	*0.11*	0.22	***2.40***	**2.86**	*-0.13*	-0.05	*-0.16*	-0.05	*-0.13*	-0.03	***0.90***	**0.95**	*-0.05*	0.00

C≡N*		C≡N		HN=CNH$_2$*		HN=CNHC		C=NNH$_2$*		C=NNH$_2$		C=NN=C		C=NC		C=NH*	
-0.16	-0.11	*-0.16*	-0.11	*-0.16*	-0.11	*-0.16*	-0.11	*-0.16*	-0.11	*-0.16*	-0.11	*-0.16*	-0.11	*-0.13*	-0.05	*-0.16*	-0.11
0.06	0.08	*0.06*	0.05	*0.06*	0.08	*0.03*	0.05	*0.03*	0.05	*0.03*	0.05	*0.06*	0.11	*0.08*	0.14	*0.03*	0.08
0.03	0.03	*0.03*	0.05	*0.00*	0.00	*-0.08*	-0.05	*-0.02*	0.00	*-0.05*	-0.03	*0.08*	0.11	*0.06*	0.11	*-0.02*	0.00
0.03	0.05	*0.08*	0.11	*0.00*	0.03	*-0.02*	0.00	*-0.02*	-0.03	*-0.02*	0.00	*0.22*	0.24	*0.14*	0.16	*0.00*	0.03
0.06	0.05	*0.19*	0.19	*0.03*	0.03	*-0.13*	-0.11	*-0.02*	0.00	*-0.13*	-0.11	*0.30*	0.33	*0.25*	0.30	*0.00*	0.03
0.08	0.08	*0.30*	0.30	*0.03*	0.03	*0.36*	0.44	*0.00*	0.00	*0.25*	0.30	***1.25***	**1.41**	*0.25*	0.30	*0.03*	0.05
0.11	0.14	*0.68*	0.76	*0.06*	0.05	***2.15***	**2.53**	*0.00*	0.00	***1.12***	**1.36**			***1.31***	**1.50**	*0.03*	0.08
0.17	0.19	*1.66*	1.80	*0.08*	0.08			*0.00*	0.00	*0.46*	0.49					*0.08*	0.11
0.25	0.27	*0.68*	0.76	*0.11*	0.14	***1.44***	**1.50**	*0.03*	0.05	*0.52*	0.54	***1.25***	**1.41**	***0.79***	**0.87**	*0.11*	0.16
0.36	0.38	*0.27*	0.33	*0.17*	0.19	*0.66*	0.63	*0.06*	0.08	*0.33*	0.35	*0.30*	0.33	*0.00*	0.00	*0.17*	0.22
0.57	0.60	*0.19*	0.22	*0.25*	0.30	*0.49*	0.46	*0.08*	0.14	*0.27*	0.27	*0.22*	0.24	*0.06*	0.08	*0.30*	0.33
0.87	0.93	*0.08*	0.11	*0.38*	0.44	*0.36*	0.35	*0.19*	0.24	*0.22*	0.22	*0.08*	0.14	*0.00*	0.03	*0.46*	0.52
1.69	1.82	*0.08*	0.11	*0.63*	0.71	*0.33*	0.33	*0.25*	0.33	*0.22*	0.24	*0.06*	0.11	*0.03*	0.08	*0.60*	0.68
1.31	**1.41**	*-0.13*	-0.08	***2.23***	**2.61**	*0.08*	0.14	***1.01***	**1.25**	*0.00*	0.05	*-0.16*	-0.11	*-0.16*	-0.11	***1.53***	**1.74**

CN=O		C=NOC		C=NOH*		C=NOH		$CONH_2$*		$CONH_2$		CNHOC		CNHOH*		CNHOH	
-0.16	-0.11	*-0.13*	-0.05	*-0.16*	-0.11	*-0.13*	-0.08	*-0.16*	-0.11	*-0.16*	-0.11	*-0.13*	-0.11	*-0.16*	-0.11	*-0.13*	-0.05
0.06	0.08	*0.08*	0.16	*0.03*	0.05	*0.08*	0.11	*0.06*	0.05	*0.06*	0.05	*0.06*	0.09	*0.03*	0.05	*0.08*	0.14
0.03	0.05	*0.06*	0.14	*-0.02*	0.00	*0.03*	0.05	*0.00*	0.00	*0.00*	0.00	*0.03*	0.03	*-0.02*	0.00	*0.03*	0.05
0.08	0.08	*0.17*	0.30	*0.00*	0.00	*0.06*	0.08	*0.00*	0.03	*0.00*	-0.03	*0.08*	0.08	*-0.02*	-0.03	*0.00*	0.05
0.17	0.16	*0.36*	0.44	*0.00*	0.00	*0.11*	0.11	*0.00*	-0.03	*0.00*	0.00	*0.00*	-0.03	*0.00*	0.00	*0.03*	0.05
0.25	0.24	***1.12***	**1.39**	*0.00*	0.03	*0.22*	0.22	*0.00*	0.00	*0.00*	-0.03	***0.82***	**0.87**	*0.00*	-0.03	*-0.05*	0.00
0.52	0.52			*0.03*	0.03	*0.36*	0.38	*0.00*	0.00	*-0.02*	-0.03			*0.00*	0.00	*0.17*	0.16
1.25	**1.36**			*0.06*	0.05	***1.31***	**1.55**	*0.00*	0.03	***1.39***	**1.47**			*0.00*	0.03	***1.06***	**1.12**
0.55	0.52	***1.39***	**1.50**	*0.08*	0.08	*0.44*	0.49	*0.03*	0.00	*0.00*	-0.03	***1.25***	**1.36**	*0.03*	0.03	*0.11*	0.11
0.25	0.24	*-0.02*	-0.05	*0.11*	0.14	*0.00*	0.00	*0.03*	0.03	*0.00*	-0.03	*-0.08*	-0.08	*0.06*	0.05	*-0.11*	-0.11
0.17	0.16	*0.11*	0.11	*0.19*	0.22	*0.06*	0.05	*0.06*	0.05	*-0.08*	0.00	*0.08*	0.08	*0.11*	0.11	*-0.02*	0.00
0.08	0.08	*0.03*	0.03	*0.33*	0.38	*0.00*	0.00	*0.08*	0.14	*0.00*	0.00	*0.00*	0.03	*0.19*	0.19	*-0.05*	-0.03
0.08	0.11	*0.06*	0.08	*0.52*	0.57	*0.06*	0.08	*0.14*	0.05	*0.03*	0.05	*0.06*	0.08	*0.25*	0.24	*0.03*	0.08
-0.13	-0.08	*-0.16*	-0.11	***1.28***	**1.50**	*-0.16*	-0.11	***1.31***	**1.41**	*-0.16*	-0.11	*-0.16*	-0.11	***0.85***	**0.90**	*-0.16*	-0.08

	CN=O*		O=CNHC		$O=CNH_2$*		O=CNHC=O		O=CN(OH)C		O=CN(OH)H*		COC(=O)NHC		$COC(=O)NH_2$*	
	-0.11	*-0.16*	-0.11	*-0.16*	-0.11	*-0.16*	-0.11	*-0.16*	-0.11	*-0.16*	-0.11	*-0.16*	-0.11	*-0.11*	-0.11	*-0.16*
	0.08	*0.03*	0.08	*0.06*	0.08	*0.06*	0.11	*0.08*	0.08	*0.06*	0.08	*0.03*	0.05	*0.11*	0.08	*0.06*
	0.00	*-0.02*	0.03	*0.00*	0.00	*0.00*	0.08	*0.06*	0.03	*0.00*	0.03	*-0.02*	0.08	*0.11*	0.00	*0.00*
	0.03	*0.00*	0.11	*0.08*	0.00	*0.00*	0.22	*0.19*	0.11	*0.06*	0.03	*0.00*	0.16	*0.22*	0.03	*0.00*
	0.03	*0.00*	0.11	*0.11*	0.03	*0.00*	0.27	*0.22*	0.08	*0.03*	0.05	*0.00*	0.19	*0.22*	0.03	*0.03*
	0.05	*0.03*	0.54	*0.44*	0.00	*0.00*	0.87	*0.79*	0.57	*0.46*	0.05	*0.03*	**1.77**	***1.63***	0.05	*0.03*
	0.08	*0.06*	**3.40**	***2.91***	0.03	*0.00*	**4.00**	***3.54***	**3.73**	***3.19***	0.08	*0.06*			0.08	*0.06*
	0.11	*0.08*			0.03	*0.00*					0.11	*0.08*	**4.71**	***4.14***	0.11	*0.08*
	0.14	*0.11*	**1.22**	***1.17***	0.05	*0.03*	**4.00**	***3.54***	**1.25**	***1.23***	0.16	*0.14*			0.19	*0.17*
	0.22	*0.19*	0.46	*0.46*	0.08	*0.06*	0.87	*0.79*	0.35	*0.38*	0.24	*0.19*	**1.20**	***1.28***	0.30	*0.27*
	0.30	*0.27*	0.30	*0.30*	0.16	*0.14*	0.27	*0.22*	0.27	*0.30*	0.41	*0.33*	0.30	*0.11*	0.33	*0.30*
	0.49	*0.46*	0.22	*0.22*	0.19	*0.14*	0.22	*0.19*	0.22	*0.22*	0.60	*0.49*	0.19	*0.11*	**1.88**	***1.74***
	0.71	*0.68*	0.19	*0.19*	0.71	*0.60*	0.14	*0.11*	0.19	*0.19*	1.03	*0.93*	0.16	*0.08*		
	1.41	***1.25***	0.00	*-0.05*	**3.70**	***3.21***	-0.05	*-0.11*	0.00	*-0.02*	**4.11**	***3.51***	-0.08	*-0.16*	**5.03**	***4.38***

Appendix D5 – Calculated ΔCEBEs of the tocopherol-like components

Table D5a. Simplified chemical structure of α-tocopherol, showing carbon (**black**) and oxygen (**red**) atoms. The numbers refer to the ΔCEBEs (in eV), the carbon-based components are relative to the averaged [CH_2] of the PE model structure (i.e., [CH_{PE}]) and all oxygen-based components are relative to the centred hydroxyl (i.e., [COH]), as calculated by HF (normal) and wB97X-D (*italic*).

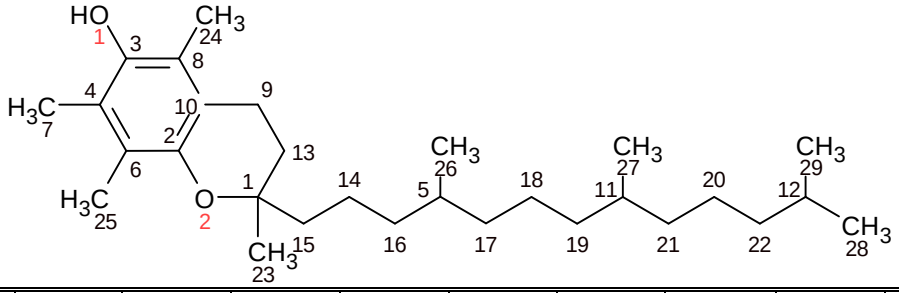
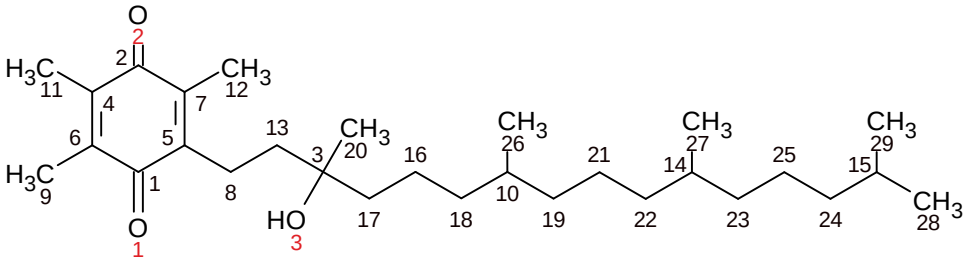
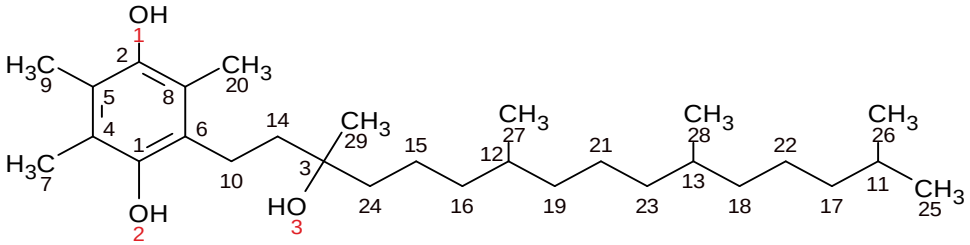
α-Tocopherol **[αTH]**											
1	**2**	**3**	**4**	**5**	**6**	**7**	**8**	**9**	**10**	**11**	**12**
2.12	1.80	1.50	0.60	0.46	0.46	0.38	0.38	0.35	0.33	0.27	0.24
2.10	*1.61*	*1.61*	*0.46*	*0.38*	*0.38*	*0.36*	*0.36*	*0.36*	*0.33*	*0.33*	*0.30*
13	**14**	**15**	**16**	**17**	**18**	**19**	**20**	**21**	**22**	**23**	**24**
0.19	0.16	0.16	0.16	0.08	0.08	0.08	0.05	0.05	0.03	0.00	-0.03
0.30	*0.22*	*0.19*	*0.14*	*0.06*	*0.06*	*0.03*	*0.03*	*0.00*	*0.00*	*-0.02*	*-0.08*
25	**26**	**27**	**28**	**29**	**1**	**2**					
-0.03	-0.03	-0.08	-0.08	-0.11	0.54	0.27					
-0.08	*-0.08*	*-0.13*	*-0.13*	*-0.16*	*0.63*	*0.46*					

Table D5b. Simplified chemical structure of α-tocopherol quinone, showing carbon (**black**) and oxygen (**red**) atoms. The numbers refer to the ΔCEBEs (in eV), the carbon-based components are relative to the averaged [CH_2] of the PE model structure (i.e., [CH_{PE}]) and all oxygen-based components are relative to the centred hydroxyl (i.e., [COH]), as calculated by HF (normal) and wB97X-D (*italic*).

α-Tocopheryl quinone **[αTQ]**											
1	**2**	**3**	**4**	**5**	**6**	**7**	**8**	**9**	**10**	**11**	**12**
3.59	3.48	2.12	1.47	1.41	1.41	1.36	0.71	0.52	0.46	0.46	0.41
3.21	*3.13*	*2.04*	*1.34*	*1.34*	*1.34*	*1.28*	*0.71*	*0.44*	*0.41*	*0.41*	*0.38*
13	**14**	**15**	**16**	**17**	**18**	**19**	**20**	**21**	**22**	**23**	**24**
0.35	0.35	0.33	0.27	0.19	0.16	0.16	0.11	0.08	0.05	0.05	0.05
0.38	*0.33*	*0.30*	*0.27*	*0.19*	*0.19*	*0.08*	*0.06*	*0.06*	*0.06*	*0.03*	*0.03*
25	**26**	**27**	**28**	**29**	**1**	**2**	**3**				
0.03	-0.03	-0.08	-0.08	-0.11	0.24	0.22	0.05				
0.00	*-0.05*	*-0.13*	*-0.16*	*-0.16*	*0.22*	*0.14*	*0.03*				

Continued on the next page…

Table D5c. Simplified chemical structure of α-tocopheryl hydroquinone, showing carbon (**black**) and oxygen (**red**), and hydrogen (light grey). The numbers refer to the ΔCEBEs, the carbon-based components are relative to the averaged [CH_2] of the PE model structure (i.e., [CH_{PE}]) (**black**) atoms and all oxygen-based components are relative to the centred hydroxyl (i.e., [COH]), as calculated by HF (normal) and wB97X-D (*italic*).

α-Tocopheryl hydroquinone **[αTHQ]**	

1	**2**	**3**	**4**	**5**	**6**	**7**	**8**	**9**	**10**	**11**	**12**
2.15	2.15	1.93	0.93	0.87	0.84	0.82	0.76	0.71	0.54	0.46	0.41
1.99	*1.96*	*1.85*	*0.85*	*0.82*	*0.76*	*0.74*	*0.71*	*0.68*	*0.52*	*0.46*	*0.44*
13	**14**	**15**	**16**	**17**	**18**	**19**	**20**	**21**	**22**	**23**	**24**
0.41	0.22	0.16	0.16	0.16	0.14	0.14	0.14	0.11	0.11	0.11	0.03
0.44	*0.27*	*0.19*	*0.17*	*0.17*	*0.17*	*0.17*	*0.14*	*0.14*	*0.14*	*0.14*	*0.06*
25	**26**	**27**	**28**	**29**	**1**	**2**	**3**				
0.03	0.00	0.00	0.00	-0.11	1.03	0.84	-0.33				
0.00	*0.00*	*0.00*	*0.00*	*-0.16*	*1.14*	*0.90*	*-0.33*				

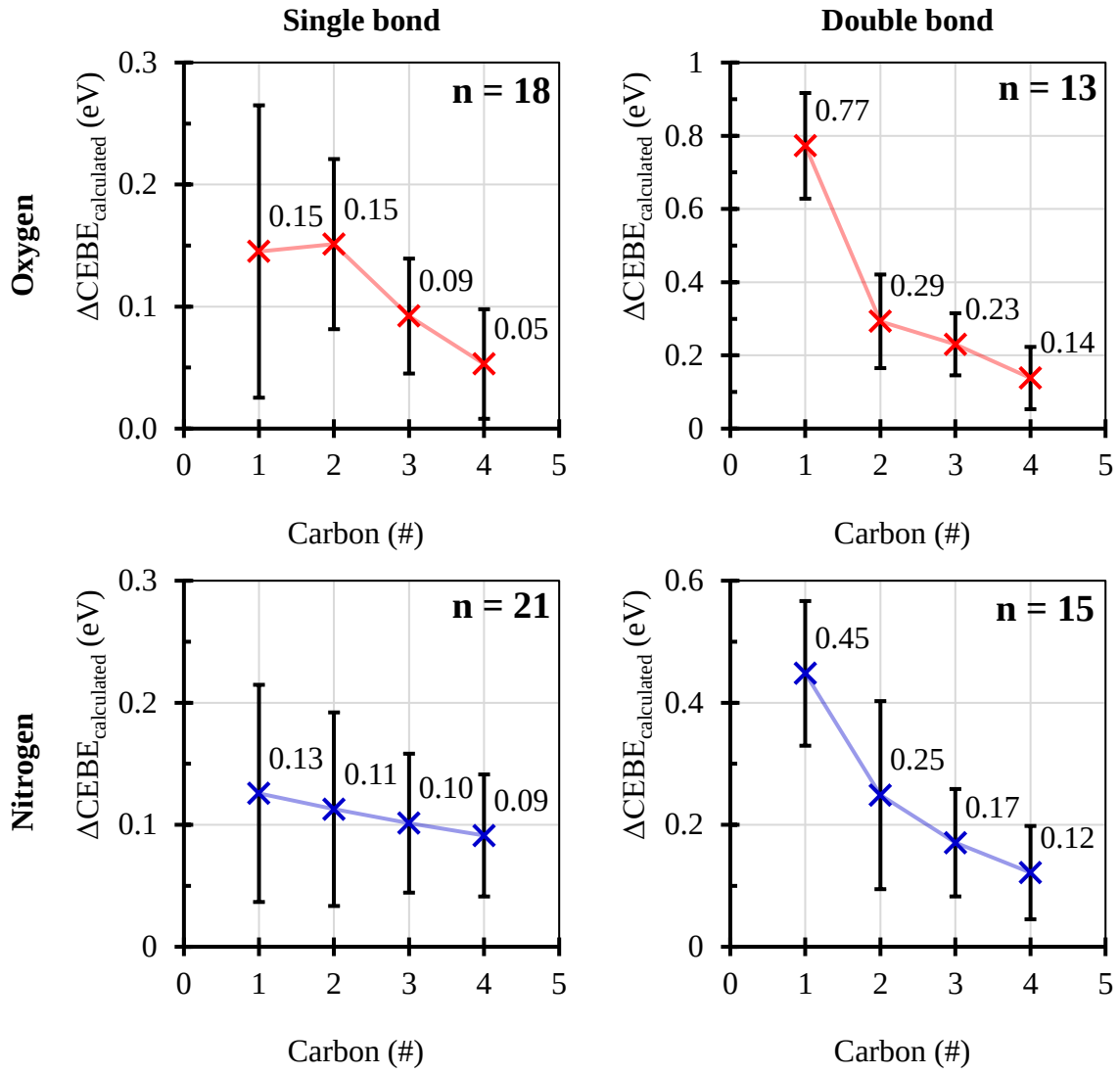
Appendix D6 – ΔCEBE deviations between centred and end-chain positioning

Table D6. ΔCEBE deviations between centred and end-chain positioning, relative to the respective ΔCEBE of the centred functionality, as calculated by HF (normal) and wB97X-D (*italic*).

ID	C 1s (eV)		N 1s (eV)		O 1s (eV)	
	1	2	1	2	1	2
COH	-0.16				0.00	
	-0.22				*0.00*	
COC_{β}	0.19	0.05			0.22	
	0.16	*0.03*			*0.19*	
C=O	0.08				0.38	
	0.08				*0.38*	
O=COR	0.30				0.41	0.16
	0.30				*0.27*	*0.14*
CNH_2	-0.27		-0.05			
	-0.24		*-0.03*			
$CNHC_{\beta}$	0.05	-0.11	0.05			
	0.05	*-0.14*	*0.03*			
$CNH_3^{\{+\}}$	0.00		0.27			
	-0.05		*0.24*			
$CNHNH_2$	-0.41		-0.22	-0.19		
	-0.38		*-0.14*	*-0.22*		
C≡N	0.03	-0.14	-0.16			
	0.03	*0.16*	*0.08*			
C=NH	-0.11		0.27			
	-0.14		*0.22*			
$C=NNH_2$	-0.11		0.35	0.08		
	-0.11		*0.19*	*0.24*		
HN=CNHR	0.08		-0.24	0.11		
	0.08		*-0.30*	*0.05*		
CNHOH	-0.22		0.00		-0.08	
	-0.22		*0.00*		*-0.05*	
$CONH_2$	-0.05		0.00		0.19	
	-0.08		*0.00*		0.11	
C=NOH	-0.05		0.38		0.14	
	-0.03		*0.35*		*0.11*	
CN=O	0.05		0.19		0.14	
	0.00		*0.16*		*0.08*	
O=CNHR	0.30		0.11		0.27	
	0.30		*0.03*		*0.24*	
O=CN(OH)R	0.38		0.33		-0.27	0.41
	0.33		*0.30*		*-0.30*	*0.38*
COC(=O)NHR	0.33	0.19	0.24		0.27	0.27
	0.27	*0.14*	*0.11*		*0.19*	*0.19*

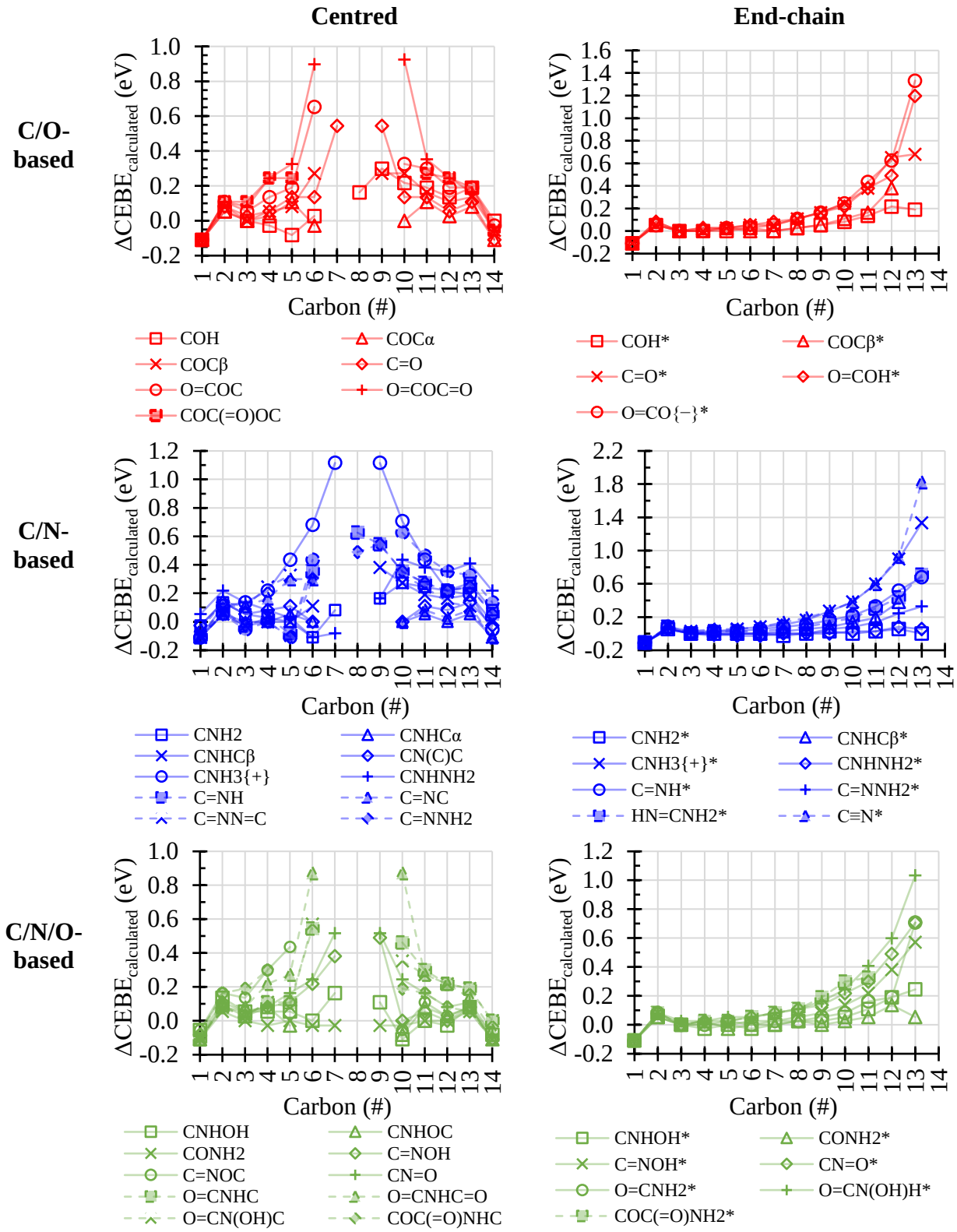
Appendix D7 – Mean influence of carbon-oxygen/nitrogen functionalities on the ΔCEBEs of the PE carbon backbone calculated with HF

Figure D7. Mean secondary (x=1), tertiary (x=2), quaternary (x=3) and quinary (x=4) carbon ΔCEBEs for [CH_2] groups in the vicinity of carbon-oxygen and carbon-nitrogen functionalities, calculated with 'HF' relative to [CH_{PE}]. Values are separated by atom type and bond type, error analysis with α = 0.01 and n as shown per group.



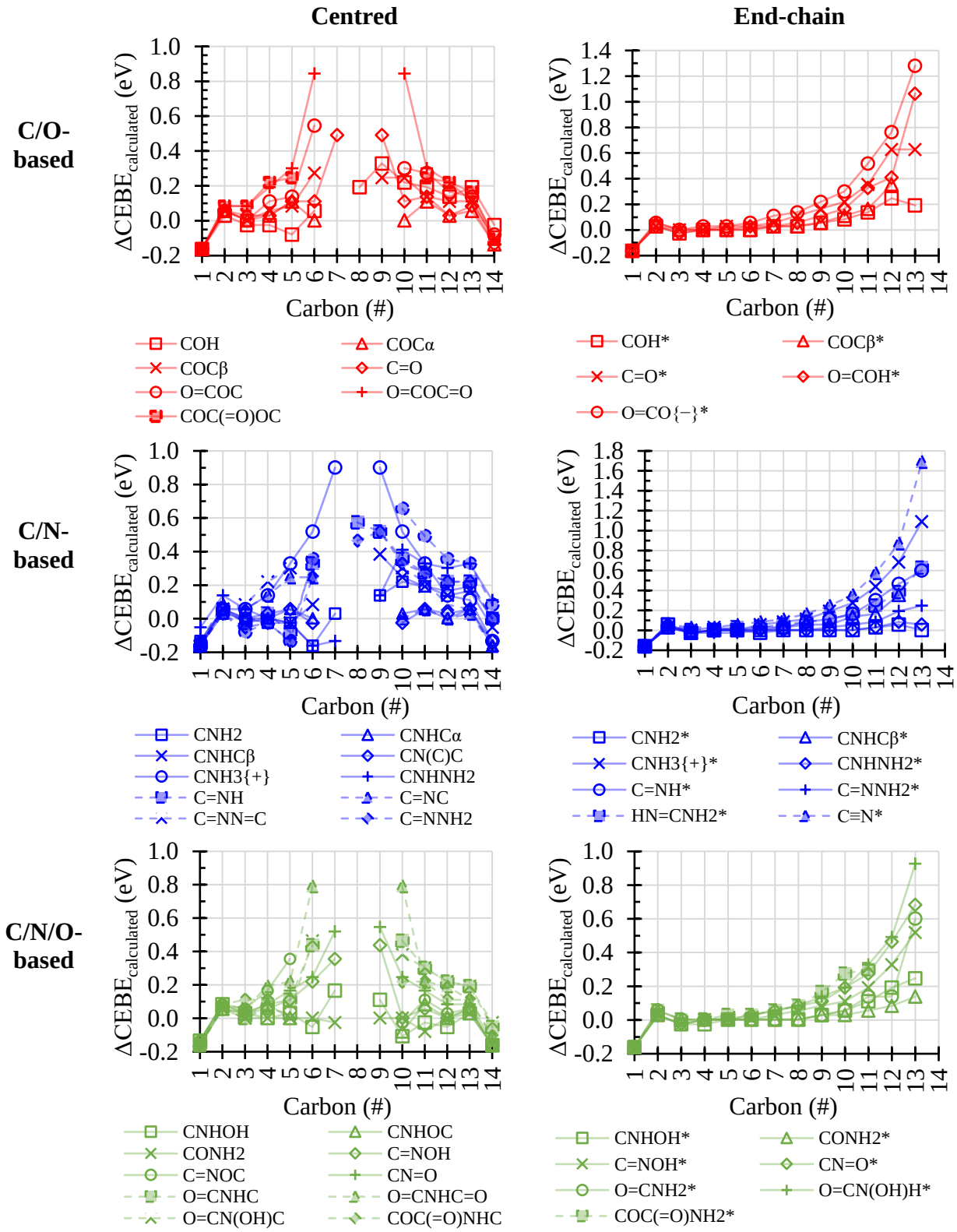
Appendix D8 – Individual influence of carbon-oxygen/nitrogen functionalities on the ΔCEBEs of the PE carbon backbone calculated with HF

Figure D8. Carbon ΔCEBEs for [CH_2] groups in the vicinity of oxygen and/or nitrogen containing functional groups, calculated with 'HF' relative to [CH_{PE}]. The number (#) represents the position in the model structure, primary carbon ΔCEBEs are omitted.



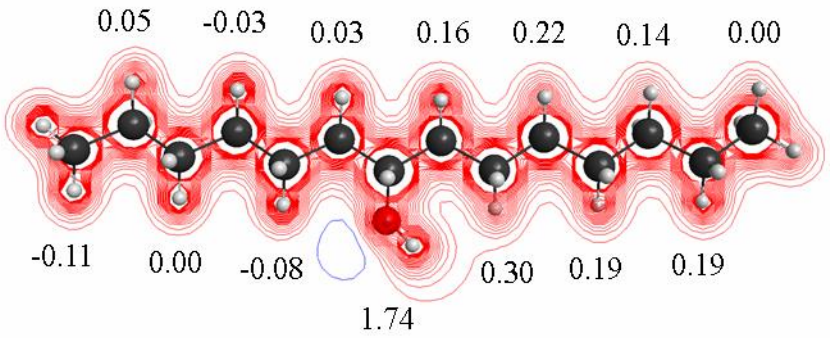
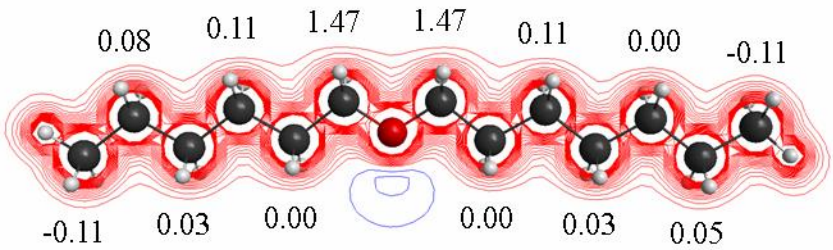
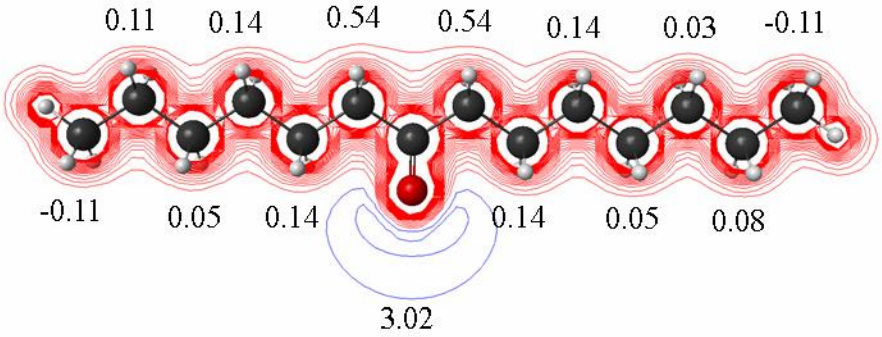
Appendix D9 – Individual influence of carbon-oxygen/nitrogen functionalities on the ΔCEBEs of the PE carbon backbone calculated with wB97X-D

Figure D9. Carbon ΔCEBEs for [CH_2] groups in the vicinity of oxygen and/or nitrogen containing functional groups, calculated with 'wB97X-D' relative to [CH_{PE}]. The number (#) represents the position in the model structure, primary carbon ΔCEBEs are omitted.



Appendix D10 – Two-dimensional molecular electrostatic potential contour maps

Figure D10. Examples of 3D model structures showing carbon (**black**), oxygen (**red**), and hydrogen (light grey) atoms, including their 2D molecular electrostatic potential contours showing the negative (**red**) and positive (**blue**) potential contours. The numbers refer to the carbon ΔCEBEs relative to [CH_{PE}] as calculated by HF.

ID	3D Model structure
COH	
COC_{α}	
C=O	

Appendix D11 – Origin of the reference data within the Beamson and Briggs database

Table D11. Origin of data within the Beamson and Briggs reference database (Hantsche, 1993).

ID	C1s	N1s	O1s
COH	Appendix 1	-	Appendix 3.1
COC	Appendix 1	-	Appendix 3.1
C=O	Appendix 1	-	Appendix 3.1
O=COC	Appendix 1	-	Appendix 3.1
O=COH	Appendix 1	-	Appendix 3.1
O=COC=O	Appendix 1	-	Appendix 3.1
COC(=O)OC	Appendix 1	-	Appendix 3.1
CNH_2	Appendix 1	-	-
CNHC	-	Polyethyleneimine	-
C≡N	Poly(acrylonitrile) + Poly(methacrylonitrile)		-
O=CNHC	Nylon 6 + Nylon 6,6 + Nylon 12		
O=CNH2	Poly(methacrylamide) + Poly(acrylamide)		
O=CNHC=O	Kapton HN + Ultem 1000™		

Appendix D12 – CEBEs used in the linear correlation fits for the C 1s region

Table D12. The calculated and experimental CEBEs for the C 1s region used for the linear correlation fits.

	ID	HF				wB97X-D			
		CEBE (eV)		ΔCEBE (eV)		CEBE (eV)		ΔCEBE (eV)	
		1	2	1	2	1	2	1	2
C 1s	CH_2	304.97		0.00		279.45		0.00	
	COH	306.71		1.74		281.11		1.66	
	COC	306.44		1.47		280.81		1.36	
	C=O	307.99		3.02		282.17		2.72	
	$O=C^1OC^2$	309.27	306.87	4.30	1.90	283.21	281.19	3.76	1.74
	O=COH	309.57		4.60		283.51		4.06	
	O=COC=O	309.79		4.82		283.72	279.45	4.27	
	$C^2OC^1(=O)OC^2$	310.55	306.90	5.58	1.93	284.32	281.25	4.87	1.80
	CNH_2	306.09		1.12		280.49		1.04	
	C≡N †	306.77	306.52	1.80	1.55	281.14	280.76	1.69	1.31
	$O=C^1NHC^2$	308.37	306.19	3.40	1.22	282.36	280.62	2.91	1.17
	$O=CNH_2$*	308.67		3.70		282.66		3.21	
	O=CNHC=O	308.97		4.00		282.99		3.54	

	ID	Experimental (Hantsche, 1993)							
		$CEBE_{mean}$ (eV)		ΔCEBE (eV)					
		1	2	1			2		
				min	mean	max	min	mean	max
C 1s	CH_2	285			0.00				
	COH	286.55		1.47	1.55	1.73			
	COC	286.45		1.13	1.45	1.75			
	C=O	287.9		2.81	2.90	2.97			
	$O=C^1OC^2$	288.99	286.64	3.64	3.99	4.23	1.12	1.64	1.98
	O=COH	289.26		4.18	4.26	4.33			
	O=COC=O	289.41		4.36	4.41	4.46			
	$C^2OC^1(=O)OC^2$	290.35	286.76		5.35			1.76	
	CNH_2	285.94		0.56	0.94	1.41			
	C≡N	286.74	286.41	1.73	1.74	1.74	1.35	1.41	1.46
	$O=C^1NHC^2$	288.00	285.97	2.97	3.00	3.02	0.90	0.97	1.02
	$O=CNH_2$*	288.45		3.30	3.45	3.59			
	O=CNHC=O	288.55		3.49	3.55	3.61			

† Both the primary and secondary carbon CEBEs are evaluated due to their relatively high shifts.

Appendix D13 – CEBEs used in the linear correlation fits for the N 1s region

Table D13. The calculated and experimental CEBEs for the N 1s region used for the linear correlation fits.

	ID	HF		wB97X-D	
		CEBE (eV)	ΔCEBE (eV)	CEBE (eV)	ΔCEBE (eV)
N 1s	CNHC	422.60	0.00	392.22	0.00
	C≡N	423.39	0.79	392.57	0.35
	O=CNHC	423.82	1.22	393.44	1.22
	$O=CNH_2$*	423.93	1.33	393.47	1.25
	O=CNHC=O	424.56	1.96	394.07	1.85
	ID	**Experimental (Hantsche, 1993)**			
		$CEBE_{mean}$ (eV)	ΔCEBE (eV)		
			min	mean	max
	CNHC	399.07		0	
	C≡N	399.57	0.50	0.50	0.50
	O=CNHC	399.81	0.70	0.74	0.77
	$O=CNH_2$*	399.90	0.76	0.82	0.89
	O=CNHC=O	400.50	1.33	1.43	1.53

Appendix D14 – CEBEs used in the linear correlation fits for the O 1s region

Table D14. The calculated and experimental CEBEs for the O 1s region used for the linear correlation fits.

	ID	HF				wB97X-D			
		CEBE (eV)		ΔCEBE (eV)		CEBE (eV)		ΔCEBE (eV)	
		1	2	1	2	1	2	1	2
O 1s	COH	559.17		1.17		523.78		1.17	
	COCα	559.04		1.03		523.75		1.14	
	C=O	558.93		0.93		523.48		0.87	
	$O^2=CO^1C$	560.37	558.79	2.37	0.79	524.98	523.37	2.37	0.76
	$O^2=CO^1C=O^2$	560.94	559.34	2.94	1.33	525.44	523.89	2.83	1.28
	$CO^1C(=O^2)O^1C$	560.45	558.66	2.45	0.65	525.06	523.29	2.45	0.68
	O=CNHC	558.00		0.00		522.61		0.00	
	$O=CNH_2$*	558.28		0.27		522.86		0.24	
	O=CNHC=O	558.68		0.68		523.29		0.68	
	ID	**Experimental (Hantsche, 1993)**							
		$CEBE_{mean}$ (eV)		ΔCEBE (eV)					
		1	2	1			2		
				min	mean	max	min	mean	max
	COH	532.89		1.39	1.54	1.74			
	COCα	532.64		1.12	1.29	1.48			
	C=O	532.33		0.95	0.98	1.02			
	$O^2=CO^1C$	533.59	532.21	1.89	2.24	2.51	0.61	0.86	1.08
	$O^2=CO^1C=O^2$	533.91	532.64	2.51	2.56	2.67	1.17	1.29	1.46
	$CO^1C(=O^2)O^1C$	533.88	532.44		2.53			1.09	
	O=CNHC	531.35		-0.02	0	0.02			
	$O=CNH_2$*	531.55		0.19	0.20	0.22			
	O=CNHC=O	531.95	531.95	0.52	0.60	0.68			

Appendix D15 – Comparison of the calculated C 1s ΔCEBEs to the literature

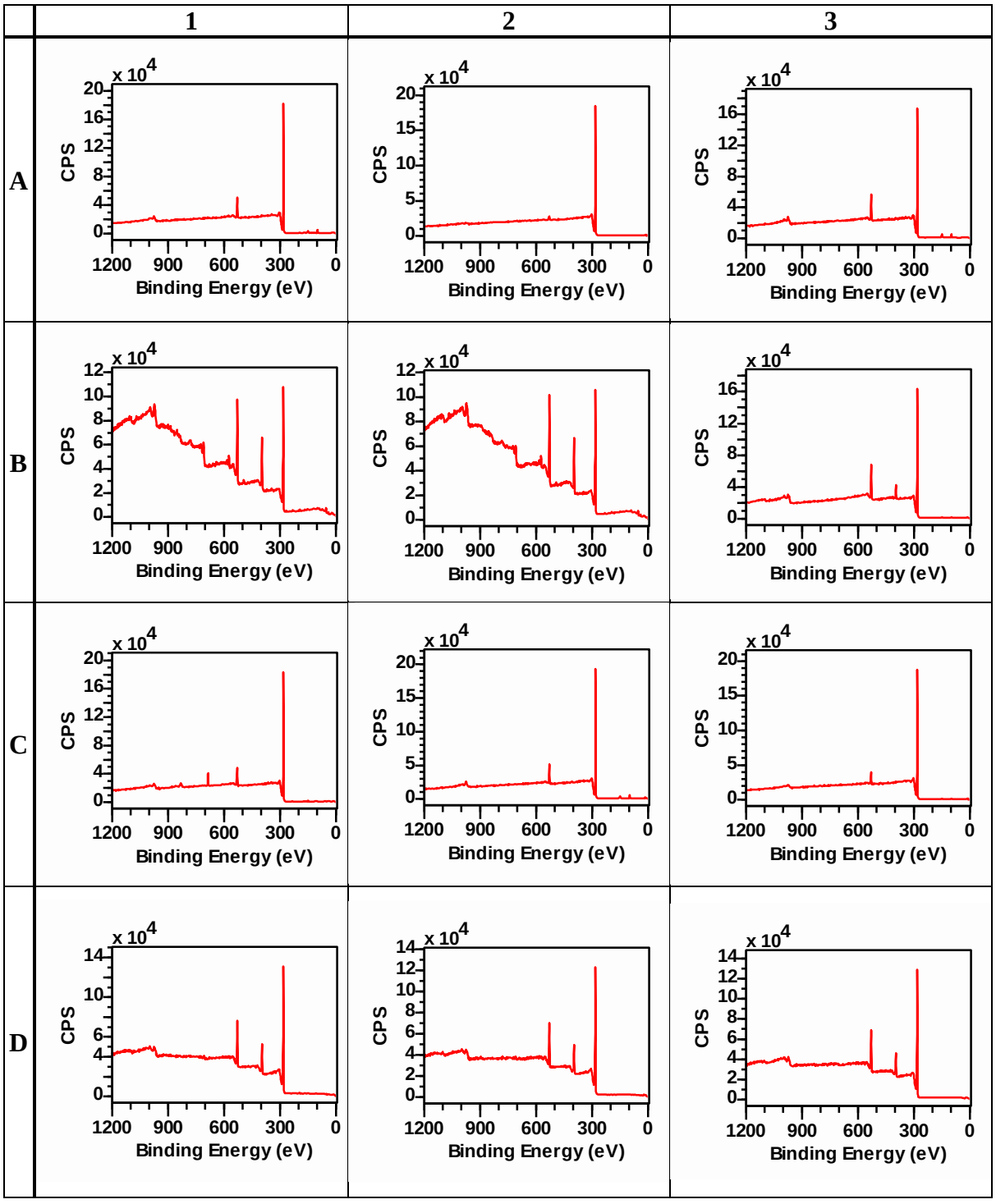
Table D15. Comparison of the calculated C 1s ΔCEBEs from this work to the literature, showing the mean absolute difference (MAD).

ID	Literature (Giesbers et al., 2013)			HF			wB97X-D		
COH*	1.2			1.6			1.4		
COC	1.5	1.6		1.5	1.5		1.4	1.4	
COC_{β}*	1.9	1.7		2.0	1.8		1.8	1.7	
CO*	0.6	3.0		0.7	3.1		0.6	2.8	
O=COH	0.9	4.3		1.2	4.6		1.1	4.1	
C(=O)NHC	0.3	3.0	1.1	0.5	3.4	1.2	0.4	2.9	1.2

ID	$\Delta_{HF - Literature}$			$\Delta_{wB97X-D - Literature}$		
COH*	0.4			0.2		
COC	0.0	-0.1		-0.1	-0.2	
COC_{β}*	0.1	0.1		-0.1	0.0	
CO*	0.1	0.1		0.0	-0.2	
O=COH	0.3	0.3		0.2	-0.2	
C(=O)NHC	0.2	0.4	0.1	0.1	-0.1	0.1
	MAD	0.2		**MAD**	0.1	

Appendix D16 – XPS survey spectra of the various UHMWPE-based samples

Figure D16. XPS survey spectra of UHMWPE undoped and untreated (UD/UT; A1-3), undoped and plasma-treated (UD/PT; B1-3), doped and untreated (D/UT; C1-3), and doped and plasma-treated (D/PT; D1-3).



Appendix D17 – Region maxima in the survey spectra after energy calibration

Table D17. Region maxima in the survey spectra after energy calibration of UHMWPE UD/UT (A1-3), UD/PT (B1-3), D/UT (C1-3), and D/PT (D1-3).

	Region maximum (eV)				
	C 1s	**N 1s**	**O 1s**	**Contaminants**	
A1	284.8	399.8	531.8	Si $2p_{3/2}$ (Si 2s)	101.8 (152.8)
				F 1s	688.8
A2	284.8		531.8	-	
A3	284.8	398.8	531.8	Si $2p_{3/2}$ (Si 2s)	101.8 (152.8)
B1	284.8	398.8	531.8	Fe $2p_{3/2}$ (Fe 3p)	710.8 (55.8)
				Cr $2p_{3/2}$ (Cr 3p)	576.8 (43.8)
				Mo $3d_{5/2}$	231.8
				Na 1s	1071.8
				Cl $2p_{3/2}$	198.8
B2	284.8	398.8	531.8	Fe $2p_{3/2}$ (Fe 3p)	710.8 (55.8)
				Cr $2p_{3/2}$ (Cr 3p)	576.8 (43.8)
				Mo $3d_{5/2}$	231.8
				Na 1s	1071.8
				Cl $2p_{3/2}$	198.8
B3	284.8	399.8	531.8	Si $2p_{3/2}$ (Si 2s)	101.8 (152.8)
C1	284.8	-	531.8	F 1s	688.8
				Si $2p_{3/2}$ (Si 2s)	101.8 (152.8)
C2	284.8	-	531.8	Si $2p_{3/2}$ (Si 2s)	101.8 (152.8)
				Al $2p_{3/2}$ (Al 2s)	73.8 (118.8)
C3	284.8	-	532.8	Si $2p_{3/2}$ (Si 2s)	101.8 (152.8)
D1	284.8	398.8	531.8	-	
D2	284.8	399.8	531.8	-	
D3	284.8	399.8	531.8	-	

Appendix D18 – Reference-based BEs used to identify the minor contaminants

Table D18. Mean BEs for various components as observed in the NIST database (NIST, 2008) – including the observed average deviation (Δ) and number of references (No.).

	1s			**1s**		
	BE	**Δ**	**No.**	**BE**	**Δ**	**No.**
CH_2CHF	689.10	0.00	2	285.72 / 287.86	0.02 / 0.06	z2 / 2
CH_2CF_2	688.78	0.63	2	286.34 / 290.80	0.22 / 0.20	5 / 4
CF_2CF_2	689.89	0.29	5	292.26	0.35	9
Na	1071.65	0.17	3			
[Na]Cl	1071.91	0.47	8			
	$2p_{3/2}$			**2s**		
	BE	**Δ**	**No.**	**BE**	**Δ**	**No.**
Al	72.88	0.06	5	118.05	0.08	6
Al_2O_3	74.01	0.19	10	119.02	0.22	11
Na[Cl]	198.58	0.33	4			

Appendix D19 – Reference-based BEs used to identify the silicon contaminants

Table D19. Mean BEs for various Si components as observed in the NIST database (NIST, 2008)(NIST, 2008) – including the observed average deviation (Δ) and number of references (No.).

	$2p_{3/2}$			**2s**		
	BE	**Δ**	**No.**	**BE**	**Δ**	**No.**
Si	99.40	0.20	48	150.62	0.10	5
SiC	100.80	0.30	8	151.70	-	1
$Si(CH_3)_2O$	102.15	0.30	6	153.20	-	1
SiO2	103.49	0.19	39	154.61	0.20	17
Si_3N_4	101.91	0.24	14			

Appendix D20 – Reference-based BEs used to identify the chromium contaminants

Table D20. Mean BEs for various Cr components as observed in the NIST database (NIST, 2008)(NIST, 2008) – including the observed average deviation (Δ) and number of references (No.).

	$2p_{3/2}$			2s			3p			3s		
	BE	**Δ**	**No.**	**BE**	**Δ**	**No.**	**BE**	**Δ**	**No.**	**BE**	**Δ**	**No.**
Cr	574.17	0.19	19	696.20	0.10	2	42.40	0.27	8	74.38	0.04	4
Cr_2O_3	576.63	0.33	41	699.30	-	1	43.81	0.21	10	75.27	0.08	6
Cr_2O_3 sat.	587.20	0.13	3									
CrO_3	579.27	0.54	14				48.27	0.18	6			
CrO2	575.85	0.45	2				43.50	-	1	75.10	-	1
$Cr(OH)_3$	577.20	0.14	7				44.80	0.00	2			
Cr(OH)O	577.00	-	1				44.10	-	1			
CrOOH	576.90	-	1									
CrN	575.73	0.07	4				43.00	-	1			
$CrN_{(alt)}$ †	574.60	0.10	2									
Cr_2N	575.45	0.65	2									
FeCr	574.40	0.10	2									
$FeCr_2O_4$	576.30	0.20	4				43.93	0.23	4	74.93	0.42	3

† Not from NIST, but averaged BE as observed in (Bertóti, 2002; Biesinger, 2017).

Appendix D21 – Reference-based BEs used to identify the iron contaminants

Table D21. Mean BEs for various Fe components as observed in the NIST database (NIST, 2008)(NIST, 2008) – including the observed average deviation (Δ) and number of references (No.).

	$2p_{3/2}$			3p			3s		
	BE	**Δ**	**No.**	**BE**	**Δ**	**No.**	**BE**	**Δ**	**No.**
Fe	707.24	0.55	30	52.90	0.24	11	91.15	0.21	8
FeO	709.87	0.43	6	55.05	0.47	4	93.07	0.51	3
Fe_2O_3	710.98	0.31	17	55.70	0.37	7	93.43	0.32	4
Fe_3O_4	709.78	1.02	9	55.15	1.45	4	94.00	-	1
Fe(OH)O	711.34	0.23	4	56.23	0.18	2	94.00	-	1
FeOOH	711.50	-	1						
$Fe_{(2-4)}N$	706.70	-	1						
$FeN_{(alt)}$ †	707.14	0.08	3						
FeCr	707.05	0.05	2						
$FeCr_2O_4$	710.55	0.05	2	56.20	0.85	4	93.18	0.39	4

† Not from NIST, but averaged BE as observed in (Meskinis et al., 2005; Flori et al., 2008; Hattori et al., 2018).

Appendix D22 – Reference-based nitrogen/oxygen BEs related to the contaminants

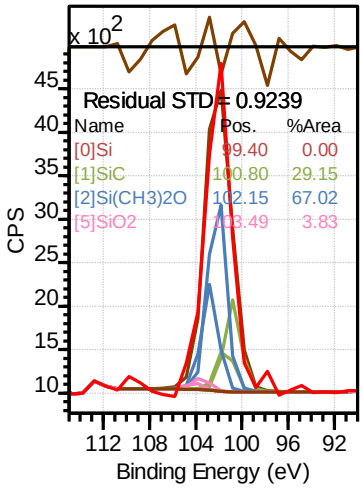
Table D22. Corresponding N 1s and O 1s BEs of the evaluated contaminants as observed in the NIST database (NIST, 2008) – including the observed average deviation (Δ) and number of references (No.).

	O 1s			N 1s		
	BE	**Δ**	**No.**	**BE**	**Δ**	**No.**
Al_2O_3	531.22	0.47	58			
$Si(CH_3)_2O$	532.53	0.23	15			
SiO2	532.87	0.29	83			
Si_3N_4				397.98	0.36	24
Cr_2O_3	530.26	0.27	20			
CrO_3	530.33	0.37	8			
CrO_2	529.30	-	1			
$Cr(OH)_3$	531.33	0.33	4			
Cr(OH)O	531.40	-	1			
CrOOH	531.20	-	1			
CrN				396.63	0.13	4
Cr_2N				397.30	0.10	2
FeO	529.95	0.15	2			
Fe_2O_3	530.00	0.35	16			
Fe_3O_4	529.91	0.36	8			
Fe(OH)O	530.10 / 531.40	0.00 / 0.27	3 / 3			
FeOOH	531.70 / 529.70	-	1 / 1			
FeN				397.30	-	1

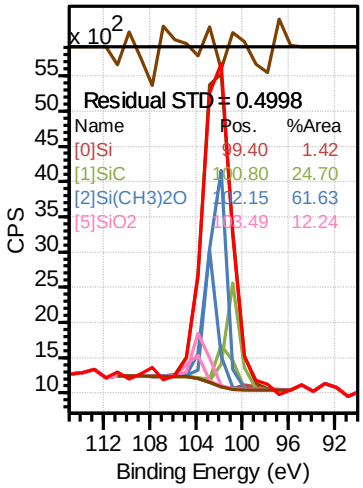
Appendix D23 – XPS survey peak fits of the silicon contaminants

Figure D23a. Si 2p constrained survey spectrum peak fits of UHMWPE UD/UT (A1,3), UD/PT (B3), and D/UT (C1-3).

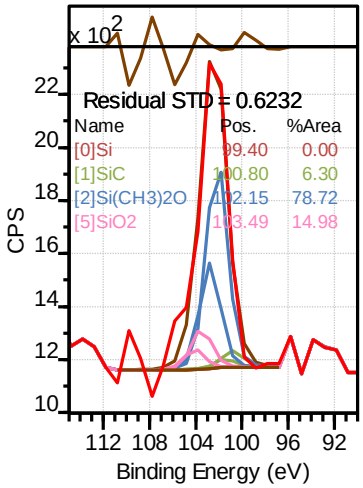
A1



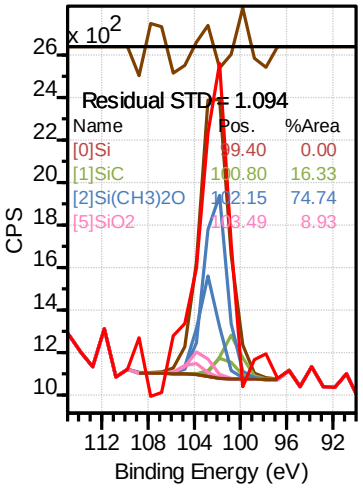
A3



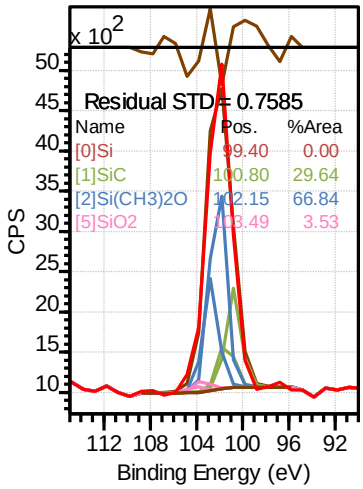
B3



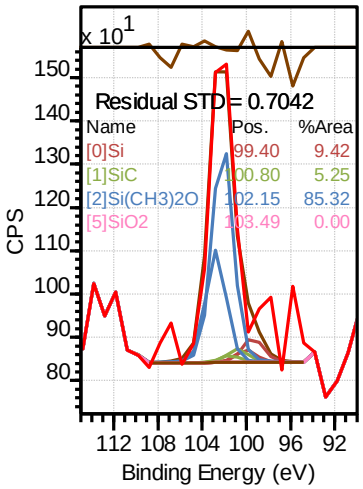
C1



C2



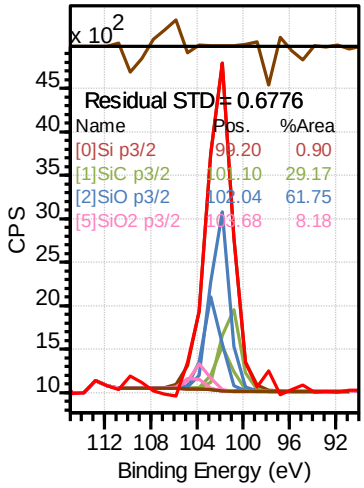
C3



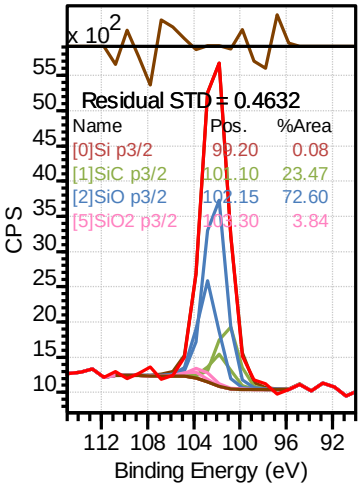
Continued on the next page…

Figure D23b. Si 2p unconstrained survey spectra peak fits of UHMWPE UD/UT (A1,3), UD/PT (B3), and D/UT (C1-3).

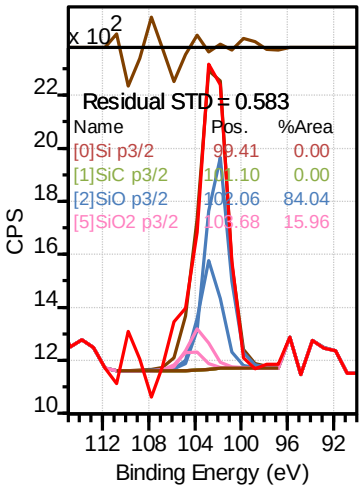
A1



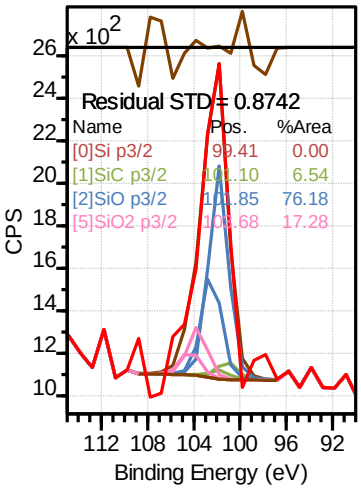
A3



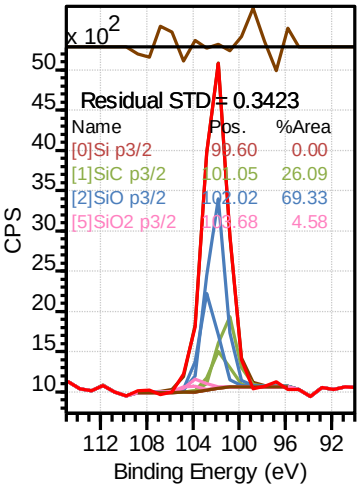
B3



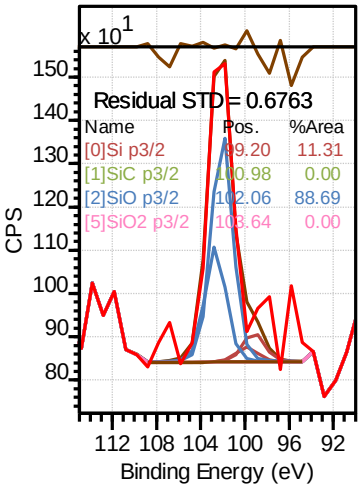
C1



C2

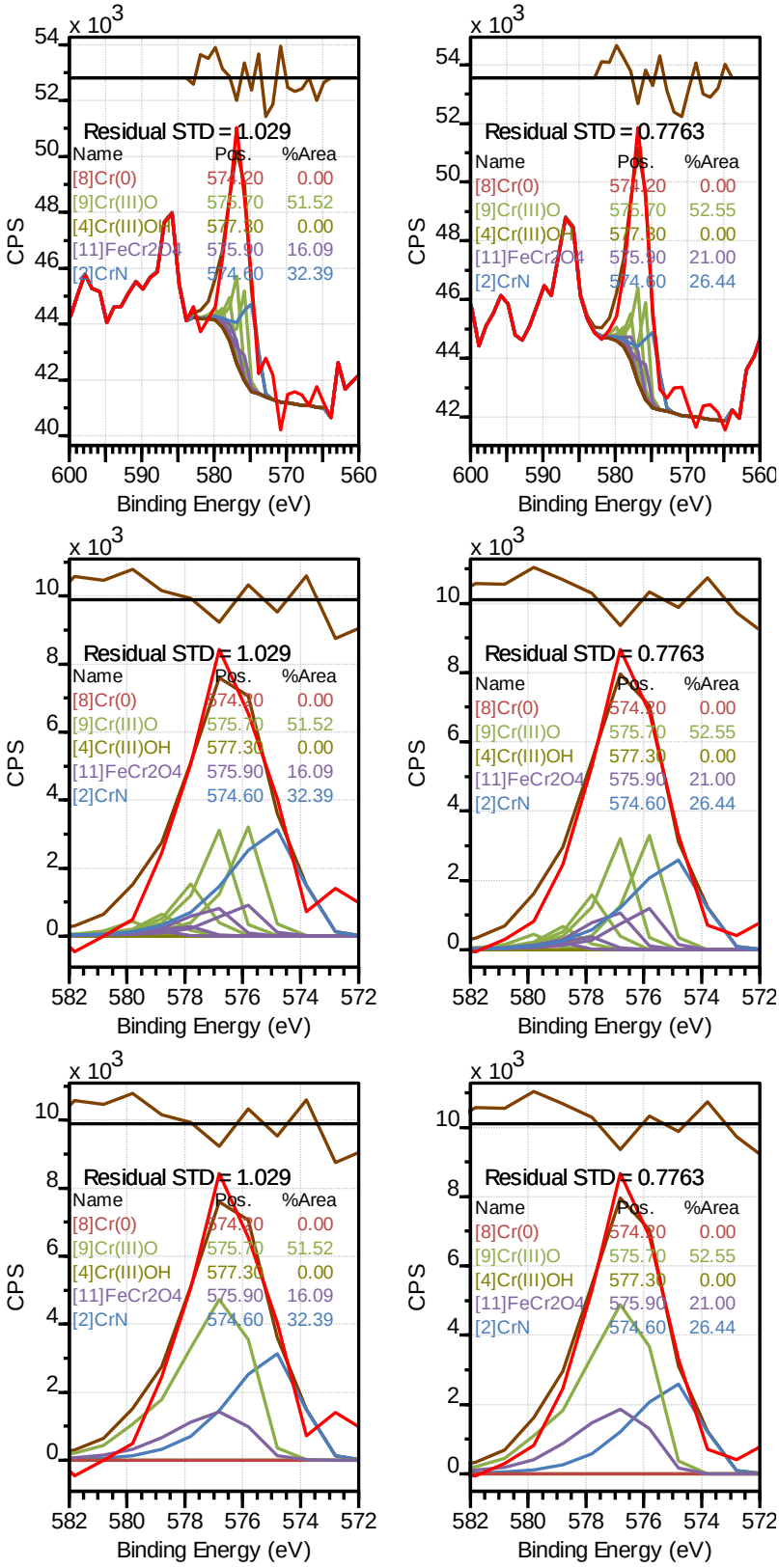


C3



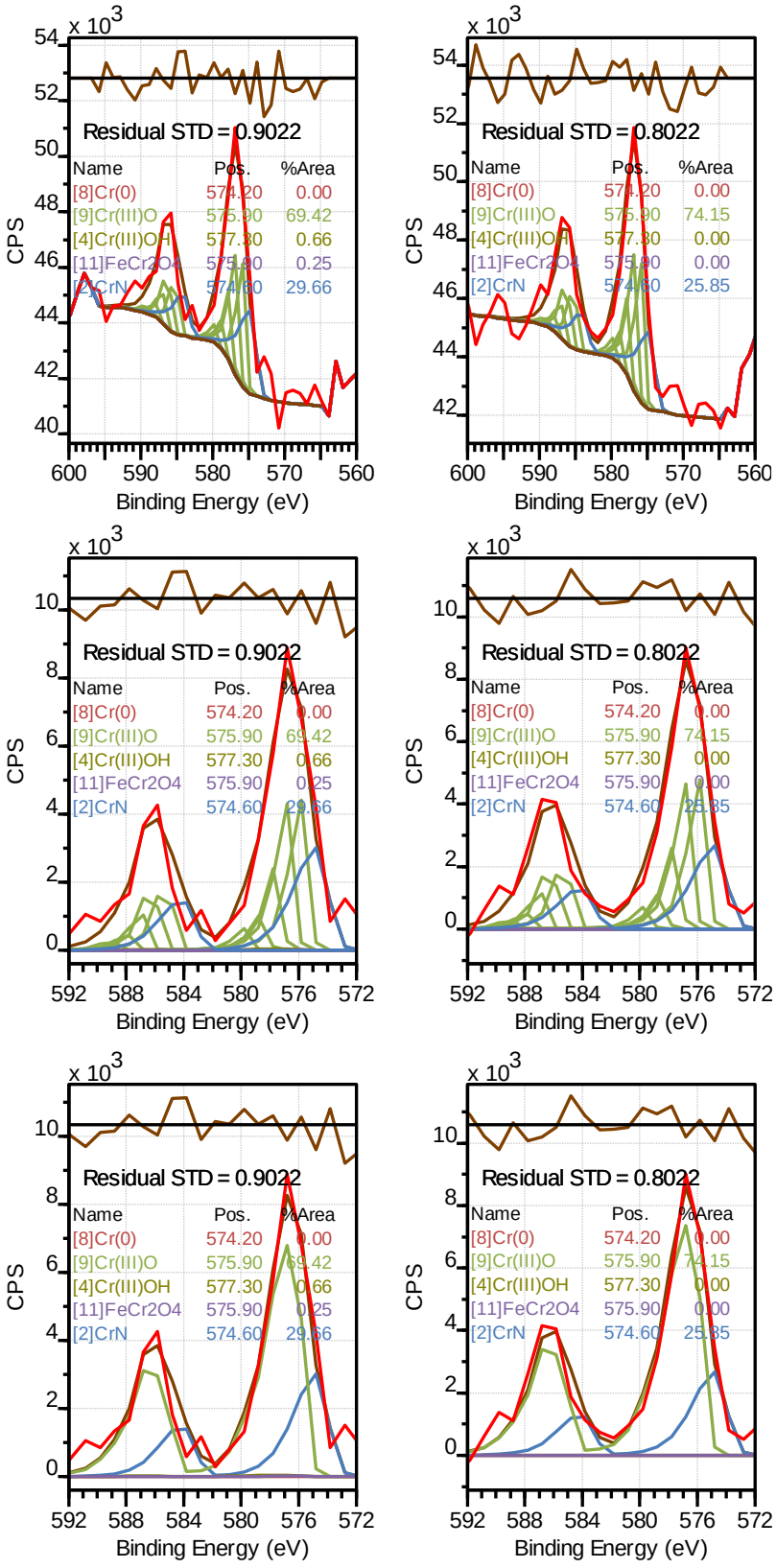
Appendix D24 – XPS survey peak fits of the chromium contaminants

Figure D24a. Cr $2p_{3/2}$ constrained survey spectrum peak fits of UHMWPE UD/PT 'B1' (left) and 'B2' (right).



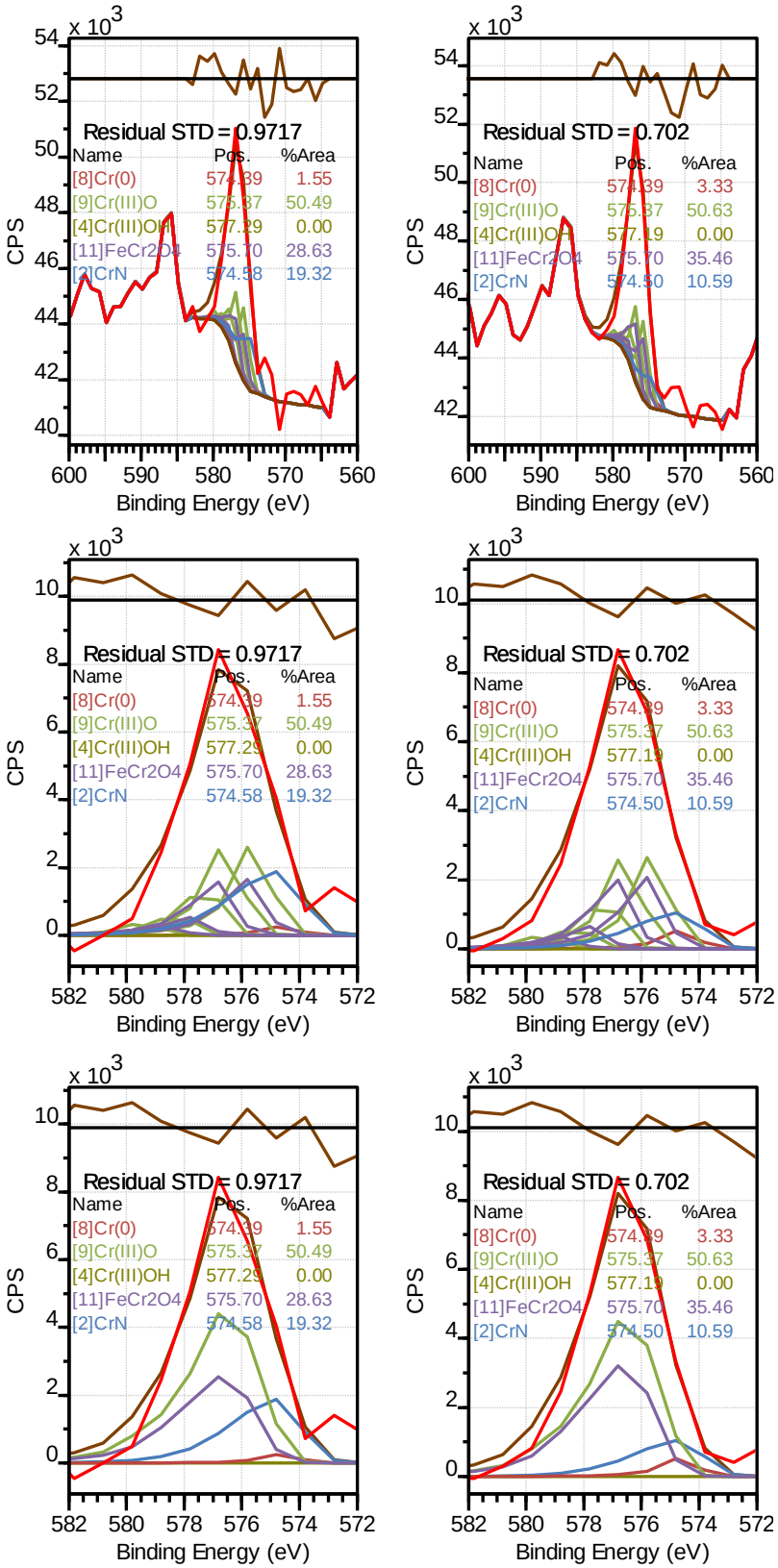
Continued on the next page…

Figure D24b. Cr 2p constrained survey spectrum peak fits of UHMWPE UD/PT ‘B1’ (left) and ‘B2’ (right).



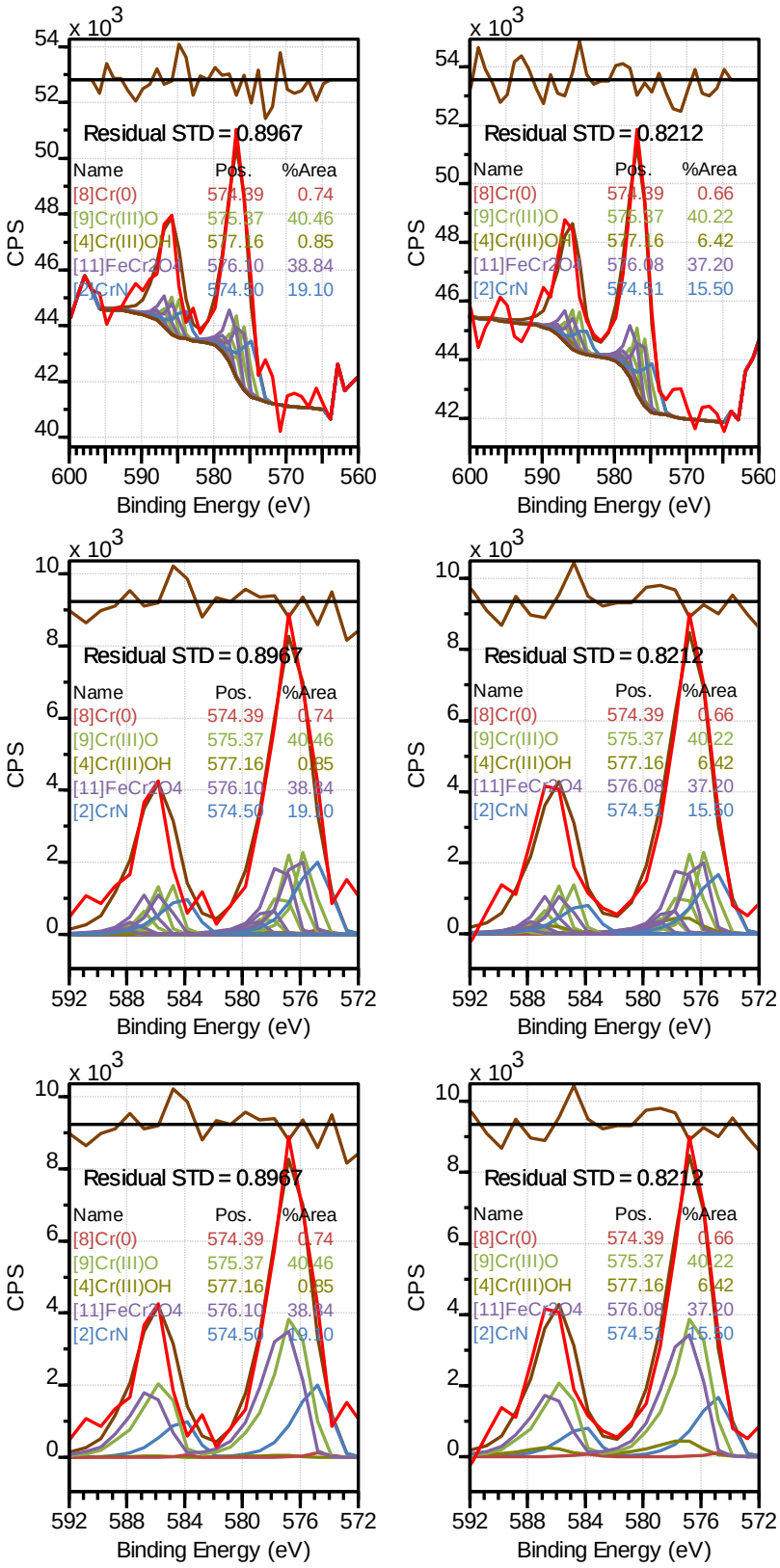
Continued on the next page…

Figure D24c. Cr $2p_{3/2}$ unconstrained survey spectrum peak fits of UHMWPE UD/PT 'B1' (left) and 'B2' (right).



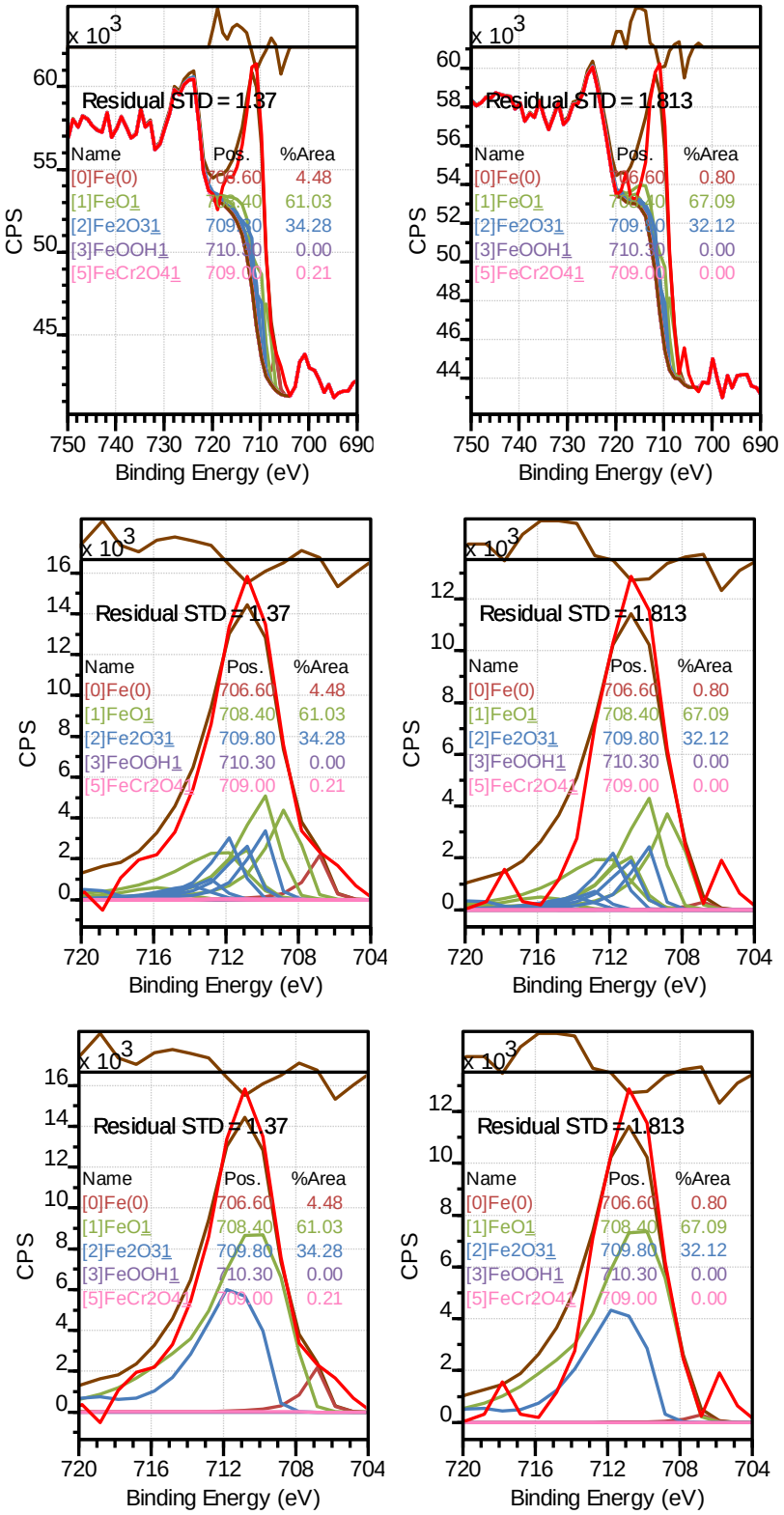
Continued on the next page…

Figure D24d. Cr 2p unconstrained survey spectrum peak fits of UHMWPE UD/PT ‘B1’ (left) and ‘B2’ (right).



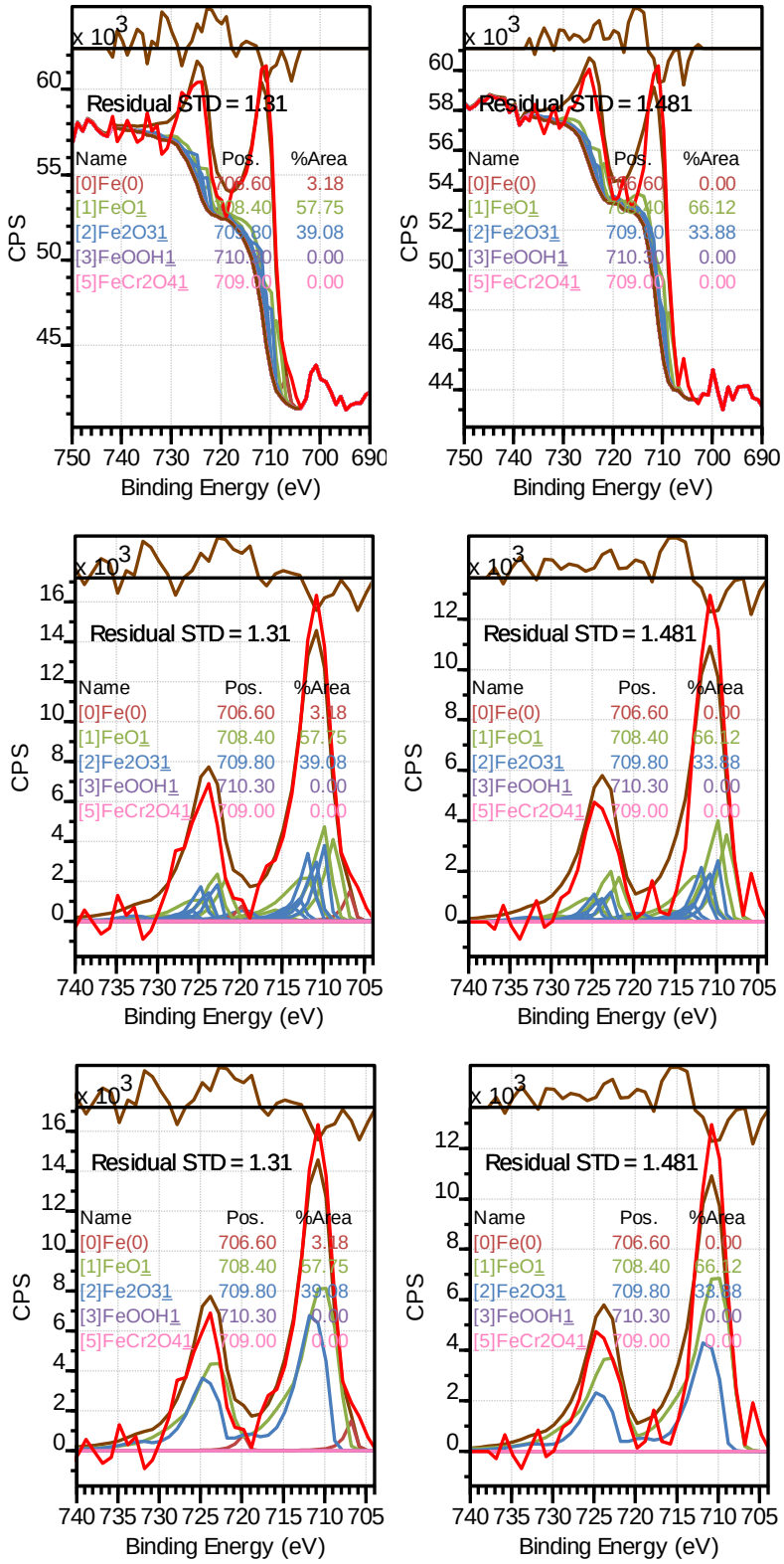
Appendix D25 – XPS survey peak fits of the iron contaminants

Figure D25a. Fe $2p_{3/2}$ survey spectrum peak fits of UHMWPE UD/PT 'B1' (left) and 'B2' (right), with peak positioning constrained.



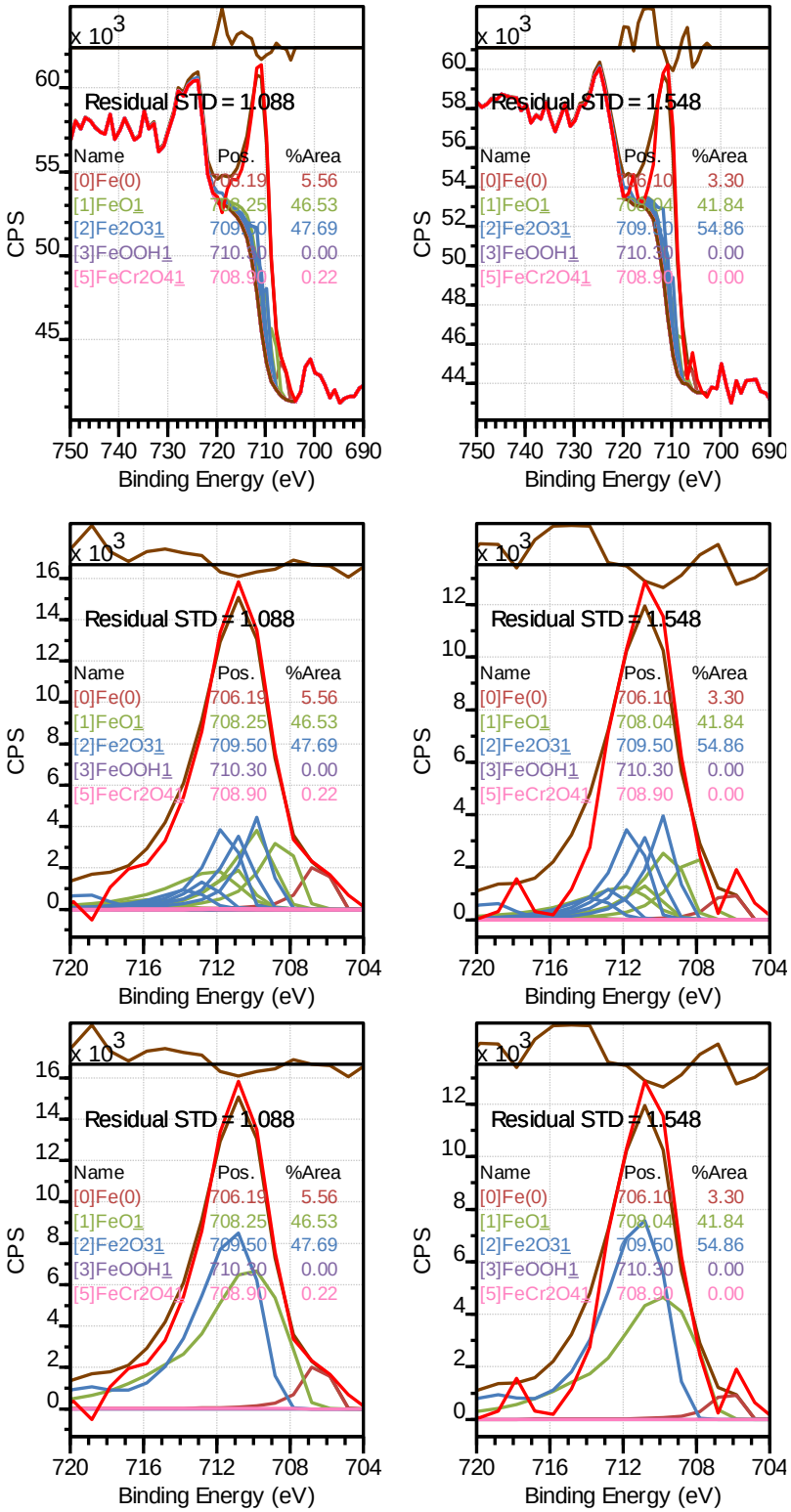
Continued on the next page…

Figure D25b. Fe 2p survey spectrum peak fits of UHMWPE UD/PT ‘B1’ (left) and ‘B2’ (right), with peak positioning constrained.



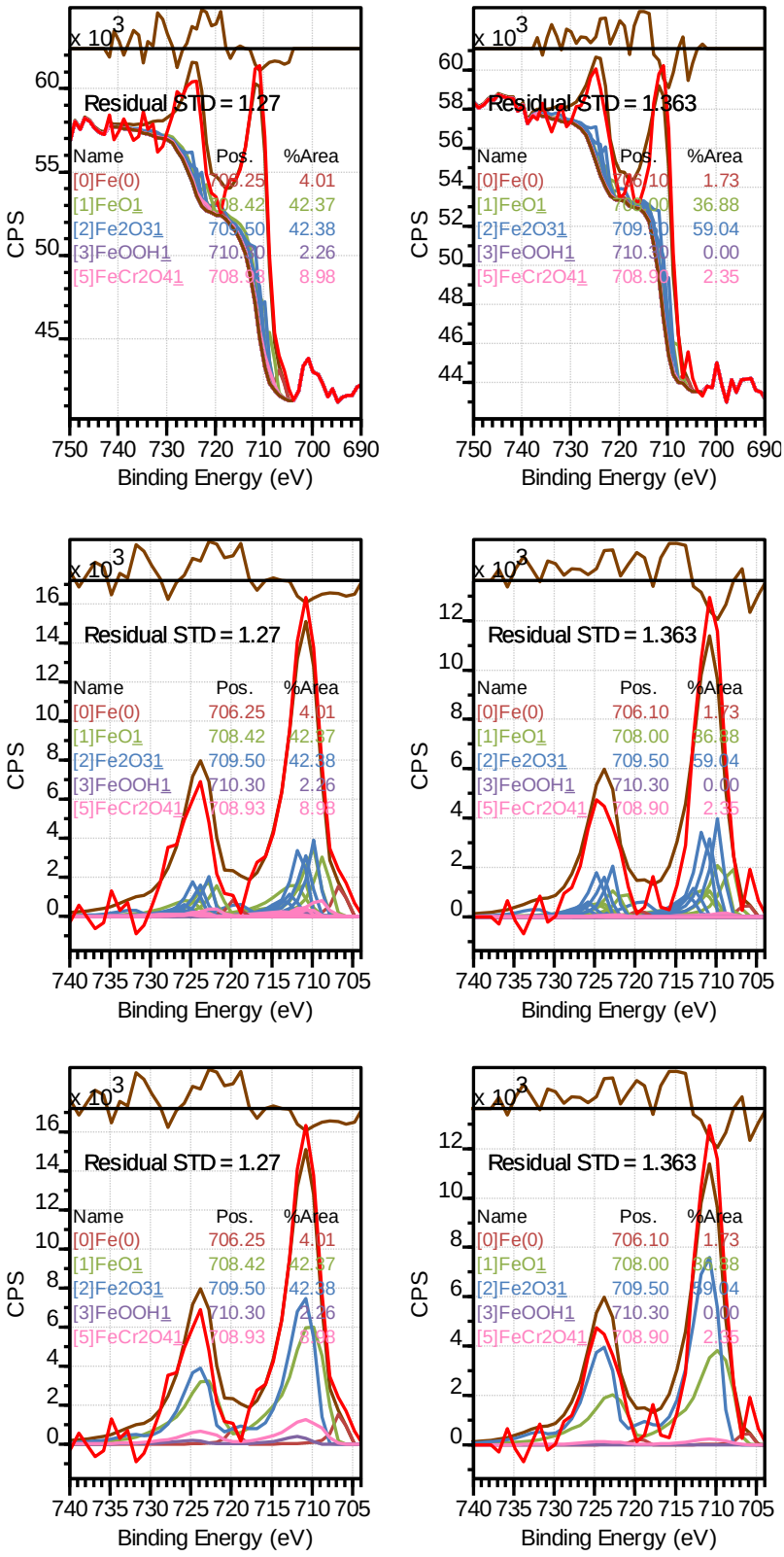
Continued on the next page…

Figure D25c. Fe $2p_{3/2}$ survey spectrum peak fits of UHMWPE UD/PT 'B1' (left) and 'B2' (right), with peak positioning unconstrained.



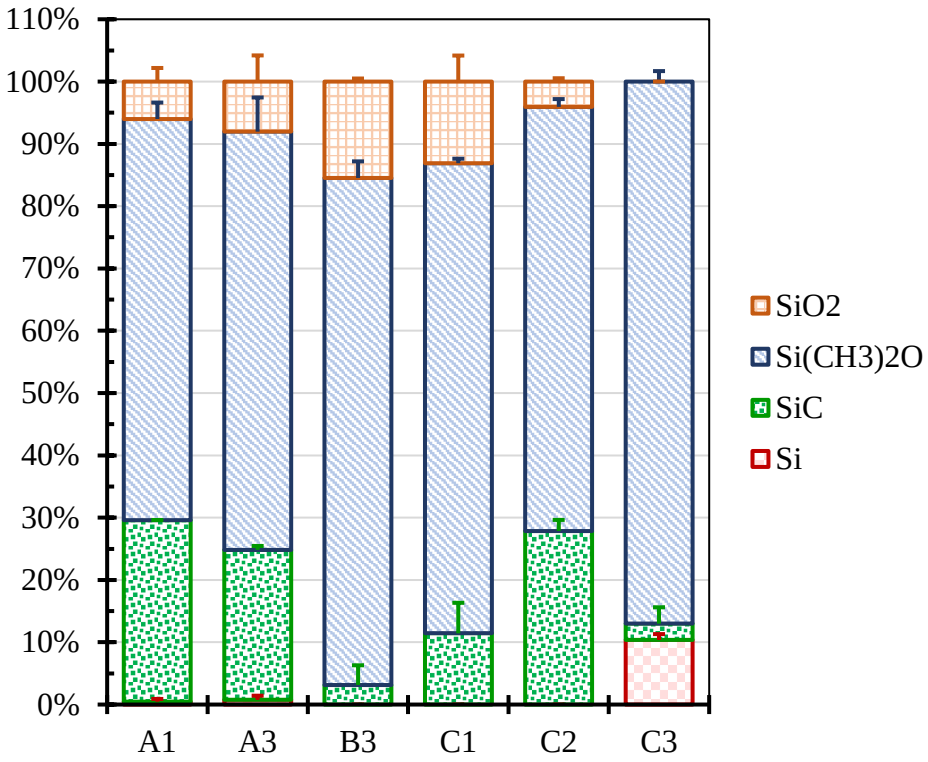
Continued on the next page…

Figure D25d. Fe 2p survey spectrum peak fits of UHMWPE UD/PT ‘B1’ (left) and ‘B2’ (right), with peak positioning unconstrained.



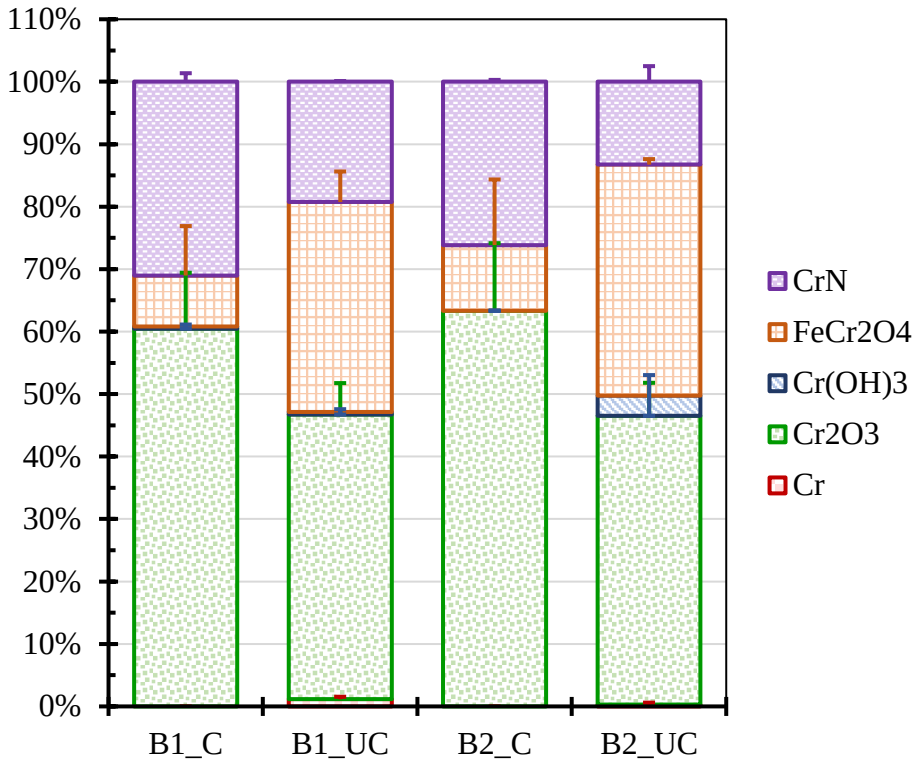
Appendix D26 – Averaged atomic composition of the silicon contaminants

Figure D26. Averaged atomic composition as observed by the survey spectra Si 2p peak fits of UHMWPE UD/UT (A1,3), UD/PT (B3), and D/UT (C1-3), errors bars show average deviation between the constrained and unconstrained fits.



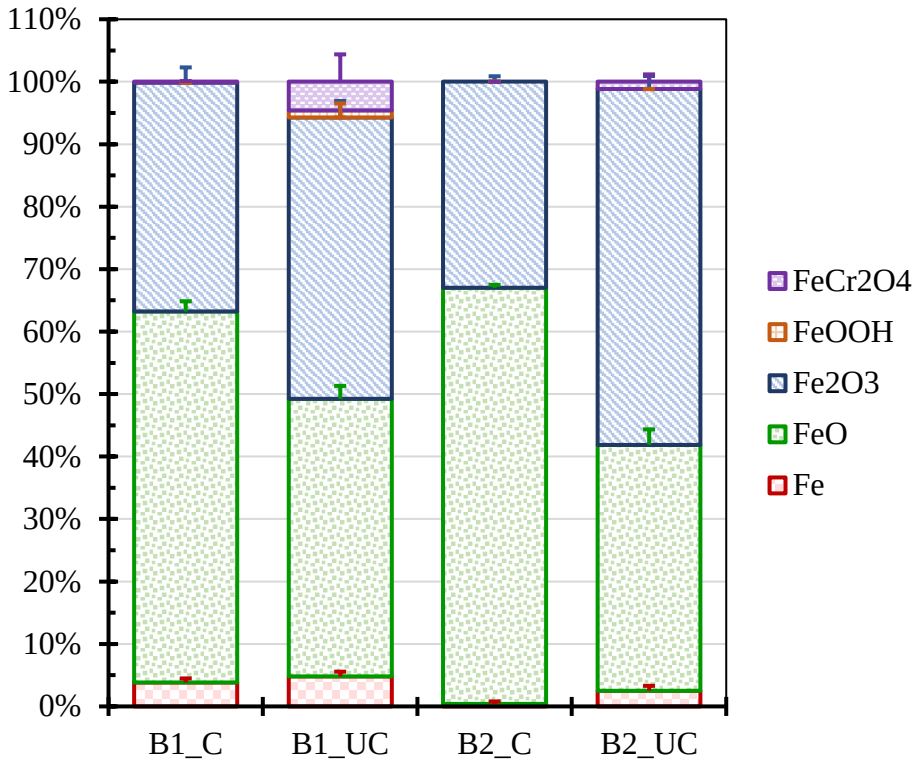
Appendix D27 – Averaged atomic composition of the chromium contaminants

Figure D27. Averaged atomic composition as observed by survey spectra Cr 2p peak fits of UHMWPE UD/PT 'B1' and 'B2', showing the constrained (C) and unconstrained (UC) fits separated, errors bars show average deviation between the 2p and $2p_{3/2}$ fits.



Appendix D28 – Averaged atomic composition of the iron contaminants

Figure D28. Averaged atomic composition as observed by the survey spectra Fe 2p peak fits of UHMWPE UD/PT 'B1' and 'B2', showing the constrained (C) and unconstrained (UC) fits separated, errors bars show average deviation between the 2p and $2p_{3/2}$ fits.



Appendix D29 – Atomic composition of the silicon survey peak fits

Table D29. Atomic composition of Si 2p survey peak fits of UHMWPE UD/UT (A1,3), UD/PT (B3), and D/UT (C1-3), using the constrained/(unconstrained) peak model.

	Atomic concentration ± St.Dev. (%)			
	Si	**SiC**	**$Si(CH_3)_2O$**	**SiO_2**
A1	0.00 ± 0.00 (0.90 ± 2.17)	29.15 ± 6.88 (29.16 ± 11.62)	67.02 ± 9.96 (61.76 ± 11.73)	3.83 ± 5.31 (8.19 ± 6.60)
A3	1.42 ± 2.49 (0.08 ± 0.24)	24.70 ± 4.77 (23.46 ± 12.67)	61.63 ± 6.23 (72.41 ± 10.84)	12.24 ± 5.08 (3.85 ± 4.50)
B3	0.00 ± 0.00 (0.00 ± 0.00)	6.30 ± 12.45 (0.00 ± 0.00)	78.72 ± 20.16 (84.03 ± 17.20)	14.98 ± 17.97 (15.95 ± 17.20)
C1	0.00 ± 0.00 (0.00 ± 0.00)	16.33 ± 16.23 (6.53 ± 12.42)	74.74 ± 22.84 (76.17 ± 17.42)	8.93 ± 11.23 (17.30 ± 12.44)
C2	0.00 ± 0.00 (0.00 ± 0.00)	29.63 ± 7.30 (26.07 ± 12.00)	47.36 ± 8.39 (69.34 ± 11.59)	3.43 ± 4.77 (4.59 ± 5.10)
C3	9.42 ± 9.78 (11.28 ± 10.89)	5.25 ± 16.80 (0.00 ± 0.00)	85.32 ± 14.77 (88.71 ± 10.89)	0.00 ± 0.00 (0.00 ± 0.00)

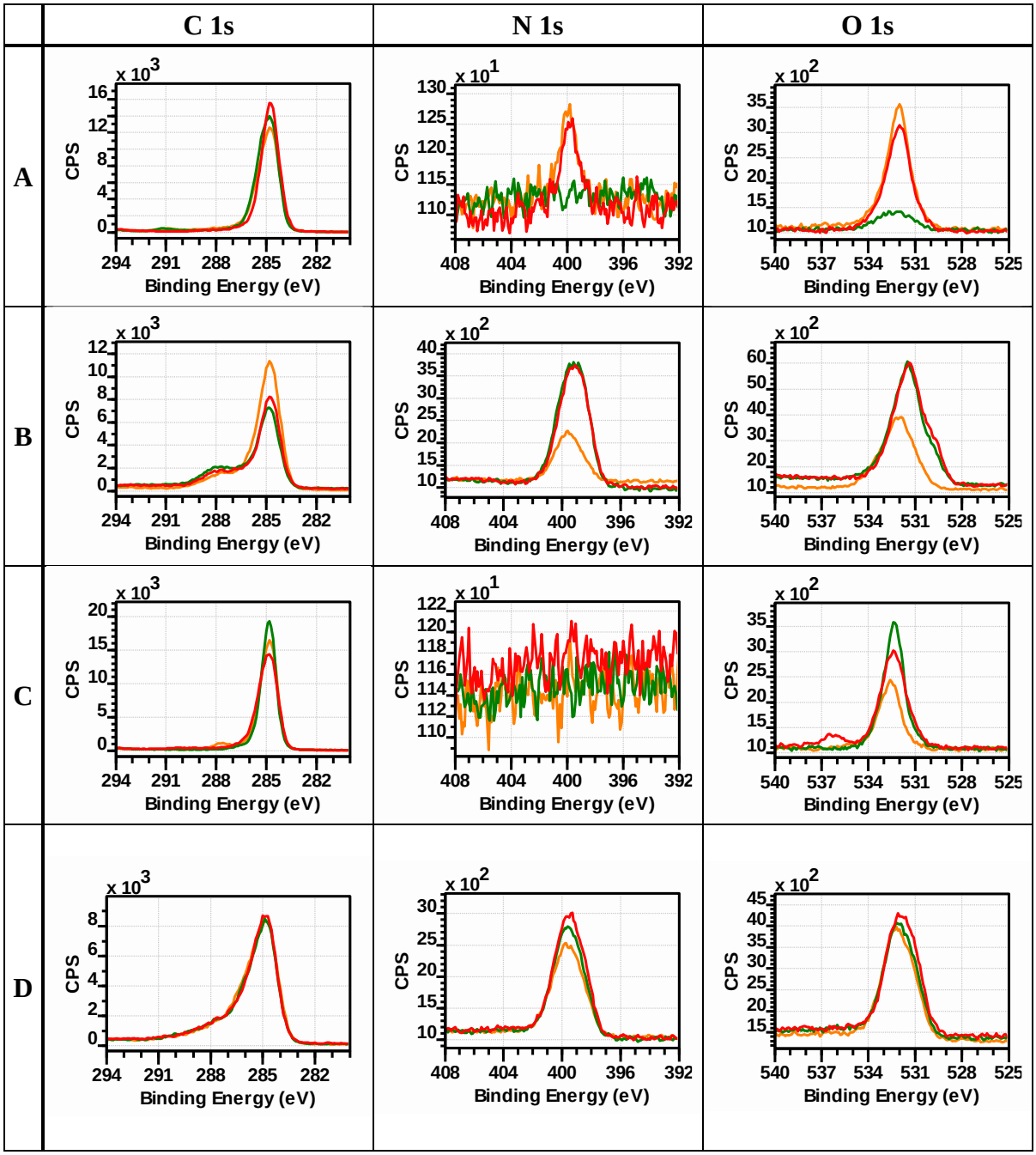
Appendix D30 – Atomic composition of the chromium and iron survey peak fits

Table D30. Atomic composition of Cr 2p and Fe 2p survey peak fits of UHMWPE UD/PT (B1,2) using the constrained/(unconstrained) peak models.

		B1		B2	
		$2p_{3/2}$	**2p**	**$2p_{3/2}$**	**2p**
Atomic concentration ± St.Dev. (%)	**Cr**	0.00 ± 0.00 (1.55 ± 3.83)	0.00 ± 0.00 (0.74 ± 3.03)	0.00 ± 0.00 (3.33 ± 7.23)	0.00 ± 0.00 (0.66 ± 1.91)
	Cr_2O_3	51.52 ± 34.20 (50.49 ± 32.21)	69.42 ± 19.12 (40.46 ± 40.69)	52.55 ± 34.90 (50.63 ± 18.97)	74.15 ± 38.68 (40.22 ± 35.50)
	$Cr(OH)_3$	0.00 ± 0.00 (0.00 ± 0.00)	0.66 ± 2.48 (0.85 ± 3.39)	0.00 ± 0.00 (0.00 ± 0.00)	0.00 ± 0.00 (6.42 ± 16.89)
	$FrCr_2O_4$	16.09 ± 30.55 (28.63 ± 28.17)	0.25 ± 2.06 (38.84 ± 43.13)	21.00 ± 22.68 (35.46 ± 20.10)	0.00 ± 0.00 (37.20 ± 41.12)
	CrN	32.39 ± 27.68 (19.32 ± 17.99)	29.66 ± 26.85 (19.10 ± 26.97)	26.44 ± 25.69 (10.59 ± 16.71)	25.85 ± 38.69 (15.50 ± 26.09)
	Fe	4.48 ± 2.55 (5.56 ± 3.71)	3.18 ± 2.62 (4.01 ± 4.23)	0.80 ± 1.37 (3.30 ± 3.34)	0.00 ± 0.00 (1.73 ± 5.46)
	FeO	61.03 ± 12.49 (46.53 ± 15.15)	57.75 ± 35.24 (42.37 ± 42.60)	67.09 ± 17.08 (41.84 ± 16.97)	66.12 ± 33.24 (36.88 ± 55.40)
	Fe_2O_3	34.28 ± 12.85 (47.69 ± 15.46)	39.08 ± 35.66 (42.38 ± 38.85)	32.12 ± 17.83 (54.86 ± 15.59)	33.88 ± 30.76 (59.04 ± 53.35)
	FeOOH	0.00 ± 0.00 (0.00 ± 0.00)	0.00 ± 0.00 (2.26 ± 5.78)	0.00 ± 0.00 (0.00 ± 0.00)	0.00 ± 0.00 (0.00 ± 0.00)
	$FeCr_2O_4$	0.21 ± 0.72 (0.22 ± 0.72)	0.00 ± 0.00 (8.98 ± 22.03)	0.00 ± 0.00 (0.00 ± 0.00)	0.00 ± 0.00 (2.35 ± 9.61)

Appendix D31 – High-resolution XPS spectra of UHMWPE-based samples

Figure D31. High-resolution XPS spectra of UHMWPE undoped and untreated (UD/UT; A1-3), undoped and plasma-treated (UD/PT; B1-3), doped and untreated (D/UT; C1-3), and doped and plasma-treated (D/PT; D1-3); overlaid per samples series showing sample 1 (**red**), 2 (**green**) and 3 (**orange**), for each of the respective elemental regions.



Appendix D32 – Conversion table of the silicon contaminants for the HR spectra

Table D32. Expected presence of silicon contaminants in the high-resolution (HR) spectra of UHMWPE UD/UT (A1,3), UD/PT (B3), and D/UT (C1-3), determined by the averaged survey spectra peak fits.

		A1	A3	B3	C1	C2	C3
Average area% survey peak fits	**Si**	0.45	0.75	0.00	0.00	0.00	10.37
	SiC	29.17	24.09	3.15	11.44	27.86	2.63
	$Si(CH_3)_2O$	64.38	67.12	81.38	75.46	68.08	87.01
	SiO_2	6.01	8.04	15.47	13.10	4.06	0.00
At% in survey	**Si 2p**	1.72	2.23	0.49	0.66	2.18	0.51
	C 1s	91.46	89.2	84.39	90.55	90.91	95.38
	O 1s	5.92	7.74	9.66	6.03	6.5	4.11
Area% in HR–C 1s	**SiC**	0.55	0.60	0.02	0.08	0.67	0.01
	$Si(CH_3)_2O$	2.42	3.36	0.95	1.10	3.27	0.93
Area% in HR–O 1s	**$Si(CH_3)_2O$**	18.71	19.34	4.13	8.26	22.83	10.80
	SiO_2	3.49	4.63	1.57	2.87	2.72	0.00

Appendix D33 – Conversion table of the Cr and Fe contaminants for the HR spectra

Table D33. Expected presence of chromium and iron contaminants in the high-resolution (HR) spectra of UHMWPE UD/PT (B1,2), determined by the averaged survey spectra peak fits.

		B1	**B2**		**B1**	**B2**
Average area% survey peak fits	**Cr**	0.57	0.15	**Fe**	4.31	1.46
	Cr_2O_3	74.28	80.09	**FeO**	53.38	53.28
	CrN	25.15	19.76	**Fe_2O_3**	42.32	45.27
At% in survey	**Cr 2p**	0.98	1.03	**Fe 2p**	2.10	1.34
	N 1s	15.55	16.37	**N 1s**	15.55	16.37
	O 1s	16.42	16.28	**O 1s**	16.42	16.28
Area% in HR–N 1s	**CrN**	1.59	1.24			
Area% in HR–O 1s	**Cr_2O_3**	6.65	7.60	**FeO**	6.83	4.39
				Fe_2O_3	8.12	5.59

Appendix D34 – Difference in the atomic composition due to the change in background

Table D34. Atomic composition of UHMWPE UD/UT (A1-3), UD/PT (B1-3), D/UT (C1-3), and D/PT (D1-3), determined by the high-resolution spectra with a Shirley/(U Poly Tougaard) background.

	Atomic concentration ± St.Dev. (%)		
	C 1s	**N 1s**	**O 1s**
A1	92.25 ± 0.27 (92.49 ± 0.31)	0.95 ± 0.26 (0.757± 0.25)	6.80 ± 0.12 (6.74 ± 0.21)
A2	98.47 ± 0.12 (98.47 ± 0.15)	-	1.53 ± 0.12 (1.53 ± 0.15)
A3	91.43 ± 0.30 (91.37 ± 0.34)	0.83 ± 0.26 (0.83 ± 0.31)	7.75 ± 0.17 (7.80 ± 0.18)
B1	66.34 ± 0.22 (65.57 ± 0.28)	16.39 ± 0.21 (16.12 ± 0.27)	17.27 ± 0.17 (18.31 ± 0.22)
B2	65.77 ± 0.21 (65.45 ± 0.28)	17.31 ± 0.18 (17.39 ± 0.25)	16.93 ± 0.16 (17.16 ± 0.22)
B3	84.16 ± 0.22 (84.12 ± 0.38)	5.77 ± 0.20 (5.77 ± 0.37)	10.07 ± 0.14 (10.11 ± 0.20)
C1	93.38 ± 0.15 (93.93 ± 0.17)	-	6.62 ± 0.15 (6.61 ± 0.17)
C2	93.41 ± 0.13 (93.52 ± 0.22)	-	6.59 ± 0.13 (6.48 ± 0.20)
C3	96.00 ± 0.14 (96.02 ± 0.20)	-	4.00 ± 0.14 (3.98 ± 0.20)
D1	78.21 ± 0.32 (77.70 ± 0.34)	11.60 ± 0.24 (11.82 ± 0.28)	10.19 ± 0.21 (10.49 ± 0.22)
D2	79.08 ± 0.27 (78.71 ± 0.34)	10.68 ± 0.23 (11.01 ± 0.29)	10.24 ± 0.19 (10.28 ± 0.22)
D3	81.55 ± 0.27 (87.30 ± 0.34)	8.82 ± 0.24 (8.83 ± 0.28)	9.63 ± 0.18 (9.87 ± 0.23)

Appendix D35 – Component compositions of the UD/UT high-resolution peak fits

Table D35. Composition as obtained by the high-resolution C 1s, N 1s and O 1s spectra peak fits of UHMWPE UD/UT (A1-3), using a 'Shirley' background and the wB97X-D-based peak model including the respective symmetric higher-order carbon shifts (1°-4°).

ID	A1_1°	A1_2°	A1_3°	A1_4°	A2_1°	A2_2°	A2_3°	A2_4°	A3_1°	A3_2°	A3_3°	A3_4°
CH	88.16	86.08	83.32	81.32	97.09	97.00	97.04	97.02	83.91	81.09	79.98	82.39
COH	2.25	3.44	3.51	4.23	0.00	0.00	0.00	0.00	0.67	0.13	0.02	2.58
COH*	0.00	0.00	0.00	0.00	0.00	0.00	0.00	0.00	0.19	0.00	1.58	2.15
COC_{α}	0.00	0.00	0.00	0.00	0.00	0.00	0.00	0.00	3.40	5.23	3.54	0.39
COC_{β}	0.00	0.00	0.00	0.00	0.00	0.00	0.00	0.00	0.00	0.09	0.96	0.00
COC_{β}*	0.00	0.00	0.00	0.00	0.00	0.00	0.00	0.00	0.00	0.00	0.00	0.29
C=O	0.97	1.93	2.13	0.86	0.31	0.43	0.00	0.00	1.21	3.71	0.91	0.00
C=O*	0.46	0.04	0.06	1.26	1.15	1.11	1.58	1.60	1.97	0.00	2.25	3.03
O=COC	0.38	1.43	1.55	1.13	0.08	0.25	0.00	0.00	0.00	0.00	0.00	0.00
O=COH*	1.04	0.06	0.00	0.09	0.06	0.03	0.43	0.49	0.00	0.00	0.00	0.00
O=CO{-}*	0.03	0.00	0.00	0.00	0.52	0.06	0.22	0.31	0.00	0.00	0.00	0.00
O=COC=O	0.97	1.45	1.48	1.57	0.79	1.13	0.74	0.58	2.60	2.28	2.22	2.55
COC(=O)OC	0.63	0.00	0.00	0.00	0.00	0.00	0.00	0.00	0.76	0.91	0.74	0.20
CNH_2	0.00	0.00	0.00	0.00	0.00	0.00	0.00	0.00	0.00	0.00	0.00	0.00
CNH_2*	0.00	0.00	0.00	0.00	0.00	0.00	0.00	0.00	0.00	0.00	0.00	0.00
$CNHC_{\alpha}$	1.59	3.52	0.00	0.00	0.00	0.00	0.00	0.00	0.00	0.00	0.00	0.00
$CNHC_{\beta}$	0.00	0.00	0.00	0.00	0.00	0.00	0.00	0.00	0.00	0.00	0.00	0.00
$CNHC_{\beta}$*	0.00	0.00	0.00	0.00	0.00	0.00	0.00	0.00	0.00	0.00	0.00	1.56
CN(C)C	0.00	0.00	6.06	8.37	0.00	0.00	0.00	0.00	2.38	4.26	5.29	1.99
$CNH_3^{\{+\}}$	0.00	0.00	0.00	0.00	0.00	0.00	0.00	0.00	0.00	0.30	0.78	0.85
$CNH_3^{\{+\}}$*	0.00	0.00	0.00	0.00	0.00	0.00	0.00	0.00	0.06	0.00	0.00	0.00
$CNHNH_2$	0.00	0.00	0.00	0.00	0.00	0.00	0.00	0.00	0.00	0.00	0.00	0.00
$CNHNH_2$*	0.00	0.00	0.00	0.00	0.00	0.00	0.00	0.00	0.00	0.00	0.00	0.00
C=NH	0.00	0.00	0.00	0.00	0.00	0.00	0.00	0.00	0.00	0.00	0.00	0.00
C=NH*	0.00	0.00	0.00	0.00	0.00	0.00	0.00	0.00	0.00	0.00	0.00	0.00
C=NC	0.00	0.00	0.00	0.00	0.00	0.00	0.00	0.00	0.00	0.00	0.00	0.00
C=NN=C	0.00	0.00	0.00	0.00	0.00	0.00	0.00	0.00	0.00	0.00	0.00	0.00
$C=NNH_2$	0.00	0.00	0.00	0.00	0.00	0.00	0.00	0.00	0.00	0.00	0.00	0.00
$C=NNH_2$*	0.00	0.00	0.00	0.00	0.00	0.00	0.00	0.00	0.00	0.00	0.00	0.00
HN=CNHC	0.00	0.00	0.00	0.00	0.00	0.00	0.00	0.00	0.00	0.00	0.00	0.00
$HN=CNH_2$*	0.00	0.00	0.00	0.00	0.00	0.00	0.00	0.00	0.00	0.00	0.00	0.00
C≡N	0.00	0.00	0.00	0.00	0.00	0.00	0.00	0.00	0.00	0.00	0.00	0.00
C≡N*	0.00	0.00	0.00	0.00	0.00	0.00	0.00	0.00	0.00	0.00	0.00	0.59
CNHOH	0.00	0.00	0.00	0.00	0.00	0.00	0.00	0.00	0.00	0.00	0.00	0.00
CNHOH*	1.45	0.94	1.07	0.00	0.00	0.00	0.00	0.00	0.00	0.00	0.00	0.00
$CONH_2$	0.00	0.00	0.00	0.00	0.00	0.00	0.00	0.00	0.00	0.00	0.00	0.00
$CONH_2$*	0.00	0.00	0.00	0.00	0.00	0.00	0.00	0.00	0.00	0.00	0.00	0.00
CNHOC	0.00	0.00	0.00	0.00	0.00	0.00	0.00	0.00	0.00	0.00	0.00	0.00
C=NOH	0.00	0.00	0.00	0.00	0.00	0.00	0.00	0.00	0.00	0.00	0.00	0.00
C=NOH*	0.00	0.00	0.00	0.00	0.00	0.00	0.00	0.00	0.00	0.00	0.00	0.00
C=NOC	0.00	0.00	0.00	0.00	0.00	0.00	0.00	0.00	0.00	0.00	0.00	0.00
CN=O	0.00	0.63	0.78	0.82	0.00	0.00	0.00	0.00	0.00	0.00	0.00	0.00
CN=O*	0.51	0.00	0.00	0.00	0.00	0.00	0.00	0.00	0.00	0.00	0.00	0.00
O=CNHC	0.17	0.00	0.00	0.00	0.00	0.00	0.00	0.00	1.26	0.00	0.00	0.00
$O=CNH_2$*	1.39	0.16	0.00	0.00	0.00	0.00	0.00	0.00	0.06	0.00	0.00	0.00
O=CNHC=O	0.00	0.05	0.03	0.19	0.00	0.00	0.00	0.00	1.52	2.00	1.73	1.44
O=CN(OH)C	0.00	0.10	0.00	0.10	0.00	0.00	0.00	0.00	0.00	0.00	0.00	0.00
O=CN(OH)H*	0.00	0.17	0.00	0.04	0.00	0.00	0.00	0.00	0.00	0.00	0.00	0.00
COC(=O)NHC	0.00	0.00	0.00	0.00	0.00	0.00	0.00	0.00	0.00	0.00	0.00	0.00
$COC(=O)NH_2$*	0.00	0.00	0.00	0.00	0.00	0.00	0.00	0.00	0.00	0.00	0.00	0.00
aT	0.00	0.00	0.00	0.00	0.00	0.00	0.00	0.00	0.00	0.00	0.00	0.00
aTQ	0.00	0.00	0.00	0.00	0.00	0.00	0.00	0.00	0.00	0.00	0.00	0.00
aTHQ	0.00	0.00	0.00	0.00	0.00	0.00	0.00	0.00	0.00	0.00	0.00	0.00

Appendix D36 – Component compositions of the UD/PT60 high-resolution peak fits

Table D36. Composition as obtained by the high-resolution C 1s, N 1s and O 1s spectra peak fits of UHMWPE UD/PT (B1-3), using a 'Shirley' background and the wB97X-D-based peak model including the respective symmetric higher-order carbon shifts (1°-4°).

ID	B1_1°	B1_2°	B1_3°	B1_4°	B2_1°	B2_2°	B2_3°	B2_4°	B3_1°	B3_2°	B3_3°	B3_4°
CH	47.06	38.52	44.98	52.71	42.38	38.60	43.30	51.53	70.54	61.33	62.28	64.12
COH	1.20	0.50	0.00	0.00	0.00	0.00	0.00	0.00	0.00	0.00	0.00	0.00
COH*	0.00	0.00	0.00	0.00	0.00	0.00	0.00	0.00	0.00	0.00	0.00	0.00
COC_{α}	0.00	0.00	0.00	0.00	0.00	0.00	0.00	0.00	0.00	0.00	0.00	0.00
COC_{β}	0.00	2.30	0.00	0.00	0.00	0.00	0.00	0.00	0.00	0.00	0.29	0.00
COC_{β}*	0.03	1.60	3.76	1.31	0.00	0.00	0.00	0.00	0.00	0.00	0.76	1.86
C=O	0.06	4.20	1.98	0.00	0.02	0.82	0.10	0.00	0.00	0.00	0.47	0.00
C=O*	7.78	4.39	5.38	5.94	9.75	7.71	6.12	5.10	6.84	6.64	5.50	5.24
O=COC	0.04	0.00	0.00	0.00	0.00	0.00	0.00	0.00	1.70	4.72	2.96	0.45
O=COH*	0.00	0.00	0.00	0.00	0.00	0.00	0.00	0.00	0.00	0.00	0.00	0.00
O=CO{-}*	0.91	0.00	0.00	0.00	0.00	0.00	0.00	0.00	0.21	0.00	0.00	0.15
O=COC=O	3.93	7.21	3.73	2.29	6.95	9.07	2.98	0.00	3.92	3.26	3.58	3.81
COC(=O)OC	0.00	0.90	0.00	0.00	0.00	1.76	0.00	0.00	0.83	1.85	1.99	2.40
CNH_2	0.00	0.15	0.00	0.00	0.00	1.94	0.00	0.00	0.00	0.00	0.00	0.24
CNH_2*	2.71	0.00	6.09	2.65	0.54	0.84	3.84	1.46	0.00	0.00	0.00	0.00
$CNHC_{\alpha}$	0.98	6.96	0.00	0.00	3.80	0.01	0.00	0.00	0.00	0.00	0.00	0.00
$CNHC_{\beta}$	0.00	0.00	0.00	0.00	0.00	0.00	0.00	0.00	0.00	0.00	0.00	0.25
$CNHC_{\beta}$*	0.00	0.00	0.00	0.00	0.00	0.00	0.00	0.00	0.00	0.00	0.00	0.00
CN(C)C	0.00	1.71	0.00	0.00	0.00	0.01	0.00	0.00	0.00	7.98	4.54	0.00
$CNH_3^{\{+\}}$	0.00	0.19	0.00	0.00	0.00	0.29	0.00	0.00	0.00	0.00	0.12	0.00
$CNH_3^{\{+\}}$*	0.00	0.00	0.06	0.00	0.19	0.15	0.42	0.00	0.51	0.83	0.75	0.93
$CNHNH_2$	0.00	1.48	0.00	0.00	0.00	1.00	0.00	0.00	0.00	0.00	0.00	0.00
$CNHNH_2$*	4.56	3.20	3.38	2.00	3.73	3.42	1.79	1.19	1.16	0.00	0.00	0.00
C=NH	2.56	5.97	0.00	0.00	4.89	7.34	0.00	0.00	0.00	0.00	0.14	0.00
C=NH*	3.57	0.00	3.94	4.57	2.74	1.59	6.25	4.75	2.05	0.00	0.00	0.00
C=NC	0.00	1.54	0.00	0.00	0.00	0.41	0.00	0.00	0.00	0.00	0.30	0.91
C=NN=C	0.00	0.36	0.00	0.00	0.00	0.04	0.00	0.00	0.00	0.00	0.00	0.00
$C=NNH_2$	0.00	1.82	0.00	0.00	0.00	0.00	0.00	0.00	0.00	0.00	0.00	0.00
$C=NNH_2$*	0.00	1.03	1.00	0.00	2.45	1.69	0.00	0.00	0.00	0.00	0.00	0.00
HN=CNHC	0.00	0.33	0.50	0.00	0.00	3.47	0.00	0.00	0.28	3.30	2.07	2.15
$HN=CNH_2$*	6.73	4.86	6.98	7.10	7.62	5.24	9.02	7.47	1.49	0.00	0.21	0.00
C≡N	0.00	0.00	0.00	0.00	0.00	0.03	0.00	0.00	0.49	0.67	2.50	1.49
C≡N*	0.00	0.00	0.00	0.00	0.00	1.38	0.00	0.00	2.04	4.21	4.48	6.55
CNHOH	0.00	0.00	0.00	0.00	0.00	0.00	0.00	0.00	0.00	0.00	0.00	0.00
CNHOH*	3.21	0.00	0.00	2.06	0.00	0.00	0.00	0.00	0.00	0.00	0.00	0.00
$CONH_2$	0.47	0.00	0.00	0.00	0.44	0.00	0.00	0.00	0.00	0.00	0.00	0.00
$CONH_2$*	0.88	0.00	0.00	0.00	0.00	0.00	0.00	0.00	0.00	0.00	0.00	0.00
CNHOC	0.00	0.00	0.00	0.00	0.00	0.00	0.00	0.00	0.00	0.00	0.00	0.00
C=NOH	0.00	0.00	0.00	0.00	0.00	0.00	0.00	0.00	0.00	0.00	0.00	0.00
C=NOH*	0.00	0.00	0.00	0.00	0.00	0.00	0.00	0.00	0.00	0.00	0.00	0.00
C=NOC	0.00	0.00	0.00	0.00	0.00	0.00	0.00	0.00	0.00	0.00	0.00	0.00
CN=O	0.00	0.00	0.00	0.00	0.00	0.00	0.00	0.00	0.00	0.00	0.00	0.00
CN=O*	0.00	0.00	0.00	0.00	0.00	0.00	0.00	0.00	0.00	0.00	0.00	0.00
O=CNHC	0.00	0.00	0.00	0.00	0.00	0.00	0.00	0.00	0.08	0.04	0.45	0.65
$O=CNH_2$*	2.64	0.00	0.19	2.85	1.32	0.00	1.32	1.97	5.17	2.90	3.26	3.90
O=CNHC=O	8.49	10.81	11.47	8.10	12.05	13.19	15.15	13.10	2.69	2.26	3.33	4.90
O=CN(OH)C	0.00	0.00	0.00	0.00	0.00	0.00	0.00	0.00	0.00	0.00	0.00	0.00
O=CN(OH)H*	1.30	0.00	0.21	0.79	1.13	0.00	0.00	1.04	0.00	0.00	0.00	0.00
COC(=O)NHC	0.00	0.00	0.19	0.00	0.00	0.00	0.00	0.00	0.00	0.00	0.00	0.00
$COC(=O)NH_2$*	0.89	0.00	6.15	7.61	0.00	0.00	9.71	12.39	0.00	0.00	0.00	0.00
aT	0.00	0.00	0.00	0.00	0.00	0.00	0.00	0.00	0.00	0.00	0.00	0.00
aTQ	0.00	0.00	0.00	0.00	0.00	0.00	0.00	0.00	0.00	0.00	0.00	0.00
aTHQ	0.00	0.00	0.00	0.00	0.00	0.00	0.00	0.00	0.00	0.00	0.00	0.00

Appendix D37 – Component compositions of the D/UT high-resolution peak fits

Table D37. Composition as obtained by the high-resolution C 1s, N 1s and O 1s spectra peak fits of UHMWPE D/UT (C1-3), using a 'Shirley' background and the wB97X-D-based peak model including the respective symmetric higher-order carbon shifts (1°-4°).

ID	C1_1°	C1_2°	C1_3°	C1_4°	C2_1°	C2_2°	C2_3°	C2_4°	C3_1°	C3_2°	C3_3°	C3_4°
CH	62.27	64.74	65.25	65.08	63.39	68.79	71.78	72.01	79.22	78.87	77.71	77.16
COH	0.00	0.00	0.00	0.00	0.00	0.21	0.47	0.66	0.00	0.00	0.00	0.00
COH*	0.54	1.60	1.62	1.77	1.11	0.74	1.11	1.32	0.00	0.00	0.00	0.00
COC_{α}	0.79	0.00	0.00	0.00	0.00	0.15	0.00	0.00	0.00	0.00	0.00	0.00
COC_{β}	0.00	0.00	0.00	0.00	0.00	0.00	0.00	0.00	0.00	0.00	0.00	0.00
COC_{β}*	0.00	0.00	0.00	0.00	0.00	0.00	0.00	0.00	0.00	0.00	0.00	0.00
C=O	0.00	0.00	0.00	0.00	0.23	0.57	0.66	0.68	0.00	0.00	0.00	0.00
C=O*	0.89	1.08	1.12	1.08	0.21	0.02	0.00	0.00	5.85	5.51	5.25	5.11
O=COC	0.00	0.04	0.00	0.00	0.00	0.21	0.30	0.09	0.00	0.00	0.00	0.00
O=COH*	0.00	0.00	0.00	0.00	0.96	0.64	0.61	0.67	0.00	0.00	0.00	0.00
O=CO{-}*	0.03	0.00	0.00	0.00	0.13	0.00	0.00	0.00	0.00	0.00	0.00	0.00
O=COC=O	1.89	1.92	1.90	1.84	0.00	0.05	0.00	0.00	0.00	0.00	0.00	0.00
COC(=O)OC	0.00	0.00	0.00	0.00	0.00	0.34	0.36	0.06	0.00	0.00	0.00	0.00
CNH_2	0.00	0.00	0.00	0.00	0.00	0.00	0.00	0.00	0.00	0.00	0.00	0.00
CNH_2*	0.00	0.00	0.00	0.00	0.00	0.00	0.00	0.00	0.00	0.00	0.00	0.00
$CNHC_{\alpha}$	0.00	0.00	0.00	0.00	0.00	0.00	0.00	0.00	0.00	0.00	0.00	0.00
$CNHC_{\beta}$	0.00	0.00	0.00	0.00	0.00	0.00	0.00	0.00	0.00	0.00	0.00	0.00
$CNHC_{\beta}$*	0.00	0.00	0.00	0.00	0.00	0.00	0.00	0.00	0.00	0.00	0.00	0.00
CN(C)C	0.00	0.00	0.00	0.00	0.00	0.00	0.00	0.00	0.00	0.00	0.00	0.00
$CNH_3^{\{+\}}$	0.00	0.00	0.00	0.00	0.00	0.00	0.00	0.00	0.00	0.00	0.00	0.00
$CNH_3^{\{+\}}$*	0.00	0.00	0.00	0.00	0.00	0.00	0.00	0.00	0.00	0.00	0.00	0.00
$CNHNH_2$	0.00	0.00	0.00	0.00	0.00	0.00	0.00	0.00	0.00	0.00	0.00	0.00
$CNHNH_2$*	0.00	0.00	0.00	0.00	0.00	0.00	0.00	0.00	0.00	0.00	0.00	0.00
C=NH	0.00	0.00	0.00	0.00	0.00	0.00	0.00	0.00	0.00	0.00	0.00	0.00
C=NH*	0.00	0.00	0.00	0.00	0.00	0.00	0.00	0.00	0.00	0.00	0.00	0.00
C=NC	0.00	0.00	0.00	0.00	0.00	0.00	0.00	0.00	0.00	0.00	0.00	0.00
C=NN=C	0.00	0.00	0.00	0.00	0.00	0.00	0.00	0.00	0.00	0.00	0.00	0.00
$C=NNH_2$	0.00	0.00	0.00	0.00	0.00	0.00	0.00	0.00	0.00	0.00	0.00	0.00
$C=NNH_2$*	0.00	0.00	0.00	0.00	0.00	0.00	0.00	0.00	0.00	0.00	0.00	0.00
HN=CNHC	0.00	0.00	0.00	0.00	0.00	0.00	0.00	0.00	0.00	0.00	0.00	0.00
$HN=CNH_2$*	0.00	0.00	0.00	0.00	0.00	0.00	0.00	0.00	0.00	0.00	0.00	0.00
C≡N	0.00	0.00	0.00	0.00	0.00	0.00	0.00	0.00	0.00	0.00	0.00	0.00
C≡N*	0.00	0.00	0.00	0.00	0.00	0.00	0.00	0.00	0.00	0.00	0.00	0.00
CNHOH	0.00	0.00	0.00	0.00	0.00	0.00	0.00	0.00	0.00	0.00	0.00	0.00
CNHOH*	0.00	0.00	0.00	0.00	0.00	0.00	0.00	0.00	0.00	0.00	0.00	0.00
$CONH_2$	0.00	0.00	0.00	0.00	0.00	0.00	0.00	0.00	0.00	0.00	0.00	0.00
$CONH_2$*	0.00	0.00	0.00	0.00	0.00	0.00	0.00	0.00	0.00	0.00	0.00	0.00
CNHOC	0.00	0.00	0.00	0.00	0.00	0.00	0.00	0.00	0.00	0.00	0.00	0.00
C=NOH	0.00	0.00	0.00	0.00	0.00	0.00	0.00	0.00	0.00	0.00	0.00	0.00
C=NOH*	0.00	0.00	0.00	0.00	0.00	0.00	0.00	0.00	0.00	0.00	0.00	0.00
C=NOC	0.00	0.00	0.00	0.00	0.00	0.00	0.00	0.00	0.00	0.00	0.00	0.00
CN=O	0.00	0.00	0.00	0.00	0.00	0.00	0.00	0.00	0.00	0.00	0.00	0.00
CN=O*	0.00	0.00	0.00	0.00	0.00	0.00	0.00	0.00	0.00	0.00	0.00	0.00
O=CNHC	0.00	0.00	0.00	0.00	0.00	0.00	0.00	0.00	0.00	0.00	0.00	0.00
$O=CNH_2$*	0.00	0.00	0.00	0.00	0.00	0.00	0.00	0.00	0.00	0.00	0.00	0.00
O=CNHC=O	0.00	0.00	0.00	0.00	0.00	0.00	0.00	0.00	0.00	0.00	0.00	0.00
O=CN(OH)C	0.00	0.00	0.00	0.00	0.00	0.00	0.00	0.00	0.00	0.00	0.00	0.00
O=CN(OH)H*	0.00	0.00	0.00	0.00	0.00	0.00	0.00	0.00	0.00	0.00	0.00	0.00
COC(=O)NHC	0.00	0.00	0.00	0.00	0.00	0.00	0.00	0.00	0.00	0.00	0.00	0.00
$COC(=O)NH_2$*	0.00	0.00	0.00	0.00	0.00	0.00	0.00	0.00	0.00	0.00	0.00	0.00
aT	0.00	0.00	0.00	0.00	25.46	21.15	20.24	10.09	0.00	0.00	0.00	0.00
aTQ	4.39	3.65	3.99	4.39	0.00	0.00	0.00	0.00	14.93	15.61	17.04	17.74
aTHQ	29.20	26.98	26.12	25.84	8.50	7.11	4.48	14.42	0.00	0.00	0.00	0.00

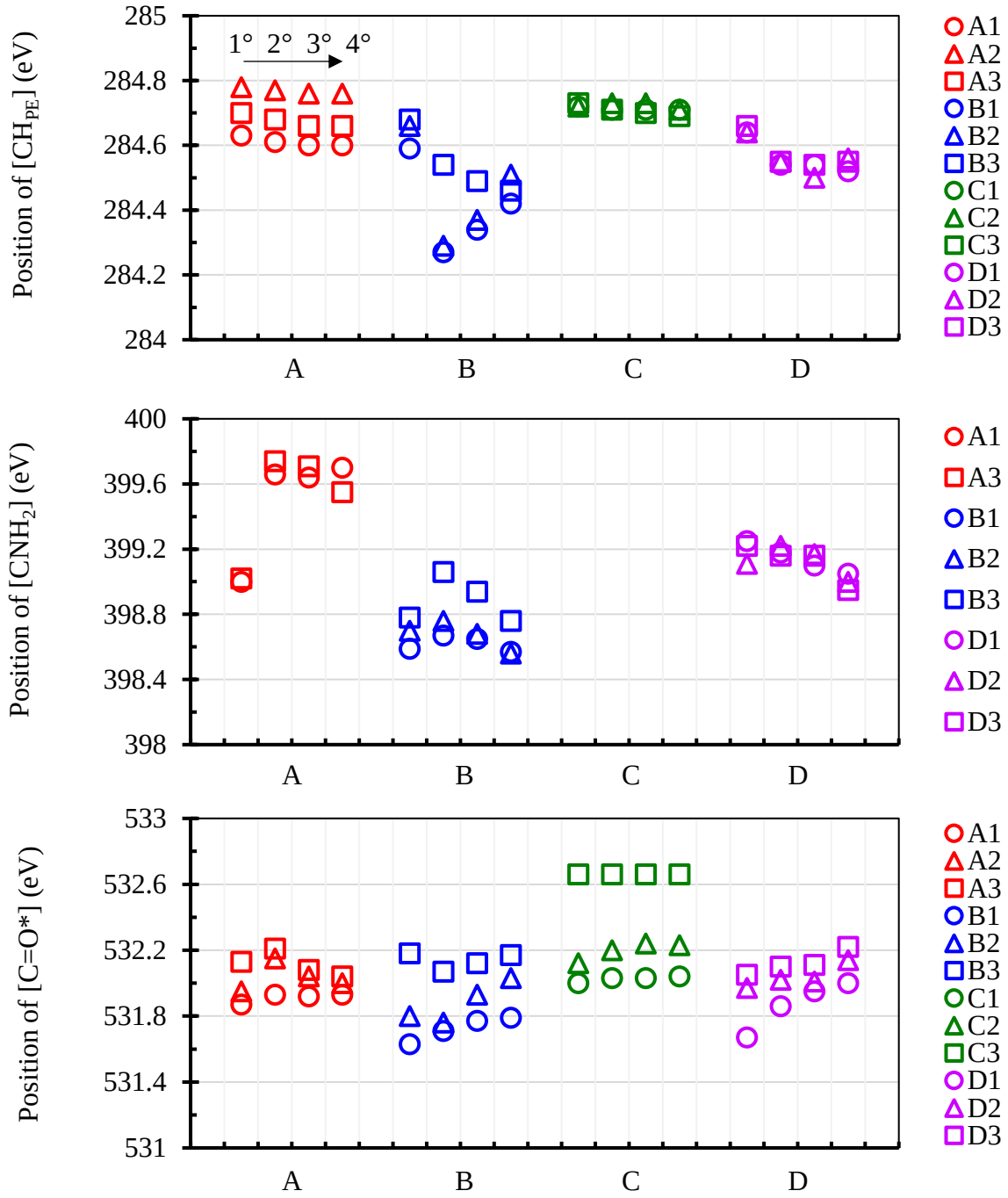
Appendix D38 – Component compositions of the D/PT60 high-resolution peak fits

Table D38. Composition as obtained by the high-resolution C 1s, N 1s and O 1s spectra peak fits of UHMWPE D/PT (D1-3), using a 'Shirley' background and the wB97X-D-based peak model including the respective symmetric higher-order carbon shifts (1°-4°).

ID	D1_1°	D1_2°	D1_3°	D1_4°	D2_1°	D2_2°	D2_3°	D2_4°	D3_1°	D3_2°	D3_3°	D3_4°
CH	14.73	25.79	45.83	50.50	20.34	37.71	42.59	54.33	20.42	29.84	46.17	55.17
COH	0.00	0.00	0.00	0.00	0.00	0.00	0.00	0.00	0.00	0.00	0.00	0.00
COH*	0.00	0.00	0.00	0.00	0.00	0.00	0.00	0.00	0.00	0.00	0.00	0.00
COC_{α}	0.00	0.00	0.00	0.00	0.00	0.00	0.00	0.00	0.00	0.00	0.00	0.00
COC_{β}	0.00	0.00	0.00	0.00	0.00	0.00	0.00	0.00	0.00	0.00	0.00	0.00
COC_{β}*	0.00	0.00	3.00	4.98	0.00	0.00	1.26	4.14	0.00	1.77	4.86	7.26
C=O	0.00	0.00	0.04	0.00	0.00	0.00	0.00	0.00	0.00	0.00	0.04	0.00
C=O*	4.84	5.64	5.84	4.22	4.10	5.26	5.68	4.26	3.44	3.82	4.60	3.08
O=COC	0.00	0.00	0.00	0.00	0.00	0.00	0.00	0.00	0.00	0.00	0.00	0.00
O=COH*	0.00	0.00	0.00	0.00	0.00	0.00	0.00	0.00	0.00	0.00	0.00	0.00
O=CO{-}*	2.34	0.00	0.00	0.00	0.00	0.00	0.00	0.00	0.00	0.00	0.00	0.00
O=COC=O	2.13	3.22	2.55	2.80	2.92	3.00	2.33	1.83	2.20	0.50	2.20	1.87
COC(=O)OC	0.00	1.98	1.54	1.18	2.64	3.30	4.00	2.78	3.00	3.80	2.62	2.22
CNH_2	1.00	3.18	2.98	0.30	0.10	0.40	2.34	0.64	0.00	0.00	2.36	0.00
CNH_2*	0.00	0.00	0.76	2.74	0.00	0.00	0.00	0.62	0.00	0.00	0.00	0.36
$CNHC_{\alpha}$	0.00	0.00	0.00	0.00	0.00	0.00	0.00	0.00	0.00	0.00	0.00	0.00
$CNHC_{\beta}$	1.39	0.78	0.04	0.00	0.84	0.00	0.00	0.00	0.00	0.00	0.00	0.00
$CNHC_{\beta}$*	8.22	0.00	0.00	0.00	0.00	0.00	0.00	0.00	4.29	0.00	0.00	0.00
CN(C)C	0.84	0.87	0.33	0.00	4.76	0.00	0.00	0.00	0.00	3.12	0.00	0.00
$CNH_3^{\{+\}}$	0.00	0.00	0.00	0.00	0.00	0.00	0.00	0.00	0.52	0.66	0.00	0.00
$CNH_3^{\{+\}}$*	0.68	0.80	0.68	0.68	0.70	0.58	0.84	0.56	0.00	0.00	0.88	0.76
$CNHNH_2$	0.00	0.00	0.00	0.00	0.00	0.00	0.00	0.00	0.00	0.00	0.00	0.00
$CNHNH_2$*	0.00	0.00	0.00	0.00	0.00	0.00	0.00	0.00	0.00	0.00	0.00	0.00
C=NH	0.22	0.06	0.02	0.00	1.42	2.80	0.00	0.00	0.00	0.50	0.34	0.00
C=NH*	0.00	0.00	0.00	0.00	0.56	2.92	2.60	2.10	0.00	0.00	0.00	0.00
C=NC	0.00	4.35	1.89	0.00	1.65	1.35	0.21	0.00	0.00	0.00	0.00	0.00
C=NN=C	0.00	0.00	0.00	0.00	3.36	0.32	0.00	0.00	0.00	0.00	0.00	0.00
$C=NNH_2$	0.00	0.00	0.00	0.00	0.00	0.00	0.00	0.00	0.00	0.00	0.00	0.00
$C=NNH_2$*	0.00	0.00	0.00	0.00	0.00	0.00	0.00	0.00	0.00	0.00	0.00	0.00
HN=CNHC	3.44	6.00	5.56	0.92	5.08	5.44	11.12	8.96	8.80	6.00	8.56	7.36
$HN=CNH_2$*	7.38	4.14	4.11	7.17	2.01	2.73	0.00	0.00	0.00	1.65	0.00	0.00
C≡N	1.02	0.87	0.00	0.00	2.19	0.21	0.00	0.00	6.78	3.87	0.06	0.00
C≡N*	1.02	4.05	5.85	7.92	2.49	4.92	6.42	6.63	1.68	5.82	8.31	9.96
CNHOH	0.00	0.00	0.00	0.00	0.00	0.00	0.00	0.00	0.00	0.00	0.00	0.00
CNHOH*	0.00	0.00	0.00	0.00	0.00	0.00	0.00	0.00	0.00	0.00	0.00	0.00
$CONH_2$	0.00	0.00	0.00	0.00	0.00	0.00	0.00	0.00	0.00	0.00	0.00	0.00
$CONH_2$*	0.00	0.00	0.00	0.00	0.00	0.00	0.00	0.00	0.00	0.00	0.00	0.00
CNHOC	0.00	0.00	0.00	0.00	0.00	0.00	0.00	0.00	0.00	0.00	0.00	0.00
C=NOH	0.00	0.00	0.00	0.00	0.00	0.00	0.00	0.00	0.00	0.00	0.00	0.00
C=NOH*	0.00	0.00	0.00	0.00	0.00	0.00	0.00	0.00	0.00	0.00	0.00	0.00
C=NOC	0.00	0.00	0.00	0.00	0.00	0.00	0.00	0.00	0.00	0.00	0.00	0.00
CN=O	0.00	0.00	0.00	0.00	0.00	0.00	0.00	0.00	0.00	0.00	0.00	0.00
CN=O*	0.00	0.00	0.00	0.00	0.00	0.00	0.00	0.00	0.00	0.00	0.00	0.00
O=CNHC	0.00	0.00	0.00	0.00	0.12	0.00	0.00	0.00	0.28	0.00	0.00	0.00
$O=CNH_2$*	0.00	0.69	1.29	2.73	0.72	1.02	0.00	1.11	0.00	0.00	1.23	2.91
O=CNHC=O	1.85	3.63	4.75	5.72	3.25	4.35	5.42	7.98	3.28	5.55	4.32	6.27
O=CN(OH)C	0.00	0.00	0.00	0.00	0.00	0.00	0.00	0.00	0.00	0.00	0.00	0.00
O=CN(OH)H*	0.00	0.00	0.00	0.00	0.00	0.00	0.00	0.00	0.00	0.00	0.00	0.00
COC(=O)NHC	0.00	0.54	2.70	1.80	0.00	0.00	0.96	0.96	0.00	0.00	0.00	0.00
$COC(=O)NH_2$*	0.20	0.00	0.00	0.00	0.00	0.00	0.00	0.45	0.00	0.25	0.00	0.00
aT	13.38	12.18	0.00	0.00	8.04	2.28	0.00	0.00	11.56	9.69	0.41	0.00
aTQ	33.53	19.46	8.39	4.74	30.97	19.59	12.28	0.71	31.93	21.13	11.13	0.74
aTHQ	0.00	0.00	0.00	0.00	0.00	0.00	0.00	0.00	0.00	0.00	0.00	0.00

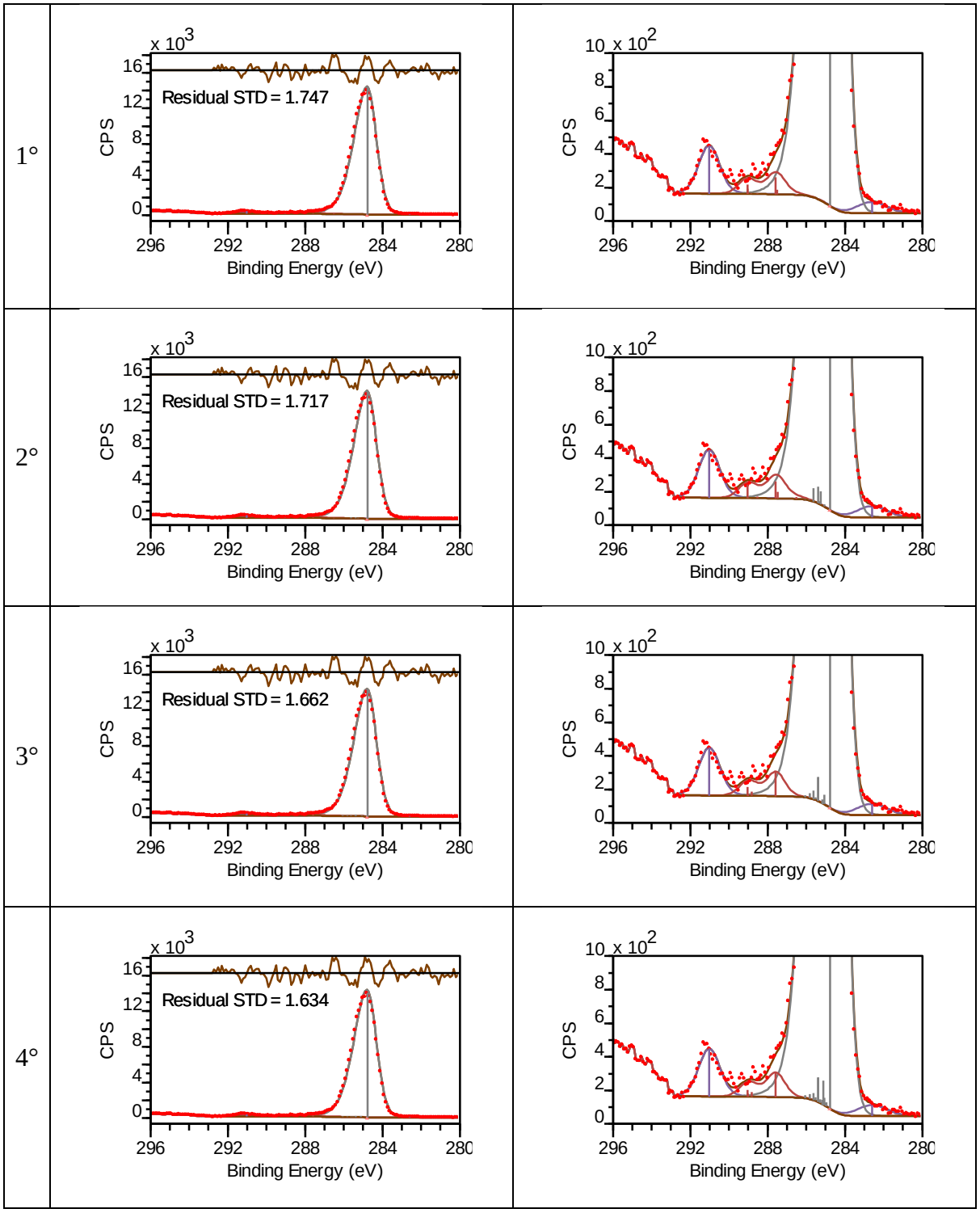
Appendix D39 – Positioning of the reference components within the HR spectra

Figure D39. Positioning of the peak model reference components within the high-resolution C 1s, N 1s and O 1s spectra of UHMWPE UD/UT (A1-3, **red**), UD/PT (B1-3, **blue**), D/UT (C1-3, **green**), and D/PT (D1-3, **purple**), including the higher-order [CH_x] ΔCEBEs (1°, 2°, 3°, and 4°) within the wB97X-D-based peak model (from left to right, per sample series; see arrow).



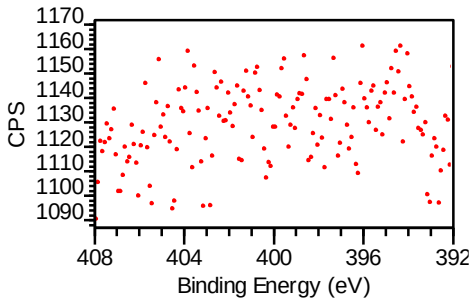
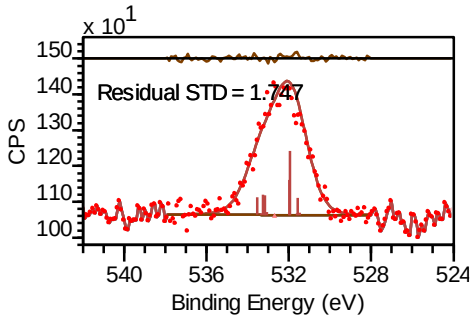
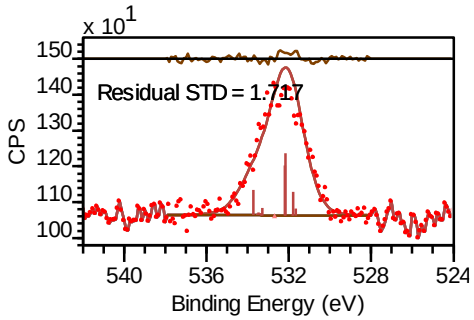
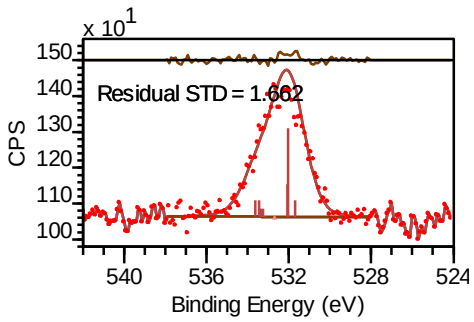
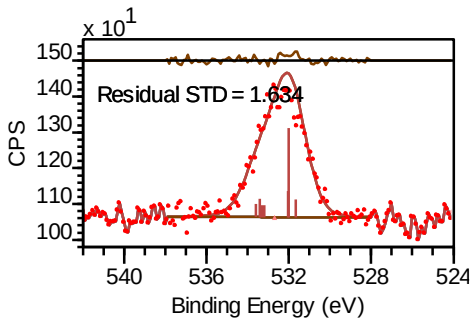
Appendix D40 – High-resolution XPS spectra peak fits of UD/UT

Figure D40a. High-resolution C 1s spectra peak fits of UHMWPE UD/UT (A2), using a 'Shirley' background and the wB97X-D-based peak model including the respective symmetric [CH_x] higher-order shifts. The spectra display the recorded experimental data (**red**, dotted) and the summed peak model envelope (**brown**, solid). The colours represent the various component groups: [CH] (**grey**), [CO] (**dark red**), and contaminants (**purple**).



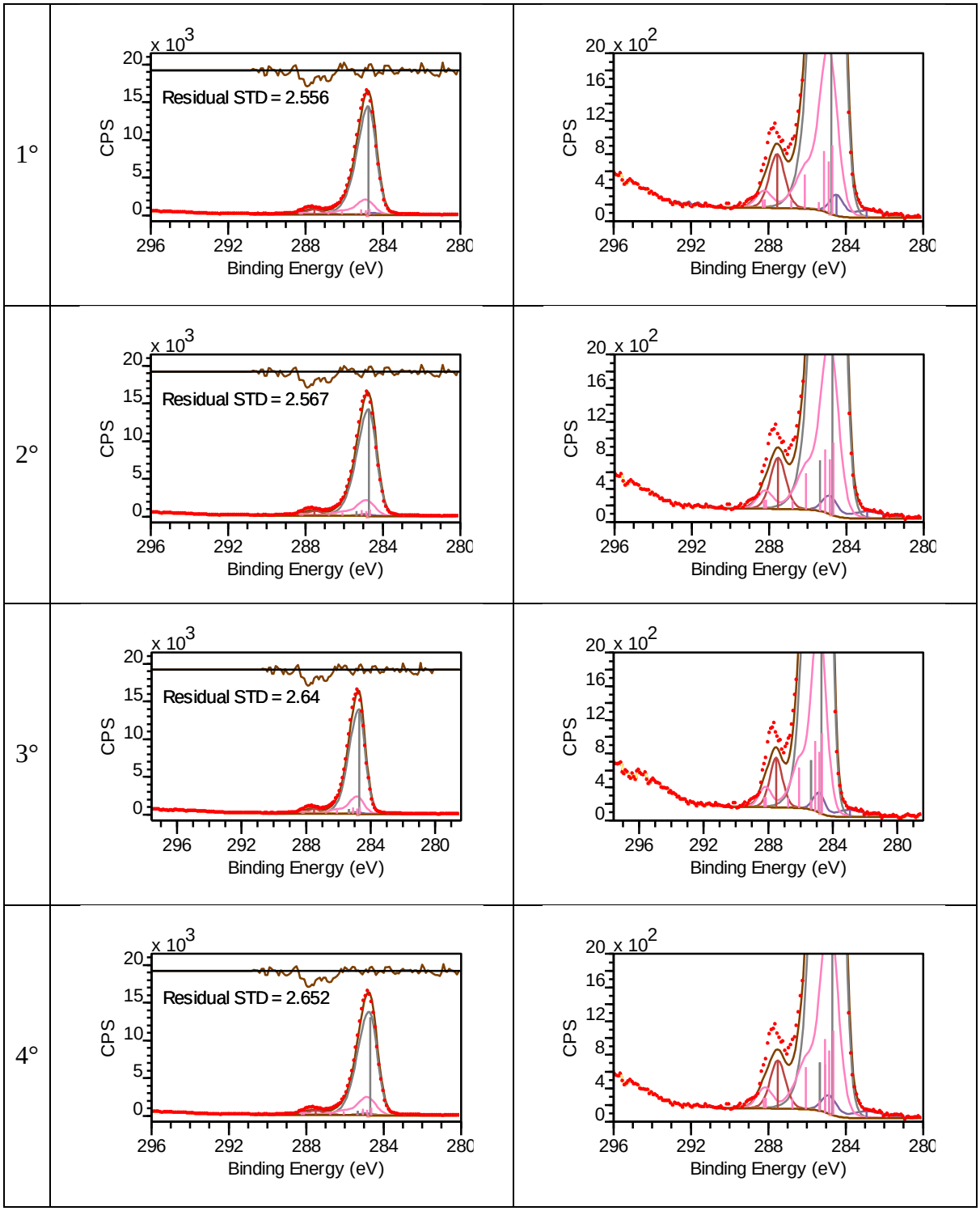
Continued on the next page…

Figure D40b. High-resolution N 1s and O 1s spectra peak fits of UHMWPE UD/UT (A2), using a 'Shirley' background and the wB97X-D-based peak model including the respective symmetric [CH_x] higher-order shifts. The spectra display the recorded experimental data (**red**, dotted) and the summed peak model envelope (**brown**, solid). The colour represents the component group [CO] (**dark red**).

	N 1s	O 1s
1°		
2°	N/A	
3°	N/A	
4°	N/A	

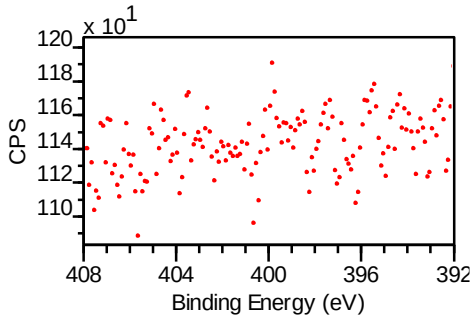
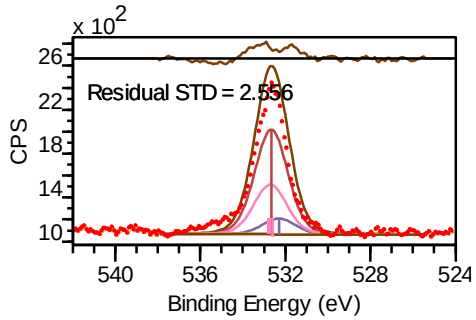
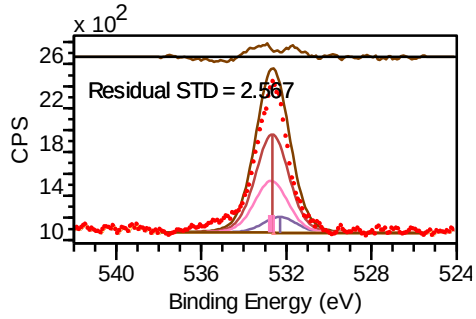
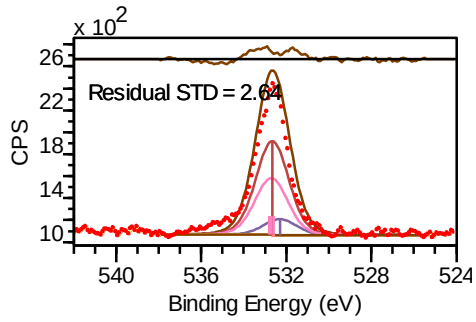
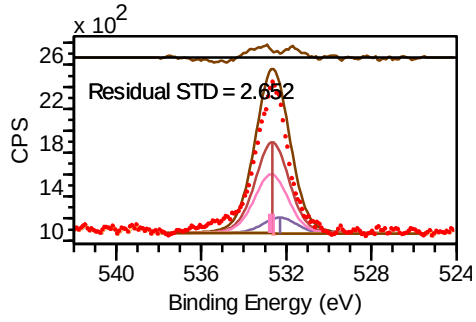
Appendix D41 – High-resolution XPS spectra peak fits of D/UT

Figure D41a. High-resolution C 1s spectra peak fits of UHMWPE D/UT (C3), using a 'Shirley' background and the wB97X-D-based peak model including the respective symmetric [CH_x] higher-order shifts. The spectra display the recorded experimental data (**red**, dotted) and the summed peak model envelope (**brown**, solid). The colours represent the various component groups: [CH] (**grey**), [CO] (**dark red**), [aT] (**orange**), [aTQ] (**pink**), [aTHQ] (**yellow**), and contaminants (**purple**).



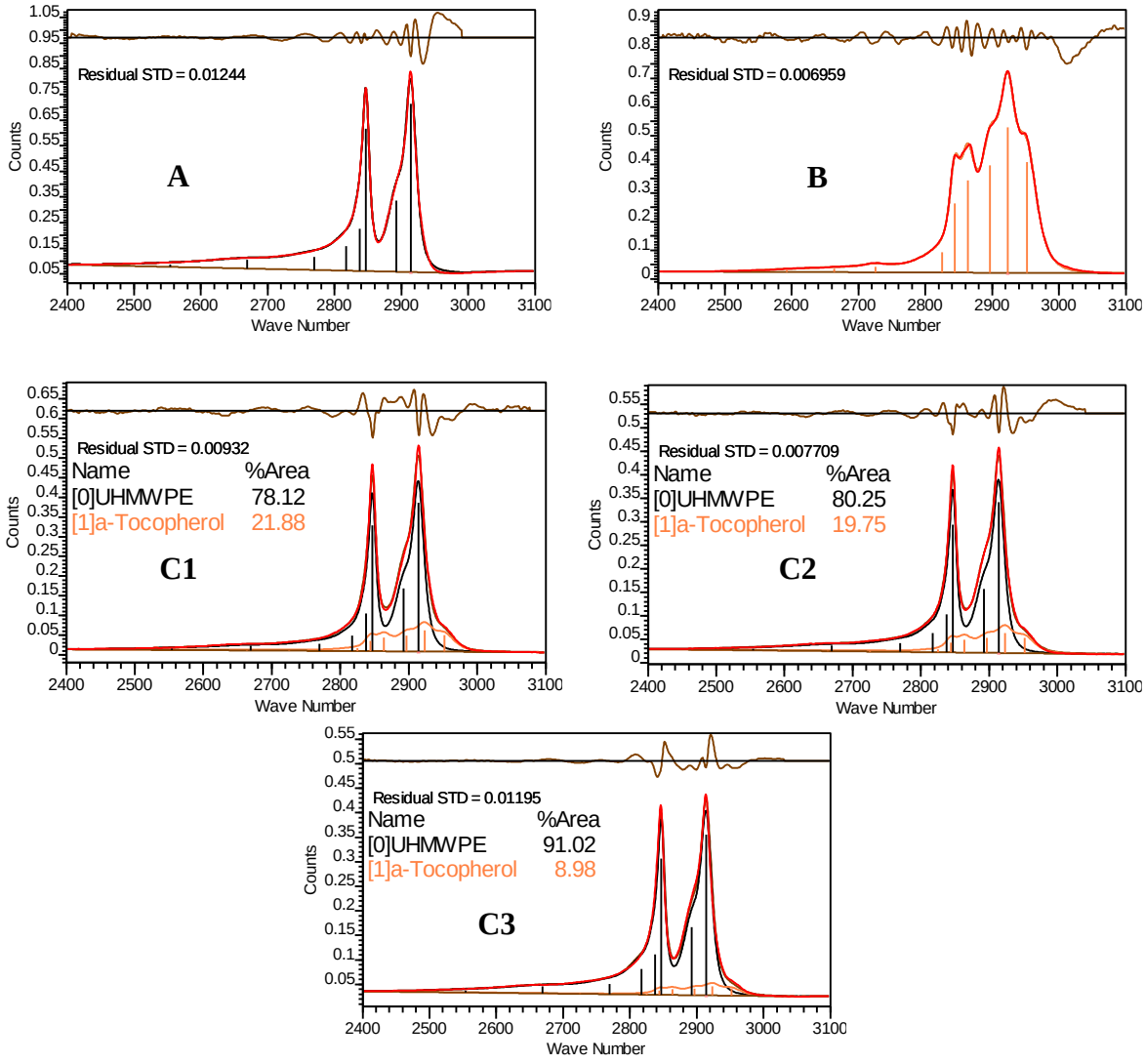
Continued on the next page…

Figure 41b. High-resolution N 1s and O 1s spectra peak fits of UHMWPE D/UT (C3), using a 'Shirley' background and the wB97X-D-based peak model including the respective symmetric [CH_x] higher-order shifts. The spectra display the recorded experimental data (**red**, dotted) and the summed peak model envelope (**brown**, solid). The colours represent the various component groups: [CH] (**grey**), [CO] (**dark red**), and contaminants (**purple**).

	N 1s	O 1s
1°		
2°	N/A	
3°	N/A	
4°	N/A	

Appendix D42 – Presence of the tocopherol-like components determined by FTIR

Figure D42. ATR-FTIR peak fits of UHMWPE UD/UT (A, sum of 3 samples, **black**), α-tocopherol (B, sum of 3 samples, **orange**), and UHMWPE D/UT (C1-3). Spectra were taken with a *Nicolet™ 8700* FT-IR (Thermo Scientific) in combination with a single-reflectance diamond *Golden Gate™* ATR module (Specac), samples were clamped onto the ATR crystal with a force of 80 cNm. After a background scan prior to each measurement, spectra were collected in absorbance mode with 100 scans between 700 – 4000 cm^{-1} and with a data spacing of 0.482 cm^{-1}.



Appendix D43 – High-resolution XPS spectra peak fits of UD/PT60

Figure D43a. High-resolution C 1s spectra peak fits of UHMWPE UD/PT (B1), using a 'Shirley' background and the wB97X-D-based peak model including the respective symmetric [CH_x] higher-order shifts. The spectra display the recorded experimental data (**red**, dotted) and the summed peak model envelope (**brown**, solid). The colours represent the various component groups: [CH] (**grey**), [CO] (**dark red**), [CN] (**blue**), [CNO] (**green**), and contaminants (**purple**).

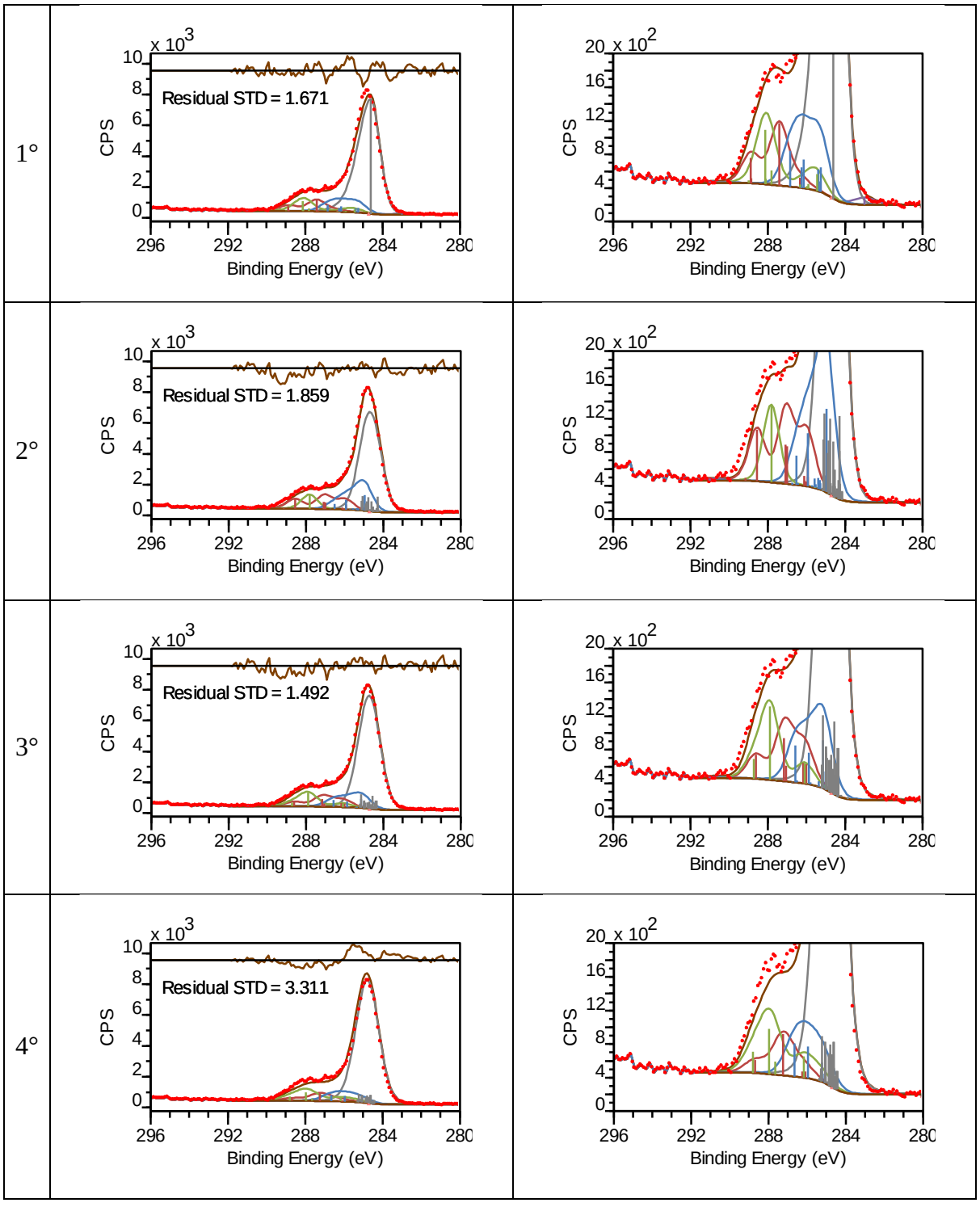
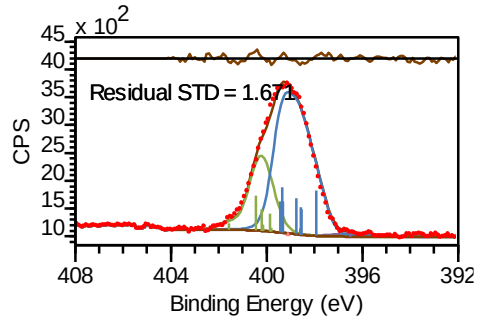
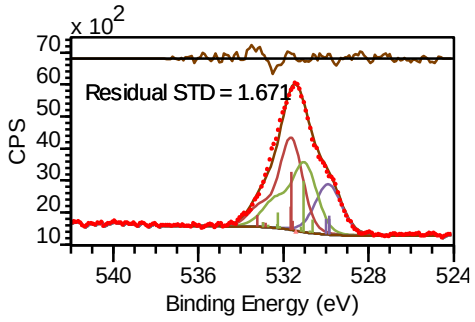
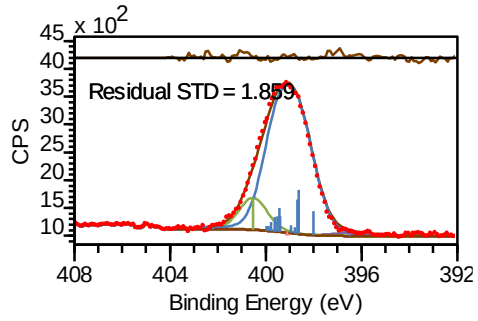
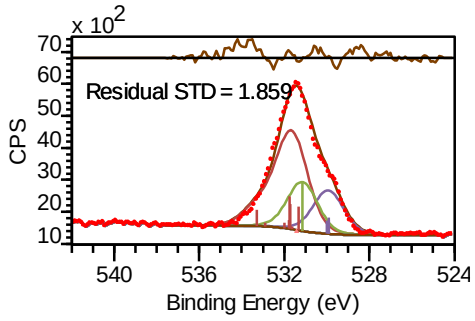
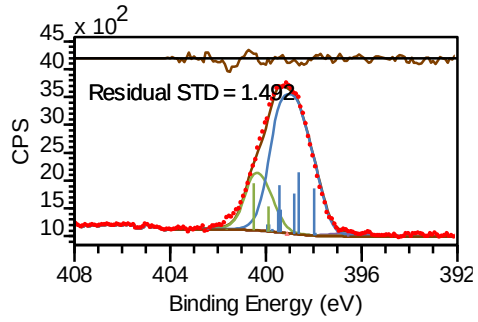
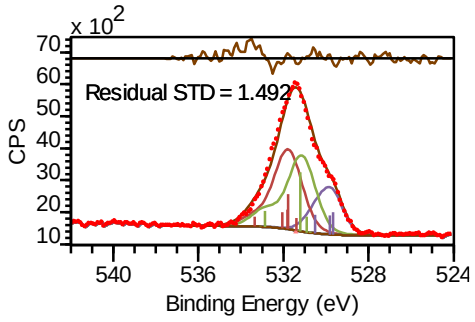
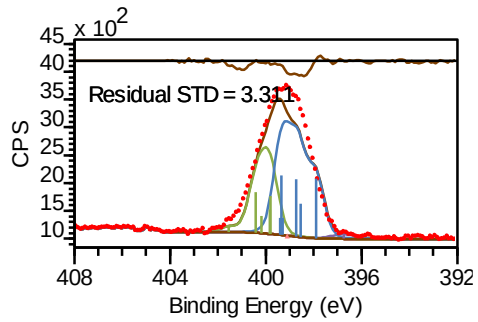
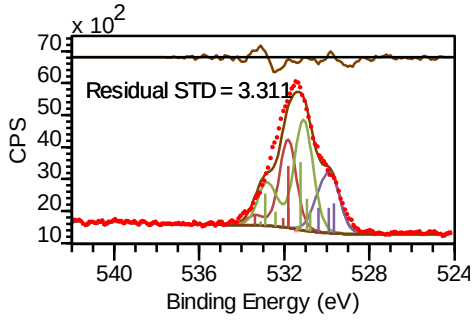
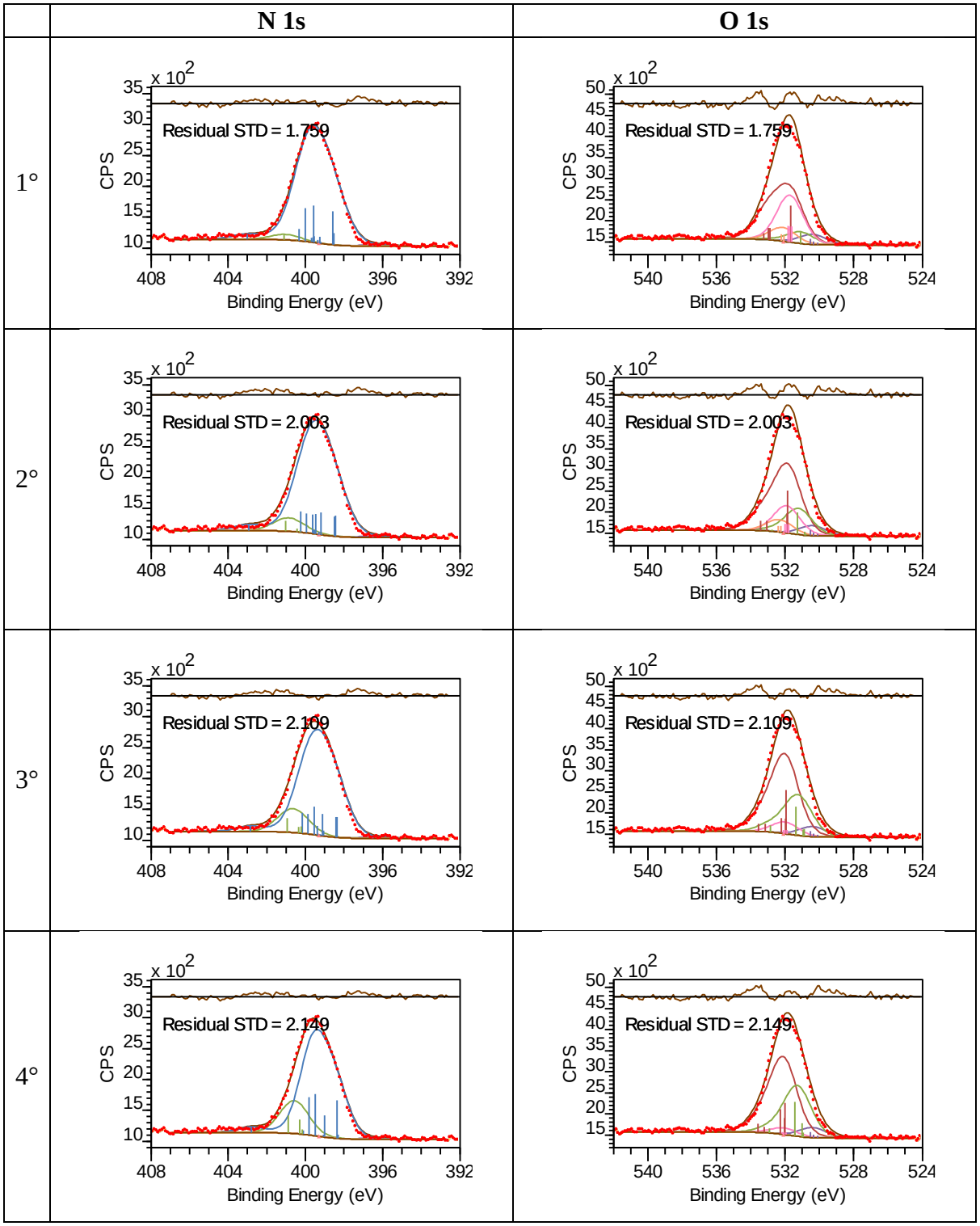


Figure 43b. High-resolution N 1s and O 1s spectra peak fits of UHMWPE UD/PT (B1), using a 'Shirley' background and the wB97X-D peak model including the respective symmetric [CH_x] higher-order shifts. The spectra display the recorded experimental data (**red**, dotted) and the summed peak model envelope (**brown**, solid). The colours represent the various component groups: [CH] (**grey**), [CO] (**dark red**), [CN] (**blue**), [CNO] (**green**), and contaminants (**purple**).

	N 1s	O 1s
1°		
2°		
3°		
4°		

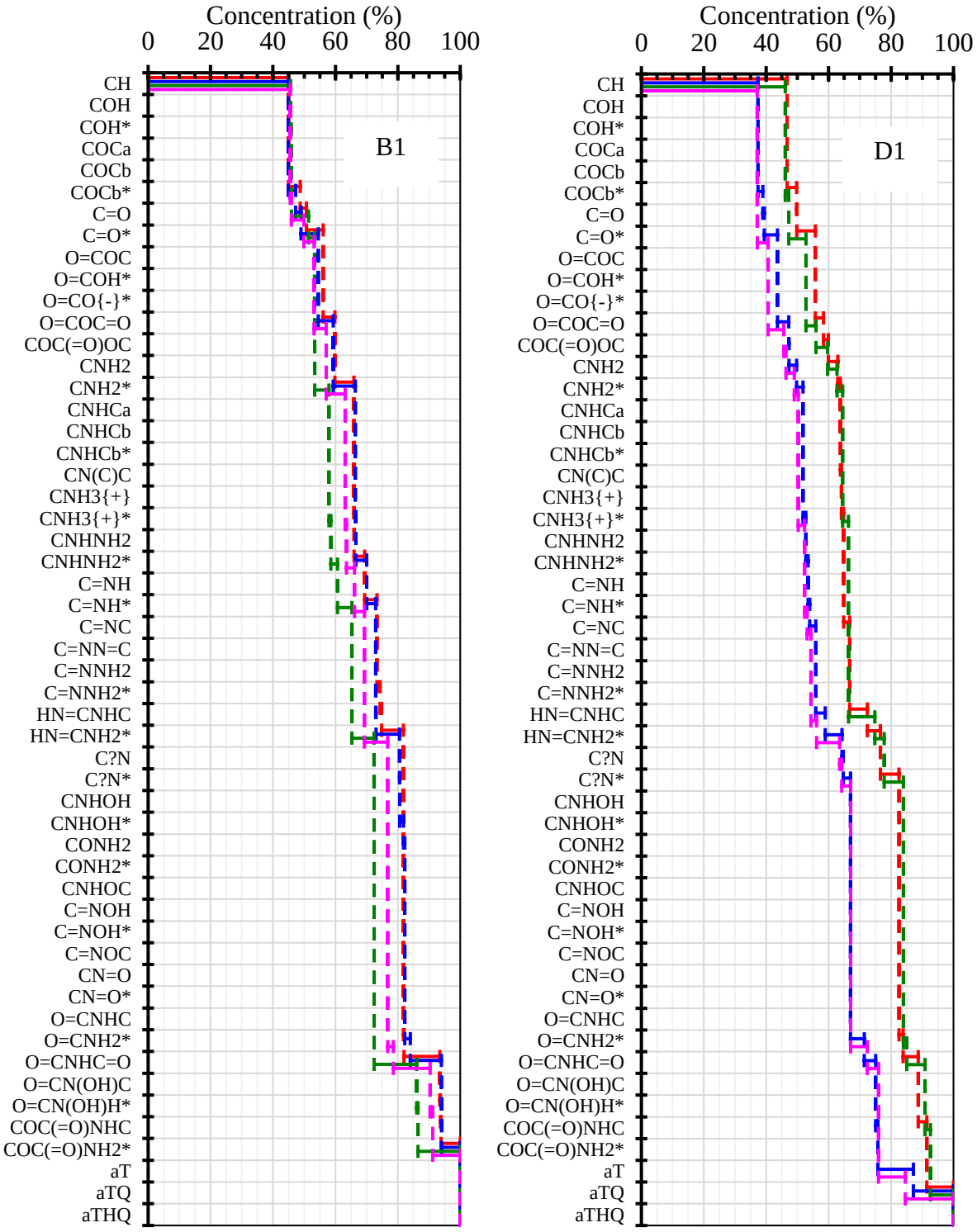
Appendix D44 – HR XPS N 1s and O 1s spectra peak fits of D/PT60

Figure D44. High-resolution N 1s and O 1s spectra peak fits of UHMWPE D/PT (D1), using a 'Shirley' background and the wB97X-D-based peak model including the respective symmetric [CH_x] higher-order shifts. The spectra display the recorded experimental data (**red**, dotted) and the summed peak model envelope (**brown**, solid). The colours represent the various component groups: [CH] (**grey**), [CO] (**dark red**), [CN] (**blue**), [CNO] (**green**), [aT] (**orange**), [aTQ] (**pink**), [aTHQ] (**yellow**), and contaminants (**purple**).



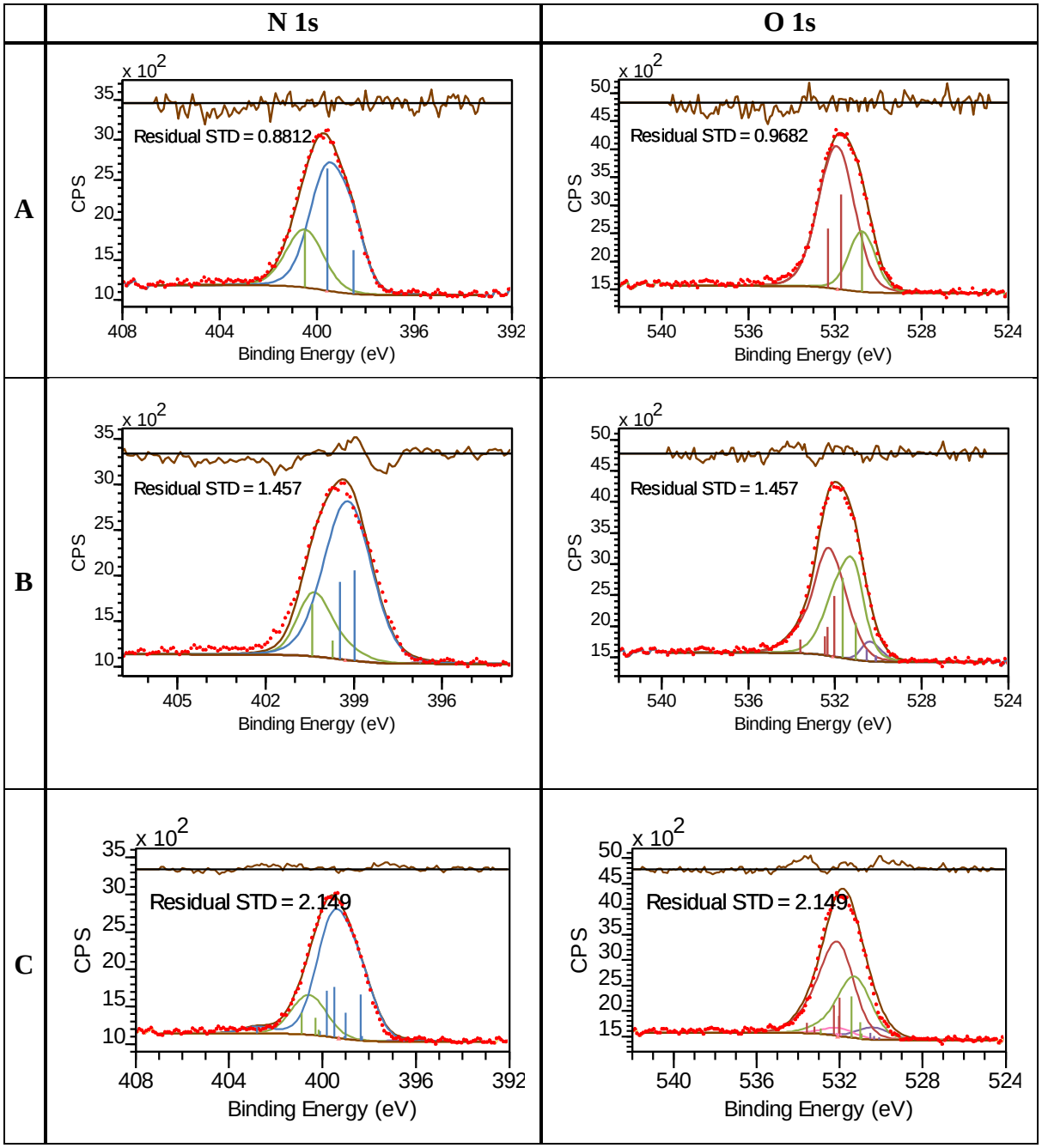
Appendix D45 – Change in composition due to the background and peak asymmetry

Figure D45. Composition of UHMWPE UD/PT (B1, left) and D/PT (D1, right) determined by the high-resolution spectra peak fits using the wB97X-D-based peak model including the symmetric or asymmetric 3° [CH_x] fine structure with a 'Shirley' background (**red** or **blue**, respectively) or an 'Universal Polymer Tougaard' background (**green** or **pink**, respectively). The bars depict the component presence, stacking up to 100%.



Appendix D46 – HR XPS N 1s and O 1s spectra of the reference-based peak fits

Figure D46. High-resolution N 1s and O 1s spectra peak fits of UHMWPE D/PT (D1) using a 'Shirley' background following conventional peak fitting (A), reference-based advanced peak fitting (B) and the wB97X-D-based peak fitting using the 3° symmetric [CH_x] higher-order shifts (C). The spectra display the experimental data (**red**, dotted) and the summed peak model envelope (**brown**, solid). The colours represent the various component groups: [CO] (**dark red**), [CN] (**blue**), [CNO] (**green**), [aTQ] (**pink**), and contaminants (**purple**).



Appendix E1 – Bacterial adhesion assay CFUs, dilution factors, and CFUs/mL

Table E1a. Bacterial adhesion assay CFUs, dilution factors, and CFUs/mL with *S. Aureus*.

	Sample	Repeat	Control	UD/UT	UD/PT60	D/UT	D/PT60
CFU	1	1	24	17	16	28	31
		2	19	21	14	22	38
		3	23	18	16	26	33
	2	1	25	12	20	23	34
		2	21	15	21	33	42
		3	23	10	23	33	35
	3	1	14	8	17	21	23
		2	18	13	20	27	16
		3	19	11	29	31	26
Average			20.67	13.89	19.56	27.11	30.89
Standard deviation			3.30	3.96	4.30	4.31	7.55
Conf. interval (α=0.05)			2.16	2.58	2.81	2.81	4.93
Dilution factor (/mL)			$50*10^6$	$55*10^6$	$65*10^6$	$45*10^6$	$55*10^6$
CFU/mL			$1.03*10^9$	$7.64*10^8$	$1.27*10^9$	$1.22*10^9$	$1.70*10^9$

Continued on the next page…

Table E1b. Bacterial adhesion assay CFUs, dilution factors, and CFUs/mL with *S. Epidermidis*.

	Sample	Repeat	Control	UD/UT	UD/PT60	D/UT	D/PT60
CFU	1	1	27	27	23	20	22
		2	22	22	21	25	24
		3	26	21	24	20	31
	2	1	32	18	29	22	38
		2	27	22	21	27	45
		3	31	29	18	28	47
	3	1	21	21	19	17	44
		2	18	23	22	16	46
		3	24	26	20	17	50
Average			25.33	23.22	21.89	21.33	38.56
Standard deviation			4.32	3.26	3.07	4.22	9.84
Conf. interval (α=0.05)			2.82	2.13	2.01	2.75	6.43
Dilution factor (/mL)			$50*10^6$	$35*10^6$	$65*10^6$	$35*10^6$	$55*10^6$
CFU/mL			$1.27*10^9$	$8.13*10^8$	$1.42*10^9$	$7.47*10^8$	$2.12*10^9$

Appendix E2 – Additional statistic results for bacterial adhesion assay

Table E2a. Additional statistic results from one-way ANOVA on bacterial adhesion of *S. Aureus* on UHMWPE-based samples.

	SS	df	MS	F	P-value	F crit
Between Groups	4.25E+18	4	1.06E+18	13.03	7.01E-07	2.61
Within Groups	3.26E+18	40	8.16E+16			

Table E2b. Additional statistic results from Tukey-Kramer post-hoc analysis on bacterial adhesion of *S. Aureus* on UHMWPE-based samples.

Var1	Var2	Diff.	SE	Q	*p*
Control	UD_UT	2.69E+08	9.52E+07	2.83	2.84E-01
Control	UD_PT60	2.38E+08	9.52E+07	2.50	4.06E-01
Control	D_UT	1.87E+08	9.52E+07	1.96	6.40E-01
Control	D_PT60	6.66E+08	9.52E+07	6.99	1.30E-04
UD_UT	UD_PT60	5.07E+08	9.52E+07	5.33	4.58E-03
UD_UT	D_UT	4.56E+08	9.52E+07	4.79	1.31E-02
UD_UT	D_PT60	9.35E+08	9.52E+07	9.82	1.00E-05
UD_PT60	D_UT	5.11E+07	9.52E+07	0.54	9.95E-01
UD_PT60	D_PT60	4.28E+08	9.52E+07	4.49	2.27E-02
D_UT	D_PT60	4.79E+08	9.52E+07	5.03	8.25E-03

Continued on the next page…

Table E2c. Additional statistic results from one-way ANOVA on bacterial adhesion of *S. Epidermidis* on UHMWPE-based samples.

	SS	df	MS	F	P-value	F crit
Between Groups	1.11E+19	4	2.77E+18	29.67	1.71E-11	2.61
Within Groups	3.73E+18	40	9.33E+16			

Table E2d. Additional statistic results from Tukey-Kramer post-hoc analysis on bacterial adhesion of *S. Epidermidis* on UHMWPE-based samples.

Var1	Var2	Diff.	SE	Q	*p*
Control	UD_UT	2.69E+08	9.52E+07	2.83	1.36E-02
Control	UD_PT60	2.38E+08	9.52E+07	2.50	8.13E-01
Control	D_UT	1.87E+08	9.52E+07	1.96	3.49E-03
Control	D_PT60	6.66E+08	9.52E+07	6.99	< .00001
UD_UT	UD_PT60	5.07E+08	9.52E+07	5.33	4.80E-04
UD_UT	D_UT	4.56E+08	9.52E+07	4.79	9.90E-01
UD_UT	D_PT60	9.35E+08	9.52E+07	9.82	< .00001
UD_PT60	D_UT	5.11E+07	9.52E+07	0.54	1.00E-04
UD_PT60	D_PT60	4.28E+08	9.52E+07	4.49	6.00E-05
D_UT	D_PT60	4.79E+08	9.52E+07	5.03	< .00001

Appendix E3 – Cell viability assay luminescence data, standard curve, and cell counts

Table E3a. Luminescence data for UD/UT, UD/PT60, D/UT, and D/PT60 samples.

	Day 1			Day 4			Day 7		
	1	**2**	**3**	**1**	**2**	**3**	**1**	**2**	**3**
Control	34662	29790	25227	153874	177578	174932	275427	234812	243187
UD/UT	27048	32598	20287	121603	146214	145012	265292	358111	312936
D/UT	23769	26501	19936	73438	108333	128719	302919	301425	242239
Control	33042	37232	42072	43476	101556	48965	166697	250167	125454
UD/PT60	10578	12965	8395	66474	29650	57641	93440	196149	133623
D/PT60	12784	23025	22985	32196	42512	28496	162953	103461	114256

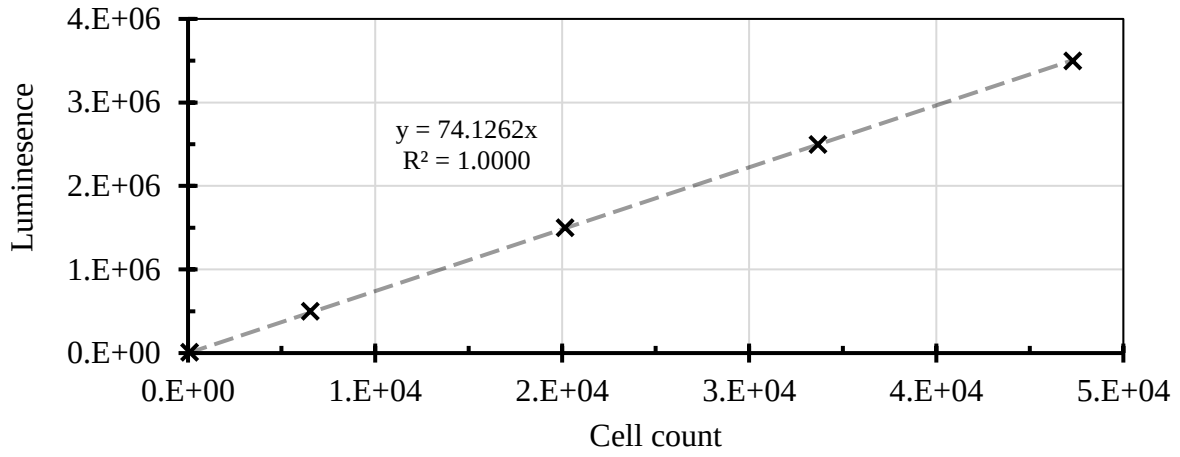


Figure E3. Luminescence vs. cell count standard curve reproduced from the assay protocol (Promega, 2002).

Table E3b. Cell count data for UD/UT, UD/PT60, D/UT, and D/PT60 samples.

	Day 1			Day 4			Day 7		
	1	**2**	**3**	**1**	**2**	**3**	**1**	**2**	**3**
Control	468	402	340	2076	2396	2360	3716	3168	3281
UD/UT	365	440	274	1640	1972	1956	3579	4831	4222
D/UT	321	358	269	991	1461	1736	4087	4066	3268
Control	446	502	568	587	1370	661	2249	3375	1692
UD/PT60	143	175	113	897	400	778	1261	2646	1803
D/PT60	172	311	310	434	574	384	2198	1396	1541

Appendix E4 – Additional statistic results for cell viability assay

Table E4a. Additional statistic results from one-way ANOVA on cell viability of UT samples.

Day 1	SS	df	MS	F	P-value	F crit
Between Groups	1.15E+04	2	5.75E+03	1.33	0.33	5.14
Within Groups	2.59E+04	6	4.32E+03			
Day 4	**SS**	**df**	**MS**	**F**	**P-value**	**F crit**
Between Groups	1.16E+06	2	5.82E+05	8.40	0.02	5.14
Within Groups	4.16E+05	6	6.93E+04			
Day 7	**SS**	**df**	**MS**	**F**	**P-value**	**F crit**
Between Groups	1.01E+06	2	5.07E+05	2.19	0.19	5.14
Within Groups	1.39E+06	6	2.31E+05			

Table E4b. Additional statistic results from Tukey-Kramer post-hoc analysis on cell viability of UT samples.

	Var1	Var2	Diff.	SE	Q	*p*
Day 1	Control	UD/UT	4.38E+01	3.79E+01	1.16	7.07E-01
	Control	D/UT	8.76E+01	3.79E+01	2.31	3.04E-01
	UD/UT	D/UT	4.37E+01	3.79E+01	1.15	7.08E-01
Day 4	Control	UD/UT	4.21E+02	1.52E+02	2.77	2.04E-01
	Control	D/UT	8.81E+02	1.52E+02	5.79	1.50E-02
	UD/UT	D/UT	4.60E+02	1.52E+02	3.03	1.61E-01
Day 7	Control	UD/UT	8.23E+02	2.78E+02	2.96	1.71E-01
	Control	D/UT	4.19E+02	2.78E+02	1.51	5.66E-01
	UD/UT	D/UT	4.04E+02	2.78E+02	1.45	5.88E-01

Continued on the next page…

Table E4c. Additional statistic results from one-way ANOVA on cell viability of PT60 samples.

Day 1	SS	df	MS	F	P-value	F crit
Between Groups	2.03E+05	2	1.02E+05	27.71	0.00	5.14
Within Groups	2.20E+04	6	3.67E+03			
Day 4	**SS**	**df**	**MS**	**F**	**P-value**	**F crit**
Between Groups	2.51E+05	2	1.26E+05	1.43	0.31	5.14
Within Groups	5.28E+05	6	8.80E+04			
Day 7	**SS**	**df**	**MS**	**F**	**P-value**	**F crit**
Between Groups	8.52E+05	2	4.26E+05	0.91	0.45	5.14
Within Groups	2.81E+06	6	4.68E+05			

Table E4d. Additional statistic results from Tukey-Kramer post-hoc analysis on cell viability of PT60 samples.

	Var1	Var2	Diff.	SE	Q	*p*
Day 1	Control	UD/PT60	3.62E+02	3.50E+01	10.34	8.20E-04
	Control	D/PT60	2.41E+02	3.50E+01	6.89	6.69E-03
	UD/PT60	D/PT60	1.21E+02	3.50E+01	3.45	1.10E-01
Day 4	Control	UD/PT60	1.81E+02	1.71E+02	1.06	7.46E-01
	Control	D/PT60	4.08E+02	1.71E+02	2.38	2.85E-01
	UD/PT60	D/PT60	2.27E+02	1.71E+02	1.33	6.38E-01
Day 7	Control	UD/PT60	5.36E+02	3.95E+02	1.36	6.27E-01
	Control	D/PT60	7.27E+02	3.95E+02	1.84	4.45E-01
	UD/PT60	D/PT60	1.91E+02	3.95E+02	0.48	9.38E-01

Appendix references

Allen, F. H., Watson, D. G., Brammer, L., Orpen, A. G., and Taylor, R. (1995). International Tables for Crystallography, 2006. *Wilson, AJC, Ed*, 685–760.

Bagus, P. S., Sousa, C., and Illas, F. (2016). Consequences of electron correlation for XPS binding energies: Representative case for C(1s) and O(1s) XPS of CO. *J. Chem. Phys.* 145, 144303. doi:10.1063/1.4964320.

Barca, G. M. J., Bertoni, C., Carrington, L., Datta, D., De Silva, N., Deustua, J. E., et al. (2020). Recent developments in the general atomic and molecular electronic structure system. *J. Chem. Phys.* 152, 154102. doi:10.1063/5.0005188.

Bellafont, N. P., Illas, F., and Bagus, P. S. (2015). Validation of Koopmans' theorem for density functional theory binding energies. *Phys. Chem. Chem. Phys.* 17, 4015–4019. doi:10.1039/c4cp05434b.

Bertóti, I. (2002). Characterization of nitride coatings by XPS. *Surf. Coatings Technol.* 151–152, 194–203. doi:10.1016/S0257-8972(01)01619-X.

Biesinger, M. C. (2017). Chromium Nitride (CrN). Available at: https://www.xpsfitting.com/2017/01/chromium-nitride-crn.html [Accessed January 31, 2021].

Bruggeman, M., Zelzer, M., Dong, H., and Stamboulis, A. (2022). Processing and interpretation of core-electron XPS spectra of complex plasma-treated polyethylene-based surfaces using a theoretical peak model. *Surf. Interface Anal.* 54, 986–1007. doi:10.1002/SIA.7125.

Cavigliasso, G., and Chong, D. P. (1999). Accurate density-functional calculation of core-electron binding energies by a total-energy difference approach. *J. Chem. Phys.* 111, 9485–9492. doi:10.1063/1.480279.

Chong, D. P. (1995). Accurate calculation of core-electron binding energies by the density-functional method. *Chem. Phys. Lett.* 232, 486–490. doi:10.1016/0009-2614(94)01378-9.

Cline, J. P. (2015). NIST: Standard Reference Material 676a. 1–7. Available at: https://www-s.nist.gov/srmors/certificates/676A.pdf.

El-Azazy, M. (2019). Introductory chapter: infrared spectroscopy-A synopsis of the fundamentals and applications. *Infrared Spectrosc. Adv. Appl.* 3.

Endo, K., Shimada, S., Kato, N., and Ida, T. (2016). Analysis of valence XPS and AES of (PP, P4VP, PVME, PPS, PTFE) polymers by DFT calculations using the model molecules. *J. Mol. Struct.* 1122, 341–349. doi:10.1016/j.molstruc.2016.04.087.

Ermrich, M., and Opper, D. (2013). XRD for the analyst. *Get. acquainted with Princ. Second. Panalytical*.

Fawcett, T. G., Crowder, C. E., Brownell, S. J., Zhang, Y., Hubbard, C., Schreiner, W., et al. (1988). Establishing an Instrumental Peak Profile Calibration Standard for Powder Diffraction Analyses: International Round Robin Conducted by the JCPDS-ICDD and the U.S. National Bureau of Standards†. *Powder Diffr.* 3, 209–218. doi:10.1017/S0885715600013506.

Flori, M., Gruzza, B., Bideux, L., Monier, G., Robert-Goumet, C., Cherré, J. P., et al. (2008). XPS, EPMA and microstructural analysis of a defective industrial plasma-nitrided steel. *Surf. Coatings Technol.* 202, 5887–5894. doi:10.1016/j.surfcoat.2008.06.164.

Giesbers, M., Marcelis, A. T. M., and Zuilhof, H. (2013). Simulation of XPS C1s spectra of organic monolayers by quantum chemical methods. *Langmuir* 29, 4782–4788. doi:10.1021/la400445s.

Goldstein, J. I., Newbury, D. E., Michael, J. R., Ritchie, N. W. M., Scott, J. H. J., and Joy, D. C. (2017). *Scanning electron microscopy and X-ray microanalysis*. Springer.

Graves, P., and Gardiner, D. (1989). Practical raman spectroscopy. *Springer* 10, 973–978.

Greczynski, G., and Hultman, L. (2020). Compromising Science by Ignorant Instrument Calibration—Need to Revisit Half a Century of Published XPS Data. *Angew. Chemie - Int. Ed.* 59, 5002–5006. doi:10.1002/anie.201916000.

Griffiths, D. J. (2004). Introduction to Quantum Mechanics, 2nd udg.

Griffiths, P. R. (1983). Fourier transform infrared spectrometry. *Science (80-.).* 222, 297–302.

Hammes, G. G. (2005). *Spectroscopy for the biological sciences*. John Wiley \& Sons.

Hantsche, H. (1993). High resolution XPS of organic polymers. The scienta database. *Anal. Chim. Acta* 276, 469–470. doi:10.1016/0003-2670(93)80419-l.

Hariharan, P., and Braun, C. (1992). Basics of Interferometry. *Appl. Opt.* 31, 6583.

Harris, D. C., and Bertolucci, M. D. (1989). *Symmetry and spectroscopy: an introduction to vibrational and electronic spectroscopy*. Courier Corporation.

Hattori, T., Iimori, T., Miyamachi, T., and Komori, F. (2018). Lattice distortion of square iron nitride monolayers induced by changing symmetry of substrate. *Phys. Rev. Mater.* 2, 44003. doi:10.1103/PhysRevMaterials.2.044003.

Henke, B. L., Gullikson, E. M., and Davis, J. C. (1993). X-ray interactions: Photoabsorption, scattering, transmission, and reflection at E = 50-30, 000 eV, Z = 1-92. *At. Data Nucl. Data Tables* 54, 181–342. doi:10.1006/adnd.1993.1013.

Herres, W., and Gronholz, J. (1984). Understanding FT-IR data processing. *Part* 1, 352–356.

Holland, T. J. B., and Redfern, S. A. T. (1997). Unit cell refinement from powder diffraction data: the use of regression diagnostics. *Mineral. Mag.* 61, 65–77. doi:10.1180/minmag.1997.061.404.07.

Kelly, A., and Knowles, K. M. (2012). *Crystallography and Crystal Defects: Second Edition*. John Wiley \& Sons doi:10.1002/9781119961468.

Komornicki, A., and McIver, J. W. (1979). An efficient ab initio method for computing infrared and Raman intensities: Application to ethylene. *J. Chem. Phys.* 70, 2014–2016. doi:10.1063/1.437627.

Koopmans, T. (1933). Ordering of wave functions and eigenenergies to the individual electrons of an atom. *Physica* 1, 104–113.

Kröner, D., Ehlert, C., Saalfrank, P., and Holländer, A. (2011). Ab initio calculations for XPS chemical shifts of poly(vinyl- trifluoroacetate) using trimer models. *Surf. Sci.* 605,

1516–1524. doi:10.1016/j.susc.2011.05.021.

Lorenzo, V., Pereña, J. M., and Fatou, J. M. G. (1989). Relationships between mechanical properties and microhardness of polyethylenes. *Die Angew. Makromol. Chemie* 172, 25–35. doi:10.1002/apmc.1989.051720103.

McCreery, R. L. (2001). Raman spectroscopy for chemical analysis. *Meas. Sci. Technol.* 12, 653.

Meskinis, S., Andrulevicius, M., Kopustinskas, V., and Tamulevicius, S. (2005). XPS study of the ultrathin a-C:H films deposited onto ion beam nitrided AISI 316 steel. *Appl. Surf. Sci.* 249, 295–302. doi:10.1016/j.apsusc.2004.12.007.

Mills, I. M., and Robiette, A. G. (1985). On the relationship of normal modes to local modes in molecular vibrations. *Mol. Phys.* 56, 743–765.

NIST (2008). NIST Standard Reference Database, National Institute of Standards and Technology. *NIST X-ray Photoelectron Spectrosc. Database*, [27/05/2018].

Peters, R. F. (2014). Fabrication and testing of surface-enhanced Raman spectroscopy substrates for the detection of biomolecules.

Promega (2002). CellTiter-Glo ® Luminescent Cell Viability Assay Cell Viability Assay. 8–10. Available at: https://www.promega.co.uk/-/media/files/resources/protocols/technical-bulletins/0/celltiter-glo-luminescent-cell-viability-assay-protocol.pdf?rev=0d95c232094b41daa06d0c110d1d916f&sc_lang=en.

Schwerdtfeger, P. (2011). The pseudopotential approximation in electronic structure theory. *ChemPhysChem* 12, 3143–3155. doi:10.1002/cphc.201100387.

Sherrill, C. D., and Schaefer, H. F. (1999). “The Configuration Interaction Method: Advances in Highly Correlated Approaches,” in *Advances in Quantum Chemistry* (Academic Press Inc.), 143–269. doi:10.1016/S0065-3276(08)60532-8.

Siegbahn, K. (1982). Electron spectroscopy for atoms, molecules, and condensed matter. *Rev. Mod. Phys.* 54, 709.

Steele, D. (2006). Infrared spectroscopy: theory. *Handb. Vib. Spectrosc.*

Tardio, S., and Cumpson, P. J. (2018). Practical estimation of XPS binding energies using widely available quantum chemistry software. *Surf. Interface Anal.* 50, 5–12. doi:10.1002/sia.6319.

Triguero, L., Plashkevych, O., Pettersson, L. G. M., and Ågren, H. (1999). Separate state vs. transition state Kohn-Sham calculations of X-ray photoelectron binding energies and chemical shifts. *J. Electron Spectros. Relat. Phenomena* 104, 195–207. doi:10.1016/s0368-2048(99)00008-0.

Turner, D. W., and Jobory, M. I. Al (1962). Determination of ionization potentials by photoelectron energy measurement. *J. Chem. Phys.* 37, 3007–3008.

Viñes, F., Sousa, C., and Illas, F. (2018). On the prediction of core level binding energies in molecules, surfaces and solids. *Phys. Chem. Chem. Phys.* 20, 8403–8410. doi:10.1039/c7cp08503f.

Waasmaier, D., and Kirfel, A. (1995). Data activities in crystallography, factor function for free atoms and ions. *Acta Cryst. A* 51, 416–431.

Warren, B. E. (1990). *X-ray Diffraction*. Courier Corporation.

Watts, J. F. (1998). *Surface analysis of polymers by XPS and static SIMS*. Cambridge University Press doi:10.1179/sur.1998.14.4.290.

Zamfirova, G., Lorenzo, V., Benavente, R., and Pereña, J. M. (2003). On the relationship between modulus of elasticity and microhardness. *J. Appl. Polym. Sci.* 88, 1794–1798. doi:10.1002/app.11788.